



ADVANCES IN QUATUM CHEMISTRY

Volume 27

Per-Olov Löwdin

ADVANCES IN
QUANTUM CHEMISTRY

VOLUME 27

EDITORIAL BOARD

Jiri Cizek (Waterloo, Canada)
David P. Craig (Canberra, Australia)
Raymond Daudel (Paris, France)
Ernst R. Davidson (Bloomington, Indiana)
Inga Fischer-Hjalmars (Stockholm, Sweden)
Kenichi Fukui (Kyoto, Japan)
George G. Hall (Kyoto, Japan)
Frederick A. Matsen (Austin, Texas)
Roy McWeeney (Pisa, Italy)
Joseph Paldus (Waterloo, Canada)
Ruben Pauncz (Haifa, Israel)
Siegfried Peyerimhoff (Bonn, Germany)
John A. Pople (Pittsburgh, Pennsylvania)
Alberte Pullman (Paris, France)
Klaus Ruedenberg (Ames, Iowa)
Henry F. Schaefer III (Athens, Georgia)
Au-Chin Tang (Kirin, Changchun, China)
Rudolf Zahradnik (Prague, Czech Republic)

ADVISORY EDITORIAL BOARD

David M. Bishop (Ottawa, Canada)
Jean-Louis Calais (Uppsala, Sweden)
Giuseppe del Re (Naples, Italy)
Fritz Grein (Fredericton, Canada)
Mu Shik Jhon (Seoul, Korea)
Mel Levy (New Orleans, Louisiana)
Jan Linderberg (Aarhus, Denmark)
William H. Miller (Berkeley, California)
Keiji Morokuma (Okazaki, Japan)
Jens Oddershede (Odense, Denmark)
Pekka Pyykkö (Helsinki, Finland)
Leo Radom (Canberra, Australia)
Mark Ratner (Evanston, Illinois)
Dennis R. Salahub (Montreal, Canada)
Isaiah Shavitt (Columbus, Ohio)
Per Siegbahn (Stockholm, Sweden)
Harel Weinstein (New York, New York)
Robert E. Wyatt (Austin, Texas)
Tokio Yamabe (Kyoto, Japan)

ADVANCES IN QUANTUM CHEMISTRY

EDITOR-IN-CHIEF

PER-OLOV LÖWDIN

PROFESSOR EMERITUS

QUANTUM CHEMISTRY GROUP

UPPSALA UNIVERSITY

UPPSALA, SWEDEN

AND

QUANTUM THEORY PROJECT

UNIVERSITY OF FLORIDA

GAINESVILLE, FLORIDA

EDITORS

JOHN R. SABIN AND MICHAEL C. ZERNER

QUANTUM THEORY PROJECT

UNIVERSITY OF FLORIDA

GAINESVILLE, FLORIDA

VOLUME 27



ACADEMIC PRESS

San Diego

London

Boston

New York

Sydney

Tokyo

Toronto

Academic Press Rapid Manuscript Reproduction

This book is printed on acid-free paper. (∞)

Copyright © 1996 by ACADEMIC PRESS

All Rights Reserved.

No part of this publication may be reproduced or transmitted in any form or by any means, electronic or mechanical, including photocopy, recording, or any information storage and retrieval system, without permission in writing from the publisher.

Academic Press, Inc.

525 B Street, Suite 1900, San Diego, California 92101-4495, USA

<http://www.apnet.com>

Academic Press Limited

24-28 Oval Road, London NW1 7DX, UK

<http://www.hbuk.co.uk/ap/>

International Standard Serial Number: 0065-3276

International Standard Book Number: 0-12-034827-6

PRINTED IN THE UNITED STATES OF AMERICA

96 97 98 99 00 01 QW 9 8 7 6 5 4 3 2 1

Contents

<i>Contributors</i>	ix
<i>Preface</i>	xi

Freeon Dynamics: A Novel Theory of Atoms and Molecules

F. A. Matsen

1. Introduction	4
2. The Spin Paradigm	9
3. The Polyenes	10
4. The Heisenberg Exchange Hamiltonian	25
5. Mean-Field Theories of the Second-Order, Phase-Change	30
6. The Freeon Theory of Ferromagnetism	32
7. Superconductivity and Mean-Field Theory	35
8. The Ising, Small-Bipolaron Theory of Cuprate Superconductivity	39
9. Critique of the Freeon Theory of Ferromagnetism	53
10. Atomic Structure	54
11. Nuclear Structure	60
12. Summary and Conclusions	67
13. Dedication and Acknowledgments	69
References	70

Response Theory and Calculations of Spin-Orbit Coupling Phenomena in Molecules

Hans Ågren, Olav Vahtras, Boris Minaev

1. Abstract	71
2. Introduction	74
3. Theory	76
4. Computation of Spin-Orbit Response Functions	86
5. Miscellaneous Applications	91
6. Selected Singlet-Triplet Transitions	104
7. Phosphorescence of Aromatic Compounds	129
8. The External Heavy Atom Effect on S-T Transitions	148
9. Outlook	153
References	155

Functional Groups in Quantum Chemistry

Paul G. Mezey

1. Introduction	165
2. Molecular Fragments, Chemical Functional Groups	167
3. The Density Domain Approach to Functional Groups and Local Molecular Properties	178
4. An Application of the MEDLA Method for the Direct Computation of Electron Densities of Functional Groups	192
5. Local Shape Analysis of Functional Groups	206
6. Shape Similarity and Shape Complementarity Measures of Functional Groups in Different Molecular Environments	210
7. Energy Relations for Functional Groups and Their Interactions	214
8. Summary	216
9. Acknowledgments	217
10. References	217

Characterization of Shape and Auger Resonances Using The Dilated One Electron Propagator Method

Manoj K. Mishra, Milan N. Medikeri

1. Introduction	225
2. The General Theoretical Framework	227
3. Shape Resonances in Atom and Molecule Scattering	243
4. The Auger Resonances	260
5. The Orbital Picture of Resonances from Different Decouplings of the Dilated Electron Propagator	266
6. Conclusions and Future Directions	286
Acknowledgments	288
References	289

Recent Developments in Configuration Interaction and Density Functional Theory Calculations of Radical Hyperfine Structure

Bernd Engels, Leif A. Eriksson, Sten Lunell

1. Introduction	298
2. Configuration Interaction Methods	300
3. Density Functional Methods	333
4. Concluding Remarks	358
Acknowledgments	359
References	360

Some Properties of Linear Functionals and Adjoint Operators

Per-Olov Löwdin

Introduction	372
1. Some Properties of Linear Functionals	372
2. Mappings of the Dual Space A^d on the Original Space A	379
3. Mapping of the Dual Space A^d on Another Linear Space	389
4. Mapping of a Space $A = \{x\}$ on Another Space $B = \{y\}$	393
References	397
<i>Index</i>	399

It has come to our attention that substantial portions of the paper

Yi Lao, Hans Ågren, Poul Jorgensen, and Kurt V. Mikkelsen (1995). Response theory and calculations of molecular hyperpolarizabilities. *Adv. Quantum Chem.* **26**, 168–237.

were taken nearly unaltered from

Henne Hettema, Hans Jorgen Aa. Jensen, Poul Jorgensen, and Jeppe Olsen (1992). Quadratic response functions for a multi-configurational self-consistent-field wave-function. *J. Chem. Phys.* **97**, 1174–1190.

and republished without proper copyright permission. The Editors regret this breach of courtesy and offer their sincere apologies to the authors of the *Journal of Chemical Physics* paper and to the American Institute of Physics for any resulting inconvenience or embarrassment.

The Editors

Contributors

Numbers in parentheses indicate the pages on which the authors' contributions begin.

Hans Ågren (71), Institute of Physics and Measurement Technology, Linköping University, S-58183 Linköping, Sweden

Bernd Engels (297), Department of Physical and Theoretical Chemistry, University of Bonn, D-53115 Bonn, Germany

Leif A. Eriksson (297), Department of Physics, University of Stockholm, S-113 85 Stockholm, Sweden

Per-Olov Löwdin (371), Quantum Chemistry Group, Uppsala University, S-752 36 Uppsala, Sweden, and Quantum Theory Project, University of Florida, Gainesville, Florida 32611

Sten Lunell (297), Department of Quantum Chemistry, Uppsala University, S-751 20 Uppsala, Sweden

F. A. Matsen (1), Departments of Chemistry and Physics, The University of Texas, Austin, Texas 78712

Milan N. Medikeri (223), Department of Chemistry, Indian Institute of Technology, Powai, Bombay 400 076, India

Paul G. Mezey (163), Department of Chemistry and Department of Mathematics and Statistics, University of Saskatchewan, Saskatoon S7N 5C9, Canada

Boris Minaev (71), Institute of Physics and Measurement Technology, Linköping University, S-58183 Linköping, Sweden

Manoj K. Mishra (223), Department of Chemistry, Indian Institute of Technology, Powai, Bombay 400 076, India

Olav Vahtras (71), Institute of Physics and Measurement Technology, Linköping University, S-58183 Linköping, Sweden

This Page Intentionally Left Blank

Preface

In investigating the highly different phenomena in nature, scientists have always tried to find some fundamental principles that can explain the variety from a basic unity. Today they have shown not only that all the various kinds of matter are built up from a rather limited number of atoms but also that these atoms are composed of a few basic elements or building blocks. It seems possible to understand the innermost structure of matter and its behavior in terms of a few elementary particles: electrons, protons, neutrons, photons, etc., and their interactions. Since these particles obey not the laws of classical physics but the rules of modern quantum theory of wave mechanics established in 1925, there has developed a new field of "quantum science" which deals with the explanation of nature on this basis.

Quantum chemistry deals particularly with the electronic structure of atoms, molecules, and crystalline matter, and describes it in terms of electronic wave patterns. It uses physical and chemical insight, sophisticated mathematics, and high-speed computers to solve the wave equations and achieve its results. Its goals are great, and today the new field can boast of both its conceptual framework and its numerical accomplishments. It provides a unification of the natural sciences that was previously inconceivable, and the modern development of cellular biology shows that the life sciences are now, in turn, using the same basis. "Quantum Biology" is a new field which describes the life processes and the functioning of the cell on a molecular level and a submolecular level.

Quantum chemistry is hence a rapidly developing field which falls between the historically established areas of mathematics, physics, chemistry, and biology. As a result there is a wide diversity of backgrounds among those interested in quantum chemistry. Since the results of the research are reported in periodicals of many different types, it has become increasingly difficult for both the expert and the nonexpert to follow the rapid development in this new multidisciplinary area.

The purpose of this serial publication is to present a survey of the current development of quantum chemistry as it is seen by a number of internationally leading research workers in various countries. The authors have been invited to give their personal points of view of the subject freely and without severe space limitations. No attempts have been made to avoid overlap—on the contrary, it seems desirable to have certain important research areas reviewed from different points of view.

The response from the authors and the referees has been so encouraging that a series of new volumes is being prepared. However, in order to control pro-

duction costs and speed publication time, a new format involving camera-ready manuscripts was initiated with Volume 20. A special announcement about the new format was enclosed in that volume (page xiii).

In the volumes to come, special attention will be devoted to the following subjects: the quantum theory of closed states, particularly the electronic structure of atoms, molecules, and crystals; the quantum theory of scattering states, dealing also with the theory of chemical reactions; the quantum theory of time-dependent phenomena, including the problem of electron transfer and radiation theory; molecular dynamics; statistical mechanics and general quantum statistics; condensed matter theory in general; quantum biochemistry and quantum pharmacology; the theory of numerical analysis and computational techniques.

As to the content of Volume 27, the Editors thank the authors for their contributions, which provide an interesting picture of part of the current development of quantum chemistry. The topics range from freeon dynamics of atoms and molecules, over response theory and calculations of spin-orbit coupling phenomena in molecules, functional groups in quantum chemistry, and characterization of shape and Auger resonances by means of dilated one-electron propagators, to investigations of radical hyperfine structure by means of configuration interaction and density functional methods and a study of certain properties of linear functionals and adjoint operators.

In contrast to the regular review volumes with a rather eclectic content, the Editors tried instead in Volume 21 to focus interest on a single topic, in that case, on "The Density-Functional Theory of Many-Fermion Systems." Since this experiment turned out very well, the Editors are now planning—in addition to the regular review volumes—a few more "thematic volumes" with contributions concentrating specifically on recent advances, and with specialists in the field as Guest Editors.

PER-OLOV LÖWDIN

FREEON DYNAMICS: A NOVEL THEORY OF ATOMS AND MOLECULES

F. A. Matsen

Departments of Chemistry and Physics
The University of Texas, Austin TX 78712-1167

1. INTRODUCTION
2. THE SPIN PARADIGM
3. THE POLYENES
 - 3.1. Introduction
 - 3.2. The Electronic Structure and the Spectra of Polyenes
 - 3.3. The Hückel-Hubbard Hamiltonian
 - 3.4. The π Theory of Ethylene
 - 3.5. The Allyl Radical and Larger Polyenes
4. THE HEISENBERG EXCHANGE HAMILTONIAN
 - 4.1. Introduction
 - 4.2. The Heisenberg Exchange Hamiltonian
 - 4.3. Freeon Waves
5. MEAN-FIELD THEORIES OF THE SECOND-ORDER, PHASE-CHANGE
6. THE FREEON THEORY OF FERROMAGNETISM
 - 6.1. Introduction
 - 6.2. The Uniform-Interaction Model
7. SUPERCONDUCTIVITY AND MEAN-FIELD THEORY
 - 7.1. Introduction
 - 7.2. Perfect Conductivity
 - 7.3. The Meissner Effect
8. THE ISING, SMALL-BIPOLARON THEORY OF CUPRATE SUPERCONDUCTIVITY
 - 8.1. Introduction
 - 8.2. The Properties of the Cuprate Superconductors.
 - 8.3. The NUHH Hamiltonian and its Spectrum
 - 8.4. The Ising, Small-Bipolaron Model of Mean-Field Theory
 - 8.5. The Chemical Structure of Bipolarons and Holes
 - 8.6. Doping and the Lattice Parameter

9. CRITIQUE OF THE FREEON THEORY OF FERROMAGNETISM

10. ATOMIC STRUCTURE

- 10.1. Introduction
- 10.2. The Periodic Table
- 10.3. Crystal Field States
- 10.4. Symmetry-Quantization
- 10.5. The Group-Theoretical Analysis of p^N Spectra
- 10.6. The Group Theoretical Analysis of d^N Spectra

11. NUCLEAR STRUCTURE

- 11.1. Introduction
- 11.2. The $(1s)^A$ Gel'fand Diagrams
- 11.3. The Isospin Paradigm
- 11.4. The $(j)^A$ Configurations
- 11.5. The Quark Structure of Baryons
- 11.6. Nuclear Freeon Dynamics

12. SUMMARY AND CONCLUSIONS

13. DEDICATION AND ACKNOWLEDGMENTS

1. INTRODUCTION

In the first volume of *Advances in Quantum Chemistry* [1] I published an article called *Spin-Free Quantum Chemistry*. Since then I have broadened this concept considerably and have changed the name of the subject to "freeon dynamics". The word "freeon" means "free-of-spin" and not the common refrigerant. Freeon dynamics is a viable alternative (for light atoms and for molecules with light atoms) to the more-conventional fermion dynamics. The *raison d'être* for freeon dynamics is that it is conceptually and computationally simpler than fermion dynamics and so is consistent with Ockham's razor:

"A satisfactory proposition should contain no **unnecessary** complications."

William of Ockham, 14th century

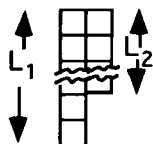
Al Sherman, who introduced me to quantum mechanics while I was an undergraduate at the University of Wisconsin, was co-author with Van Vleck of a classic paper on quantum chemistry which contained the following significant statement:

"Actually, **the only forces between spin are magnetic forces which are exceedingly small** and the only reason that spin figures in the answer is that the constraints imposed by the Pauli principle correlate different spin alignments with different electrostatic exchange energies. Thus **spin is only an indicator...**", J. H. Van Vleck and A. Sherman, *Rev. Mod. Phys.* **7**, 167 (1935).

Central to freeon dynamics is the indistinguishability of electrons; this property is a symmetry which is expressed in terms of the symmetric group, S_N , the group of permutations on the indices of the N identical electrons. The irreducible-representation-spaces (IRS) of S_N are uniquely labeled by Young diagrams denoted $YD[\lambda]$ where $[\lambda]$ is a partition of N and where $YD[\lambda]$ is an array of N boxes in columns of nondecreasing lengths. The Hamiltonian for a system of N identical particles commutes with the elements of S_N . By the

Wigner-Eckart theorem the Hamiltonian-state-spaces (HSS) are uniquely labeled by Young diagrams.

In 1926 (*Zeitschr f, Phys.*, **40**, 492) Eugene Wigner, who taught me group theory at Princeton, wrote the first paper on freeon dynamics. He used the Frobenius algebra of S_N as described in my first article in the *Advances*. To satisfy the fermion antisymmetry principle he required the IRS of the spin and the freeon spaces be conjugate to each other. Since there are two, and only two spin orbitals, the spin IRS are labeled by Young diagrams with no more than two rows. The conjugate freeon IRS are then labeled by Young diagrams with no more than two columns of lengths, $L_1 \geq L_2 \geq 0$.



(1.1)

The number of electrons is then

$$L_1 + L_2 = N \quad (1.2)$$

Because of the conjugacy of the spin IRS to the freeon IRS the Pauli Principle spin can be used as a label of the freeon IRS as follows:

$$S(\text{spin}) = (L_1 - L_2)/2 \quad (1.3)$$

Freeon Young diagrams, $YD[\lambda]$ with no more than two columns are graphical realizations of partitions of the form,

$$[\lambda] = [2p, 1^{N-2p}] \quad (1.4)$$

where $0 \leq p \leq N/2$ is the "freeon quantum number"; it is related to the spin quantum number by

$$S = N/2 - p \quad (1.5)$$

The use of spin to label the freeon spaces, which carry the dynamics of the system, has confused those chemists who are locked into the spin paradigm.

In 1929 (*Phys. Rev.*, **34**, 1203) John Slater published his famous (non-group-theoretical) determinantal method for constructing antisymmetric fermion functions. In 1927 (*Proc. Roy. Soc.*, **114A** 243) Paul Dirac introduced the

second-quantized procedure into field theory in which N is allowed to vary. The second-quantized algebra proved to be both convenient and glamorous for chemists who used it in the construction of antisymmetric functions for fixed N . In 1930 Herman Weyl responded to these two developments as follows.

"It is rumored that the **group pest** is gradually being cut out of quantum physics and as far as the permutation group is concerned it does indeed seem possible to avoid it with the aid of the Pauli exclusion principle. Nevertheless, the theory must retain the representations (the IRS) of the **permutation group** as a natural tool to obtain an understanding of the relationships due to the introduction of spin so long as its specific dynamic effect is neglected." (H. Weyl, *Theory of Groups and Quantum Mechanics* (1930))

From all this one must conclude that the determinantal and second-quantized formulations should be regarded as a poor man's group theory which, while convenient, hides the basic freeon dynamics. These fermion methods have the additional disadvantage that their antisymmetric fermion functions are not normally pure spin (freeon) states so that spin-projection may be required. A method for avoiding (approximately) spin projection is the employment of the variation principle to approximate the ground state; e. g., unrestricted Hartree-Fock theory. Finally the use of the fermion formulations has lead to the spin paradigm as a replacement for the more fundamental freeon dynamics.

These facts appear to be unknown to most chemists even after thirty years. During this period I have presented freeon dynamics, on separate occasions, to Nobel-Laureate Robert Mulliken and to my research professor, Henry Eyring, after which I was asked by each whether "they had to learn that stuff?". I was able to assure them that their reputations would not suffer through the neglect of freeon dynamics. Even now after thirty years freeon dynamics does not appear in the standard quantum chemistry texts with the noteworthy exception of Roy McWeeny's *Methods of Molecular Quantum Mechanics* [2] Consequently the title of this article has been taken to be *Freeon Dynamics. A Novel Theory of Atoms and Molecules*. When, at the onset of my research on freeon dynamics, I told Norman Hackerman, a former office-mate and at that time president of the University of Texas, that I had an idea for a novel way to do quantum mechanics but that I did not know whether I would be able to acquire the necessary

mathematical skills, he replied characteristically: "Why do you think we pay you fat-cat professors good salaries? We expect you to take chances and if no papers on your novel theory appear in your vita, I will personally see that you do not get a pay raise". While this was a joke, it was a very encouraging one. In contrast, I could not get NSF support (i. e., freeon dynamics is not relevant to chemistry). Fortunately, the Welch Foundation has come through every year for the past thirty years.

In the eleventh volume of *Advances* [3] I showed that an equivalent, but more elegant, formulation of freeon dynamics can be based on the unitary group, $U(M)$ where M is the number of freeon orbitals. The following question was put to me a reviewer: Since unitary group theory has been formulated in terms of the second quantized operators (principally by my good friends, Marcos Moshinsky and Larry Biedenharn) should second quantization be called a poor man's group theory? But of course it should because the second-quantized operators act only as the scaffold of a house which is torn down after the house is completed. It is comforting to know that Larry agrees with my assessment.

The IRS of $U(M)$ are also labeled by Young diagrams so that much of the S_N formulation can be carried over directly. An added feature of the $U(M)$ formulation is that the IRS are spanned by orthonormal Gel'fand states, named after I. M. Gel'fand (1920 -) the famous Russian mathematician. These states are uniquely labeled by Gel'fand diagrams constructed by adding, to the proper, N -electron Young diagram, N of the M freeon orbitals in nondescending order along rows and ascending order down columns. A corollary to the freeon exclusion principle is that no more than two electrons may be added to the same freeon orbital. A Gel'fand diagram identifies both the spin ($S = (L_1 - L_2)/2$) and the freeon electron configuration. Valence bond states are constructed from atomic-orbital Gel'fand states and their number provides a theoretical basis for Rumer's rule. In my contribution to the festschrift [4] celebrating the fortieth anniversary of the publication of Coulson's *Valence* I applied the Coulson phrase "primitive patterns of understanding" to these ubiquitous Gel'fand diagrams.

The theory of the application of the unitary group to quantum chemistry (together with relevant references) has been developed in Roy Mcweeny's text [2] and in *The Unitary Group in Quantum Chemistry* (1986)[5] written in collaboration with Ruben Pauncz. The freeon unitary-group formulation is the

basis of the Paldus-Shavitt GUGA (graphical-unitary-group approach), an efficient algorithm for large-scale configuration-interaction calculations. The theory and vocabulary of freeon dynamics is quite technical and intimidating particularly to those unfamiliar with group theory. Fortunately its application is actually quite simple as was demonstrated by three articles [6] I wrote in 1985 with Marye Anne Fox for the *Journal of Chemical Education*; she is a member of the National Science Board and has just been appointed Vice President for Research at the University of Texas. This work is discussed in Section 3.

In this, my third contribution, I apply freeon dynamics to problems of interest in chemistry and physics and compare with the results obtained by the spin paradigm. In particular I will apply freeon dynamics to the following "spin phenomena": i) spin exchange, ii) spin superexchange, iii) spin polarization, iii) spin density, iv) high-and low-spin states of the transition-metal ions, v) the periodic table, vi) ferromagnetism, vii) spin waves and viii) high- T_C superconductivity.

An important feature of the unitary group formulation is that $U(M)$ is the head group of a lattice of group chains which have spectral significance for atoms, molecules, solids and nuclei. Of even greater importance is the role that $U(M)$ plays in symmetry-quantization. Quantum mechanics was invented to describe discrete spectra. In wave mechanics quantum numbers are by imposing physical boundary conditions on solutions of the Schrödinger equation. It was later shown that quantum numbers and quantization are the consequence of symmetry. In the $U(M)$ theory the major quantum number is the particle number N . For freeon dynamics the group chain, with N fixed, is

$$U(M) \supset R(3) \supset G(\text{point group}) \quad (1.6)$$

quantum numbers: $N, p(S) \quad L \quad K$

These matters are discussed in detail in Sections 10-13, where they are used in theories of atoms, nuclei and baryons.

2. THE SPIN PARADIGM

The spin paradigm, widely-used by the chemical community, is the replacement of fermion dynamics by spin dynamics in the discussion of spectra, structure and mechanism. The average chemist feels very comfortable with this spin paradigm and resists passionately any attempt to break it. The spin paradigm does have a number attractive features:

- i) The spin arrows provide an extremely elementary "primitive pattern of understanding".
- ii) At this elementary level spin-arrows are often represented by bar magnets. Here bar magnets with the north and south poles opposed attract each other while magnets with north and with south poles opposed repel. This interpretation gives a comforting feeling of objective reality. Unfortunately this model does not make correct prediction in all cases; e. g. Hund's rule.
- iii) At a higher level the spin paradigm is justified by the Heisenberg spin Hamiltonian which is interpreted as a magnetic dipole-dipole interaction between the magnetic moments of the two spins. There are two strong objections to this interpretation:
 - a) The strength of the spin dipole moment is too small to predict the observed interaction.
 - b) The origin of the Heisenberg spin Hamiltonian lies in freeon dynamics.
- iv) At a higher level theoretical chemists avoid freeon dynamics by employing the poor man's group theory; e. g., the Slater-determinantal and second-quantized fermion formulations. These techniques often require spin projection to obtain pure spin states (i.e. freeon states).

Freeon dynamics provides a dynamically-correct replacement for the faulty spin paradigm. In particular its freeon Gel'fand diagrams are a dynamically correct replacement for spin arrows as a "primitive pattern of understanding".

3. THE POLYENES

3.1. Introduction

In this section the simplicity of freeon dynamics is illustrated by its application to polyenes [6]. Here I relate molecular-orbital Gel'fand states to atomic-orbital Gel'fand states and then relate the atomic-orbital Gel'fand states to valence bond states. Note that this construction provides a theoretical basis for the Rumer rule; i.e., for the number of linearly independent valence bond states. We then use this freeon dynamics to explicate the spin paradigm.

3.2. The Electronic Structure and the Spectra of Polyenes

The procedure for the construction of the freeon Gel'fand states of polyenes consists of the following simple steps:

- i) Specify M , the number of carbon atoms in the polyene chain.
- ii) Specify N , the number of electrons
- iii) Specify S , the spin
- iv) Compute the freeon quantum number

$$p = N/2 - S \quad (3.1)$$

- iv) Determine the appropriate Young diagram; i. e., specify $L_1 \geq L_2 \geq 0$ from the following relations:

$$L_1 = \frac{N+2S}{2} \quad (3.2)$$

and

$$L_2 = \frac{N-2S}{2} \quad (3.3)$$

- v) Construct Gel'fand diagrams by adding freeon atomic or freeon molecular orbitals in nondecreasing order along rows and in ascending order down columns.
- vi) Construct valence bond states from linear combinations of atomic-orbital Gel'fand states by requiring that chemically-bonded atoms be invariant under the exchange of the freeon orbitals of the bonded atoms.

3.3. The Hückel-Hubbard Hamiltonian

We have outlined above the procedure for the construction of orthonormal molecular-orbital and atomic-orbital Gel'fand states and for the conversion of the latter to the non-orthogonal valence bond states. We require, in addition, a freeon Hamiltonian to compute the spectra of the several polyene systems. For this we employ the freeon, reduced Hückel-Hubbard Hamiltonian which has the following form:

$$\mathbf{H} = (z-1) \sum_{\langle rs \rangle} (\mathbf{E}_{rs} + \mathbf{E}_{sr}) + z\mathbf{d} \quad (3.4)$$

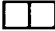

Here $\mathbf{E}_{rs} \equiv \sum_i |r_i\rangle \langle s_i|$ where the freeon orbitals are summed over their electron numbers, \mathbf{d} counts the number of doubly-occupied, freeon atomic orbitals and

$$0 \leq z \equiv \frac{U}{U+t}, \leq 1 \quad (3.5)$$

is the coupling strength. Further t is the one-electron transfer integral (the negative of Hückel β) and U is the repulsive energy of two electron on same carbon atom. At $z = 0$ and at $z = 1$ the molecular-orbital spectrum and the atomic-orbital spectrum occur. For simple systems the polyene spectra can be obtained, without calculation, by linear interpolation between these two limits. As examples I present the π theory of ethylene and the allyl radical.

3.4. The π Theory of Ethylene

3.4.1. The IRS for Two Electrons

$[\lambda]$	$Y[\lambda]$	$S = (L_1 - L_2)/2$	p
[2,0]		0 (singlet)	1
[1,1]		1 (triplet)	0

3.4.2. Freeon Atomic-Orbital Gel'fand States

Atomic orbitals are denoted $|a\rangle$ and $|b\rangle$ and their orbital energies are taken to be zero.

$[\lambda]$	$Y[\lambda]$	p	$V_2[\lambda]$								
$[2,0]$	<table><tr><td></td><td></td></tr></table>			1	<table><tr><td>a</td><td>a</td></tr></table> , <table><tr><td>a</td><td>b</td></tr></table> , <table><tr><td>b</td><td>b</td></tr></table>	a	a	a	b	b	b
a	a										
a	b										
b	b										
$[1,1]$	<table><tr><td></td></tr><tr><td></td></tr></table>			0	<table><tr><td>a</td></tr><tr><td>b</td></tr></table>	a	b				
a											
b											

3.4.3. Freeon Molecular-Orbital Freeon Gel'fand States

The molecular orbitals and their energies are given by

$$|1\rangle = (1/\sqrt{2})(|a\rangle + |b\rangle); \epsilon_1 = -t \quad (3.6)$$

$$|2\rangle = (1/\sqrt{2})(|a\rangle - |b\rangle); \epsilon_2 = +t$$

Then

$[\lambda]$	$Y[\lambda]$	p	$V_2[\lambda]$								
$[2,0]$	<table><tr><td></td><td></td></tr></table>			1	<table><tr><td>1</td><td>1</td></tr></table> , <table><tr><td>1</td><td>2</td></tr></table> , <table><tr><td>2</td><td>2</td></tr></table>	1	1	1	2	2	2
1	1										
1	2										
2	2										
$[1,1]$	<table><tr><td></td></tr><tr><td></td></tr></table>			0	<table><tr><td>1</td></tr><tr><td>2</td></tr></table>	1	2				
1											
2											

3.4.4. The Interpolated Ethylene Spectrum

The calculation of the ethylene spectrum from the Hückel-Hubbard Hamiltonian is a freshman exercise. However a good approximation to the spectrum is obtained by linear interpolation between the MO and AO limits. See Fig. 3.1

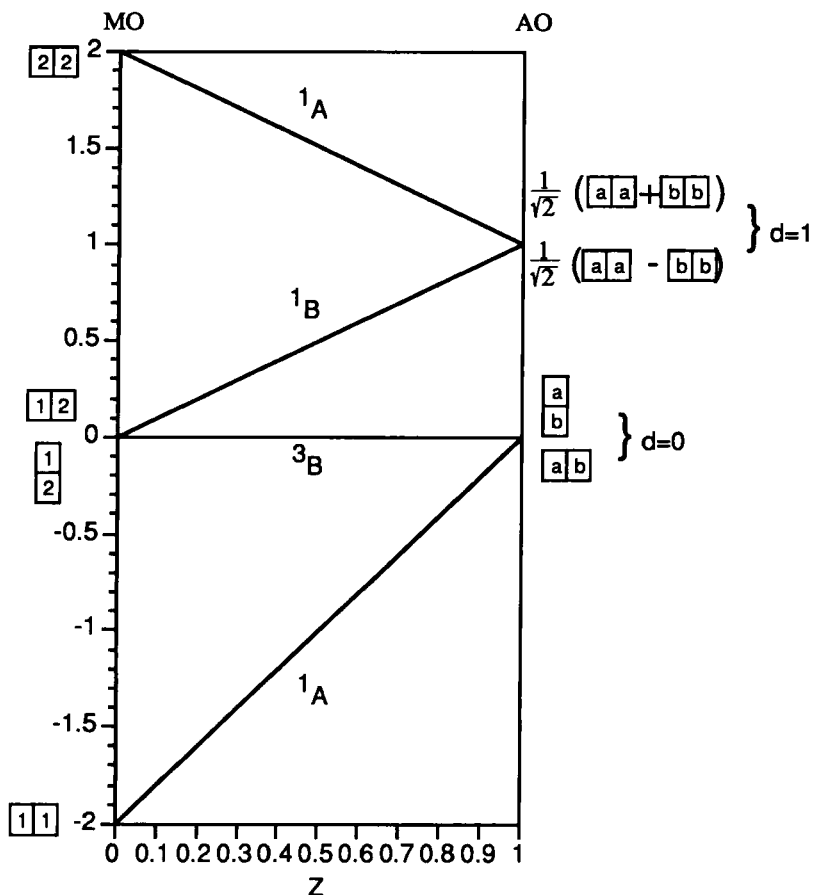


Fig. 3.1. The linear Hückel-Hubbard spectrum of ethylene. The letters constitute a point group classification of states.

The interpolation proceeds as follows:

- (i) Plot the energies for each Gel'fand state at $x=0$ (MO limit) and at $x=1$ (AO limit).
- (ii) Correlate the lowest MO singlet state $[1|1]$ with the lowest AO singlet state $[a|b]$.
- (iii) Correlate the remaining AO triplet state $[a|b]$ with the MO triplet state $[1|2]$.

- (iv) Correlate the remaining MO singlet state $\begin{bmatrix} 1 & 2 \end{bmatrix}$ with one of the two highest singlets $\{\begin{bmatrix} a & a \end{bmatrix}, \begin{bmatrix} b & b \end{bmatrix}\}$, leaving behind one singlet state which is then correlated with the highest MO singlet state $\begin{bmatrix} 2 & 2 \end{bmatrix}$.
- (v) Note that the MO singlet-triplet pair is split; with the MO triplet state $\begin{bmatrix} 1 \\ 2 \end{bmatrix}$ lying lower because it correlates with the lower lying covalent AO state $\begin{bmatrix} a \\ b \end{bmatrix}$, while the MO singlet state $\begin{bmatrix} 1 & 2 \end{bmatrix}$ correlates with one of the higher-lying ionic AO states $\{\begin{bmatrix} a & a \end{bmatrix}, \begin{bmatrix} b & b \end{bmatrix}\}$. This splitting obeys Hund's rule; i. e., states of higher spin lie lower. We see that this splitting, is not as is often claimed, due to the interaction between spins, but is due to the coulomb repulsion between two electrons on one site.
- (vi) Note further that the AO singlet-triplet pair is also split; the AO singlet state $\begin{bmatrix} a & b \end{bmatrix}$ lying lower because it correlates with the ground MO state $\begin{bmatrix} 1 & 1 \end{bmatrix}$, while the AO triplet state $\begin{bmatrix} a \\ b \end{bmatrix}$ (II) correlates with the higher-lying MO triplet state $\begin{bmatrix} 1 \\ 2 \end{bmatrix}$. We see that the stability of the singlet $\begin{bmatrix} a & b \end{bmatrix}$ relative to the triplet $\begin{bmatrix} a \\ b \end{bmatrix}$ is also not due to the interaction between spins, but rather to the correlation of these two states with the ground and the first excited MO states, respectively. This splitting obeys the Heitler-London rule.

The electronic spectra of ethylene is well-fit at $x \approx 0.6$.

3.4.5. The Valence bond Structures of Ethylene

A covalent bond between two atoms is defined as one which is invariant under the exchange of the two orbitals. We can see this most simply by expressing the singlet and triplet Gel'fand states in terms of atomic orbital products:

$$\begin{bmatrix} a & b \end{bmatrix} = (1/\sqrt{2})(|a_1\rangle|b_2\rangle + |b_1\rangle|a_2\rangle) \quad (3.7)$$

and

$$\begin{bmatrix} a \\ b \end{bmatrix} = (1/\sqrt{2})(|a_1\rangle|b_2\rangle - |b_1\rangle|a_2\rangle) \quad (3.8)$$

and

$$\begin{bmatrix} a & a \end{bmatrix} = |a_1\rangle|a_2\rangle \quad (3.9)$$

and

$$\begin{bmatrix} b & b \end{bmatrix} = |b_1\rangle|b_2\rangle. \quad (3.10)$$

Covalent States (d = 0)

i) Singlet State

$$P_{ab} \begin{bmatrix} a & b \end{bmatrix} = +1 \begin{bmatrix} a & b \end{bmatrix} \quad (3.11)$$

The electrons on sites a and b are paired to form a covalent bond;.

$$\begin{bmatrix} a & b \end{bmatrix} \Rightarrow |C=C\rangle \quad (3.12)$$

ii) Triplet State

$$P_{ab} \begin{bmatrix} a & \\ b & \end{bmatrix} = - \begin{bmatrix} a & \\ b & \end{bmatrix} \quad (3.13)$$

$$\begin{bmatrix} a & \\ b & \end{bmatrix} \Rightarrow | \dot{C}-\dot{C} \rangle \quad (3.14)$$

Here the electrons on sites a and b are anti-paired to form the triplet biradical. Note that by the Gel'fand construction a triplet state cannot be formed from a pair of identical freeon, atomic orbitals.

Ionic States (d = 1)

$$\begin{bmatrix} a & a \end{bmatrix} \Rightarrow | \bar{C}-\dot{C}^+ \rangle$$

$$\begin{bmatrix} b & b \end{bmatrix} \Rightarrow | \dot{C}-\bar{C}^+ \rangle$$

The two electrons on the same site are paired

3.4.6. Freeon Heisenberg Antiferromagnetic Exchange Hamiltonian

The application of second-order perturbation theory to the Hückel-Hubbard Hamiltonian for z close to one (Section 4.2) yields the freeon, antiferromagnetic, Heisenberg exchange Hamiltonian,

$$H = JP_{ab} \quad (3.15)$$

where \mathbf{P}_{ab} acts on the freeon Gel'fand states and where

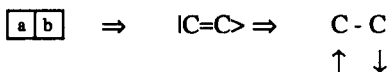
$$J = -2t^2/U \quad (3.16)$$

is the exchange parameter. If t is taken to be inversely proportional to the distance between the paired atoms, the freeon antiferromagnetic Heisenberg Hamiltonian provides a qualitative theory of chemical bonding; i. e., as the paired atoms approach each other the pair becomes more stable relative to dissociation. This supports the association of the covalent state $\begin{bmatrix} a & b \end{bmatrix}$ with the chemical bond, $|C=C\rangle$.

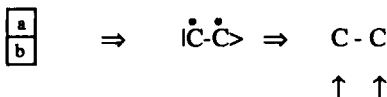
3.4.7. Spin-Arrow Diagrams

The spin paradigm employs spin arrows to indicate electron pairing and antipairing. Here I compare the spin-arrow diagrams for ethylene to their Gel'fand and the valence bond counterparts:

i) The singlet covalent state



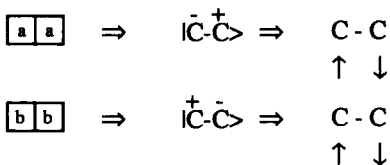
ii) The triplet covalent state



The following spin-paradigmatic statement is often found in the organic literature: "By Hund's rule electrons with parallel spin cannot occupy the same atomic orbital". This is not precise; the statement should be the following: by the

Gel'fand construction a triplet Gel'fand state, $\begin{bmatrix} \\ \end{bmatrix}$, cannot be constructed from two identical freeon atomic orbitals.

Ionic States ($d = 1$)



3.4.8. "Spin Exchange"

The equivalent Heisenberg, antiferromagnetic, spin-exchange Hamiltonian

$$\mathbf{H} = +JS_{\mathbf{a}} \cdot \mathbf{S}_{\mathbf{b}} \quad (3.17)$$

is obtained from the freeon antiferromagnetic Heisenberg Hamiltonian by replacing the permutation by a dot product of spins according to the Dirac identity. Dirac was a great walker and when he visited Austin several of us were assigned to walk with him in relays. While he was a great walker he was not a great talker so that during my watch I had to carry-on the conversation. I talked to him about freeon dynamics and told him that the Dirac identity had misled many chemists and physicists into the spin paradigm. His only comment was, "is that what they call it?". In the spin paradigm, the Heisenberg spin Hamiltonian is interpreted as the magnetic dipole-dipole interaction of the spin magnetic moments on neighboring atoms. This is clearly not a physical interpretation since the spin magnetic moments are not large enough to predict the observed splitting

3.4.9. Hund's Rule and the Heitler-London Rule

The spin paradigm can lead to serious inconsistencies. Consider for example the Hund and the Heitler-London rules discussed in Section 4.2. The spin-arrow description of the states assigns parallel spins to triplet states and antiparallel spins to singlet states as follows:

Hund Rule, $Z \approx 0$

$$E\left(\begin{array}{|c|} \hline 1 \\ \hline 2 \\ \hline \end{array}\right) < E\left(\begin{array}{|c|c|} \hline 1 & 2 \\ \hline \end{array}\right)$$

$\uparrow\uparrow \qquad \uparrow\downarrow$

Heitler-London Rule, $Z \approx 1$

$$E\left(\begin{array}{|c|} \hline a \\ \hline b \\ \hline \end{array}\right) > E\left(\begin{array}{|c|c|} \hline a & b \\ \hline \end{array}\right)$$

$\uparrow\uparrow \qquad \uparrow\downarrow$


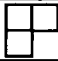

From these spin assignments we conclude the following:

Electrons with parallel spins attract or maybe they repel? Of course electrons always repel!

3.5 The Allyl Radical and Larger Polyenes

3.5.1. The Three-Electron Spaces

For the allyl radical $N = M = 3$. For $N = 3$ there are three IRS one of which is excluded because its Young diagram contains more than two columns.

$[\lambda]$	YD $[\lambda]$	Spin
$[1^3]$		$S = (3-0)/2 = 3/2$, quartet
$[2,1]$		$S = (2-1)/2 = 1/2$, doublet
$[3]$		excluded

3.5.2. The Interpolated Spectrum

Proceeding as for ethylene we arrive at the following interpolated spectrum for the allyl radical shown in Fig. 3.2.

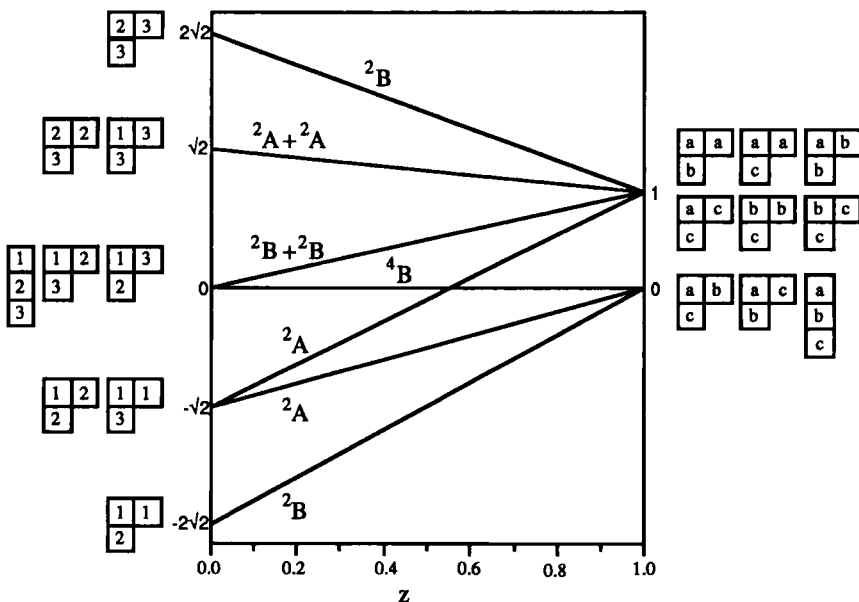
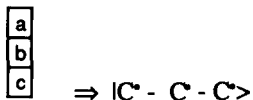


Fig. 3.2. The linear Hückel-Hubbard spectrum of the allyl radical

3.5.3. The Valence Bond Structures of the Allyl Radical

Covalent Structures, $d = 0$

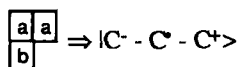
i) The quartet state



A dot denotes an unpaired electron

ii) The doublet space

a) Ionic states. Two electrons assigned to the same freeon orbital product from a unique ionic state; e.g.,

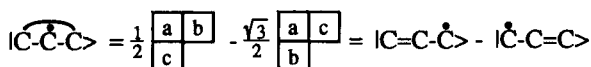
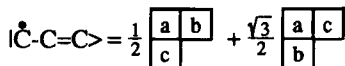
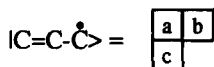


b) Covalent states

The valence bond structures of the doublet allyl radical are more complicated. The transformation properties under orbital permutation of the doublet, covalent Gel'fand states are shown below:

	$\begin{array}{ c c } \hline a & b \\ \hline c & \\ \hline \end{array}$	$\begin{array}{ c c } \hline a & c \\ \hline b & \\ \hline \end{array}$
P_{ab}	$\begin{array}{ c c } \hline a & b \\ \hline c & \\ \hline \end{array}$	$-\begin{array}{ c c } \hline a & c \\ \hline b & \\ \hline \end{array}$
P_{bc}	$-\frac{1}{2}\begin{array}{ c c } \hline a & b \\ \hline c & \\ \hline \end{array} + \frac{\sqrt{3}}{2}\begin{array}{ c c } \hline a & c \\ \hline b & \\ \hline \end{array}$	$\frac{\sqrt{3}}{2}\begin{array}{ c c } \hline a & b \\ \hline c & \\ \hline \end{array} + \frac{1}{2}\begin{array}{ c c } \hline a & c \\ \hline b & \\ \hline \end{array}$
P_{ac}	$-\frac{1}{2}\begin{array}{ c c } \hline a & b \\ \hline c & \\ \hline \end{array} - \frac{\sqrt{3}}{2}\begin{array}{ c c } \hline a & c \\ \hline b & \\ \hline \end{array}$	$-\frac{\sqrt{3}}{2}\begin{array}{ c c } \hline a & b \\ \hline c & \\ \hline \end{array} - \frac{1}{2}\begin{array}{ c c } \hline a & c \\ \hline b & \\ \hline \end{array}$

The valence bond states for the allyl radical are then

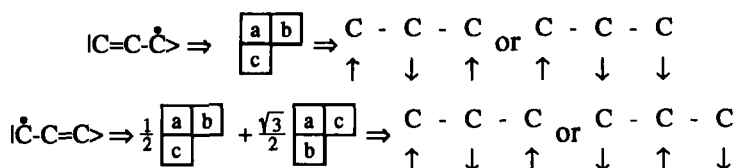


Note that the three valence bond states are linearly dependent. This is a corollary of the Rumer rule. The C_2 symmetry-adapted covalent states are

$$|^2B\rangle = (|C=C-\dot{C}\rangle + |\dot{C}-C=C\rangle)/\sqrt{2} \quad \text{and} \quad |^2A\rangle = |C-\dot{C}-C\rangle$$

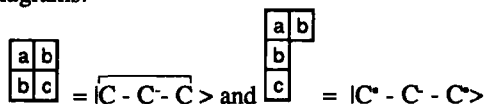
which are antisymmetric and symmetric, respectively, under P_{ac} . These states are good approximations to the two lower energy eigenvectors, for z close to one. The ground state, $|^2B\rangle$, is called a resonating valence bond (RVB) state, a concept which has been used in Anderson's theory of superconductivity.

3.5.4. Spin Arrow Diagrams



3.5.5. Freeon Superexchange

Superexchange is the exchange between a pair of next-nearest neighbors. We illustrate superexchange by the following four-electron, three-atom, singlet and triplet Gel'fand diagrams:



where the singlet state lies lower than the triplet state. In both states the electrons on the central atom (b) are paired while the electrons on the two terminal atoms (a,c) are paired and antipaired respectively. The freeon Heisenberg superexchange Hamiltonian is written

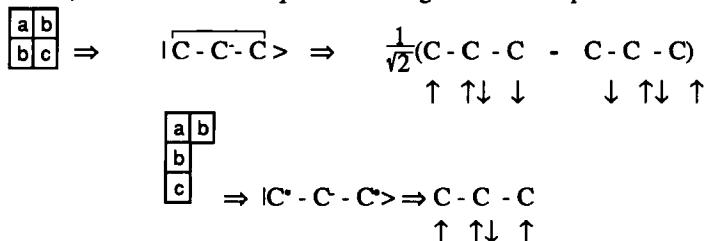
$$H = -JP_{ac} \quad (3.18)$$

3.5.6. "Spin Superexchange"

The spin exchange Hamiltonian is written

$$H = JS_a \cdot S_c \quad (3.19)$$

The Gel'fand, valence bond and spin-arrow diagrams are compared below



But again the magnetic spin dipoles are too weak to produce the observed splitting between the singlet and the triplet states which is, of course, the consequence of freeon dynamics. In public lectures spin superexchange has been illustrated as follows: the lecture's head is taken to be the central atom and the several spin arrangements are represented by the lecturer's arms arranged parallel or antiparallel to each other. While this is vivid and amusing it is dynamically incorrect (the spin magnetic moments are too small to cause the splitting).

3.5.7. "Spin Polarization"

"Spin polarization" has been used in the interpretation of the hyperfine structure of ESR spectra. As described above the strength of the spin-magnetic dipoles is too small to effect such a polarization and is the consequence of freeon dynamics. It requires the interaction of the electronic spin of the π system with the nuclear spin of the hydrogen atom and is based on the mixing of a low-lying excited freeon Gel'fand state with the ground freeon Gel'fand state. The freeon dynamics employs three freeon orbitals, $|h\rangle$ the orbital on the hydrogen atom, $|s\rangle$ and $|p\rangle$ the sigma and π orbitals on the carbon atom. The two lower-lying, doublet, freeon Gel'fand states are

$$|I\rangle = \begin{array}{c} \boxed{h} \boxed{s} \\ \boxed{p} \end{array}$$

and

$$|II> = \begin{array}{|c|c|} \hline h & p \\ \hline s & \\ \hline \end{array}$$

State $|I>$ is the zero order ground state because of the strong sigma bond between $|s>$ and $|h>$. However the $|s>$ orbital cannot couple with the angular momentum of the proton spin. In the excited state $|II>$, $|h>$ is paired with a p orbital which has a nonzero component angular momentum and so can couple to the nuclear spin and produce the hyperfine interaction. Note that the concept of freeon dynamics is an electronic phenomena which does not exclude the magnetic dipole-magnetic dipole interaction between nuclear spin and the electronic orbital angular momentum.

The first order wavefunction is

$$|\Psi> = |I> + \lambda |II> \quad (3.20)$$

The unpaired electron density on the hydrogen atom is $\rho_H \approx \lambda^2$, and the spin density at the hydrogen atom is given

$$S_H \approx \rho_H S_z \quad (3.21)$$

The spin-arrow picture is

$$|I> = \frac{1}{\sqrt{2}} \begin{pmatrix} h & s & p & - & h & s & p \\ \uparrow & \downarrow & \uparrow & & \downarrow & \uparrow & \uparrow \end{pmatrix} \quad (3.22)$$

$$|II> = \frac{1}{\sqrt{6}} \begin{pmatrix} h & s & p & - & h & s & p & - & h & s & p \\ \uparrow & \uparrow & \downarrow & & \uparrow & \downarrow & \uparrow & & \downarrow & \uparrow & \uparrow \end{pmatrix}$$

The spin-dynamic interpretation is that the up spin associated with the p orbital polarizes (unpairs) the paired spins on s and h. This is of course dynamically incorrect because the electron spin magnetic moments are not large enough to produce the observed polarization.

3.5.8. Negative Spin Density

The electron spin resonance of certain paramagnetic compounds e. g., diphenyl picryl hydrosil (DPPH) and the allyl radical are said to exhibit negative spin density. The negative spin density is determined by the freeon unpaired

electron density. The unpaired electron density for the allyl radical is computed for the allyl radical whose ground state is

$$|^2B\rangle = \frac{1}{\sqrt{3}}(|C=C-\dot{C}\rangle + |\dot{C}-C=C\rangle) \quad (3.23)$$

and whose first excited state is

$$|^2A\rangle = |\overset{\curvearrowright}{C-C-C}\rangle \quad (3.24)$$

The unpaired electron density on the center carbon atom in the ground state is given by

$$\begin{aligned} \rho_2 &= \langle ^2B | \rho_2 | ^2B \rangle \\ &= (0 + 0 + 2\langle I | \rho_2 | II \rangle) / 3 \end{aligned} \quad (3.25)$$

where ρ_2 is the unpaired electron density operator on the center carbon atom. Now the unpaired electron density on the center carbon for the $|^2A\rangle$ state is from its valence bond form is equal to one so

$$\begin{aligned} 1 &= \langle ^2A | \rho_2 | ^2A \rangle \\ &= 0 + 0 - 2\langle I | \rho_2 | II \rangle \end{aligned} \quad (3.26)$$

and so

$$\rho_2 = -1/3 \quad (3.27)$$

Further the total unpaired electron density is

$$1 = \rho = \rho_1 + \rho_2 + \rho_3 \quad (3.28)$$

so

$$\rho_1 = \rho_3 = 2/3 \quad (3.29)$$

This gives good agreement with the observed hyperfine ESR spectrum

3.5.9 Benzene

Benzene played an important role in my development of freeon dynamics. I knew, by the Rumer rule, that benzene had five canonical structures (i. e., five linearly independent wave functions). These are the two Kekule structures and the three Dewar structures. From this I surmised that the singlet IRS for $N = M = 6$ should be of five dimensions. On consulting the symmetric group textbooks I

found this to be the case, so I knew then I was on the right track. The number five can be shown most easily by constructing the five Gel'fand states for $M = N = 6$:

a	b
c	d
e	f

II>

a	b
c	e
d	f

III>

a	c
b	d
e	f

III>

a	c
b	e
d	f

IIV>

a	d
b	e
c	f

IV>

Like the allyl radical only the first Gel'fand state, II>, is a pure valence state

3.5.10. Kekule', Sylvester and Young

It is appropriate that since this Section has dealt with organic chemistry we should give credit to Kekule, one of the great organic chemists who, strangely enough, can be regarded as one of founders of the algebra of freeon dynamics. In 1878 James Sylvester, a mathematics professor at John's Hopkins, wrote a paper entitled, *On The Application of the New Atomic Theory to the Graphical Representation of the Invariants and Covariants of Binary Quantics*. He introduced the paper with the following sentence: " By the New Atomic Theory, I mean that sublime invention of Kekule' which stands to the old in a somewhat similar relation as astronomy of Kepler to Ptolemy, or the System of Nature of Darwin to that of Linnaeus - like the latter it lies outside the immediate sphere of energetics basing its laws on pure relations of form and like the former as perfected by Newton, these laws admit an exact arithmetical definition". Initially chemists like Frankland and Mallet (the first dean of the University Texas) expressed considerable interest in the algebraic representation of chemical structure. Fifty years later Texas chemist H.R. Henze [7] extended the Sylvester concept by assigning to valence bond structures mathematical indices. Currently Texas Ph.D. D.J. Klein [8] continues the tradition by basing many-body theory on valence bond structures.

In 1937 Yamanouchi [9] clearly demonstrated the *group pest* had not yet been cut out of physics. Additional demonstration has been provided by Kotani^[10] and associates. The Japanese developments have been summarized by the Russian Kaplan [11]. Paldus and Li have recently used a freeon, valence bond algebra to study excited polyene states [12].

In 1903 Alfred Young (with J. H. Grace) in his famous book, *The Algebras of Invariants* stated "the so-called Chemico-Algebraic theory - an idea originally due to Sylvester which has attracted perhaps more attention than its intrinsic merits deserve". Young clearly did not recognize that his own research was in the genre of Sylvester and would play a leading role in the formulation of freeon dynamics. Incidentally when I studied Young's work I felt as if he had been reading my mail. In 1964 J. S. Griffith agreed with my assessment of Sylvester and stated that "Sylvester had anticipated by fifty years the essential and central role of a certain type of algebra in modern theories of chemical valency. In summary Kekule' on the basis of the nonexistence of two ortho disubstituted isomers of benzene actually defined a two-dimensional vector space and represented benzene as a vector in that space Griffith goes on to state that "In particle theory a certain amount of order is apparent and as yet the significance of much of that order is entirely obscure. As did Sylvester, so today people try to affix algebraic schemes onto physical theory and interpret the order as arising from the structural features of the algebra. In modern theory the algebraic schemes are the Lie algebras of the unitary group which describe electrons, nucleons and quarks. (See Sections 10-13)

4. THE HEISENBERG EXCHANGE HAMILTONIAN

4.1. Introduction

In the previous Sections we have made considerable use of the freeon exchange Hamiltonian. In this Section we give a little history of this concept.

Ferromagnets spontaneously magnetize below some critical temperature. T_C While spins are necessary to detect magnetization, the spin-spin interaction is not strong enough to account for spontaneous magnetization. This became apparent as early as 1907 when Weiss proposed his molecular-field theory of spontaneous magnetization. The assumption that the electron-electron interaction was a magnetic spin-spin interaction led to the prediction of $\approx 0.25K$ for the ferromagnets, two to three orders of magnitude smaller than observed values. Undaunted Weiss commented on this discrepancy as follows:

"I believe, however, that the molecular-field theory is supported by a sufficient number of facts that one can be certain that it contains an important part of the truth and that the difficulty of interpretation should be considered less an objection than a stimulus for research on new hypotheses of atomic structure".

Thirty years later Heisenberg showed that the new hypothesis of atomic structure was the freeon exchange interaction expressed by the freeon Heisenberg Hamiltonian,

$$H = JP_{ab} \quad (4.1)$$

Here $J > 0$ for a ferromagnet and $J < 0$ for antiferromagnet.

In this Section the ferromagnetic and the antiferromagnetic Heisenberg exchange Hamiltonians are derived from the Hückel-Hubbard Hamiltonian in which the value of the coupling constant, z takes on values from -1 to +1. The $M = N = 2$, linear, extended Hückel-Hubbard spectrum is plotted in Fig. 4.1. (Compare with Fig. 3.1)

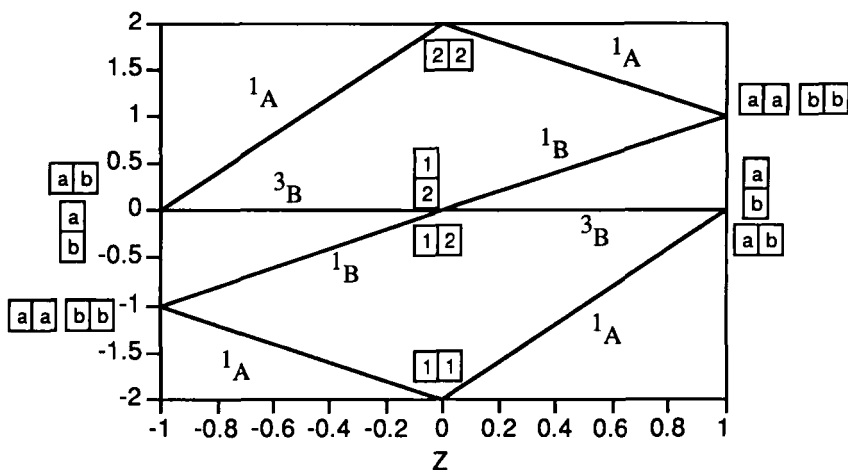


Fig. 4.1. The freeon extended linear Hückel-Hubbard spectrum for $M = N = 2$

The Heisenberg Hamiltonians are derived by the application of second-order perturbation theory to the extended Hückel-Hubbard Hamiltonian at z close to -1 (ferromagnet) and at z close to $+1$ (antiferromagnet) respectively.

In Section 4.4 the freeon ferromagnetic Hamiltonian is used to develop the freeon theory of spin-waves.

4.2. The Heisenberg Exchange Hamiltonian

4.2.1. Second Order Perturbation Theory

The second-order perturbation energy is given by

$$E^{(2)} = \langle P | V R V | P \rangle \quad (4.2)$$

where

$$R = |Q\rangle (H^0 - IE^0)^{-1} \langle Q| \quad (4.3)$$

is called the resolvent. The second-order perturbation energy theory is computed for Hückel-Hubbard Hamiltonian with z close to plus and to minus one. Here the singlet primary state is

$$|P\rangle = |\boxed{a} \boxed{b}\rangle, E^0 = 0 \quad (4.4)$$

the secondary state is

$$|Q\rangle = \frac{1}{\sqrt{2}} (|\boxed{a} \boxed{a}\rangle + |\boxed{b} \boxed{b}\rangle), E^0 = \pm U \quad (4.5)$$

for z close to minus and plus one respectively. (See Fig. 4.1). The perturbation operator is

$$V = -t(E_{ab} + E_{ba}) \quad (4.6)$$

so the singlet, second order energy is

$$\begin{aligned} E^{(2)}(\text{singlet}) &= \langle P | H | P \rangle \\ &= \pm \frac{t^2}{2U} \langle \boxed{a} \boxed{b} | (E_{ab} + E_{ba}) (|\boxed{a} \boxed{a}\rangle + |\boxed{b} \boxed{b}\rangle) (\langle \boxed{a} \boxed{a}| + \langle \boxed{b} \boxed{b}|) (E_{ab} + E_{ba}) |\boxed{a} \boxed{b}\rangle \\ &= \pm \frac{4t^2}{U} \end{aligned} \quad (4.7)$$

The triplet primary state is

$$|P\rangle = \left| \begin{array}{c} a \\ b \end{array} \right\rangle \quad (4.8)$$

so

$$E^{(2)}(\text{triplet}) = 0 \quad (4.9)$$

4.2.2. The Heisenberg Freeon Hamiltonians

The Heisenberg coupling constants are defined by

$$\begin{aligned} 2J &= E^{(2)}(\text{triplet}) - E^{(2)}(\text{singlet}) \\ &= 0 - \left(\pm \frac{2t^2}{U} \right) \text{ (for } z = \pm 1) \end{aligned} \quad (4.10)$$

or

$$J_F = + \frac{2t^2}{U} \text{ (ferromagnetic)} \quad (4.11)$$

and

$$J_A = - \frac{2t^2}{U} \text{ (antiferromagnetic)} \quad (4.12)$$

Since

$$P_{ab} \left| \begin{array}{c} a \\ b \end{array} \right\rangle = +1 \left| \begin{array}{c} a \\ b \end{array} \right\rangle \quad (4.13)$$

and since

$$P_{ab} \left| \begin{array}{c} a \\ b \end{array} \right\rangle = - \left| \begin{array}{c} a \\ b \end{array} \right\rangle \quad (4.14)$$

the freeon Heisenberg (effective) Hamiltonian is

$$H_H = J P_{ab} \quad (4.15)$$

for both the ferromagnetic ($J > 0$) and antiferromagnetic ($J < 0$) interactions.

4.2.3. The Spin Paradigm

The freeon Heisenberg Hamiltonian is converted to the spin Heisenberg Hamiltonian by the Dirac identity,

$$P_{ab} = -\frac{1}{2} (I + 4S_a \cdot S_b) \quad (4.16)$$

which relates a permutation in the freeon space to a spin operator acting on the conjugate spin space. On neglecting the additive constant we have

$$\mathbf{H} = - 2JS_a \cdot \mathbf{S}_b \quad (4.17)$$

4.3. Freeon Waves

4.3.1. Introduction

Freeon waves are detected in magnetic materials by neutron diffraction acting on the spin space. The frequency of the waves is observed to be

$$\omega(\mathbf{k}) = Jk^2a^2 \quad (4.18)$$

4.3.2. Theory of the Freeon-Wave Spectrum

The imposition of cyclic symmetry, C_N on the S_N -IRS decomposes them into a direct sum of the C_N -IRS, each of which are labeled by $K = 0, 1, 2, \dots$. For $[\lambda] = [1^N]$, ($p = 0$), the $K = N/2$ space is one-dimensional and no others occur. For $[\lambda] = [1^{N-2}]$ ($p = 1$) the $K = 0$ space does not occur and all other K 's are one-dimensional. The eigenvalues $E(p, K)$ of these two lowest energy states of the freeon Heisenberg Hamiltonian are

$$E([0,0]) = -NJ \text{ (ground state)} \quad (4.19)$$

and

$$E(1, K > 0) = -NJ + 2J[1 - \cos(2\pi K/N)] \text{ (excited states)}$$

The excitation energy from the ground state is then

$$\omega(K) = 2J (1 - \cos(Ka)) \quad (4.20)$$

$$\approx JK^2a^2 \text{ for } N \text{ large and } K \text{ small}$$

This is called the freeon-wave dispersion. It is expressed in terms of a lattice parameter, a , by the substitution

$$K = Nak/2\pi \quad (4.21)$$

so

$$\omega(k) = Jk^2a^2 \quad (4.22)$$

The coupling of the freeon waves with the appropriate spin function produces a wave function which has nonzero matrix elements with the wave function of a neutron scatterer so that permutation dispersion relation can be and has been experimentally verified.

For $p > 1$ more than one permutation wave state occurs in the same C_N -IRS and gives rise to freeon wave-freeon wave interaction.

4.3.3. The Spin Paradigm

The freeon theories are converted in to spin theories by means of the Dirac identity, which converts the freeon Heisenberg to the spin Hamiltonian

$$H = 2 \sum_{i \neq j} J_{ij} S_i \cdot S_j \quad (4.23)$$

The theory employs the spin quantum number which is related to the freeon quantum number, p by

$$S = N/2 - p \quad (4.24)$$

The $p = 0$, freeon ground state becomes the spin ground state with $S = N/2$ and the $p = 1$ freeon excited state becomes the $S = N/2 - 1$, one-magnon, excited state. The $p > 1$, $S < N/2 - 1$, states become multimagnon states and exhibit the so-called magnon-magnon interaction. Dyson has given an elegant treatment of this magnon-magnon interaction inside the spin paradigm [13]. In a recent interview, he stated this was the best thing he had ever done. He, however, did not respond to my query about a freeon formulation of the spin waves.

5. MEAN-FIELD THEORIES OF THE SECOND-ORDER, PHASE-CHANGE

The second-order, phase-change exhibited by ferromagnets (Section 6), antiferromagnets (Section 7) and by superconductors (Section 8) have a phenomenological description in terms of the mean-field equation,

$$\Omega = \tanh(\Omega/t) \quad (5.1)$$

where $0 \leq \Omega \leq 1$ is the order parameter and where $0 \leq t \equiv T/T_C \leq 1$ is the reduced temperature. See Fig. 5.1.

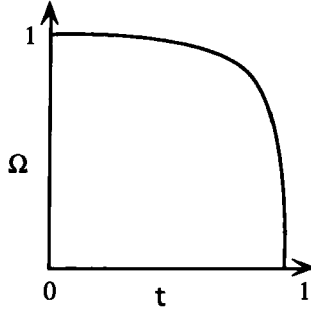


Fig. 5.1. The temperature-dependence of the order parameter

At $t = 0$ the system is completely ordered ($\Omega = 1$) while at $t = 1$ the system is completely disordered ($\Omega = 0$). As $t \rightarrow 1$

$$\begin{aligned} \Omega^2 &\rightarrow 3[t^{-1} - 1]t^3 \\ &\approx 3(1 - t) \end{aligned} \quad (5.2)$$

By analogy to the liquid-vapor equilibrium the system is said to be condensed for $\Omega \geq 0$. The critical temperature is expressed in terms of a Heisenberg exchange parameter

$$T_C = 2zJ/k \quad (5.3)$$

where z is the number of nearest neighbors

The mean-field equation will be derived from two models: the uniform interaction model and the Ising model. Neither of the two derivations depend explicitly on spin. They will be applied to the freeon theory of ferromagnetism Section 6 and freeon theory of high- T_C superconductivity in Section 7.

6. THE FREEON THEORY OF FERROMAGNETISM

6.1. Introduction

In this section we give the freeon theory of ferromagnetism. As pointed out above ferromagnetism is a second order-phase change which is well-defined by mean-field theory. In Section 6.2 we give the uniform interaction derivation of mean-field theory and in Section 6.3 we compare prediction with observation.

6.2. The Uniform-Interaction Model

6.2.1. The Theory

The uniform interaction (UI) model assumes that the freeon, Heisenberg ferromagnetic exchange interaction is uniform for all pairs in the sample: i. e.,

$$H = J \sum_{ab} P_{ab} \quad (6.1)$$

This is the freeon analogue [14] of the spin model of Kittel and Shore [15]. Since the UI Hamiltonian is the sum over all pairs with a uniform interaction strength it can be expressed in the following form

$$H = JK_2 \quad (6.2)$$

where K_2 commutes with all permutations; it is an invariant of the S_N algebra and so by Schur's lemma is diagonal in the several IRS. Further its eigenvalues are shown to be

$$E(p) = J[p(N+1) - p^2 - N(N-1)/2] \quad (6.3)$$

The dimension (the weight) of the p^{th} covalent space is

$$\begin{aligned} f[\lambda] &= f_p \\ &= \frac{N! (N-2p+1)}{p! (N-p+1)!} \end{aligned} \quad (6.4)$$

where p is the freeon quantum number. For example for $N = 3$ and $p = 1$

$$f[2,1] = 2 \quad (6.5)$$

The two Gel'fand states are

$$\begin{array}{|c|c|} \hline a & b \\ \hline c & \\ \hline \end{array} \quad \text{and} \quad \begin{array}{|c|c|} \hline a & c \\ \hline b & \\ \hline \end{array} \quad (6.6)$$

I will now compute the most probable value of the freeon quantum number, p by means of the canonical partition function. Here it is finally necessary to acknowledge the existence of the conjugate spin space whose dimension (statistical weight) is

$$\begin{aligned} f_S^{[\lambda]} &= f_p^S \\ &= 2S + 1 \\ &= N - 2p + 1 \end{aligned} \quad (6.7)$$

Consequently the total weight of the p^{th} state

$$\begin{aligned} F_p &= f_p f_p^S \\ &= (N - 2p + 1)^2 \frac{N!}{p! (N - p + 1)!} \end{aligned} \quad (6.8)$$

The partition function is then

$$Z = \sum_p F_p \exp(-\beta E(p)) \quad (6.9)$$

where $\beta = (kT)^{-1}$. I follow Kittel and Shore and rewrite the partition function as follows:

$$Z \approx \sum_p \exp(-\phi(p)) \quad (6.10)$$

where

$$\phi(p) = N \ln N - (N - p) \ln(N - p) - p \ln p + \beta E(p) \quad (6.11)$$

The most probable value of the freeon quantum number p is given by the condition,

$$\frac{\partial \phi}{\partial p} = 0 \quad (6.12)$$

or

$$\ln(N - p) - \ln p + 2p\beta J = 0 \quad (6.13)$$

Kittel and Shore define the freeon order parameter by

$$\Omega = (N - 2p)/N \quad (6.14)$$

so

$$\ln\left(\frac{1+\Omega}{1-\Omega}\right) = \alpha\Omega \quad (6.15)$$

where

$$\alpha = kT_C/kT \quad (6.16)$$

Alternately

$$\Omega = \tanh(\alpha\Omega/2) \quad (6.17)$$

This transcendental equation has a zero root only for $\alpha \geq \alpha_0 = 2$ so the critical temperature is

$$kT_C = NJ/2 \quad (6.18)$$

Consequently

$$\Omega = \tanh(\Omega T_C/T) = \tanh(\Omega/t) \quad (6.19)$$

Below the critical (Curie) temperature, T_C a ferromagnet spontaneously magnetizes to a permanent magnet whose magnitude and direction is denoted by the magnetization vector, $\mathbf{M}(T)$. The experimental order parameter is defined by the ratio

$$\mathbf{M}(t)/\mathbf{M}(0) = \Omega_{\text{exp}}(t) \quad (6.20)$$

and equated to the mean field order parameter. This essentially the result obtained from Weiss molecular-field theory in the limit of a vanishing applied molecular field.

7. SUPERCONDUCTIVITY AND MEAN-FIELD THEORY

7.1. Introduction

A superconductor exhibits perfect conductivity (See Section 7.2) and the Meissner effect (See Section 7.3) below some critical temperature, T_C . The transition from a normal conductor to a superconductor is a second-order, phase-transition which is also well-described by mean-field theory. Note that the mean-field condensation is not a Bose condensation nor does it require an energy gap. The mean-field theory is combined with London-Ginzburg-Landau theory through the concentration of superconducting carriers as follows:

$$n_S(T) = n\Omega^2(T) \quad (7.1)$$

where n is the concentration ($\approx 10^{22} \text{ cm}^{-3}$) of active electrons. This produces a macrotheory which makes predictions in strong qualitative agreement with observations on both metallic (low- T_C) and cuprate (high- T_C) superconductors.

7.2. Perfect Conductivity

7.2.1. Introduction

A perfect conductor is one that exhibits zero resistance. In this Section we describe both the observations and the theory.

7.2.2. The Observations

A schematic plot of the observed resistance-temperature relations of normal and superconductors is shown in Fig. 7.1

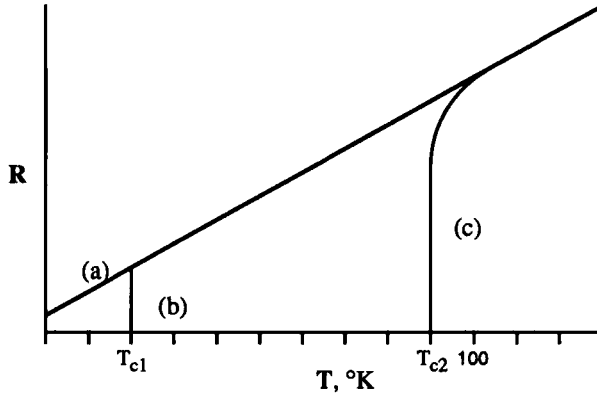


Fig. 7.1. Resistivity as a function of temperature for

(a) A normal conductor

(b) A conventional superconductor with critical temperature T_{c1}

(c) A high-temperature superconductor with critical temperature T_{c2}

The conduction in the low- T_C metallic superconductors is isotropic while in the high- T_C cuprate superconductors the conduction takes place along crystal planes

7.2.3. Theory

The London supercurrent density is

$$\mathbf{J} = -k\mathbf{A} \quad (7.2)$$

where \mathbf{A} is the vector potential and where

$$k = qn_S(t)/\mu c \quad (7.3)$$

Here q is the charge, $n_S(t)$ is the concentration and μ is the mass of the superconducting carriers. The time-derivative of the current density is

$$\partial \mathbf{J} / \partial \tau = k^2 \mathbf{E} \quad (7.4)$$

where \mathbf{E} is the electric field. For constant \mathbf{E}

$$\mathbf{J} = k^2 \mathbf{E} \tau \quad (7.5)$$

This is the equation for perfect conductivity. The temperature-dependence of the resistivity is

$$R(t) \propto \frac{1}{n\Omega^2} \quad (7.6)$$

As $t \rightarrow 1$

$$R(t) \rightarrow \frac{1}{3n(1-t)} \rightarrow +\infty \quad (7.7)$$

Further

$$\begin{aligned} \frac{\partial R(t)}{\partial t} &\approx \frac{\partial}{\partial t} \frac{1}{3n(1-t)} \\ &= \frac{1}{3n(1-t)^2} \rightarrow +\infty \end{aligned} \quad (7.8)$$

For $t > 1$ normal resistivity obtains; i. e.,

$$R_N \approx R_0 t \quad (7.9)$$

This reproduces the sharp break of the metallic superconduction shown in Fig. 7.1. The absence of the sharp break in the cuprate resistance vs. temperature plot has been attributed to their short coherence lengths which give rise to large thermal fluctuations at the critical temperature.

7.3 The Meissner Effect

The Meissner effect is the exclusion of an external magnetic field from the bulk of the superconductor. By London theory the magnetic induction is

$$B(x) = B(0) \exp\left[-\frac{x}{\lambda}\right] \quad (7.10)$$

where λ is the penetration depth. See Fig. 7.2. The penetration depth can be directly determined by the a mutual-induction bridge by muon resonance spectroscopy and by polarized neutron reflectivity . Its dependence on t is shown in Fig. 7.3.

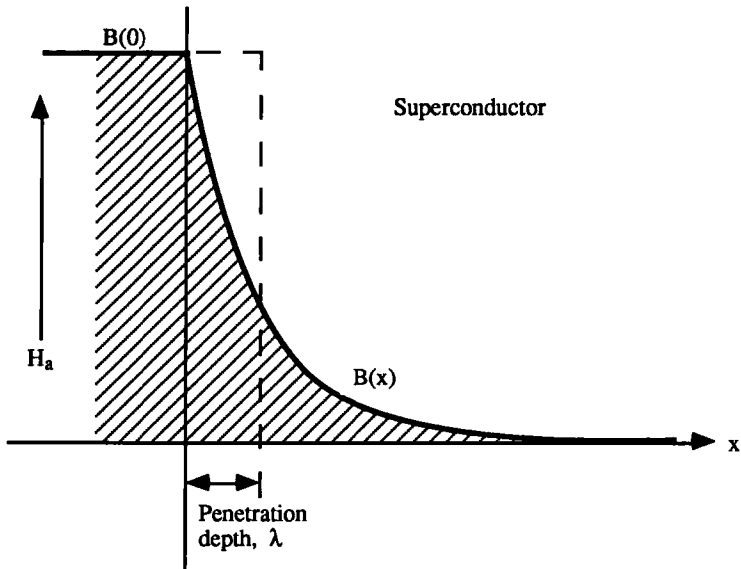


Fig. 7.2. Exclusion of a magnetic field from the body of a superconductor

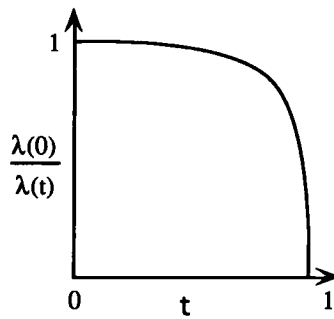


Fig. 7.3. The penetration depth vs. the reduced temperature

By London theory

$$\lambda(t) = \left(\frac{c^2}{4\pi n_S(t)} \right)^{1/2} \quad (7.11)$$

so

$$\lambda(0)/\lambda(t) = \Omega(t) \quad (7.12)$$

This prediction is in strong qualitative agreement with the observations shown in Fig. 7.3.

Note that the mean-field theory is not a Bose condensation nor does it require a gap. A macrotheory cannot predict critical temperatures, coherence lengths and other observations. For these predictions a macrotheory is required. We consider two microtheories, the BCS and the ISB theories.

8. THE ISING, SMALL-BIPOLARON THEORY OF CUPRATE SUPERCONDUCTIVITY

8.1. Introduction

The Bardeen-Cooper-Schrieffer (BCS) theory [16] is the microtheory of choice for the metallic (low- T_C) superconductors. The BCS theory has proved to be less than satisfactory for the cuprate (high- T_C) superconductors. Among the theories which have been proposed for the cuprates are the following spin theories- the spin bag theory [17] and the resonating-valence bond-spinon theory [18]. I have recently proposed a freeon theory called the Ising, small-bipolaron (ISB) theory [19]. Here "Ising" refers to the Ising theory of the second-order, phase-transition and "small bipolaron" refers to the short-coherence-length of the electron-pair, supercurrent carriers.

8.2. The Properties of the Cuprate Superconductors.

8.2.1. Introduction

The crystal structures (Section 8.2.2) and the phase-relations (Section 8.2.3) of the cuprate superconductors are considerably more complex than for the metallic superconductors. It is not surprising that, while there a common macrotheory, different microtheories are required.

8.2.2. The Crystal Structures

The high- T_C cuprate superconductors are perovskites. See for example Fig. 8.1.

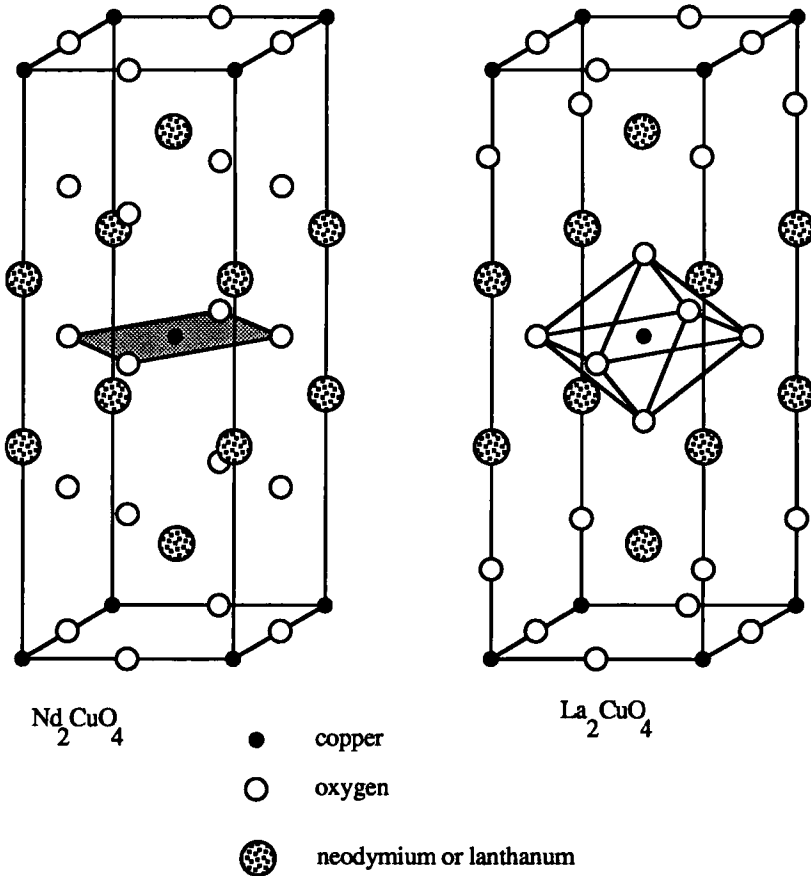


Fig. 8.1. The crystal structure of two cuprate superconductors

The parent ($\text{A}_2\text{B}_0\text{Cu-O}_4$) cuprates are antiferromagnetic semiconductors which, on doping to $\text{A}_{2-x}\text{B}_x\text{Cu-O}_4$, become superconductors where x is called the doping parameter. The replacement of Nd^{3+} by Ce^{4+} produces an electron superconductor

while the replacement of La^{3+} by Sr^{2+} or Ba^{2+} produces a hole superconductor. It is assumed that the supercurrent is transmitted along the Cu-O planes marked by the shaded areas and that the remaining atoms act as sources (electron superconductors) or as sinks (hole superconductors) of electrons.

8.2.3. The Phase Diagram

Cuprate superconductors exhibit complicated phase diagrams which are functions of the doping parameter, x which controls the amount of the electron-transfer into or out of the cuprate plane. See for example Fig. 8.2.

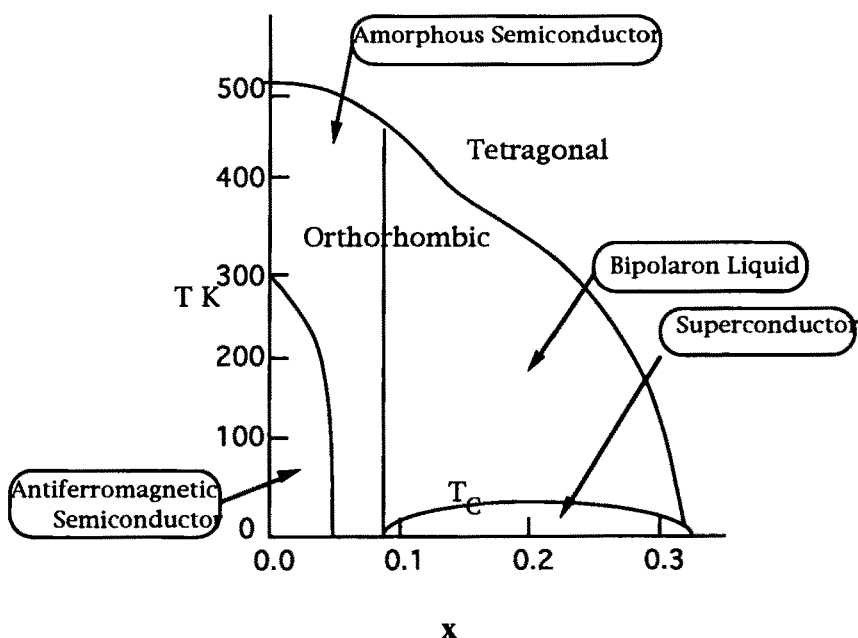


Fig. 8.2. Phase diagram for $\text{La}_{2-x}\text{Sr}_x\text{CuO}_4$

Note that the undoped cuprate is an antiferromagnet and that doping converts it into a superconductor. We have shown above that antiferromagnetic behavior arises from the $z \approx +1$ side of the extended Hückel-Hubbard spectrum in Fig. 4.1. In the ISB theory the superconducting behavior comes from the $z \approx -1$ side of Fig. 4.1 just as does the freeon theory of ferromagnetism.

8.3. The NUHH Hamiltonian and its Spectrum

The Negative-Hubbard Hückel-Hubbard Hamiltonian (NUHH) at $z = -1$ is

$$H = -|U|d \quad (8.1)$$

where $|U|$ is the Hubbard parameter and where d counts the number of doubly occupied sites. The site-orbital Gel'fand states, are eigenvectors of this Hamiltonian with eigenvalues

$$E(d) = -|U|d \quad (8.2)$$

where d is a quantum number which specifies the number of doubly-occupied sites. It will be convenient to define a second quantum number, the *valence* (seniority), by

$$v = N/2 - d \quad (8.3)$$

The singlet spectrum and the states of the four-site, four-electron system are shown in Fig. 8.3

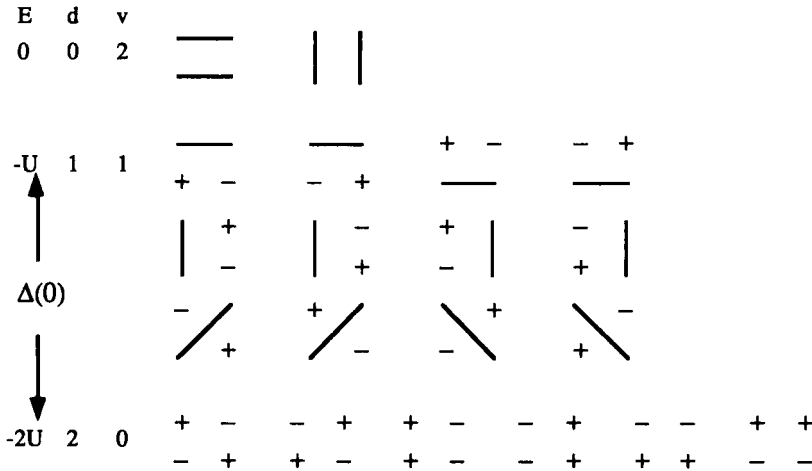


Fig. 8.3. Singlet states of the four-electron, four-site system for the strongly-coupled NUHH ($\Delta(0)$ defines the gap in ISB)

The $v = 2$ states in Fig. 8.4 are Anderson RVB states which are ignored here because they are highly-excited states for the strongly-coupled NUHH. Note that the ground state, $v = 0$, is composed exclusively of small bipolarons, $(-)$ and bipolaron holes, $(+)$. Of particular importance is the fact that the $v = 0$ states are Ising states so that Ising condensation obtains with

$$T_C = 2zJ_{BH}/k \quad (8.4)$$

where J_{BH} is the exchange interaction between a neighboring small bipolaron and a bipolaron hole. The ISB gap is defined spectroscopically as the energy required to break a bipolaron pair and so is temperature-independent.

8.4. The Ising, Small-Bipolaron Model of Mean-Field Theory

8.4.1. The Two-Dimensional Representation of Condensation

The Ising mean-field theory assigns to each site in an N -site, two-dimensional solid, two states labeled $(+)$ and $(-)$. The order parameter is related to the numbers of the two types of nearest neighbors (bipolaron and/or hole) for an N -site system as follows:

a) Unlike nearest neighbors

$$A = (N/2)(1 + \Omega) \quad (8.5)$$

b) Like nearest neighbors

$$B = (N/2)(1 - \Omega) \quad (8.6)$$

The conventional choice for the internal energy is

$$U = -zNJ_{BH}\Omega^2 \quad (8.7)$$

Fig. 8.4 gives a pictorial realization of condensation in terms of the Ising unit structure $\begin{bmatrix} + & - \\ - & + \end{bmatrix}$. Note that each of these structural units have d-wave character, which are phased in the condensed areas but lose their phasing in the uncondensed area.

+	-	+	-	+	-	+	-
-	+	-	+	-	+	-	+
+	-	+	-	+	-	+	-
-	+	-	+	-	+	-	+
+	-	+	-	+	-	+	-
-	+	-	+	-	+	-	+
+	-	+	-	+	-	+	-
-	+	-	+	-	+	-	+

Fig. 8.4a. Ising condensation $\Omega = 1$; $t = 0$, fully condensed

+	+	-	-	+	+	-	-
+	+	-	-	+	+	-	-
-	-	+	+	-	-	+	+
-	-	+	-	+	-	+	+
+	+	-	+	-	+	-	-
+	+	-	-	+	+	-	-
-	-	+	+	-	-	+	+
-	-	+	+	-	-	+	+

Fig. 8.4b. Partial condensation
 $0 < \Omega < 1$; $0 < t < 1$

+	-	-	+	+	-	-	+
-	+	+	-	-	+	+	-
-	+	+	-	-	+	+	-
+	-	-	+	+	-	-	+
+	-	-	+	+	-	-	+
-	+	+	-	-	+	+	-
-	+	+	-	-	+	+	-
+	-	-	+	+	-	-	+

Fig. 8.4c. Uncondensed
 $\Omega = 0$; $t = 1$

8.4.2. The ISB Derivation of the Mean-Field Equation.

The ISB derivation of the mean-field equation begins with the free-energy functional,

$$F(\Omega, T) = U(\Omega) - TS(\Omega, T) \quad (8.8)$$

Each site is assigned the same energy ($-zJ_{BH}\Omega^2$) (where z is the number of nearest neighbors) so the internal energy functional is

$$U = -NzJ_{BH}\Omega^2 \quad (8.9)$$

The entropy functional is

$$S(\Omega, T) = Nk\ln Z(\Omega) \quad (8.10)$$

where

$$Z(\Omega) = W(\Omega) \quad (8.11)$$

is the partition function with

$$W(\Omega) = N!/[A!][B!] \quad (8.12)$$

The equilibrium condition on the free-energy functional is

$$(\partial F(T, \Omega)/\partial \Omega)_T = 0 \quad (8.13)$$

By Stirling's approximation,

$$\ln Z(\Omega) = \ln N! - (A \ln A - A + B \ln B - B) \quad (8.14)$$

so

$$\begin{aligned} \partial(A \ln A - A)/\partial \Omega &= (\ln A + A/A - 1) \partial A/\partial \Omega \\ &= (N/2) \ln A \end{aligned} \quad (8.15)$$

and

$$\partial(B \ln B - B)/\partial \Omega = - (N/2) \ln B \quad (8.16)$$

In consequence

$$\begin{aligned} \partial \ln Z/\partial \Omega &= - (N/2) \ln(A/B) \\ &= - (N/2) \ln(1 + \Omega)/(1 - \Omega) \\ &= - (N/2) W \end{aligned} \quad (8.17)$$

where

$$W = \ln(1 + \Omega)/(1 - \Omega) \quad (8.18)$$

so

$$\Omega = \tanh(W/2) \quad (8.19)$$

The variation principle yields

$$2NzJ_{BH}\Omega = NkTW/2 \quad (8.20)$$

or

$$W = 4zJ_{BH}\Omega/kT \quad (8.21)$$

so

$$\Omega = \tanh(2zJ_{BH}\Omega/kT) \quad (8.22)$$

To relate J_{BH} to the critical temperature we expand Eq. 8.22 as follows:

$$\Omega = 2zJ_{BH}\Omega/kT - (1/3)(2zJ_{BH}\Omega/kT)^3 + \dots \quad (8.23)$$

so

$$1 = (2zJ_{BH}/kT - (1/3)(2zJ_{BH}/kT)^3)\Omega^2 + \dots \quad (8.24)$$

and so

$$\Omega^2 \approx 3(2zJ_{BH}/kT - 1)(kT/2zJ_{BH})^3 \quad (8.25)$$

As $T \rightarrow T_C$ (from below) $\Omega \rightarrow 0$

$$J_{BH} = kT_C/2z \quad (8.26)$$

so

$$\Omega = \tanh(\Omega T_C/T) \quad (8.27)$$

$$= \tanh(\Omega/t) \quad (8.28)$$

8.5. The Chemical Structure of Bipolarons and Holes

8.5.1. The Site Orbital Space

We take for the freeon orbital space,

$$V_2: \{ |Cu\rangle, |O\rangle \} \quad (8.29)$$

where $|Cu\rangle$ is the $d(x^2 - y^2)$ orbital centered on copper and $|O\rangle$ is a normalized, linear combination of p_σ orbitals centered on the four neighboring oxygen atoms. See Fig. 8.5 .

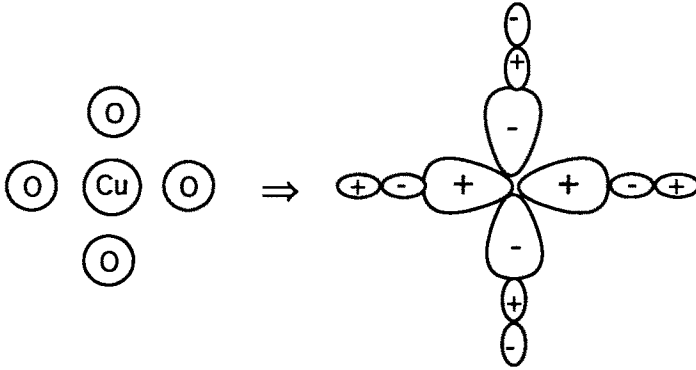


Fig. 8.5. The copper and oxygen orbitals for the cuprates

8.5.2. The Two-Electron Spaces

For two electrons there are two freeon, irreducible representation spaces, each labeled by a Young diagram:

- i) The triplet space, $\begin{array}{|c|} \hline \square \\ \hline \end{array}$
- ii) The singlet space, $\begin{array}{|c|c|} \hline \square & \square \\ \hline \end{array}$

8.5.3. The Freeon Gel'fand States

The spin-free Gel'fand states span the several irreducible representation spaces. They are uniquely labeled by Gel'fand diagrams constructed by adding spin-free orbitals in nondescending order along rows and ascending order down columns:

- i) The triplet space:

$$V\left(\begin{array}{|c|} \hline \square \\ \hline \end{array}\right): \left\{ \begin{array}{|c|} \hline \text{Cu} \\ \hline \text{O} \end{array} \right\}$$

- ii) The singlet space:

$$V\left(\begin{array}{|c|c|} \hline \square & \square \\ \hline \end{array}\right): \left\{ \begin{array}{|c|c|} \hline \text{Cu} & \text{Cu} \\ \hline \text{O} & \text{O} \end{array}, \begin{array}{|c|c|} \hline \text{Cu} & \text{O} \\ \hline \text{O} & \text{O} \end{array}, \begin{array}{|c|c|} \hline \text{O} & \text{O} \\ \hline \text{O} & \text{O} \end{array} \right\}$$

The two-electron NUHH spectrum is as follows.

Energy	State
0	$\begin{array}{ c } \hline \text{Cu} \\ \hline \text{O} \\ \hline \end{array} \equiv \text{triplet biradical state}; \begin{array}{ c c } \hline \text{Cu} & \text{O} \\ \hline \end{array} \equiv \text{single covalent state}$
- U	$\begin{array}{ c c } \hline \text{Cu} & \text{Cu} \\ \hline \end{array} \equiv (-), \text{bipolaron state}; \begin{array}{ c c } \hline \text{O} & \text{O} \\ \hline \end{array} \equiv (+), \text{hole state}.$

The singlet, covalent Gel'fand state $\begin{array}{|c|c|} \hline \text{Cu} & \text{O} \\ \hline \end{array}$ and the triplet, covalent state $\begin{array}{|c|} \hline \text{Cu} \\ \hline \text{O} \\ \hline \end{array}$ lie higher than the small bipolaron (-) and hole (+) states (See Fig. 8.3) and are ignored.

8.6. Doping and the Lattice Parameter

8.6.1. Introduction

$\text{La}_{2-x}\text{Sr}_x\text{CuO}_4$ is a superconductor for $0.09 \leq x \leq 0.31$. See Fig. 8.2. Over this doping range a continuous change of lattice parameters occurs with no change in crystal structure. From this it is inferred that a simultaneous continuous change in electronic structure occurs on doping. I follow Burdett [20] and employ the bipolaron-lattice-parameter model in which the bipolaron and the hole energies are assumed to vary linearly with the lattice parameter. From this assumption is obtained a microtheory of J_{BH} , a microtheory of the dependence of T_{C} on doping and a microtheory of the vibronic interaction which produces NUHH.

A two dimensional realization of doping is obtained by taking the parent electron-superconductor and hole-superconductor to consist solely of bipolarons and holes respectively. See Fig. 8.6. This model is consistent with the observed volume-fraction Meissner effect since the Meissner effect can occur only in condensed areas. The dependency of the Meissner effect on doping parallels the parabolic dependency of T_{C} . See Section 8.6.3.

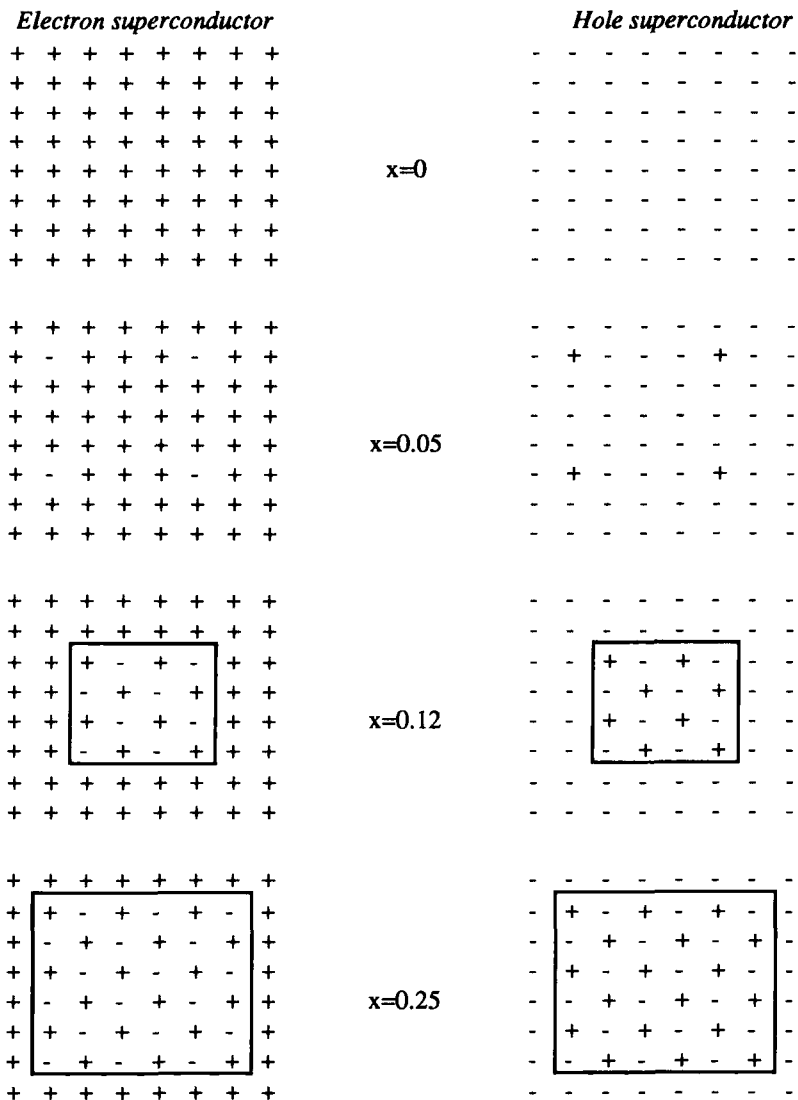


Fig. 8.6. Doping in a 64 site system (The condensed areas are outlined in black)

8.6.2. The Bipolaron-Lattice-Parameter Model

The bipolaron-lattice-parameter model is based on the following assumptions:

- i) A reduced lattice parameter, $-1 \leq \rho \leq +1$ which is proportional to x .
- ii) The dependence of the bipolaron and hole energies on ρ

$$E[\boxed{\text{Cu}}\boxed{\text{Cu}}] = -E[\boxed{\text{O}}\boxed{\text{O}}] = -\rho \quad (8.30)$$

- iii) The bipolaron-hole interaction:

$$J_{BH} = \langle \boxed{\text{Cu}}\boxed{\text{Cu}} | H | \boxed{\text{O}}\boxed{\text{O}} \rangle \quad (8.31)$$

The energies of the two bipolaron-hole system states are then

$$\left. \begin{matrix} E_G \\ E_E \end{matrix} \right\} = \pm K \quad (8.32)$$

where $K = (J_{BH}^2 + \rho^2)^{1/2}$. The eigenvalues are plotted in Fig. 8.7.

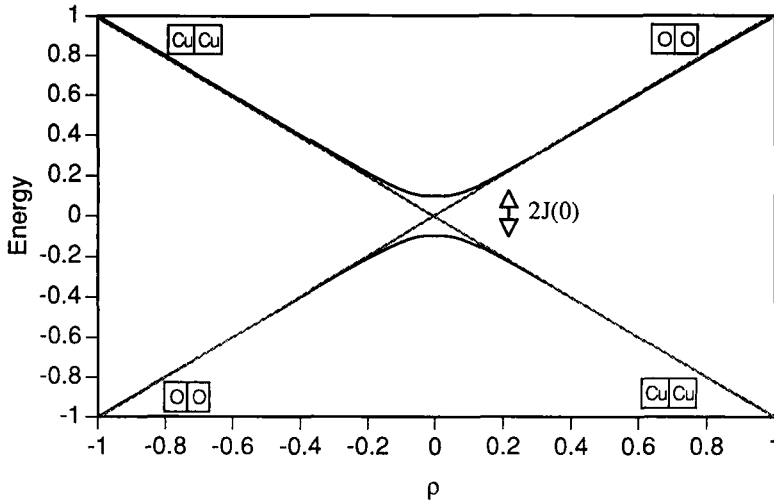


Fig. 8.7. The cuprate spectrum

8.6.3. The Doping-Dependence of J_{BH} and T_C

The resonance exchange integral, $J_{BH}(0)$ is indicated in Fig. 8.7. For the off-resonance exchange integral we take

$$J(\rho) = E(\rho^*) - E(\rho) \quad (8.33)$$

where ρ^* is that value of ρ for which

$$E(\rho^*) \approx \rho^* \quad (8.34)$$

By mean-field theory

$$T_C(\rho) = 2zJ(\rho)/k \quad (8.35)$$

and by the assumption of a linear relation between x and ρ

$$J(\rho)/J(0) = T_C(\rho)/T_C(0) \quad (8.36)$$

$$= T_C(x)/T_C(x_{\max}) \quad (8.37)$$

See Fig. 8.8 which reproduces the T_C parabola of Fig. 8.2.

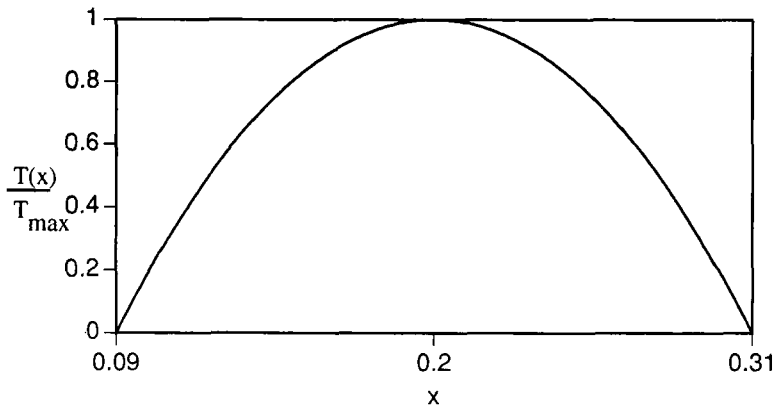


Fig. 8.8. The dependence of resonance exchange integral on doping parameter

8.6.4. Vibronic Interaction

The strength of the vibronic interaction is dependent on the amplitudes of the bipolaron and hole wavefunctions in bipolaron-lattice wavefunction. The ground-state eigenvector is

$$\begin{aligned}\Psi(\chi) &= (U|\boxed{\text{Cu}}\boxed{\text{Cu}}\rangle + V|\boxed{\text{O}}\boxed{\text{O}}\rangle) (U^2 + V^2)^{-1/2} \\ &= A_B|\boxed{\text{Cu}}\boxed{\text{Cu}}\rangle + A_H|\boxed{\text{O}}\boxed{\text{O}}\rangle\end{aligned}\quad (8.38)$$

The amplitudes of the bipolaron and hole states are plotted as functions of ρ in Fig. 8.9

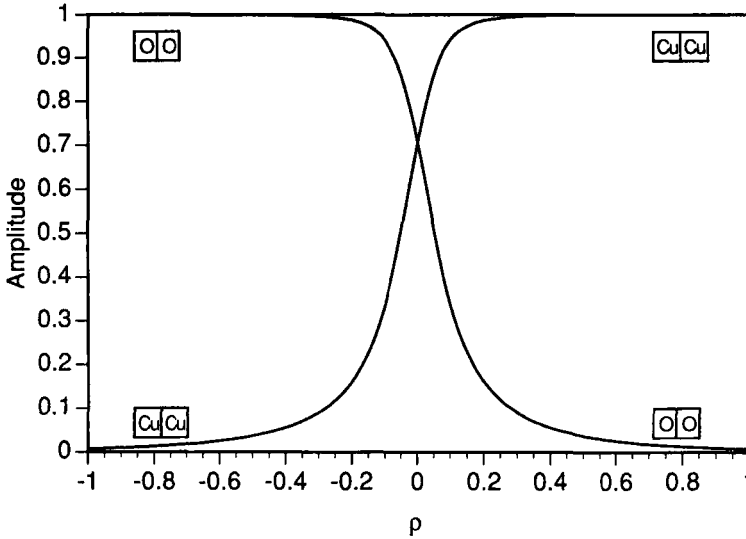


Fig. 8.9. The bipolaron and hole amplitudes

It is now assumed that the distance variable, ρ is also the variable in a harmonic cell potential with states $\{|n\rangle, n = 0, 1, 2, \dots\}$ and with energies, $E_n = \hbar\omega(n + 1/2)$. The zero-order states of the vibronic system are then the product states, $\{\Psi(x)|n\rangle, n = 0, 1, \dots\}$. The electronic ground state eigenvector is expanded about $\rho = 0$ as follows:

$$\Psi(\rho) = \Psi(0) + (d\Psi(\rho)/d\rho)_0 + \dots \quad (8.39)$$

where the second term is taken as the vibronic perturbation with

$$(d\Psi(\chi)/d\chi)_0 = d(A_B|\boxed{\alpha\alpha}\rangle + A_H|\boxed{\alpha\alpha}\rangle)_0/d\chi \quad (8.40)$$

Then

$$(d\Psi(\rho)/d\rho)_0(d\Psi(\rho)/d\rho)_0^\dagger = (dA_B/d\rho)_0^2 + (dA_H/d\rho)_0^2 \quad (8.41)$$

$$\equiv K$$

The second-order energy is then

$$E^{(2)} = -K \langle 0|\rho|n\rangle \langle n|\rho|0\rangle / n\hbar\omega$$

$$= -2K/\hbar\omega$$

$$= -S_{\text{vib}} \quad (8.42)$$

where S_{vib} is the vibronic stabilization energy. From an inspection of Fig. 8.9 this is a very large number.

9. CRITIQUE OF THE FREEON THEORY OF FERROMAGNETISM

The freeon theory of ferromagnetism is based on the negative-U, Hückel-Hubbard Hamiltonian (NUHH). However the conventional positive-U, Hückel-Hubbard (PUHH) Hamiltonian employs a positive U which is a measure of the repulsion of a bare pair of electrons on a single site. From whence comes NUHH? There are three positions to take with respect to NUHH:

- 1) The Ising, small-bipolaron (ISB) theory of cuprate superconductivity (Section 8) employs NUHH where, just as in BCS theory, it is a consequence of vibronic interaction which overrides the positive U.
- 2) Ferromagnetism cannot be explained by a site theory and requires a delocalized band theory. Support for this point of view is provided by UHF band calculations which produce a surplus of up spins over down spins for a number of the ferromagnetic materials.
- 3) Adopt the cavalier attitude of Weiss and claim that the use of NUHH in a theory of ferromagnetism "is supported by a sufficient number of facts that one can be certain that it contains an important part of the truth and that

the difficulty of interpretation should be considered less an objection than a stimulus for research on new hypotheses of atomic structure".

10. ATOMIC STRUCTURE

10.1. Introduction

In this Section we apply freeon theory to atomic structure. In Section 10.2 we give the freeon Gel'fand structures of the second row of the periodic table and in Section 10.3 Gel'fand diagrams are used to describe the splitting of d-electron configurations in an octahedral field.

The initial incentive for the invention of quantum mechanics was the observed, discrete spectra of atoms and molecules which could not be predicted by classical mechanics. The Schrödinger differential equation is constructed from the classical energy and its physically-significant solutions were restricted to those which satisfied certain physically-significant boundary-conditions. This quantized the energy and supplied quantum numbers which identified the quantized states. In the Section 10.4 we take a different view of quantization. It is used, in the following Sections, to analyze atomic spectra.

10.2. The Periodic Table

One of the early great triumphs of atomic theory was the *aufbau* principle which explained the periodic table. In it the atomic orbital energies were assigned the following order: $1s < 2s < 2p < 3s < \dots$. The occupation number of freeon orbitals was limited to no more than two as was discussed in Section 1. Further Hund's rule was imposed; i. e. states of highest spin lie the lowest. The Gel'fand state reconstruction of the *aufbau* for the second row of the periodic table (with $m_l = +1$ or zero) is shown in Fig. 10.1 where $2p_+ = +1$, $2p_0 = 0$ and $2p_{-1} = -1$:

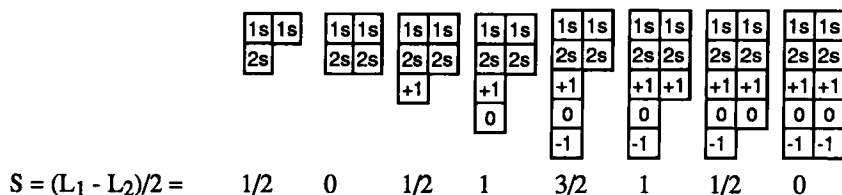


Fig. 10.1. Gel'fand structures for the second row of the periodic table.

10.3. Crystal Field States

A transition metal ion confined to a weak crystal field exhibits the high spin spectrum while in a strong field exhibits the low spin spectrum. The d orbitals of the ion have a five-fold degeneracy which is split by an octahedral field into an excited, doubly-degenerate (denoted e1 and e2) orbital and a ground, triply-degenerate (denoted t1, t2 and t3) orbital. The Gel'fand state correlation among the relevant free ion configurations \rightarrow high-spin states \rightarrow low-spin states is shown below for the d^4 , d^5 and d^6 ions

The weak-field case like the free ion obeys Hund's rule while in the strong-field case Hund's rule is overcome by the increased relative stability of the t-type relative to the e-type orbitals

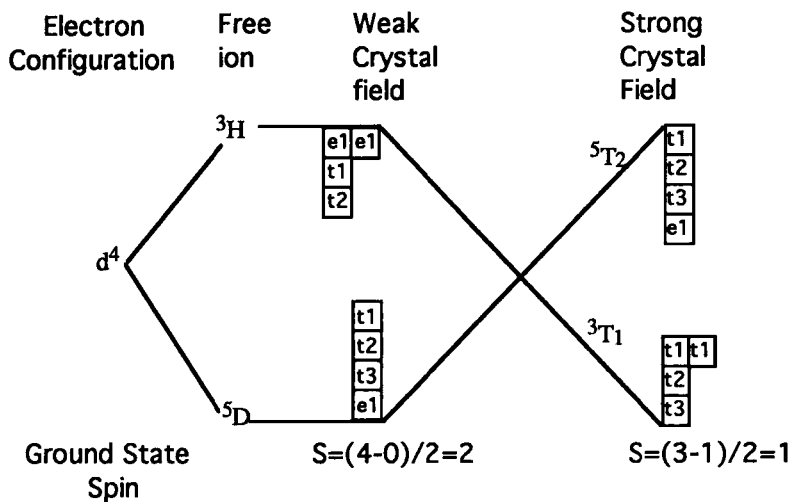


Fig. 10.2. The Gel'fand state correlation diagram for d^4

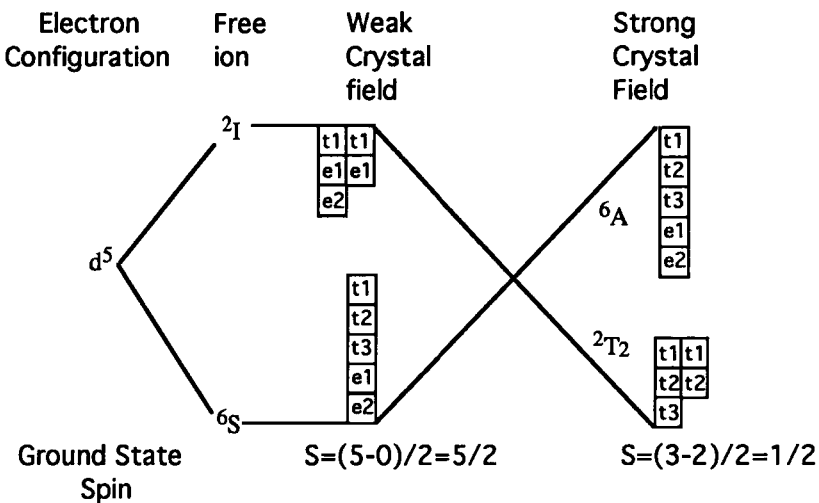


Fig. 10.3. The Gel'fand state correlation diagram for d^5

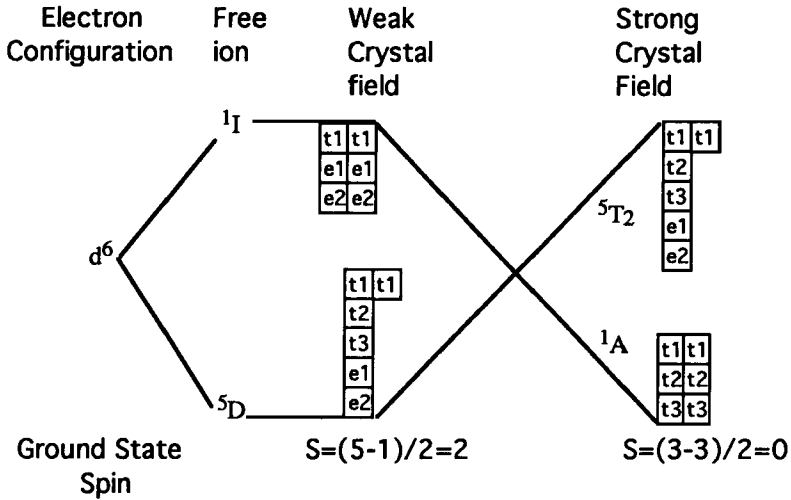


Fig. 10.4. The Gel'fand state correlation diagram for d^6

10.4. Symmetry-Quantization

It has been shown that quantization is a consequence of symmetry. This permits an alternate, and perhaps more fundamental, view of quantization called symmetry quantization because it is based the symmetries of atoms expressed through chains of compact groups for which $U(M)$ is the head group. With this concept there can be constructed a group-theoretical Hamiltonian which can be used to analyze atomic spectra. The Hamiltonian consists of a linear combination of the invariants of a group chain which is diagonal in a space symmetry-adapted to that chain. The several groups each supply a quantum number. The general, group-theoretical Hamiltonian has the following form:

$$H(\alpha_k) = \sum_k \alpha_k C_k \quad (10.1)$$

where k identifies the groups in the chain. where α_k is an empirical parameter evaluated from the spectra and where C_k is a Casimir operator for the k^{th} group and where C_k is a Casimir operator which commutes with every element of G_k and so is diagonal in the several IRS (j) of G_k with an eigenvalue denoted E_k^j .

This model Hamiltonian is diagonal in an IRS of $U(M)$ which has been symmetry adapted to the above chain with eigenvalues denoted

$$E\{\alpha_k, j\} = \sum_k \alpha_k E_k^j \quad (10.2)$$

Since for light atoms only freeon dynamics is relevant we consider only freeon chains,.

$$U(M) \supset \dots \supset G_k \supset \dots \supset R(3) \quad (10.3)$$

In Section 10.5 the above model Hamiltonian is applied to the analysis of the spectra of the p^N configuration. In Section 4 the model Hamiltonian is used to analyze the spectra of the d^N configuration.

10.5. The Group-Theoretical Analysis of p^N Spectra

For the p^N group chain and quantum numbers are

$$U(3) \supset R(3) \quad (10.4)$$

quantum numbers: $[v], S \quad L$

The group-theoretical analysis of the several p shell configurations is given below:

N	$[\lambda]$	S	L
0	[0]	0	S
1	[1]	1/2	P
2	[2,0]	0	S,D
	[1,1]	1	P
3	[2,1]	1/2	P,D
	[1 ³]	3/2	S
4	[2 ²]	0	S,D
	[2,1 ²]	1	P
5	[2 ² ,1]	1/2	P
6	[2 ³]	0	S

The spectrum of the model Hamiltonian is for each value of N

$$E(S,L) = E_0 - \alpha S(S+1) - \beta L(L+1) \quad (10.5)$$

so that

	Obs	Freeon Spectrum	
C(p ²)	1S	21.6	E ₀
	1D	10.2	E ₀ - 6β
	3P	0.0	E ₀ - 2α - 2β
N(p ³)	2P	28.8	E ₀ - 3α/4 - 2β
	2D	19.2	E ₀ - 3α/4 - 6β
	4S	0.0	E ₀ - 15α/4
O(p ⁴)	1S	33.8	E ₀
	1D	15.9	E ₀ - 6β
	3P	0.0	E ₀ - 2α - 2β

$$r(3) = \frac{E(^2P) - E(^2D)}{E(^2D) - E(^4S)} = \frac{4\beta}{3\alpha - 6\beta} = 0.500 \text{ (exp)} \quad (10.6)$$

$$r(2) = r(4) = \frac{E(^1S) - E(^1D)}{E(^1D) - E(^3P)} = \frac{6\beta}{2\alpha - 4\beta} = 1.13, 1.14 \text{ (exp)} \quad (10.7)$$

$$\frac{r(2)}{r(3)} = \frac{r(4)}{r(3)} = 2.25 \text{ (2.26, exp)} \quad (10.8)$$

The last ratio is independent of the parameters, α and β and may be regarded as a purely group theoretical (kinematic) result. The same result is obtained dynamically without group theory through the Slater-Condon parameters which are integrals of e^2/r_{ij} over analytic hydrogenic orbitals. The chain has been interpreted as the sum of a p orbital-p orbital and a spin orbital-spin orbital magnetic dipole interaction. This interpretation is clearly nonphysical.

10.6. The Group Theoretical Analysis of d^N Spectra

The d^N group chain and quantum number are

$$U(5) \supset R(5) \supset R(3) \quad (10.9)$$

quantum numbers: $[v], S \quad v \quad L$

where v is the seniority quantum number

N	$[\lambda]$	$v(\text{seniority})$	S	L
1	[1]	1	1/2	D
2	[2,0]	0	0	S
		2	0	D,G
	[1,1]	2	1	P,F
3	[2,1]	1	1/2	D
		3	1/2	
	P,D,F,G,H			
	$[1^3]$	2	3/2	P,F
4	[2,2]	0	0	S
		2	0	D,G
		4	0	
	P,D,F,G,I			
	$[2,1^2]$	2	1	P,F
		3	1	
	P,D,F,G,H			
	$[1^4]$	1	2	D

The analysis of the d^N spectra is more complicated than for p^N due to intershell interactions and will not be discussed further here.

11. NUCLEAR STRUCTURE

11.1. Introduction

There exists a pleasing isomorphism between atomic and nuclear structure [21]. In 1937 Wigner pointed out that isospin is the nuclear analogue of ordinary spin. In this view there are two isospin states:

$$V_2: \{ |p\rangle (\text{proton}), |n\rangle (\text{neutron}) \}$$

The number of nucleons is denoted by the mass number, A . By analogy to freeon dynamics, the isofreeon states are labeled by Young diagrams with no more than two columns, $L_1 \geq L_2 \geq 0$. The mass number and the isospin quantum number are then

$$A = L_1 + L_2 \quad (11.1)$$

and

$$T = (L_1 - L_2)/2 \quad (11.2)$$

The nuclear fermion orbital is product of a spatial (superfreeon) orbital, an ordinary spin (ordspin) orbital and an isospin orbital (which determine the atomic number). In isofreeon dynamics the quantum number, J replaces the ordinary freeon quantum number, L .

The superfreeon orbitals are taken to be the three-dimensional harmonic oscillator orbitals which lie the following energy sequence

$$\epsilon_{1s} < \epsilon_{1p} < \epsilon_{2s} = \epsilon_{1d} < \dots \quad (11.3)$$

This energy sequence together with the Gel'fand construction leads to the nuclear periodic table

11.2. The $(1s)^A$ Gel'fand Diagrams

The superfreeon $1s$ orbital can carry up to 4 nucleons. The $1s^A$ isofreeon Gel'fand state are listed Fig. 11.1 together with the isospin, the ordspin and the nuclear species which are associated with each Gel'fand state.

A	$[\lambda]$	Gel'fand States		T	J	Species
1	[1]	$\boxed{1s\alpha}$	$\boxed{1s\beta}$	1/2	1/2	n,p
2	$[1^2]$	$\boxed{1s\alpha} \boxed{1s\alpha}$	$\boxed{1s\alpha} \boxed{1s\beta}$	0	1	H ²
3	$[2,1]$	$\boxed{1s\alpha} \boxed{1s\beta}$ $\boxed{1s\beta}$	$\boxed{1s\alpha} \boxed{1s\alpha}$ $\boxed{1s\beta}$	1/2	1/2	H ³ , He ³
4	$[2^2]$	$\boxed{1s\alpha} \boxed{1s\alpha}$ $\boxed{1s\beta} \boxed{1s\beta}$		0	0	He ⁴

Fig. 11.1. The isofreeon ground Gel'fand states to $A = 4$

11.3. The Isospin Paradigm

The isospin Young diagrams are conjugate to the isofreeon Young diagrams. By analogy to the z components, M_S of electron spin, the "z" components of isospin are

$$M_T = -T, -T+1, \dots, T-1, T \quad (11.4)$$

They determine the nuclear charge and the nuclear species by the formula

$$Z = (M_T + A)/2 \quad (11.5)$$

By analogy to the ordinary-spin Heisenberg exchange Hamiltonian the isospin exchange Hamiltonian is

$$H = JT_i \cdot T_j \quad (11.6)$$

where $J > 0$ is the analogue of a ferromagnetic analogue of a ferromagnetic interaction. By this Hamiltonian, which neglects the coulomb interaction, the low isospin states lie the lowest in energy, and the number of protons will be roughly equal to the number of neutrons for such states. The isospin Gel'fand states to $A = 4$ are listed in Fig. 11.2.

A=1 Isobars			A=2 Isobars			
	$\begin{array}{ c } \hline p \\ \hline \\ \hline n \\ \hline \end{array}$ ${}_1\text{H}^1$	$\begin{array}{ c } \hline n \\ \hline \\ \hline \\ \hline \end{array}$ ${}_0n^1$	$\begin{array}{ c } \hline p \\ \hline n \\ \hline \end{array}$ ${}_1\text{H}^2$	$\begin{array}{ c c } \hline p & p \\ \hline \\ \hline \\ \hline \end{array}$ ${}_2\text{He}^2$	$\begin{array}{ c c } \hline p & n \\ \hline \\ \hline \\ \hline \end{array}$ ${}_1\text{H}^2$	$\begin{array}{ c c } \hline n & n \\ \hline \\ \hline \\ \hline \end{array}$ ${}_0n^2$
T	$\frac{1}{2}$	$\frac{1}{2}$	0	1	1	1
M_T	$\frac{1}{2}$	$-\frac{1}{2}$	0	1	0	-1
$\frac{Z}{N}$	∞	0	1	∞	1	0

A=3 Isobars						
	$\begin{array}{ c c } \hline p & p \\ \hline n & \\ \hline \end{array}$ ${}_2\text{He}^3$	$\begin{array}{ c c } \hline p & n \\ \hline n & \\ \hline \end{array}$ ${}_0n^1$	$\begin{array}{ c c c } \hline p & p & p \\ \hline \\ \hline \\ \hline \end{array}$ ${}_3\text{Li}^3$	$\begin{array}{ c c c } \hline p & p & n \\ \hline \\ \hline \\ \hline \end{array}$ ${}_2\text{He}^3$	$\begin{array}{ c c c } \hline p & n & n \\ \hline \\ \hline \\ \hline \end{array}$ ${}_1\text{H}^3$	$\begin{array}{ c c c } \hline n & n & n \\ \hline \\ \hline \\ \hline \end{array}$ ${}_0n^3$
T	$\frac{1}{2}$	$\frac{1}{2}$	$\frac{3}{2}$	$\frac{3}{2}$	$\frac{3}{2}$	$\frac{3}{2}$
M_T	$\frac{1}{2}$	$-\frac{1}{2}$	$\frac{3}{2}$	$\frac{1}{2}$	$-\frac{1}{2}$	$-\frac{3}{2}$
$\frac{Z}{N}$	2	$\frac{1}{2}$	∞	2	$\frac{1}{2}$	0

A = 4 Isobar				
	$\begin{array}{ c c } \hline p & p \\ \hline n & n \\ \hline \end{array}$ ${}_2\text{He}^4$	$\begin{array}{ c c c } \hline p & p & p \\ \hline n & & \\ \hline \end{array}$ ${}_3\text{Li}^4$	$\begin{array}{ c c c } \hline p & p & n \\ \hline n & & \\ \hline \end{array}$ ${}_2\text{He}^4$	$\begin{array}{ c c c } \hline p & n & n \\ \hline n & & \\ \hline \end{array}$ ${}_1\text{H}^4$
T	0	1	1	1
M_T	0	1	0	-1
$\frac{Z}{N}$	1	3	1	$\frac{1}{3}$

Fig. 11.2. Isospin Gel'fand states to A=4. N is the number of neutrons

11.4. The $(j)^A$ Configurations

11.4.1. Introduction

A useful chain for the $(j)^A$ configurations of light nuclei is

$$U(2j+1) \supset Sp(2j+1) \supset SU(2) \quad (11.7)$$

where $Sp(2j+1)$ is a symplectic group for which the quantum numbers are v (seniority) and t (reduced isospin). The spectrum for this U-chain is

$$E(T, v, t, J) = \alpha T(T+1) + \beta(v(4j+8-v) - t(t+1)) + \gamma J(J+1) \quad (11.8)$$

Note that the signs are the opposite of the atomic U chain.

11.4.2. The $j = 3/2$ Configurations

The $1p_{3/2}$ is the lowest energy orbital outside the $1s$ core. So $M = 2j+1 = 4$. We take for the U chain

$$U(4) \supset Sp(4) \supset SU(2) \quad (11.9)$$

The decomposition of the irreducible representations are listed in Fig. 11.3 together with the labels of the ground states.

A	$[\lambda]$	(v, t)	T	J	Ground State $\{T, J\}$
1	[1]	(1, 1/2)	1/2	3/2	--
2	[2, 0] [1, 1]	(2, 0)	0	1, 3	$Li^6\{0, 1\}$
		(0, 0)	1	0	
		(2, 1)	1	2	
3	[2, 1]	(1, 1/2)	1/2	3/2	$Li^7, B^7\{1/2, 3/2\}$
		(3, 1/2)	1/2	1/2, 5/2, 7/2	
4	$[1^3]$	(1, 1/2)	3/2	3/2	$Be^8\{0, 0\}$
	$[2^2]$	(0, 0)	0	0	
		(2, 1)	0	2	
		(4, 1)	0	2, 4	
	$[2, 1^2]$	(2, 0)	1	1, 3	$Li^8\{1, 2\}$
		(2, 1)	1	2	
	$[1^4]$	(0, 0)	2	0	

Fig. 11.3. The decomposition of the irreducible spaces and the ground states for $(3/2)^A$

11.5. The Quark Structure of Baryons

11.5.1. Introduction

Nuclei are constructed from protons and neutrons. The proton and the neutron are members of a class of elementary particles called baryons (the heavy ones) which are constructed from quarks. The quark orbital is the product

$$|q\rangle = |\phi\rangle|\sigma\rangle|\chi\rangle \quad (11.10)$$

where $|\phi\rangle$ is a flavor orbital whose space is

$$\phi: \{ |u\rangle \text{ (up)}, |d\rangle \text{ (down)}, |s\rangle \text{ (strange)} \} \quad (11.11)$$

where $|\sigma\rangle$ is an ordinary spin orbital whose space is

$$\sigma: \{ |\alpha\rangle, |\beta\rangle \} \quad (11.12)$$


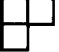

and where $|\chi\rangle$ is a color orbital whose space is

$$\chi: \{ |R\rangle \text{ (red)}, |G\rangle \text{ (green)}, |B\rangle \text{ (blue)} \} \quad (11.13)$$

In Section 11.5.2 we give the Gel'fand structures of the flavor states which serve to identify the several baryons and in Section 11.5.3 we treat the freeon dynamics of nuclei.

11.5.2. The Flavor Gel'fand Structures.

We use three-particle Young diagrams for the construction of flavor Gel'fand states:

$[\lambda]$	YD $[\lambda]$	Spin
$[1^3]$		excluded (See Section 11.5.3)
$[2,1]$		octet
$[3]$		decuplet

The flavor Gel'fand states for the octet and the decuplet spaces are shown as follows.

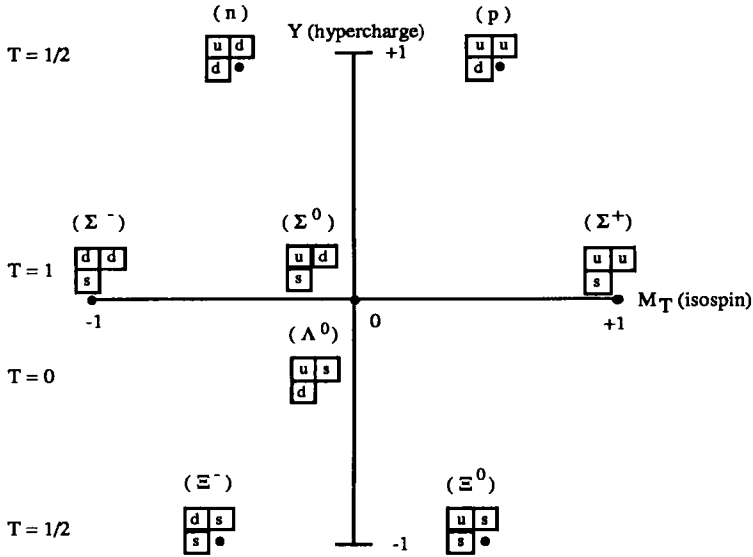


Fig. 11.4. The octet flavor Gelfand states ($J=1/2$)

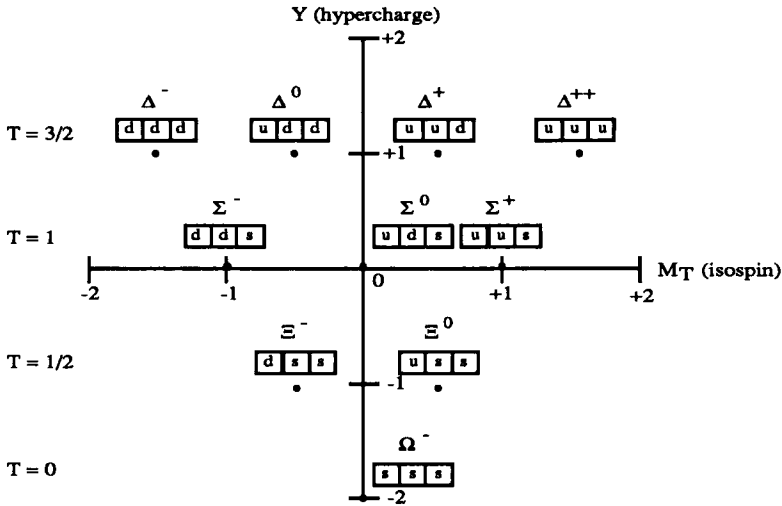

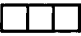


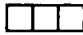

Fig. 11.5. The decuplet flavor Gelfand states ($J=3/2$)

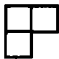

11.6. Nuclear Freeon Dynamics


The flavor and the ordinary orbitals are inert and it is the color orbital which carries the freeon dynamics in the same ways as the freeon (spatial) orbitals carry the dynamics for electronic systems. It should be noted that the two basic field theories are quantum electrodynamics (QED) and quantum chromodynamics (QCD). The color force is also an exchange force in which the several colors are exchanged.



The three quark color states are restricted to the color singlet, , which together with the fermion antisymmetry principle leads to requirement that the flavor-ordinary spin space must be totally symmetric; i. e., . This, in turn, leads to the following relationships between the flavor space and the ordinary spin space:

i) The Decuplet Space. The  flavor space \Rightarrow the  ordinary spin space $\Rightarrow S = J = 3/2$

ii) The Octet Space. The  flavor space \Rightarrow the  ordinary spin space $\Rightarrow S = J = 1/2$

iii) The Singlet Space. The  flavor space \Rightarrow no ordinary spin space and is therefor excluded.

This unitary-group calculus accounts for all the observed baryons.

12. SUMMARY AND CONCLUSIONS

We have shown that the unitary group provides an organizing principle for much of matter - atoms, molecules, solids, nuclei and baryons. Note the particle number, N , is a unitary group-quantum number. Thus, the Greek concept of pure form, i.e. the group, is extended to include substance. The $N = 0$ space is a space without particle-number and hence without substance. The group theoretical history of our universe is shown in Fig. 12.1.

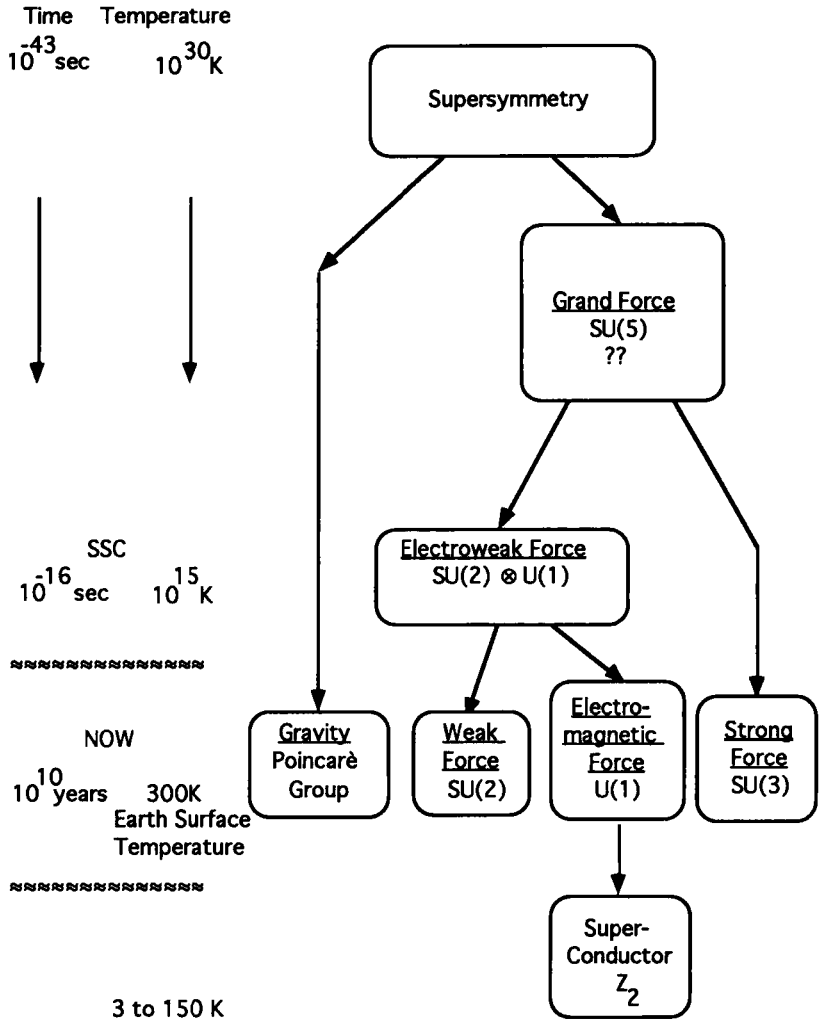


Fig. 12.1. Group theoretical history of the universe

The modern theory of creation begins at Planck time (10^{-43} seconds) when the universe was very hot and supersymmetric. As the universe cooled supersymmetry was spontaneously-broken into the Poincaré symmetry (gravity) and the grand symmetry, SU(5) (the grand force). On further cooling SU(5) was spontaneously broken into the electroweak force $SU(2) \otimes U(1)$ and the strong force

SU(3) which holds quarks and nucleons together. On further cooling SU(2)⊗U(1) is spontaneously-broken into SU(2) (the weak force which causes beta decay) and U(1) the electromagnetic force. On the cooling of certain solids the local U(1) symmetry of Maxwell's equations is spontaneously broken and superconductivity occurs. Clearly God is a skilled group-theorist!

Finally we should ask the question: Why is our universe so well-described by group theory? My best guess is that it is an important aspect of some general principle of least action.

Electron freeon dynamics, which is also based on group theory, claims the following

- 1) The unitary group is sufficient for light-atom, many-electron systems
- 2) Slater determinants and second-quantization constitute a poor-man's group theory which is "ungodly" and leads to the nefarious spin paradigm.
- 3) Freeon Gel'fand diagrams provide primitive patterns of understanding which are superior to and which should replace spin arrows as the primitive patterns of understanding of N particle systems.
- 4) The freeon unitary group formulation provides fast methods of computation in configuration interaction (CI) calculations for freeon states (pure eigenstates of the spin) [22,23].

13. DEDICATION AND ACKNOWLEDGMENTS

I respectfully dedicate, this my third contribution to *Advances*, to Per-Olov Löwdin, a good friend and a staunch defender of freeon dynamics. In addition, I am happy to acknowledge the technical support of Dr. Loudon Campbell and the financial support of the Robert A. Welch Foundation of Houston, Texas.

REFERENCES

1. F.A. Matsen, *Adv. Quantum Chem.* **1**, 59 (1964).
2. R. McWeeny, *Methods of Molecular Quantum Mechanics.*, Academic Press (1992)
3. F.A. Matsen, *Adv. Quantum Chem.* **11**, 233 (1978).
4. F.A. Matsen, *J. Molecular Structure.* **259**, 65 (1992).
5. F.A. Matsen and R. Pauncz, *The Unitary Group in Quantum Chemistry*, Elsevier (1986).
6. M.A. Fox and F.A. Matsen, *J. Chem. Ed.* **62**, 367, 477, 551 (1985)
7. H.R. Henze and C.M. Blair, *J. Am. Chem. Soc.* **53**, 3042-3046 (1931) and **55**, 680-686 (1933).
8. D.J. Klein, *et. al.* , *J. Chem. Phys.* **101**, 5281, 5641 (1994)
9. T. Yamanouchi, *Proc. Phys. Math. Soc. Jap.* **19**, 436 (1937)
10. M. Kotani, A. Amemiya, E. Ishiguro, and T. Kimura, *Tables of Molecular Integrals*, Maruzen, Tokyo (1963)
11. I.G. Kaplan, *Symmetry of Many-Electron Systems*, Academic Press 1975
12. J. Paldus and X. Li, *Group Theory in Physics, AIP Conference Proceedings*, **216**, 159 (1991).
13. F.J. Dyson, *Phys., Rev.* **102** 1217 (1956).
14. F.A. Matsen, J. E. Sugar, and J. M. Picone, *Int J. Quantum Chem.* **7**, 1063 (1973).
15. C. Kittel and H.B.Shore, *Phys. Rev.* **138**, 1165 (1963)
16. J. Bardeen, L. N. Cooper, and J. R. Schrieffer, *Phys. Rev.* **108**, 1175 (1955).
17. J. R. Schrieffer, X. G. Wen, and S. C. Zhang, *Phys. Rev.*, **B39**, 11663 (1989)
18. P. W. Anderson, *Science* **235**, 1196 (1987); P. W. Anderson, G. Baskaran, Z. Zhou and T. Hsu, *Phys. Rev. Lett.* **58**, 2790 (1987).
19. F. A. Matsen, *J. Phys. Chem.*, (submitted).
20. J. K. Burdett, *J. Solid State Chem.* **100**, 393 (1992); *Inorg. Chem.* **32**, 3915 (1993).
21. F. A. Matsen, *Group Theory in Physics, AIP Conference Proceedings* **216**, 131 (1991).
22. I. Shavitt, in *The Unitary Group for the Evaluation of Electronic Energy Matrix Elements*, J. Hinze, Ed. (Springer-Verlag, Berlin, 1981), p. 51.
23. L.L. Campbell, *Int. J. Quant. Chem.* **41**, 187 (1992).

RESPONSE THEORY AND CALCULATIONS OF SPIN-ORBIT COUPLING PHENOMENA IN MOLECULES

Hans Ågren, Olav Vahtras and Boris Minaev

Institute of Physics and Measurement Technology
Linköping University
S-58183, Linköping, Sweden

1 Abstract

We review response theory and calculations of molecular properties involving spin-orbit interactions. The spin-orbit coupling is evaluated for reference states described by single- or multi-configuration self-consistent field wave functions. The calculations of spin-orbit related properties rest on the formalism of linear and quadratic response functions for singlet and triplet perturbations when no permutational symmetry in the two-electron operators is assumed and from which various triplet as well as singlet response properties are derived. The spin-orbit coupling matrix elements between singlet and triplet states are evaluated as residues of (multi-configuration) linear response functions, and are therefore automatically determined between orthogonal and non-interacting states. Spin-forbidden radiative transition intensities and lifetimes are determined from the spin-orbit coupling induced dipole transitions between two electronic states of different multiplicity and are obtained as residues of quadratic response functions. The potential of the theory and its range of applications is illustrated by a selection of recent investigations covering different molecular phenomena. The applications include second-order energy contributions, intensity rearrangement in electron spectra, calculation of predissociative lifetimes of dicationic states, assignment of triplet bands in absorption spectra, intersystem crossings and reactivity, external heavy atom effects on S-T transitions, phosphorescence spectra and radiative lifetimes of triplet states. We give an outlook on spin-orbit interaction induced phenomena in extended systems and on applications to general spin catalysis phenomena.

Contents

1 Abstract

2 Introduction

3 Theory

- I General
- II Multiconfiguration response functions
- III Implementation
- IV Spin-orbit response properties

4 Computation of Spin-orbit Response Functions

- I Background
- II Computational features
- III Test of response theory SOC calculation

5 Miscellaneous Applications

- I Second order spin-orbit coupling contribution to the total energy
- II Intensity modulation of electronic spectra due to spin-orbit coupling . .
- III Spin-orbit induced dynamic properties
- IV Intersystem crossings and reactivity
- V Assignments of optical and ultraviolet spectra

6 Selected Singlet-Triplet Transitions

- I Formaldehyde $^3A'' \rightarrow ^1A'$ emission
- II Singlet-Triplet Transitions in diatomics
 - II-A N_2 : The Vegard-Kaplan system
 - II-B N_2 : The $W^3\Delta_u \leftarrow X^1\Sigma_g^+$ Saum-Benesch system
 - II-C N_2 : The $B'^3\Sigma_u^- - X^1\Sigma_g^+$ Ogawa-Tanaka-Wilkinson system

II-D	N_2 : The $C^3\Pi_u \leftarrow X^1\Sigma_g^+$ Tanaka system
II-E	CO: The Cameron band
II-F	Comments on diatomic calculations
III	Conjugated Hydrocarbons
III-A	Ethylene
III-B	Butadiene
III-C	Hexatriene
III-D	Comparison of singlet-triplet transition intensities in polyenes . .

7 Phosphorescence of Aromatic Compounds

I	Benzene
I-A	History of the benzene phosphorescence problem
I-B	Vibronic structure of benzene phosphorescence in the response formalism
II	Naphthalene
III	Comparison between naphthalene, benzene and polyenes
IV	Nitrogen substituted heterocycles
IV-A	Azabenzenes
IV-B	Azanaphthalenes

8 The external heavy atom effect on S-T transitions

9 Outlook

I	Spin Catalysis
II	Extended Systems

2 Introduction

Although the overwhelming part of applications of quantum methods on molecules still are based on the Born-Oppenheimer, non-relativistic, Hamiltonian picture, one has increasingly realized the important role of spin-orbit coupling for the interpretation of a number of experiments referring to spectroscopy, reactivity and to catalysis in general. Spectroscopic assignments have traditionally been carried out in terms of spatial- and spin-symmetry of states, intensity distributions and fine structures. These applications have referred to a number of spectroscopies using photons, electrons or charged ions as exciting agents, in more recent times also high-resolution coincidence techniques involving photons, photoions and electrons in various combinations. With these techniques detailed information is gained on fine structures, potential energy surfaces, finite lifetimes. Much of this information, e.g. finiteness of the lifetimes, result from intersystem and non-adiabatic crossings that are abundant in molecules and molecular ions. This abundance of state crossings can be derived from the compact nature of the potentials and a high density of states with different multiplicity. For ionic systems, for example, a bond breaking Coulomb repulsion gives sharp variations of the potentials with respect to intermolecular distance. The manifold of states of different multiplicities may thus be grossly intermixed already for low-lying optical excitations, and even more so for charged molecular species. In the absence of strict selection rules or even propensity rules this leads to complex spectra rich of structure. Due to these features one can anticipate intensity borrowing to occur as an effect of spin-orbit coupling (SOC), non-adiabatic coupling or of other smaller coupling terms in the Hamiltonian not included in the conventional non-relativistic Born-Oppenheimer (BO) treatment. Such couplings may lead to intensity rearrangement, and in particular, they may serve as sources of intensity for states that are forbidden by normal selection rules.

It is clear that with a high density of states the theoretical investigations of electronic spectra must sometimes go beyond a traditional BO and non-relativistic analysis that only refers to energy criteria, and that in the description of spectroscopic properties smaller terms of the Hamiltonian must be accounted for. The major corrections to the BO electrostatic Hamiltonian is the non-adiabatic coupling induced by the nuclear kinetic energy operator, and the electronic SOC treated in the present review.

For many types of electron spectroscopies there are still comparatively few studies of SOC effects in molecules in contrast to atoms, see, e.g., [1, 2, 3, 4, 5, 6, 7] and references therein. This can probably be referred to complexities in the molecular analysis due to the extra vibrational and rotational degrees of freedom, increased role of many-body interaction, interference and break-down effects in the spectra, but can also be referred to the more difficult nature of the spin-orbit coupling itself in polyatomic species. Modern *ab initio* formulations, as, e.g., spin-orbit response theory [8] reviewed here, have made such investigations possible using the full Breit-Pauli spin-orbit operator.

In the present work we review a recent development sorting under the broad con-

text of response theory methods, namely response functions for properties that involve spin-orbit interaction in molecules, and illustrate the potential of this development with applications within the field of molecular spectroscopy and reactivity. This development fall under the general branch of quantum methods that obtain linear and non-linear properties using variational type wave functions, that is the random phase approximation (RPA, time-dependent Hartree-Fock (TDHF)) and the multi-configuration response methods [9, 10, 11]. These methods are based on non-correlated, self-consistent field (SCF), and correlated, multi-configuration self-consistent field (MCSCF) reference wave functions, respectively. One has recently witnessed a rather drastic development of the response theory methods for calculations of different molecular properties, be it electric or magnetic, time-independent or time-dependent, linear or non-linear properties [12, 13, 14, 15, 16, 17, 18, 19, 10, 11]. This development has been documented in a number of original and review-type articles, see, for example, works of Olsen and Jørgensen [15], Pickup [20], Fowler [21], Oddershede [22] and Luo *et al.* [23]. Although spin-orbit coupling phenomena is just one out of several categories of properties towards which response theory has been diversified lately, it has proven particularly fruitful for molecular applications as we intend to demonstrate with the present review.

Also outside the field of spectroscopy there is a great potential for applications of SOC response theory. One can here refer to reactivity of radicals, biradicals and to spin catalysis phenomena in general. The term *spin catalysis* denotes a large range of phenomena for which the overcoming of spin-forbiddness in a chemical reaction and an increase of rate constants can be introduced by interaction with additional substances. The majority of stable chemical products are diamagnetic; they have a singlet ground state with the excited triplet state well separated in energy. However, in many situations, for example in predissociation of diatomic species or in the vicinity of activated transition states in metal catalytic complexes where chemical bonds grow weak, the S-T crossing occurs and intersystem crossings can compete with other chemical processes. The state of higher multiplicity has often an additional stabilization by exchange interaction in the transition region and lower the activation barrier. The possibility of intersystem crossings (ISC) must be taken into account for a large number of chemical reactions because the ISC can be crucial for the determination of the reaction rates and paths. A lot of reactions can thus be explained by the account of S-T transitions in intermediate diradicals, induced by SOC [24, 25, 26]. The S-T transitions can be caused by perturbations of a catalytic nature (SOC, paramagnetic exchange) and contribute to the lowering of activation energy and the increase in the reaction rate constant. It is obvious that the role of an ISC as an intermediate step of chemical rearrangement is underestimated in contemporary chemistry and catalysis.

In the present work we illustrate the potential of response theory for SOC in the areas briefly referred to above and review a set of recent applications that represent different physical aspects. We first give, in the next section, those aspects of linear and quadratic response theory that directly relate to spin-orbit coupling phenomena. We refer to the original work of Olsen and Jørgensen [15] and to the recent review by Luo *et al.* [23] for a general account of basic aspects of the response theory employed, but not

described, here. The following section, section 4, reviews some of the computational performances and the requirements, like basis sets and active space expansions. Section 5 reviews the selection of different applications: Section 5.I describes the second order energy contribution of the spin-orbit interaction illustrated by an application on the potential energy curve of Cr_2 ; section 5.II describes first- and second-order approaches for calculating the SOC between a full manifold of states, and illustrates the use of this for predicting intensity rearrangement in electronic spectra. In section 5.III the calculated SOC are further used to solve the dynamical equations (multi-channel Schrödinger equation) in order to determine the predissociative lifetimes of such states. In section 5.IV it is shown how spin-orbit response calculations can be used to estimate intersystem crossings in chemical reactions. Section 5.V illustrates the potential of spin-orbit response theory for assignment problems in optical absorption spectra, and show how such calculations have made it possible to make a completely new assignment of the origin of the lowest lying absorption band in ozone. The use of quadratic response theory involving simultaneous dipole and SOC to determine singlet-triplet absorption and phosphorescence moments and triplet state radiative lifetimes is illustrated in section 6 with calculations on a large variety of small and big molecules. Section 7 is devoted to phosphorescence of aromatic compounds, such as benzene, naphthalene and the nitrogen substituted heterocycles; azabenzenes and azanaphthalenes. With the last application, given in section 8, we discuss a related problem, namely the role and the interpretation of the internal and, in particular, the external heavy atom effect on S-T transitions. Finally, in section 9 we give an outlook for possible future developments emphasizing spin catalysis and applications on extended systems.

3 Theory

I General

There are different approaches to calculating physical and chemical properties from Rayleigh-Schrödinger perturbation theory. A straightforward formulation, one that is usually presented in textbooks, is to express the results of perturbation theory in terms of summations over excited states. Consider *e.g.* a system described by the Hamiltonian H_0 , with the energy eigenvalue E_0 corresponding the ground state $|0\rangle$. The second-order energy correction due to a perturbation V is

$$E^{(2)} = \sum_{k>0} \frac{|\langle 0|V|k\rangle|^2}{E_0 - E_k}. \quad (1)$$

The main difficulty with this formulation is that it requires complete knowledge of the excited states, so one is forced to pray for rapid convergence and truncate the series after the first few excited states. A more general form of Eq. (1) is [27]

$$E^{(2)} = \langle 0|VR(E_0)V|0\rangle \quad (2)$$

where R is a resolvent operator involving the inverse of the Hamiltonian,

$$R(E) = (E - H_0)^{-1}. \quad (3)$$

The resolvent operator as a function of E has poles at the eigenvalues of H_0 . Strictly speaking, for the expression in Eq. (2) to be meaningful, the singular component of the resolvent must be removed, but we choose not to clutter the notation with formalism that is unnecessary for our purposes. We note that Eq. (1) can be derived from Eq. (2) if we insert a resolution of the identity (and removing the ground state) on each side of the resolvent,

$$R(E) = \sum_k |k\rangle\langle k| (E - H_0)^{-1} \sum_l |l\rangle\langle l| = \sum_k \frac{|k\rangle\langle k|}{E - E_k}. \quad (4)$$

If the sum over states is incomplete Eq. (4) is an *outer projection* of the resolvent R onto the subspace spanned by the states $|k\rangle$.

Another approach to perturbation theory is response functions, which is the subject of this paper. The basis for all response function methods is an *inner projection* [28] of the resolvent,

$$R(E) = |\mathbf{k}\rangle\langle\mathbf{k}|E - H_0|\mathbf{k}\rangle^{-1}\langle\mathbf{k}| \quad (5)$$

where $|\mathbf{k}\rangle$ are the states $|k\rangle$ collected in a row matrix and $\langle\mathbf{k}|$ the corresponding column matrix. If the functions k indeed are the eigenstates of H_0 , then Eqs. (4) and (5) are identical. There is a clear advantage with the inner projection scheme. We can let $|\mathbf{k}\rangle$ be some other basis than the one formed by the energy eigenfunctions. In that case the evaluation of the second order energy in (one) is a two-step procedure; solve the linear system of equation

$$\langle\mathbf{k}|E_0 - H_0|\mathbf{k}\rangle\mathbf{N} = \langle\mathbf{k}|V|0\rangle \quad (6)$$

and form

$$E^{(2)} = \langle 0|V|\mathbf{k}\rangle\mathbf{N}. \quad (7)$$

The summation over excited states is effectively replaced by solving a linear system of equations, and this is done without prior knowledge of the excited states.

Taking these introductory comments as a motivation, we shall turn to the formalism of response theory. Response theory is first of all a way of formulating time-dependent perturbation theory. In fact, time-dependent and time-independent perturbation theory are treated on equal footing, the latter being a special case of the former. As the name implies, response functions describe how a property of a system responds to an external perturbation. If initially, we have a system in the state $|0\rangle$ (the reference state), as a weak perturbation $V(t)$ is turned on, the average value of an operator A will develop in time according to

$$\langle A \rangle = \langle A \rangle_0 + \langle A \rangle_1 + \langle A \rangle_2 \cdots, \quad (8)$$

where $\langle A \rangle_0$ is the average value with respect to the reference state, and $\langle A \rangle_1$ and $\langle A \rangle_2$ the first and second-order responses respectively. These may be written in their Fourier

representations,

$$\langle A \rangle_1 = \int d\omega_1 \langle \langle A; V \rangle \rangle_{\omega_1} e^{-i\omega_1 t + \epsilon t}, \quad (9)$$

and

$$\langle A \rangle_2 = \frac{1}{2} \int \int d\omega_1 d\omega_2 \langle \langle A; V, V \rangle \rangle_{\omega_1, \omega_2} e^{-i\omega_1 t - i\omega_2 t + 2\epsilon t}. \quad (10)$$

Eq. (9) defines the linear response function

$$\langle \langle A; V \rangle \rangle_{\omega_1} = \left\langle \frac{AV_{\omega_1}}{\omega_1 - \hat{\omega} + i\epsilon} - \frac{V_{\omega_1}A}{\omega_1 + \hat{\omega} + i\epsilon} \right\rangle \quad (11)$$

where $\hat{\omega} = H_0 - E_0$ and we use the notation

$$\frac{AV}{\omega - \hat{\omega}} \equiv A(\omega - \hat{\omega})^{-1}V \quad (12)$$

The linear response function in Eq. (11) has the same structure as the second-order energy expression in Eq. (2) and we note that for $A = V$ and $\omega_1 = 0$ they are identical, except for a factor of two. Similarly, Eq. (10) defines the quadratic response function

$$\begin{aligned} \langle \langle A; V, V \rangle \rangle_{\omega_1, \omega_2} &= \left\langle \frac{AV_{\omega_1}V_{\omega_2}}{(\omega_1 + \omega_2 - \hat{\omega} + 2i\epsilon)(\omega_2 - \hat{\omega} + i\epsilon)} \right\rangle \\ &+ \left\langle \frac{V_{\omega_2}V_{\omega_1}A}{(\omega_2 + \hat{\omega} + i\epsilon)(\omega_1 + \omega_2 + \hat{\omega} + 2i\epsilon)} \right\rangle \\ &- \left\langle \frac{V_{\omega_1}AV_{\omega_2}}{(\omega_1 + \hat{\omega} + i\epsilon)(\omega_2 - \hat{\omega} + i\epsilon)} \right\rangle + P_{12} \end{aligned} \quad (13)$$

where P_{12} is a permutation that denotes symmetrization with respect to frequencies ω_1 and ω_2 . We note that by taking the residue of the quadratic response function at an excitation energy ω_k , one obtains a second-order transition moment, *i.e.* a transition matrix element of an operator A between the ground state and the excited state $|k\rangle$ that is induced by the perturbation V . The double residue of the quadratic response function at two excitation energies, ω_f and $-\omega_g$ gives a matrix element between the corresponding excited states, $\langle g|A|k\rangle$.

II Multiconfiguration response functions

In multiconfiguration response theory, the space of excited states, the orthogonal complement of the reference state, is described in terms of operators acting on the reference state; orbital excitation operators

$$q_k^\dagger = E_{rs}^\pm = a_{r\alpha}^\dagger a_{s\alpha} \pm a_{r\beta}^\dagger a_{s\beta}, \quad r > s \quad (14)$$

and state transfer operators

$$R_j^\dagger = |j\rangle\langle 0| \quad (15)$$

We consider either singlet perturbations or triplet perturbations, which in Eq. (14) correspond to the $+$ and $-$ signs, respectively. In Eq. (15) the same distinction corresponds to interpreting $|k\rangle$ as a singlet or a triplet configuration state function (CSF).

The matrices and vectors of this formalism refer to the basis which is formed by the operators Eqs. (14) and (15) together with their deexcitation (hermitean conjugate) counterparts,

$$T = \begin{pmatrix} q^\dagger & R^\dagger & q & R \end{pmatrix} \quad (16)$$

and a general vector is written

$$N = \begin{pmatrix} \kappa \\ S \\ \kappa' \\ S' \end{pmatrix} \quad (17)$$

where κ refers to orbital excitation amplitudes and the S to configuration amplitudes.

The response functions in the multiconfiguration formalism are indeed complicated but their derivation is straightforward, only tedious. For detailed derivations we refer to Ref. [15]. A recent review on the calculation of hyperpolarizabilities [23] may also serve as a reference for the response formalism and its computer implementations. The present review must however address the particular complications pertaining to spin-dependent perturbations.

The linear response function is given by

$$\langle\langle A; V \rangle\rangle_{\omega_1} = -A^{[1]}(E^{[2]} - \omega_1 S^{[2]})^{-1}V_{\omega_1}^{[1]} \quad (18)$$

where $A^{[1]}$ and $V^{[1]}$ are gradient-type vectors,

$$A_j^{[1]} = \langle 0|[A, T_j]|0\rangle \quad (19)$$

$$V_j^{[1]} = \langle 0|[T_j^\dagger, V]|0\rangle \quad (20)$$

and $E^{[2]}$ and $S^{[2]}$ are hessian and metric matrices given by,

$$E_{jk}^{[2]} = - \begin{pmatrix} \langle 0|[T_{oj}^\dagger, [T_{ok}, H_0]]|0\rangle & \langle 0|[T_{ck}, [T_{oj}^\dagger, H_0]]|0\rangle \\ \langle 0|[T_{cj}^\dagger, [T_{ok}, H_0]]|0\rangle & \langle 0|[T_{cj}^\dagger, [T_{ck}, H_0]]|0\rangle \end{pmatrix} \quad (21)$$

and

$$S^{[2]} = \langle 0|[T^\dagger, T]|0\rangle \quad (22)$$

respectively, where we have decomposed the operator basis T into orbital and configuration parts, T_o and T_c (the coupling between the two sets becomes more intricate for higher orders matrices).

We would like to stress the similarity between Eqs. (5) and (18). The main difference is that the poles of the linear response function are excitation energies rather than energy eigenvalues (*c.f.* Eq. (11)) but in both cases, the residues correspond to transition moments between the ground state and excited states. The two-step procedure for evaluating the linear response function is now (*c.f.* Eqs. (6) and (7)); solve

$$(E^{[2]} - \omega S^{[2]})N_\omega^V = V_\omega^{[1]} \quad (23)$$

and form

$$\langle\langle A; V \rangle\rangle_{\omega} = -A^{[1]}N_{\omega}^V \quad (24)$$

The quadratic response function is given by

$$\begin{aligned} \langle\langle A; V, V \rangle\rangle_{\omega_1, \omega_2} &= N_{\omega_1 + \omega_2}^A (E^{[3]} - \omega_1 S^{[3]}) N_{\omega_1}^V N_{\omega_2}^V \\ &- N_{\omega_1 + \omega_2}^A V_{\omega_1}^{[2]} N_{\omega_2}^V \\ &+ A^{[2]} N_{\omega_1}^V N_{\omega_2}^V + P_{12} \end{aligned} \quad (25)$$

where

$$N_{\omega}^A = A^{[1]}(E^{[2]} - \omega S^{[2]})^{-1} \quad (26)$$

$$N_{\omega}^V = (E^{[2]} - \omega S^{[2]})^{-1} V_{\omega}^{[1]} \quad (27)$$

and where $E^{[3]}$ is the MCSCF third-order energy derivative matrix,

$$E_{jkl}^{[3]} = \begin{pmatrix} \frac{1}{2}\langle 0|[T_{oj}^{\dagger}, [T_{ok}, [T_{ol}, H_0]]]0\rangle & \langle 0|[T_{ck}, [T_{oj}^{\dagger}, [T_{ol}, H_0]]]0\rangle & \frac{1}{2}\langle 0|[T_{ck}, [T_{cl}, [T_{oj}^{\dagger}, H_0]]]0\rangle \\ \frac{1}{2}\langle 0|[T_{cj}^{\dagger}, [T_{ok}, [T_{ol}, H_0]]]0\rangle & \langle 0|[T_{cj}^{\dagger}, [T_{ck}, [T_{ol}, H_0]]]0\rangle & 0 \end{pmatrix} \quad (28)$$

$S^{[3]}$ a third-order generalization of the metric,

$$S_{jkl}^{[3]} = \begin{pmatrix} -\frac{1}{2}\langle 0|[T_{oj}^{\dagger}, [T_{ol}, T_{ok}]]0\rangle & -\langle 0|[T_{cl}, [T_{oj}^{\dagger}, T_{ok}]]0\rangle & -\langle 0|[T_{cl}, [T_{oj}^{\dagger}, T_{ck}]]0\rangle \\ -\frac{1}{2}\langle 0|[T_{cj}^{\dagger}, [T_{ol}, T_{ok}]]0\rangle & -\langle 0|[T_{cj}^{\dagger}, [T_{cl}, T_{ok}]]0\rangle & 0 \end{pmatrix} \quad (29)$$

and where $V^{[2]}$ and $A^{[2]}$ are Hessian type matrices for the operators V and A respectively, with $V^{[2]}$ defined identically as in Eq. (21) and

$$A_{jk}^{[2]} = (\frac{1}{2}\langle 0|[T_{oj}, [T_{ok}, A]]0\rangle \quad \langle 0|[T_{cj}, [T_{ok}, A]]0\rangle \quad \frac{1}{2}\langle 0|[T_{cj}, [T_{ck}, A]]0\rangle) \quad (30)$$

P_{12} denotes as before the symmetrization in frequencies ω_1 and ω_2 .

III Implementation

The calculation of molecular properties using response function theory incorporates the solution of two types of linear equations, the linear response (LR) eigenvalue equation for excitation energies and transition properties, and the solution of a linear system of equations, for second and higher order response properties. The eigenvalue equation, if solved completely, gives n excitation energies, n being the dimensionality of the matrices. This would be a very impractical (if not impossible) approach for large dimensions and furthermore, only the few lowest eigenvalues are of physical interest. Analogous problems for large-scale CI- and MCSCF-calculations has spurred the development of iterative algorithms, where the equation is projected on a reduced space of trial vectors (Davidson [29]) and direct integral-driven methods (Roos [30] and Jensen and Ågren [31]) where the full matrices are never needed explicitly.

The solution of Eq. (23) is thus carried out by forming the linear transformations of trial vectors directly without constructing $E^{[2]}$ or $S^{[2]}$ explicitly,

$$E_{jk}^{[2]} N_k = - \begin{pmatrix} \langle 0 | [q_j, H_0(\kappa)] | 0 \rangle \\ \langle j | H_0(\kappa) | 0 \rangle \\ \langle 0 | [q_j^\dagger, H_0(\kappa)] | 0 \rangle \\ - \langle 0 | H_0(\kappa) | j \rangle \end{pmatrix} - \langle H_0 \rangle \begin{pmatrix} 0 \\ S_j \\ 0 \\ S'_j \end{pmatrix} - \begin{pmatrix} \langle 0^L | [q_j, H_0] | 0 \rangle + \langle 0 | [q_j, H_0] | 0^R \rangle \\ \langle j | H_0 | 0 \rangle^R \\ \langle 0^L | [q_j^\dagger, H_0] | 0 \rangle + \langle 0 | [q_j^\dagger, H_0] | 0^R \rangle \\ - \langle 0 |^L H_0 | j \rangle \end{pmatrix} \quad (31)$$

where the so-called one-index transformed Hamiltonian is defined by

$$H_0(\kappa) = [\kappa, H_0] \quad (32)$$

$$\kappa = \sum_{rs} \kappa_{rs} E_{rs}^\pm \quad (33)$$

and the modified states by

$$|0^R\rangle = - \sum_n S_n |n\rangle \quad (34)$$

$$\langle 0^L| = \sum_n S'_n \langle n| \quad (35)$$

The advantage now is that Eq. (31) has the same structure as Eq. (20), namely that of a gradient, the difference being that we have modified operators and modified states. The same features can be attributed the linear transformation of a trial vector with the metric,

$$S_{jk}^{[2]} N_k = - \begin{pmatrix} \langle 0 | [q_j, \kappa] | 0 \rangle \\ \langle j | \kappa | 0 \rangle \\ \langle 0 | [q_j^\dagger, \kappa] | 0 \rangle \\ - \langle 0 | \kappa | j \rangle \end{pmatrix} - \begin{pmatrix} \langle 0^L | q_j | 0 \rangle + \langle 0 | q_j | 0^R \rangle \\ -S_j \\ \langle 0^L | q_j^\dagger | 0 \rangle + \langle 0 | q_j^\dagger | 0^R \rangle \\ S'_j \end{pmatrix} \quad (36)$$

All formulae until now are independent of the spin character of the perturbation. The spin complications enter at the level of one-index transformations. If κ has been derived from an operator with spin, i.e. if it is given by Eq. (33) with the minus sign, the one-index transformation will change the spin properties of the Hamiltonian. In this case the transformed Hamiltonian is

$$H_0(\kappa) = h_{pq}^- E_{pq}^- + \frac{1}{2} (\widetilde{pq} | rs) e_{pqrs}^{-+} + \frac{1}{2} (pq | \widetilde{rs}) e_{pqrs}^{+-} \quad (37)$$

and the one-index transformed integrals are

$$h_{\widetilde{pq}}^- = \kappa_{pr} h_{rs} - h_{pr} \kappa_{rs} \quad (38)$$

$$(\widetilde{pq} | rs) = \kappa_{pt} (tq | rs) - (pt | rs) \kappa_{ts} \quad (39)$$

$$(pq | \widetilde{rs}) = \kappa_{rt} (pq | ts) - (pq | rt) \kappa_{ts} \quad (40)$$

For singlet perturbations we need not consider the left (39) and right (40) transformations separately, we may add these to define an integral where all indices are transformed once, since the corresponding operators (37) are the same.

From the discussion above it is clear that for the evaluation of quadratic response functions it is desirable to contract two indices of $E^{[3]}$ with two vectors simultaneously, giving

$$\begin{aligned}
 E_{jkl}^{[3]1} N_k^2 N_l &= \frac{1}{2} \begin{pmatrix} \langle 0 | [q_j, H_0(^2\kappa, ^1\kappa)] | 0 \rangle \\ \langle j | H_0(^2\kappa, ^1\kappa) | j \rangle \\ \langle 0 | [q_j^\dagger, H_0(^2\kappa, ^1\kappa)] | 0 \rangle \\ - \langle 0 | H_0(^2\kappa, ^1\kappa) | 0 \rangle \end{pmatrix} + \frac{1}{2} \begin{pmatrix} \langle 0^{1L} | [q_j, H_0] | 0^{2R} \rangle + \langle 0^{2L} | [q_j, H_0] | 0^{1R} \rangle \\ 0 \\ \langle 0^{1L} | [q_j^\dagger, H_0] | 0^{2R} \rangle + \langle 0^{2L} | [q_j^\dagger, H_0] | 0^{1R} \rangle \\ 0 \end{pmatrix} \\
 &+ \begin{pmatrix} \langle 0^{1L} | [q_j, H_0(^2\kappa)] | 0 \rangle + \langle 0 | [q_j, H_0(^2\kappa)] | 0^{1R} \rangle \\ \langle j | H_0(^2\kappa) | 0^{1R} \rangle \\ \langle 0^{1L} | [q_j^\dagger, H_0(^2\kappa)] | 0 \rangle + \langle 0 | [q_j^\dagger, H_0(^2\kappa)] | 0^{1R} \rangle \\ - \langle 0^{1L} | H_0(^2\kappa) | 0 \rangle \end{pmatrix} \quad (41)
 \end{aligned}$$

Likewise, contracting $S^{[3]}$ with two vectors gives

$$\begin{aligned}
 S_{jkl}^{[3]1} N_k^2 N_l &= -\frac{1}{2} \begin{pmatrix} \langle 0 | [q_j, ^2\kappa, ^1\kappa] | 0 \rangle \\ \langle j | ^2\kappa, ^1\kappa | 0 \rangle \\ \langle 0 | [q_j^\dagger, ^2\kappa, ^1\kappa] | 0 \rangle \\ - \langle 0 | ^2\kappa, ^1\kappa | j \rangle \end{pmatrix} \\
 &- \begin{pmatrix} \langle 0^{2L} | [q_j, ^1\kappa] | 0 \rangle + \langle 0 | [q_j, ^1\kappa] | 0^{2R} \rangle \\ \langle j | ^1\kappa | 0^{2R} \rangle \\ \langle 0^{2L} | [q_j^\dagger, ^1\kappa] | 0 \rangle + \langle 0 | [q_j^\dagger, ^1\kappa] | 0^{2R} \rangle \\ - \langle 0^{2L} | ^1\kappa | j \rangle \end{pmatrix} - \begin{pmatrix} 0 \\ ^2S_j \langle 0 | ^1\kappa | 0 \rangle \\ 0 \\ ^2S_j' \langle 0 | ^1\kappa | 0 \rangle \end{pmatrix} \\
 &+ \begin{pmatrix} \langle 0^{2L} | q_j | 0^{1R} \rangle + \langle 0^{1L} | q_j | 0^{2R} \rangle \\ 0 \\ \langle 0^{2L} | q_j^\dagger | 0^{1R} \rangle + \langle 0^{1L} | q_j^\dagger | 0^{2R} \rangle \\ 0 \end{pmatrix} + (^1S_l^2 S_l' + ^1S_l'^2 S_l) \begin{pmatrix} \langle 0 | q_j | 0 \rangle \\ 0 \\ \langle 0 | q_j^\dagger | 0 \rangle \\ 0 \end{pmatrix} \quad (42)
 \end{aligned}$$

and finally for $A^{[2]}$ we have

$$A_{jk}^{[2]} N_k = \begin{pmatrix} \frac{1}{2} \langle 0 | [q_j^\dagger, A] | 0 \rangle \\ - \langle 0 | A(\kappa) | j \rangle \\ \frac{1}{2} \langle 0 | [q_j, A] | 0 \rangle \\ \langle j | A(\kappa) | 0 \rangle \end{pmatrix} + \frac{1}{2} \begin{pmatrix} 0 \\ - \langle 0^L | A | j \rangle \\ 0 \\ \langle j | A | 0^R \rangle \end{pmatrix} + \frac{1}{2} \begin{pmatrix} 0 \\ S_j' \\ 0 \\ S_j \end{pmatrix} \quad (43)$$

It is to be noticed the all linear transformations which are obtained by contracting all but one index of a given tensor, yield vectors which all have the structure of a gradient. All that is needed is therefore a general gradient formulation which allows for all kinds of spin combinations and which does not assume hermitean symmetry or permutation symmetry in the two-electron integrals.

The key operations will be the evaluation of two types of gradients, an orbital gradient

$$F_{pq} = \langle L | [E_{qp}^S, H(S_1, S_2)] | R \rangle \quad (44)$$

and a CI gradient

$$\langle j | H(S_1, S_2) | R \rangle \quad (45)$$

where the spin indices refer to + for singlet and - for triplet, and where $H(S_1, S_2)$ is a general two-electron operator,

$$H(S_1, S_2) = \sum_{pq} f_{pq} E_{pq}^S + \sum_{pqrs} g_{pqrs} e_{pqrs}^{S_1 S_2} \quad (46)$$

or in special cases a one-electron operator. f can be any one-electron type of integrals and g any two-electron type of integrals over the Hamiltonian or any observables A, B or C . They may also refer to one-index transformed integrals. In what follows we denote inactive orbitals by i, j, k, \dots , active orbitals by x, y, z, \dots , secondary orbitals by a, b, c, \dots and general orbitals by p, q, r, \dots .

The density matrices

$$D_{xy}^S = \langle L | E_{xy}^S | R \rangle \quad (47)$$

$$d_{xyzw}^{S_1 S_2} = \langle L | e_{xyzw}^{S_1 S_2} | R \rangle \quad (48)$$

are simplified for inactive or secondary orbital indices:

$$D_{pi}^S = D_{ip}^S = (1 + S) \delta_{ip} \quad (49)$$

$$D_{pa}^S = D_{ap}^S = 0 \quad (50)$$

$$d_{ipqr}^{S_1 S_2} = d_{qrip}^{S_2 S_1} = (1 + S_1) D_{qr}^{S_2} \delta_{ip} - \delta_{ir} D_{qp}^S \quad (51)$$

$$d_{pqri}^{S_1 S_2} = d_{ripq}^{S_2 S_1} = (1 + S_2) D_{pq}^{S_1} \delta_{ir} - \delta_{pq} D_{ri}^S \quad (52)$$

$$d_{apqr}^{S_1 S_2} = d_{pqra}^{S_1 S_2} = 0 \quad (53)$$

This implies that for each special case of orbital index combinations, an orbital gradient defined by Eq. (44) can be written as

$$F_{ai} = (1 + S_g S) F_{ai}^I \langle L | R \rangle + 2 F_{ai}^A \quad (54)$$

$$F_{ia} = -2 F_{ia}^I \langle L | R \rangle - 2 F_{ia}^A \quad (55)$$

$$F_{wi} = 2 F_{wi}^I \langle L | R \rangle - F_{xi}^I D_{xw}^{S_g S} + 2 F_{wi}^A - Q_{iw}^A \quad (56)$$

$$F_{iw} = -2 F_{iw}^I \langle L | R \rangle + F_{ix}^I D_{wx}^{S_g S} - 2 F_{iw}^A + Q_{iw}^B \quad (57)$$

$$F_{aw} = F_{ax}^I D_{wx}^{S_g S} + Q_{aw}^B \quad (58)$$

$$F_{wa} = -F_{xa}^I D_{xw}^{S_g S} - Q_{aw}^B \quad (59)$$

where the generalized Fock- and Q -matrices are defined by

$$F_{pq}^I = f_{pq} + (1 + S_1)g_{kkpq} + (1 + S_2)g_{pqkk} - g_{pkkk} - g_{kqp}k \quad (60)$$

$$2F_{pq}^A = ((1 + S_g S_2)g_{xypp} + (1 + S_g S_1)g_{pqxy} - g_{pyxq} - g_{xqpy})D_{xy}^{S_g S} \quad (61)$$

$$Q_{pq}^A = g_{xpyz}d_{xqyz}^{S_g S_1, S_2} + g_{xyzp}d_{xyzq}^{S_1, S_g S_2} \quad (62)$$

$$Q_{pq}^B = g_{pxyz}d_{qxyz}^{S_g S_1, S_2} + g_{xypz}d_{xyqz}^{S_1, S_g S_2} \quad (63)$$

$$(64)$$

An expectation or transition value of the Hamiltonian in Eq. (46) is given by

$$\langle L | H(S_1, S_2) | R \rangle = \frac{1}{2}(1 + S)(h_{kk} + F_{kk}^I) \langle L | R \rangle + F_{xy}^I D_{xy}^S + g_{xyzw} d_{xyzw}^{S_1 S_2} \quad (65)$$

The CI-gradient $\langle j | H | 0 \rangle$ is constructed using the determinant based direct technique of Olsen *et al.* [32] The advantage of using a determinant based formalism is that alpha and beta spins can be treated separately which reduces the dimensionality of the problem considerably.

IV Spin-orbit response properties

The electronic spin-orbit interaction operator, referred to as the Breit-Pauli spin-orbit Hamiltonian, is given by

$$H_{SO} = \frac{\alpha^2}{2} \left[\sum_{iA} Z_A \frac{\mathbf{l}_{iA} \cdot \mathbf{s}_i}{r_{iA}^3} - \sum_{ij} \frac{\mathbf{l}_{ij} \cdot (\mathbf{s}_i + 2\mathbf{s}_j)}{r_{ij}^3} \right] \quad (66)$$

where i, j refer to electrons and A to nuclei. Note that the relative orbital angular momentum between two particles, *e.g.* $\mathbf{l}_{ij} = (\mathbf{r}_i - \mathbf{r}_j) \times \mathbf{p}_i$ is asymmetric, *i.e.* $\mathbf{l}_{ij} \neq \mathbf{l}_{ji}$. This means that the two-electron integrals over this operator do not have the permutation symmetry as do the electron repulsion integrals. They could have been symmetrized, had it not been for the asymmetry in the spin part, which has its origin in the Thomas precession [33].

The results of response theory are most conveniently cast into a formalism based on second quantization. In a second quantized representation of (66), the spin-operators will transfer to triplet excitation operators which are weighted by the integrals over the orbital parts. The z -component will have the form

$$H_{SO}^z = \sum_{ij} (\hat{i}j | Z) E_{ij}^- + \sum_{ijkl} (\hat{i}j | kl) (e_{ijkl}^{+-} + 2e_{ijkl}^{+-}) \quad (67)$$

where the one-particle excitations are given in Eq. (14), the two-particle excitations are given by

$$e_{ijkl}^{+-} = E_{ij}^+ E_{kl}^- - E_{il}^- \delta_{kj} \quad (68)$$

and the integrals, written in a Mulliken-like notation, by

$$(\hat{ij}|Z) = \frac{\alpha^2}{2} \sum_A Z_A \int d\mathbf{r} \phi_i(\mathbf{r}) \frac{l_A^z}{r_A^3} \phi_j(\mathbf{r}) \quad (69)$$

$$(\hat{ij}|kl) = -\frac{\alpha^2}{2} \int d\mathbf{r}_1 d\mathbf{r}_2 \phi_i(\mathbf{r}_1) \phi_k(\mathbf{r}_2) \frac{l_{12}^z}{r_{12}^3} \phi_j(\mathbf{r}_1) \phi_l(\mathbf{r}_2) \quad (70)$$

The Mulliken notation is being used because Eq. (70) can be seen as the electron repulsion integrals between a charge distribution kl and a differentiated charge distribution \hat{ij} . Due to the nature of the orbital angular momentum, these integrals are symmetric in kl and real antisymmetric in ij . The other components of the spin-orbit operator are obtained by assigning the proper integrals and tensor components to Eq. (67). In practice, only the operators of Eqs. (14) and (68) are needed, since matrix elements involving other components can easily be written in this form using the Wigner-Eckart theorem [8].

A large number of spin-orbit properties can now be derived from the response functions. From the linear response function we can deduce the second-order energy correction due to SOC (see section 4.I),

$$E^{(2)} = \frac{1}{2} \langle \langle H_{SO}; H_{SO} \rangle \rangle_0 = \frac{1}{2} H_{SO}^{[1]\dagger} (E^{[2]})^{-1} H_{SO}^{[1]} \quad (71)$$

where $H_{SO}^{[1]}$ is the spin-orbit gradient define by Eq. (20), and the SOC constants (see section 4.II), are derived from the residue

$$\lim_{\omega \rightarrow \omega_f} (\omega - \omega_f) \langle \langle H_{SO}; H_{SO} \rangle \rangle_\omega \rightarrow \langle 0 | H_{SO} | f \rangle \quad (72)$$

and which is formed by solving the eigenvalue equation

$$(E^{[2]} - \omega_f S^{[2]}) X_f = 0 \quad (73)$$

and forming

$$\langle 0 | H_{SO} | f \rangle = H_{SO}^{[1]\dagger} X_f \quad (74)$$

One of the most of important applications of quadratic response theory, pertaining to spin-orbit properties, is the calculation of the spin-orbit induced dipole moment (phosphorescence, see section 7), which can be derived from the residue

$$\lim_{\omega \rightarrow \omega_f} (\omega - \omega_f) \langle \langle \mathbf{r}; H_{SO}, C \rangle \rangle_{0,\omega} \rightarrow \langle {}^1 0 | \mathbf{r} | {}^3 f \rangle \quad (75)$$

where C is an arbitrary triplet operator, and $|{}^3 f\rangle$ is a triplet state. The matrix element to the right is zero in the absence of perturbations. The residue to the left corresponds to inserting the first-order corrections to the singlet state $|{}^1 0\rangle$ and the triplet state $|{}^3 f\rangle$,

due to SOC. In this case we solve the eigenvalue equation (73) for X_f and the excitation frequency ω_f and the linear response equations

$$(E^{[2]})N^{so} = H_{SO}^{[1]} \quad (76)$$

$$N^r(E^{[2]} - \omega_f S^{[2]}) = \mathbf{r}^{[1]} \quad (77)$$

to form

$$-N_j^r H_{SO,j}^{[2]} X_{lf} - N_j^{so} (\mathbf{r}_{jl}^{[2]} + \mathbf{r}_{lj}^{[2]}) X_{lf} + N_j^r (E_{jml}^{[3]} + E_{jlm}^{[3]} - \omega_f S_{jlm}^{[3]}) N_m^{so} X_{lf} \quad (78)$$

Here $H_{SO}^{[2]}$ is defined according to Eq. (21) whereas $\mathbf{r}^{[2]}$ is defined according to Eq. (30).

The matrix element $\langle l | H_{SO} | k \rangle$, where $|l\rangle$ and $|k\rangle$ are two arbitrary excited states, can be derived from the double residue

$$\lim_{\omega_1 \rightarrow \omega_k} (\omega - \omega_k) \lim_{\omega_2 \rightarrow -\omega_l} (\omega + \omega_k) \langle \langle H_{SO}, B, C \rangle \rangle_{\omega_1, \omega_2} \quad (79)$$

where B and C are two arbitrary operators, one singlet and one triplet. In this case we solve two eigenvalue equations of the form (73) one for X, ω_f and one for $X_{-g}, -\omega_g$ and the linear response equation

$$N^{so}(E^{[2]} - (\omega_f - \omega_g)S^{[2]}) = H_{so}^{[1]\dagger} \quad (80)$$

The matrix element is in this case

$$\begin{aligned} \langle g | H_{so} | f \rangle &= N_j^{so} (E_{jkl}^{[3]} (X_{k-g} X_{lf} + X_{kf} X_{l-g}) + \omega_g S_{jkl}^{[3]} X_{k-g} X_{lf} - \omega_f S_{jkl}^{[3]} X_{kf} X_{l-g}) \\ &- A_{jk}^{[2]} (X_{j-g} X_{kf} + X_{jf} X_{k-g}) \end{aligned} \quad (81)$$

Thus, from a single calculation we may calculate a complete spin-orbit matrix over a manifold of eigenstates of H_0 (see section 4.II).

4 Computation of Spin-orbit Response Functions

I Background

As for other types of response calculations the spin-orbit response calculations have greatly benefited from the progress in identifying and removing the inherent bottlenecks in the computer implementations, and of the introduction of new efficient algorithms for solution of the response equations. Initially, MCLR calculations explicitly constructed MCLR matrices and solved the equations by standard techniques. The applications were therefore limited to small configuration spaces describing non-dynamical correlation only. The range of applications widened considerably by the introduction of various "direct" methods. The basic direct technique involves solution of response equations by direct linear transformations of Hessian-like matrices on vectors (as in

direct CI) without explicit construction of the matrices [9, 15, 32]. These linear transformations are formulated in terms of gradient vectors of an operator with one-index transformed integrals, *i.e.* the commutator of the operator with generators of orbital rotations. The one-index transformation has thus made it possible to transcend direct CI [30] to direct MCSCF [31] and to direct multiconfiguration response theory methods [9, 15, 34], and is thus also a key operation in multiconfiguration response theory calculations. This operation, *i.e.* the evaluation of gradient vectors of a general operator with one-index, double one-index, or higher order one-index transformed integrals can now also be carried out in a direct fashion without pre-transforming or storing the integrals [35], which is particularly beneficial for spin-orbit response calculations since the particle permutation symmetry of the integrals is lost anyway. These integral-driven "direct" algorithms lead to a considerable reduction in disk space and timing, and are thus prerequisites for making large-scale calculations at all possible. Thirdly, direct atomic orbital (AO) techniques have been introduced at the level of the random phase approximation [36, 37] (DRPA and DQRPA) making direct Fock matrix calculations possible for very large systems and basis sets. This will be a desirable future option also for spin-orbit related properties.

The prospect for spin-orbit response and, in general, for excitations involving change of spin greatly promoted by the formulation of determinant based CI techniques [32, 38]. This was simplified enormously the construction of two-electron density matrices that contain triplet orbital excitation operators and two-electron density matrices which connect singlet and triplet states. Furthermore, the direct CI method was developed for two-electron operators with spin rank one. The determinant based direct CI technology of Olsen *et al.* [32] was generalized to include these cases, which would have been exceedingly difficult within the context of the conventional GUGA approach to the CI problem.

II Computational features

The method requires that the singlet reference state is optimized. Spin-orbit coupling constants are then simply determined from a contraction of a gradient type vector with the spin-orbit operator and an eigenvector of the multi-configuration linear response eigenvalue problem. Orbital relaxation is included through the orbital operators in the MCLR eigenvalue equation.

For a system with a singlet ground state S_0 and a first excited triplet state T_1 , the unpolarized (average) transition rate is obtained by averaging initial states (triplet components) and summing over final states (photon polarizations and directions). Direct computations of spin-sublevel rates and therefore polarization directions of triplet state emission or absorption is possible. The computational steps include; optimize the singlet wave-function S_0 ; the solution of the triplet linear response eigenvalue equation for a particular excitation energy; the solution of two sets of linear response equations, *e.g.* one for the dipole operator, and one for the spin-orbit operator; the solution vectors from the eigenvalue equation and the linear response equations are then used to

obtain the residue of the quadratic response function. The full Breit-Pauli form of the spin-orbit operator is accounted for, thus including two-electron as well as many-center contributions. The one- and two-electron electrostatic and spin-orbit integrals are obtained over generally contracted gaussian type orbitals. The reduced permutational symmetry of the spin-orbit operator with respect to the ordinary electrostatic Hamiltonian, leads to twice as many spin-orbit integrals (for each component) as electron repulsion integrals to store on disk, which effectively sets the limit for the size of this type of calculations. If only the one-electron part of the spin-orbit operator is accounted for very large basis sets can be employed.

The advantages with calculations described in this and coming sections can be summarized as: 1) The representation of the full Breit-Pauli spin-orbit operator; most previous work only include the one-electron spin-orbit operator and simulate the two-electron effects with shielded nuclear charges. 2) The sum-over-state expressions for the transition moments have been replaced by solutions of sets of linear equations. Since these solutions can be determined using direct iterative techniques of the response equations, large dimensions and therefore large orbital and configuration space MCSCF wave functions can be considered. In conventional calculations large dimensions would inevitably lead to the need to truncate the sum-over-state expressions.

The summation converges very slowly and a truncation might lead to considerable errors as shown *e.g.* in the work on H_2CO by Langhoff and Davidson [39]. Their configuration-interaction approach included 100 terms in both singlet and triplet sums, and it was concluded anyway that high-energy intermediate states cannot be neglected and that the sums converge slowly when the states are ordered according to energy (many terms are of similar magnitude but of different signs). This also leads to size-consistency errors when comparing similar calculations (*e.g.* at slightly differing geometries); 3) The method is fully analytic, *i.e.* an analytic analogue of a finite field calculation of the dipole transition moment from an MCSCF linear response calculation where the spin-orbit operator is the applied field; 4) Both orbital excitation operators and configuration excitation operators are used to describe correlation. Conventional configuration (CI) approaches use only configuration excitation operators. More elaborate calculations are therefore required in such approaches for obtaining an equal correlation level. Of these 4 items one should stress item 2 most, that the full sum-over-state result is obtained independent of the dimension of the problem. This is illustrated by the explicit summations of terms in the sum-over-state expression in Table 22. The states 1k and 3k in this Table refer to intermediate singlet and triplet states;

$$\begin{aligned}
 \langle ^10 | \mathbf{r} | ^3f \rangle^{(1)} &= \sum_{^1k} \frac{\langle ^10^{(0)} | \mathbf{r} | ^1k^{(0)} \rangle \langle ^1k^{(0)} | H_{SO} | ^3f^{(0)} \rangle}{\omega_f - \omega_k} \\
 &- \sum_{^3k} \frac{\langle ^10^{(0)} | H_{SO} | ^3k^{(0)} \rangle \langle ^3k^{(0)} | \mathbf{r} | ^3f^{(0)} \rangle}{\omega_k} \quad (82)
 \end{aligned}$$

and for a transition from the singlet ground state, 10 , to the triplet final state, 3f . This formula displays more explicitly that the source of intensity for triplet state absorp-

tion arrives from two routes, with dipole coupling in the singlet, respectively, triplet manifolds of states.

III Test of response theory SOC calculation

In order to illustrate some computational features of the response methods we show in this section convergence behavior of results for SOC with respect to correlating orbital spaces and basis sets. For this purpose we choose the particular case of the $X^3\Sigma_g^- - b^1\Sigma_g^+$ magnetic dipole transition in O_2 , partially presented in ref. [8].

For comparison with response theory results for SOC, Table 1 lists data obtained with a small basis set (6-31G) but large correlation spaces in separate state CI calculations for the $X^3\Sigma_g^- - b^1\Sigma_g^+$ matrix element of the SOC operator in O_2 . The size of the couplings shows clear trends with respect to the size of the wave function. The values are evidently somewhat dependent on geometry, *e.g.* on singlet versus triplet state optimized geometry, and also, on the choice of optimized orbitals when using CI wave functions. The full configuration interaction (FCI) limit for the spin-orbit coupling matrix element was estimated by a series of CI calculations with different levels of electron excitations from the single-configuration $b^1\Sigma_g^+$. The excitation levels refer to single-double-triple (SDT) and single-double-triple-quadruple (SDTQ) excitations.

Results from response calculations are shown in Table 2 in which a single configuration SCF is used as reference state and with two CAS representations of the $b^1\Sigma_g^+$ state [8]. Both CAS calculations contain 10 active electrons, CAS I a 5 active orbital space ($2\sigma_u, \sigma_g, \pi_u, \pi_g$) and CAS II an 8 active orbital space, thus small conventional active orbital spaces. Significant changes are observed in the SOC matrix elements from the CAS I to the CAS II calculations, however, the results in Table 1 shows that already with the CAS II calculation a correlation level is reached which give results quite close to SDTQ. Since this in turn is expected to be close to the FCI limit, a satisfactory level of correlation is reached already by a moderate active space used in the response calculation. The last value in Table 2 is in a very good agreement with the results of high quality MRCI calculations of Klotz *et al.* [5, 40] (176.6 cm^{-1} at $r = 2.3 \text{ a.u.}$). Table 2 also provides a basis set test. The results show the importance of polarization functions. The 4s3p2d1f level gives values close to saturation with respect to the basis functions in the correlated calculation. The SCF results are accurate to within ten percent and have reached basis set saturation already at the 3s2p1d level (186.3 cm^{-1}).

The quality of the SOC calculation in O_2 can be checked by estimation of the $b^1\Sigma_g^+ - X^3\Sigma_g^-$ transition probability. The transition is forbidden by selection rules for electric dipole radiation with account of SOC, and occurs as magnetic dipole spin-current borrowing intensity from microwave transitions between spin-sublevels of the ground state [41].

$$\Psi_{X,0} = |X, 0\rangle - c^{b,X} |b\rangle, \quad \Psi_b = |b\rangle + c^{b,X} |X, 0\rangle \quad (83)$$

Table 1: Spin-orbit coupling matrix element (cm^{-1}) $b^1\Sigma_g^+ - X^3\Sigma_g^-(M_s = 0)$ in O_2 at the equilibrium internuclear distance (2.281 a.u.), obtained in the same small 6-31G basis^e. From Ref. [8].

	<i>One – Electron</i>	<i>Two – Electron</i>	<i>Total</i>
Breulet ^{a,b}	261.53	-99.73	161.80
Furlani ^{c,d}	242.19	-88.96	153.23
SCF-CI ^a	261.69	-96.09	165.59
SCF-CI	253.07	-93.31	159.76
SDCI	256.40	-94.32	162.08
SDCI-1sf	256.35	-94.19	162.15
SDTCI-1sf	260.17	-95.44	164.73
SDTQCI-1sf	257.16	-94.40	162.76
RPA	274.38	-99.62	174.75
MCLR-CAS I	251.25	-92.10	159.07
MCLR-CAS II	256.96	-94.43	162.52

^{a)} Triplet SCF orbitals, all other CI results from singlet SCF orbitals.

^{b)} Ref. [43].

^{c)} Triplet SCF orbitals, π -orbitals.
reoptimised for the singlet state.

^{d)} Ref. [44].

^{e)} Ref. [45].

where the coefficient $c^{b,X}$ is equal to

$$c^{b,X} = \frac{\langle X, 0 | H_{SO} | b \rangle}{E_b - E_X}. \quad (84)$$

Here $|b\rangle$ and $|X, 0\rangle$ designate the zero order wave function of the states $b^1\Sigma_g^+$ and $X^3\Sigma_g^-$ respectively with $M_S = 0$ for the triplet ground state. The $b^1\Sigma_g^+ - X^3\Sigma_g^-(M_S = \pm 1)$ transition moment in O_2 is now magnetic dipole allowed and equal to

$$\langle \Psi_b | 2\beta_N S_{\pm} | X, \pm 1 \rangle = 2\beta_N c^{b,X}, \quad (85)$$

where only the spin part of magnetic dipole operator gives nonzero contributions, β_N is Bohr magneton and $|X, \pm 1\rangle$ denotes spin sublevels of the ground state with $M_S = \pm 1$. The orbital angular momentum contribution to the $b^1\Sigma_g^+ - X^3\Sigma_g^-, \pm 1$ transition moment is negligible [41], so Eq. (85) and hence the integral from Eq. (84) determines the intensity of the $b \rightarrow X$ red emission band of oxygen from the upper atmosphere [41]. The experimental value for the transition probability is equal to 0.089 s^{-1} [42]. With the largest CAS (CAS II B) and the most flexible basis set (6s5p3d2f) we get, taking into account the experimental energy difference (1.63 eV), the $b \rightarrow X$ transition probability equal to 0.08874 s^{-1} in an excellent agreement with the recent experiment [42].

So we claim that the last value in Table 2 (176.59 cm^{-1}) is close to the exact estimation of the SOC matrix element at the equilibrium distance in the ground state

Table 2: Spin-orbit coupling matrix element (cm^{-1}) $b^1\Sigma_g^+ - X^3\Sigma_g^-$ in O_2 at the equilibrium internuclear distance (2.281 a.u.) using various basis sets^a and configuration spaces. From Ref. [8].

		One – Electron	Two – Electron	Total
3s2p1d	SCF	286.23	-99.96	186.28
	CAS I	261.12	-92.01	169.11
	CAS II A	267.47	-94.47	173.00
4s3p2d1f	SCF	286.10	-99.79	186.31
	CAS I	262.07	-92.28	169.79
	CAS II B	273.29	-96.26	177.04
6s5p3d2f	SCF	286.09	-99.78	186.31
	CAS I	261.59	-92.15	169.44
	CAS II B	272.68	-96.08	176.59

^a) Ref. [46].

oxygen molecule. We can compare this value with result of Klotz *et al.* [5] at the similar distance (2.28 a.u.), which is 175.6 cm^{-1} . The value of this matrix element is crucial for intensity calculation of the 0,0 transition of the red atmospheric band $X^3\Sigma_g^- - b^1\Sigma_g^+$ [47, 41, 5].

5 Miscellaneous Applications

I Second order spin-orbit coupling contribution to the total energy

Calculations of spin-orbit coupling constants in diatomic and three-atomic linear molecules, which determine the SOC splittings of Π and Δ multiplets, constitute a traditional field of applications for SOC theory [1, 48]. The expectation value of the SOC operator could be non-zero (SOC constant) for orbitally degenerate states with non-zero spin. For orbitally nondegenerate states a SOC contribution to the energy can occur only in second order of perturbation theory. Zero-field splittings (ZFS) of triplet excited states of aromatic molecules [49] are therefore exclusively determined by spin-spin coupling because the SOC contribution is negligible [50, 48]. This is, however, not the general rule. For carbonyl molecules with small energy gaps between $^3,1(n\pi^*)$ and $^1,3(\pi\pi^*)$ states the SOC contributions to the ZFS parameters are comparable with spin-spin coupling and could even be larger [49, 48, 2]. The same type of energy correction (not the splitting) could be possible for the ground singlet state of a molecule, thus providing the most important relativistic correction to heat of formation. One of the possible applications of spin-orbit response theory is therefore to predict this second-order Rayleigh-Schrödinger energy correction to the BO potential energy

$$E_0^{(2)} = \sum_n \frac{\langle 0 | H_{so} | n \rangle \langle n | H_{so} | 0 \rangle}{E_n - E_0} \quad (86)$$

where $|0\rangle$ is the reference state with total energy E_0 and $|n\rangle$ is an excited state with total energy E_n . This second-order energy contribution from the spin-orbit operator can alternatively be expressed as a linear response function evaluated at zero frequency;

$$\langle\langle H_{so}; H_{so} \rangle\rangle_{\omega=0} = V^{(1)}(E^{(2)})^{-1}V^{(1)} \quad (87)$$

where

$$E^{(2)} = \begin{pmatrix} A & B \\ B^* & A^* \end{pmatrix} \quad (88)$$

and the matrices A and B given in eqs. 5 and 6 of Ref. [51]. To determine Eq. 87 we need to solve the linear set of equations

$$E^{(2)}X = V^{(1)} \quad (89)$$

with many close-lying excited states present. In such cases it is plausible that finer effects such as second-order relativistic and non-adiabatic energy contributions may perturb the binding energy and bond length. Even small energy contributions may thus be important if they show large variations with geometry. So have relativistic effects in general been claimed to be of importance for the binding of transition metal dimers [52]. A test of the conjecture that the (relativistic) second-order contribution due to spin-orbit coupling is of importance for the binding energy and bond length was presented for Cr_2 in ref. [51] using the multi-configuration spin-orbit response method. The Cr_2 molecule, with its hextuple bond and unusual electron correlation, has been a crucial test case for quantum chemical calculations with a wide spread of results for its bond length [53, 54, 52]. The MCSCF/MCLR calculations of the second-order energy contribution to the Cr_2 singlet ground state $X^1\Sigma_g^+$ potential energy showed nevertheless the effect of spin-orbit coupling on the potential energy curve is quite small. Moreover, the geometry dependence of the second order energy contribution was also found small. Thus yet another suggested cause for the problems in calculations of the binding of Cr_2 was eliminated.

II Intensity modulation of electronic spectra due to spin-orbit coupling

In many spectroscopic problems spin-orbit and non-adiabatic interactions are responsible for intersystem crossings, charge transfer and predissociation. This goes for systems with a high density of states and with rapidly changing potential functions. In the following two subsections we illustrate calculations using response theory that go beyond the usual BO non-relativistic theoretical treatment of electronic spectra and properties, namely the calculation of SOC effects in dicationic states. In the first example such couplings are used in a perturbative way to derive intensity rearrangement in Auger spectra, in the second example they are used to obtain the solutions of the multi-channel Schrödinger equation to derive dynamic properties, *viz.* stability and lifetime towards predissociation of low-lying dicationic states.

In Ref. [55] first- and second-order response theory was used to explore the role of spin-orbit coupling in the manifold of low-lying dicationic states of water and its implications on the intensity analysis of the Auger spectrum of that molecule. The choice of this model system was based on the fact it has served as a prime test case for computational methods for Auger energies and intensities, ranging from simple semi-empirical schemes to more advanced *ab initio* calculations. Of particular importance is that accurate polycenter Auger transition moments, including their phases, have been given for H_2O^{++} , which is a prerequisite for obtaining information on the role of SOC.

Auger rates were obtained assuming the electrostatic limit ("LS coupling") and given by first order perturbation theory. The spin-orbit linear response functions were computed for excitations between the ground dicationic state and all double hole valences states. Specific for dicationic problems, as for many other types of spectroscopies, is the occurrence of a large number of avoided crossings and intersystem (curve-) crossings. It can therefore be more efficient to use second order response theory in which couplings, here SOC:s, between different excited states can be obtained directly from one sole ground state calculation. This is accomplished by evaluating the SOC:s between orthogonal and non-interacting excited states as residues of (multi-configuration) quadratic response functions [11, 55]. These residues are identified as matrix elements of operators between the unperturbed states, see section 3.

The results for the second order response theory calculations are collected in Table 3 in the form of a chart of SOC matrix elements connecting singlet and triplet states defining rows and columns, respectively. Some of the SOC matrix elements are quite large ($674 \text{ a.u.} = 141 \text{ cm}^{-1}$ should be compared with the largest SOC S-T matrix element in the water molecule; 43 cm^{-1} [50]), which exhibit a substantial increase of electronic velocity upon ionization. Tables 3 and 4 collect the results for spin-orbit coupling in H_2O^{++} and Auger intensities in water using perturbation theory. The manifold of states generated by two-hole ionization among the outer 2p-carrying valence orbitals $3a_1$, $1b_2$, $1b_1$, are considered, generating 3 A_1 , 1 B_1 , 1 B_2 , 1 A_2 singlets and 1 B_2 , 1 B_1 , 1 A_2 triplets. These states are the main carriers of Auger intensity and are all well described in the one-particle picture (with a one-to-one correspondence between Auger bands and spin-coupled two-orbital vacancies). This restriction follows from that Auger moments have only been obtained in the one-particle approximation; the multi-configuration spin-orbit response method, however, makes no distinction between one-particle and correlation states.

The results infer that the spin-orbit coupling is selective in terms of states, but that overall this effect is not larger than a few percent [55]. The effect is definitely smaller than the inherent accuracy of the approximations used in the calculations of the Auger moments. Results suggested that the spin-orbit effect rather redistributes intensities between channels than changing the total rate. This parallels the effect of (electrostatic) channel interaction, which perturbs the individual rates much more than the total rate [56, 57]. The results thus also indicated that spin-orbit interaction has no net effect on the lifetime of the core hole state of water. The propensity rules used in the large bulk of analyses of molecular Auger were thus supported by the investigation

Table 3: Spin-orbit coupling matrix elements between singlet and triplet states from second order response theory calculations on H_2O^{++} (10^{-6} au). A: $6a_1, 3b_2, 3b_1, 1a_2$ active space; B: $4a_1, 2b_2, 2b_1$ active space. From Ref. [55].

Singl/Tripl	$3a_1 1b_2 {}^3B_2$	$3a_1 1b_1 {}^3B_1$	$3a_1 1a_2 {}^3A_2$
A			
$1b_1^{-2} {}^1A_1$	-89.1	-398	-439
$3a_1^{-2} {}^1A_1$	-400	620	648
$1b_2^{-2} {}^1A_1$	439	-91.2	-508
$3a_1 1b_2 {}^1B_2$	0	244	360
$3a_1 1b_1 {}^1B_1$	-205	0	296
$1b_1 1b_2 {}^1A_2$	259	-297	0
B			
$1b_1^{-2} {}^1A_1$	-71.2	-427	-438
$3a_1^{-2} {}^1A_1$	427	571	19.7
$1b_2^{-2} {}^1A_1$	-305	-63.6	347
$3a_1 1b_2 {}^1B_2$	0	-204	136
$3a_1 1b_1 {}^1B_1$	25.4	0	-306
$1b_1 1b_2 {}^1A_2$	2085	-674	0

in ref. [55]. Water was used as model system since very accurate Auger transition moments in the electrostatic limit were available for this species, but is of course still not ideal for investigating a strong SOC effect since, being a low-Z molecule, it lacks an internal "heavy-atom" effect for the SOC. Since SOC relates to the fourth power of the (screened) nuclear charge the effect would be much larger for e.g. H_2S . A second reason is that water is a relatively low-dense electronic "atomic-like" species, and already the first row diatomics deviate rather drastically with respect to properties of the dications, so also with respect to SOC.

III Spin-orbit induced dynamic properties

Many molecular excited states are unstable towards predissociation or dissociation. For example, dicationic states all contain vibrational levels that are embedded in a continuum and are therefore forced to decay through spontaneous decomposition. With new types of coincidence techniques [59], and in particular, experiments with storage rings [60], dissociation of ionic states can be observed over a large time scale, up to several seconds. Spin-orbit coupling, operating simultaneously within a manifold of states, is a main driving force behind such (pre)dissociative features. In order to understand how dynamic effects are introduced in the formation and dissociation, in particular for strong predissociation, the solution of coupled Schrödinger equations involving SOC constants is required. One can consider this on the same footing as non-adiabatic coupling constants. In the BO and non-relativistic approximation the Hamiltonian can be expressed as

$$H = T_Q + T_q + V_{QQ} + V_{qQ} + V_{qq} = H_{el} + T_Q. \quad (90)$$

Table 4: Auger rates for H₂O including SOC [55] (10⁻⁶ au.)*

State	Phases ^a	PW ^b	PW + s.o. ^c	MW ^d	MW + s.o. ^e
3a ₁ 1b ₂ ³ B ₂	-	9	11 (16)	9	11 (16)
3a ₁ 1b ₁ ³ B ₁	-	12	11 (9)	12	11 (9)
1b ₁ 1b ₂ ³ A ₂	+	0	0 (0)	0	0 (0)
1b ₁ ⁻² ¹ A ₁	+	609	610 (610)	618	619 (619)
3a ₁ ⁻² ¹ A ₁	+	446	449 (439)	440	443 (433)
1b ₂ ⁻² ¹ A ₁	-	358	357 (359)	358	357 (359)
3a ₁ 1b ₂ ¹ B ₂	+	580	579 (580)	569	568 (569)
3a ₁ 1b ₁ ¹ B ₁	+	643	644 (642)	624	625 (623)
1b ₁ 1b ₂ ¹ A ₂	+	583	570 (481)	583	570 (481)

a) Phases of Auger transition moments[58].

b) Partial Wave Auger rates[58].

c) Partial Wave Auger rates including SOC.

d) Mixed Wave Auger rates[58].

e) Mixed Wave Auger rates including SOC.

*) Numbers without parentheses from 6a₁, 3b₂, 3b₁, 1a₂ active space calculation; Numbers inside parentheses from B: 4a₁, 2b₂, 2b₁ active space.

where T and V represent kinetic and potential operators, and (*q*) and (*Q*) are the electronic and nuclear variables. The wave function is expandable as

$$\psi(Q, q) = \sum_i \chi_i(Q) \phi_i(Q; q) \quad (91)$$

where the sum in principle is evaluated over all solutions ϕ_i of the electronic equation for fixed values of the nuclear coordinates:

$$H_{el}(Q; q) \phi_i(Q; q) = E_i(Q) \phi_i(Q; q) \quad (92)$$

The simplest approximation that this scheme admits is to neglect T_Q completely. The Q 's are thus no longer dynamical variables and eq. 92 hence totally describes the system. The ϕ_i represent, then, the different molecular states. The coordinates Q in the electronic wave function ϕ enter as parameters.

The natural way to take account of dynamic effects beyond this approximation is to solve the resulting equations for χ_i , obtained when the wave function proposed in eq. 91 is inserted in the Schrödinger equation for the Hamiltonian of eq. 90. This procedure assumes differentiability in Q space. The χ_i thus obtained will describe the different vibrational levels.

In the case of only one nuclear degree of freedom, and zero nuclear angular momentum, the resulting equations become:

$$0 = \left(\left(\frac{-1}{2M} \right) \partial^2 \chi_j(Q) / \partial Q^2 + (E_j(Q) - E) \chi_j(Q) \right) \delta_{ij} + \sum_i \left(\frac{-1}{2M} \right) \times$$

$$\times (\chi_i(Q)P_{ji} + 2R_{ji}\partial\chi_i(Q)/\partial Q) \quad (93)$$

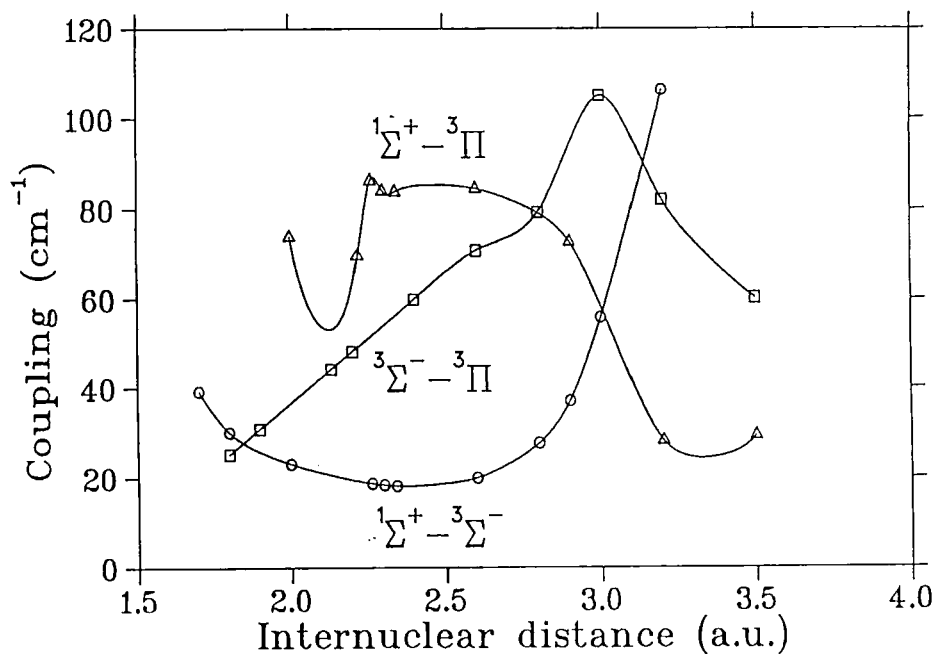
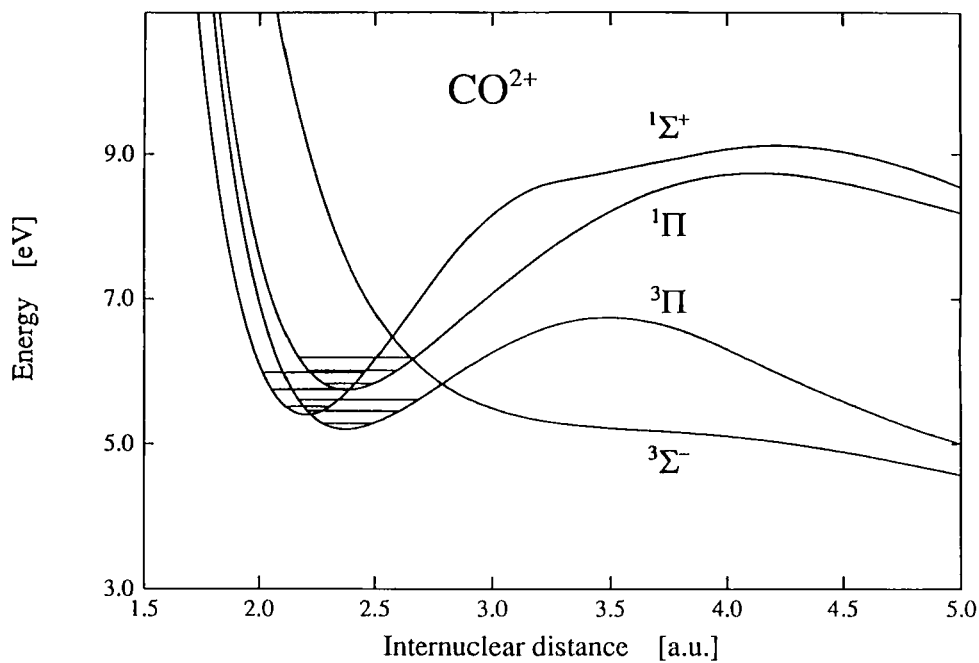
where the brackets indicate integration over the q coordinates only. i and j run over all terms in eq. 91. This number is for practical reasons finite in numerical calculations. In this set of coupled differential equations (the Multichannel Schrödinger Equation (MCS)) all χ_i 's and ϕ_i 's are separately normalized to unity, a weight factor c_i appears in eq. 91 describing the relative mixing of the different channels. The couplings between different electronic states can either be determined by non-adiabatic interactions (see ref. [61]) i.e. R and P given by the first and second non-adiabatic coupling constants given above which are the derivatives of the electronic wave function with respect to Q arising in eq.93, or by relativistic corrections to the BO hamiltonian, here given by spin-orbit interaction, which couple different electronic states. The SOC can thus be regarded, from the computational point of view, as one possible contribution to the general matrices P and/or R .

The finiteness of the low-lying dicationic lifetimes is obtained by combining accurate electronic structure calculations with molecular calculations beyond the BO approximation, where electronic state-to-state coupling due to non-relativistic effects (SOC) are taken into account [62, 60]. With such calculations the resolved vibrational structure is accounted for as well as estimates of the lifetime of different of double-hole states. The degree of mixing of electronic states due to spin-orbit or other couplings can thus be obtained, by including precisely those couplings which are neglected in standard quantum chemical calculations.

Below we briefly recapitulate some applications of the dynamic MCS technique to CO^{++} . As inferred from old [63] and recent [64, 65] reviews, applications on CO^{++} has been a popular test case for experimental dicationic studies. This goes for traditional spectroscopies for which the lowest dicationic states of CO have been used to illustrate the effect of *electronic interference* for intensity redistribution, as well as for coincidence spectroscopies like photoion-photon-of-fluorescence (PIFCO) and kinetic energy release spectroscopy (KERS) [59], and by ion-beam time-of-flight experiments. In the recent work of Andersen *et al.* [60] the energies of the four lowest electronic states of CO^{++} were determined with very high accuracy, and it was observed that the lowest state was stable on time scale of seconds whereas some higher states were spontaneously dissociating on a scale of ms. This is probably not unusual for general dicationic species. Andersen *et al.* [60] used spin-orbit response theory [8] in the solutions of the MCS equations for CO^{++} . Thus rather than using the couplings in first order perturbation theory to rearrange spectroscopic intensities (e.g. Auger electron intensities as described in the previous section), a full dynamic, vibronic picture of the interaction of the low-lying dicationic states was obtained which also is necessary in order to explore their stability and possible finite lifetimes. Any description of the different vibrational quasi-bound levels thus has to take into account the couplings between different electronic states. Higher vibrational levels of the electronic curves may lie "close enough" in energy when compared with the typical size of the couplings, thus requiring a coupled description. Andersen *et al.* [62] used a numerical finite-element method to solve the MCS equations, and focused on the the lowest states, $^1\Sigma^+$, $^3\Pi$,

Fig. 1

a) Potential energy curves for the lowest electronic states of CO^{2+} . b) Spin-orbit couplings between $^1\Sigma^+ - ^3\Pi$, $^1\Sigma^+ - ^3\Sigma^-$, and $^3\Pi - ^3\Sigma^-$ states. From ref. [60].



and $^3\Sigma^-$, as responsible for the dynamics of CO^{++} . These curves and their mutual spin-orbit couplings are recapitulated in Fig. 1.

There is a delicate dependence of the MCS technique on the underlying PES:s. For CO^{++} accurate such PES:s are obtained in e.g. refs. [66, 64, 60]. The dependence of the MCS calculations on the couplings is somewhat less crucial, and sufficient convergence in the couplings by means of the response theory calculations could be obtained. Because of the Coulomb repulsion, the potential curves are in fact *dissociative*, i.e. the local minima at equilibrium geometry lie often above the large- r limit. The typical size of the couplings range between 10 and 60 cm^{-1} , and are rather smoothly varying over a large region of the internuclear distances. The coupling strength is below one tenth of the typical energy difference between vibrational levels of the isolated state potentials, so the degree of mixing of the different electronic states is in general low. Some notable exceptions among the excited mixtures ($^1\Sigma^+ - ^3\Pi$ for CO^{++}) of up to many percent can be observed. On account of the potential curves and of the fact that the SOC is comparatively small it is to be expected that the lowest quasi-bound states are of a particular symmetry set by the BO calculation (for CO^{++} of $^3\Pi$ type). As energy increases they will alternate with states of other symmetries (for CO^{++} mostly $^1\Sigma^+$ states) and possibly some mixed states will appear. Lifetimes are expected roughly to decrease with increasing energy, considering the extension in r of the vibrational wave functions. When energy increases, the wave functions extend further and further into the region of the rapidly dissociating potentials (for CO^{++} the $^3\Pi$ and $^1\Sigma^+$ wave functions extend into the $^3\Sigma^-$ potentials). The experimental observation of many dicationic low-lying levels that are quasi-stable on *ms-μs* time scales [60] can thus be verified by taking account of SOC in a quantitatively accurate scheme beyond the BO approximation [60, 62], in ref. [60] this was thus well accomplished by response theory.

IV Intersystem crossings and reactivity

Potentially rewarding applications of the spin-orbit response method are given by calculations of spin-orbit coupling in the intersystem crossings of radical reactions. This is part of the more general field of spin catalysis phenomena involving many types of chemical reactions driven by SOC or by the overcoming of spin-forbiddance by other interactions. For example, at transition states with small or even negative S-T gaps, S-T transitions can be crucial for the determination of the reaction rates. Many reactions can thus be explained by the account of S-T transitions in intermediate diradicals induced by SOC. Of particular interest are the intersystem crossings (ISCs) between lowest triplet to singlet states occurring in the reaction of atomic oxygen with simple hydrocarbons. For example, reactions of triplet oxygen atoms with unsaturated hydrocarbons and olefins involving electrophilic addition are of great importance in combustion chemistry [67]. Some of these reactions are also thought to play important roles in photochemical processes, e.g. the carbolysis in the photosynthesis, and in the synthesis of organic compounds. The importance of SOC for the cross sections is widely recognized, and these reactions have also been useful in the classification of a

large number of SOC effects. With use of high level correlated methods, such as MCLR, one can now study such effects on a more quantitative level than given by molecular orbital theory or by semiempirical computations with simplified forms for the SOC.

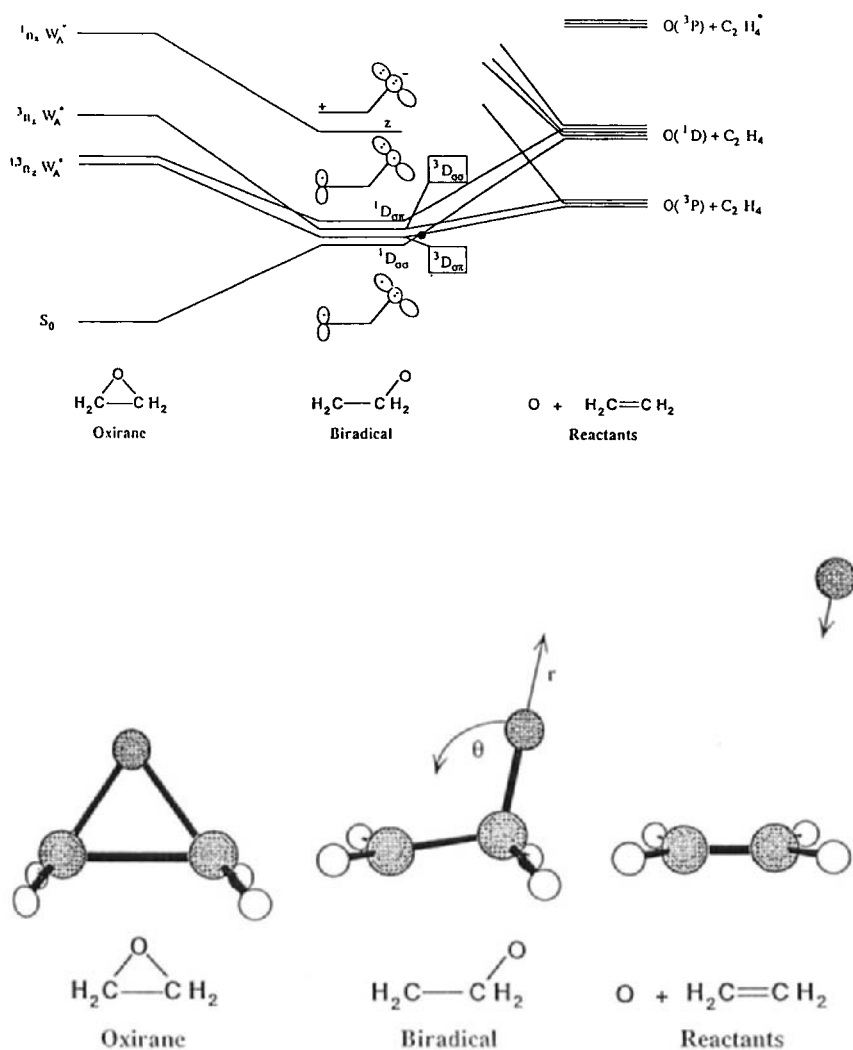
Below we illustrate possible applications of response theory in this context by commenting a recent study on the formation and the ring opening of the oxirane molecule, which we consider to represent some of the main features in these reactions. It is the simplest reaction involving $O(^3P)$ among the group of possible compounds given by $O(^3P) + C_2H_4$ leading to oxirane. Oxiranes can undergo monomolecular (thermal or photochemical) ring openings and fragmentations. A main feature of the ring opening is that it results in a system with a triplet spin function. Since the stable closed ring conformation, epoxide, has singlet spin symmetry this reaction involves necessarily a triplet-singlet crossing. The oxirane molecule is a small member of the three centre ring series and therefore reachable by *ab initio* response theory calculations, which can systemize the role of electron correlation and take full account of the Breit-Pauli form of the spin-orbit operator. A qualitatively correct description of the large electronic relocation upon the ring opening and of the biradical nature of the oxirane reactants indeed favor a multi-configuration treatment, as in the response theory study given in ref. [68].

The efficiency of SOC in the $O(^3P) + C_2H_4$ reaction forming epoxide can be derived from the biradical structure of the reactants. The CH_2CH_2O molecule forms four relevant biradical states which are nearly degenerate: $^1,^3A'(\sigma, \sigma)$ and $^1,^3A''(\sigma, \pi)$ states, and, at slightly higher energies, the $^1,^3A''(\pi, \sigma)$ and $^1,^3A'(\pi, \pi)$ states. The first character (σ or π) refers to the unpaired carbon electron, the second character (σ or π) to the oxygen unpaired electron. The biradical nature follows from the orbital diagram given Fig. 2 [68] from which also the character of the SOC can be derived qualitatively. The $^1,^3A'(\sigma, \sigma)$ states thus contain an unpaired carbon 2p-AO in the xy-plane, while the oxygen atom has a filled lone-pair 2p-orbital in the out-of-plane z-direction but an unpaired in-plane (xy) 2p orbital. The other relevant biradical states $^1,^3A''(\sigma, \pi)$ have flipped the unpaired electron to the oxygen in-plane 2p orbital leaving the out-of-plane 2p orbital unpaired. The transition between the two types of states will thus involve a rotation of the 2p AO on the oxygen atom around the C-O bond which creates a torque to flip the electronic spin. The triplet biradical initially formed will thus undergo an ISC due to the large SOC on the oxygen atom. The singlet biradical $^1A'(\sigma, \pi)$ produces the cyclization product, epoxide. The thermal ring opening necessitates an activation energy $E_a \simeq 45$ kcal/mole [68] and since no extremum appears along the CO reaction coordinate, the open form must reclose spontaneously back to the initial oxirane molecule. But because of the S-T $^1A'(\sigma, \sigma) - ^3A''(\sigma, \pi)$ crossing there is a probability to get the metastable triplet biradical form, which ought to have a non-zero lifetime.

The study of the features briefly given above involves the identification of the coupling area through geometry optimization and, possibly, transition state searches. Since the electron correlation is expected to be larger at the compound geometry than for the reactants, a careful choice of the correlating space is required. Furthermore, the correct ordering of near-lying singlet and triplet states, here the $^3A''$ and $^1A'$ states,

Fig. 2

a) A correlation diagram between reactant states and biradical states of $O(^3P)+C_2H_4$, and the first few states of the ring-closed oxirane molecule. The ISC near the biradical stage is pointed out with a dot. b) The different conformations of $O(^3P)+C_2H_4$ and a definition of the reaction coordinates θ and r . From ref. [68].



requires good quality wave functions. Ref. [68] focussed on a particular ring-opening reaction mechanism between the lowest singlet and triplet states and used a standard Landau-Zener theory for obtaining the the ISC probability from the coupling of the lowest singlet and triplet states. With small active space wave functions and small singlet triplet separations MCLR transition energies may differ significantly with state optimized excitation energies, while the restricted active space (RAS) alleviates this problem.

The S-T excitation energies and coupling elements are given in Tables 5 and 6 with respect to reaction coordinates close to the crossing point. The spin-orbit matrix elements ($M_S=-1,0,+1$) between the triplet and singlet states are computed along the reaction coordinate defined by a constant C-C-O angle at the S-T crossing point. As in the olefin reaction different components of the spin-orbit reaction contributes rather differently, in the particular case of oxirane the σ component dominates the coupling, being four times as large as the π component, the two components covary with the distance. It is thus found that SOC is large over a wide region of biradical geometries. The large size of the spin-orbit coupling is not surprising considering the fact that it is largely localized to the oxygen atom. The S-T transition rates can be further enhanced by vibronic effects, i.e. vibrational motion in the direction perpendicular to the reaction coordinate may induce multiple passages through the active transfer region thereby increasing the rate.

Specific for ISC and other predissociative curve-crossings is that the response function approach can be afflicted by instabilities which has to be treated with some care. The instabilities encountered for the MCLR eigenvalue equation near curve crossings is a structural problem of the method itself. Partitioning the MCSCF Hessian to orbital and configuration parts on one hand, and excitation and deexcitations on the other, gives the structure

$$E^{[2]} = \begin{pmatrix} A & B \\ B^* & A^* \end{pmatrix}$$

It was demonstrated by Golab *et al.* [69] that to obtain a positive excitation energy it is necessary that both the matrices $A+B$ and $A-B$ are positive definite. Also, to obtain a negative excitation energy it is necessary that both matrices $A \pm B$ have one negative eigenvalue. Hence, there will always be a region near a curve crossing where one of the matrices is positive definite and the other is not, which leads to instabilities in terms of complex eigenvalues. From calculations we find that the range of the instability region depends much on the nature of the crossing and on the orbital space employed. Thus with the smallest active space of orbitals described below this region can extend quite much, while it diminishes significantly for the larger active spaces. In the full CI (FCI) limit the B matrix is zero and the instability region reduces to a point.

V Assignments of optical and ultraviolet spectra

Response theory calculations including the manifold of triplet states make it possible to obtain a more complete picture of optical and ultraviolet (UV) spectra of free

Table 5: Spin-orbit coupling elements for the $O(^3P) + C_2H_4$ reaction around the crossing point. ($r = R(C_2O) - 1.39 \text{ \AA}$). From Ref. [68].

r (a.u.)	$S-T$	$\delta(H_{ss} - H_{tt})/\delta q$	$\langle S H_{SO} T, M_S \rangle$	
	MCLR (cm^{-1})	MCLR ($cm^{-1}/a.u.$)	$M_S = \pm 1$ (cm^{-1})	$M_S = 0$ (cm^{-1})
0.00	1087.9	442.3	12.28	47.88
0.10	1068.0	729.9	11.89	47.67
0.20	964.0	1239.7	11.31	46.48
0.30	818.7	1790.3	10.55	44.38
0.40	594.4	2686.9	9.25	39.88
0.45	437.8	3804.5	5.71	35.35
0.50	191.2	6286.9	3.91	24.39

Table 6: Spin-orbit coupling elements for the $O(^3P) + C_2H_4$ reaction along the reaction coordinate where the angle θ varies from the crossing point ($r=0.52 \text{ a.u.}$); $\theta=114.5^\circ - \Lambda(C_1C_2O)$. From Ref. [68].

θ ($^\circ$)	$S-T$	$\delta(H_{ss} - H_{tt})/\delta q$	$\langle S H_{SO} T, M_S \rangle$	
	MCLR (cm^{-1})	MCLR ($cm^{-1}/a.u.$)	$M_S = \pm 1$ (cm^{-1})	$M_S = 0$ (cm^{-1})
2.0	381.9	5106	5.0	33.1
3.0	652.1	4510	4.8	41.0
4.0	893.5	4084	3.8	45.5
5.0	1119.3	4017	2.4	48.4
6.0	1356.5	4489	0.8	50.6

molecules. The number of low-lying triplet states is often quite large, and as it turns out, the dipole forbidden radiative intensities are often far from negligible, and should hence be taken into account. Apart from ground to singlet dipole transitions the radiative spectrum contains transitions between ground state to the full triplet manifold of states. These transitions can be obtained from a one-step linear response calculation, moreover, the dipole and spin-orbit interactions and ISCs between excited singlet and triplet states can be obtained from one quadratic response calculation based on optimization of the ground state wave function only. This feature was also illustrated in section II. A particularly rewarding field of applications for the spin-orbit response method is therefore given by calculations of dipole forbidden molecular absorption bands, for instance in spectra of molecules of stratospheric interest. In order to illustrate the potential of spin-orbit response theory calculations in this respect, we briefly review results of a recent investigation in this area, namely a study on the role of triplet states for the interpretation of low-lying absorption bands of ozone [70].

In ozone as in many other molecules of atmospheric interest there is a comparatively large number of low-lying singlet and triplet states. The triplet states have largely been overlooked concerning their role in low-energy absorption and dissociation of ozone, in particular for the formation of the lowest, Wulf and Chappuis, bands [71]. Most theoretical attention has been paid to the electronic spectrum, photodissociation and dynamic behavior and photochemistry of O_3 in the ultraviolet region [72]. Important for the stratospheric UV shielding is the understanding of the Hartley strong absorption $1^1B_2(B^1A') \leftarrow X^1A_1$ and the Huggins $2^1A_1(A^1A') \leftarrow X^1A_1$ bands, including the subsequent photofragment spectra [72, 73, 74]. More difficult are the interpretations of the very weak absorption in the near infrared, observed as the Wulf band [75], and the more intense prolongation in the visible region, known as the Chappuis band [76]. The difficulties of the interpretations of the Wulf and Chappuis bands are connected with the predissociation features and the diffuse character of this absorption and also with the fact that a large manifold of ozone excited states (namely the $^3B_2, ^{1,3}A_2$ and $^{1,3}B_1$) are predicted by *ab initio* methods in the low energy region (1-2 eV). All these states must be involved in detailed kinetics of $O_2 + O$ recombination and may influence the ozone population in the atmosphere. With the accepted interpretation the weak Wulf band has been assigned as a dipole forbidden singlet-singlet transition between the ground X^1A_1 and the 1A_2 states [77, 72].

The $T^\alpha \leftarrow S_0$ transition moments to particular spin sublevels for the three lowest triplet states of the ozone molecule, $^3B_2, ^3A_2$ and 3B_1 , were calculated by the MCQR method in ref. [70] using CASSCF wave functions. Table 7 recapitulates results for electric dipole radiative activity of different S-T transitions in ozone [70]. The type of information gained from this kind of spin-orbit response calculations are; *viz.* transition electric dipole moments and oscillator strengths for each spin sublevel T^α , their polarization directions (γ), radiative lifetimes (τ_n) and excitation energies (E_n). The most prominent features of the Chappuis band are reproduced in calculations, which simulate the photodynamics of ozone visible absorption [78, 79]. Because the $C^1A''(^1A_2)$ state cannot be responsible for the Wulf bands, the only other candidates ought to

be the spin-forbidden 3B_2 , 3A_2 and 3B_1 states from energy considerations. Transition energies, geometries, and vibrational frequencies can be used to accept or reject these candidates, however, only a direct oscillator strength calculation can firmly determine the true nature of the band. As seen in Table 7 the transitions to the 3A_2 state are more intensive than the transitions to other triplet states and they fit very well to the intensity of the Wulf band. The intensity ratio to the dipole allowed Chappuis band also corresponds well to the qualitative relative experimental intensity of these two bands [79].

The response calculations referred to above provide an interpretation for the large S-T intensity of the ${}^3A_2 \leftarrow X^1A_1$ transition and for the assignment of the Wulf band and do also explain that the very first triplet state of ozone, the a^3B_2 state which has some remarkable properties [80], is unobservable by absorption. This state has a very low excitation energy (about 1 eV [77, 81, 80]) and is believed to have a significant impact on the analysis of the ozone kinetics and perhaps on ozone densities at high altitudes [82]. The a^3B_2 state is also associated with a very low infrared intensity for triplet ozone [80]. These findings are remarkable because of the importance of stratospheric ozone for the absorption of solar radiation, and because the visible spectrum is useful for atmospheric ozone monitoring. Other features used for spectral assignments are the vibronic (Franck-Condon) characters of the bands, furthermore the dissociative or predissociative character of the PES:s, avoided crossings, activation barriers etc. Avoided crossings and conical intersections do not seem to enter directly in the Wulf band analysis, however. The PES of the first triplet, a^3B_2 , state and the ground state are thus very close, and may even cross. Triplet ozone might therefore exist in large but unobservable quantities with subtle vibrational and temperature dependent production and depletion mechanisms with respect to singlet ozone. The reviewed investigations show that the manifold of singlet and triplet states of molecules of atmospheric interest indeed can be addressed by multi-configuration linear and quadratic response theory calculations that explicitly account for SOC, and that they can give not only conclusive assignments but also interpretations of the origin of intensity.

6 Selected Singlet-Triplet Transitions

In addition to interpretations of optical and ultraviolet absorption spectra, as exemplified above by the new assignment of the ozone spectrum, (subsection V), the MCQR formalism lends itself also for determining lifetimes of triplet states and thus for the phenomenon of phosphorescence. In Fig. 3 we display a modified Jablonski diagram (modified by removing the vibrational manifolds of states) which give a pictorial demonstration of the different transition pathways between singlet ground and excited singlet and triplet states and the decay mechanism from the excited states. This comprises absorption, internal conversion, inter-system crossing, fluorescence and phosphorescence. Absorption can here involve multiple photons. According to Kasha's propensity rule, emission can take place only from the lowest singlet or the lowest triplet states. Fluorescence and phosphorescence denote the emission from the singlet and the triplet states,

Fig. 3

A Jablonski diagram excluding the vibrational manifold of states.

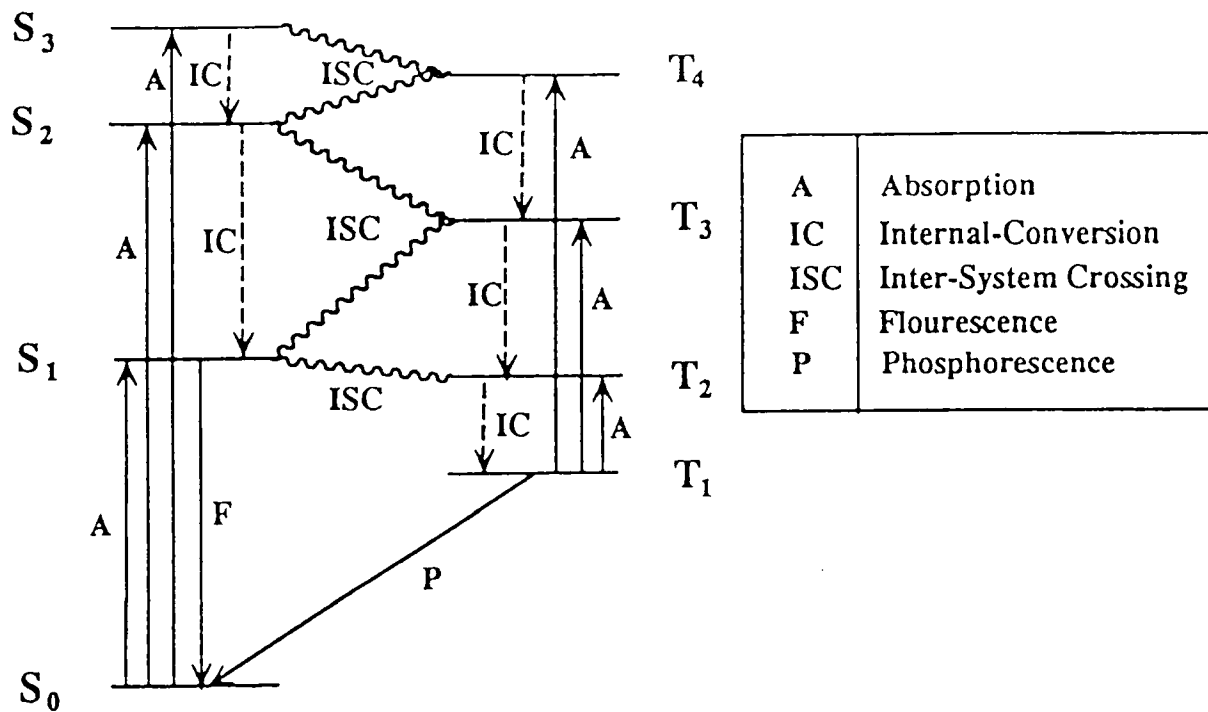


Table 7: Calculated S-T transition moments from the ground state (S_0) to the three lowest triplet states (T_n) at the ground state geometry, oscillator strengths (f), radiative lifetimes (τ_n), and vertical transition energy (E_n). From Ref. [70].

α	T_n								
Spin sublevel	3B_2			3A_2			3B_1		
	Total symm. T_1^α	$\langle T_1^\alpha \gamma S_0 \rangle$ γ	(a.u.)	Total symm. T_2^α	$\langle T_2^\alpha \gamma S_0 \rangle$ γ	(a.u.)	Total symm. T_3^α	$\langle T_3^\alpha \gamma S_0 \rangle$ γ	(a.u.)
x	A_1	z	$9.70 \cdot 10^{-8}$	B_1	x	$3.61 \cdot 10^{-3}$	A_2	forbidden	
y	A_2		forbidden	B_2	y	$6.33 \cdot 10^{-5}$	A_1	z	$1.67 \cdot 10^{-3}$
z	B_1	x	$1.78 \cdot 10^{-4}$	A_1	z	$8.63 \cdot 10^{-6}$	B_2	y	$6.97 \cdot 10^{-4}$
$f(T_n \leftarrow S_0)$	$8 \cdot 10^{-10}$			$5.67 \cdot 10^{-7}$			$1.31 \cdot 10^{-7}$		
τ_n (sec.)	83.1			0.038			0.200		
E_n (eV)	1.02			1.77			1.62		

respectively. Non-radiative deexcitations can take place within a multiplet system, so-called internal conversion, or between the multiplets systems, so-called intersystem crossing. Non-radiative deexcitation may also take place among vibrational levels, so-called vibrational quenching. Fig. 3 is close to complete as far as exceptions from Kasha's rule (e.g. emission from higher excited states) or involvement of higher multiplets (e.g. quintets) are extremely rare in molecular spectroscopy [49]. In this section we focus on singlet-triplet absorption and illustrate the capability of response theory by reviewing calculations on a selected set of transitions. In next section, section 7, we review the phenomenon of phosphorescence in more detail.

I Formaldehyde $^3A'' \rightarrow ^1A'$ emission

The lifetimes of the spin sublevels of the first triplet state, the $^3A''$ state of formaldehyde were obtained in ref. [11] as a first illustration of the MCQR method on singlet-triplet absorption and on phosphorescence. This species has previously been the object for "conventional" phosphorescence calculations as well as experiments, and was therefore suitable for demonstration of the response theory approach. It is a small non-degenerate polyatom with a comparatively simple excitation spectrum, and the computational dependencies on basis sets and different geometries and correlating active spaces could therefore be investigated rather exhaustively. Such a test for lifetimes and the excitation energies is exhibited in Table 8. The calculations illustrate that the correlation dependence can be quite different for the spin-sublevel transition moments and lifetimes. For H_2CO one thus finds large correlation effects for the slow components but small effects for the fast z-component which dominates the transition. For the average lifetime obtained at the high-temperature limit the correlation dependence is still quite weak. The experimental lifetimes are often not sufficiently accurate to favor any particular theoretical value. The final radiative rates are dependent on vibronic coupling

Table 8: Excitation energies (a.u.) and phosphorescence lifetimes (s) of the $^3A''$ triplet components of formaldehyde. From Ref. [11].

<i>Corr. Level</i>	<i>Basis set</i>	<i>Exc. Energy</i>	τ_x	τ_y	τ_z	τ^a
SCF	A 3s2p1d	0.0823	1277	2.159	0.007179	0.0215
	A ^b 3s2p1d	0.1265	4.617	1.108	0.004313	0.0129
	B4s3p2d1f	0.0815	1135	2.553	0.008124	0.0243
	B ^b 4s3p2d1f	0.1251	3.700	1.040	0.004667	0.0139
CAS	A 3s2p1d	0.1064	74.11	0.857	0.007817	0.0232
	A ^b 3s2p1d	0.1454	2.414	0.413	0.006934	0.0204
	B4s3p2d1f	0.1077	50.66	0.781	0.007110	0.0211
	B ^b 4s3p2d1f	0.1456	2.887	0.344	0.006153	0.0181

^{a)} High temperature limit (equal population of spin sublevels).

^{b)} Planar singlet ground state geometry.

and on geometry [83], e.g. the use of the singlet state geometry apparently gives an error of a factor of two at the SCF level, the difference being somewhat smaller at the CAS level.

II Singlet-Triplet Transitions in diatomics

The diatomic molecules, and the nitrogen molecule in particular, have rich electronic spectra, including a variety of transitions which are forbidden by orbital and spin symmetry restrictions [84]. Analysis of these transitions plays a crucial role for many photophysical and photochemical processes taking part in the atmosphere, including such phenomena as aurora and afterglow. Quadratic response multi-configuration self-consistent field calculations of energies and probabilities of S-T absorption transitions from the ground state $X^1\Sigma_g^+$ of N_2 to all triplet states of "ungerade" symmetry below 13 eV have been carried out recently [26, 85]. As demonstrated in this section the difference in singlet and triplet state geometries affects the phosphorescence yield significantly. Both on experimental [86] and theoretical [85] grounds the singlet-triplet transition moments are found to vary considerably over the internuclear distance. For N_2 the triplet state has an equilibrium almost 0.2 Å larger than the ground state which implies a rather complex vibrational structure and difficult transition moment calculation. In the particular case of the Vegard-Kaplan band this variation is linear close to the equilibrium where the transition moment even changes sign. The final predicted lifetime must therefore be carefully averaged vibrationally, and since the vanishing of the transition moment is caused by cancellation of a large number of terms accurate wave functions are required. Potential energy and transition moment curves for the states of interest calculated by the response method [26] are shown in Fig. 4 and Fig. 5, respectively. In the following we review some main results of these calculations. For computational details we refer to the original work. We state here that the generally contracted Atomic Natural Orbital (ANO) basis set [5s 4p 3d 2f] of Widmark *et al.* [87]

Fig. 4

Potential energy curves for the ground and few lowest triplet states of the N_2 molecule.

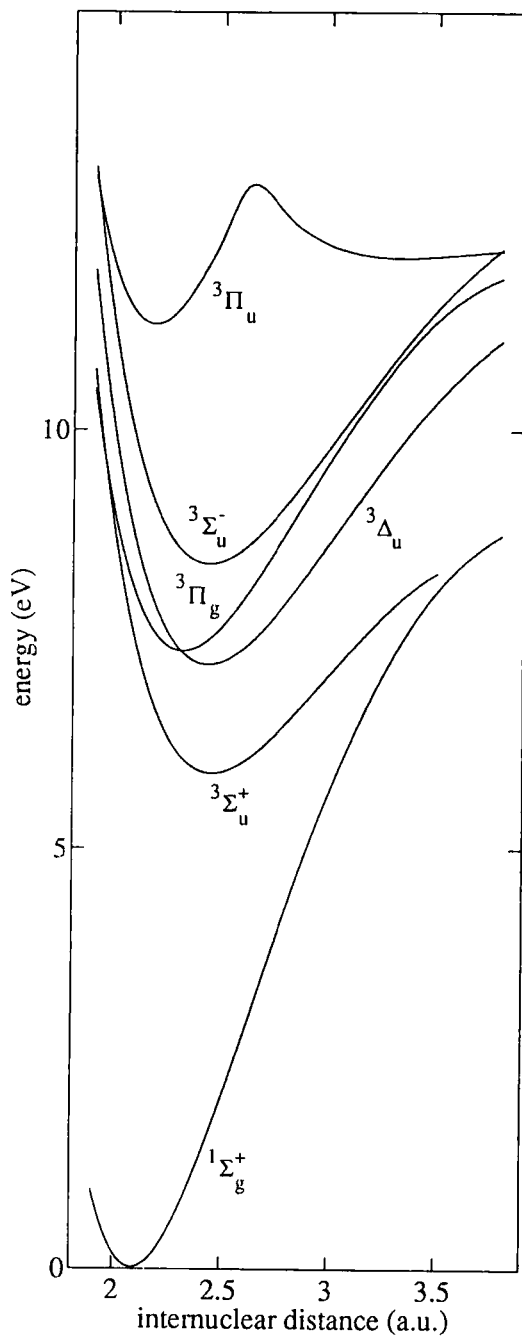
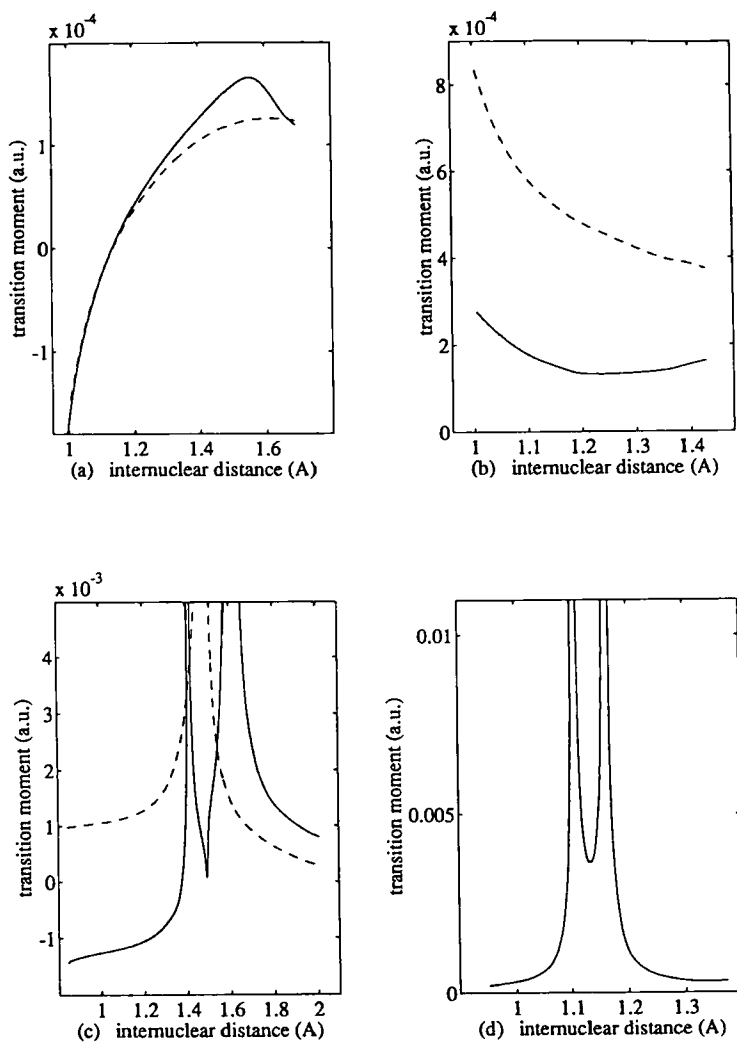


Fig. 5

Singlet-triplet transition moment curves in N_2 . All b,c,d, results correspond to valence CAS (CAS-1) calculations.

- (a) $W^3\Delta_u \leftarrow X^1\Sigma_g^+$: CAS-1 (dashed), CAS-2 (solid)
 (b) $B'^3\Sigma_u^- \leftarrow X^1\Sigma_g^+$: $\Omega=1$ (dashed), $\Omega=0$ (solid)
 (c) $C^3\Pi_u$ and $C'^3\Pi_u \leftarrow X^1\Sigma_g^+$ $\Omega=0,2$ (dashed), $\Omega=1$ (solid)
 (d) $D^3\Sigma_u^+ \leftarrow X^1\Sigma_g^+$.

From ref. [26].



were used, and that various correlating complete active spaces were evaluated. We review results from two of these; a valence active space (denoted "CAS-1" in the Tables) and an extended active space including also a few Rydberg orbitals ("CAS-2"). Because the potentials and response matrix elements show strong internuclear dependences the electronic calculations must be augmented by a vibronic analysis; this is accomplished in the reviewed work by numerical solutions of the vibrational Schrödinger equation in fitted potentials.

II-A N₂: The Vegard-Kaplan system

The Vegard-Kaplan transitions $A^3\Sigma_u^+ - X^1\Sigma_g^+$ have been observed both in emission and in absorption [88], and is the most studied T-S system in N₂. Shemansky [86] measured the absorption spectrum, identifying seven vibrational bands (6,0)-(12,0) and extracted from the obtained data an absolute transition moment curve in the interval 1.08-1.4 Å. The transition moment curve was found to be quite close to linear in the important interval 1.08-1.2 Å. The important feature of the curve is that it changes sign at $r = 1.173$ Å, i.e at the vicinity of $r_e \approx 1.1$ Å.

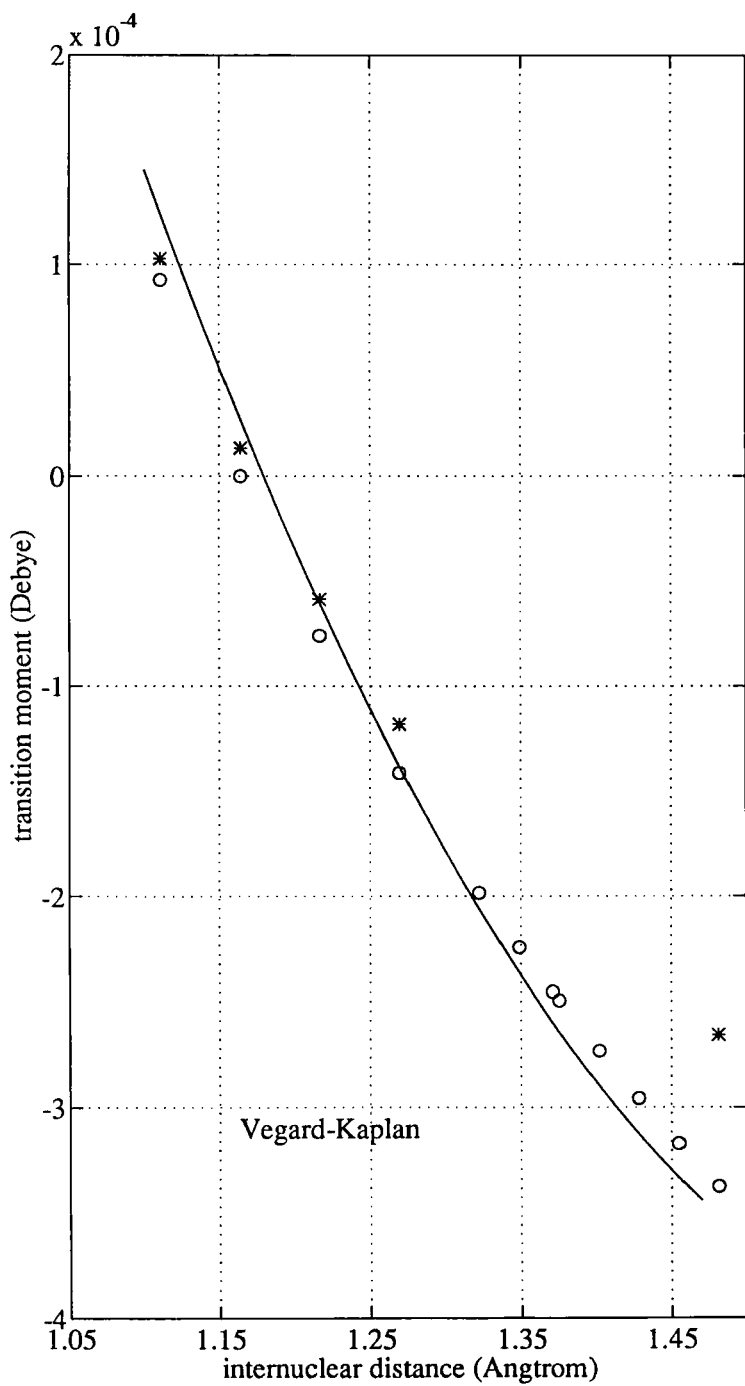
Recently, Piper [89] measured the relative intensities in a large number of Vegard-Kaplan emission bands and performed a profound revision of the transition moment function. The new transition moment curve deviates from linearity at large internuclear distances ($r > 1.3$ Å), much more than the previous one, and changes sign at $r = 1.179$ Å. It is shown in Fig. 6 together with transition moment values calculated by the response method for different active spaces. Even a moderate valence type active space was found to give good convergence characteristics for MCQR calculations of all transition moments at all distances. Inclusions of Rydberg orbitals (n.b. the $4\sigma_g$ orbital) implied some improvement of the Vegard-Kaplan transition moment curve, especially at large interatomic distances.

The complete active space response curve changes sign close to the equilibrium (1.175 Å), just as the experimental curve does. It is also close to being linear in a wide region (1.08 - 1.2 Å). Since the vanishing of the transition moment is caused by the cancellation of a sum of terms, the exact point where this cancellation occurs is very sensitive to the accuracy of the representation of the whole spectrum. The response theory calculations were here able to distinguish the quality of older data on transition moments of the Vegard-Kaplan system (Chandraiah and Shepherd [90], Broadfoot and Maran [91], Shemansky [86] and Piper [89]) holding the transition moment curve of Piper [89] as the best one.

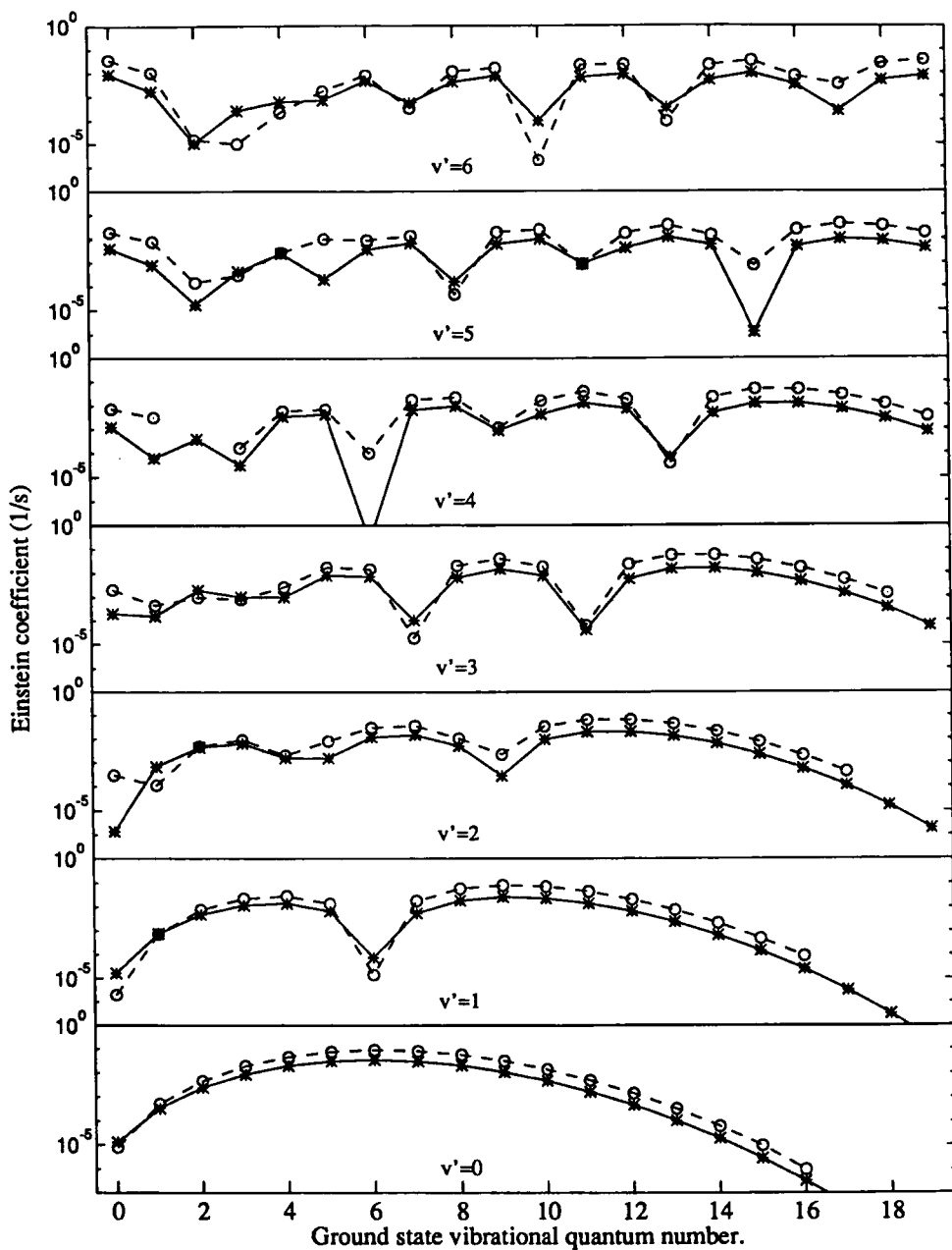
In Fig. 7 we recapitulate the spin-averaged Einstein coefficients for the Vegard-Kaplan emission from the lowest vibrational state of the triplet as well as the corresponding values reported by Piper [89]. The relative transition probabilities for different vibronic phosphorescence bands are quite good [26]. The absolute and the relative intensities of the higher vibrations v'' are very sensitive to the transition moment curve

Fig. 6

Transition moments for the Vegard-Kaplan system. Piper's function (solid) [89], CAS-1 (*), CAS-2 (circles). From ref. [26].



Einstein coefficients for the Vegard-Kaplan system in a logarithmic scale. Valence + Rydberg CAS (CAS-2, solid line), experimental data (dashed line) [89]. From ref. [26].



in the region 1.25 - 1.45 Å. The theoretical transition moments are somewhat underestimated at these distances, and lead therefore to some deviations for the lifetimes of the most intensive vibronic bands ($v'' = 5, 6$ and 7) and hence in the phosphorescence radiative lifetimes. This region is also sensitive to the design of the correlating active space of orbitals.

From the largest CAS calculation ("CAS-2" in ref. [26]) a lifetime of 2.58 s was predicted for one of the $\Omega = 1$ spin-sublevels ($M_S = \pm 1$) of the lowest triplet vibrational level. In a rotationless molecule the $\Omega = 0$ sublevel does not radiate, so the observed spin-averaged radiative lifetime of the Vegard-Kaplan emission is equal to $(3/2)\tau_{\Omega=1} = 3.87$ s. It should be compared with Piper's value, 2.37 s [89]. We can see from Fig. 7 that for the lower v'' vibronic quantum numbers the agreement is much better than for the most intensive transitions to the upper vibronic levels. The underestimation of the transition moment in the range 1.3-1.4 Å is more serious for the small active spaces. In the valence type CAS ("CAS-1" in ref. [26]) an averaged lifetime equal to 5.48 s was obtained.

II-B N₂: The $W^3\Delta_u \leftarrow X^1\Sigma_g^+$ Saum-Benesch system

Saum and Benesch found in 1970 the weak $W^3\Delta_u \leftarrow X^1\Sigma_g^+$ absorption. This constituted the upper state progressions $v' = 5, 6$ and 7 from the $v'' = 0$ level of the ground state. Benesch measured the oscillator strength for the $W(v' = 6) \leftarrow X(v'' = 0)$ transition to be equal to $f = 8.5 \times 10^{-11}$ [92]. The calculated CAS $W^3\Delta_u(\Omega = 1) \leftarrow X^1\Sigma_g^+$ transition moment functions are quite similar to that of the Vegard-Kaplan absorption. The $W - X$ transition function changes sign at 1.140 Å, i.e. a shorter internuclear distance than the $A - X$ transition curve does. The calculated oscillator strengths for the $W^3\Delta_u(v') \leftarrow X^1\Sigma_g^+(v'' = 0)$ transitions rise with increasing v' quantum number up to $v' = 13$ and then starts to decrease. The deviation from this trend occurs for $v' = 4$ which is connected with the zero crossing of the transition moment. The intensity of the $W - X(6-0)$ transition is very sensitive to the positions of minima of both potentials. A small shift of the potential curves would strongly change intensities for the $v' = 5$ and 6 bands. The calculated r_e values for the X and W states are shifted in the order of 0.007 Å from the experimentally derived values [93, 94]. The complete response calculation produces too low intensity for the $W - X(6-0)$ band but the results are improved by using the experimental ground state potential and shifting the W potential in order to reproduce the experimental equilibrium distance. In this case the oscillator strength for the $W - X(6-0)$ band is calculated to be 1.97×10^{-11} (valence CAS) which can be compared with the measurement of Benesch; $f = 8.5 \times 10^{-11}$ [92]. The upper bands have larger intensities which are comparable with the measured 6-0 band. From the known frequencies and Franck-Condon factors Benesch recalculated transition probabilities for other vibrational levels of the $W - X$ system, assuming a constant transition moment. The response calculations show that this assumption is definitely not correct; Benesch's estimation of the radiative lifetime for the $W(v' = 0)$ state (5.5 s) [92] deviates from the results of the response calculations by orders of

magnitude.

The 0-0 band is predicted to be extremely weak ($f = 10^{-12}$) in the response calculations [26]. Emission $W \rightarrow X$ could not be observed from the vibrational levels above $W(v' = 0)$, since these levels are more rapidly depleted by the allowed $W^3\Delta_u \rightarrow B^3\Pi_g$ transition in the infrared region. The $W(v'=0)$ level is quite unique, because the probability of IR transitions to the $B^3\Pi_g$ state is very low ($\omega_{0,0} \simeq 0$); it is several order of magnitude lower than that for the $W(v'=1)$ and upper levels [92]. For the lowest vibronic level $W^3\Delta_u(v' = 0)$ the ω^3 factor so heavily favors the $W^3\Delta_u(v' = 0) \rightarrow X^1\Sigma_g^+$ transition that this emission band was proposed by Benesch to be detectable [92] (when collision deactivation is low). The $W(v' = 0)$ state could bear a considerable portion of the auroral energy at the top of the atmosphere. It was found that the total cross section for the excitation of the W state by low-energy electrons is so large that no other nitrogen states attain as high an excitation rate in either auroras or glow discharges [95]. The small probability of spontaneous emission from the $W(v' = 0)$ state, obtained by the response calculations, supports the unique metastable character of this level.

II-C N_2 : The $B'^3\Sigma_u^- - X^1\Sigma_g^+$ Ogawa-Tanaka-Wilkinson system

The results of response calculations of this transition using valence CAS wave functions are recapitulated in Table 9 and Fig. 5. All three spin sublevels are active, the transitions to the $M_S = 1$ ($\Omega = 1$) sublevels being more intensive than those to the $M_S = 0$ ($\Omega = 0$), which is in qualitative agreement with the intensities of the rotational branches [96]. Tilford *et al.* [96] used the theoretical expressions for the intensity distribution of the $^3\Sigma^- - ^1\Sigma^+$ transition given by Schlapp [97] and extracted the ratio $\frac{B^2}{A^2} = 1.52$ for the (7-0) vibronic band, where A and B are related to the SOC anisotropy. A^2 and B^2 correspond almost, but not exactly, to $0.5m_1^2$ and to m_0^2 , respectively, where m_1 and m_0 are transition moments for the spin sublevels $M_S = 1$ and 0, respectively [98]. The ratio $\frac{m_0}{m_1} = 0.3$ was obtained for the (7-0) band, whereas Tilford *et al.* obtained 0.87 [96]. The ratio changes along the internuclear distance. Both the m_0 and m_1 transition moment curves exhibit a weak dependence on r in the important region of internuclear distances $1.15 < r < 1.25$ Å, though at smaller r the m_1 values increase to a marked degree (Fig. 5). The calculated oscillator strengths increase with the increase of the v' quantum number up to $v' = 8$ ($f_{8-0} = 1.63 \cdot 10^{-8}$), the most intensive transitions reside in the interval $v' = 5$ to 10. Experimental eye estimated relative vibronic intensities have a maximum at $v' = 7$ [99] and the most intensive transitions cover the same interval of vibrational quantum numbers [99, 96]. The $B' - X$ transition is much more intensive than the $W - X$ and $A - X$ transitions in agreement with experiment [99].

II-D N_2 : The $C^3\Pi_u \leftarrow X^1\Sigma_g^+$ Tanaka system

The Tanaka band, $C^3\Pi_u \leftarrow X^1\Sigma_g^+$, [100] is the most intensive known S-T transition of N_2 in the wavelength region above 100 nm. Ching, Cook and Becker measured the

Table 9:

Spin averaged Einstein coefficients and oscillator strengths for the Ogawa-Tanaka-Wilkinson band $B'^3\Sigma_u^-, \Omega(v') \longleftrightarrow X^1\Sigma_g^+(v'')$ for CAS-1 transition moment curve averaged over potentials from Lofthus and Krupenie [88].

$v'' = 0$ v'	$A^{xy}(\Omega = 1)$ s^{-1}	$A^z(\Omega = 0)$ s^{-1}	A^{av} s^{-1}	f^{tot}
0	2.308e-01	1.884e-02	1.601e-01	1.664e-10
1	1.289e+00	1.059e-01	8.945e-01	8.875e-10
2	3.875e+00	3.218e-01	2.691e+00	2.556e-09
3	8.300e+00	6.989e-01	5.766e+00	5.255e-09
4	1.401e+01	1.199e+00	9.742e+00	8.531e-09
5	2.002e+01	1.744e+00	1.393e+01	1.174e-08
6	2.558e+01	2.270e+00	1.781e+01	1.446e-08
7	2.917e+01	2.638e+00	2.032e+01	1.591e-08
8	3.088e+01	2.848e+00	2.154e+01	1.629e-08
9	3.140e+01	2.952e+00	2.191e+01	1.603e-08
10	2.982e+01	2.858e+00	2.084e+01	1.475e-08
11	2.723e+01	2.660e+00	1.904e+01	1.307e-08
12	2.413e+01	2.400e+00	1.689e+01	1.124e-08
13	2.051e+01	2.076e+00	1.437e+01	9.288e-09
14	1.714e+01	1.763e+00	1.201e+01	7.549e-09
15	1.428e+01	1.491e+00	1.001e+01	6.123e-09
16	1.155e+01	1.223e+00	8.106e+00	4.825e-09
17	9.323e+00	9.988e-01	6.548e+00	3.799e-09
18	7.485e+00	8.098e-01	5.260e+00	2.977e-09

Table 10:

Oscillator strengths for the Tanaka absorption band $C^3\Pi_u, \Omega(v') \longleftarrow X^1\Sigma_g^+(v'' = 0)$ for CAS-1 transition moment curve averaged over potentials from Lofthus and Krupenie [88]. x, y, z indexes show the light polarization.

$v'' = 0$ v'	$f^{xy}(\Omega = 1)$	$f^z(\Omega = 0)$	f^{tot}	f^{exp}
0	4.02e-07	3.94e-07	7.96e-07	2.2e-06
1	2.11e-07	2.44e-07	4.55e-07	1.1e-06
2	6.85e-08	8.88e-08	1.57e-07	5.6e-07
3	1.89e-08	2.64e-08	4.53e-08	-
4	5.31e-09	7.78e-09	1.31e-08	-

oscillator strength for the 0-0 transition of the Tanaka band to be equal to 2.2×10^{-6} [101], which is one of the strongest bands in this wavelength region.

In the case of the 0-0 transition, overlapping with the $(v' = 15) - (v'' = 0)$ band of the Lyman-Birge-Hopfield system occurred, but the principal absorption is undoubtedly the $C - X$ transition [101]. However the oscillator strength for the $C(v' = 0) \leftarrow X(v'' = 0)$ transition, presented by Ching *et al.* [101] should be regarded as an upper limit. The results of valence CAS response calculations are of the right order, but approximately three times lower (Table 10). Relative intensities are again much more reasonable. In agreement with experiment [96, 99, 101] only the first three bands have large intensities; the transitions with $v' > 3$ could not be observed at the small nitrogen pressures (< 1 atm) used in the experiments [96, 99, 101].

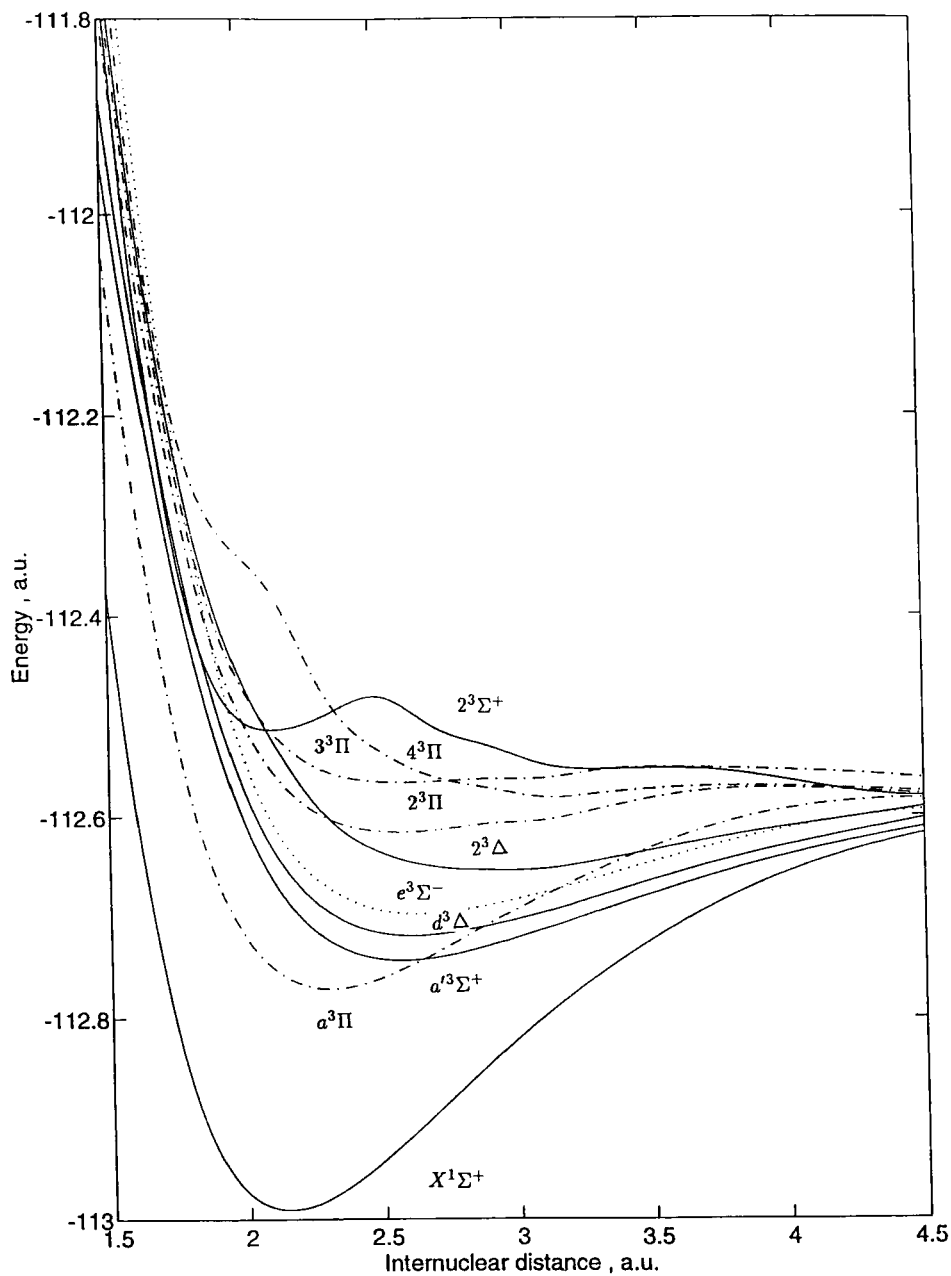
The $C - X$ transition moment curves are shown in Fig. 5. The $m_1(M_S = \pm 1)$ values have a positive sign while the $m_0(M_S = 0)$ transition moment values have a negative sign in the interval 0.8-1.2 Å, which is relevant for the $C - X$ intensity calculation. To the right of $r = 1.35$ Å, (i.e. in the vicinity of the equilibrium distance of the $C^3\Pi_u$ state) the two curves rise drastically [26], but this singularity has no relevance to the Tanaka $C - X$ system. The important region for the $C^3\Pi_u \leftarrow X^1\Sigma_g^+$ transition is to the left of $r = 1.25$ Å in Fig. 5. The transition moment curves m_0 and m_1 are smooth functions in this region and are quite close to being constant for $r < 1.2$ Å. The weak dependence of both transition moments on r in the important region is well supported by the arguments presented by Ching *et al.* [101]. They have shown that transition intensities are proportional to the Franck-Condon factors. The calculated total oscillator strength for the first three bands is 1.42×10^{-6} (valence CAS) while the experimental upper limit is 3.86×10^{-6} [101]. As it follows from Table 10, all spin sublevels have approximately equal transition probabilities. This qualitatively corresponds to the rotational analysis by Tilford *et al.* [96]. The spin-uncoupling effect in the $C^3\Pi_u$ state is quite large $Y = (A/B) = 21.5$ [96]. This means that the three Ω components are mixed even at the low rotational levels. Both parity (*e* and *f*) rovibronic transitions should have similar intensity. The case is opposite to the well-known Cameron transition $a^3\Pi - X^1\Sigma^+$ in the CO molecule where the $^3\Pi_1$ sublevel produces much larger intensity than the $^3\Pi_0$ and $^3\Pi_2$ sublevels, which determine characteristic rotational structure of the Cameron bands [102, 103] (see next subsection).

II-E CO: The Cameron band

The $a^3\Pi$ state is the lowest excited state of the CO molecule, see Fig. 8. The spin-forbidden transition from the $a^3\Pi$ state to the ground $X^1\Sigma^+$ state constitutes the well-known Cameron band system [104] which has been studied in the gas phase and in the solid matrices by many different experimental techniques [105, 106, 107, 108, 109, 110, 111, 112]. Theoretical calculations of the intensity of the Cameron bands and the lifetime of the $a^3\Pi$ state are though quite scarce [113, 112]. James [113] accounted for one perturbing state $A^1\Pi$, i.e. the SOC perturbation between the singlet and triplet

Fig. 8

Potential energy curves calculated by MCSCF and MCLR methods for the ground $X^1\Sigma^+$ state and for the excited triplet states of the CO molecule. From ref. [115].



states, $A^1\Pi - a^3\Pi_1$ of the same orbital configuration. Fournier *et al.* [112] accounted for the $X^1\Sigma^+ - a^3\Pi_0$ mixing and intensity borrowing from the permanent dipole moment difference in these two states in order to estimate the lowest $a^3\Pi_0$ lifetime component. Experimental values for the lifetime of the $a^3\Pi$ state have been found from about 1 msec (Borst and Zipf [114]) to 60 msec (Johnson [109]), depending on the experimental techniques for the determination. It is clear that the true lifetime of the $a^3\Pi$ state is a subject of great uncertainty and that it is difficult to determine accurately. The theoretical value of the $a^3\Pi$ lifetime obtained by James [113], 8.75 msec, is in good agreement with the value of Lawrence, 7.5 ± 1 msec [105]. It is therefore interesting to verify this simple theoretical prediction by the MCQR method where the explicit summations over intermediate states are replaced by the solution of a few sets of linear equations. Such calculations on the Cameron band system in carbon monoxide were recently carried out in ref. [115]. Vibrational averaging was performed using computed potentials.

The intensity of the Cameron bands arises from the mixture of some $^1\Pi_1$ character into the $^3\Pi_1$ level and some $^1\Sigma$ character into the $^3\Pi_0$ level. The $a^3\Pi_2 \rightarrow X^1\Sigma^+$ transition is forbidden for the nonrotating molecule. In the CO molecule the mixing is the most effective through the SOC operator between the $^3\Pi_1$ and the $^1\Pi_1$ sublevels referring to the same configuration, but when the molecule rotates, the three sublevels mix and three subbands can appear [113]. The spectroscopic constants of the ground and upper states are shown in Tables 11 and 12. The quality of CAS "10 in 12" results seems to be reasonable. The response calculations have been carried out for a non-rotating molecule and the electric dipole transition moments were determined for the transition from $a^3\Pi_1$ and $a^3\Pi_0$ spin-sublevels. Transitions from the $a^3\Pi_1$ spin-sublevel to the $X^1\Sigma^+$ state are represented as the $m_0 = \langle X^1\Sigma^+ | \hat{M}_{xy} | a^3\Pi_1 (M_S = 0) \rangle$ matrix elements with light polarization perpendicular to the molecular axis and the transition from the $a^3\Pi_0$ spin-sublevel to the $X^1\Sigma^+$ state as the $m_1 = \langle X^1\Sigma^+ | \hat{M}_z | a^3\Pi_0 \rangle$ transition matrix elements with the polarization along the axis. The results of the MCSCF calculation and of vibrational analysis for the $X^1\Sigma^+$ states are presented in Table 11 in comparison with the experimental data from Krupenie [116]. The molecular constants for the $a^3\Pi$ state obtained by MCLR are presented in Table 12. Although calculated vibronic transition probabilities are quite sensitive to the quality of the potential curves, the response theory results are in a reasonable agreement with experimental data [116].

The electric dipole transition moments for the Cameron system are shown in the Fig. 9. The dependences for the M_1 and M_0 transition matrix elements on the internuclear distances are completely different from one another. At the short internuclear distances the values of the m_0 transition matrix elements are more than three times larger than for m_1 , but with the increase of internuclear distances the difference between the components is decreasing, changes sign and then increases drastically in the opposite direction.

The electric dipole T-S transition moments calculated as functions of the internuclear distances were used for the estimation of the vibronic transition probabilities by a vibrational averaging procedure. The calculated Einstein coefficients for emission from

Fig. 9

Dependences of the transition matrix elements (a.u.) on the internuclear distances (a.u.) calculated by MCQR :

- (a) the $a^3\Pi_1 \rightarrow X^1\Sigma^+$ transition;
- (b) for $a^3\Pi_0 \rightarrow X^1\Sigma^+$ transition;

From ref. [115].

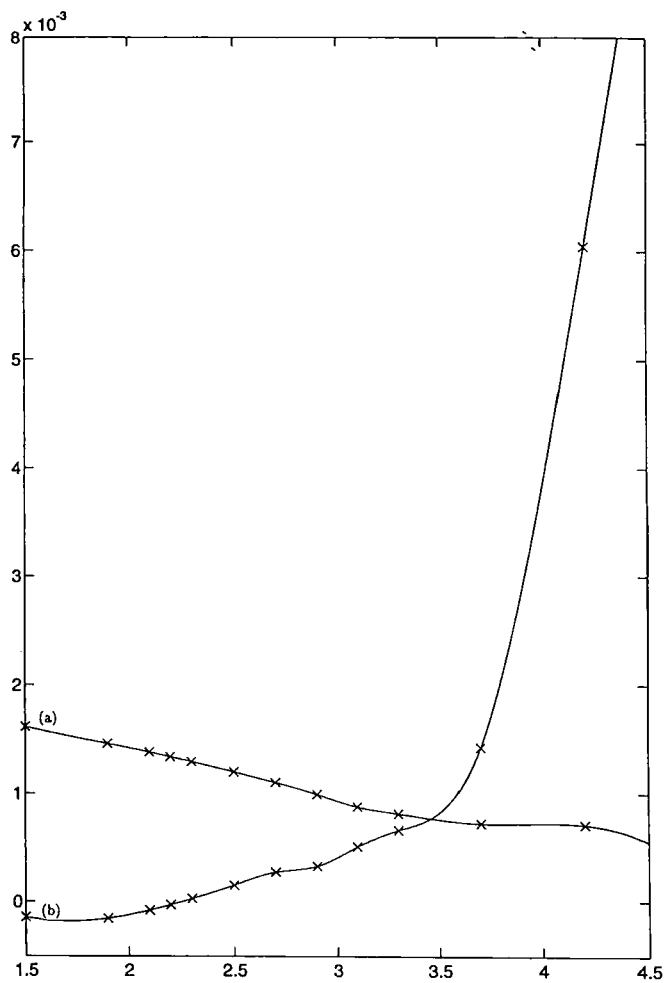


Table 11:

Spectroscopic constants of the $X^1\Sigma^+$ state of CO molecule obtained by vibrational averaged over potential energy curve calculated by MCSCF method.

	Experimental values [116]	CAS "10 in 9"	CAS "10 in 12"
$T_e(\text{eV})$	0	0	0
$D_e(\text{eV})$	11.2258	12.5939	12.7147
$r_e(\text{\AA})$	1.1283	1.1332	1.1381
$\omega_e(\text{cm}^{-1})$	2169.82	2224.39	2130.61
$\omega_e X_e(\text{cm}^{-1})$	13.29	18.42	9.50
$\omega_e Y_e(\text{cm}^{-1})$	—	$-1.97 \cdot 10^{-1}$	$-7.37 \cdot 10^{-2}$
$B_e(\text{cm}^{-1})$	1.9313	1.9149	1.9054
$\alpha_e(\text{cm}^{-1})$	0.0175	0.0153	0.0176
$\gamma_e(\text{cm}^{-1})$	$2.96 \cdot 10^{-6}$	$4.48 \cdot 10^{-5}$	$7.08 \cdot 10^{-6}$
$\delta_e(\text{cm}^{-1})$	$6.12 \cdot 10^{-6}$	$5.83 \cdot 10^{-6}$	$5.68 \cdot 10^{-6}$
$\beta_e(\text{cm}^{-1})$	$-0.99 \cdot 10^{-9}$	$6.24 \cdot 10^{-8}$	$1.19 \cdot 10^{-8}$
$D_0(\text{eV})$	11.091	12.4563	12.5840
$E_{\min}(\text{a.u.})$		-112.947347	-112.99070

Table 12:

Spectroscopic constants of the $a^3\Pi$ state of CO molecule obtained by vibrational averaged over potential energy curve calculated MCLR.

	Experimental values [116]	CAS "10 in 9"	CAS "10 in 12"
$T_e(\text{eV})$	6.036	5.518	5.981
$D_e(\text{eV})$	5.212	6.2383	3.9515
$r_e(\text{\AA})$	1.2058	1.2019	1.2186
$\omega_e(\text{cm}^{-1})$	1743.55	1821.37	1707.13
$\omega_e X_e(\text{cm}^{-1})$	14.47	9.41	14.27
$\omega_e Y_e(\text{cm}^{-1})$	—	$-2.01 \cdot 10^{-1}$	$-5.45 \cdot 10^{-2}$
$B_e(\text{cm}^{-1})$	1.6911	1.6936	1.6541
$\alpha_e(\text{cm}^{-1})$	0.0195	0.0202	0.0172
$\gamma_e(\text{cm}^{-1})$	—	$2.68 \cdot 10^{-4}$	$-2.14 \cdot 10^{-4}$
$\delta_e(\text{cm}^{-1})$	—	$5.24 \cdot 10^{-6}$	$6.29 \cdot 10^{-6}$
$\beta_e(\text{cm}^{-1})$	—	$1.35 \cdot 10^{-7}$	$4.31 \cdot 10^{-8}$
$D_0(\text{eV})$	5.0984	6.1577	3.8454
$E_{\min}(\text{a.u.})$		-112.74465	-112.770904

Table 13:

The Einstein coefficients (sec^{-1}) for the CO emission from $v' = 0, 1$ vibronic levels of the $a^3\Pi_1$ spin-substate to the $v''=0 - 10$ vibronic levels of the $X^1\Sigma^+$ state.

v'	James's results [113]		Calculated values			
			CAS "10 in 9"		CAS "10 in 12"	
v''	0	1	0	1	0	1
0	255	335	597.2	630.8	207.0	291.6
1	272	11.8	634.0	9.6	246.6	25.6
2	122	94.1	276.2	289.4	135.4	8.4
3	31.2	14.6	68.4	396.4	43.2	137.0
4	4.92	67.5	11.52	177.0	9.0	86.0
5	0.44	15.4	1.38	43.4	1.4	27.6
6	0.03	2.2	0.12	6.8	0.14	5.48
7	<0.01	0.19	0.004	0.66	0.01	0.74
9	0	0.03	0	0.04	0	0.08
10		<0.01		0.002		0.006

Table 14: MCQR results for transition energy (eV) and oscillator strength ($\times 10^{-12}$) for the $^3B_{1u} \leftarrow ^1A_g$ transition in ethylene. CAS-1 includes 2 electrons on two π -MO's, CAS-2 includes 8 electrons on 8 MO's, CAS-3 includes 12 electrons on 12 MO's,

		sz	dz	tz	tzp	tzpd
Transition energy	CAS-1	4.08	3.88	3.82	3.80	3.80
	CAS-2	4.31	4.06	4.00	3.96	3.96
	CAS-3	4.72	4.41	4.34	4.27	4.27
Osc. strength T_1^y	CAS-1	400	1890	503	121	112
	CAS-2	466	2200	593	374	387
	CAS-3	513	2460	668	176	164
Osc. strength T_1^x	CAS-1	3.61	6.79	7.30	8.04	8.66
	CAS-2	1.91	2.64	3.30	8.43	9.56
	CAS-3	3.63	7.96	8.16	10.6	11.5

the $v'=0,1$ vibronic sublevels of the $a^3\Pi$ state to the $v''=0-10$ vibronic sublevels of the ground $X^1\Sigma^+$ state are given in Table 13 in comparison with the results of James [113]. The calculated oscillator strength $f_{0-0} = 1.345 \cdot 10^{-7}$ can be compared with the results of Hasson and Nicholls, $(1.62 \pm 0.08) \cdot 10^{-7}$ [117] in absorption experiments and with a value $(1.51 \pm 0.15) \cdot 10^{-7}$ obtained by Fairbairn with using lower resolution and pressure broadening [118]. We can see from Table 13 that the valence CAS overestimates the transition probabilities more than two times, and that inclusion of highly diffuse 3π and 8σ orbitals (analogous to $2\pi_u$ and $5\sigma_g$ MO:s of the N_2 molecule) is quite important for the Cameron band intensity calculation of CO. It was shown in ref. [115] that the phosphorescence transition probabilities of the Cameron bands can be adequately explained by the response theory approach.

II-F Comments on diatomic calculations

The set of applications on H_2CO , N_2 and CO molecules reviewed above illustrates the current feasibility for studying triplet state properties in small molecules by means of response theory. This goes for details, such as excitation energetics, radiative transition probabilities, potential energy curves and individual state-to-state couplings, as well as for an effective *global* characterization of the multiplet systems. This is accomplished by using one common set of parameters, namely of one-particle and N-particle basis sets for the reference wave function, and the ease of the calculations in this respect must be emphasized. It was found that already limited correlating valence spaces provide a good global account of the triplet multiplet system. On the other hand, the lowest order response theory, the random phase approximation, may be instable for singlet-triplet transitions, as it indeed is for N_2 . It should also be noted, that although response theory is designed for property calculations, the obtained S-T excitation energies and triplet state potential energy curves are of very good quality. In fact, the solutions of the response eigenvalue equations gave better triplet state energies than if these were optimized individually by MCSCF (with the parameterization used for the ground state). This is certainly not the case for the singlet system, and might reflect the different nature of electron correlation for singlet and triplet states.

As mentioned in the theory section (3) the response theory approach provides an effective implementation of perturbation theory in that the response functions are obtained by solving equations rather than by making explicit summations. Large dimensional problems can therefore be addressed. The response calculations of the type described above illustrate that convergence of the sum-over-state approach is slow. This may be seen by comparing the exact transition moment obtained from the MCQR calculation with the transition moment calculated from a limited number of low-lying states of each spin multiplicity. In general it turns out that higher intermediate states cannot be neglected. The contributions from the individual intermediate states vary considerably and may be both positive and negative.

For the diatomic calculations reviewed above the complete sum-over-state procedure is of particular importance, because it provides a *size consistent* approach to the

singlet-triplet transition moment curves. In general these curves vary strongly over a limited region of internuclear distances; for the Vegard-Kaplan and the Saum-Benesch systems they even displayed a zero-crossing point close to the equilibrium distance. Any truncation of the sum-over-state would severely flaw these curves, since there are many small contributions of arbitrary sign that would be truncated differently at different geometries. Truncation of the summation over states could occasionally still be desirable for the purpose of interpretation, as also exemplified above. This is warranted only if there are few dominating contributions. It can be accomplished either by re-optimizing excited state wave functions and employing linear response calculations to get the excited state matrix elements, or by employing a decomposition analysis by computing the double residues of the quadratic response functions, which gives these matrix elements from optimization of the ground state wave function only. A complication with this is that the evaluation of each matrix element requires the solution of one set of linear response equations as well as the calculation of two roots of the linear response eigenvalue equations. Therefore, the cost for performing such interpretations is comparable to that of calculating the phosphorescence matrix element itself.

Implementing perturbation theory, some of the limitations of the response function approach are predictable. These become apparent for higher excited states where singlet-triplet crossings become abundant. These crossings render a blow up of the transition moments as a result of the singularities. In such cases the perturbation theory should rather include vibrational states which may remove the singularities (leading to avoided crossings). In state-specific approaches the vibronic wave function can be determined by solving the coupled electronic state vibrational Schrödinger equation [119, 120, 121]. Such approaches have even been applied in diabatic representations [122, 119, 120, 123]. The implementation of such procedures for sum-over-state, response, calculations for the spin-forbidden dipole spectra does, however, not seem to be straightforward. Fortunately, the singularities can be monitored; in the work described above they enter in regions which do not contribute much to the vibronic S-T transition intensities. Instabilities in the solutions of the response equations can also be encountered when closing the dissociation limit, or when very diffuse orbitals are included in the active reference space. By large however, a limited correlating active space gives a good account of the global spectrum.

Summarizing this section, we find that MCQR theory reproduces a variety of known features of the S-T spectra of small molecules quite well, and that it also predicts some new assignments which could be checked by modern spectroscopic methods. For high energy VUV transitions the results may be of more qualitative use because the calculated potentials in these regions are less accurate. These states have often not yet been determined by experiments, and the qualitative predictions by response theory could be used for a search for absorptions in this region. The results for the small molecules infers optimism for applications of response theory to S-T transition also of somewhat larger molecules of more chemical interest. We exemplify this by reviewing applications of spin-orbit response theory on organic π -electronic molecules in the following sections.

III Conjugated Hydrocarbons

The low-lying excited states of conjugated hydrocarbons are primarily associated with delocalized π -electrons. Semi-empirical π -electron theory describes the singlet-triplet (S-T) splitting of low-lying excited states and singlet-singlet $\pi - \pi^*$ transition energies and intensities quite well [49]. These properties represent a great challenge for *ab initio* theory [124, 60]. The so-called V state in Mulliken's terminology (the HOMO - LUMO $\pi - \pi^*$ singlet excited state) involves valence and Rydberg character with different type of dynamic correlation and basis set dependence, so it is difficult to get a proper balance of these properties [60]. The role of $\sigma - \sigma^*$ configurations and dynamic polarization of the σ core in V excited states are also important [125, 60]. In addition to response theory methods [126] a good general agreement with experimental data has been obtained using such methods as the multi-reference configuration interaction (MRCI) [124, 127], the multi-configuration perturbation theory (CASPT2) [60]

The role of S-T transitions in electron spectroscopy of unsaturated hydrocarbons has been little investigated in comparison with the role of the manifold of singlet states. In general the importance of triplet states of organic compounds for spectra and reactivity has been well recognized for a long time [49]. For short polyenes the first information about lowest triplet state was obtained by Evans from optically induced S-T absorption spectra in the presence of oxygen under pressure [128]. In addition to the studies using the optical method the S-T transitions in these molecules have been detected by threshold electron impact excitation techniques [129, 130] and by electron energy-loss spectroscopy [131]. The triplet valence and Rydberg state excitation energies are well known from these studies, but the information about transition probabilities are scarce or even absent. At the same time such information is important for photochemistry of polyenes and for systematization of the main characteristic features of S-T transitions in unsaturated hydrocarbons in a framework of *ab initio* theory [132].

Recently, the response theory formalism was applied for the calculation of singlet-triplet spectra in polyenes and aromatic hydrocarbons [83, 133, 134, 132]. In this section we shall discuss mainly the vertical $T_n \leftarrow S_0$ transitions probability in polyenes. The minimum level of accuracy includes CAS calculations of the ground state correlating all π electrons followed by linear and quadratic multi-configuration response calculations. Because the ethene molecule is the simplest representative of unsaturated hydrocarbons, different types of active spaces and AO basis sets were tested more thoroughly for this molecule in order to study the convergence of the S-T transition probability with respect to the level of accuracy.

III-A Ethylene

The ground state ethylene molecule belongs to the D_{2h} point group and we shall consider the vertical spectrum using notations of this group. Calculations were based on large active space and basis sets and on optimized ground state geometries. The results

obtained by different CAS and basis sets are shown in Table 14. The $^3B_{1u}$ state has the following total symmetry for the three ZFS (T^i) spin-sublevels: $B_{2u}(T^x)$, $B_{3u}(T^y)$, $A_u(T^z)$. It means that the $^3B_{1u} \leftarrow X^1A_g$ transition to the T^x spin-sublevel is polarized along the y axis. In semiempirical CNDO/S CI calculations this transition is forbidden, because the triplet configurations of $\pi\pi^*$ and $\sigma\sigma^*$ types do not interact and the lowest $T_1(\pi\pi^*)$ state has no orbitals in common with the singlet $^1B_{2u}$ states. The commonly effective one-electron SOC approximation [135] can not produce non-zero SOC matrix elements between the $^3B_{1u}^x$ spin-sublevel and the $^1B_{2u}$ states. In the *ab initio* MCQR method these restrictions are removed and the transition probability to the T_1^x spin-sublevel can be estimated and the validity of the earlier applied semi-empirical approximations can be verified. As can be seen from Table 14, this transition intensity is negligible in comparison with the main contribution of the $T_1 \leftarrow S_0$ absorption produced by transitions to the T_1^y spin-sublevel. In the large (TZPD) basis set and large ("CAS-2" [132]) active space the oscillator strength for the T_1^x and the T_1^y states are 9.56×10^{-12} and 3.87×10^{-10} , respectively (Table 14). Such a large difference is typical for other hydrocarbons and are observed in PMDR spectra of aromatics [48, 136, 137]. Transitions to the T_1^z spin-sublevel are strictly forbidden for the vertical $T_1 \leftarrow S_0$ excitation. From Table 14 we can see that correlation effects are quite important for the $T_1 - S_0$ transition probability especially in calculations with the largest basis sets. All CAS calculations predict the vertical transition energy of the order of 4 eV and are not very basis set dependent (Table 14). The experimental value, obtained from optical and electron energy loss spectra, is 4.36 eV [131, 138]. The $T_1^y \leftarrow S_0$ transition intensity is borrowed from the $\pi - \sigma$ excitations ($^1B_{3u} - X^1A_g$ and $^3B_{2g} - a^3B_{1u}$ transitions). The upper states are of highly diffuse character; because of this, the results are sensitive to correlation and basis set. Addition of polarized orbitals (TZP-type basis sets) leads to diminishing oscillator strengths for the T_1^y spin-sublevel, in the active spaces CAS-1 and CAS-3 it decreases more than 3 times (Table 14). The $T_1 \leftarrow S_0$ transition is 98% out-of-plane polarized and connected mostly with light absorption by the T_1^y spin-sublevel. The MCQR method gives here credit to the old CNDO/S CI SOC approach [139, 50, 140]. The calculated $T_1 - S_0$ transition moment in this approach was 1.28×10^{-4} a.u. [140] which is only twice as large as our best (TZPD) CAS-2 result 6.38×10^{-5} a.u. and is quite close to the CAS-3 TZ prediction.

III-B Butadiene

There has been a great amount of theoretical and experimental studies on the spectra of stereoisomers of butadiene (BD) and their photochemistry [141, 60, 142]. In spite of this interest in the electronic excited states of BD there exist no other theoretical considerations of the intensity of the lowest energy transition $a^3B_u \leftarrow X^1A_g$, besides the short communication in Ref. [125] using a semi-empirical SOC method (CNDO/S CI).

The low-lying triplet states of BD were investigated optically by Evans [128] using the high pressure oxygen perturbation technique. The broad absorption band with

maxima at 387 nm was assigned to the $T_1(^1B_u) \leftarrow S_0(X^1A_g)$ transition, the assignment of which has been confirmed by an electron impact study [129] and by *ab initio* calculations [124, 60]. In Table 15 we present the results of MCQR calculations for the s-trans butadiene $T_1 - S_0$ transition intensity in two basis sets [132]. The transition energies are also given from Δ MCSCF and response calculations, for comparison. The vertical transition energy for the 1B_u state is calculated to be equal to 2.97 eV (MCQR) and 3.36 eV (Δ MCSCF), the response value being somewhat lower than the experimental energy, 3.2 eV [129]. The same tendency occurs for other molecules studied by MCQR calculations [134, 83]. The calculated energies are not strongly dependent on basis set, but the SOC induced transition probabilities changed drastically. We now discuss the highest level TZP results for the vertical $T_1 \leftarrow S_0$ absorption from the ground state geometry (S_0 column). The most intensive transition is connected with the T_1^y spin-sublevel and is out-of-plane polarized; the transition moment is 6.55×10^{-5} a.u. which corresponds to the oscillator strength $f = 3.12 \times 10^{-10}$ and to the hypothetical radiative lifetime 8.33 s. The T_1^x sublevel also produces the out-of-plane polarized T-S absorption, but its oscillator strength is extremely small 5×10^{-12} , so only the T_1^y sublevel is active (y is a short in-plane axis, perpendicular to C=C bonds). The in-plane polarization (transition to the T_1^z spin-sublevel) has negligible intensity ($M_x = 1.68 \times 10^{-6}$ a.u., $M_y = 1.09 \times 10^{-5}$ a.u.); its oscillator strength is equal to 8.9×10^{-12} .

These qualitative features are reproduced also in a small (DZ) basis set, but the total oscillator strength is much higher; the same results have been obtained for the ethylene molecule. At the highest TZP level the total oscillator strength for the $T_1 \leftarrow S_0$ absorption in BD is 3.3×10^{-10} and the hypothetical spin-averaged radiative lifetime is 23.9 s. The oscillator strength of the $T_1 \rightarrow S_0$ transition at the optimized trans-BD geometry of the T_1 state is also presented in Table 15, in the T_1 column. Because of the fall of energy of the upper state and the rise of energy in the ground state, the transition energy from the response calculation is now much lower, 1.44 eV. The transition moment is also diminished leading to a smaller total oscillator strength of 1.03×10^{-10} . Because of the lower frequency the phosphorescence radiative lifetime of the equilibrium T_1 state is extremely large, here predicted to over 5 minutes. This is one of the reasons for that the phosphorescence of BD has never been observed. The additional possible explanation for the lack of phosphorescence could be obtained from analysis of geometry optimization for the three lowest states of trans-BD and their vibrational frequencies [132].

In spite of the fact that the total energy minimum of the T_1 state corresponds to a planar structure, the potential energy surface (PES) is quite flat with respect to some internal rotations [132]. The low frequency modes are greatly decreased on going from the ground singlet to the first triplet state. It means that the T_1 state PES becomes much more flexible upon out-of-plane distortions. The calculations show that the large amplitude disrotatory vibrations of terminal methene groups in the T_1 state with simultaneous internal rotation around the central C-C bond (the first step of trans-cis isomerization reaction) lead to a small energy gap towards the ground

Table 15: Transition energy (eV), oscillator strength ($\times 10^{-12}$), and phosphorescence lifetime (s) for the ${}^3B_u - {}^1A_g$ transition in butadiene (CAS44) and hexatriene (CAS66), calculated at the S_0 and T_1 state optimized geometries

Molecule Basis set Reference state geometry	BD				HT	
	dz		tzip		dz	
	S_0	T_1	S_0	T_1	S_0	T_1
Transition energy						
MCQR	3.02	1.49	2.97	1.44	2.44	1.03
Δ MCSCF	3.35	1.85	3.36	1.86	2.78	1.40
Osc. strength						
T_1^x	0.87	2.33	5.08	2.98	7.51	5.20
T_1^y	1645	490	312	98.7	1460	290
T_1^z	6.37	0.83	8.93	1.02	5.51	0.532
total	1653	494	327	103	1470	296
Lifetime						
τ_x	2917	4427	513	3749	516	4157
τ_y	1.54	21.1	8.33	113	2.66	74.5
τ_z	398	12510	292	10983	704	40650
spin averaged	4.60	62.8	23.9	327	7.90	219

Table 16: Relative intensities of different vibronic bands in benzene phosphorescence (%).

Mode Wilson not.	Frequency (cm^{-1})		Expt.[157]	Intensity %			
	$\nu_{exp.}$	$\nu_{calc.}$		DZ	DZR	TZ	TZR
b_{2g} ν_4	707	738	2.2	3.1	3.6	3.8	2.2
ν_5	1005	1064	5.0	4.8	7.5	9.7	6.4
e_{2g} ν_6	606	602	2.1	0.3	0.1	0.3	0.1
ν_7	3057	3374	0.2	0.2	0.4	0.1	0.1
ν_8	1601	1726	65.8	64.5	61.9	54.3	58.4
ν_9	1178	1293	24.7	27.3	28.3	32.2	33.0

singlet state. The first stage of the *trans* \rightarrow *cis* isomerization reaction distorts toward the quasi-tetraradical structure from the s-*trans* minimum region [142]. Even a small SOC will in this case induce ultrafast radiationless intersystem transitions to the S_0 ground state of trans-butadiene. The passage to the S_0 state will then follow the pathway associated with the most favorable spin recoupling process; a structure which favors the s-*trans* conformation of BD will obviously disfavor the recoupling of unpaired electrons of the two terminal CH_2 groups leading to cyclobutene. This corresponds to some photochemical observations. Comparison between the direct and the sensitized irradiations [143] shows that the triplet state of BD does not participate in valence photoisomerization to cyclobutene. It was also shown that the photolysis of butadiene derivatives in the vapor phase cannot be quenched by O_2 [144]. These results together with previous analysis imply that the T_1 state is very quickly quenched by intersystem crossing to the ground state before reaching the region of conical intersection [142] of two singlet states.

III-C Hexatriene

The DZ results for the $T_1 - S_0$ transition energy and intensity in s-*trans* hexatriene (HT) are shown in Table 15. As for butadiene the most intensive $T_1 \leftarrow S_0$ transition is connected with the T_1^y spin-sublevel and is out-of-plane polarized with transition moment 1.56×10^{-4} a.u. Both T_1^x and T_1^z spin-sublevel transitions have negligible intensities. The MCQR transition energy 2.44 eV can be compared with the experimental value 2.61 eV [145]. The total oscillator strength for the $T_1 \leftarrow S_0$ absorption equals 1.47×10^{-9} , corresponding to a spin averaged lifetime of 7.90 s. At the optimized geometry of the T_1 state the transition energy is much lower, 1.03 eV (MCQR) and since the transition moment changes only by a small amount to 1.07×10^{-4} a.u. for the dominating T_1^y spin-sublevel, the effect will be a greatly reduced total oscillator strength; 2.96×10^{-10} . The corresponding spin averaged lifetime is as long as 219 s. This is in complete analogy with the results obtained for butadiene and we can expect these considerations to hold also for the T_1 state of longer polyenes, thereby explaining the lack of phosphorescence in experimental observations. The $T_1 \leftarrow S_0$ transition moments calculated at the same level of accuracy (DZ basis, π -CAS) in all three molecules are almost identical (close to 1.6×10^{-4} a.u.).

III-D Comparison of singlet-triplet transition intensities in polyenes

The studies of the singlet-triplet absorption and emission spectra of the short conjugated polyenes; ethylene, trans-1,3-butadiene and trans-1,3,5-hexatriene by means MCQR SOC calculations [132] lead to the following general conclusions. Extensive test calculations on ethylene show quite strong basis set and active space dependences of the T-S transition probabilities. The increase of the basis set (starting from DZ-basis) systematically lowers the $T_1^y - S_0$ transition moment. The account of correlation is also important. Enlargement of CAS wave functions generally increases the T-S intensity

for the SZ, DZ and TZ basis sets. Inclusion of polarization functions changes this trend. This sensitivity to the active space and basis set extension is connected with the role of highly excited $\sigma - \pi$ Rydberg and valence states in the forming of SOC and intensity borrowing for the $T_1 - S_0$ transition in hydrocarbons [48, 83]. Despite the sensitivity of computational parameters a comparative analysis of the ethylene, butadiene and hexatriene molecules at a given computational level shows that the fundamental radiative quantities relating to the triplet state of these molecules (transition moments and polarization ratios) are remarkably similar.

From the results presented in Ref. [132] the absence of observed phosphorescence in the short polyenes is understood as a combination of small $T_1 \rightarrow S_0$ transition probability and vibrational quenching. Because of the similarity of results for all triplet state quantities of the ethylene, butadiene and hexatriene molecules investigated here, one can propose that these arguments also hold as explanation for the lack of phosphorescence in the longer polyenes [132].

7 Phosphorescence of Aromatic Compounds

In contrast to polyenes the aromatic molecules exhibit not only the $T_1 \leftarrow S_0$ absorption, but also the longlived $T_1 \rightarrow S_0$ emission, which gives rise to phosphorescence phenomena of rigid solvents and crystals. This is another important field of applications of spin-orbit quadratic response theory. Such calculations refer to lifetimes, transition moments, oscillator strengths and polarization directions for the radiative decay of molecular triplet states. These quantities may either be averaged over the triplet levels or refer to specific triplet spin sublevels depending on the conditions for the relevant experimental measurements.

The phosphorescence phenomenon was early identified as a radiative intercombination process between the lowest triplet state and the singlet ground state [146, 147], but can refer to any emissive passage between two states of the same molecule which are of different multiplicity. In practice, it refers to the lowest in the manifold of the excited states because higher lying states preferably decay through internal conversion. The triplet nature of phosphorescence radiation has been established by magnetic resonance measurements; the electric dipole character by interferometric studies [148]; the involvement of SOC through heavy atom substituents effects [149]. MCQR calculations performed for the small molecules; of N_2 [85, 26], CO [115] and H_2CO [11], reviewed here in section 6 in the context of singlet-triplet transitions, can also be used to explore phosphorescence in these compounds. S-T transition probability calculations in ethylene and halogen anion complexes in Ref. [150] are referring to the model of the external heavy atom effect on phosphorescence and are discussed in next section (section 8). Phosphorescence has been studied also for a series of aromatic molecules by means of response theory calculations, namely benzene [83, 133], azabenzenes [151], naphthalene and azanaphthalenes [134]. The latter series of investigations are presented at the

end of this section. The benchmark problem in this respect is the phosphorescence of benzene molecule.

I Benzene

The $T_1 - S_0$ transition in benzene molecule is a great challenge to theory. The phosphorescence spectrum of benzene is particularly rich in vibronic structure and provides the most well-known example of a spectrum of electronic transitions that is both spin and orbital symmetry forbidden. The assignment of the first excited triplet state in benzene is now firmly established as a $^3B_{1u}$ state [136, 152]. Basic to the benzene phosphorescence problem is the fact that the $\hat{a}^3B_{1u} \rightarrow \hat{X}^1A_{1g}$ transition is doubly forbidden by spin and orbital symmetry (0-0 transition is missing). Perturbation due to spin-orbit coupling alone can therefore not provide electric dipole intensity for this transition without involving vibronic interactions. Results from semi-empirical calculations of benzene phosphorescence have not considered all channels nor all the interacting electronic states and have given rather different values for the radiative lifetimes. The experiments have been undertaken with different glassy media or with benzene isolated in crystal matrices and have not been completely unambiguous concerning the triplet state lifetime, quantum yield and polarization of radiation. The question of the true radiative (phosphorescent) lifetime of benzene has therefore been considered open, although one seems to agree upon a "best experimental" value that focus on 30 sec [153, 154]. Because of the obvious importance of benzene in theoretical organic chemistry it is desirable to investigate its singlet-triplet spectra from first principles. In recent works [83, 133] the vibronically induced phosphorescence have been treated by means of multi-configuration quadratic response theory calculations and explored the vibronic intensities, polarization directions for benzene phosphorescence and the radiative lifetime of triplet benzene have been explored. Such transitions, which are allowed through the coupling of nuclear and electronic motions, including SOC perturbation, are notoriously difficult to analyze on theoretical grounds and only MCQR theory seems to be adequate so far on the *ab initio* level. Before considering the results of MCQR calculations [83, 133] we shall briefly summarize the experimental facts and the previous theories.

I-A History of the benzene phosphorescence problem

Vibrational analysis of the benzene phosphorescence bands indicates that the radiative activity is induced predominantly by e_{2g} vibrations [155, 156]. A weak but observable activity of b_{2g} vibrations has also been found [156, 155, 157]. By introducing spin-orbit- and vibronic coupling through second order perturbation theory Albrecht [158] showed that the vibronic interaction within the triplet manifold is responsible for the larger part of the phosphorescence intensity. This also follows from comparison of the vibrational structure in phosphorescence and fluorescence spectra [159]. The benzene phosphorescence spectrum in rigid glasses [155] reveals a dominant vibronic activity of

the ν_8 (1601 cm^{-1}) and ν_9 (1178 cm^{-1}) e_{2g} vibrations. The ν_6 (608 cm^{-1}) mode is very active in fluorescence ($^1B_{2u} \rightarrow ^1A_{1g}$), but appears only weakly in the phosphorescence spectrum [155, 159, 157, 136] (the Wilson numbering of benzene vibrations are used [160]). The explanation of these features has been proposed by Moffitt and Liehr on the ground of "pseudo-Jahn-Teller" interactions between $\pi - \pi^*$ states induced by different e_{2g} vibrations [161, 162]. They have shown that C-C stretching vibrations ν_8 are most effective for coupling between B_{1u} and E_{1u} states, whereas the benzene skeletal bending mode ν_6 is most effective for $B_{2u} - E_{1u}$ mixing. These ideas explain well the observed vibronic fluorescence $^1B_{2u} \rightarrow ^1A_{1g}$ and phosphorescence $^3B_{1u} \rightarrow ^1A_{1g}$ spectra. The first one borrows intensity from a very strong $^1E_{1u} - ^1A_{1g}$ transition ($^1E_{1u} - ^1B_{2u}$ mixing by ν_6 mode), the second one borrows from the spin-forbidden $^3E_{1u} - ^1A_{1g}$ transition, which becomes allowed by the account of spin-orbit coupling (SOC) [163, 164, 158].

The importance of $^3E_{1u} \leftrightarrow ^3B_{1u}$ mixing by ν_8 vibrations was directly supported by the analysis of the $^3B_{1u} \leftarrow ^1A_{1g}$ absorption spectrum [165] and its Zeeman effect [166]. The intense lines at 250 cm^{-1} above the 0-0 transition in the absorption spectrum of the O_2 induced $T_1 \leftarrow S_0$ absorption in gas phase and in low temperature crystals were attributed to the ν_8 vibration, the frequency of which is drastically reduced in the $^3B_{1u}$ state in comparison with the ground state value (1601 cm^{-1}) [165]. This is a consequence of the above mentioned "pseudo-Jahn-Teller" interaction; the potential energy surface (PES) in the benzene lowest triplet state (T_1) is extremely flat and has few shallow minima, slightly distorted ($\approx 0.02 \text{ \AA}$) from the D_{6h} conformation [167, 152]. We suppose that this difference in PES:s of S_0 and T_1 states does not influence much the vibronic structure of phosphorescence spectrum described on the basis of vibrations of the S_0 state alone. This follows from two arguments: i) The vibrational wave function of the zero-point level demonstrates that the molecule in the T_1 state is not confined to the minima but makes large excursions over the complete well [152]. The free molecule thus appears hexagonal, but even a weak crystal field can explain the host-dependent effects in ESR [168, 169] and ODMR spectra [136, 170] of low temperature doped crystals and glasses: ii) In spite of the large differences in ν_8 vibrations in the upper and lower states (including the anharmonicity) [152], the normal modes are qualitatively similar. We have used the ground state vibrational analysis for the spin-vibronic treatment of the benzene phosphorescence [83]. The ground state vibrations determine the frequencies of the phosphorescence vibronic bands in low temperature crystals and also the spin-vibronic perturbations, which govern the intensity to a large extent.

Account of Moffitt's idea together with an effective one-center SOC approximation leads in the framework of this approach to the consistent interpretation of the benzene phosphorescence spectra by the mechanisms represented in Fig. 10 and Fig. 11. This is a summary of all schemes considered by Albrecht [158], and is supported by CNDO/S-CI calculations of vibronic and spin-orbit coupling [48]. The major part of the phosphorescence intensity is determined here by channels I + II; this radiative activity induced by the e_{2g} (mainly ν_8) modes, is determined by one-center SOC integrals and by intensity borrowing from high energy $\pi - \sigma$ excitation of $^1A_{1g} - ^1A_{2u}$ and $^3E_{1u} - ^3E_{1g}$ types, which are out-of-plane polarized [139, 48].

Fig. 10

Main mechanisms of benzene phosphorescence. Triplet and Singlet manifolds of states.
From ref. [83].

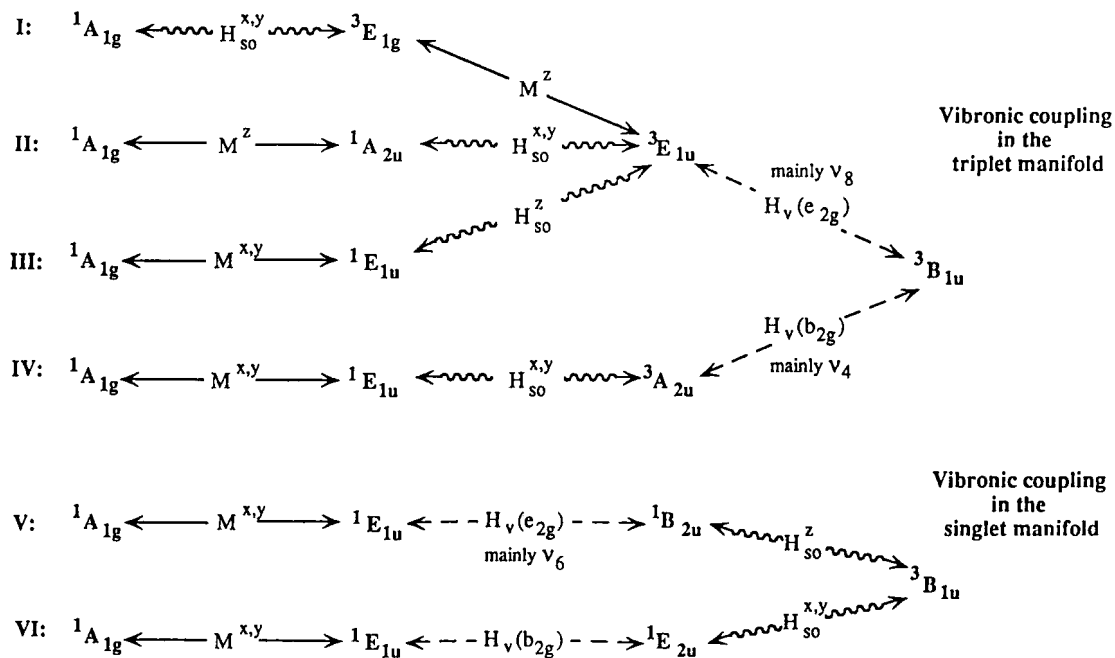
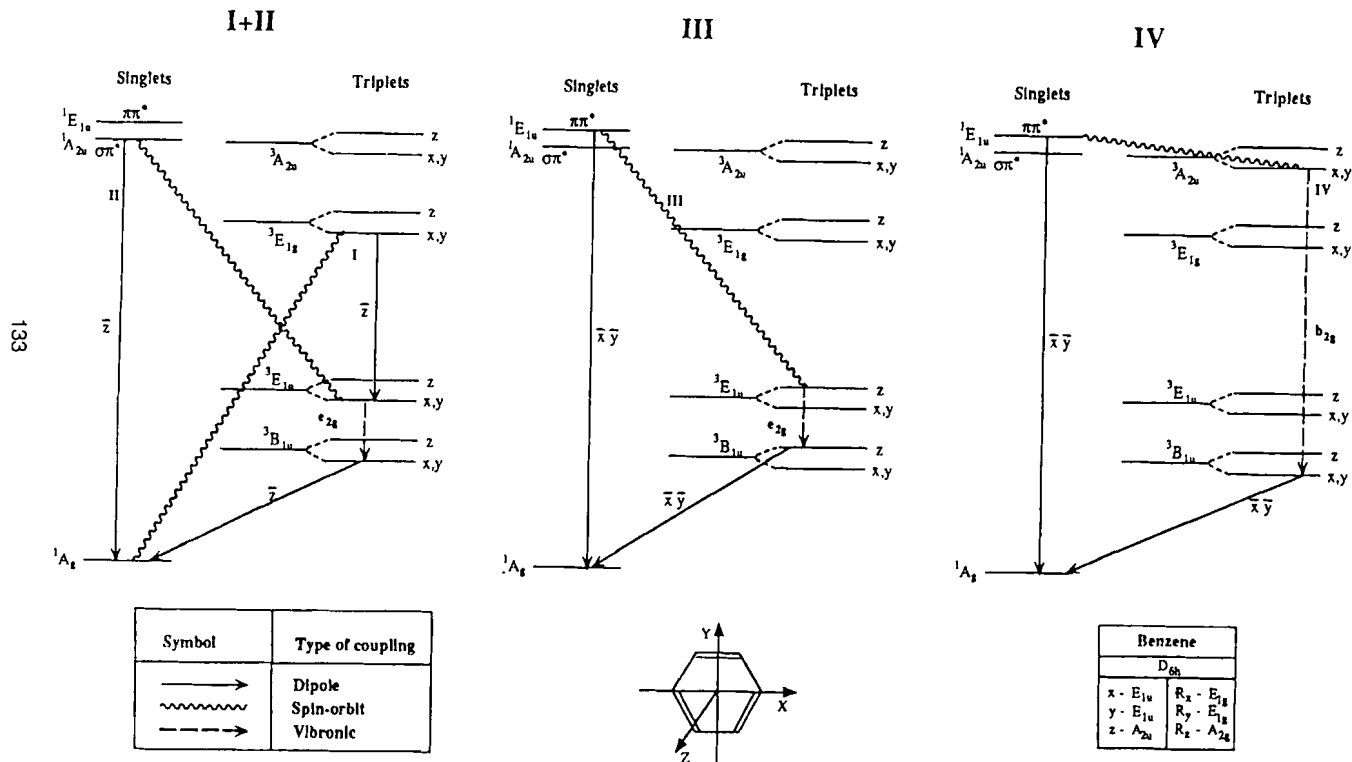


Fig. 11

Level diagrams for the main mechanisms of benzene phosphorescence. Triplet manifolds of states. From ref. [83].



Albrecht's analysis indicated that the strongest e_{2g} phosphorescence bands in rigid glass at 77 K are uniformly polarized out-of-plane with approximately 60-70% of the total intensity [158, 171]. The microwave induced delayed phosphorescence (MIDP) experiments for a C_6H_6/C_6D_6 doped crystal at 4.2 K shows that more than 90% of the e_{2g} phosphorescence must be out-of-plane polarized [136]. This discrepancy relates to the relative importance of the channels I + II and III, see Fig. 11. The latter channel [164] does not include one-center SOC integrals and is supposed to be less effective [158]. The estimations of SOC with one- and two-electron parts of the SOC operator [172, 164] $\langle {}^3E_{1u} | H_{so} | {}^1E_{1u} \rangle = 0.41 \text{ cm}^{-1}$, together with the account of σ orbitals as sp^2 -hybrids for the simple construction of the $\sigma, \pi^* {}^1A_{2u}$ state wave function [164], leads to comparable intensity for the in-plane (the channel III) and out-of-plane (the channel II) polarization for the phosphorescence [158]. This concurs with the old photoselection experiment on benzene glass at 77 K [171], but contradicts the later MIDP experiment at 4.2 K [136], which must be considered more reliable (the glass results are affected by rotation of the excited molecules before decaying [136]). Up to now this contradiction has not been resolved theoretically. Recent semiempirical calculations within the π -approximation with an account of the complete form of the SOC operator [173] seem to support a large in-plane polarization character for aromatic phosphorescence. The other unresolved question is connected with the role of the $e_{2g} \nu_9$ mode in the benzene phosphorescence spectrum. Besides ν_8 it also bears considerable activity [155]. The ν_9 vibration, however, is not expected to be active in the coupling between ${}^3B_{1u}$ and ${}^3E_{1u}$ states [161, 48] and its frequency does not change much upon $S_0 - T_1$ excitation [165].

I-B Vibronic structure of benzene phosphorescence in the response formalism

The occurrence of strong vibronic coupling among triplet states, see e.g. ref. [174], and of distorted triplet state geometries, see e.g. refs. [137, 175], might have important consequences for the calculation of phosphorescence yields. The best example is obviously benzene, the triplet state of which is doubly - orbital and spin - forbidden and which is only activated through vibronic coupling among the manifold of triplet states [158, 83]. However, even for allowed phosphorescent transitions vibronic coupling may be important, e.g. in aza-compounds the lifetime of electronically long-lived ${}^3(\pi\pi^*)$ states are significantly reduced by vibronic coupling to electronically short-lived ${}^3(n\pi^*)$ states. That the difference in singlet and triplet state geometries affect the phosphorescence yield was also demonstrated in the subsection on diatomic molecules, for instance for the $A^3\Sigma_u^+ \rightarrow X^2X\Sigma_g^+$, Vegard-Kaplan, band of N_2 , the triplet absorption moments of which varied considerably over different bond distances.

The mechanisms described above for benzene as well as a few others have been computed by direct MCQR calculations of vibronic phosphorescence intensity in Ref. [83]. For the Born-Oppenheimer wave functions the transition moment between the singlet ground state S_0 with v' -th vibrational excitation and the first triplet T_1 excited state

with v -th vibrational level, is equal to

$$M_{S,T_k}^{v',v} = \int X_{S,v'} M_{S,T_k}(Q) X_{T,v} dQ \quad (94)$$

where $M_{S,T_k}(Q)$ is the electronic $S_0 - T_1$ transition dipole moment for k -th spin sublevel

$$M_{S,T_k}(Q) = \int {}^1\Psi_0(r, Q) M^3 \Psi_1^k(r, Q) dr \quad (95)$$

Here Ψ and X are the electronic and nuclear vibrational wave functions, respectively. To the first order of the nuclear displacement we can expand this transition moment in a series

$$M_{S,T_k}(Q) = M_{S,T_k}(Q_0) + \sum_{\alpha} \eta_{\alpha}^k Q_{\alpha} \quad (96)$$

where

$$\eta_{\alpha}^k = \frac{\partial}{\partial Q_{\alpha}} [M_{S,T_k}(Q)]_{Q_0=0} \quad (97)$$

Finally the intensity of the vibronic phosphorescence band is determined by

$$M_{S,T_k}^{v',v} = M_{S,T_k}(Q_0) \int X_{S,v'} X_{T,v} dQ + \eta_{\alpha}^k \int X_{S,v'} Q_{\alpha} X_{T,v} dQ \quad (98)$$

In a simple harmonic approximation the first term gives the 0-0 band if the transition is allowed for non-distorted symmetrical structure. But in the case of benzene phosphorescence the ${}^3B_{1u} \rightarrow {}^1A_{1g}$ transition is forbidden in D_{6h} symmetry even if the SOC Hamiltonian is taken into account. In this case only vibronic phosphorescence bands ($v = 0 \rightarrow v' = 1$) appear through non-totally symmetrical b_{2g} and e_{2g} vibrations as follows from the scheme given in Fig. 7 and as discussed in the previous section. Their transition moments are equal to (in a.u.):

$$M_{S,T_k}^{0,1} = \eta_{\alpha}^k (2\pi\nu_{\alpha})^{-\frac{1}{2}} \quad (99)$$

The ground state force field, vibrational normal modes and frequencies have been obtained with MCSCF analytic gradient and hessian calculations [176]. Frequencies computed with the DZ basis set are compared with experimental ones in Table 16. The $T_1 - S_0$ transition moments were obtained using distorted benzene geometries with atomic displacements along the normal modes, and with the derivatives in Eq. 97 obtained by numerical differentiation. The normal modes active for phosphorescence in benzene are depicted in Fig. 12. The final formula for the radiative lifetime of the k spin sublevel produced by radiation in all (ν_1^0) bands is (ZFS representation x,y,z is used [49]):

$$\frac{1}{\tau_k} = \frac{4\omega^3}{3 \cdot 137^3} \sum_{\alpha} |\eta_{\alpha}^k|^2 2\pi\nu_{\alpha} \quad (100)$$

where $\omega = {}^3E_1 - {}^1E_0$ is the frequency of the transition. The average lifetime τ_{av} at the fast lattice relaxation limit is given by $\frac{3}{\tau_{av}} = \sum_k \frac{1}{\tau_k}$.

The basis sets employed in the MCQR calculations are the DZ and TZ gaussian basis sets of Dunning [177, 178] augmented with Rydberg-like functions (R), DZR and

Table 17: The $T_1 - S_0$ oscillator strengths in benzene calculated with direct vibronic coupling along e_{2g} modes (ν_i). Results are displayed for different basis sets and for the π -active space.

		Level	Osc. strength, f_i	Σf_i
		Calculated by transition moment $ \langle {}^3B_{1u}^{x,y} z {}^1A_{1g} \rangle $		
Mechanisms I+II	e_{2g}	$\nu_8(1601)DZ(II B)$	0.73e-10	1.05e-10
		$\nu_9(1178)$	0.31e-10	
		$\nu_6(606)$	0.03e-11	
		$\nu_7(3057)$	0.02e-11	
		$\nu_8(1601) DZR$	0.52e-10	
		$\nu_9(1178)$	0.248e-10	0.76e-10
		$\nu_6(606)$	0.01e-11	
		$\nu_7(3057)$	0.04e-11	
		$\nu_8(1601) TZ$	0.15e-10	
		$\nu_9(1178)$	0.09e-10	
		$\nu_6(606)$	0.04e-12	0.23e-10
		$\nu_7(3057)$	0.03e-12	
		$\nu_8(1601) TZR$	0.24e-10	
		$\nu_9(1178)$	0.13e-10	
		$\nu_6(606)$	0.01e-13	
		$\nu_7(3057)$	0.03e-12	0.37e-10
		Calculated by transition moment $ \langle {}^3B_{1u}^z x(y) {}^1A_{1g} \rangle $		
Mechanism III	e_{2g}	$\nu_8(1601) DZ$	0.39e-12	0.40e-12
		$\nu_9(1178)$	0.06e-13	
		$\nu_6(606)$	0.04e-13	
		$\nu_7(3057)$	0.04e-15	
		$\nu_8(1601) DZR$	0.38e-12	
		$\nu_9(1178)$	0.06e-12	0.46e-12
		$\nu_6(606)$	0.08e-13	
		$\nu_7(3057)$	0.02e-13	
		$\nu_8(1601) TZ$	0.24e-12	
		$\nu_9(1178)$	0.12e-13	
		$\nu_6(606)$	0.03e-12	0.29e-12
		$\nu_7(3057)$	0.06e-13	
		$\nu_8(1601) TZR$	0.23e-12	
		$\nu_9(1178)$	0.02e-12	
		$\nu_6(606)$	0.03e-12	
		$\nu_7(3057)$	0.07e-13	0.29e-12

Table 18: The $T_1 - S_0$ oscillator strengths calculated with direct spin-vibronic coupling along b_{2g} modes (ν_i , $i=4,5$). Results are displayed for different basis sets and for the active space described in text.

		Level	Osc. strength, f_i	Σf_i
Calculated by transition moment $ \langle {}^3B_{1u}^{x,y} x(y) {}^1A_{1g} \rangle $				
Mechanism IV	b_{2g}	$\nu_4(707)$ DZ(Π)	3.48e-12	8.87e-12
		$\nu_5(990)$	5.39e-12	
		$\nu_4(707)$ DZR(Π)	3.06e-12	8.78e-12
		$\nu_5(990)$	5.72e-12	
		$\nu_4(707)$ TZ($\Sigma\Pi$)	1.02e-12	3.62e-12
		$\nu_5(990)$	2.59e-12	
		$\nu_4(707)$ TZR($\Sigma\Pi$)	0.90e-12	3.46e-12
		$\nu_5(990)$	2.57e-12	

Table 19: Phosphorescence lifetimes τ_k (s) for different k spin-sublevels of the ${}^3B_{1u}$ state of benzene and of the ${}^3B_{2u}$ state of naphthalene. The benzene values refer to the four mechanisms depicted in Fig. 10; o and i denote the out-of-plane and in-plane polarization, respectively. τ_{av} denotes the average lifetime at the high temperature limit. Excitation energies given in eV.

Benzene						
level	Exc. energy	$\tau_{x,y}^{I+II}(o)$	$\tau_{x,y}^{IV}(i)$	$\tau_{x,y}^{Vot}$	$\tau_{x,y}^{III}(i)$	τ_{av}
DZ-CAS	3.3	16.4	194.2	15.1	4620	22.6
DZR-CAS	3.3	22.5	195.9	20.2	3779	30.3
TZ-CAS	3.3	74.3	475.2	64.3	5803	95.9
TZR-CAS	3.3	46.6	497.0	42.6	5871	63.7
Naphthalene						
level	Exc. energy			$\tau_x(o)$	$\tau_x(i)$	τ_{av}
SZ-CAS	2.41			23.4	$6 \cdot 10^8$	70.2
DZ-CAS	2.39			13.7	2838	40.9
DZR-CAS	2.38			17.6	2466	52.8

TZR, expanded at the center of symmetry. The quadratic response calculations were performed for various complete π active spaces comprising $1-2a_{2u}$, $1-2e_{2u}$, $1-2b_{2g}$ and $1-2e_{1g}$ orbitals correlating all π electrons. The out-of-plane b_{2g} vibration breaks the σ - π separability. The differentiation along this mode has been carried out also with an active space that includes the $1a_{2u}$, $1e_{2g}$ and $1e_{1g}$ highest occupied and the $1e_{2u}$, $1e_{1u}$ and $1b_{2g}$ lowest unoccupied orbitals. Table 16 gives the relative intensities for the vibronic bands of benzene phosphorescence as calculated with different basis sets. The important vibrational modes are $\nu_4 - \nu_9$ with the standard Wilson classification. The e_{2g} C-C stretching mode, ν_8 , appears to produce the most intensive phosphorescence band, with predominantly (92-98 %) out-of-plane polarization in all basis sets. The other C-C stretching mode, ν_9 , is also intensive in agreement with observations, however, it is not suspected to be pseudo Jahn-Teller active (the ν_9 frequency is largely unchanged upon $S_0 \rightarrow T_1$ excitation, while the frequency of ν_8 is changed drastically).

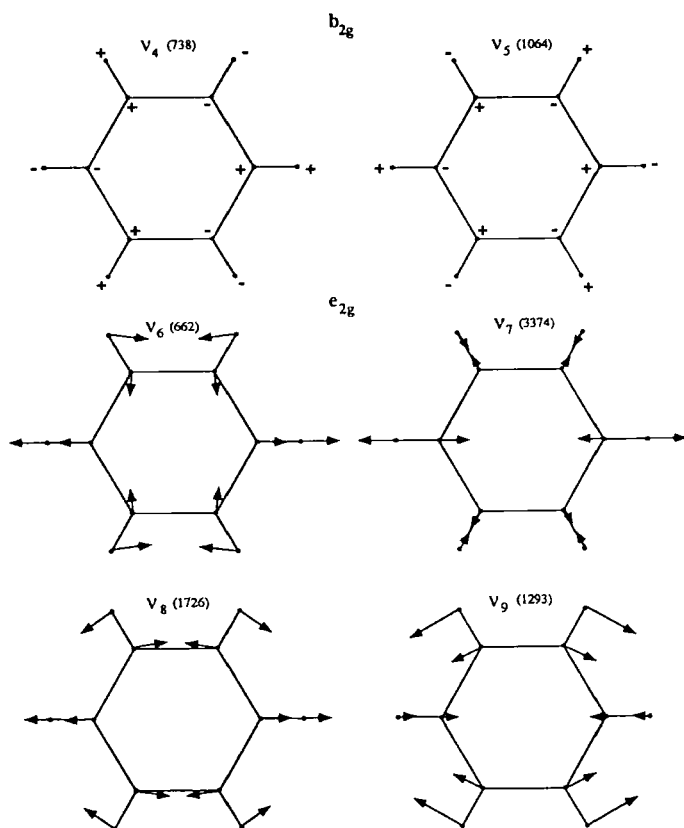
As seen in Table 16 the relative intensities are very stable towards enlargements of the basis set, and they agree well with those experimentally measured. The two b_{2g} vibronic bands have comparable activity, ν_5 being somewhat more intensive than ν_4 in all basis sets. These results are in good agreement with microphotometer recordings of phosphorescence [155] and with $^3B_{1u} \rightarrow ^1A_{1g}$ absorption measurements [165]. From Table 17 one notes that all e_{2g} bands, except ν_6 , are predominantly polarized out-of-plane. For ν_6 the in-plane and out-of-plane polarizations are approximately of equal strength in the TZ basis set, in the TZR basis set the in-plane polarization is even more intensive. This finding corresponds quite well with the microwave induced delayed phosphorescence (MIDP) experiment by van der Waals et al [136] for a C_6H_6/C_6D_6 doped crystals at 4.2 K.

The radiative lifetimes for the different spin sublevels, τ_k , and the average lifetimes, τ_{av} , at the high-temperature limit are presented in Table 19. As seen in this Table the lifetimes for the spin sublevels τ_x and τ_y , corresponding to out-of-plane polarization, are the shortest. In-plane polarized emission from the $T_1^{x,y}$ spin sublevels, represented by the b_{2g} vibrations, leads to approximately an order of magnitude longer radiative lifetime than for the e_{2g} bands (mainly ν_8 and ν_9). By contrast, the in-plane polarization from the T_1^z spin sublevel has negligible intensity, which means that this sublevel decays by very long radiative lifetimes (4-6 10^3 s for all basis sets). Because of these peculiarities the average lifetime, τ_{av} , is approximately equal to 1.5 $\tau_{x(y)}$. All these features concord very well with results from the MIDP experiments.

The average phosphorescence radiative lifetime calculated with different basis sets vary between 23 (DZ) and 96 (TZ) seconds. The DZ and DZR results overestimate the $T_1 - S_0$ transition probability in unsaturated hydrocarbons; their τ values are too small. Discussion of these results has sense only in context of comparison with other molecules, but the absolute DZ values have no credit; this basis set produces bad energies for $\sigma - \pi$ excitations, which are highly important for the T-S intensity borrowing. The best quality basis set (TZR) gives 64 seconds, which is much more credible. The so-called "best experimental" value is 30 seconds [154], but the proper estimation of non-radiative channels and the quantum yields still presents an open problem. From

Fig. 12

The active vibrational modes for benzene phosphorescence. From ref. [83].



direct measurements of $T_1 \leftarrow S_0$ absorption in pure crystalline benzene by an impurity phosphorescence - photoexcitation method, Burland et al. [165] obtained an oscillator strength of $\approx 10^{-10}$ which leads to the estimated value of 52 s for the average lifetime. Although we find a lifetime of this order with the largest of the wave functions employed we recall that the theoretical lifetime is the result of a delicate sum of different contributions from singlet-singlet and triplet-triplet $\sigma - \pi$ transition moments and excitation energies [48], which are supposed to be quite basis set dependent, especially on the account of diffuse, polarized and Rydberg orbitals.

II Naphthalene

For naphthalene there are several radiative lifetimes quoted from experiment; e.g. 28 [179], 22 [180] and 63 [181] s, the first one is close to the commonly accepted "best value" for benzene, 30 s, which was supposed to be the common radiative lifetime for all aromatics [182]. The uncertainty refers to the way for estimation of nonradiative decay by scaling the observed total lifetime through the quantum yield [179]. For long lifetime states this quantum yield is often hard to measure. The lifetime of the T_1 state of naphthalene- h_8 in dilute solution in durene host crystal at 77 K is increased from 2.1 to 16.9 s by perdeuteration [183], so the deuteration effect in naphthalene is larger than in most hydrocarbons. The commonly accepted explanation is based on Franck-Condon factor analysis and the leading role of C-H bond vibrations in inducing the non-radiative quenching [184]. The deuteration reduces the $T_1 \rightarrow S_0$ quenching considerably but the lower limit of this rate constant is unknown. Polarization of both out-of-plane ($> 75\%$ of total emission) and in-plane long-axis (18%) is observed in the (0,0) band phosphorescence in the doped crystals [180].

Table 19 recapitulate results from MCQR calculations of the phosphorescence radiative lifetime of naphthalene, given together with the benzene data. From Table 19 we see that only one triplet spin sublevel efficiently radiates for the lowest $^3B_{2u}$ state in the MCQR approach; namely the x -spin sublevel, where x is the long-axis of the C-C skeleton, leading to out-of-plane polarization of phosphorescence. This is the common polarization direction for all studied $T_1(\pi\pi^*) - S_0$ transitions of polyenes and aromatic compounds. The MCQR values are relatively well grouped; for SZ, DZ and DZR basis sets they are 23, 14 and 18 s for the x spin-sublevel, and 70, 41 and 52 s for the averaged radiative lifetime at the high spin-lattice relaxation limit (77 K). The basis set dependence is not as strong as for ethylene. We can not calculate naphthalene in the TZR basis set, but we can expect that enlargement of the basis set would increase the radiative lifetime to some extent, so our results support Ermolaev's value, 63 s, [185]. In contrast to the widely accepted opinion that triplet deuterionaphthalene does not display significant radiationless decay, Ermolaev's data indicate that the rate constant of the nonradiative $T_1 \rightsquigarrow S_0$ degradation for $C_{10}D_8$ is six times as great as that of radiation [185].

Radiative probabilities of T-S transitions have been presented by Hansen and Robinson [186] from absorption measurements of pure crystalline naphthalene. The $T_1 \leftarrow S_0$

absorption oscillator strength of the order $(1.6-16) \cdot 10^{-10}$ was measured by these authors, the lower limit being more credible [186]. From the DZ and DZR response calculations of naphthalene the values $3 \cdot 10^{-10}$ and $2.3 \cdot 10^{-10}$, respectively, were obtained [134] which are within the boundary limits of the measurements. Accounting for the fact that it is only one spin sublevel that is radiatively active, we can see that the lower limit of the S-T oscillator strength values corresponds to an average radiative lifetime of 62 s, and a radiative lifetime for the x spin sublevel of 21 s, which are close to the DZR results 53 s and 17.6 s, respectively. These data are also close to the more careful lifetime and quantum yield measurements of Langelaar *et al.* [187], giving 75 ± 25 s. The MCQR calculations give also good results for the second $T_2 \leftarrow S_0$ transition dipole moment of naphthalene [134]. The absorption intensity of this T_2 state is measured by Hansen and Robinson [186] to be a factor of 10-100 times larger than that of the $T_1 \leftarrow S_0$ transition. Accounting for the most reliable value for the first triplet state transition, it corresponds to an oscillator strength for the $T_2 \leftarrow S_0$ absorption of the order of $f = 1.6 \cdot 10^{-9} - 1.6 \cdot 10^{-8}$. The response theory result (DZ basis set) is in this range ($f = 4.8 \cdot 10^{-9}$) [134], so the calculated $T_2 \leftarrow S_0$ transition intensity is approximately 20 times higher than that for the first triplet state absorption.

III Comparison between naphthalene, benzene and polyenes

It is interesting to compare the aliphatic ethylene, butadiene and hexatriene molecules with the aromatic benzene and naphthalene molecules with respect to radiative activity of their triplet states. In the benzene molecule we must consider the S-T transition between the second triplet state ${}^3E_{1u}$ and the ground state since it is the first allowed one in a pure electronic approximation with account of SOC [133]. MCQR calculations show that the oscillator strengths for this transition have strong basis set and active space dependences [133]. The oscillator strengths for the x and y spin sublevels with a perpendicular polarization of the light determine more than 90% of the intensity of this transition (one must take into account that the total oscillator strength is equal to $2f_{x,y}$). The transition for the z -spin sublevel is negligible. The final response result for the oscillator strength in different basis sets for the second triplet state in benzene are DZ: $73.2 \cdot 10^{-10}$, DZR: $43.7 \cdot 10^{-10}$, TZR: $8.3 \cdot 10^{-10}$, TZP: $4.3 \cdot 10^{-10}$ [133]. The ethylene results (Table 14) show the same trend. The S-T transition intensity in hydrocarbons is very sensitive to the balanced description of these states. It is natural to compare electric dipole transition moments (M) on the same level of accuracy. For ethylene and butadiene the $M_z(T_1^y - S_0)$ values are equal to $6.38 \cdot 10^{-5} a.u.$ and $6.55 \cdot 10^{-5} a.u.$, respectively in the TZP basis set (CAS-2 and CAS-1 results, respectively); y axis is perpendicular to the long in-plane axis, z is out-of-plane axis. For the second triplet state in benzene the TZP CAS- π -A (six π electrons in 8-MO's) result is $M_z(T_2^y - S_0) = 4.32 \cdot 10^{-5} a.u.$ So these transition moments values are quite similar.

The DZR results for polyenes are close to $1.6 \cdot 10^{-4} a.u.$ and are also similar to the T_2 benzene value $1.35 \cdot 10^{-4} a.u.$ It is interesting to note that the DZR result for the $M_z(T_1^y - S_0)$ transition moment in naphthalene is $6.3 \cdot 10^{-5} a.u.$, so it is twice as small in

comparison with $T_2 - S_0$ transition in benzene. The vibronically induced $M_z(T_1^y - S_0)$ transition moment in benzene, summing all four e_{2g} modes, is $4.46 \cdot 10^{-5} a.u.$ in the same DZR basis. We must conclude that the $T_1 - S_0$ radiative probability in polyenes is larger than in aromatics.

Response theory describes the S-T transition probabilities in unsaturated hydrocarbons quite well; more than 99 % of the $S_0 - T_1$ transition intensity is out-of-plane polarized in agreement with experiment for aromatics; in ethylene, butadiene and naphthalene the y spin-sublevel of the T_1 state is the most active one, where y is the long in-plane axis of the molecules [134, 132]. The main difference between the triplet states of aromatic and aliphatic compounds is the lack of phosphorescence for the latter. We have related this to the fact that polyenes also lack fluorescence (or have very weak fluorescence). This has been explained from the effective quenching of singlet excited ($\pi\pi^*$) states, which is an inherent property for the short polyenes. Our results suggest that this situation also prevails for the lowest triplet states.

The large flexibility of the triplet excited molecules upon torsion and the non-zero SOC matrix elements that this nuclear movement induces, indicates that the rate constant for nonradiative intersystem crossings should be very large without any chance for radiative rate competition. A second reason for missing phosphorescence is a very large radiative lifetime due to the small transition energy at the equilibrium T_1 state geometry (in ethylene this energy is close to zero), the electronic $T - S$ transition moment is also much lower at this point than at the ground state equilibrium. Aromatic molecules are much more rigid, because of the cyclization, but their C-H vibrations are quite active in nonradiative quenching of phosphorescence. Our calculations of the radiative phosphorescence lifetime (τ_r) definitely show that the nonradiative rate constants in benzene and naphthalene are underestimated in earlier analysis (Siebrand analysis [188, 182]) and that the τ_r values for these molecules are larger than the generally accepted constant limit of 30 s.

IV Nitrogen substituted heterocycles

The benzene and azabenzenes form iso-electronic series of molecules, as naphthalene and the azanaphthalenes also do. The ground state electronic and geometric structures are therefore quite similar within one series. The substitution of CH groups with nitrogens introduces lone-pair to π^* transitions, and lowers the benzene and naphthalene symmetries. Small and systematic trends are found for linear response properties of the azabenzenes [189]. Each molecule is, however, very specific with respect to phosphorescence due to the delicate nature of the SOC and electric dipole activity interactions.

In the phosphorescence process the spin-orbit interaction between the singlet-triplet manifolds is strongest for $^1,3(n, \pi^*) \leftrightarrow ^{3,1}(\pi, \pi^*)$. This can be understood by the rotation of the lone-pair electron into the π -electron system by the spin-orbit operator. This type of atomic interaction motivates the approximations of one-electron, one-center spin-orbit operators cherished in semi-empirical work. The benzene-type of strong

dipole intensities for the $^1(\pi, \pi^*)$ states are retained for the other aromatic compounds. In particular, the aza-states derived from the benzene $^3E_{1u}$ state with super-strong absorption strength dominate their dipole spectra. The transition moment for the $^1(n, \pi^*)$ transition is about a third in strength compared to that of $^1(\pi, \pi^*)$. Furthermore there is only one symmetry (out-of-plane) which is dipole allowed for the $^1(n, \pi^*)$ transitions in comparison with (in-plane) two symmetries for $^1(\pi, \pi^*)$. With these propensity rules in mind the results of phosphorescence lifetime calculations are more easily interpreted. In Fig. 13 the phosphorescence interaction is pictorially displayed for pyrazine and pyrimidine, with two contributing processes.

In the following we discuss the phosphorescence lifetimes of $^3(n, \pi^*)$ and $^3(\pi, \pi^*)$ states of the azabenzenes and the azanaphthalenes, which can differ by several orders of magnitude. The symmetry axes and geometries of the discussed compounds are reproduced in Fig. 14. Since benzene and naphthalene lack (n, π^*) transitions their triplet state radiative lifetimes are, as for other hydrocarbons, considerably longer.

IV-A Azabenzenes

Among the sequence of N-heterocycles, n.b. the 1,2,3,4 N-substituted azabenzenes, the response investigations have focussed on pyridine, pyrazine, pyridazine, pyrimidine, s-triazine, and s-tetrazine [151]. The calculations of phosphorescence of these compounds utilize π type complete active spaces, the general rule of thumb has been to use one correlating π orbital for each occupied π orbital. All azabenzenes, except pyridazine, take the same Hartree-Fock orbital configuration in C_{2v} symmetry; $11a_1, 7b_2, 2b_1, 1a_2$, including 18 and 3 doubly occupied σ and π orbitals, respectively. For pyridazine it reads $10a_1, 8b_2, 2b_1, 1a_2$.

Pyrazine and pyrimidine are of particular interest because their $^3(n, \pi^*)$ states are thought of being the lowest triplet states in these molecules (although this is still not completely agreed upon, see below). In the works from the 1960's of Cohen and Goodman [175] on the high temperature phosphorescence, strong emission for the $^3(n, \pi^*)$ state of both pyrazine and pyrimidine was reported. For pyrazine a quantum yield (Φ_p) of 0.30 gave a radiative lifetime of 0.02 s, and for pyrimidine the corresponding values are 0.14, and 0.01 - 0.02 s, respectively. Comparative lifetime calculations with response theory give results in the same range, around 0.03 s for pyrazine and slightly less for pyrimidine [151].

Burland and Schmidt [190] performed microwave induced delayed phosphorescence (MIDP) experiments using a sample preparation with a benzene host crystal for both pyrazine and pyrimidine. With this technique they found that the relative radiative rates closely resembled the relative total rates for the different spin sublevels, indicating a high quantum yield and low non-radiative rate. The spin sub-level rates of pyrazine for Γ_x and Γ_y were given as 284 and 6.3 ms, respectively, to be compared with the best response theory result of 282 and 12 ms. The z (out-of-plane) spin component is symmetry forbidden, and its lifetime (400 ms) derives from the lattice perturbation.

For pyrimidine we get two strongly emitting spin-sublevels, Γ_x and Γ_y , instead of only one, Γ_z , for pyrazine, in full agreement with MIDP measurements of Burland and Schmidt [190]. They have obtained the lifetimes 11.8, 16.6 and 324 ms for the x , y and z spin sub-levels, respectively. These values are reproduced quite well even at the Hartree-Fock level: 13 ms, 44 ms and ∞ , respectively. The averaged lifetime, obtained in the TZP CAS calculation is 0.019 s, which falls into the experimental limit (0.01-0.02 s) [175]. The other type of triplet-singlet transition from the $^3(\pi, \pi^*)$ state has been determined for pyridine with averaged radiative lifetime 0.3-3 s [191] and 0.8 s in ref. [192]. We have obtained the lowest T_1 state in pyridine of the $^3(\pi, \pi^*)$ nature with an averaged lifetime 1.3 s by means of CAS response calculations.

For a majority of the azanaphthalenes and azaanthracenes the lowest $^3(\pi, \pi^*)$ state is phosphorescent, in ref. [49] lifetimes are listed between 1 to 2 seconds at the high temperature limit. Pyridine shows a quantum yield which is extremely small in the vapour phase. From a total lifetime of only 1.5 μ s a radiative lifetime of 0.8 s was given by Sushida *et al.* [192]. Response calculations are in reasonable agreement with this result (1.3 s [151]). Recent applications of electron spin-echo modulation spectroscopy have given new clues to the pyridine phosphorescence problem. Using this technique Buma *et al.* [137] were able to determine the structure as well as the spin-density distribution of the T_1 state of pyridine. The results showed a distorted, boat-like structure for this state. Buma *et al.* [137] considered this observation to be a manifestation of strong vibronic coupling between the $^3B_1(n\pi^*)$ and the $^3A_1(\pi\pi^*)$ states, and that the lowest state of triplet pyridine is neither pure $^3(n\pi^*)$ nor $^3(\pi\pi^*)$ but of mixed character (this was also substantiated by *ab initio* calculations [193, 194]). We have reproduced these results by CAS (8 electrons in 9 MO's) calculation. The optimized T_1 state geometry is distorted along the normal coordinate corresponding to ν_{16b} mode and is a boat conformer. In spite of some $^3(n\pi^*)$ and $^3(\pi\pi^*)$ mixing at the optimized C_s distorted T_1 state geometry, the $T_1 - S_0$ transition dipole moment does not change much (only 19 % less compared with the transition moment at the ground state geometry). So the radiative property and the frequency of the (0,0) transition are quite similar to the nondistorted result (the lowering of the T_1 state energy is only 0.2 eV upon distortion). However, the vertical energy of the $T_1 \rightarrow S_0$ transition at the optimized T_1 state boat form geometry diminished drastically (from 3.5 eV to 1.6 eV). This explains a very effective nonradiative decay of the T_1 state of pyridine. The potential energy surface of the T_1 state is quite flat upon the ν_{16b} mode movement [193, 194], but it is highly repulsive in the ground S_0 state. So the ν_{16b} vibration is very effective in promoting of nonradiative energy flow to the ground state vibronic reservoir, because of strong modulation of the S-T energy gap; the gap is close to zero at large distortion [194].

The radiative lifetime of the order of 1 second and the small quantum yield of pyridine phosphorescence could be easily understood from the MCQR calculations [151]. For most of the other azabenzenes one finds that $^3(\pi\pi^*)$ states also radiate in the order of 1 second. The averaged lifetimes in Table 20 for the $^3(n, \pi^*)$ states vary from 32 ms for pyrazine to 242 ms for tetrazine. The dependence of these lifetimes on the quality

Symmetry axes for the aza-compounds discussed in text. From ref. [222].

Pyridine

Pyrazine

Pyrimidine

Pyridazine

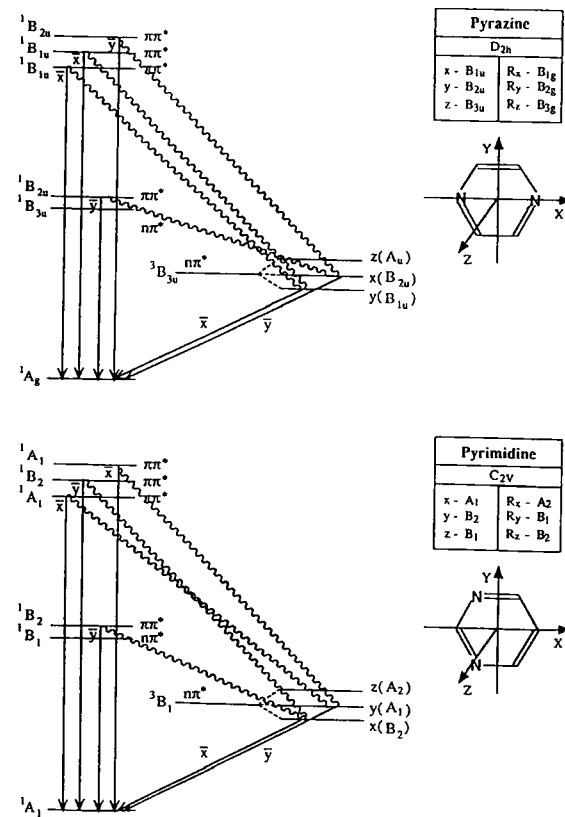
Triazine

Tetrazine

Figure 1 displays six chemical structures of bicyclic compounds, arranged in two rows of three. Each structure is shown with a coordinate system (X, Y, Z) centered on the central five-membered ring.

- Top Row:**
 - Quinoxaline:** The central five-membered ring is fused to two six-membered rings, with nitrogen atoms at the 1 and 8 positions.
 - 1,8-Naphthyridine:** The central five-membered ring is fused to two six-membered rings, with nitrogen atoms at the 1 and 8 positions.
 - 1,5-Naphthyridine:** The central five-membered ring is fused to two six-membered rings, with nitrogen atoms at the 1 and 5 positions.
- Bottom Row:**
 - Phthalazine:** The central five-membered ring is fused to two six-membered rings, with nitrogen atoms at the 1 and 4 positions.
 - 2,7-Naphthyridine:** The central five-membered ring is fused to two six-membered rings, with nitrogen atoms at the 2 and 7 positions.
 - 2,6-Naphthyridine:** The central five-membered ring is fused to two six-membered rings, with nitrogen atoms at the 2 and 6 positions.

Main mechanisms of pyrazine and pyrimidine phosphorescence. From ref. [151].



of wave functions is indicated in Table 20.

IV-B Azanaphthalenes

Out of the azanaphthalenes quinoxaline seems to be the most well investigated member. An averaged radiative lifetime of 0.56 s (in a doped crystal at 4 K) was given by Yamauchi *et al.* [195, 196]. This value is shorter than general $^3(\pi\pi^*)$ state lifetimes but somewhat longer than the $^3(n\pi^*)$ state lifetimes for azabenzenes (5 - 100 ms). The predicted average values by electronic response calculations (without vibronic coupling) are in the order 1.6 and 3.4 sec for the SZ and DZ basis sets, respectively. The x spin sub-level is the most active in agreement with ODMR experiments [195]. Next compound listed in Table 20 is phthalazine, which has rather special properties due to the neighbour positions of its two N-atoms. This leads to particularly strong solvent effects (hydrogen bonding). Phthalazine has a very weak phosphorescence in contrast to quinoxaline, because its radiative lifetime is much higher (in addition to a strong quenching). The response calculations reproduce this trend and especially the large difference in radiative activity of the x spin sub-level (Table 20).

Two of the four investigated naphthyridines (1,8- and 2,7-naphthyridine with C_{2v} symmetry) have one spin sublevel that is radiatively forbidden, the other two have all spin sub-levels active. Phosphorescent emission have been observed for all naphthyridines, but the radiative lifetimes are not available. The measured lifetime of 1,5-naphthyridine (0.02 s) is much shorter, than our radiative value. This again indicates that vibronic coupling (leading to non-radiative or radiative decay) is a strong contributor to the lifetimes of the triplet states of azanaphthalenes, in a perturbative sense thus stronger than the action of dipole and spin-orbit coupling.

A basic difference between the azabenzenes and azanaphthalenes is that for the latter the lowest states are exclusively of $^3(\pi\pi^*)$ character (notably except for a few hosted species). From molecular orbital arguments the phosphorescence strengths can be rationalized in terms of spin-orbit and dipole interaction between the excited state configurations of $\pi\pi^*$ and $n\pi^*$ character. Even simplifying one-center approximations for the spin-orbit coupling [197] imply that the coupling between $^1(n, \pi^*) \leftrightarrow ^3(\pi, \pi^*)$ or $^1(\pi, \pi^*) \leftrightarrow ^3(n, \pi^*)$ in the N-heterocycles are much stronger than between states of the same type [181]. The strength for spin-orbit coupling for $^3(n\pi^*)$ states derives from the localized nature of the n orbital, leading to a factor of hundred stronger coupling than for $^3(\pi\pi^*)$ states. This was confirmed by response theory calculations on the azabenzenes; the $^3(n\pi^*)$ states radiate with approximately 10 ms, the $^3(\pi\pi^*)$ states more than 1 second, see above. Furthermore, the $^3(n\pi^*)$ states and the $^3(\pi\pi^*)$ states are known to interact vibronically for the aza-compounds, on occasions very strongly [198]. The reverse order of $^3(n\pi^*)$ and $^3(\pi - \pi^*)$ states in the azanaphthalenes has therefore a rather pronounced effect on the interpretation of their phosphorescence; in azabenzenes the strong spin-orbit coupling between the $^1(\pi\pi^*)$ and the $^3(n\pi^*)$ states and the strong dipole coupling of the former with the ground state leads to a strong

Table 20: Triplet excitation energies (eV) and phosphorescence lifetimes τ (s) of azabenzenes and azanaphthalenes calculated for different state symmetries and spin sublevel components by random phase approximation (HF) and MCQR with double zeta (DZ) basis set.

level	$^3(\pi - \pi^*)$					$^3(n - \pi^*)$			
	Exc. energy	τ_x	τ_y	τ_z	τ_{av}	Exc. energy	τ_x	τ_y	τ_{av}
C_{2V}	A_1					B_1			
Pyridine									
HF	4.76	0.007		28.7	0.021	3.88	3.1	0.008	0.024
CAS	3.44	0.437		1666	1.3	4.51	0.056	0.010	0.025
Expt.	4.1					4.1			
Pyrimidine									
HF	5.03	0.020		25	0.058	3.65	0.013	0.044	0.030
CAS	3.26	0.361		688	1.1	4.09	0.018	0.074	0.042
Expt.						3.6			
D_{2h}	B_{1u}					B_{3u}			
Pyrazine									
HF	4.72	0.010		8.7	0.031	3.05	0.97	0.011	0.032
CAS	3.14	0.033		6.9	0.098	3.53	0.282	0.012	0.035
Expt.	4.04					3.26			
C_{2V}	B_2					B_1			
Pyridazine									
HF	4.90	0.381		23	1.1	2.60	0.030	0.404	0.082
CAS	3.21	0.450		62804	1.3	3.18	0.026	0.687	0.076
Expt.	4.0					2.9			
C_{2V}	A_1					B_1			
Triazine									
HF	4.81	0.000006		21	0.00002	4.14	3.7	3.7	5.6
CAS	3.08	0.697		3540	2.1	3.75	0.068	0.023	0.052
Expt.	3.27								
Tetrazine									
HF	4.92	0.439		4.9	1.2	1.17	0.354	2.384	0.926
CAS	2.94	0.00009		198	0.0003	2.12	0.087	1.05	0.242
Expt.						1.69			
C_{2V}	B_2					B_1			
Quinoxaline									
CAS	2.10	1.14		98.2	3.42	3.42	0.247	0.075	
Expt.	2.68	0.19		20	0.55	3.04			
Phthalazine									
CAS	2.26	27.5		71.4	59.6	3.53	1.041	0.036	
Expt.	2.74	25		50	16				
C_{2V}	B_2					B_1			
1,8-Naphthyridine									
CAS	2.19	1.65		113.8	4.95	3.91	0.0007	0.027	
Expt.	2.92								
2,7-Naphthyridine									
CAS	2.23	27.2		79.4	60.8	4.01	0.017	2.39	
Expt.	2.61								
C_{2h}	B_u					A_u			
1,5-Naphthyridine									
CAS	2.19	2.11	4711	104	6.20	4.13	0.162	0.186	
Expt.	2.88								
2,6-Naphthyridine									
CAS	2.21	3.95	54.4	76.3	10.5	4.03	0.021	0.123	
Expt.	2.57								

electronically induced radiative decay of the triplet state and to short lifetimes, while for the azanaphthalenes, with the $^3(\pi\pi^*)$ state as lowest triplet, vibronic coupling mechanisms (spin-orbit - vibronic or vibronic coupling to other radiative states) will compete heavily with the pure radiative (spin-orbit - dipole) decay.

8 The external heavy atom effect on S-T transitions

In this subsection we describe a more specific type of application that now is possible within the framework of the response methodology, namely the computation and interpretation of heavy atoms effects on S-T absorption spectra. In ref. [150] a new interpretation for the cause of the external heavy atom effect on S-T transitions was thus proposed basing on response theory results for $X + C_2H_4$, $X = F^-, Cl^-, Br^-, HCl, Ar$ as model systems. It was found that this effect should be interpreted as an increased SOC due to back-charge-transfer from the heavy atom, which contrasted the more conventional interpretations in terms of hydrocarbon charge penetration into the heavy atom or in terms of an exchange induced effect.

The internal and external heavy atom effects, IHA and EHA, have attracted a considerable attention in the community of molecular spectroscopists. This is part of an old problem of understanding environmental effects from solvents or solid matrices on S-T absorption or on phosphorescence of solute molecules. For higher temperature studies the triplet decay is quenched either by collision or by vibrational interaction with the matrix or the solvent. The molecules subject to studies in this respect have mostly been aromatic molecules perturbed by molecular oxygen, nitric oxide or other paramagnetic molecules, molecules either with heavy atoms and/or forming charge transfer complexes.

For IHA the underlying mechanism is well established; a substitution of an atom with equivalent valency but larger nuclear charge (Z) increases the S-T transition probability by virtue of the Z -dependence of the spin-orbit operator, see eq. 66. Some explanations of the EHA effect have been based on analogous arguments; charge transfer to the heavy atom leads to an enhanced S-T transition probability in the complex. The earlier understanding of the mechanism behind EHA was, however, far from satisfactory [199, 200]. The first qualitative interpretation was given by Kasha [201], who suggested that S-T ($T_1 \leftarrow S_0$) absorption was enhanced by collisional perturbation on the SOC (SOC) among the π -electron orbitals of the aromatic molecule. This enhancement grows in magnitude with the strength of the acid-base interaction between the aromatic donor and the alkyl halide acceptor [202]. The now prevailing two main types of interpretations of EHA rest on exchange [203, 49] and charge transfer [204, 205, 49] type mechanisms. The EHA mechanism has been studied also on a quantitative level with more detailed interpretations for the perturbation of the SOC, viz. one - versus two-center contributions, selectivity of triplet state spin-sublevels, but also with respect to the nature of the lowest excited states of the perturber, mixing of excited singlet states associated with the perturber EHA molecule (1P_1) into the T_1 state of the UHC

molecule, etc. see e.g. refs. [206, 207, 50, 208, 209]. All proposed CT mechanisms behind halide EHA effects [49, 210] include a consideration of the UHC aromatic molecule as a donor and the halide EHA as an acceptor, which follows from their acid-base properties. It has, however also been proposed [24, 208] that only the charge transfer in the back direction can be responsible for the EHA effect and for the SOC in the aromatic molecule, and that the normal acid-base concept is not applicable. This latter notion was favored by MCQR response theory calculations in ref. [150], i.e. that the enhanced SOC is due to that charge is donated *from* rather than *to* the external heavy atom. Fig. 15 gives a qualitative representation of a few important orbitals and of different charge transfer states relevant for the EHA effect in the $C_2H_4 + O_2$ collision complexes.

Ethylene presents a good test for the EHA effect because the $T_1 \leftarrow S_0$ absorption in this molecule is more intensive than in any other UHC molecule. The calculations of the EHA effect in ethylene produced by the three anions F^- , Cl^- , Br^- , are represented in Table 21. The calculations indicate regular trends for the triplet state lifetime with respect to the internuclear distance and the charge of the heavy atom. All anions are effective as EHAs at short distances and that the $T_1 \leftarrow S_0$ intensity enhancement strongly depends on the nuclear charge of the EHA. The transition moment ratios correspond quite well to the relation between atomic SOC constants. The combined charge-transfer and SOC nature of the EHA effect explains its strong intermolecular distance dependence. A more direct way of displaying the back-charge-transfer of EHA is to make a state-by-state decomposition of the source of triplet intensity in the conventional sum-over-state expression for the S-T matrix elements. Analysis of sum-over-state decompositions of quadratic response residues show that the EHA enhanced S-T, out-of-plane polarized, transition intensity of ethylene + F^- is borrowed from charge transfer states. As for the case of phosphorescence discussed in subsection 7 the state contributions are very slowly convergent with respect to the sum-over state, response function, value. The individual contributions vary in both magnitude and sign. Thus any accurate sum has to be obtained with many more states than those displayed in the Table. One can anyway discern that a few intensive contributions from the lower states. Table 22 indicates that the triplet states in free ethylene (with singlet to triplet spin-orbit and triplet to triplet dipole interactions) play the dominating role for the sum-over-state value. Particularly, in the triplet spectra the SOC matrix elements are several times larger than the SOC elements in pure ethylene. On the other hand, the dipole transition moments are not much larger with an F^- ion present. An analysis of the response vectors shows that the states with increased transition moments and SOC:s have leading configurations that are characterized as charge transfer configurations. This brief analysis gives a good illustration that response theory can provide both interpretation and accuracy in prediction.

Fig. 15

a) A qualitative representation of few important orbitals in the $\text{C}_2\text{H}_4 + \text{O}_2$ collision complexes. b) A pictorial representation of different charge transfer states relevant for the EHA effect in the $\text{C}_2\text{H}_4 + \text{O}_2$ collision complexes. Left side indicates charge-transfer states, right side indicates internal excitations in C_2H_4 . From ref. [150].

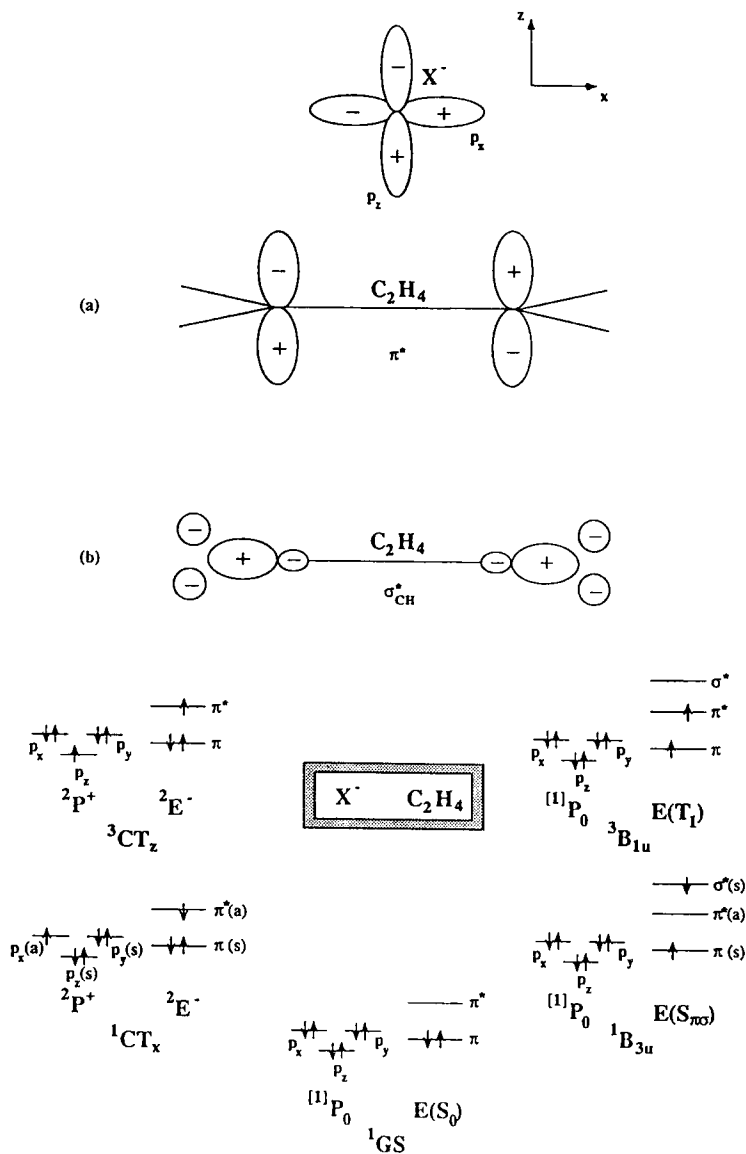


Table 21: A comparison between free ethylene and ethylene in a sudden collision complex with a heavy atom (F^- , Cl^- and Br^-) Transition moments (a.u.) and lifetimes (sec.) at different distances (Å) between ethylene center of mass and heavy atom are displayed. From Ref. [150].

Distance (Å)	j	k	F^-		Cl^-		Br^-	
			$\langle {}^1A_g j {}^3B_{1u}^k \rangle$	τ_k	$\langle {}^1A_g j {}^3B_{1u}^k \rangle$	τ_k	$\langle {}^1A_g j {}^3B_{1u}^k \rangle$	τ_k
3.5	z	y	$6.356e-4$	0.044				
	y	z	$1.822e-4$	0.535				
	av			0.122				
4.0	z	y	$1.740e-4$	0.563	$3.617e-4$	0.138	$3.492e-3$	0.001
	y	z	$3.471e-5$	14.1	$1.193e-5$	127	$5.064e-4$	0.066
	av			1.62		0.414		0.004
4.5	z	y	$3.679e-5$	12.3	$1.665e-4$	0.593	$1.767e-3$	0.005
	y	z	$1.533e-5$	71.0	$1.352e-6$	8999	$1.687e-4$	0.568
	av			31.4		1.779		0.015
5.0	z	y			$5.605e-5$	5.17	$1.148e-3$	0.012
	y	z			$8.917e-6$	204	$2.687e-4$	0.220
	av					15.1		0.034
∞	z	y	$6.313e-5$	3.79				
	y	z	$9.220e-6$	153				
	av			11.1				

Table 22: Different contributions to the final transition moment $T_1^y \leftarrow S_0$ for free ethylene. Transition moments are shown for both the triplet and singlet manifold of states. 0 denotes ground, k intermediate and f the final states. The last two columns describe the final contribution to the transition moment from state k. Term(k) is the k+1:th term of the final sum and Sum(k) is the accumulative term. ΔE_k is equal to ${}^3E_k - {}^1E_0$ for the triplet manifold and equal to ${}^1E_k - {}^3E_1$ for the singlet manifold.

Triplet manifold					
k	$\langle 0 H_{SO} k\rangle$ (cm^{-1})	$\langle k z f\rangle$ (a.u.)	ΔE_k (eV)	Term(k) (10^{-3} a.u.)	Sum(k) (10^{-3} a.u.)
1	-2.639	0.321	8.408	0.012	0.012
2	18.709	-0.486	9.590	0.118	0.130
3	-0.241	0.956	10.808	0.003	0.133
4	3.434	-0.343	11.274	0.013	0.146
5	0.848	-1.233	12.175	0.011	0.156
6	1.911	-0.139	12.959	0.003	0.159
7	-8.590	-0.043	14.231	-0.003	0.156
8	6.624	0.104	15.194	-0.006	0.150
9	-6.794	0.371	15.426	0.020	0.170
10	6.850	-0.075	16.363	0.004	0.174
11	4.653	0.387	17.503	-0.013	0.161
12	2.747	-0.171	18.072	0.003	0.165
13	10.365	0.046	19.107	-0.003	0.161
14	-2.875	-0.161	19.648	-0.003	0.159
15	0.580	0.772	19.732	-0.003	0.156
Singlet manifold					
k	$\langle 0 z k\rangle$ (a.u.)	$\langle k H_{SO} f\rangle$ (cm^{-1})	ΔE_k (eV)	Term(k) (10^{-3} a.u.)	Sum(k) (10^{-3} a.u.)
1	-0.438	0.976	6.272	-0.008	-0.008
2	-0.544	3.442	7.958	-0.029	-0.038
3	0.144	0.837	9.634	-0.002	-0.039
4	-0.869	1.738	10.015	-0.019	-0.058
5	0.166	-4.344	10.935	-0.008	-0.066
6	-0.092	-16.965	13.239	+0.015	-0.051
\sum Triplet and Singlet states :					0.063

9 Outlook

I Spin Catalysis

The potential for diversified applications of response theory involving spin-orbit interactions is great, in particular in the field of spin catalysis. Because of the multi-configuration treatment a large range of reactions involving radicals and paramagnetic species are within reach. In general a paramagnetic spin catalysis takes place when a catalyst with unpaired electrons assists in an S-T transitions in the reacting system through intermolecular exchange interaction. The spin-forbiddness is then lifted by supplying unpaired electrons without magnetic (SOC) perturbations. Molecular oxygen, with its triplet ground state and three low-lying excited singlet states, forms a particularly interesting agent in this context; investigations of intermolecular complexes between O₂ and organic substances, and of various types of S-T switching in chemical reaction paths, mainly in oxidation reactions of hydrocarbons by molecular oxygen, are called for. The $a^1\Delta_g$ degeneracy of molecular oxygen is removed during such reactions and the possibility of an S-T crossing must be accounted for when describing O₂ reactivity. The ground state oxygen, ³O₂, cannot react directly with diamagnetic substances to produce chemically stable diamagnetic products of oxidation because of spin-forbiddness. This is a reason for that a large variety of such processes proceed through radical chain reactions. What is presently needed is a consistent theoretical treatment explaining why some O₂-substrate couples undergo such a thermally induced ISC and others do not. We believe spin-orbit response calculations can assist in this respect.

Another rewarding field of applications is given by cluster simulations of the role of SOC in surface catalysis, for instance oxidation on the surface. Dissociative adsorption of O₂ on metal surfaces leads to inclusion of atomic oxygen in the oxidation reaction. Ground state O(³P) atom insertion in the C=C bond is spin forbidden, so the epoxidation of olefins on metal surfaces must find a way to overcome this prohibition. Other types of surface reactions can also illustrate the importance of SOC effects in spin catalysis [211].

The external heavy atom effect in photochemistry provides direct examples of spin catalysis [211, 212]. Because the nature of this effect is determined by charge-transfer SOC enhancements, we can predict important S-T nonadiabatic transitions during electron transfer reactions [213]. Degeneracy or quasidegeneracy of orbitals which are involved in charge-transfer is of great importance for the SOC enhancement and for the induced S-T mixing [214, 208]. In the case of heterogeneous catalysis the interface electron transfer with spin change could involve quasidegenerate atomic states of the metal surface [211]. A comparatively long lifetime of metastable intermediates obtained in such processes (with respect to the electron-hole recombination) is obvious for heterogeneous spin catalysis.

Spin changes can easily occur in reactions of 3d metal compounds. There are

many isomerization reactions of transition metal complexes with multiplicity changes [215, 216]. Transition metal complexes typically have few near-degenerate states with different orbital and spin symmetry, which often is the reason that SOC effects manifest themselves in UV and ESR spectra of such systems (rather than because of the "heavy-atom" nature of these metals). By the supply of 3d-orbitals to the catalyzing system a transition metal atom can promote a large shift of orbital angular momentum during the S-T transition of the reacting system and effectively remove the spin-forbiddness. We can add that many organic reactions have completely different behaviour for singlet and triplet states (for example, with respect to activation of C=C bonds), so the S-T transition catalyzed by a transition atom complex could be very important in spin catalysis.

Studies of transition metal ion reactions with gases such as hydrogen, water, methane, ethylene etc. [217] in ion-molecular beams have shown many examples of spin changes in these processes. It was proposed that the effective overcoming of spin-prohibition in the formation of metal-hydroxide or metal-hydride intermediates is the important stage of some catalytic processes [211]. As a simple model of a catalyst preparation the reaction $\text{Ni} + \text{H}_2\text{O}$ could be considered [218]. From the gas phase kinetic studies it was shown that the triplet-singlet intersystem crossing occurs at on the first stage of the reaction [218]. From the analysis of hybridization changes [218] a large orbital angular momentum shift during the S-T transition and a large SOC matrix element were inferred at the stage of a weak complex formation [211]. The highly effective double $T \rightleftharpoons S$ transitions during formation of the insertion product HNiOH could be explained from these arguments.

II Extended Systems

In addition to semiempirical-like approximations of the spin-orbit operator, *viz.* one-electron approximations, "shielded nuclei" etc., we can foresee a development of the spin-orbit response methodology towards extended systems along two lines. These two lines have already been exploited for other types of response properties [37, 219]. The first refers to techniques where the spin-orbit related response vectors and Fock matrices containing spin-orbit integrals are computed in a direct atomic-orbital (AO) fashion, that is in the same way as in AO-direct (or double direct) techniques in use for calculations of properties like dipole spectra and polarizabilities [37, 36]. In these methods the computationally demanding operations, *n.b.* matrix times vector operations are integral driven and integrals are computed in AO basis whenever needed, they are neither stored nor transformed. Such operations are more difficult to carry out for spin-orbit properties than for ordinary electrostatic properties due to the more complex nature of the spin-orbital integrals, with lower permutational symmetry, more difficult prescreening and identification and small integrals, etc. An implementation of this option would nevertheless make it possible to perform calculations of the kind reviewed in this article for very large systems within the random phase approximation. The other extension to large systems rely on the modeling of the long-range interactions in terms

of dielectric reaction fields. Such, self-consistent reaction field, methods have for long been available for total energy and wave function calculations with different quantum approaches. The recent generalization [219] of the multi-configuration self-consistent reaction field method [220] to response theory calculations [219] with a reaction field representation of the Hamiltonian, has made it possible to simulate the influence of the medium on specific linear response properties. With this method the solvent induced SOC can be directly simulated quantum mechanically. In the prolongation such work refers also spin-orbit induced chemical reactions in solutions modeled by the reaction field approach. Recent updates of molecular gradient and hessian MCSCF approaches [221] make it possible to conduct potential and transition state searches on both singlet and triplet state the molecular hypersurfaces with a dynamical coupling to the medium. Such calculations can thus be augmented by solvent induced SOC computations at geometrical points selected by these searches, e.g. conformations close to ISCs. Since at transitions states the S-T gap is small and the chemical bonds are weak with radical or ionic ingredients in the wave functions, the influence of a surrounding medium is crucial. Knowledge of how the solvent can change the spin-orbit properties of solvated molecules may thus provide much insight in the mechanisms by which a chemical reaction proceeds in solution.

Acknowledgements

We thank Sören Knuts, Poul Jørgensen, Trygve Helgaker, Hans Jørgen Aa. Jensen, Jeppe Olsen, Patrik Norman, Dan Jonsson and Olexandre Plachkevitch for a rewarding collaboration on linear and quadratic response theory and applications involving SOC. This work was supported by CRAY Research Inc.

References

- [1] W.G. Richards, H.P. Trivedi, and D.L. Cooper. In *Spin-Orbit Coupling in Molecules*. Clarendon Press, Oxford, 1981.
- [2] S.R. Langhoff and C.W. Kern. In H.F. Schaeffer, editor, *Methods of Electronic Structure Theory*, volume 4. Plenum Press, New York, 1977.
- [3] M.R. Manaa and D.R. Yarkony. *J. Chem. Phys.*, 95:6562, 1991.
- [4] S. Koseki, M.H. Schmidt, and M.S. Gordon. *J. Phys. Chem.*, 96:10678, 1992.
- [5] R. Klotz, C.M. Marian, S.D. Peyerimhoff, B.A. Hess, and R.J. Buenker. *Chem. Phys.*, 89:223, 1984.
- [6] P. Palmieri, R. Tarroni, G. Chamband, and P. Rosmus. *J. Chem. Phys.*, 99:456, 1993.
- [7] C. Ribbing and C. Daniel. *J. Chem. Phys.*, 100:6951, 1994.
- [8] O. Vahtras, H. Ågren, P. Jørgensen, H.J.Aa. Jensen, T. Helgaker, and J. Olsen. *J. Chem. Phys.*, 96:2118, 1992.

- [9] P. Jørgensen, J. Olsen, and H. J. Aa. Jensen. *J. Chem. Phys.*, 74:265, 1988.
- [10] H. Hettema, H.J.Aa. Jensen, P. Jørgensen, and J. Olsen. *J. Chem. Phys.*, 97:1174, 1992.
- [11] O. Vahtras, H. Ågren, P. Jørgensen, H.J.Aa. Jensen, T. Helgaker, and J. Olsen. *J. Chem. Phys.*, 97:9178, 1992.
- [12] J. Oddershede and P. Jørgensen. *J. Chem. Phys.*, 66:1541, 1977.
- [13] D.L. Yeager and P. Jørgensen. *Chem. Phys. Lett.*, 65:77, 1979.
- [14] E. Dalggaard and H.J. Monkhorst. *Phys. Rev. A*, 28:1217, 1983.
- [15] J. Olsen and P. Jørgensen. *J. Chem. Phys.*, 82:3235, 1985.
- [16] P. Swanstrøm, J.T. Golab, D.L. Yeager, and J.A. Nichols. *Chem. Phys.*, 110:339, 1986.
- [17] J. Geertsen, J. Oddershede, and G.E. Scuseria. *J. Chem. Phys.*, 87:2138, 1987.
- [18] I. Cacelli, V. Carravetta, R. Moccia, and A. Rizzo. *J. Phys. Chem.*, 92:979, 1988.
- [19] F. Müller-Plathe and G.H. Diercksen. *Phys. Rev. A*, 40:696, 1989.
- [20] B.T. Pickup. Theory and computation of molecular properties. In S. Wilson, editor, *Methods in Computational Chemistry, Volume 5: Atomic and Molecular Properties*, pages 157–265. Plenum Press, New York, 1992.
- [21] P.W. Fowler. *Ann. Rept. Chem. Soc. Sect. C*, 84:3–42, 1987.
- [22] Jens Oddershede. Propagator methods. *Adv. Chem. Phys.*, 69:201–239, 1987.
- [23] Y. Luo, H. Ågren, P. Jørgensen, and K.V. Mikkelsen. *Adv. Quant. Chem.*, 00:000, 1995.
- [24] B.F. Minaev. In *Theoretical analysis and prognostication of spin-orbit coupling effects in molecular spectroscopy and chemical kinetics*. Dr. Sc. Thesis, Chem. Phys. Institute, Moscow, 1983.
- [25] B.F. Minaev and S. Lunell. *Zeitschr. fur Physik. Chemie*, 182:263, 1993.
- [26] B.F. Minaev, P. Norman, D. Jonsson, and H. Ågren. *Chem. Phys.*, 190:11, 1995.
- [27] P.O. Löwdin. *Int. J. Quant. Chem.*, 4:31, 1971.
- [28] J. Oddershede. *Adv. Chem. Phys.*, 69:201, 1987.
- [29] E. Davidson. *J. Comput. Phys.*, 17:87, 1975.
- [30] B.O. Roos. *Chem. Phys. Lett.*, 15:153, 1972.
- [31] H.J.Aa. Jensen and H. Ågren. *Chem. Phys. Lett.*, 110:140, 1984.
- [32] J. Olsen, B.O. Roos, P. Jørgensen, and H.J.Aa. Jensen. *J. Chem. Phys.*, 89:2185, 1988.
- [33] L.T. Thomas. *Phil. Mag.*, 3:1, 1927.
- [34] J. Olsen, P. Jørgensen, and H.J.Aa. Jensen. *J. Comp. Phys.*, 74:265, 1988.
- [35] O. Vahtras and H.J.Aa. Jensen, to be published.
- [36] H. Koch, H. Ågren, P. Jørgensen, T. Helgaker, and H. J. Aa. Jensen. *Chem. Phys.*, 172:13, 1993.
- [37] H. Ågren, O. Vahtras, H. Koch, P. Jørgensen, and T. Helgaker. *J. Chem. Phys.*, 98:6417, 1993.
- [38] J. Olsen, D.L. Yeager, and P. Jørgensen. *J. Chem. Phys.*, 91:381, 1989.
- [39] S.R. Langhoff and E.R. Davidson. *J. Chem. Phys.*, 64:4699, 1976.

- [40] R. Klotz and S.D. Peyerimhoff. *Mol. Phys.*, 57:573, 1986.
- [41] B.F. Minaev. *Int. J. Quant. Chem.*, 17:367, 1980.
- [42] K.J. Ritter and T.D. Wilkerson. *J. Mol. Struct. (TEOCHEM)*, 121:1, 1987.
- [43] J. Breulet. *J. Comp. Chem.*, 2:244, 1981.
- [44] T.R. Furlani and H.F. King. *J. Chem. Phys.*, 82:557, 1985.
- [45] W.J. Hehre, R. Ditchfield, and J.A. Pople. *J. Chem. Phys.*, 56:2257, 1969.
- [46] P.-O. Widmark, P.Å. Malmquist, and B.O. Roos. *Theor. Chim. Acta*, 77:291, 1990.
- [47] B.F. Minaev. *Izv. Vysch. Ucheb. Zaved.*, 9:115, 1978.
- [48] B.F. Minaev. *Fizika Molekul, Naukova Dumka, Kiev*, 7:34, 1979.
- [49] S. P. McGlynn, T. Azumi, and M. Kinoshita. *Molecular Spectroscopy of the Triplet State*. Engelwood Cliffs, New Jersey: Prentice Hall, 1969.
- [50] B.F. Minaev. Ph.D. Dissertation, Tomsk State University, USSR, 1973.
- [51] O. Vahtras, H. Ågren, P. Jørgensen, H.J.Aa. Jensen, and T. Helgaker. *Int. J. Quant. Chem.*, 41:729, 1992.
- [52] H.J. Werner and P.J. Knowles. *J. Chem. Phys.*, 89:5803, 1988.
- [53] S.P. Walch, C.W. Bauchlicher, B.O. Roos, and C. Nelin. *Phys. Lett.*, 103:175, 1983.
- [54] D.R. Salahub. Ab initio methods in quantum chemistry part ii, advances in chemical physics. volume LXIX. Wiley, New York, 1987.
- [55] H. Ågren and O. Vahtras. *J. Phys B: At. Mol. Phys.*, 26:913, 1993.
- [56] G. Howat, T. Åberg, and O. Goscinski. *J. Phys B: At. Mol. Phys.*, 11:1575, 1978.
- [57] H. Ågren, C. Medina-Llanos, and K. Mikkelsen. *Chem. Phys.*, 115:43, 1987.
- [58] V. Carravetta and H. Ågren. *Phys. Rev. A*, 35:1022, 1987.
- [59] G. Dujardin, L. Hellner, M. Hamdan, A.G. Brenton B.J. Olsson, and M.J. Besnard-Ramage. *J. Phys B: At. Mol. Phys.*, 23:1165, 1990.
- [60] L. Serrano-Andres, M. Merchán, I. Nebot-Gil, R. Lindh, and B.O. Ross. *J. Chem. Phys.*, 98:3151, 1993.
- [61] M.A. Natiello and A.R. Engelmann. In Erkki Brändas and Nils Elander, editors, *Lecture notes in Physics 325*. Springer, Berlin, 1989.
- [62] M. Natiello and H. Ågren and O. Vahtras, Technical Note, Institute of Quantum Chemistry, Uppsala.
- [63] R.W. Wetmore, R.J. Le Roy, and R.K. Boyd. *J. Phys. Chem.*, 88:6318, 1984.
- [64] M. Larsson, B.J. Olsson, and P. Sigraý. *Chem. Phys.*, 139:457, 1989.
- [65] H. Ågren, S. Knuts, K.V. Mikkelsen, and H.J.Aa. Jensen. *Chem. Phys.*, 159:211, 1992.
- [66] N. Correia, A.F. Flores, H. Ågren, K. Helenelund, L. Asplund, and U. Gelius. *J. Chem. Phys.*, 83:2035, 1985.
- [67] R.J. Cvetanovic. *Adv. Photochem.*, 1:115, 1963.
- [68] S. Knuts, B.F. Minaev, O. Vahtras, and H. Ågren. *Int. J. Quant. Chem.*, 00:000, 1995.
- [69] J.T. Golab, D.L. Yeager, and P. Jørgensen. *Chem. Phys.*, 93:83, 1985.

- [70] B.F. Minaev and H. Ågren. *Chem. Phys. Lett.*, 217:531, 1994.
- [71] Recently, Braunstein and Pack[79] used a dynamic model for calculation of vibrational profiles to assign the Wulf band as due to a singlet-triplet ${}^3A_2 \leftarrow X^1A_1$ transition. The source of intensity was tentatively suggested to origin from spin-orbit coupling with the extremely strong UV absorbing 1B_2 state.
- [72] J.I. Steinfeld, S.M. Adler-Golden, and J.W. Gallagher. *J. Phys. Chem. Ref. Data*, 16:911, 1987.
- [73] B.R. Johnson and J.L. Kinsey. *J. Chem. Phys.*, 91:7638, 1989.
- [74] A. Banichevich, S.D. Peyerimhoff, and F. Grein. *Chem. Phys. Lett.*, 173:1, 1990.
- [75] O.R. Wulf. *Proc. Nat. Acad. Sci. (Paris)*, 16:507, 1930.
- [76] M.J. Chappuis. *C.R. Acad. Sci. (Paris)*, 91:985, 1880.
- [77] P.J. Hay and T.H. Dunning Jr. *J. Chem. Phys.*, 67:2290, 1977.
- [78] A. Banichevich, S.D. Peyerimhoff, J.A. Beswick, and O. Atabek. *J. Chem. Phys.*, 96:6580, 1992.
- [79] M. Braunstein and R.P. Pack. *J. Chem. Phys.*, 96:6378, 1992.
- [80] D. Nordfors, H. Ågren, and H.J.Aa. Jensen. *Int. J. Quant. Chem.*, 40:475, 1991.
- [81] M. Braunstein, P.J. Hay, R.L. Martin, and R.T. Pack. *J. Chem. Phys.*, 95:8239, 1991.
- [82] J.A. Jones. *J. Geophys. Res.*, 91:14533, 1986.
- [83] B.F. Minaev, S. Knuts, H. Ågren, and O. Vahtras. *Chem. Phys.*, 175:245, 1993.
- [84] W.C. Ermler, J.P. Clark, and R.S. Mulliken. *J. Chem. Phys.*, 86:370, 1987.
- [85] J. Olsen, B.F. Minaev, O. Vahtras, H. Ågren, P. Jørgensen, H.J.Aa. Jensen, and T. Helgaker. *Chem. Phys. Lett.*, 213:387, 1994.
- [86] D.E. Shemansky. *J. Chem. Phys.*, 51:689, 1969.
- [87] P.-O. Widmark, P.Å. Malmquist, and B.O. Roos. *Theor. Chim. Acta*, 77:291, 1990.
- [88] A. Lofthus and P.H. Krupenie. *J. Phys. Chem. Ref. Data*, 6:1113, 1977.
- [89] L.G. Piper. *J. Chem. Phys.*, 99:3174, 1993.
- [90] G. Chandraiah and G.G. Shepherd. *Can. J. Phys.*, 46:221, 1968.
- [91] A. L. Broadfoot and S. P. Maran. *J. Chem. Phys.*, 51:678, 1969.
- [92] W. Benesch. *Phys. Rev. A*, 19:445, 1979.
- [93] G. Zumofen, J. Sedlacek, R. Taubenberger, S.L. Pan, O. Oehler, and K. Dressler. *J. Chem. Phys.*, 81:2305, 1984.
- [94] D. Cerny, F. Roux, C. Effantin, J. D'Incan, and J. Verges. *J. Mol. Spectroscopy*, 81:2165, 1980.
- [95] D.C. Cartwright. *J. Geophys. Res.*, A83:2517, 1978.
- [96] S.G. Tilford, J.T. Vanderslice, and P.G. Wilkinson. *Astrophys. J.*, 141:1226, 1965.
- [97] R. Schlapp. *Phys. Rev.*, 39:806, 1932.
- [98] J.K.G. Watson. *Can. J. Phys.*, 46:1637, 1968.
- [99] Y. Tanaka, M. Ogawa, and A.S. Jursa. *J. Chem. Phys.*, 40:3690, 1964.

- [100] Y. Tanaka. *J. Opt. Soc. Am.*, 45:663, 1955.
- [101] B.K. Ching, G.R. Cook, and R.A. Becker. *J. Quant. Spectrosc. Radiat. Transfer*, 7:323, 1967.
- [102] K.P. Huber and G. Herzberg. In *Molecular Spectra and Molecular Structure. Vol. 4. Constants of Diatomic Molecules*. Van Nostrand Reinhold, New York, 1979, 1979.
- [103] I. Kovacs. In *Rotational Structure in the Spectra of Diatomic Molecules*, page 123. Elsevier, New York, 1969.
- [104] W.H.B. Cameron. In *The production of some spectra of carbon oxygen and nitrogen in the presence of neon*, volume 1, page 405. Phil. Mag., 1926.
- [105] G.M. Lawrence. *Chem. Phys. Lett.*, 9:575, 1971.
- [106] R.S. Freund. *J. Chem. Phys.*, 55:3579, 1971.
- [107] T.G. Slinger and G. Black. *J. Chem. Phys.*, 55:3169, 1971.
- [108] J.M. Ajello. *J. Chem. Phys.*, 55:3158, 1971.
- [109] C.E. Johnson. *J. Chem. Phys.*, 57:576, 1972.
- [110] J. Fournier, J. Deson, and C. Vermeil. *Opt. Commun.*, 16:111, 1976.
- [111] P.W. Erdman and E.C. Zipf. *Planet. Space Sci.*, 31(3):317, 1983.
- [112] J. Fournier, H.H. Mohammed, J. Deson, C. Vermeil, and J. Schamps. *J. Chem. Phys.*, 73(12), 1980.
- [113] T.C. James. *J. Chem. Phys.*, 53(8), 1971.
- [114] W.L. Borst and E.C. Zipf. *Phys. Rev. A*, 3:979, 1971.
- [115] B.F. Minaev, O.N. Plashkevich, and H. Ågren. *J. Chem. Soc. Faraday Trans.*, 00:000, 1995.
- [116] P.H. Krupenie. In *The Band Spectrum of Carbon Monoxid*, volume 5. Natl.Std.Ref.Data Sys., Natl.Bur.Std.(U.S.), 1966.
- [117] V. Hasson and R.W. Nicholls. *J. Phys. B*, 4:681, 1971.
- [118] A.R. Fairbairn. *J. Quant. Spectry. Radiative Transfer*, 10:1321, 1970.
- [119] R. de Vivie, C.M. Marian, and S.D. Peyerimhoff. *Chem. Phys.*, 12:349, 1987.
- [120] D.R. Yarkony. *J. Chem. Phys.*, 89:7324, 1988.
- [121] L.H. Andersen, J.H. Posthumus, O. Vahtras, H. Ågren, N. Elander, A. Nunez, A. Scrinzi, M. Natiello, and M. Larsson. *Phys. Rev. Lett.*, 71:1812, 1993.
- [122] C.M. Marian, R. de Vivie, and R. Klotz. In W.P. Kraemer, editor, *Computation of lifetimes by ab initio methods. Proceedings of the 6th seminar on computational methods in quantum chemistry*, 1984.
- [123] D.R. Yarkony. *Intern. Rev. Phys. Chem.*, 11:195, 1992.
- [124] C. Petrongolo, R. J. Buenker, and S.D. Peyerimhoff. *J. Chem. Phys.*, 76:3655, 1982.
- [125] B. F. Minaev. *Izv. Vyssh. Uchebn. Zaved. Fiz.*, 4:146, 1971.
- [126] Y. Luo, H. Ågren, and S. Stafström. *J. Phys. Chem.*, 98:7782, 1994.
- [127] J. Anders, V.S. Safont, and O. Tapia. *Chem. Phys. Lett.*, 198:515, 1992.
- [128] D.F. Evans. *J. Chem. Soc.*, page 1735, 1960.

- [129] O.A. Mosher, W.H. Flicker, and A. Kuppermann. *J. Chem. Phys.*, 59:6502, 1973.
- [130] W. Flicker, O.A. Mosher, and A. Kuppermann. *Chem. Phys.*, 3:307, 1978.
- [131] D.G. Wilden and J. Comer. *J. Phys B: At. Mol. Phys.*, 13:1009, 1980.
- [132] B.F. Minaev, P. Norman, D. Jonsson, and H. Ågren. *Chem. Phys.*, 194:19, 1995.
- [133] S. Knuts, B.F. Minaev, H. Ågren, and O. Vahtras. *Theor. Chim. Acta*, 87:343, 1994.
- [134] H. Ågren, B.F. Minaev, and S. Knuts. *J. Phys. Chem.*, 98:3943, 1994.
- [135] B.F. Minaev. *Izv. Vysch. Ucheb. Zaved. Fizika*, 8:118, 1971.
- [136] J. van Egmond and J.H. van der Waals. *Mol. Phys.*, 26:1147, 1973.
- [137] W.J. Buma, J.H. van der Waals, J. Schmidt, and R. de Beer. *J. Chem. Phys.*, 91:6549, 1989.
- [138] A.J. Merer and R.S. Mulliken. *Chem. Rev.*, 69:639, 1969.
- [139] B.F. Minaev. *Izv. Vysch. Ucheb. Zaved.*, 5:93, 1971.
- [140] I.S. Irgibaeva, B.F. Minaev, Z.M. Muldahmetov, and D.M. Kizner. *J. Appl. Spectrosc. (USSR)*, 32:66, 1980.
- [141] K.B. Wiberg, C.M. Haad, C.B. Ellison, and J.B. Foresman. *J. Phys. Chem.*, 97:13586, 1993.
- [142] Olivucci, I.N. Ragazos, F. Bernardi, and M.A. Robb. *J. Am. Chem. Soc.*, 115:3710, 1993.
- [143] W.G. Dauben, R.L. Cargill, R.M. Coates, and J. Saltiel. *J. Am. Chem. Soc.*, 88:2742, 1966.
- [144] R. Srinivasan. *J. Am. Chem. Soc.*, 84:4141, 1962.
- [145] W. M. Flicker, A. Mosher, and A. Kuppermann. *Chem. Phys. Lett.*, 45:492, 1977.
- [146] G.N. Lewis and M. Kasha. *J. Am. Chem. Soc.*, 66:2100, 1944.
- [147] G.N. Lewis and M. Kasha. *J. Am. Chem. Soc.*, 67:994, 1945.
- [148] S. Weissman and D. Lipkin. *J. Am. Chem. Soc.*, 64:1916, 1942.
- [149] D. McClure. *J. Chem. Phys.*, 17:905, 1949.
- [150] B.F. Minaev, S. Knuts, and H. Ågren. *Chem. Phys.*, 181:15, 1994.
- [151] H. Ågren, O. Vahtras, S. Knuts, and P. Jørgensen. *Chem. Phys.*, 181:291, 1994.
- [152] W.J. Buma, J.H. van der Waals, and M.C. van Hemert. *J. Chem. Phys.*, 93:3733, 1990.
- [153] E.C. Lim. *J. Chem. Phys.*, 36:3497, 1962.
- [154] J.W. Rabalais, H.J. Maria, and S.P. McGlynn. *J. Chem. Phys.*, 51:2259, 1969.
- [155] H.J. Shull. *J. Chem. Phys.*, 17:295, 1949.
- [156] P.P. Dikun and B. Ya. Sveshnikov. *Zhur. Eksptl. i Teoret. Fiz. (Soviet JETP)*, 19:1000, 1949.
- [157] G.C. Nieman. *J. Chem. Phys.*, 50:1660, 1969.
- [158] A.C. Albrecht. *J. Chem. Phys.*, 38:354, 1963.
- [159] T.V. Ivanova and B. Ya. Sveshnikov. *Optics and Spectroscopy (USSR)*, 11:322, 1961.

- [160] E.B. Wilson, J.C. Decious, and P.C. Cross. In *Molecular Vibrations*. McGraw-Hill, New York, 1955.
- [161] W. Moffitt. *J. Chem. Phys.*, 22:320, 1954.
- [162] W. Mofitt and A.D. Liehr. *Phys. Rev.*, 106:1195, 1957.
- [163] M. Mizushima and S. Koide. *J. Chem. Phys.*, 20:765, 1952.
- [164] E. Clementi. *J. Mol. Spectroscopy*, 6:497, 1961.
- [165] D.M. Burland, G. Castro, and G.W. Robinson. *J. Chem. Phys.*, 52:4100, 1970.
- [166] J. van Egmond, D.M. Burland, and J.H. van der Waals. *Chem. Phys. Lett.*, 12:206, 1971.
- [167] Y. Osamura. *Chem. Phys. Lett.*, 145:541, 1988.
- [168] J. van Egmond, D.M. Burland, and J.H. van der Waals. *Mol. Phys.*, 28:457, 1974.
- [169] S.R. Langhoff, E.R. Davidson, and C.W. Kern. *J. Chem. Phys.*, 63:4800, 1975.
- [170] M.A. El-Sayed. In A.D. Ramsey and D.A. Ramsay, editors, *MTP International Review of Science, Spectroscopy*, page 119. Butterworth, London, 1972.
- [171] P.G. Russell and A.C. Albrecht. *J. Chem. Phys.*, 41:2536, 1964.
- [172] H.F. Hameka and J.L. Oosterhoff. *Mol. Phys.*, 1:364, 1958.
- [173] Yu.F. Pedash and A.V. Luzanov. *Theor. Exp. Chem.*, 27:152, 1991.
- [174] W.J. Burna, J.H. van der Waals, and M.C. van Hemert. *J. Chem. Phys.*, 93:3733, 1990.
- [175] B. J. Cohen and L. Goodman. *J. Chem. Phys.*, 46:713, 1967.
- [176] T.U. Helgaker, J. Almlöf, H.J.Aa. Jensen, and P. Jørgensen. *J. Chem. Phys.*, 84:6266, 1986.
- [177] Jr. T.H. Dunning. *J. Chem. Phys.*, 53:2833, 1970.
- [178] Jr. T.H. Dunning. *J. Chem. Phys.*, 55:716, 1971.
- [179] B. R. Henry and W. Siebrand. *J. Chem. Phys.*, 51:2396, 1969.
- [180] N. Chaudhuri and M.A. El-Sayed. *J. Chem. Phys.*, 43:1423, 1965.
- [181] S.K. Lower and M.A. El-Sayed. *Chem. Rev.*, 66:199, 1966.
- [182] W. Siebrand. *J. Chem. Phys.*, 47:2411, 1967.
- [183] C.A. Hutchison and B.W. Mangum. *J. Chem. Phys.*, 32:1261, 1960.
- [184] G.W. Robinson and R.P. Frosch. *J. Chem. Phys.*, 38:1187, 1963.
- [185] V.L. Ermolaev. *Izv. Akad. Nauk USSR, Ser. Fiz.*, 27:617, 1963.
- [186] D.M. Hanson and G.W. Robinson. *J. Chem. Phys.*, 43:4174, 1965.
- [187] J. Langelaar, R.P.H. Rettschnick, and G.J. Hoijtink. *J. Chem. Phys.*, 54:1, 1971.
- [188] B. R. Henry and W. Siebrand. *J. Chem. Phys.*, 54:1072, 1971.
- [189] S. Knuts, O. Vahtras, and H. Ågren. *THEOCHEM*, 279:249, 1993.
- [190] D.M. Burland and J. Schmidt. *Mol. Phys.*, 22:19, 1971.
- [191] L. Vanquickenborne and S.P. McGlynn. *J. Chem. Phys.*, 45:4755, 1966.
- [192] K. Sushida, M. Fujita, T. Takemura, and H. Baba. *J. Chem. Phys.*, 78:588, 1983.

- [193] W.J. Buma, E.J.J. Groenen, and M.C. van Hemert. *J. Am. Chem. Soc.*, 112:5447, 1990.
- [194] S.I. Nagaoka and U. Nagashima. *J. Phys. Chem.*, 94:4467, 1990.
- [195] S. Yamaguchi and T. Azumi. *J. Chem. Phys.*, 67:7, 1977.
- [196] S. Yamauchi, T. Ueno, and N. Hirota. *Mol. Phys.*, 47:1333, 1982.
- [197] E. Clementi and M. Kasha. *J. Mol. Spectroscopy*, 2:297, 1958.
- [198] K.K. Innes, I.G. Ross, and W.R. Moomaw. *J. Mol. Spectry.*, 132:492, 1988.
- [199] S. Yamaguchi, H. Saigusa, and T. Azumi. *J. Chem. Phys.*, 74:5335, 1981.
- [200] Y. Komada, S. Yamauchi, and N. Hirota. *J. Chem. Phys.*, 82:1651, 1985.
- [201] M. Kasha. *J. Chem. Phys.*, 20:71, 1952.
- [202] S.P. McGlynn, T. Azumi, and M. Kasha. *J. Chem. Phys.*, 40:507, 1964.
- [203] G.J. Hoijtink. *Mol. Phys.*, 3:67, 1960.
- [204] H. Tsubamura and R.S. Mulliken. *J. Am. Chem. Soc.*, 82:5666, 1960.
- [205] J.N. Murrell. *Mol. Phys.*, 3:319, 1960.
- [206] G.W. Robinson. *J. Chem. Phys.*, 46:572, 1967.
- [207] K.C. Lin and S.H. Lin. *Mol. Phys.*, 21:1105, 1971.
- [208] B.F. Minaev. *J. Appl. Spectrosc. (USSR)*, 43:131, 1985.
- [209] B.F. Minaev, I.M. Danilovich, and Yu.A. Serebrennikov. In *Dynamics of triplet excitations in molecular crystals*, page 109. Naukova Dumka, Kiev (in Russ.), 1989.
- [210] R.H. Hofeldt, R. Sahai, and S.H. Lin. *J. Chem. Phys.*, 53:4512, 1970.
- [211] B.F. Minaev and H. Ågren. *Coll. Czech. Chem. Comm.*, 60:339, 1995.
- [212] J.C. Koziar and D.O. Cowan. *Acc. Chem. Res.*, 11:334, 1978.
- [213] B.F. Minaev, I.S. Irgibaeva, and Z.M. Muldahmetov. *Teor. Eksp. Khim.*, 17:659, 1981.
- [214] B.F. Minaev. *Teor. Eksp. Khim.*, 20:209, 1984.
- [215] H. Toftlund. *Coord. Chem. Rev.*, 94:67, 1989.
- [216] M. Fisher and S.G. Sligar. *Biochemistry*, 26:4797, 1987.
- [217] P.B. Armentrout. *Ann. Rev. Phys. Chem.*, 41:313, 1990.
- [218] S.A. Mitchell, M.A. Blitz, P.E.M. Siegbahn, and M. Svensson. *J. Chem. Phys.*, 100:423, 1994.
- [219] K. Mikkelsen and P. Jørgensen. to be published.
- [220] K.V. Mikkelsen, E. Dalgaard, and P. Swanstrøm. *J. Chem. Phys.*, 79:587, 1987.
- [221] K. Mikkelsen et al. to be published.
- [222] S. Knuts, H. Ågren, and B.F. Minaev. *THEOCHEM*, 311:185, 1994.

FUNCTIONAL GROUPS IN QUANTUM CHEMISTRY

Paul G. Mezey

*Mathematical Chemistry Research Unit,
Department of Chemistry and Department of Mathematics and Statistics,
University of Saskatchewan,
110 Science Place, Saskatoon, Canada, S7N 5C9*

Table of Contents

- 1. Introduction**
- 2. Molecular Fragments, Chemical Functional Groups**
 - 2.1 Semiclassical Concepts of Molecular Bodies and Functional Groups
 - 2.2 A Fuzzy Set Formalism for Molecular Electronic Density
 - 2.3 Quantum Chemical Representations of Molecular Bodies and their Subdivisions Using Fragmentation Schemes
 - 2.4 The Pseudo-Density Scheme of Walker
 - 2.5 The Mulliken-Mezey Additive Fuzzy Electron Density Fragmentation Method
- 3. The Density Domain Approach to Functional Groups and Local Molecular Properties**
 - 3.1 The Density Domain Concept
 - 3.2 Chemical Bond as a Density Domain Relation
 - 3.3 The "Late - Early Rule"
 - 3.4 A Density Domain Definition of Functional Groups
 - 3.5 Functional Groups as Fuzzy Subsets of Molecular Electron Density
 - 3.6 A Fuzzy Set Model for Local Molecular Properties
- 4. An Application of the MEDLA Method for the Direct Computation of Electron Densities of Functional Groups**
 - 4.1 Building Molecular Electron Densities Using the Additive Fuzzy Electron Density Fragmentation Method.
 - 4.2. The MEDLA Method
 - 4.3 MEDLA Fragment Selection Based on Density Domains
 - 4.4 Functional Groups as MEDLA Superfragments
 - 4.5 Linear Homotopies of Fuzzy Electron Density Fragments
 - 4.6 Nonlinear Transformations of Fuzzy Electron Density Fragments
- 5. Local Shape Analysis of Functional Groups**
 - 5.1 Local Molecular Fragments in a Global Molecular Environment
 - 5.2 Local Shape Changes Induced by Molecular Environment
 - 5.3 Local Shapes of Non-Interacting Functional Groups
 - 5.4 Local Shapes of Interacting Functional Groups
- 6. Shape Similarity and Shape Complementarity Measures of Functional Groups in Different Molecular Environments**
 - 6.1 Shape Similarity Measures of Functional Groups Based on Local Shapes
 - 6.2 Local Shape Complementarity Measures for Functional Groups
- 7. Energy Relations for Functional Groups and their Interactions**
 - 7.1 The Fragment Energy Concept and Fragment Interaction Energies
 - 7.2 Approximate Conformation Optimization from Fragment Models
- 8. Summary**
- 9. Acknowledgements**
- 10. References**

1. INTRODUCTION

In this report the quantum chemical concept of functional groups will be described, following a topological approach based on the three-dimensional shape of fuzzy molecular bodies and the local shapes of various molecular moieties. This quantum chemical description of functional groups was first proposed in ref. [1] and further elaborated in refs. [2,3], based on the topological shape analysis of molecules [2] and on the *density domain* approach to chemical bonding [4]. Density domains are formal bodies enclosed by molecular isodensity contours; density domains play an important role in molecular shape analysis and serve as the basis of various molecular similarity measures [5]. The proposed quantum chemical model of functional groups also fits within a rather broad, essentially geometrical framework discussed in [6]. Also in ref.[6], a general algebraic structure has been proposed for families of functional groups. The suggested algebraic structure is a mathematical lattice describing the interrelations between functional groups. This general algebraic description is also applicable to the families of quantum chemical functional groups defined by topological shape conditions of the electron density [1-3,5].

A chemical functional group is a collection of nuclei and the associated electron density which occur with a similar nuclear arrangement and a similar local electron density cloud in many molecules. A functional group is a molecular moiety of a specific stoichiometry that typically undergoes similar chemical reactions in most molecules containing this moiety. In chemistry, especially in organic chemistry, the concept of functional groups is a powerful tool used for the characterization and classification of molecules and their reactions; in fact, the presence of a given functional group in a family of molecules is an expression of chemical similarity. Molecules containing common functional groups often exhibit similar physical properties in addition to their similar chemical properties. For example, organic molecules containing the OH group often generate hydrogen bonds between one another, that in turn has the usual consequence of a higher boiling point than that of molecules of similar molecular weight but containing no OH groups. There are important differences, however, depending on the local surroundings of these OH groups, and it is often justified to regard larger moieties, such as the carboxyl group, COOH, or the hydroxymethyl group, CH₂OH, as functional groups.

Apparently, the concept of *similarity* plays an important role in the chemistry of functional groups. Motivated by the recent revival of interest in molecular similarity [7-39], we shall present a systematic approach towards a quantum chemical description of functional groups. There are two main components of the approach described in this report. The first component is shape-similarity, based on the topological shape groups and topological similarity measures of molecular electron densities[2,19-34], whereas the second component is the Density Domain approach to chemical bonding [4]. The topological Density Domain is a natural basis for a quantum

chemical model of functional groups, first proposed in [1] and further elaborated in refs. [2,3] and [5].

The conventional chemical notations using either the familiar structural formulas or the more revealing stereodiagrams are especially suited for encoding the identity of molecules. Whereas structural formulas and stereodiagrams given in terms of formal bonds depicted as lines represent only the skeletal structure of molecules; nevertheless, they serve as a "shorthand notation" for molecules and the three-dimensional arrangements of their nuclei. Depending on the chemical process, a given functional group may change or may remain essentially intact during the process. The actual transformations of functional groups (if the given groups are actively participating in the reactions), as well as their simple retention while the reactants turn into products (if the actual reactions affect directly only some other parts of the molecules) are easily modeled by fragments of the bond diagrams. In such models, a functional group is represented by its local bonding pattern, for example, the OH group is represented by the symbol -O-H , indicating the bond within the group as well as a formal broken, "dangling" bond between the functional group and the rest of the molecule. Based on such notations, the various functional groups of a molecule can be recognized. If one is familiar with the typical properties and behavior of the functional groups present, then one can often predict some of the most essential physical and chemical properties of the molecules as well as the main features of their reactions. Evidently, much of our chemical knowledge is formulated and classified in terms of functional groups.

The usual representation of functional groups as a particular local bonding pattern involving a set of atoms is somewhat oversimplified, and only a few attempts have been made to provide a more rigorous, quantum chemical definition and description of functional groups. One of the difficulties is associated with the description of parts of a quantum mechanical molecule, where these parts, as functional groups, possess individual characteristics and a certain degree of autonomy within the molecules. For the quantum chemical description of functional groups, it appears natural to use models and methods also applicable for complete molecules; in particular, it is well advised to avoid models showing artificial boundaries between various parts of a molecule. Models of molecular fragments showing discontinuities of electron density at some of their formal boundaries have artificial features; such discontinuous features are clearly impossible for entire molecules. Subdividing a molecule that appears an easy task for simple, traditional models involving formal chemical bonds depicted as lines is a problem of considerable complexity within a quantum chemical context. In reality, chemical bonding in molecules is not restricted to simple lines, such as the formal lines of bond diagrams; in fact, the actual chemical bonding is due to the electron density distribution throughout a fuzzy molecular body of the electronic charge cloud. In a more realistic model, functional groups require a more precise, quantum chemical definition; in particular, it is of importance to establish the extent by which various parts of the electron density belong to one or to another functional group of the molecule.

In this contribution, an approach to the quantum chemical concept of functional groups will be discussed, with special emphasis on their shapes, similarity and complementarity relations.

2. MOLECULAR FRAGMENTS, CHEMICAL FUNCTIONAL GROUPS

2.1 Semiclassical Concepts of Molecular Bodies and Functional Groups

In principle, the semiclassical concept of a molecular body is rather simple: the molecular body is a fuzzy charge cloud of electron density surrounding a set of essentially pointlike nuclei which vibrate about a specified equilibrium nuclear arrangement. A nuclear arrangement and the surrounding electronic charge cloud form the molecule; there is nothing else there. The shape of the molecule is the shape of the fuzzy, electronic charge cloud, a dynamic object whose motion approximately follows the nuclear vibrations.

The above simple model provides important insight into various molecular properties, physical, chemical and biochemical processes. One should note, however, that this model treats nuclei on two, mutually incompatible levels: as an essentially classical set of pointlike objects with a well-defined equilibrium configuration, and also as a vibrating system of masses exhibiting quantum mechanical uncertainty as well as quantization for their vibrations. According to rigorous quantum mechanics, nuclei are subject to the Heisenberg uncertainty relation, and in a physically correct model of chemistry [40] the concept of "a precise nuclear position in a molecule" is just as meaningless as the concept of "the precise position of an electron in a molecule". In practice, however, the Heisenberg uncertainty for the position of the more massive nuclei is much less severe than it is for the much lighter electrons, and the above semiclassical model is a useful and, computationally, a rather efficient tool in the study of molecular behavior.

One approach to the approximate representation of molecular bodies is based on molecular isodensity contours, MIDCOs, defined with respect to some fixed nuclear configuration K and some electron density threshold a . A MIDCO $G(a,K)$ is defined (in the fixed nuclear configuration approximation) as the collection of all those points \mathbf{r} of the three-dimensional space where the electronic density is equal to the threshold a :

$$G(a,K) = \{ \mathbf{r} : \rho(\mathbf{r},K) = a \}. \quad (1)$$

If there is no need to include the nuclear configuration K in the notation, one

may simply write

$$G(a) = \{ \mathbf{r} : \rho(\mathbf{r}) = a \}. \quad (2)$$

For any continuous electronic density function $\rho(\mathbf{r})$ of a molecule, the set of all points \mathbf{r} fulfilling equation (2) must form a set of a finite number of continuous surfaces. For low values of the electron density threshold a , $G(a)$ is usually a single, closed surface, whereas for high values of threshold a , $G(a)$ is usually a collection of several closed surfaces, each surrounding some of the nuclei of the molecule.

In fact, the complete electronic density of a molecule can be represented by an infinite family of such MIDCOs, a family that contains one set $G(a)$ of continuous surfaces for every threshold value a from the open-closed interval

$$(0, a_{\max}], \quad (3)$$

where a_{\max} is the electron density at a nucleus of the largest nuclear charge in the molecule. Consider the simplest case, where for a given interval of threshold values there is precisely one surface $G(a)$ for each threshold value a . These MIDCOs are nested within one another, in a manner similar to a series of Russian wooden dolls, where for each pair of a and a' values,

$$a < a', \quad (4)$$

the larger MIDCO $G(a)$ contains the smaller MIDCO $G(a')$.

If the molecular body is represented by a fuzzy electronic charge density, then it is also justified to represent functional groups by electron density charge clouds of similar, fuzzy features. Although most functional groups do not retain their shape and other properties when they actually become disconnected from the rest of the molecule and become independent, separate entities, nevertheless, a consistent framework for their quantum chemical description appears to require a treatment analogous to that of complete molecules. For this end, one has to decide what contribution of the molecular electronic charge density cloud belongs to which functional group of a molecule. In a general scheme, functional groups or other molecular fragments can be treated similarly to entire molecules, leading to the new concept of fragment isodensity contour, FIDCO, analogous to the molecular isodensity contour, MIDCO.

The question of assigning nuclei to various functional groups is much simpler: it is natural to define a functional group as a given subset of the nuclei and their "share" of the electronic density of the molecule. However, even for nuclei, this approach is not fully satisfactory. For example, in some hydrogen-bonded systems the assignment of the bridging hydrogen nucleus to either of the two molecular fragments it links is somewhat ambiguous. In such cases the electronic density may decide, as we shall see in later parts of this report.

2.2 A Fuzzy Set Formalism for Molecular Electronic Density

Molecular bodies do not have actual boundaries; these bodies are fuzzy, three-dimensional charge clouds of the molecular electron density distribution. Molecular shape is the shape of this fuzzy charge cloud. The concept of molecular shape should be clearly distinguished from the concept of molecular conformation; the latter is usually interpreted as a specific nuclear arrangement and the associated three-dimensional pattern of formal chemical bonds. These bonding patterns are usually described by lines of formal chemical bonds of a structural diagram. Since the actual molecular shape is determined by the fuzzy electron distribution, it is of some importance to reflect this fuzziness in models describing molecular shapes and chemical bonding.

For a single, isolated molecule X one may consider the following problem: to what degree do various points \mathbf{r} of the three-dimensional space belong to the molecule? A fuzzy set model of molecules can be introduced that provides a simple and rather natural approach to this problem.

Take the maximum value ρ_{\max} of the electron density within a spatial domain D containing the nuclei of molecule X ,

$$\rho_{\max} = \max \{ \rho(\mathbf{r}), \mathbf{r} \in D \}, \quad (5)$$

and define a fuzzy membership function $\mu_X(\mathbf{r})$ for points \mathbf{r} of the space belonging to molecule X as

$$\mu_X(\mathbf{r}) = \rho(\mathbf{r})/\rho_{\max}. \quad (6)$$

If molecule X is not isolated, for example, if the total electron density at some point \mathbf{r} can be regarded as a sum of electron densities $\rho_X(\mathbf{r})$ and $\rho_Y(\mathbf{r})$ assigned to molecules X and Y , respectively, then the fuzzy membership function of points \mathbf{r} with respect to the two molecules are determined by the relative magnitudes of the individual electron densities.

Consider the general case of a molecular family L of *several* molecules

$$X_1, X_2, \dots, X_i, \dots, X_m, \quad (7)$$

of electron density contributions

$$\rho_{X_1}(\mathbf{r}), \rho_{X_2}(\mathbf{r}), \dots, \rho_{X_i}(\mathbf{r}), \dots, \rho_{X_m}(\mathbf{r}), \quad (8)$$

respectively, representing their "share" in the total electron density of the molecular family L .

Following the simpler case of eq.(5), first we take each individual molecule X_i , with their "share" $\rho_{X_i}(\mathbf{r})$ of the complete electron density, and this "share" will be considered as a separate, individual object in the *absence* of all other molecules. The maximum value $\rho_{\max,i}$ of the electron density $\rho_{X_i}(\mathbf{r})$ within a spatial domain D_{X_i} containing all the nuclei of molecule X_i is given as

$$\rho_{\max,i} = \max \{ \rho_{X_i}(\mathbf{r}), \mathbf{r} \in D_{X_i} \}. \quad (9)$$

The point $\mathbf{r}_{\max,i}$ is defined as a point \mathbf{r} where this maximum density value $\rho_{\max,i}$ is realized:

$$\rho_{X_i}(\mathbf{r}_{\max,i}) = \rho_{\max,i} \cdot \quad (10)$$

Then, in the absence of other molecules, definition (6) of the fuzzy membership function for points \mathbf{r} of the space belonging to molecule X_i becomes

$$\mu_{X_i}(\mathbf{r}) = \rho_{X_i}(\mathbf{r}) / \rho_{\max,i} \cdot \quad (11)$$

If, however, the rest of the molecules of the family L is also considered, then the actual "belonging" of a point \mathbf{r} to molecule X_i is affected by the electron density contributions of all molecules, hence the above membership function is no longer appropriate. If the total electron density $\rho_L(\mathbf{r})$ of the molecular family $X_1, X_2, \dots, X_j, \dots, X_m$ at point \mathbf{r} is given by

$$\rho_L(\mathbf{r}) = \sum_j \rho_{X_j}(\mathbf{r}), \quad (12)$$

then the fuzzy membership function $\mu_{X_i,L}(\mathbf{r})$ for points \mathbf{r} of the space belonging to molecule X_i of the molecular family is defined as

$$\mu_{X_i,L}(\mathbf{r}) = \mu_{X_i}(\mathbf{r}) [\rho_{\max,i} / \rho_L(\mathbf{r}_{\max,i})]. \quad (13)$$

The scaling factor $[\rho_{\max,i} / \rho_L(\mathbf{r}_{\max,i})]$ ensures proper accounting of the actual density contributions from various molecules of the family L .

This fuzzy membership function $\mu_{X_i,L}(\mathbf{r})$ can be written in another form:

$$\begin{aligned} \mu_{X_i,L}(\mathbf{r}) &= \mu_{X_i}(\mathbf{r}) [\rho_{\max,i} / \rho_L(\mathbf{r}_{\max,i})] \\ &= [\rho_{X_i}(\mathbf{r}) / \rho_{\max,i}] [\rho_{\max,i} / \rho_L(\mathbf{r}_{\max,i})] \\ &= \rho_{X_i}(\mathbf{r}) / \rho_L(\mathbf{r}_{\max,i}), \end{aligned} \quad (14)$$

that is, simply as

$$\mu_{X_i,L}(\mathbf{r}) = \rho_{X_i}(\mathbf{r}) / \rho_L(\mathbf{r}_{\max,i}). \quad (15)$$

The above fuzzy electron density membership functions reflect the relative contributions of the fuzzy, three-dimensional charge clouds of the various molecular electron density distributions to the total electronic density of molecular family L .

2.3 Quantum Chemical Representations of Molecular Bodies and their Subdivisions Using Fragmentation Schemes

A molecule contains a nuclear distribution and an electronic distribution; there is *nothing else* in a molecule. The nuclear arrangement is fully reflected in the electronic density distribution, consequently, the electronic density and its changes are sufficient to derive all information on all molecular properties. Molecular bodies are the fuzzy bodies of electronic charge density distributions; consequently, the shape and shape changes of these fuzzy bodies potentially describe all molecular properties. Modern computational methods of quantum chemistry provide practical means to describe molecular electron distributions, and sufficiently accurate quantum chemical representations of the fuzzy molecular bodies are of importance for many reasons. A detailed analysis and understanding of "static" molecular properties such as "equilibrium" structure, and the more important dynamic properties such as vibrations, conformational changes and chemical reactions are hardly possible without a description of the molecule itself that implies a description of molecular bodies.

If the conventional SCF LCAO *ab initio* method is used for the computation of a wavefunction of a molecule of some fixed conformation K , then the electronic density $\rho(\mathbf{r})$ can be constructed in terms of a set of atomic orbitals $\phi_i(\mathbf{r})$ ($i=1,2,\dots,n$), where n is the number of orbitals. If \mathbf{r} denotes the three-dimensional position vector variable, and if \mathbf{P} is the $n \times n$ dimensional density matrix, then the electronic density $\rho(\mathbf{r})$ of the molecule can be written as

$$\rho(\mathbf{r}) = \sum_{i=1}^n \sum_{j=1}^n P_{ij} \phi_i(\mathbf{r}) \phi_j(\mathbf{r}). \quad (16)$$

This electron density $\rho(\mathbf{r})$ corresponds to the fuzzy "body" of the electronic charge cloud, providing a representation for the shape of the molecule.

In the general scheme described in subsequent sections, a functional group is regarded as a fuzzy body of electronic charge cloud, a fuzzy subset of the electronic charge density cloud of the complete molecule. In this context, a functional group is a special case of a fuzzy fragment of a molecular body, obtained by some subdivision

scheme. In this section some aspects of subdivision schemes are discussed.

Any quantum chemical representation of molecular bodies must take into account the fuzzy nature of electron density clouds. This fuzziness can be described in mathematical terms by the fuzzy membership functions discussed in the previous section, or it can be represented geometrically by an infinite family of MIDCOs $G(a)$ where one MIDCO belongs to every threshold value a from the open-closed interval $(0, a_{\max}]$. As discussed in section 2.1 of this report, the maximum threshold value a_{\max} is the electron density at a nucleus of the largest nuclear charge in the given molecule. In an alternative, topological representation [41-44, see also ref. 2 for a review], one can take advantage of the fact that for non-pathological electronic densities there are only a finite number of topologically different MIDCOs, and it is sufficient to take one MIDCO $G(a)$ from each of the corresponding topological equivalence classes. This allows one to represent the essential shape features of the entire molecular electron density by a finite number of individual MIDCO surfaces.

The natural fuzziness of electron densities of complete molecules is not necessarily retained in all subdivision schemes of molecular electron densities into fragments. One subdivision scheme is based on the theory of catastrophes as applied to the electronic density by Collard and Hall [45]. This method, as further developed by Bader, involves boundary surfaces defined by the condition of zero flux of the electron density gradient across these surfaces [46-51]. This is a natural condition for compartmentalizing a molecular electron density cloud into "atomic regions" within a given molecule, and these compartments have many interesting properties [52-59]. However, these atomic compartments and their combinations into larger molecular fragments also have some properties which are fundamentally different from properties of electron densities of complete molecules: at all locations where such a fragment joins the rest of the molecule, the electron density of the individual fragment itself changes *discontinuously* to zero at the boundary surface. No complete molecule has such discontinuous electron density.

In this study the emphasis is placed on fragmentation schemes and functional group representations where the resulting molecular fragments and functional groups have no electron density discontinuities and show closer analogies with complete molecules. This approach is motivated by the fact that molecular fragments and functional groups often appear as individual objects that are actually transferred from one molecule to another; during the transfer their electron density changes but does not exhibit a discontinuous boundary surface. These, temporarily "independent" fragments show many analogies with complete molecules, including a fuzzy, boundaryless electron density cloud. This suggests that a uniform representation, that applies a fuzzy electron density model to complete molecules as well as to molecular fragments, has some advantages.

Some additional, quantum chemical and computational advantages of fuzzy fragments can be exploited in an approach designed to build electron densities of large molecules, partially motivated by an early approach of Christoffersen and Maggiora

for wavefunction generation of large systems [60-62], by some new synthetic principles using molecular building blocks [63,64], and by the quasi-invariance of the medium and high density threshold MIDCOs [65].

An important concern is the efficient detection of local shape changes introduced by chemical changes in remote locations of a molecule. One simple approach [20] applied a truncation method, compatible with the truncation process already used within the shape group methods for molecular shape analysis [41-44].

In the following two sections two approaches will be discussed where molecular fragments are represented by fuzzy electron density models.

2.4 The Pseudo-Density Scheme of Walker

One of the alternative computational methods for diagnosing local shape variations of the electron density was suggested by Walker (P.D. Walker (1992), see also [66]), by introducing a pseudo-density matrix ${}^*P^k$ of a formal molecular fragment for a subset k of the nuclei of a molecule. The pseudo-density matrix ${}^*P^k$ is defined by

$$\begin{aligned} {}^*P^k_{ij} &= P_{ij} \quad \text{if AO } \varphi_i(\mathbf{r}) \text{ or } \varphi_j(\mathbf{r}) \text{ is centered on a nucleus} \\ &\quad \text{that belongs to the subset } k, \\ &= 0 \quad \text{otherwise.} \end{aligned} \quad (17)$$

The resulting pseudo-density ${}^*\rho^k(\mathbf{r})$ for the formal molecular fragment involving the subset k of the nuclei is calculated as

$${}^*\rho^k(\mathbf{r}) = \sum_{i=1}^n \sum_{j=1}^n {}^*P^k_{ij} \varphi_i(\mathbf{r}) \varphi_j(\mathbf{r}). \quad (18)$$

Walker's pseudo-density ${}^*\rho^k(\mathbf{r})$ of the formal molecular fragment incorporates an enhanced contribution from the surroundings of the local molecular neighborhood, and it has been suggested as a sensitive diagnostic tool for the detection of shape differences induced by conformational or other changes at other locations within the molecule [66]. The assignment of all interaction matrix elements to the given molecular moiety involving set k of nuclei exaggerates the shape changes by overestimating the role of density interactions, and in fact at places the pseudo-density ${}^*\rho^k(\mathbf{r})$ is somewhat distorted when compared to the actual local shape of the molecule. Nevertheless, these pseudo-densities ${}^*\rho^k(\mathbf{r})$, used as a diagnostic tool, help the detection of interactions affecting shape variations.

An alternative, also distorted, density-based diagnostic tool, analogous to the Walker scheme, is introduced below. If a matrix $^{**}\mathbf{P}^k$ is constructed from all the actual density matrix elements P_{ij} *not* involving any of the nuclei of set k , and if this matrix is used to replace $^*\mathbf{P}^k$ in equation (18), then the resulting *pseudo-density complement* $^{**}\rho^k(\mathbf{r})$ of Walker's pseudo-density $^*\rho^k(\mathbf{r})$ can also be used for diagnosing interactions affecting local shape changes. Note that distortions of similar magnitude but of opposite sense are shown by $^{**}\rho^k(\mathbf{r})$ and $^*\rho^k(\mathbf{r})$, when compared to the actual local shapes of the molecule.

Whereas $^{**}\rho^k(\mathbf{r})$ and $^*\rho^k(\mathbf{r})$ are additive in the following sense,

$$^{**}\rho^k(\mathbf{r}) + ^*\rho^k(\mathbf{r}) = \rho(\mathbf{r}), \quad (19)$$

these two pseudo-densities $^{**}\rho^k(\mathbf{r})$ and $^*\rho^k(\mathbf{r})$ have fundamentally different definitions, their roles are nonequivalent, and they cannot serve as a basis for a general, additive fragmentation scheme involving more than two parts for a molecule. In particular, if the nuclei of a molecule are classified into m subsets, $m \geq 3$, then for the corresponding local molecular moieties neither the pseudo-densities,

$$^*\rho^1(\mathbf{r}), ^*\rho^2(\mathbf{r}), \dots, ^*\rho^m(\mathbf{r}), \quad (20)$$

nor their complements,

$$^{**}\rho^1(\mathbf{r}), ^{**}\rho^2(\mathbf{r}), \dots, ^{**}\rho^m(\mathbf{r}), \quad (21)$$

generate an additive scheme, that is, their sum differs from the electron density $\rho(\mathbf{r})$ of the molecule:

$$^*\rho^1(\mathbf{r}) + ^*\rho^2(\mathbf{r}) + \dots + ^*\rho^m(\mathbf{r}) \neq \rho(\mathbf{r}) \quad (22)$$

and

$$^{**}\rho^1(\mathbf{r}) + ^{**}\rho^2(\mathbf{r}) + \dots + ^{**}\rho^m(\mathbf{r}) \neq \rho(\mathbf{r}) \quad (22)$$

If the purpose of the analysis is the detection of shape changes, then these pseudo-densities and their complements are good diagnostic tools; however, the pseudo-density scheme is not suitable to build approximate electron densities of large molecules from pseudo-density fragments obtained from smaller molecules.

Walker's pseudo-densities and their complements are designed for enhanced detection of local shape variations and are valuable for local shape analysis. Some more advanced variants of non-additive pseudo-densities are described in ref. [66].

2.5 The Mulliken-Mezey Additive Fuzzy Electron Density Fragmentation Method

A new range of applications becomes possible if a fuzzy density fragmentation method is *additive*. The simplest of these additive fuzzy electron density fragmentation methods was proposed by the author (P.G. Mezey (1992), first applied in ref. [67] and generalized in [5,37]). In a formal sense, the additive density fragmentation method can be regarded as an "atom-group population analysis without integration", and has been motivated by Mulliken's population analysis [68,69]. Consider a molecular electronic density $\rho(\mathbf{r})$ and an arbitrary collection k of the nuclei of the given molecule. According to the simplest version of this method, the k -th fuzzy electron density fragment $\rho^k(\mathbf{r})$ is defined in terms of Mezey's *fragment density matrix*, denoted by \mathbf{P}^k .

The elements P_{ij}^k of \mathbf{P}^k are defined as follows:

$$\begin{aligned} P_{ij}^k &= P_{ij} \text{ if both } \varphi_i(\mathbf{r}) \text{ and } \varphi_j(\mathbf{r}) \text{ are AO's centered on} \\ &\quad \text{nuclei of the fragment,} \\ &= 0.5 P_{ij} \text{ if only one of } \varphi_i(\mathbf{r}) \text{ and } \varphi_j(\mathbf{r}) \text{ is centered} \\ &\quad \text{on a nucleus of the fragment,} \\ &= 0 \text{ otherwise.} \end{aligned} \quad (23)$$

This fragment density matrix \mathbf{P}^k has the same $n \times n$ dimensions as that of the density matrix \mathbf{P} of the complete molecule.

Based on the fragment density matrix \mathbf{P}^k for the k -th fragment, the electron density of Mezey's *fuzzy density fragment* $\rho^k(\mathbf{r})$ is defined as

$$\rho^k(\mathbf{r}) = \sum_{i=1}^n \sum_{j=1}^n P_{ij}^k \varphi_i(\mathbf{r}) \varphi_j(\mathbf{r}). \quad (24)$$

Consider a molecule and assume that its nuclei are distributed into m mutually exclusive families, where m can take any positive integer value. As follows from the defining equation (23) of the fragment density matrix, the sum of Mezey's fragment density matrices \mathbf{P}^k is equal to the density matrix \mathbf{P} of the molecule:

$$P_{ij} = \sum_{k=1}^m P_{ij}^k \quad (25)$$

that is,

$$\mathbf{P} = \sum_{k=1}^m \mathbf{P}^k. \quad (26)$$

Since the density expressions (16) and (24) are linear in the corresponding density matrices, the sum of fragment densities $\rho^k(\mathbf{r})$ is equal to the density $\rho(\mathbf{r})$ of the molecule:

$$\rho(\mathbf{r}) = \sum_{k=1}^m \rho^k(\mathbf{r}). \quad (27)$$

In this fragmentation scheme both the fragment density matrices \mathbf{P}^k and the fragment densities $\rho^k(\mathbf{r})$ are additive, that is, Mezey's scheme is an additive, fuzzy electron density fragmentation scheme. Whereas the method does not in general exaggerate the interactions affecting local shape features, hence for diagnostic purposes it is not as sensitive as Walker's pseudo-density method, however, this additive method avoids the significant distortions of the pseudo-density scheme.

The fuzzy electron density fragment additivity rules (23) - (27) are *exact* at any given *ab initio* LCAO level, hence the reconstruction of the calculated electronic density $\rho(\mathbf{r})$ of the given molecule from the corresponding fuzzy fragment electron densities $\rho^k(\mathbf{r})$ is also *exact*.

Generalizations of this additive fuzzy electron density fragmentation scheme have been proposed in refs. [5,37]. One of these more flexible schemes for assigning interfragment interactions is described below, leading to a generalization [5,37] of the original fuzzy electron density fragment additivity principle:

$$\begin{aligned} P_{ij}^k &= P_{ij} \text{ if both } \phi_i(\mathbf{r}) \text{ and } \phi_j(\mathbf{r}) \text{ are AO's centered on} \\ &\quad \text{nuclei of fragment } k, \\ &= w(k,i,j)P_{ij} \text{ if only one of the AO's } \phi_i(\mathbf{r}) \text{ and } \phi_j(\mathbf{r}) \text{ is} \\ &\quad \text{centered on a nucleus of fragment } k, \text{ where} \\ &\quad \text{for the weighting factors both conditions} \\ &\quad w(k,i,j) > 0, \text{ and } w(k,i,j) + w(k',i,j) = 1 \\ &\quad \text{hold, and where fragment } k' \text{ contains the} \\ &\quad \text{nucleus for the other AO,} \\ &= 0 \text{ otherwise.} \end{aligned} \quad (28)$$

Some additional conditions must be fulfilled if the function $w(k,i,j)$ is to generate a physically valid additive scheme. One choice relies on a sign-preserving scalar property $A(i)$ that can be assigned to atomic orbitals. For example, appropriately scaled electronegativity can be used as such a scalar property. The choice of

$$w(k,i,j) = A(i)/[A(i)+A(j)], \quad (29)$$

where AO $\phi_i(\mathbf{r})$ is centered on a nucleus that belongs to the k -th family, generates

a valid scheme.

Another, more convenient form of Mezey's fragmentation scheme can be given in terms of membership functions of nuclei within various molecular fragments. The set of all nuclei of the molecule is divided into m mutually exclusive families, denoted by

$$f_1, f_2, \dots, f_k, \dots, f_m, \quad (30)$$

associated with m density fragments,

$$F_1, F_2, \dots, F_k, \dots, F_m, \quad (31)$$

respectively, where the earlier notation is used for the fragment density functions

$$\rho^1(\mathbf{r}), \rho^2(\mathbf{r}), \dots, \rho^k(\mathbf{r}), \dots, \rho^m(\mathbf{r}). \quad (32)$$

We denote by $m_k(i)$ the membership function of AO $\varphi_i(\mathbf{r})$ in the set of AOs centered on a nucleus of nuclear set f_k of fragment F_k . Formally, this membership function is defined as follows:

$$m_k(i) = \begin{cases} 1 & \text{if AO } \varphi_i(\mathbf{r}) \text{ is centered on one of the nuclei of set } f_k, \\ 0 & \text{otherwise.} \end{cases} \quad (33)$$

Using these membership functions $m_k(i)$, the elements P_{ij}^k of Mezey's $n \times n$ fragment density matrix \mathbf{P}^k for the k -th fragment F_k can be written as

$$P_{ij}^k = 0.5 [m_k(i) + m_k(j)] P_{ij}. \quad (34)$$

The generalized fragmentation scheme can also be introduced using the membership function formalism of eq. (33), by taking

$$P_{ij}^k = [m_k(i) w_{ij} + m_k(j) w_{ji}] P_{ij}, \quad (35)$$

where the following constraint applies for the weighting factors:

$$w_{ij} + w_{ji} = 1. \quad (36)$$

The original additive fuzzy fragmentation scheme corresponds to the choice of

$$w_{ij} = w_{ji} = 0.5. \quad (37)$$

For the generalized scheme, involving a scalar property $A(i)$, the function w_{ij} can be

chosen as

$$w_{ij} = A(i)/[A(i)+A(j)], \quad (38)$$

an expression analogous to that given in eq. (29). This formulation differs from the previous one by no longer having any need to specify the fragment index k in the weighting factor w_{ij} , since the membership function formalism ensures proper additivity.

The additive fuzzy electron density fragmentation scheme of Mezey is the basis of the Molecular Electron Density Lego Assembler (MEDLA) method [67,70-72], reviewed in section 4. of this report, where additional details and applications in local shape analysis are discussed. The MEDLA method was used for the generation of the first *ab initio* quality electron densities for macromolecules such as proteins [71,72] and other natural products such as taxol [66].

3. THE DENSITY DOMAIN APPROACH TO FUNCTIONAL GROUPS AND LOCAL MOLECULAR PROPERTIES

3.1 The Density Domain Concept

The density domain approach was first proposed [4] as a tool for the description of chemical bonding where the complete shape information of the molecular electron density was taken into account. Density domains are formal bodies of electron density clouds enclosed by MIDCOs defined by eq. (1) [or by eq. (2) if there is no need to specify the nuclear configuration K].

The electronic charge density function $\rho(\mathbf{r},K)$ becomes exactly zero only at infinite distance from the nuclei of the molecule; however, in an approximate sense the electronic density converges to zero very rapidly already at few bohrs from the nuclei. In fact, the electronic density charge cloud is approximately localized near the nuclei. For computational purposes, one may take a small enough threshold a and regard only those regions of the 3D space to belong to the molecule of nuclear configuration K , where the electronic density $\rho(\mathbf{r},K)$ is larger than this threshold.

This approach, however, can be generalized for any threshold value a , and one may consider the fuzzy molecular body as being viewed at various density thresholds, for the whole range of possible densities. An infinite family of formal bodies is obtained, and all these formal bodies, collectively, represent the actual *molecular body*. For each threshold value a , the formal, threshold-dependent molecular body is the *density domain* $DD(a,K)$, defined as the collection of all those points \mathbf{r} of the 3D space where the electronic density is greater than or equal to the threshold a ,

$$DD(a,K) = \{ \mathbf{r} : \rho(\mathbf{r},K) \geq a \} . \quad (39)$$

If the specification of the nuclear configuration K is not required, then one may simply write

$$DD(a) = \{ \mathbf{r} : \rho(\mathbf{r}) \geq a \} . \quad (40)$$

Since the electronic density $\rho(\mathbf{r},K)$ is a continuous function of the 3D space variable \mathbf{r} , the set of all points \mathbf{r} fulfilling the conditions of defining equation (2) of MIDCOs, that is, the set of boundary points of the density domains defined above, does form a continuous surface.

A pictorial analogy between macroscopic clouds of various densities and molecular charge densities can be used here. A density domain $DD(a)$ is analogous to a cloud we could see if our eyes were adjusted to notice only densities equal to or higher than the threshold a . By readjusting our eyes, different "density domains" of clouds of higher or lower density threshold values could be observed.

Most properties of density domains follow from the properties of MIDCOs. We have seen before that for low values of the electron density threshold a , the MIDCO $G(a,K)$ is usually a single, closed surface, consequently, the density domain $DD(a,K)$ is also a single, connected body. For high values of density threshold a , the MIDCO $G(a,K)$ is often a collection of several closed surfaces, where each closed surface surrounds some of the nuclei of the molecule. Consequently, for such a density threshold, the formal density domain $DD(a,K)$ is in fact a collection of several, disconnected bodies $DD_i(a,K)$.

A density domain $DD(a,K)$ represents a formal *molecular body at an electronic density threshold a and nuclear configuration K* . A body $DD(a,K)$ may be a single piece or it may be a collection of several disconnected pieces, the maximum connected components $DD_i(a,K)$ of $DD(a,K)$:

$$DD(a,K) = \bigcup_i DD_i(a,K). \quad (41)$$

In precise mathematical terminology, the term "domain" should be applied only to a single maximum component. However, for simplicity, the term "density domain" is used for both the individual maximum connected components $DD_i(a,K)$ and the union $DD(a,K)$ in eq. (41).

The entire electronic density of a molecule can be represented by an infinite family of density domains, a family that contains one set $\{DD_i(a,K)\}$ of density domains for every threshold value a from the open-closed interval $(0, a_{\max}]$, where, as in eq. (2), a_{\max} can be chosen as the electron density at a nucleus of the largest nuclear charge in the molecule. Due to the nesting properties of MIDCOs for

threshold values a and a' fulfilling condition (4), a density domain $DD(a,K)$ of lower density threshold value a contains density domains $DD(a',K)$ of higher threshold values a' .

Both the shape and the size of a density domain $DD(a,K)$ depend on the choice of the threshold value a . Selecting an arbitrary value for a is highly unlikely to result in a valid description and it is better to consider a whole range of possible threshold values a for the density domains $DD(a,K)$. Some important simplifications are possible. First of all, it is not necessary to consider very high a values which occur only in the vicinity of heavy nuclei. By selecting an appropriate small but nonzero lower limit for the threshold values, formal density domains involving two distant, essentially independent molecules can also be eliminated from the analysis. For the purposes of molecular shape analysis, additional and more fundamental simplifications can be obtained by applying topological methods and the GSTE principle [2] (Geometrical Similarity as Topological Equivalence).

If the electron density is regarded as a function $\rho(r,K)$ of the nuclear arrangement K , then the MIDCOs $G(a,K)$ and the enclosed density domains $DD(a,K)$ are also functions of the nuclear configuration K . How these functions vary with K is one of the main questions of chemistry. It is worthwhile to study this question using the nuclear configuration space approach [2,40].

The set of all possible nuclear configurations K of a given stoichiometric family of N nuclei defines a formal nuclear configuration space. This space can be defined so that a proper distance function $d(K,K')$ can be specified that applies to any two nuclear arrangements K and K' . This turns the configuration space into a $(3N-6)$ -dimensional metric space M [40]. This metric configuration space has many properties analogous to those of the ordinary, three-dimensional space, but it also has fundamentally different properties that are a source of many misconceptions. For example, the nuclear configuration space M is not a vector space, and what is especially misleading, it cannot even be turned into one [40].

If the electronic state is specified, then a formal potential energy value can be assigned to each nuclear arrangement K . The molecular potential energy of the given electronic state is a function of the nuclear arrangements K , and it can be pictured as a hypersurface $E(K)$ over the space M [40]. Each chemical species, such as a stable conformation vibrating about a configuration corresponding to an energy minimum, can be associated with an open set, called a *catchment region* of the given energy hypersurface $E(K)$. The catchment region model formally relaxes the classical constraints of rigid nuclear geometry and avoids the conflict with the Heisenberg uncertainty relation [40]. The concept of dynamic molecular shape can be associated with an entire family of $\rho(r,K)$ charge density distributions occurring within the catchment region representing the given stable, vibrating conformation of the molecule [2].

3.2 Chemical Bond as a Density Domain Relation

One of the most deeply held notions of chemistry is the concept of chemical bond. Such bonds, almost always depicted as formal lines between atomic symbols, have their counterpart within the quantum chemical description of electron densities; often [45-51], but not always [54-60], a correspondence can be made between conventional chemical bonds and specific lines defined by the electron density gradient maps. These lines usually interconnect nuclear positions. However, as has been pointed out by Cioslowski [54-60], there are cases where this correspondence fails.

It is clear that the entire electronic density in a molecule has the role of determining the nuclear distribution hence bonding, consequently, chemical bonding cannot be confined to lines in space. It is well understood that bond diagrams represent only an oversimplified, "short-hand" notation for the actual molecular structure, nevertheless, as most successful notations do, chemical bonds as formal lines have acquired an almost unquestioned reputation of their own as if they were truly responsible for holding molecules together.

Formal chemical bonds as lines in space represent only a drastically oversimplified representation of chemical bonding, a mere skeletal model, introduced and in use since the early days of chemistry when there was no hope yet to detect, model, visualize, and understand the intricate, fuzzy, three-dimensional features and the wealth of shape information of molecular electron densities.

A more realistic model is obtained by regarding each molecule as a collection of atomic nuclei embedded in an electron density cloud interacting with the nuclei, where quantum mechanical uncertainty affects the motion of electrons as well as nuclei. The electronic density closely "follows" the nuclear motions, nearly instantaneously readjusting to new nuclear arrangements. In simplistic terms, electronic density is a deformable "glue" holding the mutually repelling nuclei together, where this glue is thick near the nuclei and becomes thinner and thinner further away from nuclear locations, eventually fading out at large distances. The bonding is provided by the *entire body* of this boundaryless "blob" of glue. A description of chemical bonding compatible with the above picture requires a fully three-dimensional model, where the boundaryless, "fading out" features of electronic density is properly represented.

Today we can easily obtain detailed shape information on electron densities, by experiment or by quantum chemical computations, and the best utilization of these methodologies, possibly in combination, is one fertile area of research [73-84]. Yet, there has been little progress in replacing the simplistic bond-line diagrams with more accurate, more descriptive, and better predictive models of chemical bonding.

There is no longer any inherent difficulty in computing reasonably accurate electron densities for small molecules by either of the two main computational approaches: wavefunction methods [85,86] and density functional methodologies [87-89]. With the introduction of the MEDLA technique [67,70], *ab initio* quality electron densities can be computed for virtually any macromolecule, including

proteins [66,71,72]. The actual molecular body, the electronic density cloud, has become accessible to rigorous study. Whereas conventional chemical bond diagrams are still useful, they are no longer a choice dictated by necessity, and today reasonably accurate electron density descriptors are easily available for anyone with a workstation. It is surprising how little mainstream chemical thinking has taken advantage of the new computational possibilities, and of the new, deeper understanding accurate electron density computations have already provided. Most of the efforts of contemporary electron density analysis have been focused on justifying the old, skeletal model of chemical bonds as formal lines in space, ignoring the rich details the full, three-dimensional fuzzy electron density has to offer. Today, when detailed electron densities are readily available, the conventional "skeletal" image of chemical bonding using line diagrams is more an impediment than help.

One of the exceptions, that offers an alternative to the conventional bond diagrams is the density domain approach [4,5] to chemical bonding. This approach is based on the following observation: for a given molecule with a specified nuclear configuration K , the infinite family $\{DD(a,K)\}$ of density domains for the range $(0, a_{\max}]$ of density thresholds,

$$\{DD(a,K), a \in (0, a_{\max}]\}, \quad (42)$$

contains only a *finite number* of topologically different density domains. The density domains in the above infinite family can be classified into a finite number of topological equivalence classes, representing the essential features of the bonding within the molecule. The topological aspects of the bonding pattern of the three-dimensional electron density can be represented by a finite number of density domains, one taken from each equivalence class. The sequence of critical points of the electronic density can produce the same classification of density domains, however, the location and electron density values of these critical points contain much less shape information than the density domains themselves. It is important to realize that within each equivalence class there are more invariant shape features than the mere pattern of interconnectedness of local regions. These shape features are present in the actual density domains selected to represent each equivalence class [2].

Consider a molecule with a fixed nuclear configuration K and select an initial high density threshold a_{\max} . By gradually decreasing this threshold to a small enough value a such that all the nuclei of the molecule are enclosed within a single density domain $DD(a,K)$, one may study the gradual buildup of the electron density in the molecule, and both the sequence of interconnection patterns and the actual shapes and shape changes associated with this imaginary process. By monitoring the topological and essential geometrical changes (where the latter can also be described by topological, in fact algebraic, means [2]), a detailed description of chemical bonding is obtained.

It is useful to indicate which nuclei are enclosed within each maximum connected component, that is, within each density domain $DD_i(a)$. If the nuclei A, B , etc., are

enclosed within a density domain component $DD_i(a_j)$ at a threshold a_j , then the detailed notation $DD_i(a_j, K; A, B, \dots)$ can be used.

As an illustration, we take the simple example of the equilibrium arrangement of the methane molecule from ref.[3]. Using a semiclassical model and a fixed nuclear configuration K , there are only three topologically distinguishable sets of density domains of the methane molecule. At a high density threshold a_1 , electronic density is found only near the carbon nucleus, hence there is only a single density domain. That is, at the high density threshold a_1 the set of density domains has a single element,

$$\{DD_1(a_1, K; C)\}. \quad (43)$$

At some medium density threshold a_2 , symmetry implies that electronic density clouds appear simultaneously around each of the four hydrogen nuclei; one finds that there are five separate density domains. That is, at an intermediate density threshold a_2 , the set of density domains has five elements,

$$\{DD_1(a_2, K; C), DD_2(a_2, K; H), DD_3(a_2, K; H), DD_4(a_2, K; H), DD_5(a_2, K; H)\}. \quad (44)$$

At some low enough density threshold a_3 , the methane molecule has a single density domain that contains all five nuclei C, H, H, H , and H . At this density threshold a_3 the set of density domains has again only a single element,

$$\{DD_1(a_3, K; C, H, H, H, H)\}. \quad (45)$$

The shapes of these density domains are characteristic to the set of nuclei enclosed by them, to the nuclear geometry, and also to the location of these density domains within the molecule, collectively represented by the configuration variable K , as well as to the actual density threshold a . The sequence of density domains as a function of density threshold a , augmented with the results of a local shape analysis of these density domains [2], provides a detailed description of chemical bonding within the methane molecule.

A gradual decrease of the density threshold a , starting with a high value [2], is usually accompanied with a series of typical topological changes of the density domains. These changes provide a classification of density domains according to the various ranges of the density threshold parameter a .

The various density ranges form a hierarchy [2], indicated by boldface, underlining, and italics, as well as indentation within the list below. If a subrange in the hierarchy happens to coincide with a range, then its name is given in parentheses after the name of the range.

Localized density range, $[a_{\max}, a_g)$: a_{\max} is the maximum electron density in the molecule, whereas a_g is the threshold below which only a single density domain is found.

Atomic range, $[a_{\max}, a_f)$: a_{\max} is defined above, a_f is the lowest density threshold where two density domains join. Only individual nuclear neighborhoods appear as disconnected density domains, that is, there is precisely one nucleus within each density domain which appears.

Strictly atomic range, $[a_{\max}, a_p)$: a_{\max} is defined above, a_p is the lowest density threshold where at least one density domain is no longer convex, as it "reaches out" to join a neighboring density domain. Note that within the strictly atomic range all density domains are convex, and each density domain contains precisely one nucleus.

Prebonding range, $[a_p, a_f)$: both a_p and a_f are defined above.

Within the prebonding range each density domain contains precisely one nucleus, but not all density domains are convex.

Functional group range (*bonding range for density domains*), $[a_f, a_g)$: both a_f and a_g are defined above. Within the functional group range at least one density domain contains more than one nucleus, but not all nuclei of the molecule can be found within a single density domain. Those density domains with more than one nucleus represent "complex" functional groups, as contrasted to "simple" functional groups represented by density domains containing a single nucleus. In this density range one finds the various "complex" functional groups as individual entities. Also in this range, the bonding pattern (the actual interconnection pattern) of the density domains is revealed. Consequently, this range is referred to as the functional group range or the bonding range for density domains.

Global density range (*molecular density range*), $[a_g, a_{\min})$: a_g is defined above, whereas a_{\min} is a low threshold value below which electron density can be neglected. The molecule is represented by a single, connected density domain for each threshold value within the global density range.

Skinny molecular range, $[a_f, a_c)$: a_f is defined above, whereas a_c is the maximum threshold at and below which all locally nonconvex domains on the surface of density domains are simply connected. In simpler terms, in the skinny molecular range all nuclei are found within a single density domain, but there are formal "neck" regions on the surface of density domains. In the terminology of shape group analysis [2], rings of D_1 type can be found on the surface of density domains.

Corpulent molecular range, $[a_c, a_q)$: a_c is defined above, whereas a_q is the maximum threshold at and below which all density domains

are convex. Within the corpulent molecular range no local "neck" regions are found, but the density domains are not convex.

Quasi-spherical molecular range, $[a_q, a_{\min})$: both a_q and a_{\min} are defined above. For any threshold value within the quasi-spherical range the density domain representing the molecule is convex. If a_{\min} is small enough, then in the strict mathematical sense, for very low density thresholds all molecules have convex density domains.

3.3 The "Late - Early Rule"

The gradual decrease of the electron density threshold value reveals many interesting trends. One such trend is called the "Late - Early Rule" [2].

The Late - Early Rule:

If the threshold density a is gradually decreased in a density domain analysis of a given conformation K of a molecule, then the order of joining of various, individual density domains of a given atom type A to neighboring density domains tends to be the reversed order of their appearance.

This trend, also not necessarily followed in all instances, can be justified by simple electronegativity considerations. Consider a molecule that contains several nuclei of the same type A , in different local surroundings. In one surrounding, a higher electronegativity neighbor of A is likely to delay the appearance of the density domain of A to a lower density threshold. The density domain about this nucleus A appears *late*. A highly electronegative atom is also likely to have a more extensive charge density cloud about it, implying that an *early* joining of the density domains of this neighbor and this nucleus A is likely. The individual density domain of this nucleus A exists in a narrower threshold interval than the density domains of other nuclei of the same type A having no highly electronegative nuclei within their surroundings. This implies that the threshold interval for the individual existence of a density domain for our selected nucleus A is expected to be contained within the corresponding intervals of other density domains containing the same nucleus type A .

The trend described by the Late - Early rule can be phrased in terms of the expected inclusion relations of those electron density threshold intervals where the density domains of individual nuclei exist as separate entities. A given set of the nuclei of type A is ordered according to the increasing effective electronegativity of the neighbor nuclei $B^{(k)}$ involved in the *first* merger of each of the density domains of nuclei of type A . This ordering is represented by the index k :

$$A^{(k)}, \quad k=1,2,\dots,q, \quad (46)$$

$$B(k), k=1,2,\dots,q. \quad (47)$$

Nucleus $B(1)$ is the first nucleus to share its density domain with that of $A(1)$, and nucleus $B(q)$ is the first nucleus to share its density domain with that of $A(q)$; the effective electronegativity of nucleus $B(1)$ is the lowest, whereas the effective electronegativity of nucleus $B(q)$ is the highest.

The interval of density thresholds where a separate density domain exists for nucleus $A(k)$ is denoted by (a_k, a'_k) . Using these notations, the trend expressed by the "Late - Early Rule" is equivalent to the following, ideal sequence of inclusion relations:

$$(a_1, a'_1) \supset (a_2, a'_2) \supset (a_3, a'_3) \supset \dots \supset (a_k, a'_k) \dots \supset (a_q, a'_q). \quad (48)$$

Exceptions to the Late-Early Rule are known, however, the rule represents the expected trend.

One example that has been studied in some detail is the ethanol molecule [2]. Let us choose H as nucleus A. The density domain of the OH proton appears relatively late in the process of gradually decreasing the electron density threshold. This observation can be justified by the high electronegativity of oxygen, resulting in a depletion of the electron density at the nearby proton, that has a chance for the formation of a density domain of its own only at a somewhat lower density threshold.

We combine this observation with another: when generating a sequence of density domains by gradually decreasing the electron density threshold a , the most acidic proton of the ethanol molecule loses its separate density domain first. Considering all the minimum values of charge densities separating protons from other nuclei, the minimal electronic charge density is of the highest value between this OH proton and the nearest nucleus, the oxygen nucleus. At first sight, this might appear as a conflict with the known fact that this proton, the most acidic in the molecule, is the most easily donated to proton acceptors. This apparently counterintuitive pattern is a consequence of the high electronegativity and the resulting, more extensive high density domain about the oxygen nucleus. Apparently, the high electron density cloud about the oxygen engulfs this particular proton, resulting in the highest density threshold "bridgehead" between any proton and another nucleus within the ethanol molecule.

3.4 A Density Domain Definition of Functional Groups

The hierarchy of density domains discussed in Section 3.2 has already indicated a natural density domain condition for a functional group. If a family of nuclei has the property within a given molecule that there exists a threshold a such that a

corresponding connected density domain contains all of these nuclei while separating them from the rest of the nuclei of the molecule, then these nuclei form the nuclear family of a functional group. The fact that such a separate density domain exists for these nuclei implies that the part of the electronic density dominated by these nuclei forms an entity that has some identity of its own, and some limited "autonomy" within the molecule. This observation justifies taking this density domain as that of a functional group within the molecule. There is still the problem of assigning an electron density contribution to this functional group at lower densities, for example, for density thresholds within the molecular range. This question will be addressed in sections 4.4, 5.3, and 5.4, where local electron density representations and local shape analysis of molecules are discussed.

One of the main advantages of the density domain approach is the introduction of a natural model for a quantum chemical representation of formal functional groups [1-3]. Consider the simplest case: a single connected density domain $DD(a,K)$ and all the nuclei contained within $DD(a,K)$. The boundary MIDCO $G(a,K)$ of the density domain $DD(a,K)$ separates this subset of the nuclei of the molecule from the rest of the nuclei. This fact indicates that the nuclei embedded within $DD(a,K)$, together with a local electronic density cloud surrounding them, represent a sub-entity of the molecule. This sub-entity has an individual identity, since for a range of density threshold values including the value a , the local electron density cloud is separable from the density cloud of the rest of the molecule.

We may consider some chemical examples. Several alcohols, including ethanol and allyl alcohol, have been studied using the density domain shape analysis approach [2,3], and in all these cases a whole range $[a',a'']$ of density threshold values have been found within which the O and H nuclei of the OH group are completely surrounded by MIDCO's, separating these nuclei from all the other nuclei of the molecule. This criterion, the existence of a MIDCO that separates a group of nuclei from all other nuclei of a molecule, is used for the identification and a detailed characterization of chemical functional groups [1-3].

Most actual density domains $DD_i(a_j)$ and the nuclei enclosed by them can be transferred from one molecule to another without altering the topology of the density domains. Whereas some density domains may change their topology in the course of such a transfer if the new environment is sufficiently different, nevertheless, the density domain approach is a criterion derived from physical conditions, specifying those molecular moieties, at the given density threshold a , which can be regarded to have a well defined chemical identity. This approach represents a generalization of the usual chemical concept of functional groups: according to this generalized concept, a collection of all nuclei within a density domain $DD_i(a_j)$, together with the density domain itself can be regarded as a functional group of the molecule at the density threshold a_j .

The actual bonding pattern can be regarded as justification of this approach. Consider a family of MIDCOs for a range of threshold values a that separates a group of nuclei from the rest of the nuclei of the molecule. This indicates a stronger

chemical linkage among the local charge density clouds surrounding the nuclei within the given density domain, whereas the linkage between this group and the rest of the molecule is weaker. This is a natural property for a chemically recognizable functional group. Note, however, that in actual computational studies, for example, if the conventional *ab initio* Hartree-Fock-Roothaan-Hall method [90-93] is used within the gaussian basis set formalism of the Gaussian program system [85], the calculated density domains are dependent on the level of basis set and the quantum chemical methods used, hence conclusions whether a group of nuclei represents a functional group may be basis set dependent.

The density domain $DD(a,K)$ can then serve as a natural representative of a formal functional group. Note that this concept is rather general; by this condition, most individual atomic neighborhoods, as well as many parts of molecules seldom exhibiting special chemical properties or reactivities qualify as formal "density domain functional groups". Whereas in some instances the quantum chemical concept of "density domain functional group" deviates somewhat from the usual, intuitive, organic chemistry concept of functional group, the density-based definition provides interesting insight into the roles and "autonomy" of various molecular parts [2,3].

Additional advantages have been pointed out in the Introduction. Since density domains play a major role in molecular shape analysis and in the construction of various molecular similarity measures [5], shape analysis and molecular similarity can be formulated in terms of quantum-chemically defined functional groups. This model is also compatible with a rather general, algebraic-geometrical framework discussed in ref.[6].

3.5 Functional Groups as Fuzzy Subsets of Molecular Electron Density

The early recognition that quantum mechanical uncertainty [94] of electronic arrangement and motion within a molecule [95,96] has a special role in chemistry has been fundamental in the development of quantum chemistry. In general, the uncertainty itself can be represented by fuzzy set methods, applied in a wide range of disciplines [97-103], and both general quantum mechanical [104-108] and quantum chemical applications [40,52,109-111] have led to novel descriptions of physical and chemical properties.

With minor modifications, the fuzzy electron density membership function formalism of molecular families can also be applied to a family of functional groups within a molecule. Consider a molecule X and some electron density threshold a within the functional group range of density. Consider the functional groups appearing as separate density domains

$$DD_1(a,K), DD_2(a,K), \dots, DD_m(a,K) \quad (49)$$

at this density threshold a , and for simplicity denote them by the symbols

$$F_1, F_2, \dots, F_m. \quad (50)$$

The electron density contribution $\rho^i(\mathbf{r})$ of each functional group F_i is calculated using the Mezey scheme (eqs. 23, 24) for additive fuzzy density fragmentation of the molecular density $\rho_X(\mathbf{r})$, by simply taking the nuclear set k for each fuzzy fragment density as the nuclear set embedded in the corresponding density domain $DD_i(a, K)$ representing functional group F_i .

The fuzzy fragment electron density contributions

$$\rho_{F_1}(\mathbf{r}), \rho_{F_2}(\mathbf{r}), \dots, \rho_{F_i}(\mathbf{r}), \dots, \rho_{F_m}(\mathbf{r}), \quad (51)$$

respectively, represent the "share" of each functional group F_i within the total electron density $\rho_X(\mathbf{r})$ of molecule X .

The fuzzy electron density membership functions of functional groups described below reflect the relative contributions of the fuzzy, three-dimensional electron density charge clouds to the total electronic density of molecule X .

For the derivation of appropriate fuzzy membership functions for the electronic densities of functional groups, first we take each individual functional group F_i , with its share $\rho_{F_i}(\mathbf{r})$ of the complete electron density of molecule X , and consider this share as a separate, individual object in the absence of all other functional groups of family F_1, F_2, \dots, F_m of molecule X . Note that the special value a of the density threshold is used only to identify some of the possible functional groups of molecule X , the very family F_1, F_2, \dots, F_m , and the actual functional group electron densities $\rho_{F_1}(\mathbf{r}), \rho_{F_2}(\mathbf{r}), \dots, \rho_{F_m}(\mathbf{r})$ are not restricted to any specific threshold value.

Also note that if a different threshold value a' is chosen, a different assignment of nuclei to individual density domains may result, that is, a different set of functional groups may be identified within the same molecule X . Take the example of the ethanol molecule [3]. At some threshold a , the nuclei of the CH_2 group are separated from all other nuclei by a MIDCO, hence at this density threshold a , CH_2 is manifested as a functional group within ethanol. However, at a somewhat lower electron density threshold a' , only two nuclear families are separated by MIDCOs, the nuclei of the CH_3CH_2 and OH moieties. Hence, at this density threshold a' , the ethyl group and the hydroxyl group are manifested as functional groups within ethanol, and the fact the methylene group CH_2 is also a functional group is not revealed at the second density threshold a' .

The maximum value $\rho_{\max,i}$ of the electron density $\rho_{F_i}(\mathbf{r})$ within a spatial domain D_{F_i} containing all the nuclei of functional group F_i is used as a reference:

$$\rho_{\max,i} = \max \{ \rho_{F_i}(\mathbf{r}), \mathbf{r} \in D_{F_i} \}. \quad (52)$$

A point $\mathbf{r}_{\max,i}$ is selected as a point \mathbf{r} where this maximum density value $\rho_{\max,i}$ is realized for the given functional group:

$$\rho_{F_i}(\mathbf{r}_{\max,i}) = \rho_{\max,i} \quad (53)$$

Then, by taking functional group F_i in the absence of other functional groups, and by adapting the approach described in section 2.2 for individual molecules from a molecular family L , the definition of the fuzzy membership function for points \mathbf{r} of the space belonging to functional group F_i is given as

$$\mu_{F_i}(\mathbf{r}) = \rho_{F_i}(\mathbf{r}) / \rho_{\max,i} \quad (54)$$

The fuzzy membership function defined above reflects the actual electronic charge distribution of functional group within the given molecule X , without directly involving any other density contributions from other functional groups of the molecule.

For practical purposes, an alternative model provides more insight. If the density contributions of the rest of the functional groups of molecule X are also considered, then the actual degree of "belonging" of a point \mathbf{r} to a given functional group F_i is also affected by the electron density contributions of all other functional groups from the family F_1, F_2, \dots, F_m . Consequently, the membership function $\mu_{F_i}(\mathbf{r})$ defined by eq. (54) is no longer appropriate. An alternative fuzzy set approach, including the effects of the electron density contributions of all other functional groups of the molecule is based on Mezey's additive fuzzy electron density fragmentation method.

Molecule X is regarded as a collection of appropriately arranged, mutually interpenetrating electron densities of the functional groups $F_1, F_2, \dots, F_j, \dots, F_m$, where each fuzzy electron density fragment F_j contains the corresponding set of nuclei. As a consequence of the exact additivity property of Mezey's fragmentation scheme, at each point \mathbf{r} the total electronic density $\rho_X(\mathbf{r})$ of molecule X is given as the sum of functional group electron densities:

$$\rho_X(\mathbf{r}) = \sum_j \rho_{F_j}(\mathbf{r}) \quad (55)$$

If the simultaneous presence of all functional groups $F_1, F_2, \dots, F_i, \dots, F_m$ within molecule X is taken into account, then a new fuzzy membership function $\mu_{F_i,X}(\mathbf{r})$ for points \mathbf{r} of the space belonging to functional group F_i of molecule X can be defined as

$$\mu_{F_i,X}(\mathbf{r}) = \mu_{F_i}(\mathbf{r}) [\rho_{\max,i} / \rho_X(\mathbf{r}_{\max,i})] \quad (56)$$

The scaling factor $[\rho_{\max,i} / \rho_X(\mathbf{r}_{\max,i})]$ in the above equation is required in

order to reflect the actual density contributions from various functional groups F_i of molecule X .

This fuzzy membership function $\mu_{F_i,X}(\mathbf{r})$ can also be written in a form of a simple density ratio:

$$\begin{aligned}\mu_{F_i,X}(\mathbf{r}) &= \mu_{F_i}(\mathbf{r}) [\rho_{\max,i} / \rho_X(\mathbf{r}_{\max,i})] \\ &= [\rho_{F_i}(\mathbf{r}) / \rho_{\max,i}] [\rho_{\max,i} / \rho_X(\mathbf{r}_{\max,i})] \\ &= \rho_{F_i}(\mathbf{r}) / \rho_X(\mathbf{r}_{\max,i}).\end{aligned}\quad (57)$$

This ratio, expressed for each functional group F_i ,

$$\mu_{F_i,X}(\mathbf{r}) = \rho_{F_i}(\mathbf{r}) / \rho_X(\mathbf{r}_{\max,i}), \quad (58)$$

is convenient for computational purposes. The fuzzy membership functions $\mu_{F_i,X}(\mathbf{r})$ describe the "degree of belonging" of points \mathbf{r} of the three-dimensional space to the various functional groups $F_1, F_2, \dots, F_i, \dots, F_m$ of molecule X .

3.6 A Fuzzy Set Model for Local Molecular Properties

Local molecular properties can be represented by the properties of functional groups F_i of molecule X , that in turn can be characterized by the fuzzy membership function $\mu_{F_i,X}(\mathbf{r})$ for points \mathbf{r} of the space.

Variations in the local properties can be monitored by calculating the variations of the fuzzy membership function $\mu_{F_i,X}(\mathbf{r})$. If two functional groups F_i and F_j of a molecule X have the same chemical formula, then their differences must be due to their different local surroundings within the molecule X . These differences are necessarily manifested in differences of their fuzzy membership functions $\mu_{F_i,X}(\mathbf{r})$ and $\mu_{F_j,X}(\mathbf{r})$ in molecule X .

Considering a collection of functional groups of the same chemical formula but located in a series of *different* molecules, local similarity measures among these functional groups can be based on their fuzzy membership functions (for a discussion of local similarity measures see sections 5 and 6). These similarity measures provide clues for the similarities and differences in their reactivities, caused by the similarities and differences in their molecular environments.

4. AN APPLICATION OF THE *MEDLA* METHOD FOR THE DIRECT COMPUTATION OF ELECTRON DENSITIES OF FUNCTIONAL GROUPS

4.1 Building Molecular Electron Densities Using the Additive Fuzzy Electron Density Fragmentation Method.

Several versions of an additive fuzzy electron density fragmentation scheme have been proposed in [5,37]. The simplest version of Mezey's scheme, as implemented in [67], can be regarded as an "atom-group population analysis without integration". As pointed out in section 2.3, this simplest version can be thought of as an atom-group generalization of Mulliken's population analysis [68,69], where the integration step is omitted and instead of a formal charge value, a fuzzy electron density fragment is obtained.

The exact additivity of the fragment density matrices \mathbf{P}^k and the fuzzy fragment densities $\rho^k(\mathbf{r})$ defined according to Mezey's scheme (eqs. (23)-(27)) motivates the terminology: additive, fuzzy electron density fragmentation method. The fuzzy electron density fragment additivity rule is exact at the given *ab initio* LCAO level.

The linearity of density expressions (16) and (24) in the corresponding density matrices ensures exact additivity for the fuzzy electron density fragments, as described by eq. (27):

$$\rho(\mathbf{r}) = \sum_{k=1}^m \rho^k(\mathbf{r}).$$

The sum of all m fuzzy fragment densities $\rho^k(\mathbf{r})$ is, indeed, equal to the total electron density $\rho(\mathbf{r})$ of the molecule.

4.2. The *MEDLA* Method

The additive fuzzy electron density fragments, discussed in section 2.5, can also be used to build electron densities for molecules different from the molecules from which the fragments originate. If the local nuclear geometry and the actual local surroundings of a fuzzy electron density fragment in a molecule X coincide with those of a fragment within a different molecule Y , then the same fragment density can also be used as a component to build the electron density of molecule Y . That is,

if the local nuclear geometries as well as the local surroundings within reasonably extensive neighborhoods of the two fragments coincide, then the differences between the two fuzzy electron density fragments are expected to be negligible. The same density fragment, as a fuzzy "lego" piece, can then be used for both molecules X and Y . This "lego" principle can then be applied to build electron densities of large molecules from fuzzy fragments obtained from calculations for smaller molecules, where the local nuclear geometry as well as the extended surroundings of the fuzzy fragment in the small "parent" molecule are designed so as to mimic those in the large, "target" molecule.

The application of the additive fuzzy electron density fragments for the building of electron densities of large molecules is called the Molecular Electron Density Lego Assembler method, or MEDLA method [5,37,66,67,70-72].

Some of the fundamental properties of the fragments are important. If our goal is the construction of electron densities of large molecules from pre-calculated fragment densities obtained from smaller molecules, then both additivity and a fuzzy electron density representation appear essential. The first requirement, an additive density fragment scheme, is a natural condition, for both charge preservation and for a simple computational implementation. The second requirement, a fuzzy charge distribution for the fragments, is also natural, since in this representation fragments are analogous to complete molecules. Important computational advantages of the fuzzy representation have also been pointed out [66]. In particular, the severe local errors of combining alternative fragments with boundaries, such as those obtained by fragmentation based on zero flux density gradient surfaces (density doubling and/or density gaps, 100% error), can be avoided.

Both of the natural requirements of additivity and fuzziness are fulfilled by Mezey's fragmentation scheme that has served as the basis of the MEDLA method.

Even if each of the fuzzy electron density fragments $\rho^k(\mathbf{r})$ originate from a different molecule, a good approximation to the total electron density $\rho(\mathbf{r})$ of the target molecule can be obtained using eq. (27):

$$\rho(\mathbf{r}) = \sum_{k=1}^m \rho^k(\mathbf{r}).$$

The actual application of the MEDLA method for the construction of electron densities of large molecules requires an electron density fragment databank. In this MEDLA databank the electron densities are stored numerically. Each fragment type, for example, the electron density fragment of a methyl group, is stored in several versions in the databank. These versions differ in the local geometry of the nuclear family (C, H, H, H) where formal bond angles and bond distances may vary, and they also may differ in the share of the local electron density from the interactive effects of various possible surroundings. For example, the protein electron densities reported in [66,71,72] required 21 fragment types, whereas the taxol molecule [66]

required several additional fragments from the MEDLA density fragment databank. Each fuzzy MEDLA fragment has been previously obtained from a 6-31G** *ab initio* calculation for a smaller molecule, artificially distorted to match the nuclear geometry and local surroundings of the fragment in the target molecule. Each fragment type is stored in several versions in the databank, for a range of several possible local nuclear arrangements; if a new arrangement is needed, a new fragment can be "custom made" by computing the electron density of the fragment from a small molecule with the required local geometry and surroundings. This new fragment density can then be added to the MEDLA databank. When used for building densities of large molecules, in each case the fragment with matching or nearly matching nuclear geometry can be selected from the databank, and high accuracy can be achieved. The electron density fragments for groups CH₃, CH₂, NH₂, and COOH are typical.

Several numerical tests and detailed comparisons of MEDLA electron densities to electron densities computed by traditional *ab initio* SCF technique using 3-21G and 6-31G** basis sets have shown [67,71] that the MEDLA results are invariably of better quality than the standard 3-21G *ab initio* results, and the MEDLA results are virtually indistinguishable from the standard *ab initio* 6-31G** basis set results obtained with the traditional Hartree-Fock method.

In particular, in addition to direct, point-by-point, numerical density comparisons carried out for several molecules [67,71], the following test results have been obtained:

(a) Detailed comparisons of electron densities of β -alanine obtained by standard *ab initio* SCF calculations using both 3-21G, 6-31G** bases, and MEDLA computations have been performed.

(b) One of the early goals of applied MEDLA studies was the construction of *ab initio* quality electron densities for proteins [71,72]. For this task, a prototype peptide system, glycyl-alanine was tested first, using standard *ab initio* SCF calculations at the 3-21G and 6-31G** level of bases, as well as MEDLA computations.

(c) For nonbonded interactions, the first test involved H-bonding in a helical tetrapeptide, using standard *ab initio* SCF 3-21G and 6-31G** basis set calculations, as well as the MEDLA method.

(d) Additional nonbonded interaction, one between a sulfur atom and a phenyl ring in a molecular fragment from the pentapeptide metenkephalin has been tested in detail, using standard *ab initio* SCF 3-21G and 6-31G** basis set calculations, as well as MEDLA.

In all tests, the MEDLA method performed consistently better than standard *ab initio* SCF 3-21G basis computations, consequently, the claim of "*ab initio* quality" appears justified.

By combining the results of two of these tests, one may conclude that the MEDLA method does not appear to show a bias concerning the joining of various density domains. This is an important concern for the analysis of functional groups.

According to the $\alpha=0.007$ a.u. (atomic unit) threshold density MIDCO for the hydrogen bonded helical tetrapeptide of test c, the standard 3-21G result does not show a density domain merger at the location of the hydrogen bond, however, this merger is indicated by both the standard 6-31G** and the MEDLA results. On the other hand, according to the $\alpha=0.003$ a.u. contours for the S - Phe interaction in test d, the standard *ab initio* 3-21G result indicates a bridging of the local density contours where still a gap is indicated by both the standard 6-31G** and the MEDLA computations. Apparently, the MEDLA method outperforms the standard *ab initio* 3-21G computations in an unbiased way: MEDLA indicates a feature where the standard 6-31G** result indicates it, and shows the lack of a feature where it does not appear according to the standard 6-31G** result. Using the standard 6-31G** result as a benchmark, the MEDLA method appears to generate reliable density domain patterns.

4.3 MEDLA Fragment Selection Based on Density Domains

The MEDLA method allows considerable freedom in choosing additive fuzzy electron density fragments; the choice of nuclear family is arbitrary, constrained only by practical, computational limitations. One extreme choice, the case of single nucleus fragments, has been shown to provide good results in the first application of the MEDLA method [67]. Single nucleus MEDLA fragments may have special utility in applying MEDLA as a part of an enhanced X-ray structure refinement process, where Gaussian representations of electron densities can be replaced by more accurate MEDLA estimates, and subsequently refined in an iterative process by gradually matching nuclear locations with the X-ray diffraction data [66]. However, for most applications, probably also for structure refinement purposes, fuzzy density fragments that contain several nuclei are more practical.

One, natural criterion that can be used for MEDLA fragment selection is based on density domains. Since any error of approximation of interfragment electron density interactions is expected to be the smallest if the electron density between the fragments is low, it is natural to choose fragments so that the density is low between nuclei of different fragments. This is achieved by selecting those nuclear families for defining fragments which are separated by MIDCOS from all other nuclei within the parent molecules. This is precisely the condition for density domains within the parent molecules. Consequently, a simple density domain criterion appears as an inherent molecular property for the selection of nuclear families of fuzzy electron density fragments.

4.4 Functional Groups as MEDLA Superfragments

The approach of using density domains of parent molecules as criterion for selecting nuclear families for fuzzy density fragments has additional advantages. If the density threshold for the density domains falls within the functional group range, this guaranties that the density domains are in fact those of formal functional groups. Hence, electron density distributions of functional groups are taken as MEDLA fragments. The building of large molecules from a density fragment database can then approximately follow a simplified version of the intuitive process of synthesis planning by organic chemists, building molecules from functional groups.

In some instances it is justified to use large fragments, involving a large number of nuclei. Some of these fragments can be so large that direct determination of their electron densities from a single "parent" molecule is not feasible. In such cases, the large functional group itself can be built from smaller MEDLA fragments. Whereas such a large functional group is not a complete molecule by itself, the same MEDLA method can be used for its construction that is usually applied for complete molecules. Such large functional groups, themselves built from MEDLA fragments, are referred to as MEDLA superfragments.

The MEDLA method does not impose any size limitation on the fragments; only the feasibility of traditional *ab initio* calculations limits the actual size of the fragments and the size of the "coordination shell" around them in the small molecule imitating the actual surroundings within the target molecule. Electron densities of satisfactory accuracy have been obtained in all the test calculations.

4.5 Linear Homotopies of Fuzzy Electron Density Fragments

If the MEDLA electron density fragment database contains a fragment with the precise nuclear geometry required in the target molecule, then a simple transformation of electron density from the database to the actual position within the target molecule is carried out. In some instances, if there are only very small deviations between the required and already available nuclear arrangements, a linear homotopy (continuous deformation) of the nuclear arrangement and the associated fuzzy electron density fragment can be carried out [66]. For the purpose of direct transfer from the MEDLA database, as well as for small readjustments of the nuclear positions, a useful fragmentation scheme, typically involving four nuclei for the positioning of each fragment, is of special significance [66].

If four nuclei are not coplanar, then they define a tetrahedron. If two tetrahedral nuclear arrangements are congruent, then simple translation and rotation are sufficient to superimpose them exactly. Furthermore, even if the two tetrahedra are not

congruent (that is, if one is distorted with respect to the other), then a simple transformation can be used to convert one into the other. Any non-coplanar, tetrahedral arrangement of four nuclei can be obtained by a 3D linear transformation (a linear homotopy) from a reference tetrahedron. Unfortunately, general polyhedra of five or more nuclei do not have the analogous property, hence, the case of fragment nuclear positioning fully specified by four nuclei is special. Since the electron distribution is dominated by the nuclear arrangement, when a small distortion of the nuclear arrangement changes the electron density distribution, this change can be approximated by applying the same distortion to the density. If a required electron density fragment has a nuclear geometry that does not exactly match that of a corresponding fragment stored in the MEDLA databank, but these geometries are similar, then the same linear homotopy that interconverts the nuclear arrangements can also be applied to the electron density of the fragment of the database, providing a rapid, approximate method for the generation of an approximate electron density for a fragment with the desired nuclear geometry. As long as the geometry changes are small, this linear homotopy method generates good quality approximate electron densities for the required fuzzy density fragments.

Following the notations of ref. [66], the transformation is defined in terms of the coordinates of four reference nuclei A, B, C, and D of the actual fragment in the target molecule and the coordinates of the corresponding four nuclei A', B', C', and D' in the fragment stored in the MEDLA database. Without loss of generality we assume that nuclei A and A' are located at the origin of the coordinate system. We specify three edge-vectors of each of the corresponding two tetrahedra:

$$\mathbf{v}^{(1)} = \mathbf{A} \rightarrow \mathbf{B}, \quad (59)$$

$$\mathbf{v}^{(2)} = \mathbf{A} \rightarrow \mathbf{C}, \quad (60)$$

$$\mathbf{v}^{(3)} = \mathbf{A} \rightarrow \mathbf{D}, \quad (61)$$

$$\mathbf{w}^{(1)} = \mathbf{A}' \rightarrow \mathbf{B}', \quad (62)$$

$$\mathbf{w}^{(2)} = \mathbf{A}' \rightarrow \mathbf{C}', \quad (63)$$

$$\mathbf{w}^{(3)} = \mathbf{A}' \rightarrow \mathbf{D}', \quad (64)$$

respectively. These column vectors form two matrices, \mathbf{V} and \mathbf{W} , with elements

$$V_{ij} = v_j^{(i)} \quad (65)$$

and

$$W_{ij} = w_j^{(i)}, \quad (66)$$

respectively. We define a linear transformation T that converts the points of the ABCD tetrahedron into the corresponding points of the A'B'C'D' tetrahedron by the relation

$$TV = W, \quad (67)$$

that is, by

$$T = W V^{-1}. \quad (68)$$

If the four nuclei are not coplanar then the inverse matrix V^{-1} exists.

Whereas in the database the reference nucleus A' is always assumed to be at the origin, the initial location of nucleus A of the actual fragment in the target molecule is arbitrary. The translation placing nucleus A to the origin is denoted by S. The linear transformation TS, a linear homotopy, incorporates both translation and rotation, exactly superimposing the vertices of the two tetrahedra. Furthermore, the

$$p = TSr \quad (69)$$

assignment of points r of the target molecule and points p of the fragment in the database is general, applicable not only for nuclear locations.

The properly positioned electron density contribution $\rho_{ABCD}(r)$ to each point r of the ABCD fragment in the target molecule from the A'B'C'D' MEDLA fragment of the database is obtained as follows:

$$\rho_{ABCD}(r) = \rho_{A'B'C'D'}(TSr), \quad (70)$$

where $\rho_{A'B'C'D'}(p)$ is the electron density of fragment A'B'C'D' at point p , stored in the MEDLA database.

The TSr transformation may generate an out-of-range point p not stored in the database, in this case the

$$\rho_{ABCD}(r) = 0 \quad (71)$$

convention is used.

Degenerate tetrahedra require special treatment. If the nuclei, A, B, C, and D are coplanar but not colinear, then nucleus D is replaced by a dummy nucleus, noncoplanar with A, B, and C; in this case the chemical fragment involves only three actual nuclei. If A, B, and C are colinear, then C is also replaced by a dummy nucleus, noncolinear with A and B; in this case the fragment involves only two actual nuclei.

The TS linear homotopy generates no distortion of the tetrahedron ABCD if a

fragment with the exact required nuclear geometry is found in the MEDLA database, that is, if the two tetrahedra are congruent. In this case, an undistorted, identical replica of the fragment electron density of the MEDLA database is built into the target molecule. If the fragment nuclear geometries of the target molecule and the MEDLA database exactly coincide, then an identical technique can be applied for fragments involving more than four nuclei. If, however, the nuclear geometries of fragments of more than four nuclei do not coincide, then the TS transformation provides only an approximate density transformation from the MEDLA database to the target molecule; for small deviations from exact coincidence of nuclear geometries the TS linear homotopy method gives satisfactory results.

If high accuracy is required, then the option of generating a new fragment density with the exact required nuclear geometry is always available, and the new density fragment can be added to the database. All distortions due to the TS transformations can be avoided by using the new fragment from the MEDLA database.

4.6 Nonlinear Transformations of Fuzzy Electron Density Fragments

Whereas for the general case of five or more nuclei within the fragment no linear homotopy exists that can interconvert two arbitrary sets of nuclear coordinates, nevertheless, there are infinitely many nonlinear transformations which can accomplish this.

Two simple choices for nonlinear transformations, the DER method, and the WAT method, are described below. In both of these techniques, the main step of the transformation is linear, and nonlinearity is included in a rather transparent way.

In the first of these methods, the Dimension Expansion - Reduction (DER) method, the nuclear position vectors of the 3D Euclidean space are transformed into multidimensional vectors in a nonlinear manner, and the actual geometric transformation is carried out by a simple, *linear* matrix transformation in a multidimensional space, of dimensions $n > 3$, followed by a reduction of dimension to 3D. In the second method, the Weighted Affine Transformations (WAT) method, the transformation is confined to the 3D Euclidean space, and a nonlinearly-weighted average of linear, affine transformations by simplices of nuclear positions is used.

The Dimension Expansion - Reduction (DER) method.

This method performs well if the deviations between the actual and desired nuclear arrangements are small, if the nuclei configurations are general (as in the case of linear homotopy, if there are no four nuclei exactly coplanar and no three nuclei colinear, or if there are, they stay that way), and if the origin of the coordinate system

is not too far from the center of mass of the fragment. For large deformations, the nuclear positions are still reproduced exactly, but the nonlinearity of the transformation may excessively deform the electron density at intermediate points. The main advantage of this method is simplicity.

Consider a fragment with $n+1$ nuclei, denoted by $A_0, A_1, A_2, \dots, A_n$. For each nucleus A_i , denote the cartesian coordinates by x_i, y_i , and z_i . For simplicity, we shall use a local coordinate system attached to the fragment and assume that nucleus A_0 is located at the origin. Generate an n -dimensional vector $\mathbf{a}^{(i)}$ for each nucleus where the components are the lexicographically ordered unique products of the powers of nuclear position vector components x_i, y_i , and z_i . For example, for dimension $n=12$, the column vector $\mathbf{a}^{(i)}$ for nucleus A_i has the following components, defined as products of powers of cartesian components x_i, y_i , and z_i :

$$\mathbf{a}^{(i)} = (x_i, y_i, z_i, x_i x_i, x_i y_i, x_i z_i, y_i y_i, y_i z_i, z_i z_i, x_i x_i x_i, x_i x_i y_i, x_i x_i z_i)' \quad (72)$$

where $()'$ denotes transpose. A more general version of this approach is obtained by using other, more general functions $f_4(x_i, y_i, z_i), f_5(x_i, y_i, z_i), \dots, f_n(x_i, y_i, z_i)$ as components 4,5,...,n, as long as the components of $\mathbf{a}^{(i)}$ are linearly independent.

Based on these vectors, a simple, nonlinear transformation is defined that places all the n nuclei to the required locations and also transforms the electronic density so that it follows the nuclear distortion. The transformation for the electron density is not unique and is coordinate-dependent for most dimensions, however, the coordinate dependence is small if the distortion of the nuclear arrangement is small. The transformation based on this approach is expected to provide the best results if the dimension of vectors $\mathbf{a}^{(i)}$ is 3 (equivalent to the case of linear homotopy for four nuclei, discussed in section 4.5), or 9 (ten nuclei), or 19 (20 nuclei), and in general, for cases where all coordinate products up to a given overall degree are included as components of the vectors $\mathbf{a}^{(i)}$.

A similar n -dimensional column vector $\mathbf{b}^{(i)}$ is defined for each nucleus B_i of the fuzzy fragment stored in the MEDLA database. The components of this vector are the lexicographically ordered unique products of the nuclear position vector components x'_i, y'_i , and z'_i , where for simplicity we assume that nucleus B_0 is located at the origin of the local coordinate system. For example, for dimension $n=9$, the components of the column vector $\mathbf{b}^{(i)}$ of nucleus B_i are listed below:

$$\mathbf{b}^{(i)} = (x'_i, y'_i, z'_i, x'_i x'_i, x'_i y'_i, x'_i z'_i, y'_i y'_i, y'_i z'_i, z'_i z'_i)' \quad (73)$$

Such column vectors for $i=1, \dots, n$ form two matrices, \mathbf{A} and \mathbf{B} , with elements

$$A_{ij} = a_j^{(i)} \quad (74)$$

and

$$B_{ij} = b_j^{(i)}, \quad (75)$$

respectively.

If the relative internal coordinates of two sets of $n+1$ nuclei are compared then the dimensions of matrices **A** and **B** are the same, n . We define a linear transformation **Z** that converts matrix **A** into matrix **B**:

$$\mathbf{Z}\mathbf{A} = \mathbf{B}, \quad (76)$$

that is, by

$$\mathbf{Z} = \mathbf{B} \mathbf{A}^{-1}. \quad (77)$$

The inverse matrix \mathbf{A}^{-1} exists for most choices of nuclear arrangements except for a set of measure zero that requires special treatment.

Considering the first three rows of matrices **A** and **B**, transformation **Z** is a nonlinear transformation between the nuclear coordinates of the actual set of n nuclei in the target molecule and the corresponding set of n nuclei in the fuzzy density fragment stored in the MEDLA databank. This nonlinear transformation converts the actual nuclear coordinates of the fragment within the target molecule to the exact nuclear coordinates of the fragment within the MEDLA database, and the inverse of this transformation also deforms the corresponding MEDLA electron density fragment in a manner compatible with all the nuclear locations.

Whereas in the four-nucleus case the linear homotopy is unique, we should emphasize that a nonlinear transformation accomplishing an exact conversion of coordinates of more than four nuclei is not unique. However, the proposed scheme, as a special choice, has the advantage of extreme simplicity, requiring a formal *linear* matrix transformation to obtain a prescribed *nonlinear* coordinate distortion of a nuclear arrangement and a compatible, continuous deformation of the entire associated electron density cloud. This is performed using a direct matrix algorithm. The above DER algorithm has been implemented as a computer program [112].

The case of 10 nuclei (dimension $n=9$) provides a large enough fragment size suitable for the rapid construction of approximate electron densities of large molecules.

The Weighted Affine Transformations (WAT) method.

The basic idea of the WAT method is simple. Consider a fragment with n nuclei, denoted by $A_1, A_2, \dots, A_i, \dots, A_n$. Note that serial index i starts with 1, and there is no requirement to include the origin as a nuclear position. For each nucleus A_i , $\mathbf{v}^{(i)}$ is the 3D position vector, and the corresponding target nuclear position is denoted by $\mathbf{t}^{(i)}$. Select a nodegenerate simplex, with vertices

$$\mathbf{v}(p), \mathbf{v}(q), \mathbf{v}(r), \text{ and } \mathbf{v}(s), \quad (78)$$

and the corresponding target simplex with corresponding vertices

$$\mathbf{t}(p), \mathbf{t}(q), \mathbf{t}(r), \text{ and } \mathbf{t}(s), \quad (79)$$

from the target positions. Denote these simplices by (p,q,r,s,V) , and (p,q,r,s,T) , respectively. With respect to the simplex (p,q,r,s,V) , any vector \mathbf{v} of the 3D space can be given as an affine combination

$$\mathbf{v} = c(p)\mathbf{v}(p) + c(q)\mathbf{v}(q) + c(r)\mathbf{v}(r) + c(s)\mathbf{v}(s), \quad (80)$$

with affine coordinates

$$c(p), c(q), c(r), \text{ and } c(s), \quad (81)$$

where

$$c(p) + c(q) + c(r) + c(s) = 1. \quad (82)$$

Since our goal is to obtain a transformation that distorts the simplex (p,q,r,s,V) into the target simplex (p,q,r,s,T) , it is natural to choose a transformation defined with respect to the simplex pair (p,q,r,s,V) , (p,q,r,s,T) . This transformation is defined by assigning a vector \mathbf{t} to each vector \mathbf{v} of the 3D space, where \mathbf{t} has the same set of affine coordinates $c(p)$, $c(q)$, $c(r)$, and $c(s)$ with respect to the target simplex (p,q,r,s,T) , that is, where

$$\mathbf{t} = c(p)\mathbf{t}(p) + c(q)\mathbf{t}(q) + c(r)\mathbf{t}(r) + c(s)\mathbf{t}(s). \quad (83)$$

For a single simplex pair (p,q,r,s,V) , and (p,q,r,s,T) , this transformation is a linear homotopy.

For a set of more than 4 nuclei, the simplices (p,q,r,s,V) , and (p,q,r,s,T) can be chosen in several ways; if there is no degeneracy then there are

$$n_s = n*(n-1)*(n-2)*(n-3)/4! \quad (84)$$

different choices for simplex pairs, each pair defining a linear transformation. In the general case, different simplex pairs define different transformations; for the same point \mathbf{v} , the set of $c(p)$, $c(q)$, $c(r)$, and $c(s)$ affine coordinates can be different. A transformation that is defined in terms of simplices not including a given point pair $(\mathbf{v}(p), \mathbf{t}(p))$ may transform point $\mathbf{v}(p)$ into a point different from $\mathbf{t}(p)$. Consequently, a simple average of the results of all of these transformations, another linear transformation, is not suitable in general for transforming the set $\{\mathbf{v}^{(i)}\}$ of nuclear

positions to the set $\{\mathbf{t}^{(i)}\}$ of nuclear positions and to deform the electronic density accordingly.

However, by introducing a \mathbf{v} -dependent, nonlinear, individual weighting for each of these transformations, followed by a weighted averaging where the weights are defined by the distance of point \mathbf{v} from the various vertices of the simplices, one can construct an exact transformation that assigns each point of the set $\{\mathbf{v}^{(i)}\}$ to the corresponding point of set $\{\mathbf{t}^{(i)}\}$, while continuously deforming the electronic density that follows the nuclear deformation.

The affine representation given by eq. (80) for point \mathbf{v} can be rearranged to give

$$\mathbf{v} = c(p)\mathbf{v}(p) + c(q)\mathbf{v}(q) + c(r)\mathbf{v}(r) + (1 - c(p) - c(q) - c(r))\mathbf{v}(s), \quad (85)$$

that is,

$$\mathbf{v} - \mathbf{v}(s) = c(p)(\mathbf{v}(p) - \mathbf{v}(s)) + c(q)(\mathbf{v}(q) - \mathbf{v}(s)) + c(r)(\mathbf{v}(r) - \mathbf{v}(s)). \quad (86)$$

By collecting the column vectors $(\mathbf{v}(p) - \mathbf{v}(s))$, $(\mathbf{v}(q) - \mathbf{v}(s))$, and $(\mathbf{v}(r) - \mathbf{v}(s))$ into a matrix $\mathbf{S}(p,q,r,s,V)$,

$$\mathbf{S}(p,q,r,s,V) = \text{mat} \begin{vmatrix} (\mathbf{v}(p) - \mathbf{v}(s)) & (\mathbf{v}(q) - \mathbf{v}(s)) & (\mathbf{v}(r) - \mathbf{v}(s)) \end{vmatrix}, \quad (87)$$

and by collecting the first three affine coordinates $c(p)$, $c(q)$, $c(r)$ into a column vector $\mathbf{c}(p,q,r,s)$,

$$\mathbf{c}(p,q,r,s) = (c(p), c(q), c(r))', \quad (88)$$

eq. (86) can be rearranged to give

$$\mathbf{c}(p,q,r,s) = (\mathbf{S}(p,q,r,s,V))^{-1}(\mathbf{v} - \mathbf{v}(s)). \quad (89)$$

The inverse matrix $(\mathbf{S}(p,q,r,s,V))^{-1}$ of $\mathbf{S}(p,q,r,s,V)$ exists for every nondegenerate simplex (p,q,r,s,V) .

By definition of point \mathbf{t} , the analogous expressions apply for the transformed case:

$$\mathbf{t} - \mathbf{t}(s) = c(p)(\mathbf{t}(p) - \mathbf{t}(s)) + c(q)(\mathbf{t}(q) - \mathbf{t}(s)) + c(r)(\mathbf{t}(r) - \mathbf{t}(s)), \quad (90)$$

where for the corresponding matrix $\mathbf{S}(p,q,r,s,T)$,

$$\mathbf{S}(p,q,r,s,T) = \text{mat} \begin{vmatrix} (\mathbf{t}(p) - \mathbf{t}(s)) & (\mathbf{t}(q) - \mathbf{t}(s)) & (\mathbf{t}(r) - \mathbf{t}(s)) \end{vmatrix}, \quad (91)$$

eq. (90) can be written in the form

$$\mathbf{t} - \mathbf{t}(s) = \mathbf{S}(p,q,r,s,T) \mathbf{c}(p,q,r,s). \quad (92)$$

Combining eqs. (89) and (92) gives

$$\mathbf{t} - \mathbf{t}(s) = \mathbf{S}(p,q,r,s,T) (\mathbf{S}(p,q,r,s,V))^{-1} (\mathbf{v} - \mathbf{v}(s)). \quad (93)$$

By introducing the notations

$$\mathbf{D}(p,q,r,s) = \mathbf{S}(p,q,r,s,T) (\mathbf{S}(p,q,r,s,V))^{-1}, \quad (94)$$

and

$$\mathbf{u}(p,q,r,s) = \mathbf{t}(s) - \mathbf{D}(p,q,r,s) \mathbf{v}(s), \quad (95)$$

vector \mathbf{t} can be expressed as

$$\mathbf{t} = \mathbf{D}(p,q,r,s) \mathbf{v} + \mathbf{u}(p,q,r,s). \quad (96)$$

There are n_s simplices (p,q,r,s) and there are n_s such transformations. A set of n_s \mathbf{v} -dependent weight functions $w(p,q,r,s)(\mathbf{v})$, one weight function associated with each simplex (p,q,r,s) , is chosen so that the weighted average of the n_s transformations exactly assigns the set $\{\mathbf{v}^{(i)}\}$ of nuclear positions to the set $\{\mathbf{t}^{(i)}\}$ of nuclear positions and continuously deforms the electronic density:

$$\mathbf{t} = \sum_{(p,q,r,s)} w(p,q,r,s)(\mathbf{v}) (\mathbf{D}(p,q,r,s) \mathbf{v} + \mathbf{u}(p,q,r,s)), \quad (97)$$

where the summation is for all simplices (p,q,r,s) , and where

$$\sum_{(p,q,r,s)} w(p,q,r,s)(\mathbf{v}) = 1. \quad (98)$$

In order to construct a set of appropriate, \mathbf{v} -dependent weight functions $w(p,q,r,s)(\mathbf{v})$, first a \mathbf{v} -dependent function $f^{(i)}(\mathbf{v})$ is assigned to each vertex $\mathbf{v}^{(i)}$:

$$f^{(i)}(\mathbf{v}) = \prod_{j (j \neq i)} d(\mathbf{v}, \mathbf{v}^{(j)}), \quad (99)$$

where $d(\mathbf{v}, \mathbf{v}^{(i)})$ is the distance between points \mathbf{v} and $\mathbf{v}^{(i)}$. If point \mathbf{v} coincides with any of the nuclear positions $\mathbf{v}^{(j)}$, then this continuous \mathbf{v} -dependent function $f^{(i)}(\mathbf{v})$ becomes zero, except if $j=i$, that is, if \mathbf{v} coincides with the nuclear position $\mathbf{v}^{(i)}$.

For each simplex (p,q,r,s) , a continuous function $g(p,q,r,s)(\mathbf{v})$ is defined as

$$g(p,q,r,s)(\mathbf{v}) = f(p)(\mathbf{v}) + f(q)(\mathbf{v}) + f(r)(\mathbf{v}) + f(s)(\mathbf{v}). \quad (100)$$

If point \mathbf{v} coincides with any of the nuclear positions $\mathbf{v}^{(j)}$, then $g(\mathbf{p}, \mathbf{q}, \mathbf{r}, \mathbf{s})(\mathbf{v})$ becomes zero, except if j is one of the indices p, q, r , or s , that is, if \mathbf{v} coincides with one of the nuclear positions $\mathbf{v}^{(p)}$, $\mathbf{v}^{(q)}$, $\mathbf{v}^{(r)}$, or $\mathbf{v}^{(s)}$.

The sum of all these $g(\mathbf{p}, \mathbf{q}, \mathbf{r}, \mathbf{s})(\mathbf{v})$ functions is taken as

$$g_{\text{sum}}(\mathbf{v}) = \sum_{(\mathbf{p}, \mathbf{q}, \mathbf{r}, \mathbf{s})} g(\mathbf{p}, \mathbf{q}, \mathbf{r}, \mathbf{s})(\mathbf{v}). \quad (101)$$

The \mathbf{v} -dependent weight functions $w(\mathbf{p}, \mathbf{q}, \mathbf{r}, \mathbf{s})(\mathbf{v})$ are defined as

$$w(\mathbf{p}, \mathbf{q}, \mathbf{r}, \mathbf{s})(\mathbf{v}) = g(\mathbf{p}, \mathbf{q}, \mathbf{r}, \mathbf{s})(\mathbf{v}) / g_{\text{sum}}(\mathbf{v}). \quad (102)$$

Using these \mathbf{v} -dependent weight functions, the weighting scheme described by eq. (97) ensures that each nuclear position $\mathbf{v}^{(j)}$ is transformed to its counterpart nuclear position $\mathbf{t}^{(j)}$, while the entire electron density is deformed continuously. This method of weighted affine transformations has no origin or coordinate dependence.

The above WAT algorithm has been implemented as a computer program [113].

The weighted affine transformations scheme allows one to introduce small geometry changes relative to the MEDLA database fragments if the database contains no fragment with the exact nuclear geometry K , but h fuzzy electron density fragments $\rho_1(\mathbf{r}), \rho_2(\mathbf{r}), \dots, \rho_h(\mathbf{r})$, of nearly matching nuclear geometries, K_1, K_2, \dots, K_h , respectively, are available. If all nuclear geometries K_1, K_2, \dots, K_h , of the h different database versions $\rho_1(\mathbf{r}), \rho_2(\mathbf{r}), \dots, \rho_h(\mathbf{r})$ of fragment electron densities are transformed by the weighted affine transformations method to the same, required nuclear geometry K , than by a weighted averaging of the transformed electron densities $\rho_1'(\mathbf{r}), \rho_2'(\mathbf{r}), \dots, \rho_h'(\mathbf{r})$, a higher accuracy is obtained. One choice for the weighting factors for the individual transformed MEDLA fragment densities is taken as

$$W_i = U(K, K_1, K_2, \dots, K_h) / d(K, K_i), \quad (103)$$

where $d(K, K_i)$ is the configuration space distance [40] between the individual database configuration K_i and the actual target configuration K , whereas

$$U(K, K_1, K_2, \dots, K_h) = 1 / (\sum_i 1 / d(K, K_i)). \quad (104)$$

Using these W_i weighting factors, a MEDLA database electronic density $\rho_i(\mathbf{r})$ with a higher degree of similarity between the given database nuclear configuration K_i and the actual nuclear configuration K has a larger contribution to the resulting weighted MEDLA electron density $\rho_{WM}(\mathbf{r})$,

$$\rho_{WM}(\mathbf{r}) = W_1 \rho_1'(\mathbf{r}) + W_2 \rho_2'(\mathbf{r}) + \dots + W_h \rho_h'(\mathbf{r}). \quad (105)$$

This technique allows an efficient use of an existing MEDLA database, and when combined with shape analysis, it can be used to decide whether it is indeed needed to add a new MEDLA fragment version to the database.

5. LOCAL SHAPE ANALYSIS OF FUNCTIONAL GROUPS

5.1 Local Molecular Fragments in a Global Molecular Environment

The local shapes and shape changes of functional groups are influenced by the global molecular environment. This influence is the primary cause of differences between the reactivities of a given functional group in different molecules. It is of some importance to study these shape differences and to find out the extent of the influence the rest of a molecule can exert on a given functional group. The density domain approach provides a natural criterion for limited shape changes which preserve the identity of a functional group, and it also serves as a tool to explore the range of shape variations possible for a local molecular fragment without becoming a chemically different entity.

5.2 Local Shape Changes Induced by Molecular Environment

The reactivities of functional groups are highly dependent on the molecular surroundings, and the effects of the global molecular environment on the local shape variations can be significant.

The Walker pseudo-density scheme for diagnosing shape changes, discussed in section 2.3, is a sensitive method for detecting the effects of molecular environment. Whereas the magnitudes of formal shape changes obtained by the pseudo-density scheme are exaggerated, the very sensitivity of the method makes it a suitable diagnostic tool. Whereas the numerical changes in the computed pseudo-densities are larger than the actual density changes, the relative magnitudes of formal shape changes of the pseudo-densities are indicative of the relative magnitudes of the actual shape variations in the electron densities of functional groups.

In the following sections the actual electron density variations will be used for local shape analysis.

5.3 Local Shapes of Non-Interacting Functional Groups

The fundamental principle we shall follow in the local shape analysis of functional groups and local molecular moieties is a strict analogy with the shape analysis of complete molecules. Accordingly, instead of molecular isodensity contour (MIDCO) surfaces, the main tool of analysis will be the fragment isodensity contour (FIDCO) surfaces. Some of the ideas and concepts described in this section are illustrated in Figure 1.

We shall use the following notations: A is the actual fragment for shape analysis, B is rest of the molecule, possibly composed from several fragments, B_1, B_2, \dots, B_{m-1} .

Two choices for the representation of a local molecular moiety will be discussed. For the first choice, describing the local shapes of non-interacting functional groups within a molecule, we define a FIDCO for a fragment A in a molecule AB as follows:

$$G_{A \setminus B}(a) = \{ \mathbf{r} : \rho_A(\mathbf{r}) = a, \rho_A(\mathbf{r}) \geq \rho_{B_k}(\mathbf{r}), k=1, \dots, m-1 \}. \quad (106)$$

Two, equivalent definitions are given by

$$G_{A \setminus B}(a) = G_A(a) \cap \{ \mathbf{r} : \rho_A(\mathbf{r}) \geq \rho_{B_k}(\mathbf{r}), k=1, \dots, m-1 \}, \quad (107)$$

and

$$G_{A \setminus B}(a) = G_A(a) \setminus \{ \mathbf{r} : \exists k \in \{1, \dots, m-1\} : \rho_A(\mathbf{r}) < \rho_{B_k}(\mathbf{r}) \}. \quad (108)$$

Pictorially, in order to obtain FIDCO $G_{A \setminus B}(a)$ of fragment A in molecule AB , it is sufficient to locate those points where the electron density contribution of fragment A is dominant in molecule AB .

The actual shape analysis can be carried out on the "isolated" fragment density contour $G(a)$, where one additional domain type is introduced. These domains represent the connection of fragment A to the rest of the molecule within the actual AB system:

$$D_{-1}(G_{A \setminus B}(a)) = \{ \mathbf{r} : \mathbf{r} \in G_A(a), \exists k \in \{1, \dots, m-1\} : \rho_A(\mathbf{r}) < \rho_{B_k}(\mathbf{r}) \}, \quad (109)$$

Although the above notation $D_{-1}(G_{A \setminus B}(a))$ refers to the FIDCO $G_{A \setminus B}(a)$, the actual domain $D_{-1}(G_{A \setminus B}(a))$ exists only on the intact $G_A(a)$ contour, and $D_{-1}(G_{A \setminus B}(a))$ appears as a "cover" over the hole(s) of the FIDCO $G_{A \setminus B}(a)$ in molecule AB . The boundary $\Delta D_{-1}(G_{A \setminus B}(a))$, however, is the actual boundary of the FIDCO surface $G_{A \setminus B}(a)$:

$$\Delta D_{-1}(G_{A \setminus B}(a)) = \{ \mathbf{r} : \mathbf{r} \in G_{A \setminus B}(a), \exists k' \in \{1, \dots, m-1\} : \rho_A(\mathbf{r}) = \rho_{B_{k'}}(\mathbf{r}), \rho_{B_{k'}}(\mathbf{r}) \geq \rho_{B_k}(\mathbf{r}), k=1, \dots, m-1 \}. \quad (110)$$

An alternative, simpler choice for the representation of fragment A in molecule AB is obtained using the composite B of all fragments B_1, B_2, \dots, B_{m-1} :

$$G_{A \setminus \Sigma B}(a) = \{ \mathbf{r} : \rho_A(\mathbf{r}) = a, \rho_A(\mathbf{r}) \geq \rho_B(\mathbf{r}) \}, \quad (111)$$

where $\rho_B(\mathbf{r})$ is defined as

$$\rho_B(\mathbf{r}) = \rho_{B_1}(\mathbf{r}) + \rho_{B_2}(\mathbf{r}) + \dots + \rho_{B_{m-1}}(\mathbf{r}). \quad (112)$$

The local domains of connections between fragment A and the rest B of the molecule AB are defined as

$$D_{-1}(G_{A \setminus \Sigma B}(a)) = \{ \mathbf{r} : \mathbf{r} \in G_A(a), \rho_A(\mathbf{r}) \leq \rho_B(\mathbf{r}) \}, \quad (113)$$

whereas the boundaries of these domains are given as

$$\Delta D_{-1}(G_{A \setminus \Sigma B}(a)) = \{ \mathbf{r} : \mathbf{r} \in G_{A \setminus \Sigma B}(a), \rho_A(\mathbf{r}) = \rho_B(\mathbf{r}) \}. \quad (114)$$

5.4 Local Shapes of Interacting Functional Groups

The local shape analysis can no longer be carried out on an "isolated" FIDCO $G_A(a)$ if the interactions of various molecular fragments in a molecule AB are fully taken into account, beyond simply using these interactions for a truncation of the isolated FIDCO $G_A(a)$. If a detailed description of the interactions is required, then a new contour calculation is needed for the interactive FIDCO $G_{A(B)}(a)$ in molecule AB , where $G_{A(B)}(a)$ is defined as

$$G_{A(B)}(a) = \{ \mathbf{r} : \rho_A(\mathbf{r}) + \rho_B(\mathbf{r}) = a, \rho_A(\mathbf{r}) \geq \rho_B(\mathbf{r}) \}. \quad (115)$$

There is no surface defined where the formal "cover" domains of the hole(s) of FIDCO $G_{A(B)}(a)$ would lie, hence no such domains $D_{-1}(G_{A(B)}(a))$ are defined. However, for uniformity, the notation $\Delta D_{-1}(G_{A(B)}(a))$ will be used for the boundaries of the holes on $G_{A(B)}(a)$. These boundaries are defined as

$$\Delta D_{-1}(G_{A(B)}(a)) = \{ \mathbf{r} : \mathbf{r} \in G_{A(B)}(a), \rho_A(\mathbf{r}) = \rho_B(\mathbf{r}) \}. \quad (116)$$

For this second, more accurate choice, the definition of the interactive FIDCO

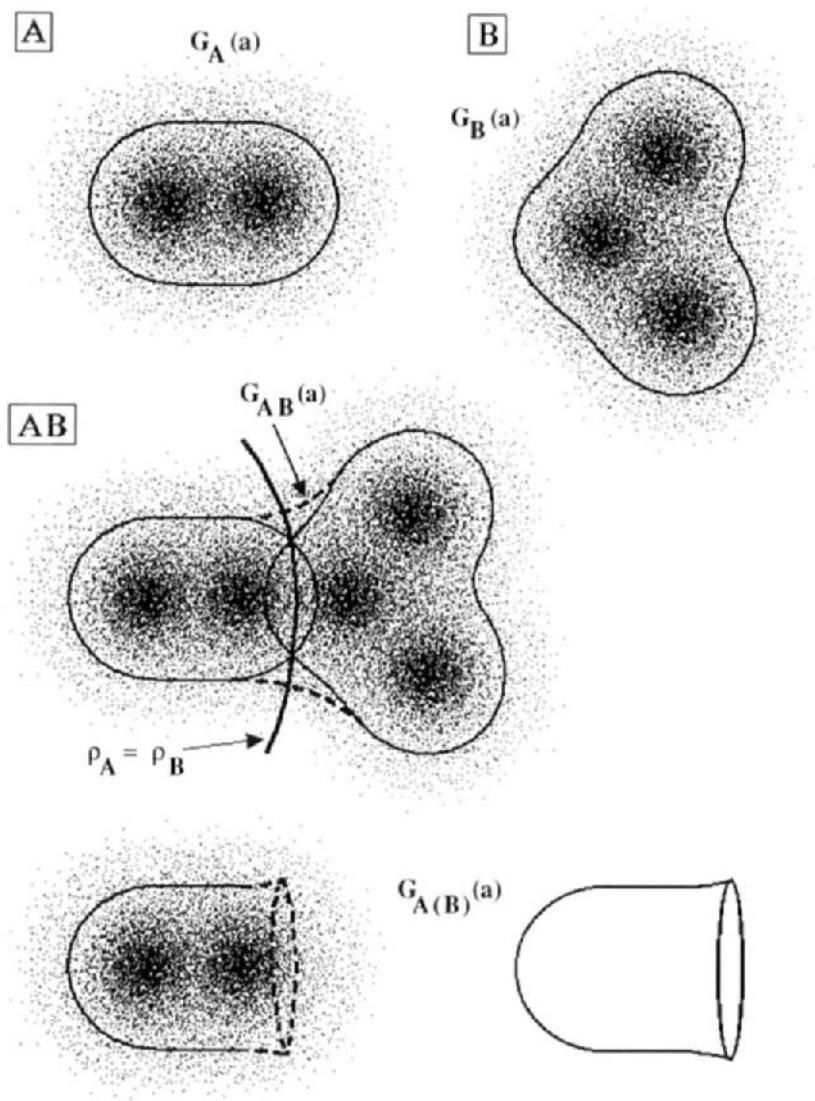


Figure 1. Illustration of the local shape description of non-interacting and interacting functional groups. See text for definitions of symbols.

for a fragment A in a molecule AB describes the local shapes of interacting functional groups within a molecule. This choice for defining interactive FIDCO surfaces $G_{A(B)}(a)$ for local shape analysis requires an additional contour calculation and is computationally more expensive than that of the non-interactive FIDCO model $G_{A \setminus B}(a)$ discussed in section 5.3.

For both types of FIDCO surfaces, the usual Shape Group method [2] of electron density shape analysis is applicable. The additional formal domain boundaries $\Delta D_{-1}(G_{A \setminus B}(a))$ and $\Delta D_{-1}(G_{A(B)}(a))$ introduce one additional index -1 , which can be treated the same way as relative curvature indices. The one-dimensional homology groups obtained by truncations using all possible index combinations are the shape groups of FIDCO surfaces. The (a,b) -parameter maps and shape codes are generated the same way as for complete molecules [2].

6. SHAPE SIMILARITY AND SHAPE COMPLEMENTARITY MEASURES OF FUNCTIONAL GROUPS IN DIFFERENT MOLECULAR ENVIRONMENTS

6.1 Shape Similarity Measures of Functional Groups Based on Local Shapes

The local shape representations by FIDCO sequences is the key to the application of the shape group method for generating shape similarity measures for functional groups and other molecular moieties. The shape of each density domain and each FIDCO $G_{A \setminus B}(a)$ or $G_{A(B)}(a)$ can be described in detail by considering local curvature variations and subdividing the surfaces according to various curvature domains. An algebraic-topological characterization of these shapes can be given, using the Shape Group Method (SGM). The shape group methods [41-44], their physical basis, and their mathematical derivation have been extensively reviewed recently [2] and will not be described in detail here.

With reference to the original derivations [41-44] given for complete molecules, it is sufficient to note that the shape groups of functional groups are the one-dimensional homology groups of FIDCO surfaces truncated according to local curvature criteria and by the boundaries $\Delta D_{-1}(G_{A \setminus B}(a))$ and $\Delta D_{-1}(G_{A(B)}(a))$ of non-interacting and interacting FIDCO surfaces, where these boundaries are defined by the interpenetration condition between the functional group and the rest of the molecule.

Since for the whole range of FIDCO surfaces of a given functional group there are only a finite number of topologically different truncated surfaces, consequently, there are only a finite number of shape groups characterizing the shape of a functional

group within a given molecule. Each shape group can be characterized by its Betti number, and the collection of the finite number of different Betti numbers as well as their distribution within an (a,b) parameter plane generate a numerical shape code for the functional group. In the (a,b) parameter plane, a is the electron density threshold for the FIDCO $G_{A \setminus B}(a)$ or $G_{A(B)}(a)$, whereas parameter b is the reference curvature parameter against which the local curvatures of the FIDCOs are compared.

Since the shape group distribution along an (a,b) parameter map of a molecule can be characterized by the distribution of the Betti numbers of these shape groups, the map can be represented by a sequence of numbers ordered into a matrix or a vector [2]. The surface truncation involved in the generation of the shape groups may lead to several disjoint surface pieces, and in some applications of the shape group method these surface pieces are characterized separately. For each given (a,b) pair of parameter values, a size-ordering of the surface pieces [33] implies an ordering of their one-dimensional Betti numbers (informally called their "first" Betti numbers) into a sequence:

$$B(1), B(2), \dots, B(k), \dots, B(m). \quad (117)$$

An electron density contour surface piece with a larger Betti number usually (but not necessarily) has the larger surface area. If this is the case, then the sequence of Betti numbers in the above ordering is the same as the decreasing sequence of the Betti numbers.

Since the number of surface pieces obtained after truncation according to a set of specified curvature conditions is dependent on the values of parameters a and b , for different (a,b) pairs within an (a,b) parameter map, both the number m of Betti numbers, and their actual values may be different. This non-uniformity of the information representation belonging to different locations within the (a,b) -map can be circumvented by applying a coding-decoding method that relies on the prime factorization of integers. By a reversible transformation it is possible to convert the family of all Betti numbers for each (a,b) location of the parameter map into a single integer number. Such an integer number, a shape ID number, can be assigned to each molecule as well as to each functional group. The shape ID number can be used as a numerical shape code. Since this coding method is uniform for all (a,b) pairs, a uniform representation of shape codes for all molecules and all functional groups is possible [2,33].

Based on this "ID number" approach, the shape similarity of molecules can be evaluated by numerical comparisons of shape codes [2]. The same technique of similarity evaluation, originally developed for complete molecules, can also be applied, in identical form, to the shape codes of functional groups as discussed in earlier parts of this report.

6.2 Local Shape Complementarity Measures for Functional Groups

In most interactions between two reactants, local shape complementarity of functional groups is of importance. A local shape complementarity of molecular electron densities represented by FIDCOs implies complementary curvatures for complementary values of the charge density threshold parameters a . For various curvature domains of a FIDCO, we shall use the notations originally proposed for complete molecules [2]. For example, the symbol $D_{2(b),i}(a, F_1)$ stands for the i -th locally convex domain of a FIDCO $G(a)$ of functional group F_1 , where local convexity, denoted by subscript $2(b)$, is interpreted relative to a reference curvature b . For locally saddle type and locally concave domains relative to curvature b , the analogous subscripts $1(b)$ and $0(b)$ are used, respectively.

In general, a locally convex domain $D_{2(b),i}(a, F_1)$ of a functional group F_1 , relative to a reference curvature b , shows local shape complementarity with a locally concave domain $D_{0(-b),j}(a', F_2)$ of a complementing functional group F_2 , relative to a reference curvature of $-b$. The threshold values a and a' are also likely to complement each other: the shape complementarity between the higher electron density contours of one functional group and the lower electron density contours of the other functional group is relevant.

For a shape complementarity analysis of functional groups we shall follow the shape complementarity approach described for molecules in ref. [2].

The electron densities of interacting functional groups penetrate each other to some extent. In stronger interactions one expects greater interpenetration than in weaker interactions. For a given pair of interacting functional groups, a common electronic density value a_0 can be chosen for the two isolated functional groups that corresponds to the threshold density of two formal "contact" FIDCO's having tangential contact in the interacting systems. For the purposes of shape complementarity analysis, we approximate the electronic density of the interacting functional groups F_1 and F_2 by the superposition of the electronic densities of the two isolated functional groups. In this case, a pair of FIDCO surfaces $G(a, F_1)$ and $G(a, F_2)$ of the same threshold value a must have one of the three possible relative arrangements:

1. $G(a, F_1)$ and $G(a, F_2)$ have no common points, or
2. $G(a, F_1)$ and $G(a, F_2)$ have a finite number of common points (usually, one common point), or
3. $G(a, F_1)$ and $G(a, F_2)$ have a continuum of common points.

We define the contact density a_0 for a given mutual arrangement of two functional groups F_1 and F_2 as the threshold value that corresponds to the unique electron density threshold of the FIDCOs of case 2.

If a contact density threshold a_0 can be chosen for a given interaction between two functional groups, then the local shape complementarity between $G(a_0, F_1)$ and $G(a_0, F_2)$ is clearly of importance. However, complementarity should also manifest itself within a whole range of density thresholds. One may consider the local shape complementarity of FIDCOs $G(a_0 - a', F_1)$ and $G(a_0 + a', F_2)$ in a density interval containing the contact density threshold a_0 ,

$$[a_0 - \Delta a, a_0 + \Delta a]. \quad (118)$$

Note that the complementarity of the local shapes of those FIDCOs are important where the thresholds deviate from the contact density value a_0 in the opposite sense.

Shape complementarity of functional groups involves matches between locally concave and locally convex domains, and also matches between properly aligned saddle-type domains, that is, between curvature domain pairs of the following combinations:

$$D_{0(b),i}(a_0 - a', F_1), D_{2(-b),i}(a_0 + a', F_2); \quad (119)$$

$$D_{1(b),i}(a_0 - a', F_1), D_{1(-b),i}(a_0 + a', F_2); \quad (120)$$

and

$$D_{2(b),i}(a_0 - a', F_1), D_{1(-b),i}(a_0 + a', F_2). \quad (121)$$

In the molecular case, similar relations formed the basis of a simple model [2] using an (a,b) parameter map approach for complementarity evaluation in a manner analogous to similarity evaluation. The same approach is applicable to fuzzy density fragments of functional groups. The local shape complementarity of matching curvature domains, for example, $D_{2(b),i}(a, F_1)$ of functional group F_1 , and $D_{0(-b),j}(a', F_2)$ of functional group F_2 , can be tested by computing complementary shape groups. This is achieved by taking complementary truncations for functional groups F_1 and F_2 , for example, by truncating the curvature domains $D_{2(b),i}(a, F_1)$ for functional group F_1 , and the curvature domains $D_{0(-b),j}(a', F_2)$ for functional group F_2 . Using the homology group notation of ref. [2], such a truncation leads to an (a,b) map for the $HP_\mu(a,b)$ shape groups of functional group F_1 , and to an (a,b) map for the complementary $HP_{2-\mu}(a,b)$ shape groups of functional group F_2 . Typical example is the pair of the (a,b) map of the $H^1_2(a,b)$ shape groups of functional group F_1 , and the (a,b) map of the $H^1_0(a,b)$ shape groups of functional group F_2 .

Complementarity of the curvature types for truncation is not sufficient for a direct comparison of the two (a,b) -maps, since one must also take into account the required complementarity of density thresholds a and reference curvatures b . This

can be accomplished by a simple transformation of one of the two (a,b)-maps. A central inversion of the (a,b)-parameter map of functional group F_2 with respect to the point $(a_0, 0)$ allows one to use a similarity evaluation method for evaluating complementarity. By comparing the centrally inverted (a,b)-map of functional group F_2 to the original (a,b)-map of functional group F_1 , and by determining the ratio of matches between the corresponding families of Betti numbers, a numerical complementarity measure is obtained. The central inversion of one of the (a,b)-parameter maps implies a proper match between curvature domain types, density thresholds, and curvature parameters, in agreement with the pairing scheme (119) - (121) specified for FIDCOs $G(a_0 - a', F_1)$ and $G(a_0 + a', F_2)$. The method ensures that the locally convex domains of FIDCO $G(a_0 - a', F_1)$ relative to the reference curvature b are tested for shape complementarity against the locally concave domains of FIDCO $G(a_0 + a', F_2)$ relative to a reference curvature $-b$, and a similar complementary match is tested when any of the roles within the pairs of FIDCOs, density thresholds, curvature types, or curvature parameters are reversed.

This generalization of the Centrally Inverted Map Method (CIMM) of molecular shape complementarity analysis [2] to FIDCOs of functional groups replaces the problem of complementarity evaluation with a conceptually and computationally simpler similarity evaluation.

7. ENERGY RELATIONS FOR FUNCTIONAL GROUPS AND THEIR INTERACTIONS

7.1 The Fragment Energy Concept and Fragment Interaction Energies

Fundamental relations of density functional theory, the Hohenberg-Kohn theorem [114], the advances made by Kohn and Sham [115], Parr [87,116,117], Levy [118,119], Ludena [88,120], Kryachko [88], March [89], Becke [121-124], Perdew [125], Ziegler [126], Salahub [127,128], Andzelm [129,130], Politzer [131,132], Tachibana [133,134], van Leuven, and Baerends [135], Koch [136], and others have provided both a detailed theoretical foundation and a variety of approximate methods for the computation of relations between electronic density and energy. Whereas most efforts have been focused on complete molecules, the fuzzy fragmentation scheme for the electron density of functional groups imply that the same methodology of density - energy relations is applicable for fuzzy density fragments and for density representations of functional groups.

Density functional theory provides the means for defining fragment energies, based on the following, simple principle: the fuzzy electron density fragment of a functional group, together with the associated set of nuclei, is treated as a complete

molecule. The molecular approximations to the $E(\rho)$ electron density - energy functional are equally applicable to functional groups represented by the fuzzy electron density fragments.

Based on this model, the molecular total energy is decomposed into two parts: fragment energies, obtained by a density functional approximation, and interfragment energies describing the interaction energies among the fragments. One area of current research is the development of approximate methods for the computation of the interfragment contributions to the molecular energy, where the consistency of the model is tested by considering alternative fragmentations within a 3D tiling scheme described earlier [66]. A method that is capable of utilizing the fuzzy fragmentation scheme for energy computation is expected to provide a new approach to the description of intermolecular interactions, nonbonding interactions and hydrogen bonds [137], important in the prediction of reactivities.

7.2 Approximate Conformation Optimization from Fragment Models

Whereas density functional theory guaranties that for the ground electronic state of molecules the electron density determines the energy, the actual construction of such energy functions from first principles is a problem of considerable complexity. The electron densities computed by the MEDLA method suggest various approximations to the molecular energy of large systems.

A simple, approximate conformational energy function can be based on a reward-and-penalty function associated with the mergers of fuzzy electron density fragments forming the molecule. According to one alternative, this reward-and-penalty function can be calibrated using conventional *ab initio* computations. A formal density threshold potential function of shape analogous to a Morse potential can be constructed where the distance variable is replaced by the value of the density threshold a where the merger of fuzzy fragments occurs. A minimization of the sum of the pairwise interfragment potentials can be used for geometry optimization where the conformational motions introduce only minor deformations within the fragments selected as functional groups, and the motion is primarily a rearrangement of the mutual positions of the functional groups.

The formal space filling characteristics of molecules are influenced by a merger of electronic density clouds between parts of the molecule not linked directly by formal bonds. The computational experience with protein MEDLA electron densities indicates that these "nonbonded" mergers of MIDCOs tend to occur simultaneously at about the same density threshold a_m , at many locations within the molecule. This trend, pointed out in [66,71], is likely to help the search for favored conformations of proteins, advantageous mutual side chain arrangements and folding patterns.

Based on this observation, the Self-Avoiding MIDCO approach has been

proposed as a simple, approximate method for macromolecular conformation analysis [66]. If the threshold value a_m corresponds to the onset of "nonbonded" mergers of MIDCOs $G(K, a_m)$, then the MEDLA method can be applied to generate a large number of MIDCOs $G(K, a_m)$ for a family R of nuclear configurations K . The self-avoiding MIDCO method is used to select from this family R of nuclear configurations those which show favorable "nonbonding" interactions. According to early experience, the optimum value of a_m falls within the range [0.003au, 0.005au] of density thresholds, and a small tolerance limit, $\Delta a \sim 0.001\text{au}$, is used for the actual mergers.

For a suitable density tolerance Δa , a simple contact principle [66] can be used for accepting and rejecting nuclear configurations from the family R :

A given configuration K is accepted if all nonbonded mergers which appear for the MEDLA MIDCO $G(K, a_m - \Delta a)$ are not yet merged in the MEDLA MIDCO $G(K, a_m + \Delta a)$.

If the above criterion is tested for the family R of nuclear configurations K , a nuclear arrangement K_{mm} with the maximum number of proper mergers can be identified. This configuration K_{mm} is expected to provide a good approximation to a preferred nuclear arrangement of the molecule.

It has been pointed out [66] that the Self-Avoiding MIDCO approach is not a MIDCO version of a hard surface contact model. Parts of a macromolecular electronic density folding back upon itself readjust, that changes the actual local shape of the MIDCO, a feature not present in simple, hard-sphere contact models, such as VdW surfaces. Since the electron densities of molecular parts placed side by side increase due to the mutual interpenetration ("overlap"), the corresponding MIDCO $G(K, a)$ of the given threshold a shows a significant "swelling" near the site of merger. This feature is in fact a manifestation of nonbonded interactions. The Self-Avoiding MIDCO method incorporates some aspects of these interactions into a simple conformation analysis approach, without actually calculating interaction energies [66].

8. SUMMARY

A quantum chemical approach is proposed for the representation of functional groups in chemistry. The approach is based on a simple density domain condition and on the additive, fuzzy electron density fragmentation method that also serves for the rapid calculation of *ab initio* quality electron densities of large molecules. Several aspects of the approach are described, including methods for similarity and complementarity analysis of functional groups.

9. ACKNOWLEDGEMENTS

The original research work leading to the methods and results described in this report was supported by both strategic and operating research grants from the Natural Sciences and Engineering Research Council of Canada.

10. REFERENCES

1. Mezey, P.G., *J. Chem. Inf. Comp. Sci.*, **32**, 650 (1992).
2. Mezey, P.G., *Shape in Chemistry: An Introduction to Molecular Shape and Topology* (VCH Publishers, New York, 1993).
3. Mezey, P.G., *Canad. J. Chem.*, **72**, 928 (1994). (Special issue dedicated to Prof. J. C. Polanyi).
4. Mezey, P.G., "Molecular Surfaces". In Lipkowitz, K.B., and Boyd, D.B., eds., *Reviews in Computational Chemistry* (VCH Publishers, New York, 1990).
5. Mezey, P.G., "Density Domain Bonding Topology and Molecular Similarity Measures". In Sen, K., ed., *Topics in Current Chemistry*, Vol. **173**, *Molecular Similarity* (Springer-Verlag, Heidelberg, 1995).
6. Dubois, J.-E., and Mezey, P.G., *Int. J. Quantum Chem.*, **43**, 647 (1992).
7. Carbó, R., Leyda, L., and Arnau, M., *Int. J. Quantum Chem.*, **17**, 1185 (1980).
8. Hodgkin, E.E., and Richards, W.G., *J. Chem. Soc. Chem. Commun.* **1986**, 1342.
9. Carbó, R., and Domingo, L.I., *Int. J. Quantum Chem.*, **32**, 517 (1987).
10. Hodgkin, E.E., and Richards, W.G., *Int. J. Quantum Chem.*, **14**, 105 (1987).
11. Carbó, R., and Calabuig, B., *Comput. Phys. Commun.*, **55**, 117 (1989).
12. Burt, C., Richards, W.G., and Huxley, P., *J. Comput. Chem.*, **11**, 1139 (1990).
13. Johnson, M.A. and Maggiora, G.M., eds., *Concepts and Applications of Molecular Similarity* (Wiley, New York, 1990).
14. Carbó, R., and Calabuig, B., *Int. J. Quantum Chem.*, **42**, 1681 (1992).
15. Carbó, R., and Calabuig, B., *Int. J. Quantum Chem.*, **42**, 1695 (1992).
16. Good, A., and Richards, W.G., *J. Chem. Inf. Sci.*, **33**, 112 (1992).
17. Johnson, M.A., *J. Math. Chem.*, **3**, 117 (1989).
18. Leicester, S.E., Finney, J.L., and Bywater, R.P., *J. Mol. Graph.*, **6**, 104 (1988).
19. Mezey, P.G., *J. Math. Chem.*, **2**, 299 (1988).

20. Arteca, G.A., Jammal, V.B., and Mezey, P.G., *J. Comput. Chem.*, **9**, 608 (1988).
21. Arteca, G.A., Jammal, V.B., Mezey, P.G., Yadav, J.S., Hermsmeier, M.A., and Gund, T.M., *J. Molec. Graphics*, **6**, 45 (1988).
22. Arteca, G.A. and Mezey, P.G., *J. Phys. Chem.*, **93**, 4746 (1989).
23. Arteca, G.A. and Mezey, P.G., *IEEE Eng. in Med. & Bio. Soc. 11th Annual Int. Conf.*, **11**, 1907 (1989).
24. Mezey, P.G., "Three-Dimensional Topological Aspects of Molecular Similarity". In Johnson, M.A. and Maggiora, G.M., eds., *Concepts and Applications of Molecular Similarity* (Wiley, New York, 1990).
25. Arteca, G.A. and Mezey, P.G., *Int. J. Quantum Chem. Symp.*, **24**, 1 (1990).
26. Mezey, P.G., *J. Math. Chem.*, **7**, 39 (1991).
27. Mezey, P.G., "New Symmetry Theorems and Similarity Rules for Transition Structures". In Formosinho, S.J., Csizmadia, I.G., and Arnaut, L.G., eds., *Theoretical and Computational Models for Organic Chemistry* (Kluwer Academic Publishers, Dordrecht, 1991).
28. Harary, F. and Mezey, P.G., *Theor. Chim. Acta*, **79**, 379 (1991).
29. Luo, X. and Mezey, P.G., *Int. J. Quantum Chem.*, **41**, 557 (1992).
30. Mezey, P.G., *J. Math. Chem.*, **11**, 27 (1992).
31. Luo, X., Arteca, G.A., and Mezey, P.G., *Int. J. Quantum Chem.*, **42**, 459 (1992).
32. Mezey, P.G., *J. Math. Chem.*, **12**, 365 (1993).
33. Mezey, P.G., *J. Chem. Inf. Comp. Sci.*, **34**, 244 (1994).
34. Mezey, P.G., *Int. J. Quantum Chem.*, **51**, 255 (1994).
35. Carbó, R., Calabuig, B., Vera, L., and Besalu, E., "Molecular Quantum Similarity: Theoretical Framework, Ordering Principles, and Visualization Techniques". In Löwdin, P.-O., Sabin, J.R., and Zerner, M.C., eds., *Advances in Quantum Chemistry*, Vol. 25 (Academic Press, New York, 1994).
36. Mezey, P.G., "Molecular Similarity Measures for Assessing Reactivity". In Carbó, R., ed., *Molecular Similarity and Reactivity: From Quantum Chemical to Phenomenological Approaches* (Kluwer Academic Publ., Dordrecht, The Netherlands, 1995).
37. Mezey, P.G., "Methods of Molecular Shape-Similarity Analysis and Topological Shape Design". In Dean, P.M., ed., *Molecular Similarity in Drug Design* (Chapman & Hall - Blackie Publishers, Glasgow, U.K., 1995).
38. Walker, P.D. and Mezey, P.G., *J. Comput. Chem.*, in press.
39. Walker, P.D., Maggiora, G.M., Johnson, M.A., Petke, J.D., and Mezey, P.G., *J. Chem. Inf. Comp. Sci.*, **35**, 568 (1995).
40. Mezey, P.G., *Potential Energy Hypersurfaces* (Elsevier, Amsterdam, 1987).
41. Mezey, P.G., *Int. J. Quant. Chem. Quant. Biol. Symp.*, **12**, 113 (1986).
42. Mezey, P.G., *J. Comput. Chem.*, **8**, 462 (1987).
43. Mezey, P.G., *Int. J. Quantum Chem., Quant. Biol. Symp.*, **14**, 127 (1987).
44. Mezey, P.G., *J. Math. Chem.*, **2**, 325 (1988).

45. Collard, K., and Hall, G.G., *Int. J. Quantum Chem.*, **12**, 623 (1977).
46. Y. Tal, Y., Bader, R.F.W., Nguyen-Dang, T.T., Ojha, M., and Anderson, S.G., *J. Chem. Phys.*, **74**, 5162 (1981).
47. Bader, R.F.W., Nguyen-Dang, T.T., *Adv. Quantum Chem.*, **14**, 63 (1981).
48. Bader, R.F.W., Slee, T.S., Cremer, D., and Kraka, E., *J. Amer. Chem. Soc.*, **105**, 5061 (1983).
49. Bader, R.F.W., *Acc. Chem. Res.*, **9**, 18 (1985).
50. Bader, R.F.W., *Atoms in Molecules: A Quantum Theory* (Clarendon Press, Oxford, 1990).
51. Chang, C., and Bader, R.F.W., *J. Phys. Chem.*, **96**, 1654 (1992).
52. Mezey, P.G., *J. Chem. Phys.*, **78**, 6182 (1983).
53. Cremer, D., and Kraka, E., *Croat. Chem. Acta*, **57**, 1265 (1984).
54. Cioslowski, J., *J. Phys. Chem.*, **94**, 5496 (1990).
55. Cioslowski, J., Mixon, S.T., and Edwards, W.D., *J. Amer. Chem. Soc.*, **113**, 1083 (1991).
56. Cioslowski, J., and Fleischmann, E.D., *J. Chem. Phys.*, **94**, 3730 (1991).
57. Cioslowski, J., O'Connor, P.B., and Fleischmann, E.D., *J. Amer. Chem. Soc.*, **113**, 1086 (1991).
58. Cioslowski, J., Mixon, S.T., and Fleischmann, E.D., *J. Amer. Chem. Soc.*, **113**, 4751 (1991).
59. Cioslowski, J., Mixon, S.T., *Can. J. Chem.*, **70**, 443 (1992).
60. Christoffersen, R.E. and Maggiora, G.M., *Chem. Phys. Lett.*, **3**, 419 (1969).
61. Christoffersen, R.E., Shipman, L.L., and Maggiora, G.M., *Internat. J. Quantum Chem.*, **5**, 143 (1971).
62. Christoffersen, R.E., Spangler, D., Hall, G.G., and Maggiora, G.M., *J. Am. Chem. Soc.*, **95**, 8526 (1973).
63. Michl, J., Kaszynski, K., Friedli, A.C., McMurdie, N.D., and Kim, T., *NATO ASI Ser., Ser. C.*, **273**, 469 (1989).
64. Mathias, J.P. and Stoddart, J.F., *Chem. Soc. Rev.*, 215 (1992).
65. Arteca, G.A., Grant, N.A., Mezey, P.G., *J. Comput. Chem.*, **12**, 1198 (1991).
66. Walker, P.D., and Mezey, P.G., *J. Math. Chem.*, **17**, 203 (1995).
67. Walker, P.D., and Mezey, P.G., *J. Am. Chem. Soc.*, **115**, 12423 (1993).
68. Mulliken, R.S., *J. Chem. Phys.*, **23**, 1833,1841,2338,2343 (1955).
69. Mulliken, R.S., *J. Chem. Phys.*, **36**, 3428 (1962).
70. Walker, P.D., and Mezey, P.G., *Program MEDLA 93* (Mathematical Chemistry Research Unit, University of Saskatchewan, Saskatoon, Canada, 1993).
71. Walker, P.D., and Mezey, P.G., *J. Am. Chem. Soc.*, **116**, 12022 (1994).
72. Walker, P.D., and Mezey, P.G., *Canad. J. Chem.*, **72**, 2531 (1994).
73. Karle, J., *Proc. Natl. Acad. Sci. USA*, **88**, 10099 (1991).
74. Massa, L., Huang, L., and Karle, J., to be published.
75. Coppens, P., and Hall, M.B., eds., *Electron Distribution and the Chemical Bond* (Plenum, New York and London, 1982).

76. Fliszár, S., *Charge Distributions and Chemical Effects* (Springer, New York, 1983).
77. Purvis III, G.D., and Culberson, C., *Int. J. Quantum Chem., Quantum Biol. Symp.*, **13**, 261 (1986).
78. Kollman, P.A., *J. Amer. Chem. Soc.*, **100**, 2974 (1978).
79. Gillespie, R.J., *Molecular Geometry* (Van Nostrand Reinhold, London, 1972).
80. Gillespie, R.J., and Hargittai, I., *The VSEPR Model of Molecular Geometry* (Allyn and Bacon, Boston, 1991).
81. Wang, J., and Smith Jr., V.H., *Internat. J. Quantum Chem.*, **52**, 1145 (1994).
82. Pichon-Pesme, V., Lecomte, C., Wiest, R., and Benard, M., *J. Am. Chem. Soc.*, **114**, 2713 (1992).
83. Wiest, R., Pichon-Pesme, V., Benard, M., and Lecomte, C., *J. Phys. Chem.*, **98**, 1351 (1994).
84. Pichon-Pesme, V., Lecomte, C., and Lachekar, H., *J. Phys. Chem.*, to be published.
85. Frisch, M.J., Head-Gordon, M., Trucks, G.W., Foresman, J.B., Schlegel, H.B., Raghavachari, K., Robb, M.A., Binkley, J.S., González, C., DeFries, D.J., Fox, D.J., Whiteside, R.A., Seeger, R., Melius, C.F., Baker, J., Martin, R., Kahn, L.R., Stewart, J.J.P., Topiol, S., and Pople, J.A., *GAUSSIAN 90* (Gaussian Inc., Pittsburgh, PA, 1990).
86. Szabo, A., Ostlund, N.S., *Modern Quantum Chemistry: Introduction to Advanced Electronic Structure Theory* (Macmillan, New York, 1982).
87. Parr, R.G., and Yang, W., *Density Functional Theory of Atoms and Molecules* (Clarendon Press, Oxford, 1989).
88. Kryachko, E.S., and Ludena, E.V., *Density Functional Theory of Many-Electron Systems* (Kluwer, Dordrecht, 1989).
89. March, N.H., *Electron Density Theory of Atoms and Molecules* (Academic, New York, 1989).
90. Hartree, D.R., *Proc. Cambridge Phil. Soc.*, **24**, 111, 426 (1928), **25**, 225, 310 (1929).
91. Fock, V., *Z. Physik*, **61**, 126 (1930).
92. Hall, G.G., *Proc. Roy. Soc. London Ser. A*, **205**, 541 (1951).
93. Roothaan, C.C., *Rev. Mod. Phys.*, **23**, 69 (1951), **32**, 179 (1960).
94. Heisenberg, W., *Z. Physik*, **43**, 172 (1927).
95. Löwdin, P.-O., *Adv. Chem. Phys.*, **18**, 365 (1950).
96. Fukui, K., in Löwdin, P.-O., and Pullman, B., eds., *Molecular Orbitals in Chemistry, Physics, and Biology* (Academic Press, New York, 1964).
97. Zadeh, L.A., *Inform. Control*, **8**, 338 (1965).
98. Zadeh, L.A., *J. Math. Anal. Appl.*, **23**, 421 (1968).
99. Kaufmann, A., *Introduction à la Théorie des Sous-Ensembles Flous* (Masson, Paris, 1973).
100. Zadeh, L.A., "Theory of Fuzzy Sets". In *Encyclopedia of Computer Science and Technology* (Marcel Dekker, New York, 1977).

101. Gupta, M.M., Ragade, R.K., and Yager, R.R., eds., *Advances in Fuzzy Set Theory and Applications* (North-Holland, Leyden, 1979).
102. Dubois, D., and Prade, H., *Fuzzy Sets and Systems: Theory and Applications*. (Academic Press, New York, 1980).
103. Sanchez E., and Gupta, M.M., eds., *Fuzzy Information, Knowledge Representation and Decision Analysis* (Pergamon Press, London, 1983).
104. Prugovecki, E., *Found. Phys.*, **4**, 9 (1974).
105. Prugovecki, E., *Found. Phys.*, **5**, 557 (1975).
106. Prugovecki, E., *J. Phys. A*, **9**, 1851 (1976).
107. Ali, S.T., and Doebner, H.D., *J. Math. Phys.*, **17**, 1105 (1976).
108. Ali, S.T., and Prugovecki, E., *J. Math. Phys.*, **18**, 219 (1977).
109. Mezey, P.G., and Maruani, J., *Mol. Phys.*, **69**, 97 (1990).
110. Maruani, J., and Mezey, P.G., *J. Chim. Phys.*, **87**, 1025 (1990).
111. Mezey, P.G., and Maruani, J., *Int. J. Quantum Chem.*, **45**, 177 (1993).
112. Mezey, P.G., *Program DER95* (Mathematical Chemistry Research Unit, University of Saskatchewan, Saskatoon, Canada, 1995).
113. Mezey, P.G., *Program WAT95* (Mathematical Chemistry Research Unit, University of Saskatchewan, Saskatoon, Canada, 1995).
114. Hohenberg, P., and Kohn, W., *Phys. Rev.*, **136**, B864 (1964).
115. Kohn, W., and Sham, L.J., *Phys. Rev.*, **140**, A1133 (1965).
116. Parr, R.G., *Proc. Natl. Acad. Sci. USA*, **72**, 763 (1975).
117. Parr, R.G., *J. Phys. Chem.*, **92**, 3060 (1988).
118. Levy, M., *Proc. Natl. Acad. Sci. USA*, **76**, 6062 (1979).
119. Levy, M., *Phys. Rev. A*, **26**, 1200 (1982).
120. Ludena, E.V., *J. Chem. Phys.*, **79**, 6174 (1983).
121. Becke, A., *Phys. Rev. A*, **33**, 2786 (1986).
122. Becke, A., *J. Chem. Phys.*, **84**, 4524 (1986).
123. Becke, A., *J. Chem. Phys.*, **88**, 1053 (1988).
124. Becke, A., *Phys. Rev. A*, **38**, 3098 (1988).
125. Perdew, J.P., *Phys. Rev. B*, **33**, 8822 (1986).
126. Ziegler, T., *Chem. Rev.*, **91**, 651 (1991).
127. Salahub, D.R., *Adv. Chem. Phys.*, **69**, 447 (1987).
128. Pápai, I., Goursoot, A., St-Amant, A., and Salahub, D.R., *Theor. Chim. Acta*, **84**, 217 (1992).
129. Labanowski, J.K., and Andzelm, J., eds., *Density Functional Methods in Chemistry* (Springer-Verlag, New York, 1991).
130. Andzelm, J., and Wimmer, E., *J. Chem. Phys.*, **96**, 1280 (1992).
131. Politzer, P., *J. Chem. Phys.*, **86**, 1072 (1987).
132. Seminario, J.M., and Politzer, P., *Int. J. Quantum Chem. Symp.*, **26**, 497 (1992).
133. Tachibana, A., *Int. J. Quantum Chem.*, **34**, 309 (1988).
134. Tachibana, A., "Density Functional Theory for Hidden High- T_c Superconductivity." In Hatfield, W.E., and Miller, J.H. Jr., eds., *High Temperature Superconducting Materials* (Dekker, New York, 1988).

135. van Leuven, R., and Baerends, E.J., *Int. J. Quantum Chem.*, **52**, 711 (1994).
136. Hertwig, R.H., and Koch, W., *J. Comput. Chem.*, **16**, 576 (1995).
137. Morokuma, K., *Accts. Chem. Res.*, **10**, 294 (1977).

**Characterization of Shape and Auger Resonances using
The Dilated One Electron Propagator Method.**

*Manoj K. Mishra and Milan N. Medikeri[†]
Department of Chemistry
Indian Institute of Technology
Powai, Bombay 400 076, India.*

[†] CSIR Senior Research Fellow.

Contents

1 Introduction

2 The General Theoretical Framework

- 2.1 The ABC Theorem
- 2.2 The Bi-variational SCF
- 2.3 The Dilated Electron Propagator
 - 2.3.1 The Bi-orthogonal Dilated Electron Propagator
 - 2.3.2 Dilated Electron Propagator based on a real SCF
 - 2.3.3 Electron Propagator with Siegert Boundary Condition
 - 2.3.4 The Trajectory Method for Resonant Pole Search
- 2.4 Molecular resonances

3 Shape Resonances in e-Atom and e-Molecule Scattering

- 3.1 Shape Resonances in e-Atom Scattering
 - 3.1.1 e-Be 2P Shape Resonance
 - 3.1.2 e-Mg 2P Shape Resonance
 - 3.1.3 e-Ca 2P Shape Resonance
 - 3.1.4 Role of Correlation and Relaxation in atomic shape resonances
- 3.2 Shape Resonances in e-Molecule Scattering
 - 3.2.1 Resonances in electron scattering by diatomic molecules
 - 3.2.2 Resonances in electron scattering by polyatomic molecules

4 The Auger Resonances

- 4.1 Energy and width of the Be⁺ ($1s^{-1}$) 2S resonance
- 4.2 Auger resonances and the need for consistent decouplings
- 4.3 Numerical considerations for the treatment of Auger Satellites

5 The Orbital Picture of Resonances from different Decouplings of the Dilated Electron Propagator

- 5.1 Feynman Dyson Amplitude as the correlated orbital
- 5.2 LUMO as the resonant orbital for molecular resonances

6 Conclusions and Future Directions

Acknowledgments

References

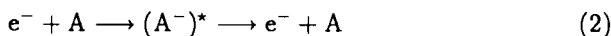
1 Introduction

Ionization energy and electron affinity are critical discriminants of systemic reactivity and the one electron propagator theory /1,2/ has provided an effective route to their accurate calculation. The spectral representation of the matrix electron propagator

$$G_{sr}(E) = \lim_{\epsilon \rightarrow 0^+} \sum_n \left[\frac{\langle {}^N_0 | a_s | {}^{N+1}_n \rangle \langle {}^{N+1}_n | a_r^\dagger | {}^N_0 \rangle}{E - (E^{N+1}_n - E^N_0) + i\epsilon} + \frac{\langle {}^N_0 | a_r^\dagger | {}^{N-1}_n \rangle \langle {}^{N-1}_n | a_s | {}^N_0 \rangle}{E - (E^N_0 - E^{N-1}_n) - i\epsilon} \right] \quad (1)$$

allows for the simultaneous and direct calculation of the ionization energy ($E^N_0 - E^{N-1}_n$) and electron affinities ($E^{N+1}_n - E^N_0$) from its appropriate poles. Varied formal and numerical developments have enriched the electron propagator method and its effectiveness as a powerful and economic tool for the correlated treatment of electronic structure and dynamics is well established. The methodology and applications of the real one electron propagator theory have been reviewed by many authors /3-10/ and newer developments /11-15/ continue to extend the scope of utility of this extensively applied technique.

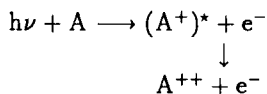
The energy and the width of resonances in scattering of an electron by an N electron target A may be associated with electron attachment involving a metastable state /16-19/. Schematically, the energetics of the electron scattering resonances may be envisaged as



whereby, the resonance energy (E_{res}), i.e., the kinetic energy of the incident electron for which resonance is observed is given by

$$E_{\text{res}} = E_{(A^-)^*} - E_A = E^{n}_{N+1} - E^0_N \quad (3)$$

where n denotes the resonance state of the target anion and E^0_N is the total ground state energy of the N electron target /20-22/. Similarly, Auger resonances may be depicted as



with

$$E_{\text{res}} = E_A - E_{(A^+)^*} = E^0_N - E^n_{N-1} \quad (4)$$

and here, the Auger resonance may be viewed as electron detachment from the n-th metastable state of the target cation /23-26/.

This association of resonance energies with electron affinity/ionization energy involving *metastable* $N \pm 1$ states immediately suggests the use of electron propagator formalism for their direct calculation in conjunction with a scheme which allows for the easy differentiation of these quasi-bound states from other states in the continuum part of the spectrum of the A^\pm Hamiltonian. Such an identification of metastable states using routine bound state methods is facilitated by the theorems of Aguilar, Balslev and Combes /27-30/. These theorems (to be referred as the ABC Theorems) characterize the pole structure of the dilated resolvent $(Z - H_\eta)^{-1}$. The dilatation transformation (or complex scaling) involves the replacement of all the electronic coordinates \vec{r}_i in the Hamiltonian by $\eta \vec{r}_i$, where $\eta = \alpha e^{i\theta}$ ($0 < \theta < \frac{\pi}{2}$) and the ABC theorems prescribe that resonances may be associated with discrete complex poles of the resolvent which once uncovered are invariant to further changes in θ .

The method of complex scaling /31-35/ has been found to be quite effective in the description of resonances and continues to generate novel applications /36-38/. We have attempted to combine the methods of complex scaling and the one particle electron propagator in a manner whereby the developments of the complex scaled electron propagator emerge as a natural and rigorous extension of the more established real unscaled electron propagator theory /22/. These complex scaled extensions of the electron propagator have been applied to many atomic and molecular resonances /21,24-26,39-50/ and our purpose in this review is to present some of the more important results obtained from these applications and sketch the emerging extensions for broadening the scope of utility of the dilated electron propagator method.

The formal and computational considerations are summarized in section 2 and in section 3 we discuss some results for atomic and molecular shape resonances and evaluate the effectiveness of different decouplings. Various decouplings of the dilated electron propagator have also been applied to the $\text{Be}^+ (1s^{-1}) \ ^2S$ Auger resonance and these results are discussed in section 4. While the poles of the dilated electron propagator furnish the resonance energies and the widths, the corresponding Feynman-Dyson Amplitudes (FDAs) $\langle N_0 | a_n | N_n^{N+1} \rangle$ and $\langle N_n^{N+1} | a_r^\dagger | N_0 \rangle$ provide a correlated orbital picture /51/ of the atomic/molecular electron attachment/detachment respectively. The energetics of molecular shape resonances has been analyzed on the basis of the attributes of the target LUMO /18,19/ and in section 5 we examine the results from the use of the FDAs in the investigation of the orbital picture of resonances. Finally, some concluding remarks summarizing the salient results and avenues for further research in this area are collected in section 6.

2 The General Theoretical Framework

Ordinarily, in quantum chemistry we concern ourselves with the solution of the Schrödinger equation

$$H\psi = E\psi \quad (5)$$

where the Hamiltonian operator H is hermitian ($H^\dagger = H$) and consequently E is real. The discrete E values correspond to wavefunctions ψ which are square integrable. The wave functions corresponding to the continua of E values are not square integrable and describe the free particle, continuum or scattering states.

For the metastable states in which the decaying electron spends some time in the vicinity of the target, Gamow /52/ and Dirac /53/ suggested that the width of these resonances Γ is related to the lifetime by the uncertainty relation $\Gamma = \hbar/\tau$ where τ is the lifetime of the metastable state and that the time development of these decaying states be described by

$$\psi(\vec{r}, t) = \psi(\vec{r})\exp(-iEt), \quad E = E_r - i\Gamma/2 \quad (6)$$

where the provision of complex E leads to finite lifetime. Using (6) in the time dependent Schrödinger equation

$$i\hbar \partial\psi/\partial t = H\psi \quad (7)$$

leads to an ordinary time independent Schrödinger equation for the spatial part

$$H\psi = E\psi \quad (8)$$

except now E is complex and consequently H must be non-hermitian. Siegert /54/ showed that solution of eqn. (5) with complex E did indeed lead to resonances, i.e., the amplitude $B(E)$ in the scattering boundary condition

$$\psi_{\text{scatt}}(\vec{r}) \xrightarrow{r \rightarrow \infty} A(E)e^{ikr} + B(E)e^{-ikr} \quad (9)$$

did vanish for certain complex values of E . This is in tune with the heuristic picture of resonances resulting from fragmentation of a point leading to only outgoing waves in all channels, i.e.,

$$\psi_{\text{res}}(\vec{r}) \xrightarrow{r \rightarrow \infty} e^{ikr}, \quad \frac{1}{2}k^2 = E_r - i\Gamma/2 \quad (10)$$

However, the Siegert function of eqn. (10) is divergent: $\int |\psi_{\text{res}}|^2 d\tau \xrightarrow{r \rightarrow \infty} \infty$ and the number of particles is not conserved. This non- L^2 nature of ψ_{res} has given rise to difficulties in the direct application of Siegert's method to resonant scattering /55/.

In order to conserve the number of particles and to be able to apply the usual bound state methods to the treatment of resonances, the following transformations are called for /56/ :

$$\phi = S\psi_{\text{res}} \xrightarrow{r \rightarrow \infty} 0 \quad (11)$$

and

$$[SHS^{-1}] S\psi_{\text{res}} = \bar{H}\phi = [E_r - i\Gamma/2] S\psi_{\text{res}} \quad (12)$$

so that calculation of resonances may be recast as the familiar eigenvalue problem

$$\bar{H}\phi = E\phi \quad (13)$$

except that \bar{H} is non-Hermitian and new algebraic considerations become necessary for the extension of routine bound-state methods in the treatment of resonances /57-63/. The basic underpinning of all these extensions is the modification of the spectrum of H induced by S as described by Aguilar, Balslev, Combes (ABC) and Simon /27-29/. Excellent pedagogical treatments of these modifications already exist /30-34,56,57/ and we merely outline some pertinent results in the following subsections.

2.1 The ABC Theorem

The theorems of Aguilar, Balslev and Combes /27-30/ prescribe that the complex scaling of all the electronic coordinates in the Hamiltonian modifies its spectrum as depicted in fig. 1.

The real discrete eigenvalues corresponding to the bound states are persistent and remain unchanged. The various ionization and excitation thresholds are also left unmodified. The continua belonging to these thresholds are however rotated by an angle 2θ where the complex scaling parameter $\eta = \alpha e^{i\theta}$. Resonances appear as complex discrete eigenvalues of the complex scaled Hamiltonian $H(\eta)$ and the corresponding wave functions are square integrable /31-35/.

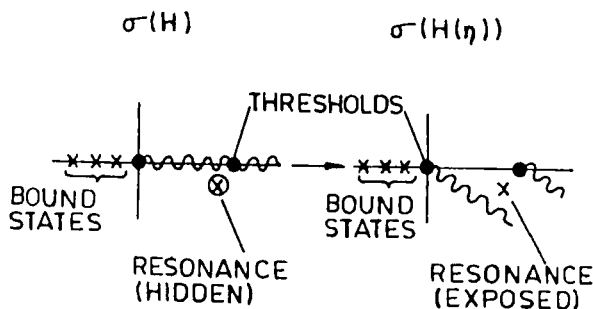


Figure 1. The spectrum $\sigma(H)$ of the unscaled and $\sigma(H(\eta))$ of the complex scaled Hamiltonian.

2.2 The Bi-variational SCF

The complex scaled Hamiltonian $\bar{H}(\eta) = SHS^{-1} \neq (\bar{H}(\eta))^\dagger$, e.g., for the dilated atomic Hamiltonian (in a.u.)

$$H(\eta) = \sum_i \left(-\frac{1}{2} \eta^{-2} \nabla_i^2 - \eta^{-1} \frac{Z}{r_i} \right) + \sum_{i>j} \frac{\eta^{-1}}{r_{ij}}; \quad \eta = \alpha e^{i\theta} \quad (14)$$

$H^\dagger(\eta) = H(\eta^*) = H^*(\eta) \neq H(\eta)$ for complex values of the dilatation parameter η , i.e., $H(\eta)$ is non-Hermitian and as such, the variational theorem does not apply. However, there exists a bi-variational theorem /57,58/ for non-Hermitian operators. The bi-variational SCF equations for the dilated Hamiltonians are derived by extremizing the generalized functional

$$\mathcal{E}(\Phi_0, \Psi_0) = \frac{\langle \Phi_0 | H(\eta) | \Psi_0 \rangle}{\langle \Phi_0 | \Psi_0 \rangle} \quad (15)$$

under the constraint that the solutions Φ_0 and Ψ_0 be of the single determinantal type and the constituent one-electron orbitals be bi-orthogonal.

$$\Phi_0 = (N!)^{-1/2} \det[\phi_1(x_1) \phi_2(x_2) \cdots \phi_N(x_N)], \quad (16)$$

$$\Psi_0 = (N!)^{-1/2} \det[\psi_1(x_1) \psi_2(x_2) \cdots \psi_N(x_N)], \quad (17)$$

$$\langle \phi_i | \psi_j \rangle = \delta_{ij} \quad (18)$$

This has been shown /59-62/ to result in a canonical bi-variational SCF procedure leading to the effective Fock operators

$$\Omega_1(\eta, \phi, \psi) = -\frac{1}{2}\eta^{-2}\nabla_1^2 - \eta^{-1}\frac{Z}{r_1} + \eta^{-1} \int_{x'_2=x_2} \frac{1-P_{12}}{r_{12}} \rho(x_2, x'_2) dx_2, \quad (19)$$

$$\Omega_1^\dagger(\eta, \phi, \psi) = -\frac{1}{2}(\eta^*)^{-2}\nabla_1^2 - (\eta^*)^{-1}\frac{Z}{r_1} + (\eta^*)^{-1} \int_{x'_2=x_2} \frac{1-P_{12}}{r_{12}} \rho^\dagger(x_2, x'_2) dx_2, \quad (20)$$

where

$$\rho = \sum_i^{\text{occ}} \psi_i \phi_i^* \quad (21)$$

Extremization of the functional in eqn. (15) defines the necessary and sufficient condition /61,62/

$$\Omega \rho = \rho \Omega \quad (22)$$

and the following SCF equations result

$$\Omega \psi_i = \epsilon_i \psi_i \quad (23)$$

$$\Omega^\dagger \phi_i = \epsilon_i^* \phi_i \quad (24)$$

The N lowest real orbital energies ϵ determine the occupied spin orbitals which define $\rho, \Omega, \Psi_0, \Omega^\dagger$ and Φ_0 . The procedure followed by us uses a finite real basic set $\mathbf{u} = \{u_i\}_{i=1}^M$, $M > N$, such that

$$\bar{\psi} = \mathbf{u} \mathbf{c} \quad \bar{\phi} = \mathbf{u} \mathbf{d} \quad (25)$$

(the bars on top of $\bar{\psi}$ and $\bar{\phi}$ denote their approximate nature), and by applying the bi-variational theorem again /59/ to the functional

$$E = \frac{\langle \bar{\phi} | \Omega \bar{\psi} \rangle}{\langle \bar{\phi} | \psi \rangle} \quad (26)$$

and its complex conjugate, one obtains the matrix equations

$$\Omega \mathbf{c} = \Delta \mathbf{c} \epsilon \quad (27)$$

$$\Omega^\dagger \mathbf{d} = \Delta \mathbf{d} \epsilon^* \quad (28)$$

and the bi-orthogonality relation

$$\mathbf{d}^\dagger \Delta \mathbf{c} = 1 \quad (29)$$

where $\Delta = \langle \mathbf{u} | \mathbf{u} \rangle$ is the real and symmetric matrix and $\Omega = \langle \mathbf{u} | \Omega \mathbf{u} \rangle$ is symmetric but complex.

The fact that $H^\dagger(\eta) = H(\eta^*) = H^*(\eta)$ suggests the assumption $\Phi_0 = \Psi_0^*$ and the consequent association $\{\phi_i\} = \{\psi_i^*\}$ /59,63/. With these assumptions the following relations hold:

$$\rho^\dagger = \rho^* \quad (30)$$

$$\Omega^\dagger = \langle \mathbf{u} | \Omega^\dagger | \mathbf{u} \rangle = \langle \mathbf{u}^* | \Omega^* | \mathbf{u}^* \rangle = \Omega^* \quad (\text{for real } \mathbf{u}) \quad (31)$$

which leads to $\mathbf{d}^\dagger = \mathbf{c}^\dagger$, and the modified bi-orthonormality condition $\mathbf{c}^\dagger \Delta \mathbf{c} = 1$ holds. We note that if \mathbf{u} were complex, then $\Omega^\dagger \neq \Omega^*$, $\mathbf{d}^\dagger \neq \mathbf{c}^\dagger$, and $\{\phi_i\} = \{\psi_i^*\}$ and $\{\psi_i\}$ are not bi-orthogonal any more. Some other approaches favor a physically motivated complex basic set \mathbf{u} /63,64/ but complex basic sets do not preserve bi-orthonormality and we have therefore employed only real primitive \mathbf{u} in all our calculations.

The assumption $\{\phi_i\} = \{\psi_i^*\}$ makes the approximate many-electron wavefunction satisfy the same relations as the exact one. This choice permits the construction of a bi-variational SCF program driven by supermatrices /59,65/ requiring a symmetric density matrix and preserves the associated storage and IO advantages. In all our numerical investigations we have used a real basic set of symmetry adapted CGTO's and have assumed $\{\phi_i\} = \{\psi_i^*\}$. With this assumption $\rho = \text{occ.} |\psi\rangle \langle \bar{\psi}| \text{occ.} = |\mathbf{u}\mathbf{c}\rangle \langle \mathbf{u}\mathbf{c}^*| = |\mathbf{u}\rangle \mathbf{c}\bar{\mathbf{c}} \langle \mathbf{u}|$. The convergence criterion $\delta\rho = 0$ demands $\delta(\mathbf{c}\bar{\mathbf{c}}) = 0$ and agreement of the absolute magnitude of the density elements from successive cycles within 1.0×10^{-5} is enforced as the convergence criterion. The results have been analyzed in some detail earlier /44,59/ and will be discussed further in the following sections.

2.3 The Dilated Electron Propagator

The bi-variational SCF furnishes the bi-orthonormal sets $\{\phi_i\}$ and $\{\psi_i\}$, and N occupied orbitals determine Φ_0 and Ψ_0 . For the ideal case of complete spin-orbital bases $\{\phi_i\}$ and $\{\psi_i\}$ the closure relation becomes

$$\delta(\mathbf{x} - \mathbf{x}') = \sum_{\mathbf{k}} \phi_{\mathbf{k}}^*(\mathbf{x}') \psi_{\mathbf{k}}(\mathbf{x}) \quad (32)$$

\mathbf{x} being a compound space-spin coordinate. We can write the appropriate zeroth order density operator as $\rho_0 = |\Psi_0\rangle \langle \Phi_0|$ with $\text{Tr } \rho_0 = 1$ and $E(\eta) = \langle H \rangle = \text{Tr} \{H(\eta)\rho_0(\eta)\}$ is stationary. The exact ground state solution can be represented by the density operator $\rho = \rho_0 + (\rho - \rho_0)$ /66/. The space of all antisymmetric tensors of different ranks corresponding to state-vectors representing different numbers of particles generated by the set $\{\psi_i\}$, under natural linear operations and exterior multiplications \wedge which increase the rank of the tensors, constitutes a Grassmann Algebra G /67/. We also introduce the

adjoint algebra G^* associated with $\{\phi_i\}$, and in terms of the duality \langle, \rangle between G and G^* , the interior multiplication of the left \rfloor , and of the right \rfloor , are defined as follows:

$$\langle \chi, a_i \wedge \xi \rangle = \langle \chi(a_i \wedge)^\dagger, \xi \rangle = \langle \chi \rfloor a_i, \xi \rangle \quad (33)$$

with $\chi, \chi \rfloor a_i \in G^*$ and $\xi, a_i \wedge \xi \in G$. Similarly, we have

$$\langle \chi \wedge a^i, \xi \rangle = \langle \chi, (\wedge a^i)^\dagger \xi \rangle = \langle \chi, a^i \rfloor \xi \rangle \quad (34)$$

$\chi, \chi \wedge a^i \in G^*$ and $\xi, a^i \rfloor \xi \in G$. The interior multiplications $a^i \rfloor$ and $\rfloor a_i$ decrease the rank of tensors in G and G^* , respectively. It is obvious that the exterior multiplications $a_i \wedge$ and $\wedge a^i$ and the interior multiplications $a^i \rfloor$ and $\rfloor a_i$ may be formalized as the familiar creation and annihilation operators on the direct $\{\psi_i\}$ and adjoint $\{\phi_i\}$ spaces, respectively, except that now the operators and their adjoints do not have the same domain. Specifically $(a_i \wedge)^\dagger = \rfloor a_i$. These concepts are part of the general theory of Dual Grassmann Algebras /67/. Some other relevant results are:

$$(a_i \wedge)^\dagger = \rfloor a_i \quad (a^i \rfloor)^\dagger = \wedge a^i \quad (35)$$

$$[a^i \rfloor, a^j \rfloor]_+ = 0 = [a_i \wedge, a_j \wedge]_+; \quad [a_i \wedge, a^j \rfloor]_+ = \delta_{ij} \quad (36)$$

The electron field operator $\hat{\psi}(x)$ for the direct space is given by

$$\begin{aligned} \hat{\psi}(x) &= \sum_i \psi_i(x) a^i \rfloor \\ &= \sum_i \psi_i(x) (\wedge a^i)^\dagger \end{aligned}$$

and the electron field operator $\hat{\phi}(x)$ for the adjoint space is defined as

$$\begin{aligned} \hat{\phi}^\dagger(x) &= \sum_i \phi_i^*(x) (\rfloor a^i)^\dagger \\ &= \sum_i \phi_i^*(x) a_i \wedge \end{aligned}$$

and in terms of the duality between G and G^* , the regular second quantized representation of the physical operators is easily generalized /22/, e.g., for the dilated Hamiltonian from eqn. (14) written as

$$H(\eta) = \sum_{i=1}^N h_i(\eta) + 1/2 \sum_i \sum_{j \neq i} g_{ij}(\eta) \quad (37)$$

$$\begin{aligned}
H(\eta) &= \int \hat{\phi}^\dagger(x_1) h_1(\eta) \hat{\psi}(x_1) dx_1 + 1/2 \int \hat{\phi}^\dagger(x_1) \hat{\phi}^\dagger(x_2) \\
&\quad \times g_{12}(\eta) \hat{\psi}(x_2) \hat{\psi}(x_1) dx_1 dx_2 \\
&= \sum_r \sum_s \langle \phi_r | h(\eta) | \psi_s \rangle a_r \wedge a^s [\\
&\quad + 1/2 \sum_r \sum_{r'} \sum_s \sum_{s'} \langle \phi_r \phi_{r'} | g(\eta) | \psi_s \psi_{s'} \rangle a_r \wedge a_{r'} \wedge a^{s'} [a^s [\quad (38)
\end{aligned}$$

We note that the number operator for electrons will be

$$N_{\text{op}} = \sum_r a_r \wedge a^r [= \sum_r n_r \quad (39)$$

and the occupation numbers are

$$\text{Tr} \{ \rho_0 a_r \wedge a^r [\} \equiv \langle n_r \rangle = \begin{cases} 1 & \text{if } \psi_r \text{ is occupied in } \Psi_0 \\ 0 & \text{otherwise} \end{cases} \quad (40)$$

Partitioning the Hamiltonian in eqn. (37) as

$$H(\eta) = H_0(\eta) + V(\eta) \quad (41)$$

where

$$H_0(\eta) = \sum_k \epsilon_k a_k \wedge a^k [\quad (42)$$

and

$$V(\eta) = \sum_i \sum_j \sum_k \sum_\ell \langle \phi_i \phi_j | \psi_k \psi_\ell \rangle [1/4 a_i \wedge a_j \wedge a^\ell [a^k [- \delta_{j\ell} \langle n_\ell \rangle a_i \wedge a^k [] \quad (43)$$

with

$$\langle \phi_i \phi_j | \psi_k \psi_\ell \rangle \equiv \langle \phi_i \phi_j | g(\eta) | \psi_k \psi_\ell \rangle - \langle \phi_i \phi_j | g(\eta) | \psi_\ell \psi_k \rangle \quad (44)$$

The linear space of fermionlike creation and annihilation operators introduced in the superoperator formulation /68/ of the propagator equations is now to be replaced by bi-orthonormal operator spaces /22/

$$\mathbf{h} = \{ a^i [, a_i \wedge a^j [a^k [, \dots \} \quad j < k \quad (45)$$

$$\bar{\mathbf{h}} = \{] a_i ,] a_k] a_j \wedge a^i , \dots \} \quad j > k \quad (46)$$

with scalar product

$$(\bar{h}_i | h_j) \equiv \text{Tr} \{ [h_j, \bar{h}_i^\dagger]_+ \rho \}. \quad (47)$$

The superoperator Hamiltonian may be partitioned as

$$\hat{H}(\eta) = \hat{H}_0(\eta) + \hat{V}(\eta) \quad (48)$$

and the superoperator $\hat{H}_0(\eta)$, $\hat{V}(\eta)$ and the identity superoperator \hat{I} /68,69/ satisfy the relations

$$\hat{H}_0 X = [X, H_0(\eta)]_-, \quad \hat{V} X = [X, V(\eta)]_-, \quad \hat{I} X = X, \quad \forall X \in \mathbf{h} \quad (49)$$

Analogous to the previous treatments /69/ the Fourier transformed equation of motion of the dilated electron propagator may now be written as

$$G(\eta) = (\tilde{\mathbf{a}} | (E\hat{I} - \hat{H}(\eta))^{-1} \mathbf{a}) \quad (50)$$

with matrix elements

$$G_{ij}(\eta) = (\tilde{\mathbf{a}}_i | (E\hat{I} - \hat{H}(\eta))^{-1} \mathbf{a}^j) \quad (51)$$

where $\tilde{\mathbf{a}}_i = |\mathbf{a}_i|$, and $\mathbf{a}^j = |\mathbf{a}^j|$ and approximation schemes can now be developed exactly as in the earlier work /3/ for the real electron propagator method and instead of the expression in eqn. (50) we study

$$G(\eta) = (\tilde{\mathbf{a}} | \mathbf{h}) (\tilde{\mathbf{h}} | (E\hat{I} - \hat{H}(\eta))^{-1} \mathbf{h})^{-1} (\tilde{\mathbf{h}} | \mathbf{a}) \quad (52)$$

obtained by inner projection /70/.

The zeroth order expression for the electron propagator is obtained by using ρ_0 from eqn. (21) as the density operator and using the inner projection manifolds

$$\mathbf{h} = \mathbf{h}^1 = \{\mathbf{a}^i | \}, \text{ and } \tilde{\mathbf{h}} = \tilde{\mathbf{h}}^1 \equiv \{ | \mathbf{a}_i \} \quad (53)$$

in eqn. (52) we get

$$G^0(\eta) = (\tilde{\mathbf{a}} | (E\hat{I} - \hat{H}_0(\eta)) \mathbf{a})^{-1} \quad (54)$$

with

$$G_{ij}^0(\eta) = \delta_{ij} / (E - \epsilon_i) \quad (55)$$

This demonstrates the equivalence of this development to that of the undiluted electron propagator. The structural equivalence at any order of perturbation theory between the dilated propagator $G(\eta)$ and the unrotated case, demonstrated by the corresponding choice of projection manifolds and density operators, guarantees the ease with which the dilated propagator coalesces into the undiluted one for $\theta = 0$ at any level of approximation. For example, choosing $\rho = \rho_0$, $\mathbf{h} = \mathbf{h}^1 \oplus \mathbf{h}^3$, and $\tilde{\mathbf{h}} = \tilde{\mathbf{h}}^1 \oplus \tilde{\mathbf{h}}^3$ with

$$\mathbf{h}^3 = \{\mathbf{a}_\alpha \wedge \mathbf{a}^p | \mathbf{a}^q |, \mathbf{a}_p \wedge \mathbf{a}^\alpha | \mathbf{a}^\beta | \} \text{ and } \tilde{\mathbf{h}}^3 = \{ | \mathbf{a}_q \rangle \mathbf{a}_p \wedge \mathbf{a}^\alpha, | \mathbf{a}_\beta \rangle \mathbf{a}_\alpha \wedge \mathbf{a}^p \} \quad (56)$$

($\alpha < \beta$ labeling occupied, $p < q$ labeling unoccupied orbitals, and i, j labeling unspecified orbitals) we can write /22/

$$G^{-1}(\eta, E) = (\mathbf{a} | E\hat{I} - \hat{H}_\eta | \mathbf{a}) - (\mathbf{a} | \hat{H}_\eta | \mathbf{h}_3) (\mathbf{h}_3 | E\hat{I} - H_\eta | \mathbf{h}_3)^{-1} (\mathbf{h}_3 | \hat{H}_\eta | \mathbf{a}) \quad (57)$$

or

$$G^{-1}(\eta, E) = E1 - [A + BM^{-1}C] \quad (58)$$

which may be recast as

$$G^{-1}(\eta, E) = E1 - A(\eta) - \Sigma(\eta, E) = E1 - L(\eta, E) \quad (59)$$

where

$$L = A + \Sigma \quad \text{and} \quad \Sigma = BM^{-1}C \quad (60)$$

Particular choices for ρ and alternative partitionings of \hat{H} lead to various decouplings of the dilated electron propagator with different actualizations for A and Σ /71/ and in the following subsections we briefly categorize these different approaches to the construction of $G(\eta, E)$.

2.3.1 The Bi-orthogonal Dilated Electron Propagator

The bi-orthogonal dilated matrix electron propagator $G(\eta, E)$ may be expressed as /22/

$$G^{-1}(\eta, E) = G_0^{-1}(\eta, E) - \Sigma(\eta, E), \quad (61)$$

where $G_0(\eta, E)$ is the zeroth order propagator for the uncorrelated electron motion, in this approach chosen as given by the bi-variational SCF approximation /59-62/ and $\eta = \alpha e^{i\theta}$ is the complex scaling (dilation) parameter. The self-energy matrix

$$\Sigma(\eta, E) = (\tilde{a}|\hat{H}(\eta)\mathbf{h}^3)(\tilde{h}^3|(E\hat{1} - \hat{H}(\eta))\mathbf{h}^3)^{-1}(\tilde{h}^3|\hat{H}(\eta)\mathbf{a}) \quad (62)$$

contains the relaxation and correlation effects and may be determined through perturbative or renormalized decouplings /22,40/.

Solution of the bi-variational SCF equations /59/ for the N -electron ground state yields a set of occupied and unoccupied spin orbitals. In terms of these spin orbitals the matrix elements of $G_0^{-1}(\eta, E)$ are

$$(G_0^{-1}(\eta, E))_{ij} = (E - \epsilon_i)\delta_{ij}, \quad (63)$$

where ϵ_i is the orbital energy corresponding to spin orbital i , i.e.; the i -th eigenvalue of the diagonal matrix ϵ of the eigenvalues of the one-electron Hamiltonian in eqn (5).

Approximation of \hat{H} by \hat{H}_0 in eqn. (62) results in the second order approximation to the dilated electron propagator /26,39/ with

$$\Sigma_{ij}^2(\eta, E) = \frac{1}{2} \sum_{\mathbf{k}, \ell, \mathbf{m}} N_{\mathbf{k}\ell\mathbf{m}} \frac{\langle \mathbf{i}\mathbf{k} \| \ell\mathbf{m} \rangle \langle \ell\mathbf{m} \| \mathbf{j}\mathbf{k} \rangle}{(E + \epsilon_{\mathbf{k}} - \epsilon_{\ell} - \epsilon_{\mathbf{m}})} \quad (64)$$

and

$$N_{\mathbf{k}\ell\mathbf{m}} = \langle n_{\mathbf{k}} \rangle - \langle n_{\mathbf{k}} \rangle \langle n_{\ell} \rangle - \langle n_{\mathbf{k}} \rangle \langle n_{\mathbf{m}} \rangle + \langle n_{\ell} \rangle \langle n_{\mathbf{m}} \rangle \quad (65)$$

If \hat{H} in eqn. (62) is retained in entirety, we obtain the full 2ph-TDA decoupling /72-74/ with

$$\Sigma_{ij}^{2\text{ph-TDA}}(\eta, E) = \frac{1}{2} \sum_{\mathbf{k}, \ell, \mathbf{m}} \sum_{\mathbf{k}', \ell', \mathbf{m}'} N_{\mathbf{k}\ell\mathbf{m}}^{1/2} N_{\mathbf{k}'\ell'\mathbf{m}'}^{1/2} \langle \mathbf{i}\mathbf{k} \parallel \ell\mathbf{m} \rangle \times \{ (\tilde{\mathbf{h}} | (\mathbf{E}\hat{\mathbf{I}} - \hat{\mathbf{H}}_0(\eta)) \mathbf{h}) - (\tilde{\mathbf{h}} | \hat{\mathbf{V}}(\eta) \mathbf{h}) \}_{\mathbf{k}\ell\mathbf{m}, \mathbf{k}'\ell'\mathbf{m}'}^{-1} \langle \ell'\mathbf{m}' \parallel \mathbf{j}\mathbf{k}' \rangle, \quad (66)$$

where

$$\mathbf{h}_{\mathbf{k}\ell\mathbf{m}} = N_{\mathbf{k}\ell\mathbf{m}}^{-1/2} [\mathbf{a}_{\mathbf{k}}^\dagger \mathbf{a}_{\ell} \mathbf{a}_{\mathbf{m}} + \delta_{\mathbf{k}\mathbf{m}} \langle n_{\mathbf{k}} \rangle \mathbf{a}_{\ell} - \delta_{\mathbf{k}\ell} \langle n_{\mathbf{k}} \rangle \mathbf{a}_{\mathbf{m}}] \quad (67)$$

$$(\tilde{\mathbf{h}}_{\mathbf{k}'\ell'\mathbf{m}'} | (\mathbf{E}\hat{\mathbf{I}} - \hat{\mathbf{H}}_0(\eta)) \mathbf{h}_{\mathbf{k}\ell\mathbf{m}}) = (E + \epsilon_{\mathbf{k}} - \epsilon_{\ell} - \epsilon_{\mathbf{m}}) \delta_{\mathbf{k}\mathbf{k}'} \delta_{\ell\ell'} \delta_{\mathbf{m}\mathbf{m}'},$$

and

$$(\tilde{\mathbf{h}}_{\mathbf{k}'\ell'\mathbf{m}'} | (\hat{\mathbf{V}}(\eta)) \mathbf{h}_{\mathbf{k}\ell\mathbf{m}}) = N_{\mathbf{k}\ell\mathbf{m}}^{1/2} N_{\mathbf{k}'\ell'\mathbf{m}'}^{-1/2} \{ \frac{1}{2} \langle \mathbf{m}\ell \parallel \mathbf{m}'\ell' \rangle \delta_{\mathbf{k}\mathbf{k}'} (1 - \langle n_{\mathbf{m}} \rangle - \langle n_{\ell} \rangle) - \langle \mathbf{k}'\mathbf{m} \parallel \mathbf{k}\mathbf{m}' \rangle \delta_{\ell\ell'} (\langle n_{\mathbf{k}} \rangle - \langle n_{\mathbf{m}} \rangle) - \langle \mathbf{k}'\ell \parallel \mathbf{k}\ell' \rangle \delta_{\mathbf{m}\mathbf{m}'} (\langle n_{\mathbf{k}} \rangle - \langle n_{\ell} \rangle) \} \quad (68)$$

As a result of the large dimension of the $\{\mathbf{h}_{\mathbf{k}\ell\mathbf{m}}\}$ operator manifold the full 2ph-TDA technique is computationally not very attractive and its diagonal approximation which restricts the summation over the spin orbitals to $\mathbf{k} = \mathbf{k}'$, $\ell = \ell'$ and $\mathbf{m} = \mathbf{m}'$ affords considerable computational savings. Applying this approximation to eqn. (66), the diagonal 2ph-TDA self-energy expression for the dilated electron propagator is given by

$$\Sigma_{ij}^{2\text{ph-TDA}}(\eta, E) = \frac{1}{2} \sum_{\mathbf{k}, \ell, \mathbf{m}} N_{\mathbf{k}\ell\mathbf{m}} \frac{\langle \mathbf{i}\mathbf{k} \parallel \ell\mathbf{m} \rangle \langle \ell\mathbf{m} \parallel \mathbf{j}\mathbf{k} \rangle}{(E + \epsilon_{\mathbf{k}} - \epsilon_{\ell} - \epsilon_{\mathbf{m}}) - \Delta}, \quad (69)$$

where $\Delta = \frac{1}{2} \langle \mathbf{m}\ell \parallel \mathbf{m}\ell \rangle (1 - \langle n_{\mathbf{m}} \rangle - \langle n_{\ell} \rangle) - \langle \mathbf{k}\mathbf{m} \parallel \mathbf{k}\mathbf{m} \rangle (\langle n_{\mathbf{k}} \rangle$

$$- \langle n_{\mathbf{m}} \rangle) - \langle \mathbf{k}\ell \parallel \mathbf{k}\ell \rangle (\langle n_{\mathbf{k}} \rangle - \langle n_{\ell} \rangle) \quad (70)$$

The results obtained from diagonal and full 2ph-TDA decouplings for the valence electrons are almost indistinguishable /75/ and this has been our preferred decoupling for the treatment of shape resonances /40/.

In addition to the usual computational demands of iterative pole search necessitating multiple passes through large self energy lists that beset all propagator calculations, resonances are identified through search for regions of quasi-stability in α and θ trajectories of complex poles of the dilated electron propagator /21,22/ making these calculations approximately 100 times more exacting in comparison to their real counterparts. The need for effective and economic approximations that preserve the accuracy of original decouplings,

therefore, assumes added significance in the case of dilated electron propagator calculations.

The quasiparticle approximation /76,77/ to the electron propagator and the related Outer Valence Green's Function (OVGF) method /6,9,77/ has emerged as an economic and remarkably accurate method and is used routinely for most of the real electron propagator calculations /6,9,77,78/. The quasiparticle approximation /48-50/ for dilated electron propagator results from an identical diagonal approximation to the self-energy matrix $\Sigma(\eta)$ with poles of the dilated electron propagator being given by

$$E(\eta) = \epsilon_i + \Sigma_{ii}(\eta, E) \quad (71)$$

which is solved iteratively beginning with $E = \epsilon_i$ and Σ_{ii} may correspond to any perturbative or renormalized decoupling or geometric approximation scheme such as the OVGF method. We have utilized both second order (Σ_{ii}^2) and diagonal 2ph-TDA ($\Sigma_{ii}^{2ph-TDA}$) decouplings, for the quasiparticle approximation /41-46/.

The computational considerations in the calculation of poles and corresponding FDAs may be outlined by rewriting the propagator eqn. (61) as

$$G^{-1}(\eta, E) = E\mathbf{I} - \mathbf{L}(\eta, E); \quad \mathbf{L} = \epsilon + \Sigma \quad (72)$$

whereby the poles of the dilated electron propagator are the energy dependent eigenvalues of $\mathbf{L}(\eta, E)$ given by

$$\mathbf{L}(\eta, E)\chi_n(\eta, E) = \mathcal{E}_n(\eta, E)\chi_n(\eta, E), \quad (73)$$

which satisfy the relation

$$\mathcal{E}_n(\eta, E) = E \quad (74)$$

Finally, in terms of the eigenfunctions and eigenvalues of \mathbf{L} , the spectral representation of the dilated electron propagator is

$$G(\eta, E) = \sum_n \frac{|\chi_n\rangle\langle\chi_n|}{E - \mathcal{E}_n(\eta, E)} \quad (75)$$

and the requisite poles of \mathbf{G} are searched by iterative diagonalization of \mathbf{L} as detailed elsewhere /21/. The Feynman-Dyson Amplitude χ_n corresponding to the n -th $N+1$ electron state is given by

$$\chi_n = \int \Psi_n^{N+1*}(1, 2, 3, \dots, N, N+1, n) \Psi_0^N(1, 2, 3, \dots, N) d(1)d(2)d(3) \dots d(N) \quad (76)$$

where Ψ_0^N is the optimal single determinantal description of the N -electron target based on the bi-variationally determined SCF orbitals $\{\psi_i\}$ and Ψ_n^{N+1} is the n -th $N+1$ state generated by the creation operator manifold $\{a_i \wedge, a_i \wedge a_j \wedge$

$a_k | j > i \rangle / 22, 40 /$. In the bi-variationally obtained bi-orthogonal orbital basis $\{\psi_i\}$, χ_n is a linear combination

$$\chi_n(\vec{r}) = \sum_i C_{ni} \psi_i(\vec{r}) \quad (77)$$

where the mixing of the canonical orbitals allows for the incorporation of correlation and relaxation effects. In the zeroth ($\Sigma = 0$) and quasiparticle approximations (diagonal Σ), there is no mixing. The difference between perturbative second order (Σ^2) or renormalized diagonal 2ph-TDA ($\Sigma^{2ph-TDA}$) decouplings manifests itself through differences between the mixing coefficients C_{ni} from these approximations /3,40/.

2.3.2 Dilated Electron Propagator based on a real SCF

In this scheme introduced by Donnelly and Simons /21,47-50/, the complex scaled Hamiltonian is partitioned as

$$H(\eta) = H_0(HF; \eta = 1) + H'(\eta) \quad (78)$$

where HF stands for Hartree-Fock and hence

$$H'(\eta) = [V(\eta) - V(HF; \eta = 1)] + [h_{HF}(\eta) - h_{HF}(\eta = 1)] \quad (79)$$

The reference state $|N_0\rangle$ in this scheme is approximated by

$$|N_0\rangle = \Psi(\eta) = \Psi(HF; \eta = 1) + \text{RSPT correction to first order} \quad (80)$$

and

$$G^{-1}(\eta, E) = E1 - (A + BM^{-1}C) = E1 - L(\eta, E) \quad (81)$$

where the detailed expressions for A , B , M and C are tabulated in reference 21.

The differences between the two approaches to the construction of the dilated electron propagator discussed so far, become obvious at this stage. The bi-orthogonal approach preserves the formal simplicity and utilizes optimal orbitals with the effect of complex scaling built into the state function $|N_0\rangle = \Psi_0(\eta)$ through a separate bi-variational SCF for each η (eqn. (19)). This, however, necessitates that a fresh set of orbitals be obtained and a complex two electron integral transformation over these orbitals be done for each new value of η . Since resonances are searched through α and θ trajectories ($\eta = \alpha e^{i\theta}$) of the corresponding poles, the bi-orthogonal procedure is computationally demanding. The approach of Donnelly and Simons /21/ bypasses these difficulties by basing its scheme on a real SCF. The accommodation of complex scaling effects through a low order perturbative analysis however,

leads to complicated formulae for Σ_{ij} and somewhat more cumbersome algorithms become necessary /21/. This approach also does not provide for easy extensions and has been restricted to only a second order decoupling. Also, one may be able to glean valuable insight by examining the bi-variational SCF orbital energies as the poles of the zeroth order dilated electron propagator /25/ and use this for economical and predictive construction and pole search of the full propagator. Such a possibility is precluded by the Donnelly-Simons approach based on real SCF. Even with these differences of approach, the results obtained from both these methods have been comparable for second order decouplings and will be discussed later in section 4.

2.3.3 Electron Propagator with Siegert Boundary Condition

The construction of the dilated electron propagator for many different values of the complex scaling parameter is computationally demanding. The advantages of complex scaling ensue from the conversion of the resonant scattering function into a square integrable function due to the Siegert boundary condition /54/. This has led to the construction of the Layzer operator L

$$L(E) = -\frac{1}{2}\nabla^2 + V(HF) + \Sigma(E) \quad (82)$$

in a basis of real Hartree-Fock orbitals $\{\phi_i\}$ augmented by a Siegert Orbital ϕ_* with a cutoff factor to take care of the divergence problems /23,24/

$$\phi_*(r) = [1 - \exp(-\beta r)]\exp(ikr - l\pi/2)/r \quad (83)$$

where k is complex with $\frac{1}{2}k^2 = E$ where E is chosen in the vicinity of known resonance energies ($E \simeq E_r - i\Gamma/2$). The pole search of the propagator once again involves the iterative solution of the Layzer eqn. (73)

$$L(\frac{1}{2}k^2)\Phi_n(\frac{1}{2}k^2) = \mathcal{E}_n(\frac{1}{2}k^2)\Phi_n(k) \quad (84)$$

with

$$\mathcal{E}_n(\frac{1}{2}k^2) = \frac{1}{2}k^2; \quad \mathcal{E}_n = \pm[E_n^{N\pm 1} - E_0^N] \quad (85)$$

once again being the convergence criterion in an iterative pole search (see eqn. (74)). This has not been applied widely. The results obtained from this method for the $(1s)^{-1} {}^2S$ Auger resonance of Be and its satellites are plausible but that for the 2P e-Be shape resonance is not so /24/ and will be discussed along with those from other approaches to the construction of complex scaled electron propagator in the following section. The major recent contribution of this approach is in the calculation of energy and width of Feshbach resonances in He /79/.

2.3.4 The Trajectory Method for Resonant Pole Search

The spectral representation of the dilated electron propagator in strict analogy to eqn. (1) is given by /20-23/ :

$$G_{rr}(\eta, E) = \lim_{\epsilon \rightarrow 0^+} \sum_n \left[\frac{\langle {}^N_0 | a_s | {}^{N+1}_n \rangle \langle {}^{N+1}_n | a_r^\dagger | {}^N_0 \rangle}{E - (E_n^{N+1}(\eta) - E_0^N) + i\epsilon} + \frac{\langle {}^N_0 | a_r^\dagger | {}^{N-1}_n \rangle \langle {}^{N-1}_n | a_s | {}^N_0 \rangle}{E - (E_0^N - E_n^{N-1}(\eta)) - i\epsilon} \right] \quad (86)$$

and the pole structure of the dilated electron propagator may be deduced by examining the poles of eqn. (86) as a function of the scaling parameter η . Since E_0^N is a persistent real eigenvalue, the imaginary part of the pole will come from $E_n^{N+1}(\eta)$ and it becomes obvious that the electron attachment poles $E_n^{N+1}(\eta) - E_0^N$ of the complex scaled electron propagator as per the modifications in the spectrum of $H(\eta)$ may be classified as follows:

1. If n denotes a bound state of the $(N+1)$ anion, $E_n^{N+1}(\eta)$ is real and persistent. Therefore, $E_n^{N+1}(\eta) - E_0^N$ is a persistent real negative pole.
2. If n denotes a resonant (metastable state) of the anion, $E_n^{N+1}(\eta) = E_r^{N+1} - i\Gamma/2$ and the corresponding pole $(E_n^{N+1}(\eta) - E_0^N) = (E_r^{N+1} - E_0^N) - i\Gamma/2$ and from the real part one may directly determine the kinetic energy of the incident electron for which resonance occurs and the imaginary part provides the half width. These poles are persistent once uncovered.
3. If n denotes a continuum state of the anion, $E_n^{N+1}(\eta) = E_0^N + E_e(\eta)$, where $E_e(\eta) = \eta^{-2}E_e$ (see fig. 1) or $E_n^{N+1}(\eta) = E_a^N + E_e(\eta)$ etc. depending on the state of the target left behind and the corresponding poles $(E_n^{N+1}(\eta) - E_0^N) = \eta^{-2}E_e$ (branch cut at 0) or $(E_a^N - E_0^N) + \eta^{-2}E_e$ (branch cut at the first threshold etc.), i.e., these poles get rotated in the fourth quadrant just as the eigenvalues of fig. 1 except here we are dealing with energy differences unlike state energies in that figure.

A similar analysis may be carried out for the electron detachment poles as well and the Auger poles $(E_0^N - E_n^{N-1}(\eta))$ will obviously be found in the first quadrant of the complex E -plane. With this brief discussion of the pole structure of the complex scaled electron propagator as a common background, its utility in direct and simultaneous treatment of resonances of $N+1$ electron and $N-1$ electron systems becomes manifest *e.g.*, for Be both $\text{Be}^+ (1s^{-1})^2\text{S}$ Auger and $^2\text{P Be}^-$ shape resonances have been calculated *simultaneously* from a *single* calculation on Be/25,26/.

While the resonant pole of the dilated electron propagator is persistent once uncovered and should be invariant to further changes in the complex

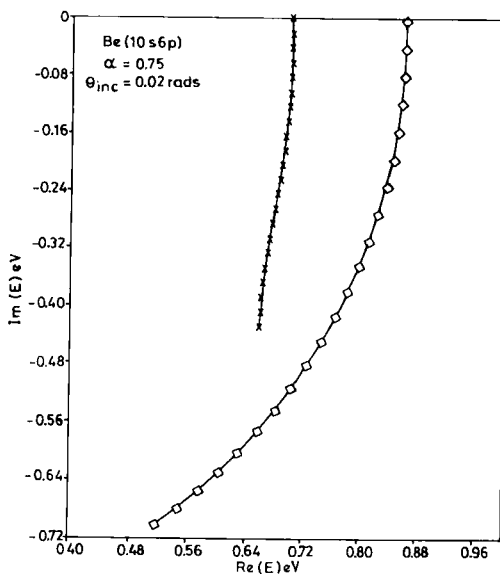


Figure 2. Theta trajectories for the e-Be 2P shape resonance and a nearby scattering root from the second order decoupling of the dilated electron propagator /26/.

scaling parameter, applications employing manageable basis sets do not fulfill the condition:

$$d^k E / d\eta^k = 0 \quad \forall k = 1, 2, 3, \dots \quad (87)$$

This condition for total stability is instead seen to manifest itself as quasi-stability in a short range of η . The stability of resonances is then examined through the following relation:

$$\frac{\partial E}{\partial \eta} = 0 \quad (88)$$

and for $\eta = \alpha e^{i\theta}$ one has the reciprocity relations:

$$(\partial E / \partial \alpha)_\theta = (\eta / \alpha) (\partial E / \partial \eta) = 0 \quad (89)$$

$$(\partial E / \partial \theta)_\alpha = i\eta (\partial E / \partial \eta) = 0 \quad (90)$$

which lead to loops/kinks in the plot of the poles as a function of the scaling parameter (trajectories) in fourth quadrant of the complex energy plane for electron attachment and in the first quadrant for the electron detachment

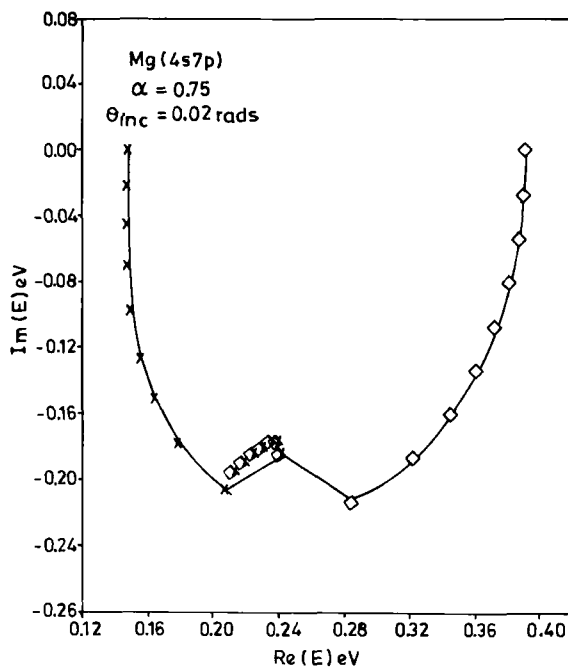


Figure 3. Theta trajectories for the e -Mg 2P shape resonance from the second order (Σ^2) decoupling of the dilated electron propagator /39/.

resonances. Fig. 2 shows the theta trajectories for the resonant and the nearest scattering poles of the dilated electron propagator for Be /25/. The complex scaling transformation is an unbounded similarity transformation and while new roots appear (resonances) old roots may also be lost. This feature is seen in fig. 3 for the case of multi-orbital 2P shape resonance in e -Mg scattering /39,40/.

2.4 Molecular resonances

The Born-Oppenheimer Hamiltonian is not dilatation analytic if only the electronic co-ordinates are scaled since $|\vec{r}e^{i\theta} - \vec{R}|$ vanishes for a continuous range of $\theta \ni |\vec{r}| = |\vec{R}|$ and $\vec{r} \cdot \vec{R} = \cos(\theta)$ /80/. The conceptual and numerical difficulties associated with complex scaling of both the nuclear and electronic coordinates and solution of the combined problem with a plethora of rotational, vibrational and electronic thresholds have prompted the formulation of (see ref. 22) two different schemes by McCurdy and Rescigno /81/ and Moiseyev and Corcoran

/82/. Both utilize the equivalence:

$$\langle \Phi(\vec{r}) | H(\eta) | \Phi(\vec{r}) \rangle \equiv \langle \Phi(\vec{r}, \eta) | H | \Phi(\vec{r}, \eta) \rangle \quad (91)$$

and since basis functions are analytic for all values of the complex scaling parameter, the non-dilatation analyticity of the Born-Oppenheimer Hamiltonian is disregarded /83/. While the McCurdy-Rescigno approach advocates the use of basis functions with exponents scaled by a complex scale parameter where only the diffuse functions are scaled, the Moiseyev-Corcoran approach uses unscaled basis functions with scaled Hamiltonian.

Since the complex scaling of the exponents of the primitive basis set will lead to a complex primitive basis set u and hence to the loss of bi-orthogonality central to our constructions, the Moiseyev-Corcoran approach has been adopted by us /44-46/ and Donnelly /21,47-50/ in the construction of the molecular dilated electron propagator.

Before concluding this section on general theoretical considerations we summarize that the bi-orthogonal approach outlined earlier provides a general and rigorous theoretical format for the construction of the infinite order or the renormalized dilated electron propagator and allows for simple, systematic and easily cognizable approximation schemes. No assumptions about the sufficiency of the first order correction to the variational ground state, as a means of accommodating complex rotation effects or the applicability of the perturbation theory to the perturbation Hamiltonian $V(\theta) = H(\theta) - F(\theta = 0)$, where F is the Fock operator /21/ need be made. The second order and other approximations of the real electron propagator theory are recovered easily and without invoking other supplementary concepts like the c-product /84/. The scheme is comprehensive and permits the treatment of cases where $\phi_i = \psi_i^*$ may not be a good approximation. All the standard decoupling procedures for the unrotated propagator may be easily incorporated and is the approach utilized by us in all our resonance calculations. Results from these applications are discussed in the following sections.

3 Shape Resonances in e-Atom and e-Molecule Scattering

The shape resonances are believed to result from a simple trapping of the impinging electron in the unoccupied orbitals of the target made metastable by the centrifugal barrier /17,18/. These belong to the continua attached to the first threshold of the target and are easiest to analyze. The multi-orbital Feshbach resonances require rearrangement of core electrons and low order decouplings with limited incorporation of correlation and relaxation effects may not be adequate for their description. Most of the application of the complex

scaled electron propagator method have therefore focused on the investigation of atomic and molecular shape resonances. In the following subsections we collect the major findings from these applications.

3.1 Shape Resonances in e-Atom Scattering

The alkaline earth elements Be, Mg and Ca have p-type orbitals as the lowest unoccupied orbital. These p-orbitals are ideally suited for providing centrifugal angular momentum barrier of adequate width and depth to temporarily trap the impinging electron, and the 2P shape resonances in e-Be, e-Mg and e-Ca scattering have been studied most extensively. The dilated electron propagator has been applied to investigate both the energetics and mechanism of shape resonance formation in electron scattering off these alkaline earth elements. In the following subsections we deal with the energetics. Mechanistic insights gleaned from the application of the dilated electron propagator to these systems are discussed in section 5.

3.1.1 e-Be 2P Shape Resonance

The 2P shape resonance in e-Be scattering has served as the test case for almost all the theoretical approaches to the treatment of electron scattering resonances and the earliest applications of the dilated electron propagator have also focused on this system [21,26,40]. Theta trajectories from different decouplings of the bi-orthogonal dilated electron propagator are displayed in fig. 4. The optimal value of $\alpha = 0.75$ has been determined through a separate α -trajectory [26].

Improvements affected by the incorporation of the correlation and the relaxation effects are quite transparent in fig. 4. The lowering of both the energy and the width of the resonance for the Σ^2 decoupling seems to indicate that relaxation of the target helps the impinging electron to see more nuclear attraction (lower energy), whereby it spends more time in the vicinity of the target (has smaller width). Just as in the real electron propagator calculations the inclusion of self-energy corrections should lead to a better description of the $(N+1)$ state. This is reflected in the dilated electron propagator calculations by the clear cusp in the θ trajectory for the propagator pole. Only a faint tendency is discernible at the level of the bi-variational SCF or the zeroth order propagator. The results from our application of the quasiparticle approximation of the shape resonances in e-Be for both second order and diagonal 2ph-TDA decouplings are also displayed in fig. 4 and the effectiveness of the quasiparticle approximation lends credence to the single orbital picture of shape resonances.

The Siegert orbital approach to the electron propagator has not been effective in the treatment of the e-Be 2P shape resonance. Both our bi-orthogonal

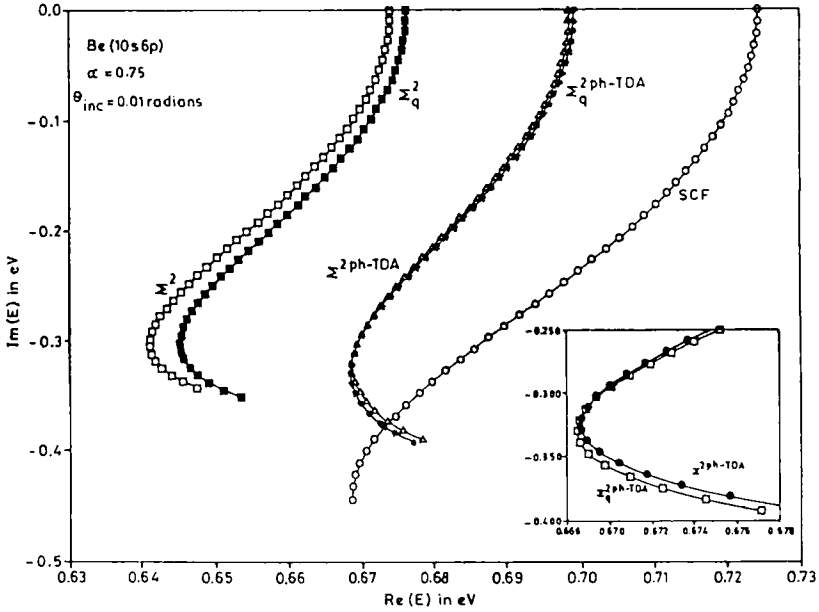


Figure 4. Theta trajectories for the $e\text{-Be } 2P$ shape resonance from the zeroth (bi-variational SCF), second order (Σ^2), quasiparticle second order (Σ_q^2), diagonal 2ph-TDA ($\Sigma^{2\text{ph-TDA}}$) and quasiparticle diagonal 2ph-TDA ($\Sigma_q^{2\text{ph-TDA}}$) decouplings of the dilated electron propagator. A magnified version of the quasiparticle diagonal 2ph-TDA ($\Sigma_q^{2\text{ph-TDA}}$) and diagonal 2ph-TDA ($\Sigma^{2\text{ph-TDA}}$) trajectories is displayed in the inset.

approach based on complex bi-variational SCF and the Donnelly-Simons construction based on real SCF find the $2P$ shape resonance in $e\text{-Be}$ scattering to be much wider when compared with the results from other techniques collected in table I.

The bi-orthogonal approach uncovers it for different α and larger θ and the two techniques give different values. Though our bi-variational SCF based method needs larger rotation to uncover this resonance ($\theta_{\text{opt}} = 0.36$ as compared to $\theta_{\text{opt}} = 0.25$ from ref. 21), the width obtained is only 0.7 of that in ref. 21. This feature, where a larger width is obtained with less rotation seems to indicate that the real SCF based method of ref. 21 may not be suitable for the characterization of wider resonances.

Table IEnergy and Width of the 2P shape resonances in e-Be scattering

Method/Reference	Energy (eV)	Width (eV)
Static Exchange Phase Shift /85/	0.77	1.61
Static Exchange plus Polarizability /85/ Phase Shift	0.20	0.28
Static Exchange Phase Shift /86/	0.75	1.64
Static Exchange plus Polarizability /86/ Phase Shift	0.14	0.13
Static Exchange Cross Section /86/	1.20	2.6
Static Exchange plus Polarizability /86/ Cross Section	0.16	0.14
Complex Δ SCF /63/	0.70	0.51
Singles and Doubles Complex CI /87/	0.58	0.38
Singles Doubles and Triples Complex CI /87/	0.32	0.30
S-Matrix pole (X_α) /127,128/	0.10	0.15
Second order Dilated Electron Propagator based on real SCF /21/	0.57	0.99
Zeroth order Bi-orthogonal Dilated Electron Propagator /40/	0.67	0.88
Second order Bi-orthogonal Dilated Electron Propagator /40/	0.64	0.60
Diagonal 2ph-TDA Bi-orthogonal Dilated Electron Propagator /40/	0.67	0.66

3.1.2 e-Mg ^2P Shape Resonance

While the $^2\text{P Be}^-$ shape resonance has served as the most popular test case, due to the toxic nature of Be, there are no experimental results for this system. The ^2P shape resonance in e-Mg scattering is well characterized /88/ and the extensive literature on this resonance utilizing many different theoretical techniques /47,64,85,86,89,90/ makes it an excellent arbiter of the efficacy of different theoretical techniques for the treatment of resonances.

The results obtained for e-Mg scattering are presented in table II. It is obvious that the perturbation theoretic accommodation of rotation effects for small θ in the Donnelly-Simons approach is quite adequate and the results obtained with or without the use of bi-variational SCF to determine the appropriate zeroth order density for the dilated electron propagator calculations are in remarkable agreement. Since the narrow resonances are uncovered with small rotations, the technique of refs. 21 and 47 is more economical and perhaps equally effective as our own.

The real merit of our work stems from the light it sheds on the parallels /47,91-94/ between the complex scaling and the stabilization method /17,93,126/ for the treatment of resonances. A notable feature of the stabilization method is that at the point of optimal stabilization of the resonant root there is an avoided crossing with another nearly degenerate root which descends from above and replaces the stabilized root when further changes in the stabilization parameter (no. of configurations as in ref. 22 or scale parameter α as in ref. 87-92) is affected.

The details of the stabilization method, especially, the superseding of a previously resonant root by a nonresonant root may be likened to the behavior of rotated scattering roots neighboring a resonance in the complex E plane. If through enough rotation, a scattering root passes by the resonance, it will uncover the neighboring resonance and lose its previous scattering character. Our trajectories from figs. 3 and 5 demonstrate this feature. It is worthwhile to note that the roots portrayed in figs. 3 and 5 approach the same resonance from the opposite directions and that the root II starts out as a typical scattering root. Similar behavior is displayed by the pair of roots displayed in other figs. 1,2 and 5 of reference 26. The pair of roots depicted in fig. 3 have entirely different orbital genealogy initially and are described by different linear combination of the SCF orbitals. This feature persists till the root II of fig 3, for example, has been rotated through $\theta = 0.16$ radians at which stage this root changes to one portrayed by root I. Thereafter the two are identical. The presence of more than one resonant root is a basic feature of all bi-orthogonal dilated electron propagator calculations for e-Mg scattering with different basis sets /26,40/. All of these roots show substantial contributions from more than one orbital (even for $\theta = 0.0$ radians). This is understandable, since if the

Table IIEnergy and Width of the 2P shape resonances in e-Mg scattering

Method/Reference	Energy (eV)	Width (eV)
Experiment /88/	0.15	0.13
Static Exchange Phase Shift /85/	0.46	1.37
Static Exchange plus Polarizability /85/ Phase Shift	0.16	0.24
Static Exchange Phase Shift /86/	0.46	1.53
Static Exchange plus Polarizability /86/ Phase Shift	0.14	0.24
Static Exchange Cross Section /86/	0.91	2.30
Static Exchange plus Polarizability /86/ Cross Section	0.19	0.30
CI /89/	0.20	0.23
S-Matrix pole (X_a) /127,128/	0.08	0.17
Complex Δ SCF /64/	0.51	0.54
Dilated Electron Propagator based on real SCF /47/	0.14	0.13
Second order Bi-orthogonal Dilated Electron Propagator /40/	0.15	0.13
Diagonal 2ph-TDA Bi-orthogonal Dilated Electron Propagator /40/	0.15	0.13

resonance is to be described as a wave packet localized by the polarization and centrifugal potentials induced in the target, the packet is made up of not just one wave but from all those with energies falling within the width of the so-called packet center /93,95/. As such, orbital bases of the kind employed here with nearly degenerate orbital energies in close proximity to the resonance energy will give rise to different roots describing different parts of the wave packet whose width is determined by the width of the widest root. Normal scattering roots *a la* complex scaling will emerge only when the poles of G are

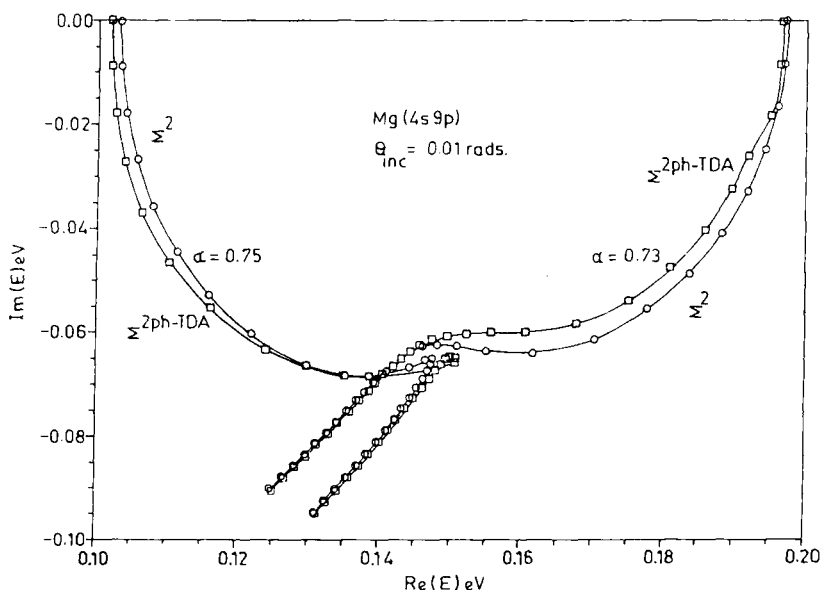


Figure 5. Theta trajectories for the $e\text{-Mg } ^2P$ shape resonance from the second order (Σ^2) and diagonal 2ph-TDA ($\Sigma^{2ph\text{-TDA}}$) decouplings of the dilated electron propagator.

sought outside this energy region. The 2P shape resonance in $e\text{-Be}$ scattering is described by a single root in figs. 2 and 4 since other roots obtained are farther than the half-width of this resonance for the basis sets used in these calculations /26,40/. The optimal results from different bases for the $e\text{-Mg } ^2P$ shape resonances are in excellent agreement with the experimental results for the 2P shape resonance in $e\text{-Mg}$ scattering, which along with the results from other calculations are collected in table II.

3.1.3 $e\text{-Ca } ^2P$ Shape Resonance

The low energy resonances are difficult to measure experimentally and there is some controversy about the energy assignment for the 2P shape resonance in $e\text{-Ca}$ scattering /96/. While the experimental results of Romanyuk et. al. /96/ and those from other theoretical calculations classify the $^2P \text{ Ca}^-$ as being metastable, more recent experimental results of Pegg et. al. /97/ and calculations of Froese-Fischer et. al. /98,129/ have found it to be stable by 0.0453 eV vis-a-vis the neutral Ca atom. Our results from both second order and diagonal 2ph-TDA calculations /40/ employing a fairly extensive

(11s/19p) basis used earlier by McCurdy et. al. /64/ identify only one of the 17 virtual orbitals to be resonant and the corresponding $^2\text{P Ca}^-$ anion to be metastable. The level of correlation and relaxation provided by second order/diagonal 2ph-TDA decouplings of the dilated electron propagator is, however, not decisive and our results are probably not accurate enough to discriminate between stability/metastability of the $^2\text{P Ca}^-$ anion, still, less than 0.1 eV separates stability/metastability and hopefully, our results from a fairly accurate calculation displaying comparative independence from complex scaling ($\alpha_{\text{opt}} = 1.0, \theta_{\text{opt}} = 0.29\text{radians}$) will spur further investigations in this area.

Theta trajectories of the resonant root for the Ca ^2P shape resonance from the various self-energy approximants are plotted in fig. 6. The results for resonance energy and width of the ^2P shape resonance in e-Ca scattering are collected in table III.

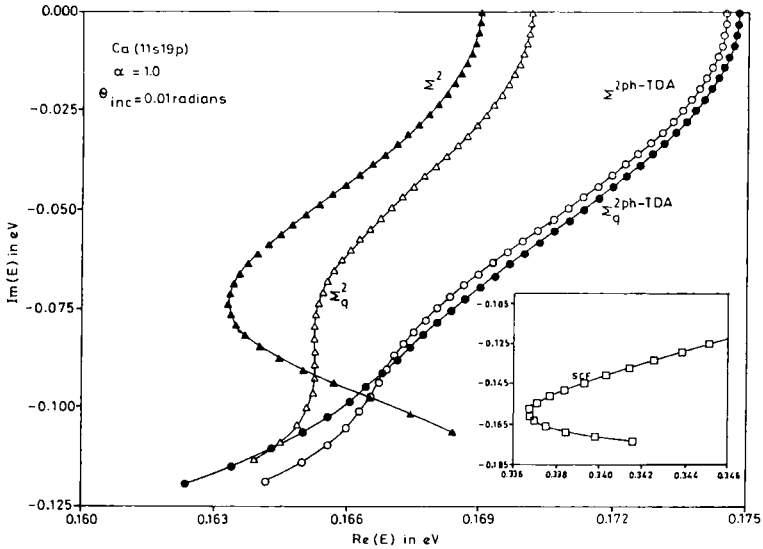


Figure. 6. Theta trajectories for the e-Ca ^2P shape resonance from the zeroth (inset), second order (Σ^2), quasiparticle second order (Σ^2_q), diagonal 2ph-TDA ($\Sigma^{2\text{ph-TDA}}$) and quasiparticle diagonal 2ph-TDA ($\Sigma^{2\text{ph-TDA}}_q$) decouplings of the dilated electron propagator.

Table IIIEnergy and Width of the 2P shape resonances in e-Ca scattering

Method/Reference	Energy (eV)	Width (eV)
Static-Exchange Phase Shift /86/	0.24	0.54
Static-Exchange plus Polarizability /86/ Phase Shift	0.06	0.10
Static-Exchange Cross Section /86/	0.40	0.70
Static-Exchange plus Polarizability /86/ Cross Section	0.08	0.10
Static-Exchange Total Cross Section /96/	0.45	0.65
Static-Exchange plus Polarizability /96/ Total Cross Section	0.10	0.14
Complex Δ SCF /64/	0.23	0.16
Zeroth order Bi-orthogonal Dilated Electron Propagator /40/	0.34	0.32
Second order Bi-orthogonal Dilated Electron Propagator /40/	0.16	0.14
Diagonal 2ph-TDA Bi-orthogonal Dilated Electron Propagator /40/	0.17	0.19

3.1.4 Role of Correlation and Relaxation in atomic shape resonances

Even though the diagonal 2ph-TDA sums diagonal ring and ladder diagrams to all orders, from tables I-III, it is obvious that unlike in other studies where increased correlation leads to lower values for resonance energy and width, the main effect of correlation in our study seems not so much on the resonance energies as on the width. Greater correlation provides for the incorporation of higher level of polarization and relaxation effects leading to a longer life time for the resonance but the resonance energies remain close to values obtained from the lower order approximations. For all the three systems, we find that the results obtained from the second order and the diagonal 2ph-TDA are more or less indistinguishable from each other. There is however, considerable

difference in results obtained from the uncorrelated zeroth order (bi-variational SCF), and the correlated second order and diagonal 2ph-TDA approximants. At the zeroth order, there is no resonant root for Mg and the resonance energy and width for the 2P shape resonance in e-Ca scattering at the zeroth order level is twice as large as that for the second order and diagonal 2ph-TDA approximants.

Relaxation effects seem to be the most important in the formation and decay of shape resonances, since there is no resonant root for Mg at the bi-variational SCF level and the values obtained for Be and Ca from the zeroth order approximation (bi-variational SCF) are much larger than that from second order and diagonal 2ph-TDA self energy approximations. In the complex Δ SCF calculations /64/ for the 2P shape resonance in e-Ca scattering, the resonance energy and width have been calculated from $E_{(Ca^-)^*}(\theta_{opt}) - E_{Ca}(\theta = 0)$, where the star denotes the resonant state. Our propagator calculations evaluate $E_{(Ca^-)^*}(\theta_{opt}) - E_{Ca}(\theta_{opt})$. Since the basis set used for both the calculations is same and exhaustive, the θ dependence of E_{Ca} is expected to be negligibly small as assumed in the Δ SCF calculation /64/. We have utilized the same basis, and since Δ SCF provides full relaxation permitted by the basis set, the difference in calculated resonance energy and width between Δ SCF values and those from our own Σ^2 and $\Sigma^{2ph-TDA}$ calculations must be due to polarization effects. We may thus surmise that the polarization has considerable effect on the resonance energy but has little impact on the width of the resonance. The results from the more demanding diagonal 2ph-TDA approximation however, offer only a marginal improvement over those obtained with the second order approximation.

3.2 Shape Resonances in e-Molecule Scattering

The basic computational difference between the use of complex scaling for the treatment of atomic and the molecular resonances stems from the non dilatation-analyticity of the Born-Oppenheimer Hamiltonian /80-83/ when only the electronic coordinates are subjected to complex scaling. As noted earlier in section 2.4 a computationally tractable solution which preserves the bi-orthogonality of the orbital basis thereby permitting the use of the same atomic bi-orthogonal dilated electron propagator apparatus is offered by the Moiseyev-Corcoran method of treating nuclear attraction integrals for the dilated Hamiltonian /82/. We have followed this modified procedure in the solution of our molecular bi-variational SCF equations /21,44-46,48-50/ and the construction of molecular bi-orthogonal dilated electron propagator rigorously follows the rules of non self-dual Grassmann algebra outlined in section 2.3. The results obtained are quite encouraging and for some representative systems we discuss them in the following subsections.

3.2.1 Resonances in electron scattering by diatomic molecules

The resonances in scattering of electrons off diatomic molecules have a long history /16/ and the initial application of the dilated electron propagator to the $^2\Pi_g$ shape resonance in e-N₂ and $^2\Pi$ shape resonance in e-CO scattering is due to their appeal as representative homo and hetero-nuclear diatomic systems which are also isoelectronic and therefore lend themselves to a comparative study /18,19/.

$^2\Pi_g$ e-N₂ Shape Resonance

Many body treatments of the $^2\Pi_g$ e-N₂ shape resonance have been done using second order self energy in complex electron propagator calculations /48/ and scattering calculations that employ many different self energy approximants as the scattering potential /13/. The scattering calculations /13/ have employed a (5s 4p 2d) basis and this same basis has been employed in bi-orthogonal dilated electron propagator calculation /99/ to compare results from complex scaling with those from scattering calculations. The role of basis set effects in bi-orthogonal dilated electron propagator calculations has been examined by calculating the $^2\Pi_g$ e-N₂ shape resonance attributes with the (4s 9p) basis employed in an earlier second order complex scaled electron propagator calculation based on real SCF /48/. The results obtained from the application of the different decouplings of the bi-orthogonal dilated molecular electron propagator employing the (5s 4p 2d) and the (4s 9p) bases are shown in figures 7a and 7b respectively. The values of the energy and width of this resonance from the different decouplings and the two different bases along with those from experiment and other theoretical methods are collected in table IV. For both the bases, the value of the width from different decouplings is almost same and the resonant trajectories for the zeroth order and the two quasi-particle (Σ_q) approximations come close at the point of quasi-stability in fig. 7. The resonance energy from the decouplings devoid of orbital relaxation (Σ^0 , Σ_q^2 , $\Sigma_q^{2ph-TDA}$) is almost same but markedly different from that given by the second order (Σ^2) and the diagonal 2ph-TDA ($\Sigma^{2ph-TDA}$) approximations. This indicates that orbital relaxation has a prominent role in metastable electron attachment. The second order resonance energy is lower compared to that from the diagonal 2ph-TDA decouplings for both the bases and this behavior of the diagonal 2ph-TDA will be seen to persist for other systems as well.

The results from the dilated electron propagator calculations using the (5s 4p 2d) basis are close to those from scattering calculations employing same decouplings (table IV) and inspire confidence in the complex scaling results. The acute basis set dependence is brought out by the considerable disparity in results from the (4s 9p) and the (5s 4p 2d) bases. The large difference between results from the two bases underscore the need for independent study

of basis set effects in resonance calculations. An attempt to understand these differences by examining the corresponding FDAs is made later in section 5.2.

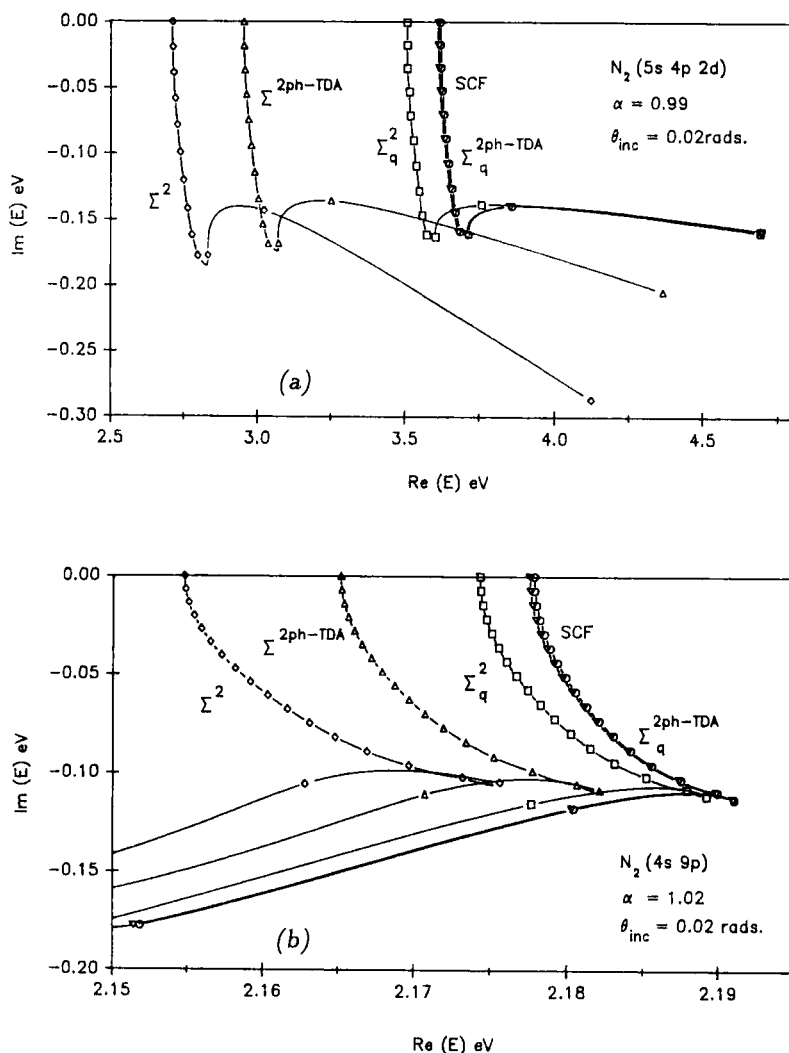


Figure 7. Resonant trajectories from different decouplings for N_2 using the (a) $(5s \ 4p \ 2d)$ and (b) $(4s \ 9p)$ bases. The resonance energy from the decouplings devoid of orbital relaxation (Σ^0 , Σ^2_q , $\Sigma^{2\text{ph-TDA}}_q$) is almost same but markedly different from that given by the second order (Σ^2) and the diagonal 2ph-TDA ($\Sigma^{2\text{ph-TDA}}$) approximations.

Table IV
Energy and Width of the $^2\Pi_g$ N_2^- Shape Resonance

Method/Reference	Energy (eV)	Width (eV)
Experiment /16,100/	2.20	0.57
Static Exchange /101//Static Exchange R-Matrix /102/	3.70/2.15	1.16/0.34
Stabilization Method /103/	2.44	0.32
R-Matrix /104/	3.26	0.80
Stieltjes Imaging Technique /105/	4.13 ^a /2.23 ^b	1.14/0.40
Many-Body Optical potential /12,13/	3.80 ^c /2.61 ^d /2.54 ^e	1.23/0.58/0.54
Complex SCF /106/	3.19	0.44
Second Order Dilated Electron Propagator (real SCF) /48/	2.14	0.26
Bi-orthogonal Dilated Electron Propagator using (4s 9p) basis /44/	2.19 ^{f,g,h} /2.18 ⁱ /2.18 ^j	0.23/0.21/0.22
Bi-orthogonal Dilated Electron Propagator using (5s 4p 2d) basis /this work/	3.72 ^{f,h} /3.61 ^g /2.83 ⁱ /3.07 ^j	0.32/0.33/0.35/0.35

^a Frozen Core

^b Configuration Interaction

^c Static Exchange

^d Second order

^e ADC(3)

^f Zeroth order

^g Quasiparticle Second order

^h Quasiparticle diagonal 2ph-TDA

ⁱ Second order

^j Diagonal 2ph-TDA

$^2\Pi$ e-CO Shape Resonance

The resonant θ -trajectories from different decouplings are displayed in figs. 8a and 8b where it is seen that optimal value of the radial scale factor α is different for the methods with (Σ^2 and $\Sigma^{2ph-TDA}$) and without (Σ^0 , Σ_q^2 , $\Sigma_q^{2ph-TDA}$) orbital relaxation.

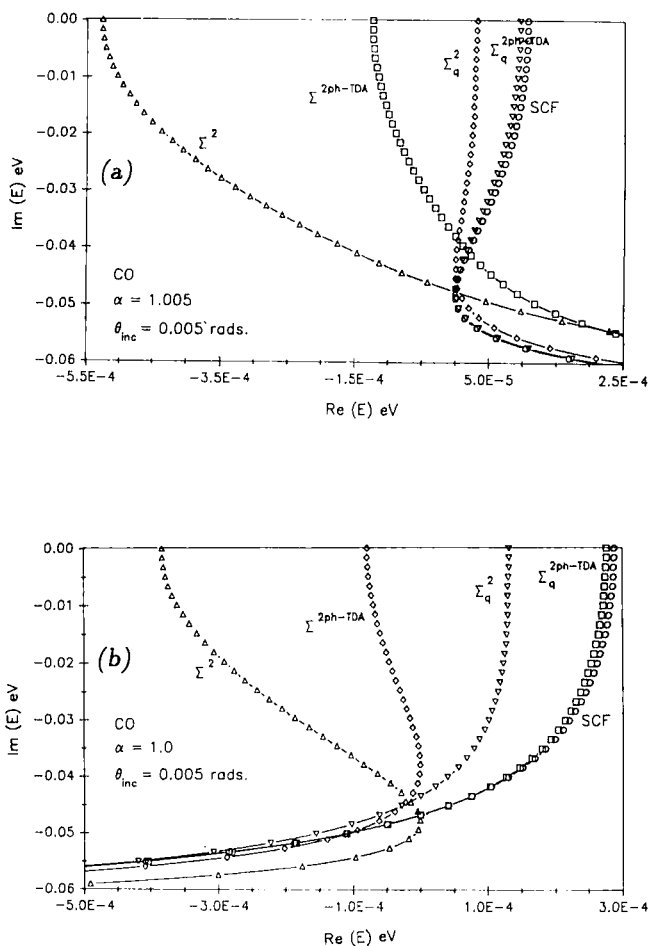


Figure 8. Resonant trajectories from different decouplings for CO. The radial scale factor required to unmask the resonance using the Σ^0 , Σ_q^2 and $\Sigma_q^{2ph-TDA}$ decouplings (a) is different from that at the Σ^2 and $\Sigma^{2ph-TDA}$ levels, (b). Trends from fig. 7 persist.

Table V
Energy and Width of the $^2\Pi$ CO $^-$ Shape Resonance

Method/Reference	Energy (eV)	Width (eV)
Experiment /100/	1.50	0.40
Boomerang Model /107/	1.52	0.80
T Matrix Method /108/	3.40	1.65
Close Coupling Method /109/	1.75	0.28
Second Order Dilated Electron Propagator (real SCF) /49/	1.71	0.08
Zeroth order, Quasiparticle Second order and Quasiparticle Diagonal 2ph-TDA Bi-orthogonal Dilated Electron Propagator /45/	1.71	0.10
Second order Bi-orthogonal Dilated Electron Propagator /45/	1.68	0.09
Diagonal 2ph-TDA Bi-orthogonal Dilated Electron Propagator /45/	1.69	0.08

Table V has the values for the resonant energy and the width for this resonance obtained by the different decouplings along with those from other methods as well as experiments. The radial scale factors required to uncover the $^2\Pi$ CO $^-$ resonance using the methods without orbital relaxation (Σ^0 , Σ_q^2 , $\Sigma_q^{2ph-TDA}$) and those with orbital relaxation and correlation (Σ^2 and $\Sigma_q^{2ph-TDA}$) are different but the energies and the widths computed by all these decouplings are close to each other (table V). The extreme sensitivity to α -values seen in figs. 8a and 8b denotes the delicate nature of the resonance characterization and its acute dependence on both the primitive and the orbital bases. It is somewhat reassuring that though the resonant pole is approached from opposite sides by the Σ^0 , Σ_q^2 , $\Sigma_q^{2ph-TDA}$ decouplings (fig. 8a) and the Σ^2 and $\Sigma_q^{2ph-TDA}$ decouplings (fig. 8b), these become resonant at almost the same point in the complex E-plane.

The value for resonance energy calculated using the bi-orthogonal dilated electron propagator is quite reasonable but the width of the $^2\Pi$ CO $^-$ using different decouplings is close only to that from the boomerang model. The

calculated width from all decouplings is much narrower than the experimental value. Narrowness of the width implies under-representation of the inter-nuclear and interelectronic repulsion and could be due to inadequacy of the primitive basis and level of correlation employed here and indicates the need for calculations employing higher order (Σ^3 , Σ_q^4 , ADC(3)) decouplings as well as more flexible and extensive basis sets.

3.2.2 Resonances in electron scattering by polyatomic molecules

The HOMO-LUMO based reactivity theories are at the heart of mechanistic pictures in organic chemistry /110/ and the simplest prototypical representative with well established pictures of HOMO and LUMO is the ethylene molecule for which Hückel theory calculations are routine in characterizing its frontier orbitals. While qualitative correlations abound /18,19/, a rigorous quantitative investigation of this simple prototypical polyatomic molecule is specially significant /45,46/ and results from our own calculations are discussed below.

$^2B_{2g}$ e- C_2H_4 Shape Resonance

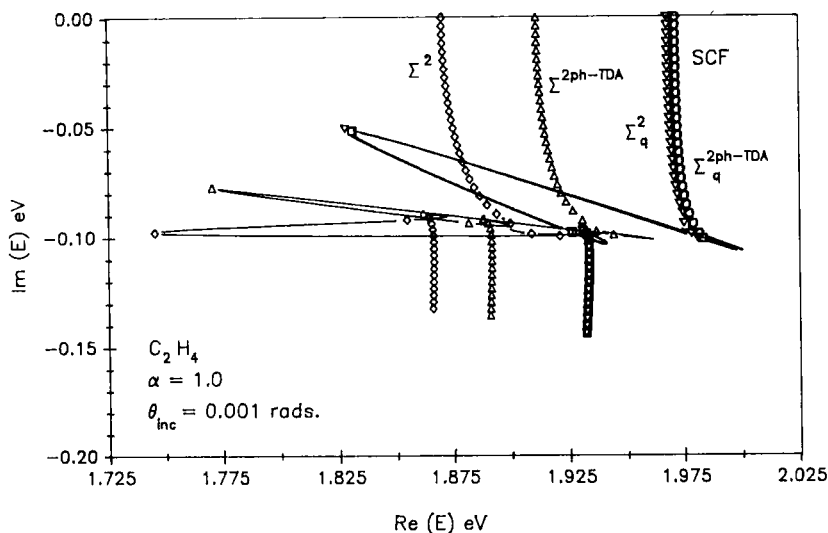


Figure 9. Resonant trajectories from different decouplings for C_2H_4 . The lowering of LUMO energy by the decouplings incorporating orbital relaxation (Σ^2 and $\Sigma^{2ph-TDA}$) is seen for this system as well.

The resonant θ -trajectories from different decouplings are plotted in fig. 9. The energy and the width for this resonance from different decouplings and those obtained by experiment and other methods are collected in table VI. That there is a cross-systemic validity to our explanations is made clear by fig. 9 where just like in the case of N_2 and CO, the decouplings devoid of orbital relaxation (Σ^0 , Σ_q^2 , $\Sigma_q^{2ph-TDA}$) clump together and once again maximum lowering of the HOMO-LUMO gap is offered by the second order self energy approximant. The resonance energy from different decouplings are quite reasonable but the calculated widths are once again much narrower, perhaps for the reasons cited earlier.

Table VI
Energy and Width of the $^2B_{2g}$ $C_2H_4^-$ Shape Resonance

Method/Reference	Energy (eV)	Width (eV)
Experiment /111/	1.78	0.70
Complex Kohn /112/	1.84	0.46
Second Order Dilated Electron Propagator (real SCF) /50/	1.71	0.08
Zeroth order, Quasiparticle Second order and Quasiparticle Diagonal 2ph-TDA Bi-orthogonal Dilated Electron Propagator /45/	1.93	0.19
Second order Bi-orthogonal Dilated Electron Propagator /45/	1.86	0.18
Diagonal 2ph-TDA Bi-orthogonal Dilated Electron Propagator /45/	1.89	0.18

4 The Auger Resonances

As discussed earlier the spectral representation of the matrix dilated electron propagator

$$G_{\text{sr}}(\eta, E) = \lim_{\epsilon \rightarrow 0^+} \sum_{\mathbf{s}} \left[\frac{\langle \mathbf{N}_0 | \mathbf{a}_{\mathbf{s}} | \mathbf{N}_{\mathbf{s}}^{N+1} \rangle \langle \mathbf{N}_{\mathbf{s}}^{N+1} | \mathbf{a}_{\mathbf{s}}^\dagger | \mathbf{N}_0 \rangle}{E - (E_{\mathbf{s}}^{N+1}(\eta) - E_0^N) + i\epsilon} + \frac{\langle \mathbf{N}_0 | \mathbf{a}_{\mathbf{s}}^\dagger | \mathbf{N}_{\mathbf{s}}^{N-1} \rangle \langle \mathbf{N}_{\mathbf{s}}^{N-1} | \mathbf{a}_{\mathbf{s}} | \mathbf{N}_0 \rangle}{E - (E_0^N - E_{\mathbf{s}}^{N-1}(\eta)) - i\epsilon} \right] \quad (92)$$

provides for the simultaneous calculation of both the energy (real part) and the width (twice the imaginary part) of electron detachment Auger ($E_0^N - E_{\mathbf{s}}^{N-1}(\eta)$) and electron attachment shape resonances ($E_{\mathbf{s}}^{N+1}(\eta) - E_0^N$) from its appropriate poles. The pole structure of the dilated electron propagator has been discussed in some detail in section 2.3 and it is obvious from eqn. (92) that since resonant eigenvalues ($E_{\mathbf{s}} - i\frac{\Gamma}{2}$) have a negative imaginary part to account for their finite life time /52,53,113/, and the target ground state energy E_0^N is completely real, the poles corresponding to the Auger resonances will have a positive imaginary part and their trajectory as a function of variations in the scaling parameter α or θ will move in the first quadrant of the complex Energy plane and the complex poles in the first quadrant displaying quasi-stability with respect to variations in η may be associated with Auger resonances /24,26/. Application of the second order, diagonal 2ph-TDA and quasiparticle decouplings to the treatment of electron detachment ($1s^{-1}$) Auger resonance in Be^+ therefore offers a complementary test for the comparative effectiveness of these decouplings of the dilated electron propagator. Recent applications /42/ have also revived the issue of balance in various self-energy approximations and these receive attention in the following subsections.

4.1 Energy and width of the $\text{Be}^+ (1s^{-1}) \ ^2\text{S}$ resonance

Results from our calculations /42/ using various decouplings of the dilated electron propagator discussed earlier are portrayed in figs. 10 and 11. The marked disparity between the theta trajectories for the uncorrelated SCF and propagator poles makes apparent the magnitude of correlation and relaxation effects attending the Auger resonance formation. From fig. 11 it is seen that the diagonal 2ph-TDA approximation predicts higher energy and smaller width (longer life time) for the $\text{Be}^+ (1s^{-1}) \ ^2\text{S}$ Auger resonance. The choice of basis set and the optimal α value (0.85) are those from an earlier study /26/. The theta trajectories for the quasiparticle diagonal 2ph-TDA for this optimal alpha shows multiple inflection points and cusps and therefore theta trajectories for other nearby alpha values have also been plotted in fig. 12.

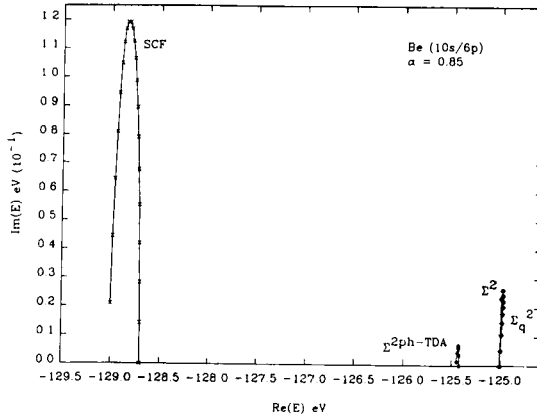


Figure 10. *Theta trajectories for the $\text{Be}^+ (1s^{-1})$ Auger pole from the zeroth (bi-variational SCF), second order (Σ^2), quasiparticle second order (Σ_q^2), diagonal 2ph-TDA ($\Sigma^{2\text{ph-TDA}}$) and quasiparticle diagonal 2ph-TDA ($\Sigma_q^{2\text{ph-TDA}}$) decouplings of the diluted electron propagator. The disparity between the theta trajectories for the SCF and propagator poles makes apparent the magnitude of correlation and relaxation effects attending the Auger resonance formation.*

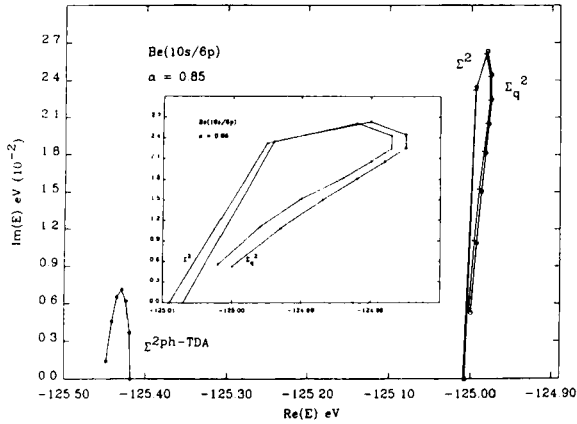


Figure 11. *Same as fig. 10 but without the zeroth order decoupling. The diagonal 2ph-TDA results predict higher energy and smaller width for the Auger resonance. A magnified version of the second order (Σ^2), and the quasiparticle second order (Σ_q^2) trajectories is displayed in the inset.*

Because of multiple regions of quasi-stability in many of these trajectories, the quasi-stable value of the Auger pole for this decoupling has been elicited from the alpha trajectory for $\theta = 0.17$ radians, the angle for which there is a clear stability in the only regular trajectory ($\alpha = 0.75$) from this decoupling. The theta trajectories for other α values also display some stability for $\theta_{\text{opt}} = 0.17$ radians in the sense of more rapid decrease in ΔE as a function of the same uniform $\Delta\theta$ stepsize (i.e. numerical stability at least to first order). This alpha trajectory for the quasi-particle 2ph-TDA decoupling is displayed in fig.

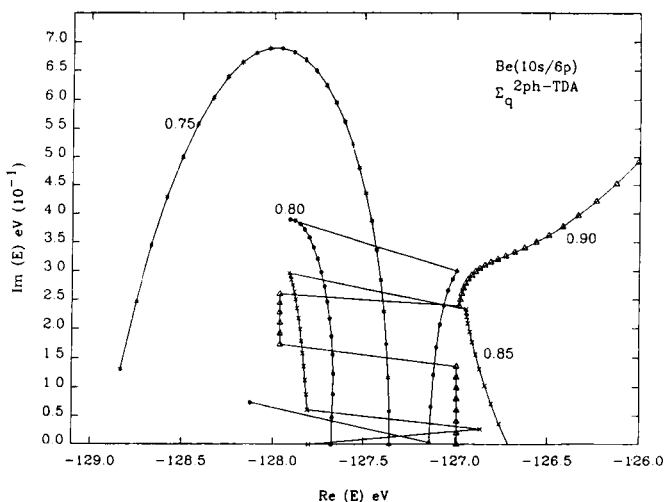


Figure 12. θ trajectories for different values of α for the quasiparticle diagonal 2ph-TDA ($\Sigma_q^{2\text{ph-TDA}}$) decoupling. Because of multiple points of quasi-stability for many trajectories, the quasi-stable value of the resonant pole is elicited from the corresponding α trajectory in fig. 13.

13 where the distances narrow as we approach $\alpha = 0.85$ and then increase again. This quasi-stable value in the alpha trajectory has been taken as the best estimate of the resonant Auger pole from this decoupling /42/. The values for the energies and widths of the $\text{Be}^+ (1s^{-1}) \ ^2\text{S}$ Auger resonance from these calculations along with experimental and other theoretical results are collected in table VII.

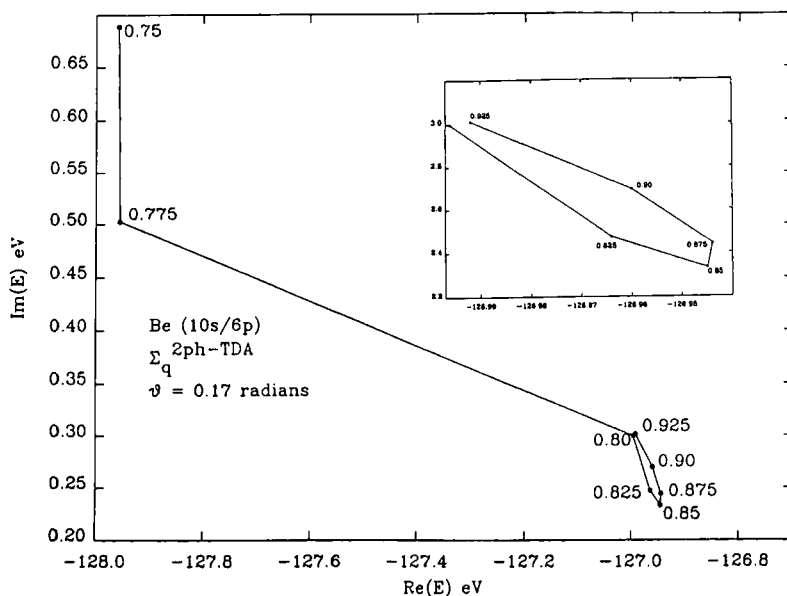


Figure 13. α trajectory for $\theta = 0.17$ radians for the quasiparticle diagonal 2ph-TDA ($\Sigma_q^{2ph-TDA}$) decoupling. The distances narrow as $\alpha = 0.85$ is approached and then increase again. The quasi-stable value of the pole at this alpha value is therefore taken to be the best estimate of the energy and width of the Auger resonance from this decoupling.

4.2 Auger resonances and the need for consistent decouplings

It is clear from figs. 10-13 and table VII that, results from both the the diagonal 2ph-TDA and quasiparticle diagonal 2ph-TDA seem to move away from the second order results towards those from the uncorrelated zeroth order bi-variational SCF calculations. Instead of being an improvement on the second order results, they deviate even more from the experimental /114,115/ and other more reliable theoretical calculations /116/. This behavior of the diagonal 2ph-TDA where they offer little or no improvement on the second order results has also been observed in our molecular shape resonance calculations /40,41,44,45/. The Auger decay is a correlated event and its description at the SCF level is not meaningful, and the energy and widths from bi-variational SCF are included only to assist in assessing the role of correlation and relaxation in the characterization of the Auger resonance, as also to highlight the relatively poor quality of diagonal and quasiparticle diagonal 2ph-TDA results

for this case.

Table VII
Energy and Width of the $\text{Be}^+ (1s^{-1}) \ ^2\text{S}$ Auger resonance.

Method/Reference	Energy (eV)	Width (eV)
Experiment /114,115/	123.63	...
Many Body Perturbation Theory /117/	...	0.09
Electron Propagator with Siegert Boundary condition /24/	125.47	0.02
Second Order Dilated Electron Propagator /26/	124.98	0.05
Quasiparticle Second order Dilated Electron Propagator /42/	124.98	0.05
Diagonal 2ph-TDA Dilated Electron Propagator /42/	125.43	0.02
Quasiparticle Diagonal 2ph-TDA Dilated Electron Propagator /42/	127.90	0.54
Zeroth order Dilated Electron Propagator /42/	128.80	0.24

The diagonal 2ph-TDA is an appealing approximation for reasons mentioned earlier and discussed in much greater detail elsewhere /3,6/. However, it is also well known that though it is consistent upto second order, it is incomplete in third and higher orders. This has led to a somewhat mixed result where the diagonal 2ph-TDA does not always offer an improvement over second order results. The imbalance is compounded by the use of an uncorrelated reference state since many important third and higher order diagrams which should have been non-zero become zero in such calculations /9/. This imbalance has been noted by von Niessen et. al. /6/ and Öhrn and Born /3/ have reviewed this with many numerical examples. A similar imbalance in the diagonal 2ph-TDA approximation even in the case of dilated electron propagator calculations is also seen and therefore care must be exercised in its use.

As seen from the results discussed earlier, the imbalance in the diagonal 2ph-TDA approximation seems to be aggravated by the quasiparticle approximation to this decoupling. The problem with quasiparticle diagonal 2ph-TDA could be again due to the inconsistent way in which non-diagonal diagrams which contribute to both the initial (2p-h term) and final (2h-p term) state correlations are excluded. This seems to lead, in this case, to a requirement of large rotation pushing the resonant pole higher into the complex energy plane thereby increasing its width in this approximation. The ADC(3) type consistent extended 2ph-TDA decouplings offer obvious advantages but are much more computationally demanding.

A comparison of equations 66, 69 and 70 makes obvious the somewhat more complicated and expensive nature of the diagonal 2ph-TDA implementation, since the calculation of the denominator shift in eqn. 69 necessitates extra calls for recovery of the transformed two electron integrals needed to compute Δ . On the other hand, as evidenced in both figs. 10 and 11, as also in table VII, the diagonal quasiparticle approximation which obviates the need for construction of the full non-diagonal self energy matrix (and thereby repeated diagonalizations as well) offers results for the second order decoupling which is more or less indistinguishable from its much more expensive full non-diagonal counterpart.

Our results therefore seem to indicate that the extra effort in implementing the diagonal 2ph-TDA approximation for the dilated electron propagator calculations is unwarranted, at least from the experience gained in this and some other investigations /40,41,44,45/.

Finally, our investigations do seem to indicate that the dilated electron propagator technique may be profitably employed in the investigation of Auger resonances. There is a need for employing consistent 2ph-TDA approximations like the ADC(3) decouplings and while the simplicity of the diagonal 2ph-TDA/ diagonal quasiparticle 2ph-TDA decouplings retain the same appeal as in the case of real electron propagator, our results in this case seem to imply that these approximations should be employed with care. The effectiveness of the quasiparticle second order approximation even for a core Auger hole calculation, however, is a pleasant surprise and we recommend this welcome economy in all dilated electron propagator calculations but with an additional caveat that such approximations are known to break down for systems with low symmetry and large number of electrons /6/ and there is a need to exercise due caution in their use. Some of this has been already evident in the case of our molecular calculations. It is also useful to recall that all quantum chemical calculations are only as good as the quality of the primitive basis set employed. The coordinate space span of the primitive basic set is critical to the description of resonances /43/. The basis set used for the Be^+ Auger calculations is same as that used for the $^2\text{P Be}^-$ shape resonance calculations /25,26,39-41,43/

and while it demonstrates the ability of the dilated electron propagator to simultaneously treat both the electron attachment and detachment resonances from a single calculation, the basis set requirements for the two are bound to be different and an exhaustive study of the basis set effects needs attention.

4.3 Numerical considerations for the treatment of Auger Satellites

While the diagonal 2ph-TDA has been indicted quite severely in the previous subsections, we should mention that results presented here are not sufficient by themselves to draw definitive conclusions regarding the techniques used and based on earlier experience /118,119/ the dilated diagonal 2ph-TDA could be quite effective in the treatment of Auger satellites. These Auger satellites however cannot be investigated using the pole search procedures currently employed in the dilated electron propagator calculations /21,47,39/. Iterative diagonalization of the $L(E)$ matrix where E^{n+1} is selected as the \mathcal{E}_n nearest to E^n automatically locks on to the principal poles and does not permit the treatment of inner valence Auger satellites. The poles may also be searched as complex E values for which $\det|G^{-1}(E)| = \det|E1 - L(E)| = 0$ but effective algorithms to find zeros of a complex function of complex argument are known to be demanding. Perhaps bi-variate interpolations coupled with two-dimensional Newton-Raphson type procedure in both variables ($\text{Re}(E)$, $\text{Im}(E)$) could be a fruitful avenue for further investigations and this promise of extending the domain of applications of the dilated electron propagator to the treatment of Auger satellites merits consideration.

5 The Orbital Picture of Resonances from different Decouplings of the Dilated Electron Propagator

The shape resonances are believed to result when the impinging electron is temporarily captured in an unoccupied orbital of the target /17-19/. While qualitative correlation between orbital shapes and electron-scattering resonances has been attempted earlier /17,18,64/, a quantitative investigation of the resonant orbital(s) has not been undertaken so far since any study of this nature first and foremost, requires a reliable mechanism for an unequivocal identification of the *resonant* orbital from other unoccupied (virtual) orbitals of the target. We have shown that the dilated electron propagator based on the bi-variational SCF may be successfully used to isolate the resonant orbital/Feynman Dyson amplitudes which characterize the 2P shape resonances in e-Be, e-Mg and e-Ca scattering /25,26,39-41/.

In this section, we examine the orbital/FD amplitudes for the resonant poles with a view to ascertain characteristics like the radial extent, nodal pattern and region of maximum localization of the captured electron in the resonant orbital. The resonant behavior of the poles is limited to a certain interval of quasi-stability with respect to variations in η and the complex scale factor plays a critical role in turning a scattering type orbital on the real line ($\eta = 1.0$) into a resonant orbital for $\eta_{\text{opt}} (= \alpha_{\text{opt}} e^{i\theta_{\text{opt}}})$. As seen earlier in section 3.1, in e-Be and e-Ca scattering /26,40/ the ^2P shape resonance is described by a single orbital/FD amplitude. The ^2P shape resonance in e-Mg scattering /39/ however, is found to be multi-orbital. A pertinent issue here is the role of the additional orbitals whose energies fall within the width of the ^2P shape resonance in e-Mg scattering and the deciphering of the role of this mixing of orbital/FD amplitudes in the stabilization of resonances, has provided important insights /43/.

SCF orbitals and Feynman-Dyson amplitudes are different linear combinations of the same primitive Gaussian Type Orbitals (GTOs) and the ultimate limitation in the orbital description of these resonances is the coordinate space span of these primitive GTOs. A plot of the resonant orbital/FD amplitude is, therefore, also useful in identifying the features in the primitive basis which will provide the requisite attributes for adequate description of shape resonances and thereby shed some light on extreme sensitivity to basis sets seen in resonance calculations. The difference between the radial density distribution given by the resonant orbital (zeroth order FD amplitude) and the corresponding FD amplitude from second order/diagonal 2ph-TDA decoupling should offer some insight in the role of correlation and relaxation effects in the formation and decay of resonances. A discussion of the results from attempts to investigate these attributes by examining *the resonant* orbital and Feynman Dyson amplitudes is the principal focus of this section. Atomic resonances are analyzed in the following subsection. The resonant molecular orbitals/FD amplitudes are discussed in subsection 5.2.

5.1 Feynman Dyson Amplitude as the correlated orbital

In this section we investigate the factors affecting the formation and decay of shape resonances by examining the radial charge density /120/ plots from the Feynman Dyson amplitudes corresponding to the resonant poles identified earlier /22,25,26,40,41/ in sections 3.1 and 3.2 for different atomic and molecular resonances.

Due to the non-hermiticity of the complex scaled Hamiltonian, there is no orthonormality among the orbitals themselves, but there exists a bi-orthonormality $\int (\psi_i^*(r, \theta, \phi))^* \psi_j(r, \theta, \phi) d\tau = \delta_{ij}$ between the orbitals and their com-

plex conjugate obtained from the bi-variational SCF procedure /60-62,84/ and a plot of $4\pi r^2 |\psi^2(r)|$ furnishes an appropriate measure of the magnitude of the radial charge density at distance r from the nucleus. For ease of differentiation between the radial charge density plots from the zeroth (bi-variational SCF orbital) and higher order (second order/diagonal 2ph-TDA) Feynman-Dyson amplitudes, even though only the radial part of ψ (orbital) or χ (FD amplitude) is being plotted, we retain the symbol for the full orbital/FD amplitude.

The maximum in the radial charge density (r_{\max}) for the outermost valence orbital for each target atom is taken as a rough guide for the radial extent of that atom and the extent of penetration of the impinging electron may be established by determining the r_{\max} for the electron density plot from the corresponding resonant FD amplitude. To discount for any effect of the deviation of α_{opt} from 1.0 on the localization of the impinging electron, the valence orbitals for Be, Mg and Ca are plotted at the same α_{opt} value as that for which the pole corresponding to the *resonant* orbital/FD amplitude shows the requisite quasi-stability /25,26,39-41/. The number of nodes in the radial charge density plots for the resonant FD amplitudes reveal the principal quantum number of the p-type target orbital/FD amplitude involved in the resonance formation. The difference between the radial charge densities from the uncorrelated zeroth order orbital and the correlated (second order/diagonal 2ph-TDA) FD amplitude(s) may be used to investigate the effect of correlation/relaxation in the formation and decay of shape resonances. Similarly, the role of the complex scaling parameter may be investigated by examining the difference between radial charge densities from orbital/FD amplitudes calculated for $\theta = 0.0$ and $\theta = \theta_{\text{opt}}$. The results for the different atomic systems investigated in this fashion are discussed below.

e-Be

A rough guideline for the radial extent of all the target atoms to be discussed here may be obtained by determining the distance from the nucleus at which the maximum in the radial charge density plot (r_{\max}) is observed for the outermost valence orbital of the target. For Be, the radial charge densities for the 2s orbital and the corresponding FD amplitudes from the 2nd order and diagonal 2ph-TDA decouplings are plotted in fig. 14.

Though the main figure cannot distinguish between the charge densities from different decouplings on the ordinate scale employed here, the difference between the densities from the second order and the zeroth order decouplings displayed in the inset makes it clear that the slightly higher ionization energy at the level of the second order decoupling /26/ ($\mathcal{E}_{2s} = -8.79$ eV as compared to $\epsilon_{2s} = -8.44$ eV) is due to a slight accumulation of the charge density at the second order level near the Be nucleus which should enhance nuclear binding and somewhat larger build up away from the nucleus to lower interelectronic

repulsion.

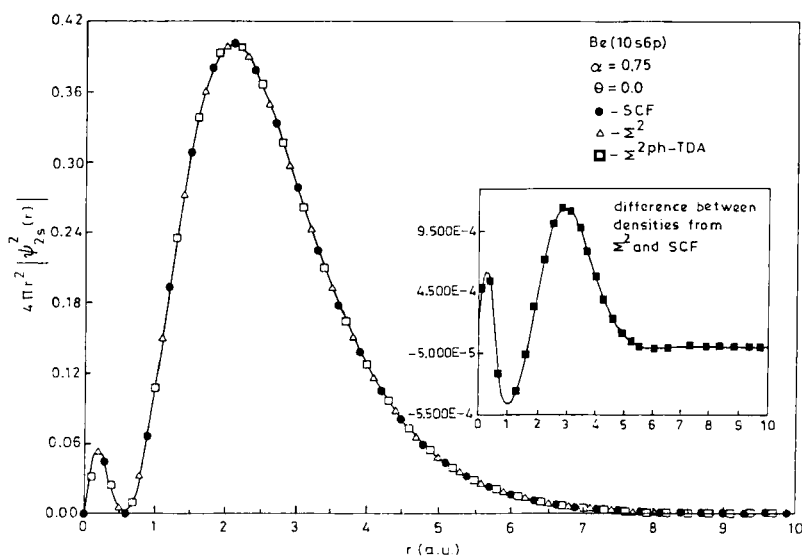


Figure 14. Radial charge density plot from the orbital/Feynman-Dyson (FD) amplitude for the $2s$ orbital in Be from zeroth order (SCF; \bullet), the second order (Σ^2 ; \triangle) and diagonal 2ph-TDA decouplings ($\Sigma^{2ph-TDA}$; \square). On the scale employed in the main plot, distinguishing the orbital/FD amplitudes from different decouplings is not possible but in the inset the difference between radial charge densities from the second and zeroth order (bi-variational SCF) decouplings clearly reveals the role of correlation and relaxation effects in changing the ionization potential from 8.44 eV at the SCF level to 8.79 eV at second order. The maximum in the electron density is at $r_{\max} = 2.1$ a.u.

In this way, the density differences depict the critical role of even the seemingly small correlation and relaxation effects incorporated by the higher order decouplings of the dilated electron propagator. The basis set employed in this calculation is the (10s/6p) Be basis used in many calculations /22,25,26/.

The radial charge density from the resonant orbital is displayed in fig. 15. and the number of radial nodes identify this as a 4p orbital and not the lowest 2p that one would have expected from the successful qualitative correlation of LUMOs with resonances in e-molecule scattering /18/. However, the accumulation of the radial charge density distribution at small r values is a strong reminder of the 2p type orbital density distribution /120/. This feature,

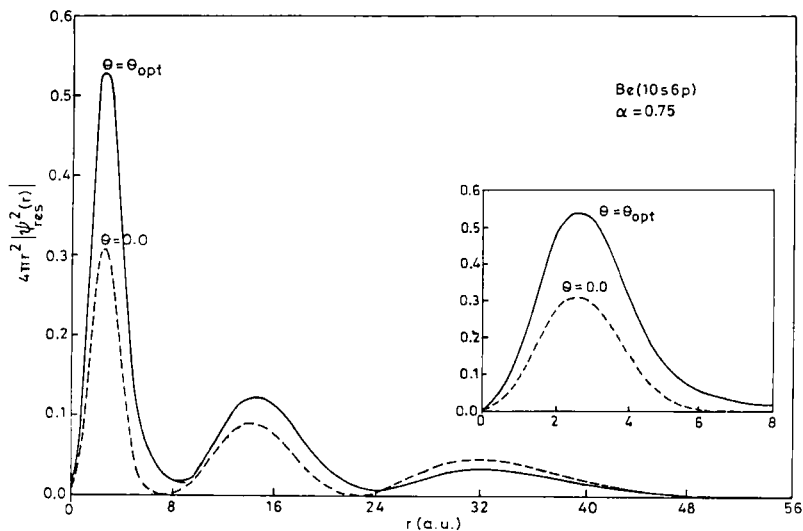


Figure 15. Radial charge density plot for the resonant p -type virtual orbital for dilation angles $\theta = 0.0$ and $\theta = \theta_{\text{opt}}$ (0.42 radians) in e -Be scattering. The role of optimal theta in the accumulation of electron density near the nucleus is clearly seen. In the inset, the maximum is seen to occur at $r_{\text{max}} = 2.5$ a.u., very close to that for the r_{max} of the outer valence $2s$ orbital, seen in fig. 14. Though a cursory look at the nodal pattern identifies this as a $4p$ orbital, the dominant contribution to the charge density distribution is mainly of $2p$ -type.

coupled with the role of multiplication by r^2 which magnifies even the small $|\psi^2|$ values at large r , suggests the resonant orbital to be predominantly a distorted $2p$ type orbital with contributions from $3p$ and $4p$ orbitals. In view of the metastable character of the binding, it is imperative that the orbital charge density should have a mechanism for accumulation near the nucleus (for resonance formation) coupled with features which pull the electron away (and allow its decay). As we shall see for the other systems as well, this competition between resonance formation facilitated by accumulation near the nucleus, with equally significant delocalization far away for its decay is a persistent feature of all resonant orbital(s)/FD amplitudes.

Fig. 15 also shows that as we move from $\theta = 0.0$ on the real line to $\theta = \theta_{\text{opt}}$, the optimal theta leads to an amplification of charge density near the nucleus. The charge density peaks at $r = 2.55$ a.u which is very close to the r_{max} (2.1

a.u.) for the 2s orbital seen in fig. 14 and indicates a localization of the captured electron near the nucleus. The correlation and relaxation provided by second order decoupling is displayed in fig. 16 where it seems that the second order decoupling provides for the building up of electron density in the vicinity of the nucleus through its depletion from large r values. Fig. 16 also shows that the diagonal 2ph-TDA decoupling has less electron density near the nucleus compared to that from the second order which explains why the resonance energy from 2ph-TDA and SCF ($E_{\text{res}} = 0.67\text{eV}$) is somewhat higher than that from the second order decoupling ($E_{\text{res}} = 0.64\text{eV}$) /26,40/.

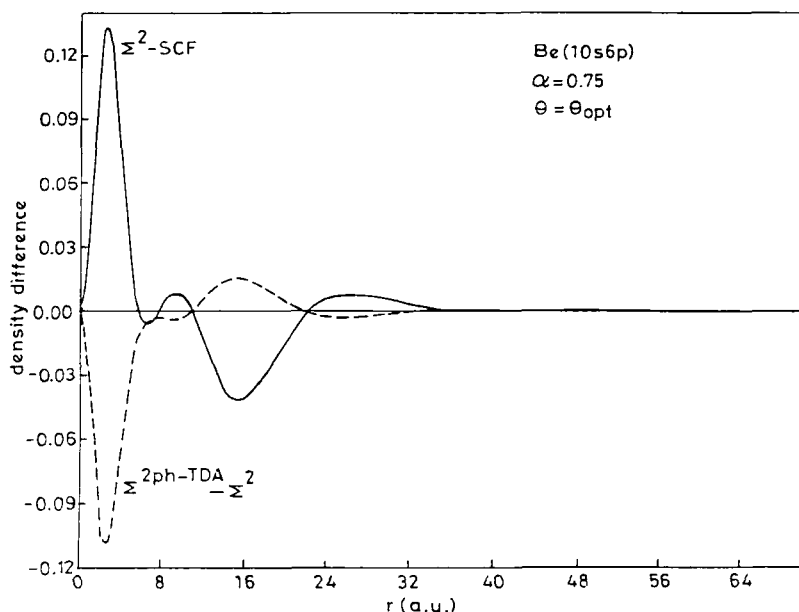


Figure 16. Plot of the difference between the densities obtained from various decouplings of the dilated electron propagator for the resonant orbital/FD amplitude in e -Be scattering at the optimal theta value ($\theta_{\text{opt}} = 0.36$ radians). The second order decoupling provides for building up of electron density in the vicinity of the nucleus as well as its depletion away from the nucleus. The difference between the charge densities from the diagonal 2ph-TDA and second order decouplings shows that the diagonal 2ph-TDA decoupling has less electron density near the nucleus compared to the second order, thereby explaining the higher value of 0.67 eV for the resonance energy at the SCF level and diagonal 2ph-TDA decouplings as compared to $E_{\text{res}} = 0.64$ eV at the second order level.

e-Mg

For the 2P shape resonance in e-Mg scattering, no orbital energy has the requisite theta trajectory to classify it as a resonant orbital /39/ and even at the level of second order and diagonal 2ph-TDA decouplings, there are three different roots which fall within the width of this resonance /39,40/, becoming resonant for different values of the radial scale factor α . The corresponding FD amplitudes have large mixing components from different orbitals. All these features have been taken to indicate that the three roots describe various parts of the same resonant wave packet /39/. The root which becomes resonant at $\alpha = 0.75$ (Root I) is seen to have a large charge density near the nucleus in fig. 17, where the role of the optimal θ in enhancing the charge density near the nucleus is clearly seen. The charge densities from other resonant roots peak far away from the nucleus providing a mechanism for decay, i.e., the three roots seem to act in tandem to achieve metastability. None of the roots has a nodal pattern in the charge density plot which has any semblance with that expected for a conventional p-type orbital and buttresses earlier conjecture about a lack

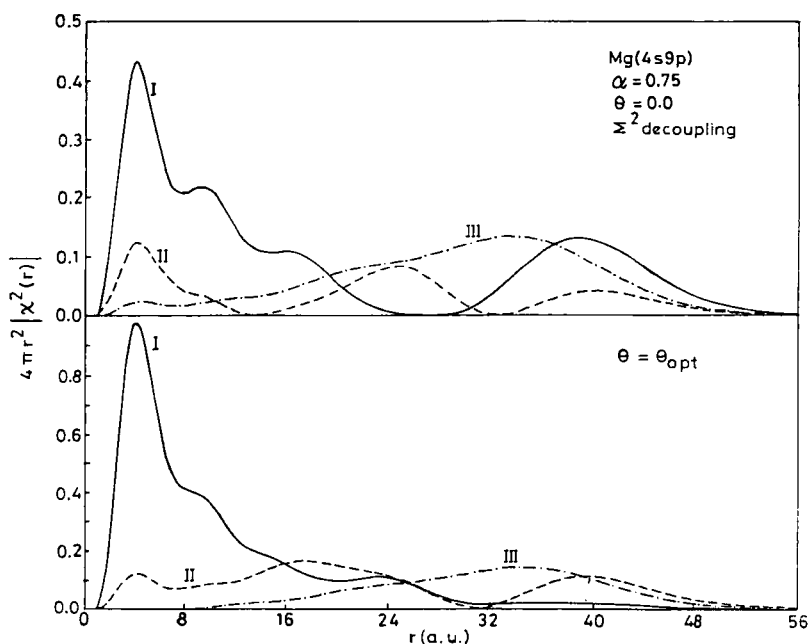


Figure 17. Radial charge density plot for the resonant FD amplitude in e-Mg scattering. For $\alpha = 0.75$ considered here, only the root labelled I is resonant. The role of optimal theta ($\theta_{opt} = 0.12$ radians) in accumulation of electron density near the nucleus is evident.

of single orbital picture for this resonance /39/. In view of the competing demands in the formation and decay of metastable resonances, the root I may be taken to provide for formation and the other two roots for the decay of the shape resonance. A comparison of figs. 17 and 18 once again establishes that the charge density distribution does permit the captured electron to be localized close to the r_{\max} for the valence 3s orbital.

The basis set employed here is the (4s9p) Mg basis used earlier for calculation of 2P shape resonance energy and width by Donnelly /21/ and Mishra et. al. /39/. Among many basis sets used in these investigations, we have selected the results from the (4s9p) basis since this gives resonance energy and width in almost complete agreement with the experimental results /88/.

Since all the three resonant roots fall within the width of the same resonance, in fig. 19 we display a plot of charge density from the linear combination $\chi(r) = \chi_I(r) + \chi_{II}(r) + \chi_{III}(r)$ where the subscripts label the resonant roots identified in fig. 17. Surprisingly, for $\theta = 0.0$, the resultant radial charge density plot is indeed characteristic of a 3p type orbital ! The accumulation of charge density near the nucleus as also at large r values for θ_{opt} seen in fig. 19 indicates large correlation and relaxation effects in the formation and decay of this shape resonance as also the critical role of the complex scale parameter in catering to the inherently contradictory demands of metastability.

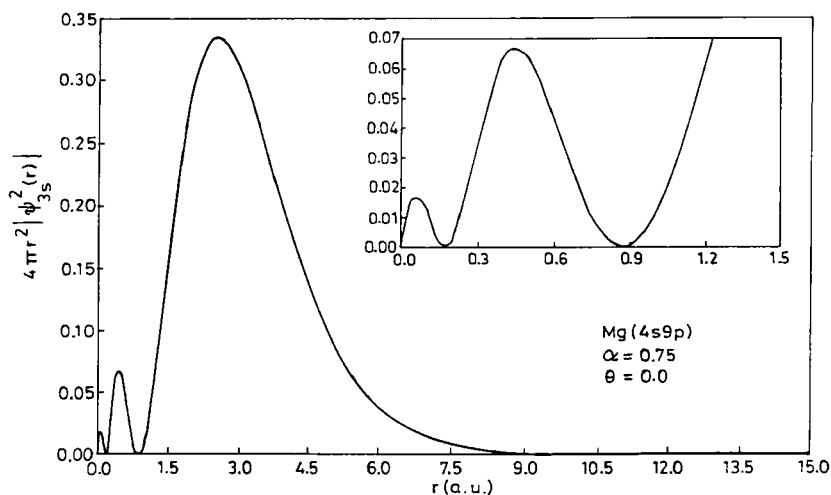


Figure 18. Radial charge density plot for the 3s orbital in Mg. The r_{\max} is at 2.55 a.u.

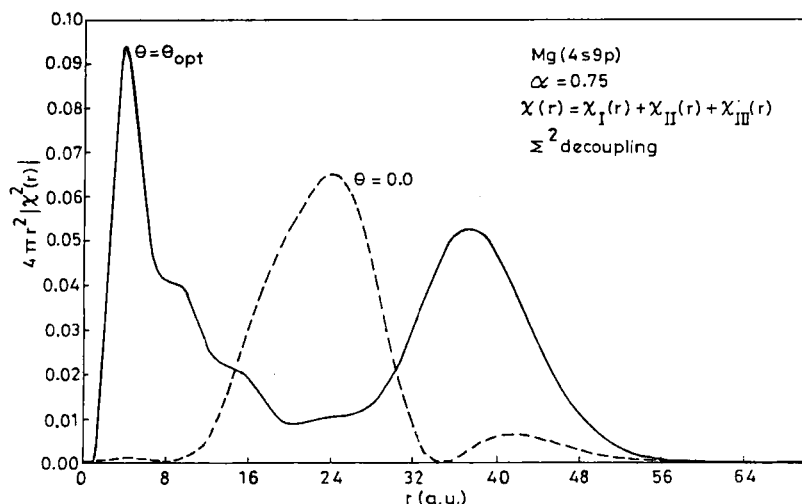


Figure 19. A plot of the charge density obtained from a linear combination of all the resonant amplitudes in e-Mg scattering with $\chi(r) = \chi_I(r) + \chi_{II}(r) + \chi_{III}(r)$, where the individual amplitudes are considered to describe different parts of the same resonant wave packet. The nodal pattern for $\theta = 0.0$ favors its identification as the lowest 3p-type unoccupied orbital of Mg. The role of optimal theta ($\theta_{opt} = 0.12$ radians) in shifting the electron density near the nucleus is clearly seen.

e-Ca

In case of the e-Ca scattering, though there is a single resonant orbital/FD amplitude both at the level of the zeroth (bi-variational SCF), second and diagonal 2ph-TDA approximations, as evidenced by figs. 20 and 21, the SCF orbital has one more node compared to the FD amplitude and consequently the resonance energy calculated at SCF level is much higher ($E_{res} = 0.34\text{eV}$) than that from the resonant propagator pole /40/ ($E_{res} = 0.16\text{eV}$). It is worth emphasizing this dramatic role of correlation in stabilization of this resonance. The charge density distribution, once again has attributes that cater to the competing demands of formation (localization near nucleus) and decay (delocalization away from the nucleus) discussed earlier for e-Be and e-Mg scattering.

The role of the complex scaling parameter θ is same as in the case of e-Be

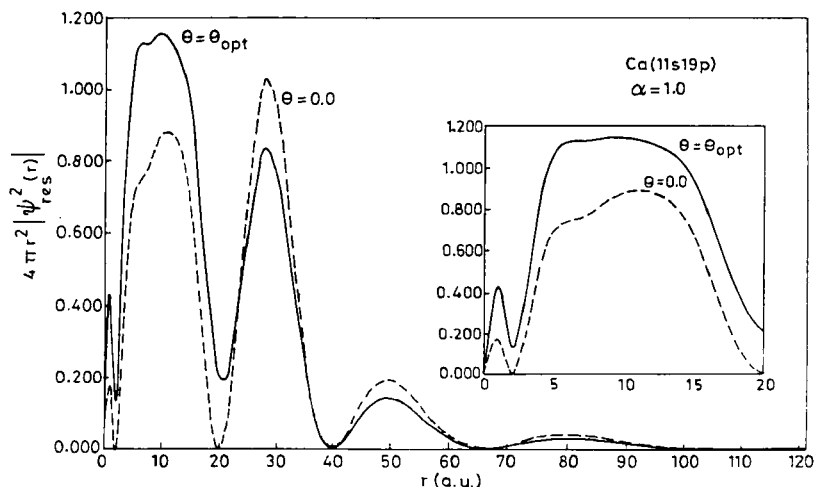


Figure 20. Radial charge density plot for the resonant orbital in e-Ca scattering. The role of optimal theta ($\theta_{\text{opt}} = 0.34$ radians) in the accumulation of electron density near the nucleus with the maximum at $r_{\text{max}} \cong 9$ a.u. is evident. The number of radial nodes identifies it as a 6p-type orbital.

and e-Mg scattering where θ_{opt} again provides greater accumulation of electron density near the nucleus both for the uncorrelated (bi-variational SCF) and the correlated second order decoupling. The role of the complex scaling parameter, however, seems much less pronounced for the second order decoupling.

The nodal pattern of the charge density plots does not lend itself to an easy identification of the resonant orbital/amplitude as a 4p or 5p type orbital and points to the common difficulty in classifying resonances as single orbital phenomena as seen earlier for e-Be and e-Mg shape resonances. A comparison between the r_{max} for the resonant orbital/amplitude with the r_{max} for the valence 4s orbital for Ca plotted in fig. 22 shows that in e-Ca scattering, the impinging electron does not penetrate as close to the target as in e-Be and e-Mg scattering. A comparison of figs. 20 and 21 further reveals that the resonant FD amplitude provides for greater correlation by shifting the r_{max} to larger r values as compared to the r_{max} from the SCF orbital in fig. 22 and yet the resonance energy is lowered because unlike in the case of the resonant orbital, the overall probability density for the resonant FD amplitude (fig. 21)

is shifted closer to the nucleus. This seems to indicate an important role for the dynamic correlation in the temporary binding of the impinging electron.

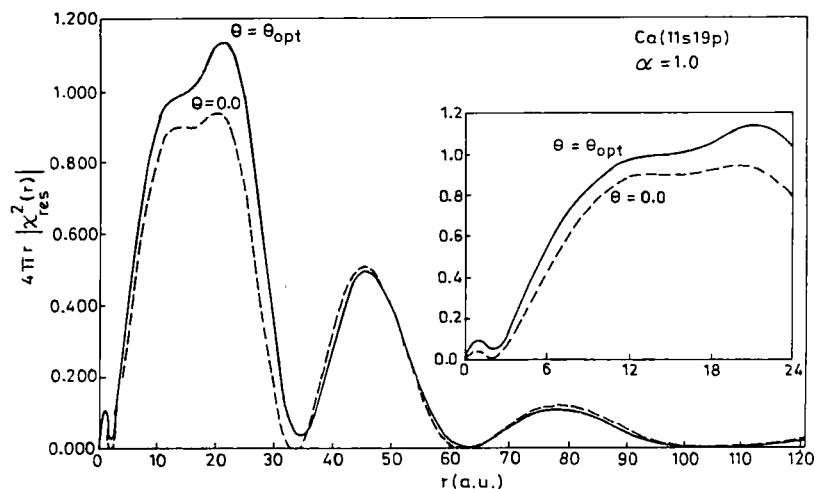


Figure 21. Radial charge density plot for the resonant FD amplitude in e -Ca scattering. The number of radial nodes for the resonant FD amplitude identifies it as a $5p$ -type orbital with a predominantly $4p$ -type character. The role of optimal theta ($\theta_{opt} = 0.29$ radians) in accumulation of electron density near the nucleus is evident. The electron density for the temporarily captured electron accumulates at $r_{max} \cong 12$ a.u. indicating that the impinging electron stays far away even from the outermost valence electrons of the target.

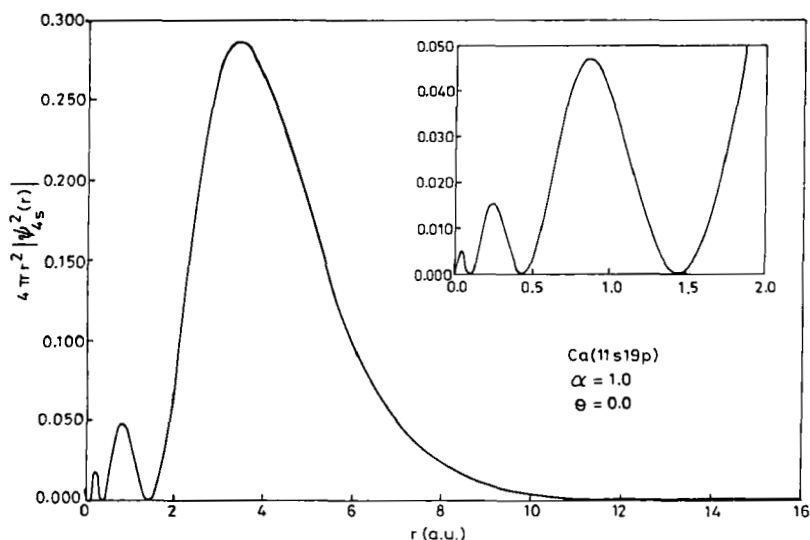


Figure 22. Radial charge density plot for the $4s$ orbital in Ca. The r_{max} is at 3.5 a.u.

5.2 LUMO as the resonant orbital for molecular resonances

The orbital picture of atoms and molecules is central to chemistry /29/ and among the many orbitals of a molecule, the Highest Occupied Molecular Orbital (HOMO) and the Lowest Unoccupied Molecular Orbital (LUMO) are critical to its reactivity /110/. While both HOMO and LUMO are well defined in the approximate parametric Self-Consistent-Field (SCF) theories like the Hückel and the Extended Hückel methods, in the *ab-initio* SCF method used routinely now, only the occupied orbitals are invariant and well defined. The orbital energies and amplitudes for all the unoccupied orbitals are arbitrarily dependent on the underlying basis and with basis-set saturation, the LUMO orbital energy may be brought arbitrarily close to zero. The concept of LUMO in reactivity theories is thus made deficient in rigour and additional mechanism for an unequivocal identification of the LUMO becomes necessary. Extensive success in the analysis of molecular shape resonance data through a qualitative correlation between the *resonant* orbital in which the impinging electron is temporarily trapped /18,19/ and the LUMO of the target molecule leaves little doubt that such an association is well founded. This intuitive no-

tion, may be investigated through identification and portrayal of the resonant orbital by using the FDAs as correlated orbitals as done earlier for atoms. The resonant poles for N_2 , CO and C_2H_4 have already been identified in section 3.2. In the following subsections we explore the corresponding Feynman Dyson Amplitudes (FDAs) for these systems.

e- N_2

The resonant Feynman Dyson amplitude on the real line from the second order decoupling employing the (5s 4p 2d) and (4s 9p) bases (FDA1 and FDA2 respectively) and difference between these are plotted in fig. 23. Fig. 23a shows that the resonant FDA1 on the real line is similar to the text book plots of the π_g^* LUMO of N_2 and is much more compact compared to the FDA2 obtained with the (4s 9p) basis in fig. 23b. This compactness of the FDA1 is made clear by the difference between the resonant FDAs from the two bases plotted in fig. 23c which confirms a sharp accumulation of the orbital amplitude near the nuclei in the case of FDA1. Orbital relaxation has been shown to be critical to the description of molecular resonances and that the resonance energy obtained with the less balanced but more diffuse (4s 9p) basis is closer to the experimental value (table IV) is made plausible by the FDA plots of fig. 23. The FDAs from other decouplings have similar features.

As per the complex scaling theorems (section 2.1), the resonance (metastable electron attachment) is uncovered by sufficient rotation (by θ_{opt}) which corresponds to quasi-stability in the θ -trajectory. The real and imaginary parts of FDA1 and FDA2 at $\theta = \theta_{opt}$ are displayed in fig. 24. The resonant FDAs at θ_{opt} are complex and the real part of these are similar to that portrayed in fig. 23. The imaginary parts of these FDAs are plotted in figs. 24b and 24d. While the nodal patterns for real and imaginary parts of the FDA1 are identical, that for FDA2 are negative of each other. The imaginary part of the FDA1 is more diffuse but smaller in comparison with the real part. The real part of FDA2 remains diffuse but the imaginary part is more compact. The magnitude of real parts at θ_{opt} is smaller than that for $\theta=0.0$ and complex scaling seems to provide an avenue for turning the compact orbitals on the real line into somewhat more diffuse anionic orbitals with imaginary parts exercising a balancing role. This role of complex scaling is explored further in figs. 25a and 25b where we plot the difference between real and imaginary parts of FDA1 and FDA2 at θ_{opt} . The difference induced in FDA1 by complex scaling is shown clearly in fig. 25a and to much lesser extent in 25b. The FDA1 at θ_{opt} is still much more compact compared to FDA2 with most of the amplitude concentrated near the nuclei. The greater orbital relaxation of FDA2 correlates well with lower resonance energy obtained from the corresponding pole (figs. 7 and table IV). Similar effect of complex scaling will be seen to persist for other systems as well and the use of FDA plots help in obtaining

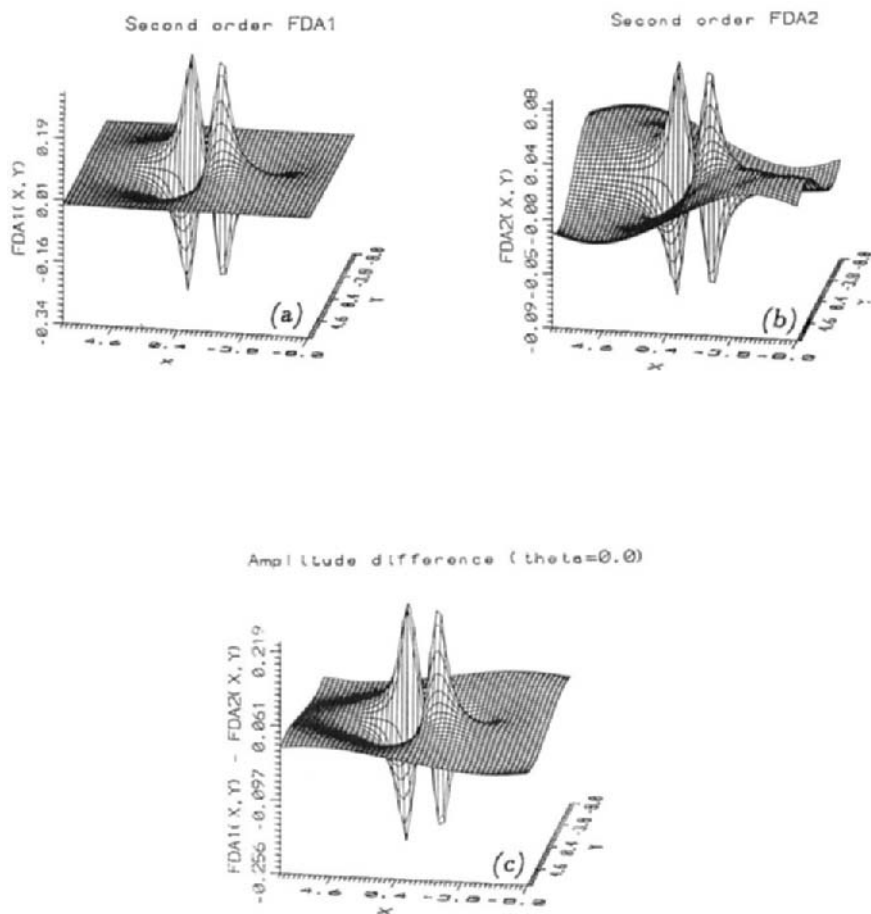


Figure 23. Second order FDAs for N_2 on the real line obtained from the (a) $(5s\ 4p\ 2d)$ and (b) $(4s\ 9p)$ bases. The difference of the FDAs plotted in (a) and (b) are shown in (c).

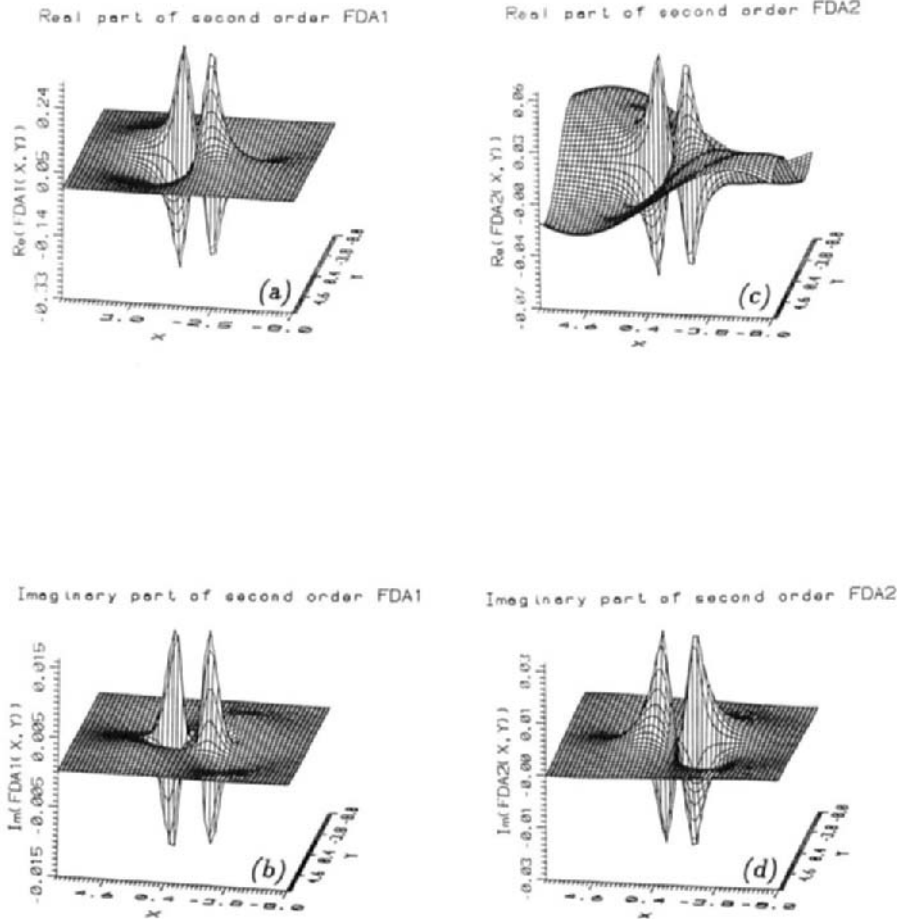


Figure 24. Real ((a) and (c)) and imaginary ((b) and (d)) parts of the second order FDAs for the (5s 4p 2d) and (4s 3p) bases at $\theta = \theta_{opt}$.

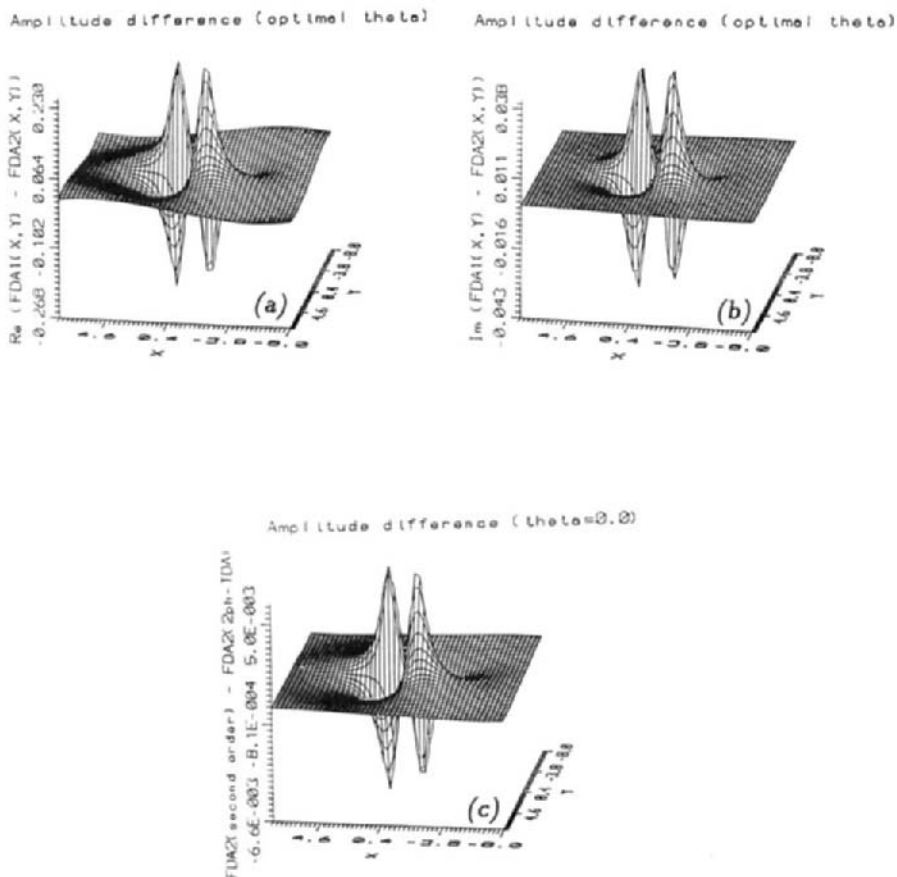


Figure 25. The real (a) and imaginary (b) parts of the difference of the second order FDAs from the (5s 4p 2d) and the (4s 9p) bases. The difference between the FDAs from the Σ^2 and $\Sigma^{2ph-TDA}$ decouplings for the (4s 9p) basis on the real line is plotted in (c).

mechanistic insights. As mentioned earlier, the overall features of the FDAs from Σ^0 and $\Sigma^{2\text{ph-TDA}}$ decouplings are similar and therefore have not been examined separately. The subtle differences can however provide important insights as in the case of atomic resonances and the difference between the Σ^2 and $\Sigma^{2\text{ph-TDA}}$ decoupling is explored using the difference between (4s 9p) FDAs obtained from these two decouplings in fig. 25c. The magnitude of the difference between the FDAs from Σ^2 and $\Sigma^{2\text{ph-TDA}}$ decouplings is indeed small which explains the closeness in the resonance energies and widths. The slightly greater amplitude near the nuclei in the Σ^2 FDA lowers the resonance energy calculated using this decoupling. In this, the molecular results are similar to the atomic results discussed earlier.

e-CO:

The resonant FDA from the second order and other decouplings on the real line once again are the familiar π^* LUMO for CO with greater amplitude on the C atom and the resonant FDA from the Σ^2 decoupling is displayed in fig. 26a. In fig. 26b the difference between FDAs from Σ^2 and Σ^0 decouplings has been plotted which shows that the major effect of the Σ^2 correction to the SCF π^* LUMO of CO is the diminution in its antibonding nature through shifting of electron amplitude to the more electronegative O atom. This lowers the LUMO energy level bringing it closer to the HOMO orbital energy. The greater effectiveness of Σ^2 vis-a-vis $\Sigma^{2\text{ph-TDA}}$ decoupling is indicated by fig. 26c where the second order approximation is seen to pull an additional amount (albeit small in magnitude) of electron amplitude on both C and O where the extra buildup on O atom is somewhat larger and more compact.

The role of complex scaling is explored in fig. 26d where the difference between the real part of the resonant FDA at $\theta = \theta_{\text{opt}}$ and the same FDA on the real line ($\theta = 0.0$) has been plotted. It is clear from fig. 26d that the role of complex scaling is to assist in diminishing the HOMO-LUMO gap by transferring of probability amplitude towards the O atom. Though the imaginary part of the FDAs from both the Σ^2 and $\Sigma^{2\text{ph-TDA}}$ decouplings is much smaller and is therefore not depicted here, the imaginary part of the resonant FDAs from both these decouplings at optimal θ has larger amplitude on the O atom. This coupled with the difference amplitude profiles of figs. 26b - 26d seem to indicate a synergy between the effects of complex scaling and corrections induced by the correlated decouplings (Σ^2 and $\Sigma^{2\text{ph-TDA}}$), with both reinforcing each other to suitably modify the antibonding SCF LUMO for metastable attachment of an additional electron.

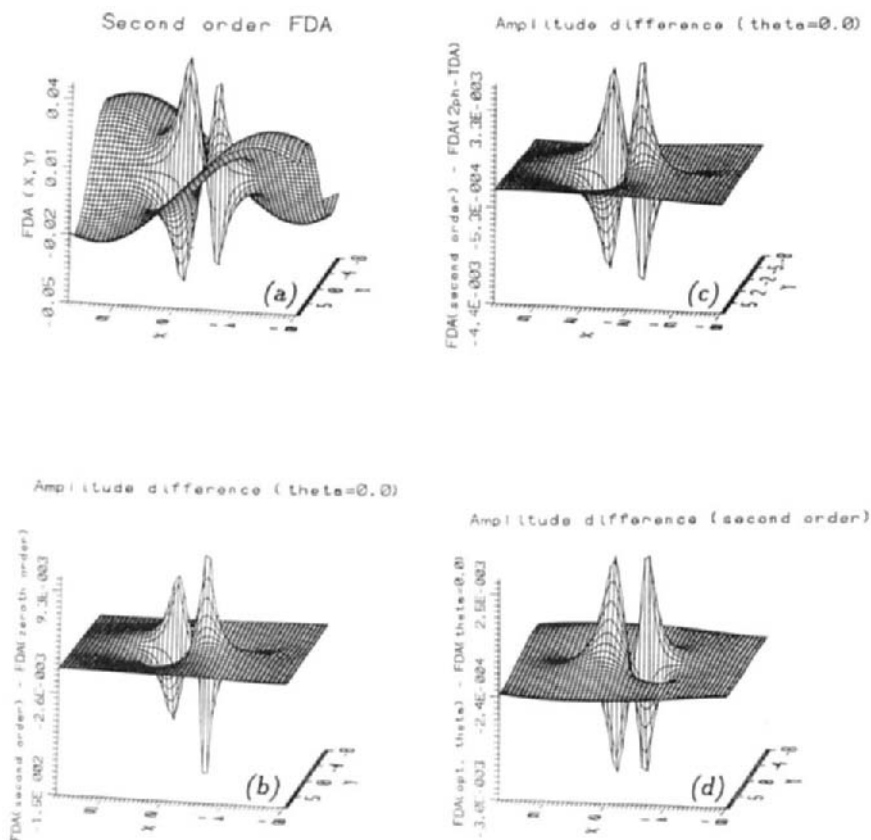


Figure 26. (a) Resonant FDA from the Σ^2 decoupling for the CO on the real line ($\theta = 0.0$). (b) Difference between the resonant FDAs from the Σ^2 and the Σ^0 decouplings and (c) between Σ^2 and $\Sigma^{2ph-TDA}$ decouplings at $\theta = 0.0$. The diminution in the antibonding nature of the π^* LUMO through shifting of the orbital amplitude towards the O atom by the correlated decouplings is seen. The difference between the real part of the resonant FDA from the Σ^2 decoupling at $\theta = \theta_{opt}$ and the same FDA on the real line is displayed in (d). The synergy between the role of complex scaling and correlation/relaxation effects in diminishing the HOMO-LUMO gap by shifting the amplitude towards the O atom is made obvious by (b), (c) and (d).

C_2H_4 :

The resonant FDA from the Σ^2 decoupling on the real line has been plotted in fig. 27c. This displays the familiar nodal pattern of the π^* LUMO of the Ethylene molecule. Those from the Σ^0 , and $\Sigma^{2ph-TDA}$ have identical features and we explore the role of correlation by plotting the difference between resonant FDAs from the Σ^2 and Σ^0 decouplings in fig. 27b. In the case of C_2H_4 the reduction of antibonding nature of the π^* LUMO through depletion of small amounts of probability amplitude away from the C-H σ bond region and its accumulation near the C-C bond seems to be the major contribution from the correlated decouplings.

That the major role perhaps is that of relaxation is indicated by fig. 27c where the real part of the resonant FDA from the Σ^2 decoupling for $\theta = \theta_{opt}$ has been plotted. The most striking feature is that the optimal value of the complex scaling parameter has turned it into a diffuse anionic orbital preparing it for the metastable electron attachment.

Differences in the description of the ${}^2B_{2g}$ $C_2H_4^-$ shape resonance by the Σ^2 and the Σ^0 decouplings may be probed by plotting the difference between the values of the resonant FDAs from these decouplings. These results show that the major effect of correlation and relaxation incorporated by the Σ^2 and $\Sigma^{2ph-TDA}$ decouplings is through greater diffusion of both the real and imaginary parts of the resonant amplitude. Though the imaginary part of the resonant FDA is two orders of magnitude smaller than the real part and is not depicted here it is responsible for accumulation of electron amplitude in the internuclear region. The complex scaling and correlation effects again seem to act in tandem to turn an antibonding LUMO for $\theta = 0.0$ into a diffuse anionic orbital for $\theta = \theta_{opt}$. The radial density plots of Donnelly /50/ have identified this resonance to be multimodal which will preclude an association of the resonant orbital with a single LUMO and the identification of LUMOs with the resonant orbital therefore requires further investigation using saturated bases and higher order decouplings.

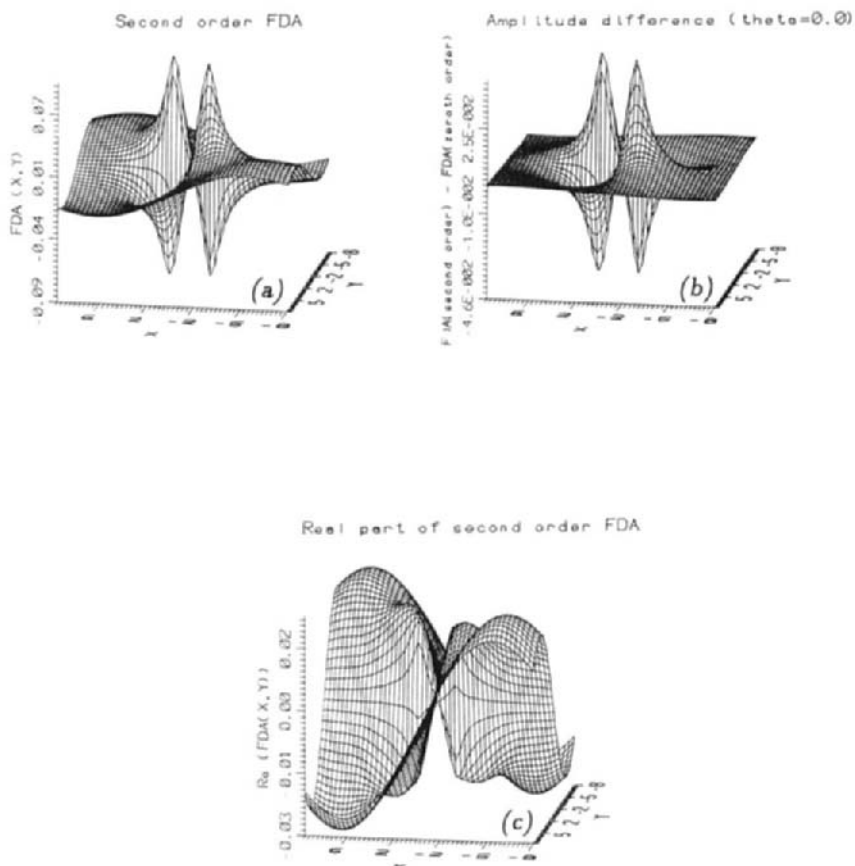


Figure 27. (a) Resonant FDA from the Σ^2 decoupling for the C_2H_4 molecule on the real line ($\theta = 0.0$). (b) Difference between the resonant FDAs from the Σ^2 and the Σ^0 decouplings for C_2H_4 on the real line. The real part of the diffuse resonant FDA at $\theta = \theta_{opt}$ is plotted in (c).

6 Conclusions and Future Directions

The basic purpose of this review is to summarize the results from our attempts to harness the electron propagator theory for the investigation of resonances in electron scattering off atoms/molecules. The bi-orthogonal approach to the construction of the dilated electron propagator does lead to the same formulae as in the case of the unscaled real propagator and all the approximations from the real electron propagator formalism may be implemented using the formal and computational strategies adopted earlier /3,6,7,121/. The use of bi-variational SCF permits easy apportioning of relaxation and correlation contributions in the formation of shape resonances. Relaxation effects seem to be the most important in the formation and decay of atomic shape resonances, since there is no resonant root for Mg at the bi-variational SCF level and the values obtained for Be and Ca from the zeroth order approximation (bi-variational SCF) are much larger than that from second order and diagonal 2ph-TDA self energy approximations.

The use of complex scaled electron propagator for the treatment of molecular resonances /48-50/ has shown extreme sensitivity to even minor variations in the scaling parameter, making the search for the resonant root much more demanding. We had speculated earlier /31-35,71/ that this may be due to the second order self energy approximant being employed in the investigation /48-50/. Later results however, show that not much improvement may be had by employing the somewhat more demanding higher order self energy approximants. The much more economic and simpler quasi-particle approximants of the type discussed in section 2.3 do provide encouraging results for the calculation of resonance energies and widths for atoms /78/. Molecular shape resonances however, are found to be critically dependent on orbital mixing and quasiparticle approximants offer little improvement to the description obtained at the level of the bi-variational SCF itself. Maximum lowering of the HOMO-LUMO gap through the lowering of the antibonding nature of the LUMO is offered by the second order decoupling and the more demanding diagonal 2ph-TDA decoupling does not seem to be worth the extra effort involved in the computation of the denominator shift Δ in eqn. 69. Also, clear isolation of a single virtual orbital of the p-type from the whole manifold of all unoccupied orbitals from the bi-variational SCF calculations for the 2P shape resonances for both e-Be and e-Ca scattering and the $^2\Pi_g$, $^2\Pi$ and $^2B_{2g}$ shape resonances in e-N₂, e-CO and e-C₂H₄ scattering respectively lends credence to the unoccupied orbital based mechanistic picture of shape resonances /17-19/.

The orbital picture is at the core of quantum-chemical thinking /122/ and a rigorous probe of this picture is clearly desirable. Though an orbital picture of resonance formation has persisted for long /18,19/, in the absence of a simple and unequivocal mechanism to identify the resonant orbital, its portrayal

had not been possible earlier. Examination of radial charge density plots from resonant orbitals and Feynman Dyson amplitudes for the 2P shape resonances in e-Be, e-Mg and e-Ca scattering has provided a preliminary outline with mixed results. The dominant features do point to the resonant orbital being the lowest p-type orbital in these systems, albeit with strong input from other orbitals in the same symmetry block. The competing demands of initial penetration and final decay are best served by a higher p-type orbital near the top and narrow end of the centrifugal barrier. On the other hand, temporary binding will be facilitated by the lower energy orbital(s) at the deeper and wider end of the barrier. These inherently contradictory attributes for the formation and decay preclude a simple orbital picture for the metastable states. In fact, the complex structure in charge density plots indicates that description of resonances will be extremely sensitive to the co-ordinate space span of the primitive basis set. The prevalent basis sets are biased in favor of occupied orbitals and our results emphasize the need for incorporation of GTOs which will provide sufficient flexibility to be able to cater to the competing demands of resonance formation and decay.

The complex scaling parameter is seen to play a critical role in providing a mechanism for the accumulation of electron density close to the target nucleus. The extensive correlation effects witnessed in the stabilization of all these shape resonances seems to indicate that the orbital picture for even the simplest of shape resonances investigated here needs to be interpreted judiciously. Optimal complex scaling is seen to turn the compact LUMOs on the real line into anionic diffuse orbitals preparing them for metastable electron attachment. That these trends persist for diverse systems like the N_2 , CO and C_2H_4 molecules generates faith in the ability of the bi-orthogonal dilated electron propagator to unmask molecular shape resonances and to unfold descriptive insights with cross-systemic validity.

Some limitations of the results obtained so far need sharper focus and the first and foremost is the inadequacy of the basis sets devoid of d-functions which might have assisted in a better description of the polarization effects. The initial applications with emphasis on complementary analysis of the molecular shape resonances through the hitherto unexplored resonant FDAs which alone can furnish mechanistic insights has necessitated the expediency of utilizing computationally convenient basis sets with proven effectiveness in the unmasking of these resonances. However, study of the basis set effects needs urgent and comprehensive attention. Furthermore, while the calculated energies are plausible, the calculated widths for all molecular resonances explored with the dilated electron propagator are much narrower than the experimental width for all the systems investigated here. The experimental widths have been obtained by fitting the cross-section data using empirical optical potential /123/. The larger experimental widths have been contested /103/ as being

due to the inadequacy of the empirical optical potential. The narrowness of the widths calculated using the dilated electron propagator technique may also be due to insufficiency of the primitive basis sets and/or the amount of correlation and relaxation incorporated by the decouplings employed here. The need for a comprehensive study of the basis set effects has been stressed earlier and an incorporation of the higher order decouplings like the third order, quasi-fourth order /14,15/ or balanced renormalized decouplings such as the Algebraic Diagrammatic Construction (ADC(3)) /6/ is an obvious extension of this technique.

The single equilibrium bond length calculation for molecules also needs to be extended by allowing bond-stretching and calculating $\mathcal{E}_{\text{res}}(R) = \frac{1}{2}k_{\text{res}}^2(R)$ as a function of the bond length R . One could then employ the Chandra /109,124/ approximation $E_{\text{res}}^{N+1}(R) = E_0^N(R) + \frac{1}{2}k_{\text{res}}^2(R)$ in conjunction with semi-classical/quantal wave packet dynamics /125/ on this complex $E_{\text{res}}^{N+1}(R)$ to unravel the vibrational dynamics attending electron attachment resonances without having to employ empirical optical potentials.

All in all, the bi-orthogonal dilated electron propagator offers a simple extension of the real electron propagator technique and with the incorporation of higher order decouplings like the Σ^3 , Σ_q^4 ADC(3) etc. and suitably large and flexible basis sets should offer same power and effectiveness in the treatment of metastable anions and cations as done by its real counterpart for stable bound systems.

Acknowledgments

MKM's work in this area has been sponsored by the Department of Science and Technology, India, through their grant no. SP/S1/F60/88. Their support is gratefully acknowledged. MNM is grateful to the CSIR, India for a predoctoral fellowship (no. 9/87(160)/93 EMR-I).

References

1. Linderberg, J., and Öhrn, Y. (1973). In "Propagators in Quantum Chemistry" (D. P. Craig and R. McWeeny eds.), Academic Press, New York.
2. Jörgensen, P., and Simons, J. (1981). In "Second Quantization Based Methods in Quantum Chemistry" Academic Press, New York.
3. Öhrn, Y., and Born, G. (1981). *Advan. Quantum Chem.* 13, 1.
4. Öhrn, Y. (1976). In "New World of Quantum Chemistry" (B. Pullman and R. G. Parr, eds.) Reidel, Dodrecht, Holland.
5. Öhrn, Y. (1978). In "Excited States in Quantum Chemistry" (B. Pullman and R. G. Parr, eds.) Reidel, Dodrecht, Holland.
6. von Niessen, W., Schirmer, J., and Cederbaum, L. S. (1984). *Computer Phys. Rept.* 1, 57.
7. Herman, M. F., Freed, K. F., and Yeager, D. L. (1981). *Advan. Chem. Phys.* 48, 1.
8. Simons, J. (1978) In, "Theoretical Chemistry : Advances and Perspectives, (H. Eyring, ed.), Vol. 3, Academic Press, New York.
9. Cederbaum, L. S., Domcke, W. (1977). *Advan. Chem. Phys.* 36, 205.
10. Öhrn, Y. (1989). "Lecture Notes in Quantum Chemistry" (D. Mukherjee, ed.), Vol. 50, p. 187, Springer-Verlag, Berlin.
11. Ortiz, J. V., (1993). *Chem. Phys. Lett.* 216, 319.
12. Berman, M., Walter, O., Cederbaum, L. S. (1983). *Phys. Rev. Letts.* 50, 1979.
13. Meyer, H-D. (1989). *Phys. Rev. A* 40, 5605.
14. Ortiz, J. V. (1992). *Chem. Phys. Letts.* 199, 530.
15. Ortiz, J. V. (1990). *Int. J. Quant. Chem.* 24, 585.
16. Schulz, G. J. (1973). *Rev. Mod. Phys.* 45, 379.
17. Taylor, H. S. (1970). *Adv. Chem. Phys.* 18, 91.
18. Jordan, K. D., Burrow, P. D. (1978). *Acc. Chem. Res.* 11, 341; Jordan, K. D., Burrow, P. D. (1987). *Chem. Rev.* 87, 557.

19. Simons, J., Jordan, K. D. (1987). *Chem. Rev.* 87, 535.
20. Winkler and Zeitschrift, (1977). *Z. Physik A.* 291, 199.
21. Donnelly, R. A., and Simons, J. (1980). *J. Chem. Phys.*, 73, 2858.
22. Mishra, M., Froelich, P., and Öhrn, Y. (1981). *Chem. Phys. Lett.* 81, 339.
23. Winkler, P., Yaris, R., and Lovett, R. (1981). *Phys. Rev. A* 23, 1787.
24. Palmquist, M., Altick, P. L., Ritcher, J., Winkler, J., Yaris, R. (1981). *Phys. Rev. A* 23, 1795.
25. Mishra, M., Goscinski, O., and Öhrn, Y. (1983). *J. Chem. Phys.* 79, 5494.
26. Mishra, M., Goscinski, O., and Öhrn, Y. (1983). *J. Chem. Phys.* 79, 5505.
27. Aguilar, J., and Combes, J. (1971). *Commun. Math. Phys.* 22, 269.
28. Balslev, E., and Combes, J. (1971). *Commun. Math. Phys.* 22, 280.
29. Simon, B. (1972). *Commun. Math. Phys.* 27, 1.
30. Simon, B. (1973). *Ann. Math.* 97, 247.
31. Reinhardt, W. P. (1982). *Ann. Rev. Phys. Chem.*, 33, 223.
32. Junker, B. R. (1982). *Adv. At. Mol. Phys.* 18, 207.
33. Ho, Y. K. (1983). *Phys. Repts.* 99, 2.
34. McCurdy, C. W., (1979). In "Electron-Molecule and Photon-Molecule Collisions" (Rescigno, T. N., McKoy, V., Schneider, B., eds.), Plenum, New York.
35. Simon, B. (1978). *Int. J. Quant. Chem.* 14, 529.
36. Gil, T. J., Rescigno, T. N., McCurdy, C. W., Lengsfeld, B. H., (1994). *Phys. Rev. A* 49, 2642; Peskin, U., and Moiseyev, N. (1994). *Phys. Rev. A* 49, 3712; Ortiz, J. V., (1993). *Chem. Phys. Lett.* 216, 319.
37. Sun, W., McCurdy, C. W., and Lengsfeld, B. H., (1992). *J. Chem. Phys.* 97, 5480.
38. Chu, S. I. (1991). *J. Chem. Phys.* 94, 7901.

39. Mishra, M., Kurtz, H. A., Goscinski, O., and Öhrn, Y. (1983). J. Chem. Phys. 79, 1896.
40. Medikeri, M. N., Nair, J., Mishra, M. K. (1993), J. Chem. Phys. 99, 1869.
41. Medikeri, M. N., Mishra, M. K. (1993). Chem. Phys. Letts., 211, 607.
42. Medikeri, M. N., Mishra, M. K. (1994). Proc. Ind. Acad. Sci., Chemical Sciences 106, 111.
43. Medikeri, M. N., Mishra, M. K. (1994). J. Chem. Phys., 100, 2044.
44. Medikeri, M. N., Mishra, M. K. (1994). Int. J. Quant. Chem. S28, 29.
45. Medikeri, M. N., Mishra, M. K. (1995). J. Chem. Phys. (in press).
46. Medikeri, M. N., Mishra, M. K. (1995). Chem. Phys. Lett. (in press).
47. Donnelly, R. A. (1982). J. Chem. Phys. 75, 5414.
48. Donnelly, R. A. (1982). Int. J. Quant. Chem. S16, 653.
49. Donnelly, R. A. (1985). S19, 337.
50. Donnelly, R. A. (1986). J. Chem. Phys. 84, 6200.
51. J. V. Ortiz, J. Chem. Phys., 92, 6728, (1990); J. V. Ortiz and J. W. Mintmire in Advances in Chemistry Series No. 224, *Silicon-Based Polymer Science : A Comprehensive Resource*, ed. John M Zeigler and F. W. Gordon Fearon, (American Chemical Society, 1990); J. V. Ortiz and Jyh-Shing Lin, Chem. Phys. Letts., 171, 197, (1990); J. V. Ortiz, Chem. Phys. Letts., 169, 116, (1990).
52. Gamow G., (1931). In "Constitution of Atomic Nuclei and Radioactivity" Oxford University Press.
53. Dirac P. A. M., (1927). Proc. Roy. Soc. (London), A14, 243; see also (1958). "The Principles of Quantum Mechanics", 4th ed. Clarendon Press, Oxford, pp 201-204.
54. Siegert A. J. F., (1939). Phys. Rev. 56, 750.
55. Isaacson A. D., McCurdy C. W. and Miller W. H., (1978). Chem. Phys. 34, 311; Isaacson A. D. and Miller W. H., (1979). Chem. Phys. Lett., 62, 374.
56. Moiseyev N. and Hirschfelder J. O., (1988). J. Chem. Phys. 88, 1063.

57. Löwdin, P. O., (1967). *Adv. Quant. Chem.* **3**, 324.
58. Löwdin, P. O. (1978). *In* "Set Theory and Linear Algebra, Part II" Department of Quantum Chemistry, Uppsala University, Uppsala, Sweden.
59. Mishra, M., Öhrn, Y., and Froelich, P. (1981). *Phys. Lett. A*, **81**, 4.
60. P. Froelich and P. O. Löwdin, *J. Math. Phys.*, **24**, 89, (1983).
61. Löwdin, P. O., Froelich, P., and Mishra, M. (1989). *Adv. Quant. Chem.* **20**, 185.
62. Löwdin, P. O., Froelich, P., and Mishra, M. (1989). *Int. J. Quant. Chem.* **2**, 867.
63. McCurdy, C. W., Rescigno, T. N., Davidson, E. R., and Lauderdale, J. G. (1980). *J. Chem. Phys.* **73**, 3268.
64. McCurdy, C. W., Lauderdale, J. G., and Mowrey, R. C. (1981). **75**, 1835.
65. Veillard, A. (1974). *In* "Computational Techniques in Quantum Chemistry and Molecular Physics" (G. H. F. Diercksen, B. T. Sutcliffe, and A. Veillard, eds.) D. Reidel, Dodrecht, Holland/Boston, Massachusetts.
66. Nehr Korn C., Purvis, G. D., Öhrn, Y. (1976). *J. Chem. Phys.* **64**, 1752.
67. Froelich, P. (1980). Quantum Theory Project, Univ. of Florida, preprint, TF 582, unpublished.
68. Goscinski, O., and Lukman, B. (1970). *Chem. Phys. Lett.* **7**, 573.
69. Pickup, B. T., and Goscinski, O. (1973). *Mol. Phys.* **26**, 1013.
70. Löwdin, P. O., (1965). *Phys. Rev. A* **139**, 357.
71. A review of the different approaches to the construction of complex scaled electron propagator is offered by Mishra. M. (1989). "Lecture Notes in Quantum Chemistry" (D. Mukherjee, ed.), Vol. 50, p. 223, Springer-Verlag, Berlin.
72. Schirmer J., and Cederbaum, L. S. (1978a). *J. Phys. B* **11**, 1889; (1978b). *ibid.* **11**, 1901.
73. Born G., and Öhrn, Y. (1979). *Chem. Phys. Lett.* **61**, 397.

74. Mishra M., and Öhrn, Y. (1980). *Chem. Phys. Letts.* 71, 549.
75. Purvis, G. D., and Öhrn, Y. (1974). *J. Chem. Phys.* 60, 4063; 62, 2045.
76. Holneicher, G., Ecker, F., Cederbaum, L. S., (1972). In "Electron Spectroscopy" (D. A. Shirley, ed.), North-Holland Amsterdam.
77. Cederbaum, L. S., (1975). *J. Phys. B.* 8, 290; (1973). *Theoret. Chim. Acta.* 31, 239.
78. Ortiz, J. V. (1989). *Chem. Phys. Lett.* 156, 489.
79. Zhan, H., Zhang, Y. and Winkler, P., (1994). *Int. J. Quant. Chem.* 28, 103.
80. Simon, B. (1979). *Phys. Letts. A* 71, 211.
81. McCurdy, C. W., Rescigno, T. N. (1978). *Phys. Rev. Lett.* 41, 1364.
82. Moiseyev, N., Corcoran, C. (1979). *Phys. Rev. A* 20, 814.
83. Morgan, J. D., Simon, B., (1981). *J. Phys. B* 14, 1167.
84. Moiseyev, N. Certain, P. R., and Weinhold, F. (1978). *Mol. Phys.*, 36, 1613.
85. Kurtz, H. A., and Öhrn, Y. (1979). *Phys. Rev. A* 19, 43.
86. Kurtz, H. A., and Jordan, K. (1981). *J. Phys. B: At. Mol. Phys.*, 14, 4361.
87. McCurdy, C. W., McNutt, J. F., (1983). *Chem. Phys. Lett.* 94, 306.
88. Burrow, P. D., Michedja, J. A., and Comer, J. (1976). *J. Phys. B.* 9, 3255.
89. Hazi, A. U. (1978). *J. Phys. B.* 11, L259.
90. Hunt, J., Moiseiwitsch, B. L., (1970). *J. Phys. B.* 3, 892.
91. Moiseyev, N., Weinhold, F. (1978). *Int. J. Quant. Chem.* 14, 727.
92. Simons, J., (1981). *J. Chem. Phys.* 75, 2465.
93. Hazi, A. U., Taylor, H. S., (1970). *Phys. Rev. A* 1, 1109.
94. Thompson, T. C., Truhlar, D. G., (1982). *Chem. Phys. Lett.* 92, 71.
95. Taylor, H. S., Hazi, A. U., (1976). *Phys. Rev. A* 14, 2071.

96. Amusia, Y. M., Cherepkov, N. A., (1975). In "Case Studies in Atomic Physics" Vol. 5, p. 47, Amsterdam: North-Holland; Romanyuk, N. I., Shpenik, O. B., Zapesochnyi, I. P., (1980). JETP Lett., 32.
97. Pegg, D. J., Thompson, J. S., Compton, R. N., Alton, G. D. (1987). Phys. Rev. Lett. 59, 2267.
98. Fischer, C. F., Lagowski, J. B., Vosko, S. H. (1987). Phys. Rev. Letts. 59, 2263.
99. Medikeri, M. N., (1995). Ph.D. thesis. Indian Institute of Technology, Bombay, India.
100. Erhardt, H., Langhans, L., Linder, F., Taylor, H. S., (1968). Phys. Rev. 173, 222.
101. Schneider, B. L., (1981). Phys. Rev. A 24, 1.
102. Schneider, B. L., Le Courneuf, M., Lan, V. K., (1979). Phys. Rev. Lett. 43, 1927.
103. Chao, J. S-Y., Falcetta, M. F., Jordan, K. D. (1990). J. Chem. Phys. 93, 1125.
104. Krauss, M., Mies, F. H., (1974). Phys. Rev. A 1, 1592.
105. Hazi, A. U., Rescigno, T. N., Kurilla, M., (1981). Phys. Rev. A 23, 1089.
106. Rescigno, T. N., Orel, A. E., McCurdy, C. W., (1980). J. Chem. Phys. 73, 6347.
107. Zubek, M., Szmytkowski, C., (1977). J. Phys. B 10, L27.
108. Levin, D. A., Fliflet, A. W., McKoy, V., Phys. Rev. A 21, 1202.
109. Chandra, N., (1977). Phys. Rev. A 16, 801.
110. a) Woodward, R. B.; Hoffmann, R.; (1970) In "The Conservation of Orbital Symmetry", Verlag Chemie GmbH Academic Press Inc. Germany, and references therein, b) Fukui, K.; (1965) In "O. Sinanoğlu : Modern Quantum Chemistry", Academic Press, New York, Vol. 1 and references therein.
111. Walker, I. C., Stamatovic, A., Wong, S. F., (1978). J. Chem. Phys. 69, 5532; Burrow, P. D., Jordan, K. D., (1975). Chem. Phys. Lett. 36, 594.

112. Schneider, B. I., Rescigno, T. N., Lengsfeld, B. H. and McCurdy, C. W., (1991). *Phys. Rev. Letts.* 66, 2728.
113. Das, A., Melissinos, A. C. (1986). In "Quantum Mechanics" p. 534, Gordon and Breach New York.
114. Bisgard, P., Bruch, R. D., Fatrup, B., Rodbro, M. (1978). *Phys. Scr.* 17, 49.
115. Rodbro, M., Bruch, R., Bisgard, P. (1979). *J. Phys. B.* 12, 2413.
116. Kelly, H. P. (1975). *Phys. Rev. A* 11, 556.
117. Kelly, H. P. (1974). *Phys. Rev. A* 9, 1582.
118. Cederbaum, L. S., Domcke, W., Schirmer, J., von Niessen, W., Diercksen, G. H. F., Kraemer, W. P. (1978). *J. Chem. Phys.* 69, 1591.
119. Cederbaum, L. S., Domcke, W., Schirmer, J., von Niessen, W. (1980). *Phys. Script.* 21, 481.
120. Slater, J. C. (1968). In *Quantum Theory of Matter* p 122, McGraw-Hill, New York.
121. Ortiz, J. V. (1991). *J. Chem. Phys.* 94, 6064, and references therein.
122. Simons, J. (1991). *J. Phys. Chem.* 95, 1017.
123. Herzenberg, A., (1968). *J. Phys. B*, 1, 548; Birtwhistle, D. T., Herzenberg, A., (1971). *J. Phys. B*, 4, 53.
124. Chandra, N., Temkin, A., (1976). *Phys. Rev. A* 13, 188.
125. McCurdy, C. W., Turner, J. L. (1983). *J. Chem. Phys.* 78, 6773.
126. Brändas, E. J., Froehlich, P. (1977). *Phys. Rev. A* 16, 2207.
127. Krylstedt, P., Rittby, M., Elander, N., Brändas, E. J. (1987). *J. Phys. B* 20 1295.
128. Krylstedt, P., Elander, N., Brändas, E. J. (1988). *J. Phys. B* 21 3969.
129. Krylstedt, P., Elander, N., Brändas, E. J. (1989). *J. Phys. B* 22 1623.

This Page Intentionally Left Blank

Recent Developments in Configuration Interaction and Density Functional Theory Calculations of Radical Hyperfine Structure.

Bernd Engels^a, Leif A. Eriksson^b and Sten Lunell^c

^aDepartment of Physical and Theoretical Chemistry,
University of Bonn, Wegelerstrasse 12, D-53115 Bonn, Germany.

^b Department of Physics, University of Stockholm,
Box 6730, S-113 85 Stockholm, Sweden.

^cDepartment of Quantum Chemistry, Uppsala University
Box 518, S-751 20 Uppsala, Sweden.

Contents

1 Introduction

2 Configuration Interaction Methods

- 2.1 Influence of different excitation classes on A_{iso}
- 2.2 The MRD-CI/ B_K method
- 2.3 Applications
 - 2.3.1 H_2CN and H_2CO^+
 - 2.3.2 Electronic triplet states

3 Density Functional Methods

- 3.1 DFT-ESR – the importance of gradient corrections
- 3.2 Basis sets for DFT calculations.
- 3.3 H_2CN and H_2CO^+ revisited
- 3.4 Applications
 - 3.4.1 Proton hyperfine coupling constants
 - 3.4.2 Heteroatom hyperfine coupling constants

4 Concluding Remarks

5 Acknowledgements

1 Introduction

Radicals and radical hyperfine structure (hfs) have been the subject of detailed experimental and theoretical studies during the past 25-30 years [1, 2, 3, 4, 5, 6, 7]. Radicals, and in particular radical ions, are generally very shortlived species, and hence special experimental techniques are required to study their properties. The most successful approaches are microwave spectroscopy (MW) and electron spin resonance (ESR; or electron paramagnetic resonance, EPR) measurements. Especially successful have been low temperature matrix isolation techniques, where the radical is trapped at very low concentrations in a surrounding of a rare gas (Ne, Ar), a chlorofluorocarbon (CF_3Cl , $\text{CF}_2\text{ClCFCl}_2$, or similar), SF_6 , or in a zeolite, at temperatures between 4 and 130 K. Although raising new questions about the influence of the matrix on the recorded ESR spectra of the trapped radicals, these techniques have opened up an extremely rich area of research on the properties of short-lived intermediates in chemical reactions [1, 2, 4].

The theoretical framework for a discussion of the hyperfine interactions in radicals is given by the so called spin Hamiltonian, which describes the interaction between the unpaired electrons and the magnetic nuclei ($I \geq 1/2$) in the sample. When the radical is placed in a static magnetic field, the electrons and the magnetic nuclei will interact with the field. These interactions give rise to the electronic and nuclear Zeeman terms,

$$\hat{\mathcal{H}}_{Zeeman} = g\beta B_z S_z - g_N \beta_N B_z I_z, \quad (1)$$

where the suffix 'N' indicates the nuclear terms (nuclear g-factor and nuclear magneton). In the electronic Zeeman term, g and β are the electronic g-factor and the Bohr magneton, respectively. The interaction between the magnetic moments of the electrons and the nuclei lead to a third term of the spin Hamiltonian, the hyperfine term:

$$\hat{\mathcal{H}}_{hf} = \vec{S} \cdot \mathbf{T} \cdot \vec{I}, \quad (2)$$

where \mathbf{T} is the 3×3 hyperfine interaction tensor. Separating out the isotropic component, which arises from a contact interaction between the electron and the nucleus in question, we have,

$$\hat{\mathcal{H}}_{hf} = A_{iso}^{(N)} (\vec{I} \cdot \vec{S}) - \vec{S} \cdot \mathbf{T}' \cdot \vec{I}. \quad (3)$$

The contact interaction is also referred to as the Fermi contact term. In a given atomic orbital basis $\{\psi_\mu\}$, the isotropic hyperfine coupling constant (hfcc) for a particular nucleus N, $A_{iso}^{(N)}$, is given by the expression,

$$A_{iso}^{(N)} = \frac{4\pi}{3} g\beta g_N \beta_N \langle S_z \rangle^{-1} \sum_{\mu,\nu} P_{\mu,\nu}^{\alpha-\beta} \langle \psi_\mu(0) | \psi_\nu(0) \rangle, \quad (4)$$

where $P_{\mu,\nu}^{\alpha-\beta}$ is an element of the unpaired spin density matrix. The remainder of the hyperfine tensor, \mathbf{T}' in Eqn. (3), is referred to as the magnetic dipolar part. The expression for the i, j 'th component of the magnetic dipolar tensor is obtained from the corresponding expression for interacting dipoles:

$$T_{ij}^{(N)} = \frac{1}{2} g \beta g_N \beta_N \langle S_z \rangle^{-1} \times \\ \times \sum_{\mu,\nu} P_{\mu,\nu}^{\alpha-\beta} \langle \psi_\mu(\vec{r}_{kN}) | r_{kN}^{-5} (r_{kN}^2 \delta_{ij} - 3 r_{kN,i} r_{kN,j}) | \psi_\nu(\vec{r}_{kN}) \rangle. \quad (5)$$

For systems with axial symmetry, the parameter $A_{dip} = 1/2 T_{zz}$ is frequently used. For direct comparison with experiment, it is also useful to calculate the components perpendicular and parallel to a particular bond (here defined as the z -axis): $A_\perp = A_{iso} + 1/2 (T_{xx} + T_{yy})$, and $A_\parallel = A_{iso} + T_{zz}$.

As a rule, the computational difficulties in hfs calculations are connected with the isotropic interaction, since the theoretically determined anisotropic parameters in general are in good agreement with experiment, and rather insensitive to computational method as well as basis set.

A major obstacle in the theoretical studies of radical hyperfine structures is the fact that in order to obtain accurate hyperfine parameters, a good description of electron correlation is essential, making configuration interaction (CI) or other high level approaches, such as coupled cluster (CC) or many-body perturbation theory (MBPT), mandatory in the case of *ab initio* calculations. Very accurate (*i.e.*, large) basis sets are also needed to obtain a satisfactory description of the electron distribution at the nuclei and outer valence regions. The combined demands of large, balanced basis sets and correlated *ab initio* treatments have so far limited these kinds of studies to relatively small systems, perhaps 10 – 15 heavy atoms plus a number of hydrogen atoms.

During the past few years, however, density functional theory (DFT) has become a serious alternative to conventional Hartree-Fock based approaches, also in the area of hyperfine structure calculations. The DFT methods have drastically expanded the size of the systems accessible to theoretical hfs studies. We will in this paper review some recent developments both in the field of *ab initio* configuration interaction techniques and in the field of density functional theory applied to hfs studies.

2 Configuration Interaction Methods

High accuracy calculations of isotropic hfcc's have proven to be an exceptionally difficult problem for conventional *ab initio* electronic structure methods. The difficulties are due to the fact that only those orbitals which possess a non-vanishing value at the position of the nucleus in question as well as a net spin density contribute to A_{iso} . The boron atom can be used as an illustration. The ground state of boron is described by the configuration $[1s^2 2s^2 2p^1]$. The unpaired electron which occupies a p orbital cannot contribute to A_{iso} because p orbitals possess a node at the position of the nucleus. The remaining s electrons are paired. Because the spatial distributions of paired electrons are taken to be identical within the restricted Hartree-Fock (RHF) approach, this approximation gives a value of zero for A_{iso} . Experimentally, however, the value of A_{iso} is 12 MHz. The deviation between the RHF value and the correct value of 12 MHz is conventionally interpreted in terms of so called spin polarization effects. Such effects arise because the paired s electrons have different interactions with the unpaired electron, i.e. the electrons of α spin experience both a Coulomb and an exchange interaction with the unpaired electron while the electrons of β experience only a Coulomb interaction.¹ This difference leads to different spatial distributions of the two electrons, from which a net spin density at the position of the nucleus arises.

This qualitative picture is taken into account in the unrestricted Hartree-Fock (UHF) approach, but it is found that UHF calculations normally overestimate A_{iso} drastically. To obtain reliable results, the interactions between the electrons must be described much more accurately. Furthermore, in difference to most other electronic properties, such as dipole moments etc., a proper treatment of the hfcc's also requires special consideration of the inner valence and the $1s$ core regions, since these electrons possess a large probability density at the position of the nucleus. Because the contributions from various shells are similar in magnitude but differ in sign, a balanced description of the electron correlation effects for all occupied shells is essential. All this explains the strong dependence of A_{iso} on the atomic orbital basis *and* on the quality of the wavefunction used for the calculation.

In the following we want to focus on some problems which arise if *ab initio* methods are used to calculate isotropic hfcc's. We will mostly concentrate on approaches where the Configuration Interaction (CI) method is used in various versions. To illustrate the performance of other theoretical methods such as Møller-Plesset perturbation theory (MP), Coupled Cluster methods (CC) or quadratic CI (QCISD), the results obtained with those approaches will be compared for a few model systems. Because an understanding of the influences

¹We consider the $M_S = 1/2$ component of the wave function.

of the various excitation classes in the CI on A_{iso} is fundamental, a discussion of this topic will be performed first. Next we will introduce the MRD-CI/ B_K method, which has been developed especially for the calculation of hfcc's. In the remaining part of the present section we want to discuss some practical problems in the *ab initio* calculation of isotropic hfcc's by investigating some selected model systems.

2.1 Influence of different excitation classes on A_{iso}

Regarding the quality of the CI wavefunction, recent investigations emphasize the importance of higher than double excitations [8, 9, 10, 11]. A good example is the X^2B_1 state of NH_2 [9], in which the value of $A_{\text{iso}}(^{14}\text{N})$ calculated with a CI wavefunction including single and double excitations (SD-CI) still possesses a deviation of about 42 % from the experimental value.

On the other hand, it is found that a single excitations CI (S-CI) treatment, as used by Chipman [12], gives isotropic hfcc's in astonishingly good agreement with experimental results. As pointed out by Feller and Davidson [16], the A_{iso} values obtained from a S-CI treatment are very often in better agreement with experimental results than those calculated with a SD-CI treatment. One example of this paradoxical behaviour is the isotropic hfcc of the ground state ($X^2\Pi$) of the CH molecule [12, 13]. For the carbon center the S-CI gives an isotropic hfcc of about 41 MHz. If a SD-CI is performed, the value drops to about 30 MHz, while it increases again to about 45 MHz if also all triple excitations are taken into account. The experimental value is $46.7 \text{ MHz} \pm 2 \text{ MHz}$. Because the configurations of a S-CI wavefunction are included in a SD-CI wavefunction, some kind of error cancellation is expected to occur in S-CI calculations.

Let us examine the influence of the different excitation classes on A_{iso} , using the ground states of the boron atom (2P_u), the carbon atom (3P_g) and the nitrogen atom (4S_u) as test systems [14]. The 4S_u ground state of the nitrogen atom was chosen because it is a standard system for calculating A_{iso} [8, 15]. The other systems were selected because, in a recent study, Feller and Davidson [15] showed that A_{iso} is much more difficult to calculate for the carbon or boron atoms than for the nitrogen atom.

The AO basis sets used in the present work are given in table 1. They were chosen to incorporate the most important features necessary for hfs calculations [11, 19], while keeping the costs of the calculations reasonable. In the present review we will focus on the results obtained with natural orbitals (NO) as underlying one-particle basis. For more information the reader is referred to reference [14]. For the multireference CI (MR-CI) calculations, 14 (boron), 12

(carbon) and 12 (nitrogen) reference configurations, respectively, were used.

Table 1: Description of the AO basis sets used for the atomic calculations in the present work.

Boron	$(13s8p) \rightarrow [8s5p]$ + 2d functions (0.2 / 0.8)	Ref. [8]
Carbon	$(13s8p) \rightarrow [8s4p]$ + 2d functions (0.318 / 1.097)	Ref. [8] Ref. [9]
Nitrogen	$(13s8p) \rightarrow [8s4p]$ + 2d functions (0.5 / 1.9)	Ref. [8]

A systematic procedure to improve the quality of the CI treatment is to start with the RHF configuration and to include the single excitations (S-CI) into the Hamilton matrix, and then add the double excitations (SD-CI), triple excitations (SDT-CI) and so on. The diagonalization of the appropriate Hamiltonian matrix leads to wavefunctions which can be used to calculate properties, e.g. A_{iso} . In the present paper the expression ‘excitation’ is employed for a replacement at the spatial orbital level, as it is used, e.g., by Chipman [12]. In the case of a single excitation at the spatial orbital level, it has to be kept in mind that for an open shell system at least one of the arising determinants represents a higher than single excitation with respect to the RHF determinant. Single excitations at the spatial level starting from the configuration $c^1a^2b^2$, for which only one determinant is needed to describe the doublet state, lead to $b^1c^1d^1a^2$ among other configurations, originating from a $b^2 \rightarrow b^1d^1$ excitation. Three determinants $\bar{b}cda^2$, $b\bar{c}da^2$ and $bc\bar{d}a^2$ arise, where the bar denotes the singly occupied orbital with β spin. While the first and the third determinants are true single excitations with respect to the starting configuration, the second determinant represents a double excitation ($\bar{b} \rightarrow d, c \rightarrow \bar{c}$) at the spin orbital level. In the Hamiltonian matrix only the interaction of double excitations with the RHF determinant is essential, due to the Brillouin theorem. The importance of those configurations within a S-CI treatment has already been discussed by Chipman [12]. While in the case of a doublet state only one double excitation appears, several double excitations and one triple excitation can be found for a triplet state.

The values of A_{iso} as a function of the level of the CI treatment for the three abovementioned systems are given in table 2. For the boron atom the S-CI

Table 2: Isotropic hyperfine coupling constant for the ground states of the boron atom (2P_u), carbon atom (3P_g) and nitrogen atom (4S_u), using different levels of the CI treatment. NO's were used as one-particle basis.

Treatment	A_{iso} (in MHz)		
	B	C	N
RHF	0.0	0.0	0.0
S-CI	-3.2	7.1	5.4
SD-CI	-1.3	6.1	3.9
SDT-CI	5.2	13.8	7.8
MR-CI	6.5	14.4	8.2
Exp	11.6 ^a	22.5 ^b	10.4 ^c

^a see Ref [15] ^b Ref [127] ^c Ref [128]

and SD-CI treatments predict the wrong sign for A_{iso} . If triple excitations are also taken into account, a large improvement in the calculated value is found. For the carbon atom and the nitrogen atom, it is found that an improvement of the CI treatment from S-CI to SD-CI makes the agreement with experiment worse. If triple excitations are also taken into account, the results become much better. Since it was not possible to include all quadruple excitations, MR-CI calculations were performed, which included the most important part of the triple and quadruple excitations. From table 2, the expected trend can be seen, i.e., for a reliable calculation of A_{iso} , the inclusion of the most significant quadruple excitations is more important than considering all triple excitations. The remaining differences with respect to the experimental results are predominantly due to deficiencies in the AO basis set used in the present work [8, 11, 19, 21]; e.g. the study of Bauschlicher et al. [8] shows that the difference between a MRCI approach and a full CI is only about 0.2 MHz.

To get more insight into the various effects seen in table 2, the different influences of the excitations on A_{iso} have to be studied. Going from a S-CI to a SD-CI treatment, the double excitations can influence A_{iso} in two ways [20]. A *direct effect* arises from the coefficients of the double excitations themselves, which are not contained in the S-CI wavefunction. A second influence of the double excitations on A_{iso} is of a more indirect nature. Due to interactions within the SD-CI Hamilton matrix between configurations already included in the S-CI and the double excitations, the coefficients of the RHF determinant and of the singly excited determinants obtained by a SD-CI treatment differ from those obtained by the S-CI treatment. From these differences in

the coefficients a further change in A_{iso} results. This can also be traced back to the influence of the double excitations. In the following, this effect is called the *indirect effect* of the double excitations on A_{iso} . The indirect effect contains both normalization effects and changes in the ratio among the individual coefficients, but the latter are found to be more important.

The size of the indirect influence of the double excitations on A_{iso} can be calculated if one projects the configurations already included in the S-CI treatment out of the wavefunction obtained from the SD-CI treatment and compares the values of A_{iso} calculated with the projected wavefunction and the value calculated with a normal S-CI wavefunction.

To avoid confusion, some terms concerning the wavefunctions and the treatments to obtain the wavefunctions should be introduced. The wavefunction which includes the RHF configuration and all single excitations will be abbreviated S-WF, if all doubles are also included it is called SD-WF, etc. Accordingly, the CI treatments from which the coefficients are determined are called S-CI, SD-CI, etc. In the following, the coefficients of a S-WF, for example, can be obtained from a S-CI treatment or by projection out of a wavefunction resulting from a more sophisticated treatment (SD-CI, SDT-CI or MR-CI).

In table 3, the splitting into direct and indirect effects is summarized. Let us first concentrate on the boron system. Using a S-CI treatment, A_{iso} is calculated to be -3.2 MHz. If the indirect effect of the double excitations is taken into account (S-WF from SD-CI), the value of A_{iso} drops by about 17 MHz to -20.5 MHz. If the direct effect of the doubles is also included (SD-WF from SD-CI) A_{iso} increases by about 19 MHz to -1.3 MHz. The indirect influence of the triple excitations on the coefficients of the single excitations is not negligible either. If this is included in the S-WF (S-WF from SDT-CI), A_{iso} increases by about 5 MHz from -20.5 MHz (S-WF from SD-CI) to -15.2 MHz (S-WF from SDT-CI). The indirect influence of the triples on the SD-WF (SD-WF from SDT-CI) raises A_{iso} by about 7 MHz from -1.3 MHz (SD-WF from SD-CI) to 5.7 MHz (SD-WF from SDT-CI). The direct contribution of the triple excitations (SDT-WF from SDT-CI) is small but possesses a negative sign (-0.5 MHz), e.g. if only the indirect effect of the triples is taken into account, the calculated value of A_{iso} is somewhat too high. With a MR-CI treatment, the effects of the most important triple and quadruple excitations (TQ) are accessible. Their indirect influence on the SD-WF (SD-WF from MR-CI) is about 6 MHz, e.g. about 1 MHz larger than the influence of the triples alone. The indirect effect on the S-WF is very similar to that found for the triples. It can be seen that the direct contribution of the most important triple and quadruple excitations is again negative.

From table 3 it is not clear whether the effect of the triple excitations on the SD-WF mostly influences the single excitations or the double excitations.

Table 3: Influence of the different excitation classes on A_{iso} for the ground states of boron 2P_u , carbon 3P_g and nitrogen 4S_u .

Excitation class in wave function ^a	Coefficients from	Boron 2P_u	Carbon 3P_g	Nitrogen 4S_u
S-WF	S-CI	-3.2	7.1	5.3
S-WF	SD-CI	-20.5	-14.6	-3.2
SD-WF	SD-CI	-1.3	6.1	3.8
S-WF	SDT-CI	-15.2	-8.2	-0.3
SD-WF	SDT-CI	5.7	14.0	7.4
SDT-WF	SDT-CI	5.2	13.8	7.7
S-WF	MR-CI	-14.9	-18.1	-0.2
SD-WF	MR-CI	6.7	14.5	7.7
MR-WF	MR-CI	6.5	14.4	8.2

^a S-WF denotes the wavefunction including the RHF determinant and all single excitations, SD-WF is used if all double excitations are also included, etc. Accordingly, the expression S-CI describes the CI treatment in which the RHF and the single excitations are included in the Hamilton matrix, etc. For further explanation, see text.

Only the sum of both can be seen. Since A_{iso} is a one-electron property, it can be written as a sum over matrix elements between configurations belonging to the same excitation class or differing in one excitation

$$\begin{aligned}
 < A_{iso} > \sim \\
 & \sum_{i,r} c_0 c_i^r < i | \delta(r - r_N) | r > \\
 & + \sum_{i,r} c_i^r c_i^r \sum_a < a | \delta(r - r_N) | a > \\
 & + \sum_{i,r < s} c_i^r c_i^s < r | \delta(r - r_N) | s > \\
 & + \sum_{i < j, r} c_i^r c_j^r < i | \delta(r - r_N) | j > \\
 & + \sum_{i < j, r < s} c_i^r c_{ij}^{rs} < j | \delta(r - r_N) | s > \\
 & + \dots
 \end{aligned} \tag{6}$$

The first term of Eqn. 6 gives the contribution arising from matrix elements between the RHF determinant and the single excitations (Single-RHF), while

the following three terms contain the contributions resulting from matrix elements between single excitations among themselves (Single-Single). The last term gives the Single-Double contributions. Further contributions arising from Doubles-Doubles, Doubles-Triples, etc., are straightforward. It should be kept in mind that the contribution from the matrix element of the RHF determinant in these cases is zero, as discussed above.

To get a better description of the effects shown in table 3, the various contributions discussed in Eqn. 6 are given in table 4.

Let us again focus on the boron atom. The value of A_{iso} calculated with the wavefunction obtained from a S-CI treatment is comprised of a large negative contribution from matrix elements between the singles and the RHF configuration (-11.4 MHz) and a large positive contribution from the interaction between the singles themselves. As discussed above the contribution from the RHF determinant itself is zero. If a SD-CI treatment is used instead of a S-CI calculation (second part of table 4), the contribution to A_{iso} arising from the matrix elements between the RHF determinant and the single excitations changes dramatically from -11.4 MHz (S-CI) to -29.1 MHz (SD-CI). Because the relative change in the coefficient of the RHF determinant is small (3%), this has to be attributed to the large relative changes of the coefficients of the single excitations which result from the indirect influence of the double excitations. Because the coefficient of the RHF determinant is large in comparison to all other coefficients (> 0.9), the influence of the changes in the coefficients of the single excitations in the Singles-RHF contribution to A_{iso} is strongly enhanced by the multiplication with the coefficient of the RHF determinant (first item in Eqn. 6). The contributions from the Singles-Singles interactions show only very small modifications (0.3 MHz) which may be traced back to the small absolute size of the single excitation coefficients and cancellation effects. The direct effect of the doubles on A_{iso} is composed of a smaller Singles-Doubles contribution (6.3 MHz) and a larger Doubles-Doubles part (12.9 MHz).

The inclusion of triple excitations (third part of table 4) in the CI treatment acts almost exclusively on contributions which are connected with the singles. Again, the largest difference is found in the Singles-RHF contribution which is shifted by about 5 MHz. As found in table 3, the direct contribution of the triples (Triples-Doubles, Triples-Triples) is small and has a negative sign.

The influence of the most important triple and quadruple excitation can be seen in the last part of table 4. The presence of the quadruple excitations (triple excitations are already included in the SDT-CI) mostly affects the Double-Double contribution.

Tables 3 and 4 also list the values calculated for the carbon and nitrogen atoms. In both systems the same trends as discussed for the boron atom are found. Only the magnitudes of the various effects are somewhat smaller. This

Table 4: Decomposition of the various contributions to A_{iso} for boron, carbon and nitrogen.

Method Contribution	Boron 2P_u	Carbon 3P_g	Nitrogen 4S_u
S-CI	-3.2	7.1	5.4
Singles-RHF ^a	-11.4	-3.4	1.1
Singles-Singles	8.2	10.5	4.3
SD-CI	-1.3	6.1	3.9
Singles-RHF	-29.1	-27.1	-6.6
Singles-Singles	8.6	12.5	3.3
Doubles-Singles	6.3	11.6	3.3
Doubles-Doubles	12.9	9.1	3.9
SDT-CI	5.2	13.8	7.7
Singles-RHF	-24.7	-18.1	-4.1
Singles-Singles	9.5	9.9	3.7
Doubles-Singles	7.6	9.9	3.7
Doubles-Doubles	13.3	13.1	4.2
Triples-Doubles	-0.7	-0.5	0.2
Triples-Triples	0.2	0.3	0.1
MR-CI	6.5	14.4	8.2
Singles-RHF	-23.9	-18.1	-3.8
Singles-Singles	9.0	9.9	3.6
Doubles-Singles	7.5	9.2	3.6
Doubles-Doubles	14.1	13.5	4.3
TQ-Doubles	-0.4	-0.5	0.3
TQ-Triples	0.2	0.4	0.2

^a Singles-RHF summarizes all contributions to A_{iso} arising from matrix elements between single excitations and the RHF determinant. The other expressions are used accordingly. For further explanations, see text.

shows that the effects discussed above are rather typical for a wide range of systems.

At a first glance, the large influence of the higher excitations on the coefficients of the single excitations is expected from the Brillouin theorem. This theorem states that the interaction between the RHF determinant and the single excitations is zero for a closed-shell system, so that the coefficients of the single excitations in closed shell systems are completely determined by the interaction with higher excitations. This was pointed out already by Chipman [12], but he also emphasized the difference between single excitations at the spin-orbital level, for which the Brillouin theorem holds, and those at the spatial-orbital level, which include some types of higher excitations (see above). Chipman assumed that the higher excitations included in a S-CI treatment were sufficient for describing the coefficients of the single excitations properly. The present calculation clearly shows that this is not true. For A_{iso} the S-CI calculations very often yield such excellent agreement with the experimental values because indirect and direct effects of the higher excitations (doubles, triples and quadruples) cancel each other to a great extent.

The discussion given above shows that the indirect influences of triples and quadruples on A_{iso} are more important than their direct contribution. A treatment which incorporates the indirect influence of triple and quadruple excitations on the wavefunction should give similar values for A_{iso} as a method in which both effects are fully included.

In the above analysis, the effects arising due to different one-particle basis sets, e.g. SCF-MO's, NO, or CASSCF-MO's, have not been discussed. The main difference lies in the number of reference configurations needed in the MR-CI treatment. If, e.g., SCF-MO's are used for the boron atom, 23 reference configurations were necessary for convergence of A_{iso} as a function of the number of reference configurations, while using NOs or CASSCF-MOs only 14 reference configurations had to be taken. This shows the greater compactness of the CI expansion if a correlated one-particle basis is used instead of SCF MO's. For more information the reader is referred to Refs. [14, 20].

2.2 The MRD-CI/ B_K method

In the previous section we showed that the influence of higher than double excitations is important to obtain accurate isotropic hfcc's. If the MR-CI approach is used to calculate A_{iso} , the importance of the higher excitation leads to a slow convergence with respect to the size of the reference space and, if truncated MR-CI approaches are employed, also with respect to the number of selected configurations. However, the discussion also shows that the indirect contribution of triples and quadruples on A_{iso} is far more important than their

direct effect. Therefore, it should be sufficient to include the indirect effect of the higher excitations by some kind of perturbation theory.

This is done in the MRD-CI/B_K method [20, 13] which we want to present in the present section. After a brief introduction of the underlying theory we will discuss the CH molecule as a test system.

The theory of the B_K method [22] is based on the partitioning technique in perturbation theory [23, 24]. Suppose the Hamiltonian matrix **H** of the MR-CI space is partitioned as

$$\begin{pmatrix} \mathbf{H}_0 & \mathbf{h}^T \\ \mathbf{h} & \mathbf{H}_1 \end{pmatrix} \begin{pmatrix} \mathbf{c}_0 \\ \mathbf{c}_1 \end{pmatrix} = \mathbf{E} \begin{pmatrix} \mathbf{c}_0 \\ \mathbf{c}_1 \end{pmatrix} \quad (7)$$

where **H**₀ is a KxK submatrix of **H** containing all important configurations. Then **H**₁ is a (N-K)x(N-K) matrix formed from configurations of lesser importance and **h** contains the connecting matrix elements between the two sets of configurations. Within selective MR-CI techniques, **h** and **H**₁ are neglected and only

$$\mathbf{H}_0 \mathbf{c}_0'' = \mathbf{E}'' \mathbf{c}_0'' \quad (8)$$

is solved. The formula of the B_K method according to Davidson and coworkers [25, 26, 27, 28] is obtained if equation 7 is written as

$$[\mathbf{H}_0 + \mathbf{h}^T (\mathbf{E} - \mathbf{H}_1)^{-1} \mathbf{h}] \mathbf{c}_0 = \mathbf{E} \mathbf{c}_0 \quad (9)$$

and **H**₁ is replaced by its diagonal part

$$[\mathbf{H}_0 + \mathbf{h}^T (\mathbf{E}' - \mathbf{D})^{-1} \mathbf{h}] \mathbf{c}_0' = \mathbf{E} \mathbf{c}_0' \quad (10)$$

Depending on how **E'** in equation 10 is chosen, one arrives at Brillouin-Wigner (**E'** is equal to **E** and the equation is solved iteratively) or Rayleigh-Schrödinger (**E'** is equal to **E''** in equation 8) perturbation theory [25, 26]. In the present work Rayleigh-Schrödinger perturbation theory was adopted. The indirect effect of the neglected configuration is accounted for because the new vector **c**₀' contains the relaxation of **c**₀'' due to the neglected configurations in second-order perturbation theory.

The coefficients of configurations not contained in **c**₀' can also be estimated in second-order perturbation theory, using the A_K method [22].

$$\mathbf{c}_1' = (\mathbf{1E} - \mathbf{D})^{-1} \mathbf{h} \mathbf{c}_0' \quad (11)$$

In the following, the efficiency of the B_K method in correcting a truncated CI wavefunction will be discussed. Such a calculation, in the following abbreviated as a MRD-CI/B_K calculation, consists of two steps. After choosing the reference space, all single and double excitations are generated. In the first

step, the \mathbf{H}_0 matrix is diagonalized. It contains all configurations which lower the energy by more than a given threshold T_{CI} . In the second step, the B_K method is applied. Since the computation of all terms in $\mathbf{h}^T(\mathbf{E}' - \mathbf{D})^{-1}\mathbf{h}$ is very time consuming, they are only calculated for the most important configurations. All configurations possessing a coefficient absolutely greater than a given threshold T_{BK} are included in the B_K correction.

Detailed investigations about the efficiency of the B_K method in correcting truncated CI wavefunction have been performed for the electronic ground states of some atoms [20] and the electronic ground state, $X^2\Pi$ of the CH molecule [13]. In the present review we only want to focus on some important points, especially the convergence of the MRD-CI/ B_K method with respect to the size of H_0 and to the number of configurations actually included within the B_K correction. For smaller systems, we could show [20, 13] that the B_K/A_K correction actually gives the exact limit, e.g. the values obtained with the full MR-CI wavefunction. However, in the present review we will focus on the investigation of the CH molecule, where larger reference spaces are necessary for a good description of the isotropic hfcc's. For these calculations our software was unable to handle the total MR-CI space. Therefore, results will be compared with experimental data. For more detailed information the reader is referred to the original literature [20, 13].

The calculation of the isotropic hfcc of the carbon center $A_{iso}(^{13}\text{C})$ in the $X^2\Pi$ ground state of CH is a great challenge for ab initio calculations, although only 7 electrons need to be correlated. The $X^2\Pi$ state is derived from the electronic configuration $1\sigma^2 2\sigma^2 3\sigma^2 1\pi^1$. Since only the π orbital is singly occupied, the restricted Hartree-Fock approach (RHF) yields a value of zero for the isotropic hfcc's of both centers. The correct value (experiment [29, 30] gives 46.8 ± 2.8 MHz for the carbon center and -57.7 ± 0.3 MHz for the hydrogen center) is determined by correlation and/or polarization effects which can be taken into account, e.g., by a MR-CI treatment. For the isotropic hfcc of the carbon center, $A_{iso}(^{13}\text{C})$, very good agreement with the experimental value of 46.8 MHz (± 2.8 MHz) can only be obtained if triple excitations are taken into account (45 MHz). A SD-CI gives a value of 30 MHz, i.e. an error of more than 30 %. As already discussed in the previous section, a CI which includes only single excitations with respect to the Hartree-Fock configuration (S-CI) gives much better agreement (41 MHz) than the SD-CI calculations.

For the study of the CH molecule, the two different AO basis sets given in table 5 were used. The smaller AO basis set $(13s8p3d1f/9s3p) \rightarrow [8s5p3d1f/6s3p]$ was used to perform less expensive calculations. Experience gained from this basis set was used in the calculations with the larger basis set $(14s9p5d1f/10s3p) \rightarrow [9s6p5d1f/7s3p]$. The latter is flexible enough for a very reliable calculation of isotropic hfcc's. All calculations were performed for $R_e = 1.118$ Å. To obtain

Table 5: Description of AO basis sets used for the CH molecule.

small AO basis		
carbon center	(13s8p) \rightarrow [8s5p] + 3d functions (2.292/0.838/0.292) + 1f function (0.761)	v. Duijneveldt, Ref. [17]
hydrogen center	(8s) \rightarrow [5s] +1s function (2.4) +3p functions (1.848/0.649/0.228)	v. Duijneveldt, Ref. [17]
large AO basis		
carbon center	small basis +1s (0.02) +1p (0.0358) +2d (8.0/0.1)	Ref. [37]
hydrogen center	small basis +1s (0.01)	Ref. [37]

faster convergence of the CI expansion, natural orbitals (NO) were used as the one-particle basis.

Besides the reliability of a method, the question of economy is also important. In connection with the B_K/A_K approach, it is therefore interesting to investigate how the isotropic hfcc's (or any other property) calculated with the perturbationally corrected wavefunction depend on the number of configurations already included in H_0 . To gain insight into the problem we varied the size of H_0 . The influence of higher excitations was studied by increasing the size of the reference space. The reference configurations were selected according to the size of their coefficients. The results of the various calculations performed with the smaller AO basis set are given in table 6.

Let us first consider $A_{\text{iso}}(^{13}\text{C})$. Using the uncorrected truncated MR-CI wavefunction, the calculated value of $A_{\text{iso}}^{\text{CI}}(^{13}\text{C})$ increases by about 15 MHz if T_{CI} is lowered from 10^{-5} hartree ($\approx 3\,000$ configurations) to 10^{-6} hartree ($\approx 8\,000 - 9\,000$ configurations). If H_0 is further enlarged, $A_{\text{iso}}^{\text{CI}}(^{13}\text{C})$ increases less rapidly but it can be seen that convergence is not yet achieved at $T_{\text{CI}} = 5 \cdot 10^{-8}$ (29 240 configurations). This behaviour is quite similar to the dependencies found in other molecules [10, 32]. The dependence of $A_{\text{iso}}^{\text{CI}}(^{13}\text{C})$ on the number of configurations handled variationally is comparable for all reference spaces

Table 6: Details of calculations performed for the $X^2\Pi$ state of CH using the smaller basis set. Energies with respect to -34.0 hartree, isotropic hfcc's in MHz. Experimental values are 46.8 ± 2.8 MHz for the carbon center and -57.7 ± 0.3 MHz for the hydrogen center.

T_{CI}^b	SAF ^c	E_{CI}^d	$A_{iso}^{CI}(^{13}C)^e$	$A_{iso}^{CI}(H)^e$	E_{MRD-CI}^f	$E_{B_K}^g$	$A_{iso}^{B_K}(^{13}C)^g$	$A_{iso}^{B_K}(H)^g$
42 reference configurations $c^2 \approx 0.980^a$ MR-space : 443 464 SAF								
10.0	2 366	-0.4360	16.7	-54.0	-0.4544	-0.4580	32.1	-57.3
1.0	8 258	-0.4486	31.1	-55.3	-0.4529	-0.4559	41.8	-57.7
0.1	21 947	-0.4524	35.6	-56.4	-0.4541	-0.4547	40.7	-57.9
0.05	29 240	-0.4529	35.0	-56.8	-0.4543			
53 reference configurations $c^2 \approx 0.984^a$ MR-space : 523 413 SAF								
10.0	2 894	-0.4362	15.2	-54.1	-0.4541			
1.0	8 575	-0.4487	31.2	-55.0	-0.4532	-0.4562	41.8	-57.3
0.1	22 582	-0.4526	36.5	-56.2	-0.4545	-0.4550	41.4	-57.6
72 reference configurations $c^2 \approx 0.987^a$ MR-space : 638 893 SAF								
1.0	11 255	-0.4492	30.2	-55.5	-0.4538	-0.4563	41.5	-58.2
0.1	24 743	-0.4527	35.3	-56.4	-0.4545	-0.4553	41.6	-58.2

^a Part of reference space of the CI wavefunction on basis on the sum of squares of coefficients

^b In 10^{-6} Hartree

^c Number of SAF included in the diagonalization procedure

^d Energy obtained by diagonalizing H_0

^e Isotropic hfcc calculated with the truncated MR-CI wavefunction

^f Obtained using the MRD-CI scheme

^g Obtained using the B_K scheme. The number of corrected SAF is 1 500 - 2 000 ($T_{B_K}=0.001$)

used in the present work. The decrease in $A_{\text{iso}}^{\text{CI}}(^{13}\text{C})$ going from 53 reference configurations to 72 reference configurations seems to be due to the selection criterion, which tests the energy contribution of the single configurations but not their importance for a given property. We will return to this point further below.

Using the B_K method, the indirect effect of the neglected configurations is taken into account. As expected, the B_K method gives the largest correction for the smallest CI calculation ($T_{\text{CI}} = 10^{-5}$ hartree; 2366 configurations handled variationally), where a correction of about 16 MHz is obtained for the isotropic hfcc of the carbon center ($A_{\text{iso}}^{\text{CI}}(^{13}\text{C}) = 16.7$ MHz; $A_{\text{iso}}^{\text{BK}}(^{13}\text{C}) = 32.1$ MHz), but comparison with the calculation with smaller T_{CI} thresholds show that the variationally handled space is too small. If more configurations are included in H_0 , $A_{\text{iso}}^{\text{BK}}(^{13}\text{C})$ shows little dependence on T_{CI} . For the thresholds $T_{\text{CI}} = 10^{-6}$, 10^{-7} hartree, the value calculated with the corrected wavefunction, $A_{\text{iso}}^{\text{BK}}(^{13}\text{C})$, only varies by about 1 MHz, while $A_{\text{iso}}^{\text{CI}}(^{13}\text{C})$ obtained from the normal truncated MR-CI wavefunction changes by about 6 MHz. Furthermore, the corrected values are higher by about 5 - 10 MHz. The direct effect of the neglected configurations on $A_{\text{iso}}(^{13}\text{C})$ was studied using the A_K method. The influence is less than 0.2 MHz, independent of the size of H_0 . This is in agreement with calculations for the boron atom, which also show a small direct contribution if NO's rather than MO's are used [14, 20].

The present study clearly shows that for a reliable description of the isotropic hfcc's, less than 2 % of the total MR-CI space has to be handled variationally, if the effects of neglected configurations are taken into account using perturbation theory. The most elaborate calculations of $A_{\text{iso}}(^{13}\text{C})$ (72 reference configurations, 25 000 configurations handled variationally, 2 000 configurations corrected perturbationally) give the value 41.6 MHz. The error with respect to experiment is about 11 %, i.e. the error of 20 % in the truncated MR-CI wavefunction has been reduced by a factor of two.

The values calculated for the hydrogen center are also given in table 6. The dependence on the quality of the calculation is smaller than was found for $A_{\text{iso}}(^{13}\text{C})$ but similar trends can be seen. The theoretically most reliable value is $A_{\text{iso}}^{\text{BK}}(\text{H}) = -58.2$ MHz.

Before discussing the reasons for the success of the B_K method, we will give a short description of the results obtained with the larger AO basis set. Several studies [15, 8, 34, 19] show that to obtain very accurate isotropic hfcc's for atomic centers belonging to the second row, the inclusion of two compact d functions in the basis set is necessary. This condition is fulfilled by the second, larger basis set. The results obtained with the larger basis set are given in table 7. The smaller reference space (52 configurations) corresponds to that used for the smaller basis set. The larger reference space (77 configurations) was

Table 7: Details of calculations performed for $X^2\Pi$ state of CH using the larger basis set. Energies with respect to -34.0 hartree, isotropic hfcc's in MHz.

T_{CI}^b	SAF ^c	E_{CI}^d	$A_{iso}^{CI}(^{13}C)^e$	$A_{iso}^{CI}(H)^e$	E_{MRD-CI}^f	$E_{B_K}^g$	$A_{iso}^{B_K}(^{13}C)^g$	$A_{iso}^{B_K}(H)^g$
		53 reference configurations		$c^2 \approx 0.984^a$	MR-space : 865 680 SAF			
1.0	13 209	-0.4506	33.2	-55.1	-0.4561	-0.4595	44.4	-57.6
0.2	24 066	-0.4541	37.0	-56.0	-0.4566	-0.4580	44.2	-57.9
		77 reference configurations		$c^2 \approx 0.987^a$	MR-space : 1 154 750 SAF			
1.0	13 218	-0.4508	33.8	-55.1	-0.4563	-0.4597	46.0	-58.2
0.2	24 135	-0.4542	37.2	-56.3	-0.4567	-0.4583	45.8	-58.3

^a Part of reference space of the CI wavefunction on basis on the sum of squares of coefficients

^b In 10^{-6} Hartree

^c Number of SAF included in the diagonalization procedure

^d Energy obtained by diagonalizing H_0

^e Isotropic hfcc's calculated with the truncated MR-CI wavefunction

^f Obtained using the MRD-CI scheme

^g Obtained using the B_K scheme

optimized with respect to the spin density. For $A_{iso}(^{13}C)$, the values calculated with the truncated MR-CI wavefunction differ by about 1 - 2 MHz from those obtained with the smaller AO basis set. The dependence of $A_{iso}(^{13}C)$ on the size of the variationally handled space H_0 is comparable to that found for the smaller basis set, i.e. it increases by about 4 MHz if the number of variationally handled configurations is increased from about 13 000 to about 24 000. The deviation from the experimental value is about 9 MHz (20 %). The difference between both reference spaces is quite small.

If the B_K method is used, $A_{iso}^{B_K}(^{13}C)$ depends only little on the underlying truncated MR-CI calculation (< 0.3 MHz). The correction of $A_{iso}(^{13}C)$ due to the B_K method is about 8 - 9 MHz. The agreement of the final theoretical value (72 reference configurations, 24 000 configurations handled variationally, 1 500 configurations corrected perturbationally) with the experimental value is excellent (45.8 MHz vs. 46.6 MHz), i.e. with the B_K correction the theoretical value lies within the experimental uncertainty (± 2.8 MHz).

As already seen for the smaller basis set, similar but less prominent trends are found for $A_{iso}(H)$ (Table 7). Using the B_K method a value of -58.5 MHz is calculated. It differs only 0.8 MHz from the experimental value (-57.7 ± 0.3 MHz).

To test the MR-CI/ B_K method used in the present study, the isotropic hfcc's were also calculated with various other methods, e.g. the UHF method, Møller-Plesset perturbation theory up to the fourth order (MP2 - MP4), Cou-

pled Cluster methods with and without an estimation of the triple excitations (CCD and CCD(T)), and the QCISD method [52] with (QCISD(T)) and without an estimation of triple excitations (QCISD). In the present study, all these treatments are based on UHF wavefunctions while RHF is the starting point for the MR-CI/ B_K method. All calculations were performed with the larger AO basis set (table 5) using the GAUSSIAN88 program package [35]. A comparison of the various theoretical methods is given in table 8, which also includes results taken from the literature.

Let us first focus on the results for the hydrogen center. Except UHF, which overestimates the absolute value of $A_{\text{iso}}(\text{H})$ by about 26 MHz and MP2 which shows a deviation of about 4 MHz, all methods give very similar results (around -57.5 MHz). This behaviour reflects the relative simplicity of the calculation, as mentioned above.

The more difficult nature of $A_{\text{iso}}(^{13}\text{C})$ can be seen from table 8. UHF overestimates $A_{\text{iso}}(^{13}\text{C})$ by more than a factor of two, and only three methods predict values larger than 41 MHz, i.e. a deviation of less than 10 % from the experimental result. If MP2 is used, a value of 37.4 MHz is found, but the value decreases to 31.6 MHz if third order perturbation theory (MP3) is also included. By incorporating the fourth order (MP4STQ), the calculated value of $A_{\text{iso}}(^{13}\text{C})$ increases to 35.0 MHz, but it is still lower than the value obtained with MP2. All parts of the fourth order seem to be important, i.e. $A_{\text{iso}}(^{13}\text{C})$ decreases to 29.5 MHz if only double substitutions within the fourth order perturbation theory (MP4D) are accounted for. The dependence of $A_{\text{iso}}(^{13}\text{C})$ on the various orders of perturbation theory indicates that the good value obtained merely with MP2 is based on fortuitous error cancellation. The reasons for this behaviour are still unknown. The CC methods used in the present study give values of 33.6 MHz (CCD) and 37.2 MHz (CCD(T)). These are in good agreement with the CCD(ST) study by Carmichael (see lower part of table 8), who calculated 36.6 MHz using the CCD(ST) and a basis set of similar quality [41]. Besides the MR-CI/ B_K method presented here, only the QCISD method (43.7 MHz) and the QCISD(T) method (42.1 MHz) are able to calculate $A_{\text{iso}}(^{13}\text{C})$ with an error of less than 10 %. It should be noted, however, that in the QCISD method the inclusion of the triple excitations lowers $A_{\text{iso}}(^{13}\text{C})$, while opposite behaviour is found for CCD calculation. The best value of the various methods presented in table 8 is obtained by the MR-CI/ B_K method (45.8 MHz).

As discussed above, the expense of the B_K method should increase almost quadratically with the size of the B_K space. The question of the dependence of the calculated value of a given property on the number of configurations actually corrected by the B_K treatment is therefore quite important. In figure 1, $A_{\text{iso}}(^{13}\text{C})$ is plotted as a function of the size of the B_K space. In the

Table 8: Comparison of isotropic hfcc's of CH calculated using various methods.

Method	$A_{iso}(^{13}\text{C})$ [MHz]	$A_{iso}(^1\text{H})$ [MHz]
Calculations performed in the present study using the large basis set (see table 5)		
UHF	100.4	-84.4
MP2	37.4	-62.1
MP3	31.4	-58.0
MP4D ^a	29.5	-56.7
MP4DQ ^a	32.1	-57.2
MP4STQ ^b	35.0	-57.6
CCD	33.6	-56.7
CCD(T) ^c	37.2	-56.7
QCISD	43.7	-58.5
QCISD(T) ^c	42.1	-57.2
MRD-CI	37.2	-56.3
MRD-CI+B _K	45.8	-58.5
Calculations taken from the literature		
SDCI / STO ^e	47.8	-42.4
MBPT / STO ^f	37.3	-59.4
MCSCF / num ^g	49.9	-57.8
CCD(ST) / CGTO ^h	36.6	-57.0
S-CI / CGTO ⁱ	41.4	-57.1
SD-CI / CGTO ⁱ	30.0	-51.8
SDT-CI / CGTO ⁱ	45.8	-58.0
Experimental data		
	46.8 ^j	-57.7 ^k
	± 2.8	± 0.3

^a Only parts of the excitation classes are included^b Full fourth order perturbation theory^c Large basis set using Slater functions, Ref. [39]^f Many-body perturbation theory, Ref. [40]^g Numerical MCSCF, polarization effects are taken into account, Ref. [38]^h Coupled Cluster with estimates of triple and quadruple contributions

(14s9p4d1f,9s3p1d)→ [8s5p4d1f,6s3p1d], Ref. [41]

ⁱ (10s6p2d1f,6s2p1d)→ [6s3p2d1f,4s2p1d], Ref. [12]^jRef [29]^kRef [30]

foregoing truncated MR-CI calculation, 24 135 configurations were handled variationally. The reference space consists of 77 configurations, leading to a total MR-CI space of 1 154 750 configurations. The isotropic hfcc's obtained with the truncated MR-CI wavefunction, ($A_{\text{iso}}^{\text{CI}}$), and the experimental values are given for comparison. The configurations included in the B_K treatment were selected according to the magnitude of their coefficients in the truncated MR-CI wavefunction. In figure 1, it can be seen that for very small B_K spaces (< 100 configurations) the calculated value of $A_{\text{iso}}(^{13}\text{C})$ increases dramatically (≈ 9 MHz), while further extension of the B_K space leads to much smaller variations (< 1 MHz) in $A_{\text{iso}}(^{13}\text{C})$. The fast convergence of $A_{\text{iso}}(^{13}\text{C})$ as a function of the number of configurations actually corrected in the B_K treatment is obvious.

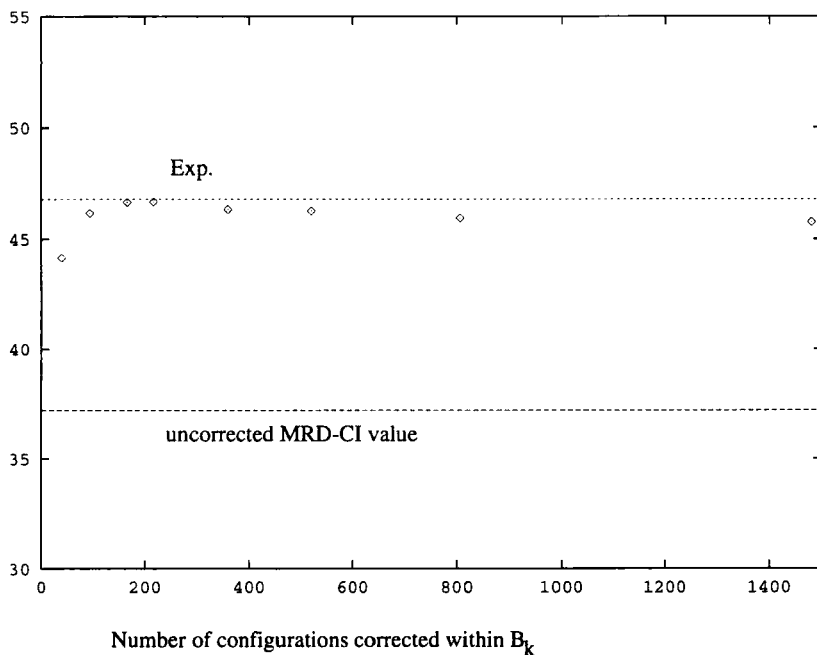


Figure 1: $A_{\text{iso}}(^{13}\text{C})$ as a function of the size of the B_K space. The foregoing MRD-CI calculation was performed with the large AO basis set and 77 reference configurations. A total of 24 135 configurations were handled variationally. The value obtained with the truncated MRD-CI wave function and the experimental value are given for comparison.

In section 2.1 we discussed the influence of higher excitations on A_{iso} . From table 4 it was obvious that the indirect influence of higher excitations leads to major changes only in the Singles-RHF contributions to A_{iso} . Therefore, within the MRD-CI/ B_K method it should be sufficient to correct the coefficients of the main configuration and of the single excitations. Confirmation of this conclusion has been given in a number of other cases [64, 44, 42, 43].

Table 9: Calculated hyperfine coupling constants for the $X^3\Sigma_g^-$ ground state of O_2 ($R=2.28$ bohr). An $[8s6p3d]$ AO basis set was employed (see text). All values are given in MHz.

	A_{iso}		A_{zz}	
	MO	NO	MO	NO
SD-CI	-27	-28	88	88
MRD-CI	-29	-37	88	89
MRD - CI/ B_K	-41	-58	89	89
Exp. ^a		-55		93

^a see Ref. [166]

The influence of the one-particle basis employed in the calculations can be seen from a study of the oxygen molecule in its electronic ground state ($X^3\Sigma_g^-$) [42]. The calculated values are given in table 9. The AO basis set used in the investigation is built upon the $(12s7p)/[7s4p]$ ‘quadruple-zeta’ basis of Koga and Thakkar [85], augmented by diffuse and polarisation functions, as given by Liu and Dykstra ($\alpha_s = 0.06$, $\alpha_p = 0.05, 0.007$, $\alpha_d = 0.9, 0.13, 0.02$) [86].

As already seen for CH, the calculated hfcc’s improve considerably if the B_K method is used to correct the wavefunction, e.g., if the indirect effects arising from the neglected configuration are taken into account. The improvement of the calculated isotropic hfcc’s if NO’s are used instead of MO’s results from the increased compactness of the wavefunction. Because the B_K correction only incorporates the indirect effect of the neglected configurations while the direct effect is not taken into account, an improvement of the calculated value of A_{iso} is found if NO’s are used instead of MO’s. As shown in test calculations performed for atomic systems [20], this effect can partly be incorporated if the A_K method is used in addition.

In summary a recipe for doing a MRD-CI/ B_K calculation is as follows:

- Choose an appropriate reference space: The reference space should include all configuration possessing a significant coefficient in a foregoing

CI calculation. In addition it should include important single excitations. Because the coefficients of the single excitations are rather small, the process of selecting important single excitations should include an analysis of the spin density matrix of a foregoing CI calculation.

- The calculated isotropic hfcc's deteriorates if the size of H_0 is too small. The convergence depends on the system under consideration but, if NO's are used, an inclusion of 1% of the generated configurations (or less) should be sufficient.
- To get convergence with respect to the B_K correction it is sufficient to include the main configurations, their single excitations, and some configurations (normally double excitations with respect to the main configurations) with medium sized coefficients.
- The AO basis set should be of triple zeta or better quality; polarization functions are important and additional basis functions with very tight and diffuse exponents are helpful. A good compromise between accuracy and cost is provided by the AO basis set given by Chipman [5], enlarged by an additional tight s function.

These points are important for isotropic hfcc's; for computations of anisotropic hfcc's, most reasonably flexible AO basis sets are sufficient.

From our experience, the effects not taken into account in such a calculation are smaller than errors arising from other sources, such as the calculated equilibrium geometry and effects arising from nuclear motion [84]

2.3 Applications

After discussing the underlying theory of the MRD-CI/ B_K method, we want to give a few examples, which illustrate some problems in the calculations of isotropic hfcc's. To give a feeling about the accuracy of various theoretical levels, we will compare the MRD-CI/ B_K method with several other theoretical approaches. As a test system we use the H_2CO^+ molecule in its electronic ground state.

Furthermore, using H_2CN as a model system, the problems of *ab initio* methods in calculating the isotropic hfcc's of β protons will be described.

2.3.1 H_2CN and H_2CO^+

Chemically, the methylene imino radical (H_2CN) is of interest, e.g., by its importance as a chemical intermediate in some ballistic propellants and in the formation of HCN in the clouds of Jupiter. A discussion of recent theoretical

and experimental work on this radical may be found in the review article by Marston and Stief [45]. In 1962, Cochran et al. [46] detected H_2CN for the first time, using Electron Spin Resonance (ESR) experiments. Many further ESR studies have been reported. In different matrices the isotropic hfcc values of the protons range from 255 MHz [47] to 240 MHz, while $A_{\text{iso}}(^{14}\text{N})$ varies between 42 MHz [46] and 26.6 MHz. A recent microwave investigation of Yamamoto and Saito [48] yielded the first experimental gas phase hyperfine parameters for the hydrogen and the nitrogen centers. For the protons $A_{\text{iso}} = 233.2$ MHz was found, while 25.9 MHz was given for the nitrogen center. This shows that matrix effects shift both parameters by about 10 % to higher values. Based on the measured rotational constants Yamamoto and Saito suggested three possible equilibrium geometries which will be discussed later on.

Less experimental information is available for H_2CO^+ (X^2B_2). In particular, a microwave investigation of this molecule is missing and to the best knowledge of the authors, no experimental geometry has been reported. As for H_2CN , matrix effects are large. The isotropic hfcc's of the protons range from 372.1 MHz [49] measured in a neon matrix to 253 MHz [50] found in sulphuric acid at 77K. For the carbon center only one value (109 MHz) was reported, by Knight and Steadman [49].

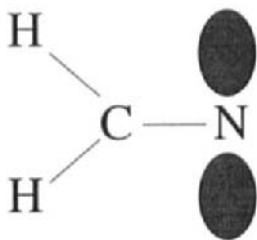


Figure 2: The shape of the singly occupied molecular orbital (SOMO) in H_2CN (X^2B_2). The SOMO of the H_2CO^+ (X^2B_2) is similar.

In the present context both molecules are very interesting. As can be seen from figure 2, which shows the singly occupied molecular orbital (SOMO) of H_2CN , the hydrogen centers represent β -protons. As shown in other studies [90], the isotropic ESR parameter of β -protons are extremely difficult to calculate so that the ground states of H_2CN and H_2CO^+ (X^2B_2) can serve as small model systems to study the problems. The arising difficulties are very

surprising because the SOMO does not vanish at the position of the β -protons, e.g. already the RHF approach gives half of the total value of A_{iso} .

Both molecules were considered in the theoretical studies of Feller and Davidson [51, 15, 16, 3], which renewed the interest in the *ab initio* studies of ESR parameters. Although the calculations seem to be at a high level of sophistication, the calculated isotropic hfcc's deviate about 30 – 50 % from the experimental values. The methylene imino radical (H_2CN) was later reinvestigated by Chipman, Carmichael and Feller [10], in the following abbreviated as the CCF study, using single excitation CI (S-CI) and QCISD(T) [52] methods, as well as configuration selected MR-CI calculations. The values predicted by configuration selected MR-CI calculations were too small for all centers (deviations of up to 40 % from the experimental results), although very large reference spaces (146 configurations) were used. The study clearly shows that configuration selection was one of the major error sources. Although more than 450 000 CSF were selected, convergence of the isotropic hfccs with respect to the selection threshold was not reached. The use of an unselected MR-CI was impossible, since the size of the MR-CI space was around 33 000 000.

The QCISD(T) method, first used in the calculation of isotropic hfcc's by Carmichael [53, 54], yielded much better agreement. For the heavier centers the agreement is nearly perfect – a deviation of less than 3 MHz is found – but the description of the isotropic hfcc of the hydrogen center turned out to be very complicated. The QCISD(T) method deviates by about 14 % (22 MHz) from the experimental value, while a deviation of about 24 % (48 MHz) was found for the configuration selected MR-CI. The H_2CN radical was also considered in the study of Cave, Xantheas and Feller [55], in the following abbreviated as the CXF study. In the CXF study, ACPF and Quasidegenerate Variational Perturbation Theory (QDVPT) [56] were used to estimate the influence of parts of those excitations not included in the MR-CI approach. However, even for $A_{\text{iso}}(\text{H})$ these contributions were found to be less important (4–6 MHz).

While vibrational effects were found to be unimportant because the isotropic hfcc's depend nearly linearly on the internal coordinates [10], the equilibrium geometry does indeed seem to be very important. This has been verified also in a number of other cases [89, 87, 88]. Therefore, in the present investigation we will concentrate on the methods used to calculate the isotropic hfcc's and on the influence of the equilibrium geometry obtained by different theoretical and experimental methods.

In order to discuss the ability of the MRDCI/ B_K method to predict the isotropic hfcc's and to study the reasons responsible for the poor agreement found in the configuration selected MR-CI calculation in the CCF [10] and CXF [55] studies, an investigation was performed at the geometry used in both these previous works. The AO basis sets used are given in table 10. The

Table 10: Definition of the van Duijneveldt AO basis set.

carbon center	(13s8p) \rightarrow [8s5p] +2d functions (1.097/0.318)
nitrogen center	(13s8p) \rightarrow [8s5p] +2d functions (1.654/0.469)
oxygen center	(13s8p) \rightarrow [8s5p] +2d functions (2.314/0.645)
hydrogen center	(9s) \rightarrow [7s] +2p functions (1.407/0.388)

calculated hfcc's are summarized in table 11, along with the outcome of the previous investigations. Let us first focus on the hydrogen center, because it is the most difficult property. Using the uncorrected MRD-CI wave function obtained with a selection threshold of $T_{CI} = 10^{-6}$ hartree, the isotropic hfcc's obtained in the present study are similar to those of previous work using the same level of sophistication (86 reference configurations, $T_{CI} = 10^{-6}$ hartree). If the number of variationally handled configurations is enlarged by decreasing T_{CI} , $A_{iso}(H)$ increases slowly but, even for the largest MR-CI calculation performed in the CCF study ($T_{CI} = 10^{-7}$ hartree, 446 932 CSF selected), no convergence is reached in $A_{iso}(H)$ (see also figures 1 and 2 of the CCF study). If instead of enlarging the variationally handled space, the indirect effect of the neglected configurations is estimated by the B_K method, $A_{iso}(H)$ jumps by about 40 MHz (MRD-CI : 171.9 MHz, MRD-CI/ B_K : 212.1 MHz) towards the experimental results. Similar effects can be seen for the isotropic hfcc's of the carbon and the nitrogen centers. This clearly shows that the reason for the failure of the configuration selected MR-CI wave function in predicting reliable isotropic hfcc's for H_2CN lies in the slow convergence of A_{iso} as a function of T_{CI} . The indirect influence of the neglected configurations, which is incorporated by the B_K treatment, is very important and cannot be neglected in the calculation of isotropic hfcc's. As found for the CH radical, the QCISD(T) gives very similar results to the MRD-CI/ B_K method.

Before we discuss the influence of the equilibrium geometry, let us focus on the effects arising from excitations not included within our treatment. The value of $A_{iso}(H)$ increases from 204 MHz to 212 MHz if the reference space is enlarged from 28 CSF to 72 CSF. Similar trends are found in the CCF and CXF studies. Further enlargement of the reference space should lead to an

Table 11: Comparison of the present study with other theoretical studies on H_2CN . The isotropic hfcc's (A_{iso}) are given in MHz. The ROHF geometry of McManus et al. was used throughout.

method	$A_{\text{iso}}(^1\text{H})$	$A_{\text{iso}}(^{13}\text{C})$	$A_{\text{iso}}(^{14}\text{N})$
^a S-CI	166.0	-68.3	24.1
^a SD-CI	152.3	-49.3	6.4
^b MRD-CI (^c 86; ^d 10.0)	169.3	-61.7	12.9
^b MRD-CI (^c 86; ^d 1.0)	173.6	-65.8	14.2
^b MRD-CI (^c 86; ^d 0.1)	184.8	-71.1	17.6
^a MRD-CI (^c 146; ^d 0.1)	187.0	-72.0	17.0
^a QCISD	211.4	-75.6	24.6
^a QCISD(T)	211.1	-77.8	26.0
^e MRD-CI (^c 28; ^d 2.0)	166.7	-56.1	10.1
^e MRD-CI/ B_K (^c 28; ^d 2.0)	204.1	-76.0	26.7
^e MRD-CI (^c 72; ^d 1.0)	171.9	-55.7	11.0
^e MRD-CI/ B_K (^c 72; ^d 1.0)	212.1	-75.0	26.6
Experiment	233.2	-80.9	25.9

^a Carmichael, Chipman and Feller [10]

^b Cave et al. [55]

^c Number of configurations in the reference space

^d Selection threshold in 10^{-6} hartree

^e Present work, using the van Duijneveldt AO basis

increase in A_{iso} of about 4 – 6 MHz. This can be seen from the calculation using 146 reference configurations and is supported by the CXF study, in which up to 375 reference configurations were used in combination with a DZP AO basis set.

Table 12: Equilibrium geometries of H_2CN obtained by different methods.

Method	R_{CN} [pm]	R_{CH} [pm]	ϕ_{HCH}	Ref.:
ROHF	124.3	108.4	119	[57]
MCSCF-ACPF	125.6	109.4	121.1	
SAITO1	126.1	108	122.3	[48]
SAITO2	124.7	111	116.7	[48]

Table 13: Isotropic hyperfine couplings in H_2CN using the MRD-CI/ B_K method with different geometries (in MHz).

geometry	A(C)	A(N)	A(H)	Energy ^a
SAITO1	-73.0	26.4	193.9	-93.808732
SAITO2	-81.1	25.7	219.1	-93.809112
ROHF [57]	-75.0	26.6	212.1	-93.808212
MCSCF-ACPF	-78.0	26.0	207.9	-93.809434
Exp.: [48]	-80.9	25.9	233.2	

^a Calculated with the MCSCF-ACPF method using the van Duijneveldt basis.

Another uncertainty in the theoretical predicted isotropic hfcc's arises from the equilibrium geometry of H_2CN (cf. table 12). As discussed above, vibrational effects are of little importance [10]. Table 13 lists the isotropic hfcc's calculated at different structures, namely the equilibrium structure obtained from the MCSCF-ACPF calculation and two geometries suggested from the microwave study of Yamamoto and Saito [48] (SAITO1, SAITO2). The third structure given by the experimental investigation was not included because at the level of MCSCF-ACPF it is higher in energy by about 700 cm^{-1} . The ROHF structure given by McManus et al. [57] is included to compare the results to those given in table 11. The geometrical parameters of the various structures are given in table 12. The energy differences between the structures

SAITO1, SAITO2 and MCSCF-ACPF are smaller than 160 cm^{-1} , indicating the very flat nature of the potential energy hypersurface around the equilibrium geometry of the molecule. The MCSCF-ACPF structure has the lowest energy but the SAITO1 structure is only 70 cm^{-1} higher in energy. The changes in the isotropic hfcc's calculated at the various geometries are significant. Comparing the two experimental structures, $A_{\text{iso}}(\text{H})$ varies by about 26 MHz, while a change of 8 MHz is found for $A_{\text{iso}}(\text{C})$. For both centers the variation amounts to about 10 % of the absolute values, while the isotropic hfcc's of the nitrogen center are less sensitive. The values obtained for the MCSCF-ACPF structure are between the ones calculated for the two experimental geometries, being closer to the values for the SAITO1 structure. The variations in $A_{\text{iso}}(\text{H})$ and $A_{\text{iso}}(\text{C})$ arise due to two opposite trends. Going from the SAITO1 structure to the SAITO2 structure, the CN distance shortens and the HCH angle decreases. While an increase in the absolute value of $A_{\text{iso}}(\text{C})$ results from the first modification (cf table 13), a decrease is found for the second. Similar effects exist for the hydrogen center. Summarizing, we expect an uncertainty of about 5 % for the isotropic hfcc's of H_2CN from inaccuracies in the equilibrium geometry.

Using the SAITO2 structure, $A_{\text{iso}}(\text{H})$ calculated in the present study deviates only 6 % from the experimental value, while a deviation of 11 % is found using the MCSCF-ACPF structure, although both geometries are very close in energy ($\Delta E = 70\text{ cm}^{-1}$). For $A_{\text{iso}}(\text{C})$ the agreement with the experimental value is good. Using the MCSCF-ACPF structure a deviation of 3 % is found, while an error of only 0.2 % is obtained at the SAITO2 structure. For $A_{\text{iso}}(\text{N})$, which is insensitive to geometrical variations, the agreement is excellent (0.2 %). To decrease the uncertainties in the isotropic hfcc's a very accurate equilibrium geometry, perhaps obtained by combining experimental and theoretical results [58], is necessary. The influences of higher excitations not taken into account in the present study (4 – 6 MHz) or of vibrational effects (3 MHz [10]) are less important. The inability of configuration selected MRD-CI studies to predict isotropic hfcc's is due to the neglect of the indirect contributions of those configurations not included in the MR-CI wave function, which in the present study have been incorporated via the B_K correction.

The anisotropic hfccs are given in table 14. All theoretical values were calculated using the MRD-CI/ B_K method but, as already mentioned, they are quite insensitive to the method of calculation. We have therefore omitted from the table most previous results given in the literature. Only the study of Feller and Davidson is included for comparison. The dependence upon the geometry is also less prominent.

For the molecule H_2CN , we compared the MRD-CI/ B_K method to S-CI, SD-CI, truncated MR-CI calculations and to the QCISD calculations reported in the very careful CCF investigation [10]. To give a feeling about the relia-

Table 14: Anisotropic hyperfine coupling constants (in MHz) of H_2CN (X^2B_2). The values of the present work were obtained with the van Duijneveldt AO basis in combination with the MRD-CI/ B_K method.

	Hydrogen			Carbon		Nitrogen	
	$^aT_{aa}$	T_{bb}	T_{ab}	T_{aa}	T_{bb}	T_{aa}	T_{bb}
$^b\text{SAITO1}$	10.4	-3.8	± 3.8	16.2	2.9	-46.3	79.3
$^b\text{SAITO2}$	8.9	-3.7	± 2.8	16.9	0.9	-45.3	77.9
$^b\text{MCSCF-ACPF}$	9.5	-3.7	± 3.1	16.7	1.7	-45.7	78.5
$^c\text{MR-CI}$	8.7	-2.2	± 4.2	16.0	1.7	-44.0	76.4
$^d\text{Exp.}$	8.3 ± 0.1	-2.2 ± 1.3				-45.1 ± 0.1	80.4 ± 0.1

- ^a For comparison with the experimental results the elements of the hyperfine tensor are given within the principal axis of the inertial tensor, with T_{aa} lying along I_a , which in the present molecule corresponds to the twofold symmetry axis. T_{bb} , lying along I_b , is the second element of the hyperfine tensor in the molecular plane. The last diagonal element (perpendicular to the molecular plane) can be obtained from the fact that the anisotropic tensor is traceless. The outer diagonal elements T_{ab} for carbon and oxygen are zero by symmetry, for the hydrogen centers they possess different signs.
- ^b The various geometrical parameters can be taken from table 12.
- ^c Reference [16].
- ^d Reference [48].

Table 15: Definition of the Chipman+Peak AO-basis set.

Chipman basis		
carbon center	(9s5p) \rightarrow [5s3p]	Huzinaga [63]
	+ 1s function (0.0479)	[37]
	+ 1s function (28217.82)	[38]
	+ 2d functions (0.28/1.12)	[37]
nitrogen center	(9s5p) \rightarrow [5s2p]	Huzinaga [63]
	+ 1s function (0.0667)	[38]
	+ 1s function (39350.32)	[38]
	+ 1p function (0.0517)	[37]
	+ 2d functions (0.37/1.48)	[37]
oxygen center	(9s5p) \rightarrow [5s2p]	Huzinaga [63]
	+ 1s function (0.0862)	[38]
	+ 1s function (52962.288)	[37]
	+ 2d functions (0.55/2.2)	
hydrogen center	(5s) \rightarrow [3s]	Huzinaga [63]
	+1s function (0.0483)	[38]
	+1s function (850.8678)	[37]
	+1p functions (1.0)	

bility of isotropic hfcc's calculated with various other theoretical approaches we want to extend our comparison using the H_2CO^+ molecule in its electronic ground state (X^2B_2). The basis set used is described in table 15. The values are collected in table 16. According to the calculated isotropic hfcc's, the methods can be divided into three groups. In terms of the absolute values, the uncorrected MRD-CI treatment gives the smallest isotropic hfcc's. The large deviations from the experimental results is due to the neglect of the indirect effects, as already discussed for H_2CN . Better results are obtained with Møller-Plesset perturbation theory (UMP2-UMP4). However, the series of the Møller-Plesset perturbation theory (UMP2-UMP4) shows similar behaviour as found for the CH molecule. The UMP2 values are surprisingly good, but comparing UMP2, UMP3 and UMP4 some sort of error cancellation is obvious. Best agreement with the experimental results is obtained in the last group of correlation treatments, consisting of QCISD(T), CCSD(T), BD(T) and MRD-CI/ B_K . All treatments yield very similar results. According to the present study the MRD-CI/ B_K results obtained with the van Duijneveldt basis set should be the theoretically most reliable.

Table 16: The isotropic hyperfine values of H_2CO^+ in its ground state (X^2B_2) using different methods (in MHz). The QCISD(T)/6-31G** optimized geometry ($R_{CO} = 121.1$ pm, $R_{CH} = 111.4$ pm, $\angle_{HCN} = 122.0$) was used throughout. All calculations were performed with the AO basis set described in table 15.

method	A(C)	A(O)	A(H)
UMP2	-108	-53	295
UMP3	-102	-61	271
UMP4	-101	-54	293
QCISD	-112	-67	313
QCISD(T)	-108	-66	319
CCSD	-111	-69	309
CCSD(T)	-107	-65	317
BD	-110	-70	306
BD(T)	-108	-67	318
MRD-CI	-86	-44	284
MRD-CI/ B_K	-107	-63	318
Exp.: [50]			253
Exp.: [49]	-109		372

A comparison of our results with theoretically predicted isotropic hfcc's

Table 17: Calculated isotropic hyperfine values (in MHz) for H_2CO^+ in its ground state (X^2B_2).

method	AO basis	A(C)	A(O)	A(H)
MR-CI	ETG	-67	-39	224 [51]
SAC-CI	DZ	-81	-37	328 [60]
SAC-CI	STO	-78	-39	312 [61]
CCSD	DZP	-104	-59	280 [62]
MRDCI + B_k	Duijneveldt	-104	-67	324
Exp.:				253 [50]
Exp.:		-109		372 [49]

taken from the literature is presented in table 17. It contains the values given by Feller and Davidson (MRD-CI/ETG) [51], which are much too small. Another study was performed by Nakatsuji and coworkers [60, 61] using the SAC-CI method in combination with very small AO basis sets. While $A_{\text{iso}}(\text{H})$ seems to be quite good, the values obtained for the heavy centers are also too small, so that some sort of error cancellation can be assumed. Especially the size of the AO basis sets used in the latter studies seems to be insufficient. In difference to the other theoretical investigations mentioned in table 17, Nakatsuji and Izawa [61] used Slater type orbitals (STO) for the calculation of the isotropic hfcc's. They claimed that the inadequacy of the calculation of Feller and Davidson was due to the use of Gaussian type orbitals (GTO). This is contrary to the present study, which clearly shows that not the use of GTOs but rather the neglect of the indirect effects is a more important reason for the bad agreement with the experimental data. A comparison of the CCSD and CCSD(T) calculations performed in the present work with the study of Sekino and Bartlett [62] reveals that the standard DZP AO basis set is not flexible enough for the calculation of spin densities.

2.3.2 Electronic triplet states

Most of the studies about ESR parameters deal with molecules possessing one unpaired electron, i.e. $S=1/2$. Investigations on systems with $S=1$ are rare. To show the ability of the MRD-CI/ B_k method we want to discuss the hyperfine structure of the isoelectronic molecules CCO, CNN and NCN [64].

As already discussed the S-CI treatment gives quantitative agreement with the experimental results [12, 5] in many cases. S-CI calculations are inexpensive, which could open a possibility for handling large molecules. However,

as discussed above, the success of S-CI is due to error cancellation which in some cases, e.g. H_2CN (X^2B_2), does even out. The performance of this method for triplet states is not as predictable, since two electrons interact with the electronic core. Therefore, S-CI and SD-CI calculations were also performed. These calculations were performed using the MELDF-X programs [31]. For the S-CI and SD-CI calculations, canonical orbitals were used as the one-electron basis.

The isoelectronic molecules CCO, CNN and NCN are reactive triplet radicals. They are linear in their $X^3\Sigma^-$ electronic ground states. Many experimental [65] – [75] and theoretical [76]–[83] investigations have been performed for these interesting molecules. Most of the studies consider the structure and the vibrational frequencies. Using the isotopic molecules $^{13}\text{C}^{12}\text{C}^{16}\text{O}$, $^{12}\text{C}^{13}\text{C}^{16}\text{O}$, $^{12}\text{C}^{15}\text{N}^{15}\text{N}$, $^{12}\text{C}^{14}\text{N}^{14}\text{N}$ and $^{13}\text{C}^{15}\text{N}^{15}\text{N}$, the hyperfine structure of CCO and CNN was investigated experimentally by Smith and Weltner [75] in noble gas matrices at 4 K. Hyperfine coupling constants could be measured for all centers except the oxygen. In the case of CNN not all of the expected lines could be resolved due to line broadening. Furthermore only the absolute values of A_\perp could be determined.

The electronic structure of the ground state of the CNN and CCO molecules is $^3\Sigma^-$, with the following configuration:

$$(1\sigma)^2(2\sigma)^2(3\sigma)^2(4\sigma)^2(5\sigma)^2(1\pi_x)^2(1\pi_y)^2(2\pi_x)^1(2\pi_y)^1,$$

while NCN has a $^3\Sigma_g^-$ ground state with the electronic configuration :

$$(1\sigma_g)^2(1\sigma_u)^2(2\sigma_g)^2(3\sigma_g)^2(2\sigma_u)^2(4\sigma_g)^2(3\sigma_u)^2(1\pi_u)^4(1\pi_g)^2,$$

For technical reasons the calculations for CNN and CCO were performed in C_{2v} symmetry, while for NCN the D_{2h} symmetry was imposed.

Natural orbitals obtained from preliminary MRD-CI calculations were used as the one-particle basis. The reference configurations in the calculations were selected according to two criteria. First, the squared coefficients of the reference configuration should be larger than 0.002 in the final wavefunctions, and secondly, their importance in the spin density matrix was analyzed. The number of the reference configurations obtained with this procedure was between 50 and 60. For CNN and CCO about $13.5 \cdot 10^6$ configurations were generated from these reference sets, while for NCN the MR-CI space consisted of about $6.5 \cdot 10^6$ configurations. The sum of the squared coefficients of the reference configurations were consistently around 0.90. The number of the selected configurations was approximately 30 000 in all MRD-CI calculations. All single excitations with respect to the main configurations were included in the B_K correction. For the calculation the Chipman AO basis [37, 38] which contains

diffuse s and p functions and d polarization functions was augmented by a tight s-function, with exponent 28191.9 for carbon, 40030.9 for nitrogen and 51962.3 for oxygen.

Table 18: Theoretical hyperfine coupling constants (in MHz) for CCO ($^3\Sigma_u^-$) CNN ($^3\Sigma_u^-$) and NCN ($^3\Sigma_g^-$) from the MRD-CI/B_K calculations ($A_\perp = A_{\text{iso}} - \frac{1}{2}T_{zz}$, $A_\parallel = A_{\text{iso}} + T_{zz}$).

$C_\alpha C_\beta O$	C_α			C_β			O		
	A_{iso}	A_\perp	A_\parallel	A_{iso}	A_\perp	A_\parallel	A_{iso}	A_\perp	A_\parallel
S-CI	17.3	43.7	-35.5	-33.8	-32.4	-36.6	-26.6	-43.3	6.8
SD-CI	-8.0	17.9	-59.7	-34.8	-32.0	-40.2	-5.2	-17.7	19.8
MRD-CI	-7.8	17.9	-59.3	-34.0	-31.7	-38.7	-12.7	-26.8	15.7
MRD-CI/B _K	30.7	56.3	-20.7	-30.7	-29.6	-32.9	-23.8	-41.3	11.2
exptl ^a		57(3)	-17(3)		-26(3)	-32(3)			
$CN_\alpha N_\beta^c$	C			N_α			N_β		
	A_{iso}	A_\perp	A_\parallel	A_{iso}	A_\perp	A_\parallel	A_{iso}	A_\perp	A_\parallel
S-CI	36.9	51.2	8.4	-16.8	-20.0	-10.5	25.3	43.6	-11.3
SD-CI	-7.6	2.3	-28.2	-13.1	-14.9	-9.4	8.0	26.6	-29.2
MRDCI	11.4	24.8	-15.2	-18.8	-21.4	-13.7	9.6	27.1	-25.6
MRDCI/B _K	35.3	52.9	-0.1	-22.3	-25.8	-15.3	19.3	35.4	-13.0
exptl ^{a,b}		50(5)			-19(5)			35(5)	
NCN ^c	C			N					
	A_{iso}	A_\perp	A_\parallel	A_{iso}	A_\perp	A_\parallel			
S-CI	-64.4	-77.2	-38.6	14.7	28.1	-12.1			
SD-CI	-44.3	-54.2	-24.75	1.6	13.6	-22.3			
MRDCI	-61.0	-72.9	-37.2	8.2	20.9	-17.2			
MRDCI/B _K	-73.8	-86.9	-47.8	14.1	27.1	-11.8			

^aRef. [75]; the numbers in parentheses are the experimental errors, the signs of the experimental values were taken from the theoretical calculations.

^bThe nitrogen centers have been interchanged.

^cValues for ^{14}N .

In table 18, the results of the hyperfine calculations are collected. A comparison with the experimental data for $A_\perp = A_{\text{iso}} - \frac{1}{2}T_{zz}$ and $A_\parallel = A_{\text{iso}} + T_{zz}$ is given. The isotropic hfcc A_{iso} is also included, because its strong dependence on the theoretical method is the reason for the variations of A_\perp and A_\parallel between different methods. Since the anisotropic term T_{zz} is nearly constant with respect to the theoretical method, it is not given. For all calculations the QCISD/6-31G* optimized geometries (CCO: $R_{\text{CC}} = 1.371$ Å, $R_{\text{CO}} = 1.173$ Å; CNN: $R_{\text{NN}} = 1.231$ Å, $R_{\text{CN}} = 1.237$ Å; NCN: $R_{\text{CN}} = 1.245$ Å) were used. All

molecules possess a linear equilibrium geometry, and vibrational effects were found to be small [64].

Comparison of the theoretical values with the experimental findings shows that only the MRD-CI/ B_K treatment yields reliable quantitative hfcc's for all the investigated molecules. Employing this method, all results lie within the experimental error bars. The S-CI method again reaches qualitative agreement with the experimental results. The deviations are between 0 and 6 MHz (0–20 %), with exception of the C_α center in $C_\alpha C_\beta O$, for which much larger errors were found. The value of A_\perp deviates more than 12 MHz (≈ 23 %) from the experimental value (43.7 MHz vs. 57 ± 3 MHz); for A_\parallel an error of 15 MHz (≈ 71 %) is found. Comparison with the MRD-CI/ B_K treatment shows that the S-CI calculations yield a value for the isotropic hfcc of C_α which is much too low (17.3 MHz vs. 30.7 MHz).

As discussed in the previous section, the agreement with experimental data deteriorates dramatically when double excitations are also taken into account. The SD-CI method yields deviations of more than 40 MHz. For truncated MRD-CI calculations, in which the most important higher excitations are accounted for, the situation improves to some extent. However, the influence of the discarded configurations is found to be substantial. If their influence is included via the modified B_K treatment, almost perfect agreement with the experimental findings is obtained; in all cases the deviations from the experimental data lie within the experimental error bars. Again the most remarkable example is the C_α center of $C_\alpha C_\beta O$ where the B_K corrections improves the isotropic hfcc from -7.8 MHz (MRD-CI) to 30.7 MHz (MRD-CI/ B_K). Due to this improvement A_\perp increases from 17.9 to 56.3 MHz (Exp.: 57 ± 3 MHz) while the value of A_\parallel goes from -50.3 MHz to -20.7 MHz (Exp.: -17 ± 3 MHz).

Considering the excellent agreement between theory and experiment for CCO it became obvious during the analysis of the $CN_\alpha N_\beta$ values that the assignment of the experimental hfcc's to N_α and N_β was wrong. In their original work, Smith and Weltner assigned the A_\perp value of 35 MHz to the N_α center while $A_\perp = 19$ MHz was attributed to the N_β center. According to our work this assignment clearly has to be interchanged.

The hfcc's of the NCN molecule are not known experimentally. The absolute values $A_\perp(^{13}C)$ and $A_\parallel(^{13}C)$ are found to be much larger than the absolute values found for C_β of $C_\alpha C_\beta O$ ($A_\perp = -86.9$ MHz vs. -29.6 MHz; $A_\parallel = -47.8$ MHz vs. -32.9 MHz). The reason for the difference lies in both the strong decrease in A_{iso} (-30.7 MHz vs. -73.8 MHz) and the strong increase in the anisotropic constants T_{zz} (-2.2 MHz vs. 26 MHz).

3 Density Functional Methods

A second method where large progress has recently been made in theoretical studies of radical hyperfine structures is density functional theory (DFT). As was seen in the previous section, the inclusion of electron correlation is of crucial importance in order to be able to generate accurate hyperfine properties. It may thus seem as a reasonable assumption that DFT based methods, where electron correlation is included already at the lowest level of theory, *via* the exchange-correlation potential (V_{xc}), can be a tractable alternative to the CPU- and memory intensive correlated *ab initio* methods. As the developments in computational quantum chemistry and in computer technology have now reached a stage where we may be able to study compounds and systems of more realistic sizes with satisfactory accuracy, the favourable scaling inherent in the DFT methods compared with HF-based techniques is a further argument for investigating its ability to predict also such intricate properties as the hyperfine structure. In the next subsection, we will briefly review the different LCGTO-DFT schemes that are used in DFT calculations of radical hfcc's (hereafter referred to as DFT-ESR calculations). Particular emphasis will be put on the various so-called gradient correction schemes presently available. Of importance when trying to obtain accurate hfcc's are also the atomic basis sets, and an overview of the different basis sets thus far employed in DFT-ESR calculations is included.

3.1 DFT-ESR – the importance of gradient corrections

It is now more than 30 years since the pioneering work by Hohenberg and Kohn [91] and Kohn and Sham [92], in which they derived and formulated the correspondence to the Hartree-Fock and Schrödinger equations in density functional theory (DFT). With the development of new gaussian-orbital based schemes and computer codes, and the appearance of a number of gradient corrections to the original local density approximation (LDA), DFT has over the last five years experienced a tremendous renaissance, and is now more or less regarded as one of the mainstream computational methods. Clearly, though, as the method in its present form is very young, new findings about its applicability, failures and successes are constantly being reported and form the basis for further understanding and developments of the theory. The various gradient corrections (reviewed in some detail below) have been found to more or less successfully, and on slightly different physical grounds, correct for the insufficient localization of the electron density obtained within the LDA, when moving from the homogeneous electron gas model to a form more suitable for describing molecular systems. What we do in DFT is es-

entially to use the electron density (ρ) as the fundamental variable, rather than the wavefunction (ψ), and to replace the HF exchange energy and its corresponding potential by an exchange-correlation energy, $E_{xc}[\rho_\uparrow, \rho_\downarrow]$, and its functional derivative, $V_{xc} = \delta E_{xc} / \delta \rho_\sigma(\mathbf{r})$. ρ_σ denotes the spin-up or spin-down density. In the spin-unrestricted formalism we thus have $\rho(\mathbf{r}) = \rho_\uparrow(\mathbf{r}) + \rho_\downarrow(\mathbf{r})$, and $\rho_\sigma(\mathbf{r}) = \sum_{i=1}^{occ} |\psi_{i\sigma}(\mathbf{r})|^2$. For more detailed accounts on density functional theory, see, *e.g.*, Refs. [93, 94, 95, 96, 97].

The LDA (or, in the case of radicals, the local spin density approximation, LSDA) exchange-correlation energy is generally expressed as

$$E_{xc}^{LDA}[\rho_\uparrow, \rho_\downarrow] = \int \rho(\mathbf{r}) \epsilon_{xc}(\rho_\uparrow(\mathbf{r}), \rho_\downarrow(\mathbf{r})) d^3r,$$

where ϵ_{xc} denotes the localized, one-particle exchange-correlation energy in a uniform electron gas. The most common form of the local density approximation is the Slater exchange term (also denoted $X\alpha$; $\alpha=2/3$) [98], together with the Vosko, Wilk and Nusair parametrization of the exact uniform electron gas model for the correlation part [99]. This form will hereafter be denoted SVWN, or simply LDA.

To improve upon this, from a chemical point of view rather crude assumption, the most widely employed corrections are based on using not only the density, but also its gradient. These corrections form the so-called generalized gradient approximation, GGA, or gradient expansion approximation (GEA) methods;

$$E_{xc}^{GGA}[\rho_\uparrow, \rho_\downarrow] = \int f(\rho_\uparrow(\mathbf{r}), \rho_\downarrow(\mathbf{r}), \nabla \rho_\uparrow, \nabla \rho_\downarrow) d^3r.$$

They are based on gradient expansions for the exchange-correlation hole density, and are designed to satisfy various constraints on the hole density, various integrated quantities, appropriate asymptotes at large distances, etc. There are three main correlation corrections commonly in use, by Perdew (P86) [100], by Lee, Yang and Parr (LYP) [101], and by Perdew and Wang (PW91) [102]. The P86 correlation correction is based on a model by Langreth and Mehl [103]. They employed a random phase approximation (RPA), in which E_{xc} was decomposed into contributions from different wave vectors of dynamic density fluctuations, and used a cut-off parameter to cure for spurious contributions to $\nabla \rho_c$ at small k . The cut-off parameter was chosen to provide a best overall fit of E_c to various atoms and metal surfaces. In the P86 version, the approximation goes beyond RPA for uniform and slowly varying electron gases. The cut-off parameter in P86 was obtained by fitting to the correlation energy of atomic neon.

The physics behind the LYP correction is quite different from the RPA models. It uses the Colle-Salvetti formula for E_c [104], but replaces the part

describing the local kinetic energy density by its second order density gradient expansion. There are four numerical constants in the LYP (and C-S) correlation correction. These were obtained by fitting the original C-S expression to the HF orbital of the helium atom. LYP has some computational advantages over P86, in that it does not contain any double derivatives of the type $\nabla|\nabla\rho|$. The PW91 correlation correction is, as P86, based on a real-space cut-off of the GEA, but uses a cut-off radius chosen to satisfy the constraint for the correlation hole:

$$\int \rho_c(\mathbf{r}, \mathbf{r}') d^3r = 0.$$

In this sense, the PW91 correction may be regarded as the "least empirical" of the various correlation corrections.

Of the corrections to the exchange energy, E_x , the most common forms are those by Perdew and Wang (PW86 and PW91) [105, 102], and by Becke (B88) [106]. To derive the PW86 GGA correction, we begin by rewriting $E_x[\rho]$ in the approximate form:

$$E_x[\rho] = A_x \int \rho^{4/3} F(s) d^3r,$$

where s is the reduced density gradient, $s = |\nabla\rho|/(2k_F\rho)$, and $k_F = (3\pi^2\rho)^{1/3}$. The PW86 exchange functional is again based on introducing a cut-off procedure to remove the spurious long-range behaviour of the second-order GEA, $F_x^{GEA}(s) = 1 + 0.1234s^2$, in order to restore the conditions defined for the exchange hole: $\rho_x(\mathbf{r}, \mathbf{r}') \leq 0$ and $\int \rho_x(\mathbf{r}, \mathbf{r}') d^3r = -1$. The final form of the PW86 function, obtained from a numerical fit to an analytical expression is $F_x(s) = (1 + 1.296s^2 + 14s^4 + 0.2s^6)^{1/15}$. This functional recovers more than 99% of the atomic exchange energies [105].

Becke's exchange functional is instead of the exchange hole cut-off procedure, based on the constraint on E_x that it should have a specified asymptotic behaviour as r goes to infinity. Its form is:

$$E_x^{B88} = E_x^{LDA} - \beta \Sigma_\sigma \int \rho^{4/3} \frac{x_\sigma^2}{(1 + 6\beta x_\sigma \sinh^{-1} x_\sigma)} d^3r,$$

where $x_\sigma = |\nabla\rho_\sigma|/\rho_\sigma^{4/3}$ [106]. It contains one empirical parameter (β), which was determined by minimizing the error in exchange energy for the rare gas atoms He-Rn. The optimal value is $\beta = 0.0042$ a.u. The more recent PW91 functional can be described as an intermediate between the two. It is based on Becke's exchange correction, modified to correct for the spurious behaviour at large s , and to restore the GEA at small s [102].

A fourth form of gradient correction has recently been proposed by Becke [107], based the adiabatic connection method (ACM). It uses a linear combination of the HF, LDA and B88 exchange contributions, together with the

LDA and PW91 correlation corrections:

$$E_{xc} = E_{xc}^{LDA} + 0.20(E_x^{HF} - E_x^{LDA}) + 0.72E_x^{B88} + 0.81E_c^{PW91}.$$

The semiempirical mixing parameters were determined from least square fittings to atomization energies, ionization potentials and proton affinities on the 'G1' set of molecules [108]. This Becke3 (or B3) exchange has also been employed together with the P86 and the LYP correlation corrections. This modification, including a portion of the gradient correction seems more appropriate than the earlier suggested "half and half" formula, where the modified functional contains 50% E_x^{HF} and 50% E_{xc}^{LSDA} [109].

There have been a number of tests of these functionals, combining the various exchange and correlation corrections and comparing geometries, atomization energies, vibrational frequencies, etc (see, *e.g.*, [106, 110, 111]). The overall consensus seems to be that the B3LYP or the PWP86 gradient correction schemes provide the most accurate results thus far. According to Perdew [112] there should in principle, however, be very little difference in the performance of the different gradient correction methods. As seen from the above descriptions all suggested improvements to the LDA are based on corrections to the exchange-correlation hole density. It is far from obvious which of the different gradient corrections, or combinations of these, that would be the most appropriate to use in hfcc calculations. None of the above has, *e.g.*, been designed under the constraint to correctly describe the distribution of unpaired electrons in a set of radical systems. One possible model that might be proposed for the future, could be to do a least square fit to minimize the error in density rather than energy, through comparisons with densities evaluated using MRCI, CCSD or QCISD wavefunctions for a number of radicals.

One of the drawbacks with density functional theory is that there is as yet no systematic way in which to improve a particular method, in a fashion similar to, *e.g.*, MBPT or CI expansions used in HF-theory. By necessity, the application of DFT based methods has to be pragmatic, and each functional form must be assessed on its own merits and improved models suggested. At present, a large body of literature is becoming available on the performance of the abovementioned correction schemes, that will form the basis for improved versions, entirely new functionals, or new combined schemes along the lines suggested through the B3 hybrid functional.

Table 19: Isotropic hyperfine coupling constants (MHz) for the atoms $^{11}\text{B}(^2P)$, $^{13}\text{C}(^3P)$, $^{14}\text{N}(^4S)$ and $^{17}\text{O}(^3P)$ computed using various DFT functionals. All calculations are done using the (18s,13p,4d,3f) basis set. From Ref [113].

Atom	UHF	SVWN	BP86	BLYP	B3P86	B3LYP	MRCISD ^a	CCSD(T) ^b	EXP
$^{11}\text{B}(^2P)$	27.8	-8.3	-16.4	16.2	-10.3	18.6	6.4	10.3	11.6 ^c
$^{13}\text{C}(^3P)$	44.9	-6.1	-6.1	21.1	1.0	25.1	17.8	21.4	22.5 ^d
$^{14}\text{N}(^4S)$	20.1	-1.9	-0.3	7.9	2.7	10.0	10.1	11.0	10.4 ^e
$^{17}\text{O}(^3P)$	-56.9	5.7	-2.3	-20.2	-10.5	-26.4	-29.1	-33.2	-34.5 ^f

^a(23s,12p,10d,4f,2g) basis; ref [15] ^b(23s,12p,10d,4f,2g) basis; ref [124]

^cRef [15]; ^dRef [127]; ^eRef [128]; ^fRef [129]

Table 20: Isotropic and anisotropic hfcc (gauss) for the OH and H_2O^+ radicals, obtained using different DFT functionals or basis sets. All calculations are on the experimental geometries. From Refs. [6] and [114].

System	Method	Hydrogen atom, ^1H			Oxygen atom, ^{17}O		
		A_{iso}	T_{xx}	T_{zz}	A_{iso}	T_{xx}	T_{zz}
OH	SVWN/IGLO-III	-21.4	-25.1	32.3	-1.0	-99.9	50.1
	BP86/IGLO-III	-23.4	-24.9	31.8	-3.5	-100.0	50.2
	PWP86/IGLO-III	-20.8	-24.6	31.4	-17.5	-101.1	50.7
	EXP ^a	-22.8	-26.2	31.1	-18.3		52.6
H_2O^+	PWP86/DZP	-22.6	-9.7	-23.3	-42.5	-110.8	56.5
	PWP86/TZP	-27.5	-8.7	-23.6	-33.0	-110.4	56.1
	PWP86/IGLO-II	-25.2	-8.7	-23.4	-27.9	-108.2	54.9
	PWP86/(9s,5p,1d)	-23.0	-8.7	-23.5	-28.1	-108.5	55.1
	PWP86/IGLO-III	-22.1	-8.2	-23.4	-24.6	-110.5	56.0
	PWP86/(11s,7p,2d)	-23.1	-8.2	-23.4	-27.8	-110.4	56.0
	SVWN/IGLO-III	-21.8	-8.7	-23.7	-5.4	-108.8	54.7
	BP86/IGLO-III	-25.1	-8.4	-23.7	-8.6	-109.6	55.5
	PW91/IGLO-III	-24.6	-8.5	-23.7	0.6	-108.9	55.0
	EXP ^b	-26.1			-29.7		

^aRef [130]; ^bRef [131].

As an example of the performance of some of the abovementioned gradient corrected schemes, we report in tables 19 and 20 some data for the atoms B–O and for the OH and H_2O^+ radicals, respectively. The atomic hfcc data are from the study by Barone [113] in which uncontracted (18s,13p,4d,3f) basis sets were employed, and the OH/ H_2O^+ results are from our studies [6, 114], using the IGLO-III family of basis sets (see next section). Common for the two studies is that the isotropic hfcc are highly sensitive to the form of the gradient correction that is introduced. For the hydrogen atoms, it seems as if the local density approximation is a sufficiently high level of theory. This may have advantages if one is interested only in the proton couplings of very large systems, where the inclusion of gradient corrections would make the calculations too costly. For the heavier atoms, however, the inclusion of a gradient corrected scheme is crucial for a balanced description of the unpaired spin density – and it is most essential to choose the correct form of the gradient corrections. As seen from the tables, and which has also been confirmed in a number of studies by now, it appears as if there are essentially only three gradient correction schemes that are sufficiently accurate for DFT-ESR calculations: the BLYP, B3LYP and PWP86 ones. Of these, BLYP seems to perform less well than the other two, which render results of comparable accuracy. For the anisotropic terms, all DFT functionals seem to perform equally well, and generally give results that are within 5% of the experimental numbers.

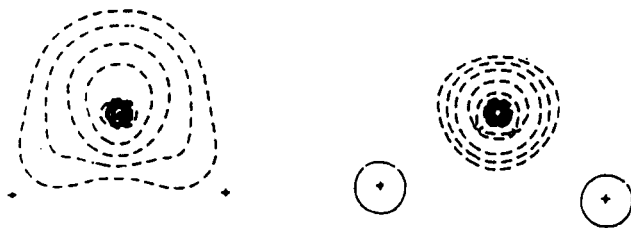


Figure 3. Spin density difference plots for H_2O^+ . Left: PWP86-SVWN; Right: PWP86-BP86 densities. All calculations are done using the IGLO-III basis set and experimental geometry. Dashed lines indicate excess SVWN/BP86 density. From ref [114].

Ziegler and coworkers [115] have found that the gradient corrections remove excess density from the tails of the core and valence regions, and place this in the core region of the atoms. This has later been verified in our work on, *e.g.*, H_2O^+ , NH_2 and similar systems [6, 116]. In figures 3 and 4 we show the differences between the LDA, BP86 and PWP86 unpaired spin densities, computed using the IGLO-III basis sets, for these two molecules. As seen, the main effects of the gradient corrections are on the heavy atoms, whereas the effects on the protons in terms of spin density redistribution are minor. We also note that the PWP86 functional gives a larger re-organisation than does the BP86 one.

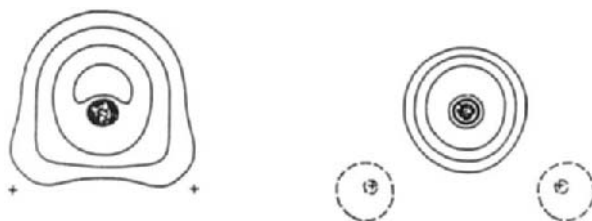


Figure 4. Spin density difference plots for NH_2 . Left: SVWN-PWP86; Right: BP86-PWP86 densities. All calculations are done using the IGLO-III basis set and experimental geometry. Solid lines indicate excess SVWN/BP86 density. From ref [116].

3.2 Basis sets for DFT calculations.

Since the appearance of the first LCAO-based DFT-ESR studies, occurring independently and almost simultaneously in three different research groups [117]-[119], a number of basis set studies are now available. Most of these have dealt with small organic or related systems, and a number of different basis sets have been utilized. We will here try to review the main features and results obtained with the various bases. A common approximation in the LCGTO-DFT formalism is to use an auxiliary basis set to fit the charge density and exchange-correlation potential to a grid. This is done in order to lower the computational costs, although it also means that the hyperfine results to some extent is relying on the accuracy of a second truncated basis set. We will comment on the effects of the auxiliary basis sets at the end of this section. First, however, we will investigate the dependence of the data on

the form of the orbital basis. All calculations using the PWP86 functionals and IGLO basis sets reported below, have been performed using the deMon program [120].

In our work on the hyperfine properties of molecules [6, 114, 116, 117, 121, 122], we have found that the IGLO family of bases [123] constitute a highly suitable set for calculating hyperfine coupling constants. For the second row atoms B-F, the IGLO bases are based on the Huzinaga 9s,5p (IGLO-II) or 11s,7p (IGLO-III) bases [63], to which are added one or two *d*-functions in order to describe polarization effects. These bases are loosely contracted in the core part, but the inner and outer valence regions are left uncontracted. For carbon, the IGLO-III basis would hence be (11s,7p,2d) in a [5111111/211111/11] contraction scheme. Although this may seem as a large basis, it is still sufficiently small to allow for full gradient corrected geometry optimizations of rather large systems, followed by hfcc calculations.

One example on the dependence of the hyperfine properties on the basis set is given for the water cation in table 20. As can be seen, the conventional DZP basis is not sufficiently accurate for generating satisfactory hfcc - just as is the case in HF-based methods. The main reason for the failure of these bases to generate accurate hfcc's is a too strong contraction of the outer-core/inner-valence regions. The TZP basis gives reasonable results, although slightly too large isotropic couplings. The fully uncontracted (9s,5p,1d) and (11s,7p,2d) bases quite naturally give the most accurate data, but are also the computationally most costly ones. In the IGLO form, these bases are partly contracted, and were estimated to give a good balance between accuracy and computational cost.

Since it was early found that the DFT-ESR/IGLO method generated good results for many different types of molecular radicals, one question that naturally also occurred was how well these IGLO bases would perform in atomic DFT-ESR calculations. It is known from extensive calculations at the MCSCF, CI and CC levels by Chipman, Feller and Davidson, Bartlett and coworkers [37, 38, 15, 124], that very large basis sets are required in order to generate accurate atomic hyperfine couplings (cf section 2). In one of the earlier DFT-ESR works [122](a), we investigated if the IGLO bases were suitable also for calculations of the hfcc for the second row atoms B-O, rather than for molecular radicals. What was found was that - just as in the case of, *e.g.*, MCSCF theory [37, 38], the atomic hfcc fluctuated significantly, and showed a dependence on both orbital and auxiliary basis set, as well as on functional form. An example of this is displayed in table 21.

Table 21: Fluctuation in isotropic hfcc (MHz) of ^{13}C , ^{14}N , ^{17}O and NH_2 (MP2/6-31G(d,p) geometry), for different functional forms and auxiliary basis sets. The atomic states are the same as in table 19. The orbital basis set IGLO-III is employed in all calculations. From ref [122](a).

Functional	Aux. Basis	^{13}C	^{14}N	^{17}O	^{14}N in NH_2	^1H in NH_2
LDA	(4,4;4,4)	-1.65	-0.91	2.45	7.91	-48.91
	(4,3;4,3)	-4.10	-2.14	0.35		
	(5,2;5,2)	-9.10	-5.16	7.56		
BP86	(4,4;4,4)	-23.84	-4.73	-1.20	17.23	-51.91
	(4,3;4,3)	-29.73	-8.87	10.15		
	(5,2;5,2)	-25.15	-9.67	14.03		
PWP86	(4,4;4,4)	-37.46	7.71	-46.12	23.21	-46.85
	(4,3;4,3)	1.45	15.70	-17.77	25.57	-46.62
	(5,2;5,2)	12.66	23.29	-43.20	27.38	-50.50
EXP		22.5 ^a	10.4 ^b	-34.5 ^c	27.9 ^d	-67.2 ^d

^aRef [127]; ^bRef [128]; ^cRef [129]; ^dRef [137]

The rationale for this failure of the method was at the time not fully understood. However, Barone's extensive study of atomic hfcc computed at different levels of density functional theory [113] (see above) was able to provide some valuable insight into the spurious fluctuations observed using the IGLO bases. In his study, he used an uncontracted (18s,13p,4d,3f) basis set - *i.e.*, essentially in the same category as the ones employed by Bartlett *et al.* [124] and by Feller and Davidson [15] in their high level post-SCF studies of atomic hfs. He furthermore employed a method that did not use an auxiliary basis, as implemented in the Gaussian92/DFT code [125]. As pointed out in the previous subsection, the choice of functional turned out to be a crucial factor also here. However, with the use of an appropriate functional (*i.e.*, BLYP or B3LYP), the results were of remarkably high accuracy, and well matched those obtained from MR-SDCI or CCSD(T) theory [37, 38, 15]; cf. table 19. Referring back to the earlier atomic IGLO-III study, the conclusion may thus be drawn that this family of basis sets is too small to be successful in atomic hfcc calculations, provided that valence orbitals with angular momenta larger than $l=0$ are populated.

Noteworthy is, however, that we have recently employed basis sets of IGLO type, constructed by decontracting a DZP basis and adding an additional very tight inner *s* function and a diffuse *d* function, in studies of alkali metal complexes and cationic magnesium clusters [132, 133]. For these systems, atomic

hyperfine couplings very close to the experimental values were obtained.

Table 22: Isotropic hfcc (gauss) for the magnesium cation; 2S state. DFT results from [133]. Experimental and CISD results: ref [134].

Method	Basis set	$A_{iso}(^{25}\text{Mg}^+)$
PWP86	DZP	-186.7
PWP86	ISO-I ^a	-206.4
PWP86	ISO-II ^b	-212.9
ROHF	(20s,15p,2d)/[8s,6p,2d]	-167.2
CISD	(20s,15p,2d)/[8s,6p,2d]	-198.6
EXP.	Ne/Ar matrix	(-)222.5/(-)211.6

^aDecontracted DZP basis. ^bAs ISO-I, with an additional tight inner s function and a diffuse d function.

In table 22, we report data for the magnesium cation. For the hydrogen atom, the [3111/11] IGLO-III basis set generates an isotropic hfcc of 496 gauss (PWP86 level of theory), to be compared with the experimental value of 507 G [135]. In other words, for atoms with an unpaired electron in an s -orbital, the IGLO bases seem to be sufficient also for atomic hfcc. The very large reference basis sets employed by Barone were furthermore concluded to be computationally impractical when going to systems much larger than atoms, and it was suggested that an extended TZP basis set (called TZ2P⁺) would be of sufficient accuracy [113]. This basis is highly compatible with the IGLO-III bases. Somewhat unfortunately, though, Barone did not saturate his basis set with respect to the atomic hfcc, so we do still not know for certain exactly how accurate results that can be achieved using the DFT-ESR methods.

A different set of bases has been employed by Suter *et al.*, in a study of small molecules such as OH, CH₃ and H₂CO⁺ [136]. They too, like Barone in the abovementioned study, used the Gaussian 92/DFT program, and tested a number of different functionals. In the work by Suter and coworkers, the van Duijneveldt (13s,9p) series [17] was used, contracted to [8s,5p], and augmented with a double set of polarization functions. This basis is commonly employed in CI calculations of hyperfine properties. For comparison, they also included in their study the corresponding IGLO bases. As stated in the paper by Suter and coworkers, the van Duijneveldt and IGLO bases should be of comparable quality; a suggestion that was validated by their results. In table 23, we have

summarized some of the data for the OH radical ($^2\Pi$) obtained using different functionals and basis sets. As was also concluded in our earlier LDA study of hydrocarbon radical cations [117](b), the differences in hfcc generated with the IGLO and van Duijneveldt basis sets are generally very small. The hydrogen couplings show very little variation irrespective of method or basis, and for the oxygen atom the hfcc primarily depend on the functional form, and less on the basis set. Once an appropriate gradient correction is selected (*i.e.*, PWP86 or B3LYP), the results are generally satisfactory also for the heavier elements.

Table 23: Summary of different theoretical data for the isotropic hyperfine couplings of the OH radical ($^2\Pi$ state), using the experimental geometry ($R=0.970$ Å). All values are in gauss.

Method	Basis	^{17}O	^1H	Ref
SVWN	IGLO-III	-1.0	21.4	[136]
	TZ2P+	-3.8	-21.1	[113]
BVWN	van Duij.	-11	-20	[136]
	IGLO-III	-11	-19	[136]
BP86	van Duij.	-6	-21	[136]
	IGLO-III ^a	-2.5	-23.4	[6]
	IGLO-III ^a	-7	-19	[136]
	TZ2P+	-9.0	-21.5	[113]
BLYP	van Duij.	-12	-22	[136]
	IGLO-III	-12	-20	[136]
	TZ2P+	-14.1	-22.3	[113]
PWP86	IGLO-III	-17.5	-20.8	[6]
B3P86	TZ2P+	-12.0	-22.7	[113]
B3LYP	TZ2P+	-17.1	-23.5	[113]
B3LYP	(18s,13p,4d,3f/10s,4p)	-16.2	-23.8	[113]
UHF	van Duij.	-34	-39	[136]
	(18s,13p,4d,3f/10s,4p)	-34.8	-38.5	[113]
MCSCF	numerical	-15	-24	[38]
UCISD(ST)	[8s,5p,4d,1f/6s,3p,1d]	-18	-25	[54]
EXP		-18	-26	[130]

^aThe first set of numbers are obtained with the deMon program, where we use 6 *d* functions (*i.e.*, the additional *s* function is retained), whereas the second set is from calculations using the G92/DFT program, that only uses 5 *d* functions.

The final type of atomic basis sets thus far employed in DFT-ESR calculations are the Slater type orbitals (STO's) by Ishii and Shimizu [119]. These basis sets usually consist of a (6s,6p,4d) set of functions for the second row atoms. The results obtained are most encouraging, and it seems as if the BP86 gradient corrections [100, 106] generate very good results. This is somewhat surprising since, as seen above, when used within the LCGTO approach, the BP86 functional has been shown to generate highly fluctuating results, very much depending on the particular system in question. No calculations have, however, been made by Ishii and Shimizu so far, in which the PWP86 or B3LYP functionals have been employed, so we do as yet not know how well these will perform within the STO approach.

The auxiliary basis sets, used in order to cut down computational costs, can from table 21 be seen to play a minor role in the properties of molecules, whereas for the atomic hfcc there is a fair degree of variation depending on the choice of basis. The auxiliary basis sets consist of an even-tempered expansion of the number of (s,spd;s',spd') functions used for the fitting of the charge density (s,spd) and the exchange-correlation potential (s',spd'), respectively, to a grid. For the charge densities the fitting is done analytically, whereas for V_{xc} a numerical fitting procedure is used. For every atom the grid usually consists of 32 radial shells that each contains up to 194 angular points. The actual number of grid points effects the hfcc very little [122](a), whereas it has been shown to have some effect on *e.g.*, the binding properties of rare gas dimers and similar compounds [120](d). For all practical purposes, we have found the (5,x;5,x) series [138] to be most satisfactory for geometries as well as hfcc calculations (x=1 for H, 2 for Li-Ne, 4 for third row atoms, 5 for the remainder). These are the bases that have been employed in the various PWP86/IGLO-III calculations reported in the different tables below.

3.3 H₂CN and H₂CO⁺ revisited

We will in this section revisit the case study from section 2.3.1, and will consider in some detail the H₂CO⁺ radical cation and the H₂CN radical. In table 24, results are given for a number of DFT and *ab initio* calculations for H₂CO⁺. Because $A_{\text{iso}}(^1\text{H})$ strongly depends on the geometry (cf. section 2.3.1), the geometries used in the different calculations are also given [136]. For a better comparison of the various functionals, most of the calculations have been performed for one and the same geometry, namely the one obtained with a 6-31G*/QCISD(T) calculation. This geometry is very similar to that given by Feller and Davidson [51] so that our value from ref. [114] can be directly included in the comparison.

Table 24: Isotropic hfcc's of H_2CO^+ ($^2\text{B}_2$) in Gauss.

H_2CO^+	Functional	Basis	C	O	H	geometry
[114]	PW86	IGLO-III	-32	-13	133	optimized
	BLYP	IGLO-III	-31	-10	137	optimized
	BP86	IGLO-III	-29	-6	130	optimized
[119]	BP86	STO	-30	-11	133	optimized
	BVWN	TZ2P	-22	-7	112	QCISD(T)
	BVWN	Chipman	-22	-8	116	QCISD(T)
	ROHF	Duij	0	0	34	QCISD(T)
	ROHF	Duij	0	0	34	QCISD(T)
	UHF	Duij	-47	-50	81	QCISD(T)
	BVWN	Duij	-20	-9	115	QCISD(T)
	BP86	Duij	-24	-6	117	QCISD(T)
	BLYP	Duij	-27	-11	123	QCISD(T)
	BLYP	IGLO-III	-28	-13	117	QCISD(T)
	BP86	IGLO-III	-24	-6	111	QCISD(T)
[114]	PW86	IGLO-III	-28	-13	117	Feller/Davidson
	MRD-CI/ B_k	Duij [44]	-37	-23	116	QCISD(T)
	Exp.: [49]		-39		133	

For a more detailed analysis, it is helpful to distinguish between 'direct' and 'indirect' contributions. In treatments which employ a one particle basis to describe the electronic structure, two different contributions to the spin density at a given center can be distinguished. The first part is proportional to the spin density of the singly occupied orbital (SOMO) at the center under consideration. In the following, this will be called the 'direct contribution'. The difference between the direct contribution and the total spin density at the given center is summarized as 'indirect contributions', and arise from spin polarization and correlation effects (cf. section 2).

As shown before, in figure 2, the SOMO in the H_2CO^+ cation represents a π in-plane orbital located mainly at the oxygen center. Due to the symmetry of the SOMO, the isotropic hfcc's of the heavier centers consist only of spin polarization effects (indirect contributions), while for the hydrogen centers

both direct and indirect contributions to A_{iso} exist.

As already found for the hydrides, no significant difference exists between the results obtained with the van Duijneveldt AO-basis set and the IGLO-III basis. Similar to the hydrides, the isotropic hfcc's of the hydrogen centers depend only slightly on the various functionals ($\pm 3\%$). The calculated values are of similar quality as those obtained in the MRD-CI/ B_K calculation.

Both the BLYP functional used in the present work and the PW86 functional in ref. [114] give $A_{\text{iso}}(^1\text{H})$ values which deviate less from the experimental data than the MRD-CI/ B_K results. The agreement with experimental data is even improved if the geometry is optimized using the DFT method itself (table 24, upper part). However, as already discussed in ref. [114], very often these geometries are not as good as *ab initio* data.

For the heavier centers, a quite different situation is found. The isotropic hfcc's at both centers depend heavily on the functional ($\pm 20\%$) and, furthermore, in comparison to the MRD-CI/ B_K treatment the absolute values are much too low. Again BLYP and PW86 performed best, but even for these functionals an error of about 25 % is found for the carbon center, while the deviation for the oxygen center is even larger (50 %). While the PW86 functional gave excellent results for the oxygen center in OH, it is considerably less successful for H_2CO^+ . The results for H_2CN (table 25) show similar trends as found for H_2CO^+ . For H_2CN , the BLYP functional which performs excellently in the case of CH and NH, possesses errors of more than 20 % for the isotropic hfcc's of the heavier centers.

Because direct contributions to the hfcc's of the heavier centers vanish in both molecules, the results indicate that the functionals employed in the comparison do not describe spin polarization effects accurately enough. On the other hand, for $A_{\text{iso}}(^1\text{H})$, which in the MRD-CI/ B_K treatment [44, 10] also is largely affected by spin-polarization effects, DFT provides excellent values. To get a better insight into this paradoxical situation, we will try to distinguish between the direct and indirect contributions to $A_{\text{iso}}(^1\text{H})$. For H_2CN the direct contributions are given in table 25; the indirect contributions are obtained from the difference between the direct contributions and the total result. As found for the heavier centers, the indirect contribution to $A_{\text{iso}}(^1\text{H})$ is much smaller in DFT calculations (16–21 Gauss) than in the MRD-CI/ B_K treatment (≈ 40 Gauss). However, this is compensated for by larger direct contributions so that, in total, very similar results are obtained in both methods. The reason for the behaviour explained above can be understood from the shape of the SOMO, which is found to be more compact in DFT-BLYP than in a ROHF approach [136]. The deviations between the various functionals arise due to differences within the indirect contribution, while the direct contribution is equal.

The examples given in the present investigation underscore that at least the functionals used in this work (and the PW86 functional used in ref. [114]) still have problems in describing the interaction between the singly occupied and the doubly occupied shells sufficiently well. In comparison with *ab initio*, the contributions to the isotropic hfcc's arising due to these spin polarization effects are computed too low, in absolute values.

Let us first consider those cases where the direct contribution vanishes due to symmetry reasons. As already discussed the net spin density at the center under consideration solely arises from the interaction between the singly and doubly occupied shells so that the indirect contributions represent an observable. The non-local nature of this interaction is obvious, since the density of the unpaired electron vanishes at the point where the effect of the interaction is measured, *i.e.* at the position of the center under consideration. The difficulties to describe non-local effects within the DFT are known [167] and explain the errors in the isotropic hfcc's computed with the DFT method.

If direct contributions are important a cancellation takes place, leading, for example, to very accurate isotropic hfcc's of β protons, as shown for H_2CN and H_2CO^+ . In such cases neither the direct nor the indirect contributions represent observables. Therefore it is unclear whether this represents an error cancellation or arises from the differences in the description of correlation effects in the MRD-CI/ B_K treatment and the DFT method.

Comparing the various examples it is obvious that the error made by DFT depends on the system under consideration. While the PW86 functional performs perfectly for $A_{\text{iso}}(^{17}\text{O})$ in the OH molecule it gives considerably worse results in the case of H_2CO^+ , although in both molecules the unpaired electron is mainly located at the oxygen. Further studies seem to be necessary to understand the underlying reasons for this behaviour. Such investigations are also interesting because isotropic hyperfine coupling constants directly probe the electron spin density at the nuclei and therefore provide a valuable measure for the quality of approximate spin density functionals. As shown in the following sections, however, DFT methods with an appropriate choice of functionals have nevertheless proven to be extremely successful in describing hyperfine interactions in a number of widely varying systems.

Table 25: Isotropic hfcc's of H_2CN ($^2\text{B}_2$). The geometry used for these calculations is the MCSCF-ACPF/Duj geometry ($R_{\text{CN}} = 1.256 \text{ \AA}$, $R_{\text{CH}} = 1.094 \text{ \AA}$, $\phi_{\text{HCH}} = 121.1$) given in reference [44]. All values are in Gauss.

Functional	Basis	C	N	H	H ^a
ROHF	Duij	0	0	31	31
UHF	Duij	-69	26	102	83
BVWN	Duij	-17	6	79	63
BLYP	Duij	-21	7	84	63
BP86	Duij	-19	4	80	63
MRD-CI	Duij [44]	-28	9	74	41
Exp.: [48]		-29	9	83	

^a Direct contribution, see text for explanation.

3.4 Applications

3.4.1 Proton hyperfine coupling constants

In the previous sections, we presented some data for the atoms B–O, and for the OH, NH_2 , H_2O^+ , H_2CN and H_2CO^+ radicals; in this section we will present some results for the proton hfcc of the systems CH_3 , NH_3^+ , CH_4^+ , $\text{C}_2\text{H}_2^{+/-}$ and $\text{C}_{17}\text{H}_{16}^-$, studied primarily at the PWP86/IGLO-III level. Several other compounds have been studied over these last three years since the DFT-ESR schemes were developed [113, 6, 114, 116, 117, 118, 119, 121, 122, 132, 133, 136, 139, 7, 140, 141, 142], but it is beyond the scope of the present paper to review them all. Instead we will focus on a relatively small yet diverse set of systems, with the aim of giving a flavour of the accuracy and applicability of the method.

Table 26: Calculated hfcc (gauss) for various neutral and charged radicals.

System	Method	Atom	A_{iso}	T_{xx}	T_{zz}	Ref
CH ₃	PWP86/IGLO-III	¹³ C	32.4	-29.2	58.4	[121]
	planar	¹ H (3)	-20.8	-14.4	14.3	
	PWP86/IGLO-III	¹³ C	40.0	-28.9	57.9	[121]
	5° pyram.	¹ H (3)	-19.4	-14.2	14.3	
	BP86/STO	¹³ C	38.9			[119]
	non-planar	¹ H (3)	-22.8			
	CIS/[631/41]	¹³ C	36.2	-25.9	51.7	[143]
	vibr.average	¹ H (3)	-23.9	-13.6	15.2	
	CISD/[10s,5p,3d/5s,2p]	¹³ C	17.1	-27.4	55.8	[3]
	planar	¹ H (3)	-21.4	-13.8	14.2	
	CCSD/DZPP	¹³ C	28			[62]
	planar	¹ H (3)	-27			
NH ₃ ⁺	PWP86/IGLO-III	¹³ C	38.3	-22.1	44±1	[143, 151]
		¹ H	-23.0	-12.5	12.5	
	UHF/6-31G(d,p)	¹⁴ N	14.8	-17.6	35.2	[122](a)
		¹ H (3)	22.7	-19.9	24.3	
		¹⁴ N	30.7	-15.6	31.1	[151]
	MRCISD/ (18s,13p,2d/10s,7p)	¹ H (3)	-48.4	-21.4	27.2	
		¹⁴ N	17.9	-16.6	33.1	[122](a)
		¹ H (3)	-28.4	-17.7	22.8	
	EXP.	¹⁴ N	19.5	-15.2	30.3	[152]
		¹ H (3)	-27.4	-19.6	22.1	
CH ₄ ⁺	PWP86/IGLO-III	¹³ C	24.2	-24.8	49.1	[6]
		¹ H (2)	127.9	-11.9	20.3	
		¹ H (2)	-18.9	-11.3	13.2	
	CISD/[5s,4p,1d/4s,1p]	¹ H (2)	137			[145]
		¹ H (2)	-17			
	EXP.	¹ H (2)	121.7			[145]
		¹ H (2)	-14.6			

^aRemoving the effects of vibrations, the isotropic data are (¹³C) 27 and (¹H) -25 G; Ref. [12].

Tab 26, *cont'd*

System	Method	Atom	A_{iso}	T_{xx}	T_{zz}	Ref
HCCH ⁺	PWP86/IGLO-III	¹³ C (2)	9.8		35.3	[147]
		¹ H (2)	-17.6		10.1	
C'CH ₂ ⁺	PWP86/IGLO-III	¹³ C'	6.7		31.1	[147]
		¹³ C	21.9		37.2	
		¹ H (2)	-16.6		10.6	
<i>t</i> -HCCH ⁻	PWP86/IGLO-III	¹³ C (2)	29.9		24.2	[147]
		¹ H (2)	48.9		6.1	
	B3LYP/IGLO-III	¹³ C (2)	29.2			[147]
		¹ H (2)	51.4			
	BLYP/IGLO-III	¹³ C (2)	29.8			[147]
		¹ H (2)	50.8			
	EXP	¹³ C (2)	14-15	2	22	[146]
		¹ H (2)	48	-5	6	
<i>c</i> -HCCH ⁻	PWP86/IGLO-III	¹³ C (2)	132.2		16.8	[147]
		¹ H (2)	65.0		5.0	
	B3LYP/IGLO-III	¹³ C (2)	130.1			[147]
		¹ H (2)	67.5			
	BLYP/IGLO-III	¹³ C (2)	131.2			[147]
		¹ H (2)	67.2			
	EXP	¹³ C (2)	130	-11	20	[147]
		¹ H (2)	65	-3	4	
C'CH ₂ ⁻	PWP86/IGLO-III	¹³ C'	18.6		48.3	[147]
		¹³ C	-16.0		3.8	
		¹ H (2)	53.8		3.0	
	B3LYP/IGLO-III	¹³ C'	22.9			[147]
		¹³ C	-17.4			
		¹ H (2)	53.2			
	BLYP/IGLO-III	¹³ C'	20.8			[147]
		¹³ C	-15.1			
		¹ H (2)	54.3			

As mentioned in section 3.2, we are with the present method able to predict the isotropic hfcc for atomic hydrogen very accurately. Since the atom lacks higher angular momenta, and the isotropic hfcc depends largely on the amount of *s*-character at the nucleus (through the overlap term, Eq. 4), one may expect that this property is well described for H irrespective of radical species. As was shown above, the dependence of the hfcc on the choice of DFT functional is much smaller than for the heavier atoms. In table 26 we present the PWP/IGLO-III (and other) computed proton hfcc for the abovementioned radicals and radical ions.

For CH₃, we have conducted a thorough study of the effects of non-planarity of the radical [121]. It has been suggested, and thoroughly investigated by Chipman [143], that the radical already at 4 K undergoes vibrational ("umbrella-like") motion. In his study, he found that a vibrationally averaged hfcc yielded results in very good agreement with experimental data; and that these strongly resembled the 'static' hfcc for a geometry with a 5° out-of-plane angle. In table 26 we list both the results for the planar and for the non-planar structure, using the experimental bond length (1.079 Å). The main effect of this umbrella motion is on the isotropic hfcc for carbon (see next section), whereas the proton hfcc are essentially unchanged for the small out-of-plane distortions. The calculated value for the planar geometry is 2 G smaller than experiment. Various high-level correlated approaches (CCSD, MPPT), applied by Sekino and Bartlett [62] as well as the CISD method used by Feller and Davidson [51] on the same geometry instead yield a 1-2 G too large isotropic proton hfcc. In the DFT-ESR calculations using STO basis sets (Ishii and Shimizu [119]), applied on a slightly non-planar geometry, the inclusion of gradient corrections and a 5s,4p basis set on hydrogen yielded results in excellent agreement with experiment.

In our early study of the effects of different functional forms, auxiliary and orbital basis sets, and grid sizes for the fitting of the charge density and the exchange-correlation potential [122](a), we found the results for the planar NH₃⁺ radical cation to be somewhat underestimated using the DFT-ESR approach. At the PWP/IGLO-III level our isotropic data for both types of nuclei were 4.7 G too low compared with experiment (MP2/6-31G** optimized geometry). No other DFT study has been reported of this system. It is possible that the deviation in hfcc on the NH₃⁺ radical is - just as for CH₃ - affected by umbrella-like vibrations even at temperatures as low as 4 K. This has, however, as yet not been tested. A second factor could be that MP2 would yield poor bond lengths, although this seems like a less likely explanation.

The methane radical cation, CH₄⁺, is known to Jahn-Teller distort from the symmetric tetrahedral neutral ground state structure to a conformation of C_{2v} symmetry, with two elongated and two shorter CH bonds (1.18 and

1.08 Å, respectively) [6, 117, 121, 144]. The HCH bond angles between each pair of equivalent hydrogens also undergoes dramatic changes relative to the neutral case; $\angle\text{HCH} = 55^\circ$ and 125° for the long bonded and short bonded pairs, respectively. The calculated $A_{iso}(\text{H})$ data also gives a very consistent picture of the system. At all levels of theory, the two long bonded protons have isotropic hfcc of 110 – 130 G, and the short bonded ones are -10 – -20 G. This should be compared with the results from neon matrix isolation experiments on CH_2D_2^+ (the deuterium atoms are required to stabilize the system in the C_{2v} ground state structure, whereas for CH_4^+ , large vibrational averaging is observed due to quantum tunnelling): $A_{iso}(2\text{H})=122$ G; $A_{iso}(2\text{H})=-14.6$ G (translated from the deuterium to the hydrogen scale) [145]. At the PWP/IGLO-III level, we obtain the hfcc 2x128 and 2x-19 G. The effects of the gradient corrections on the proton hfcc are again found to be very minor [121].

Another small set of systems is the acetylene/vinylidene radical anions and cations. No experimental data is available for the cationic system, but for the anion the *trans* conformer (ground state structure) has proton hfcc of 48 G [146], whereas the energetically ca. 5 kcal/mol higher lying *cis* conformer is known to have proton hfcc of 2x65 G [147]. In table 26, we list the data for the *cis* and *trans* HCCH anions, the linear HCCH⁺ and the vinylidene anion and cation, obtained at the PWP86, B3LYP and BLYP levels of theory for the anions, and PWP86 for the cations. We have used the IGLO-III basis sets throughout. Each structure is optimized at the corresponding level of theory. As seen, the proton couplings for the anionic systems are very similar for the different methods. We also note that the experimental proton couplings are excellently reproduced for both *cis*- and *trans*-HCCH⁻. Energetically, the two systems differ quite markedly. The *trans*-acetylene and vinylidene anions lie very close in energy; whereas the cations are more similar to the neutral system, where CCH_2 lies some 40-45 kcal/mol above the acetylene reactant. The high relative stability of the vinylidene anion has also been observed in different matrix ESR experiments, where the M^+HCCH^- charge transfer complexes are formed (M=Li, Na, K) [148]. This will be addressed in the next subsection.

Table 27: Proton hfcc of the stilbene anion depicted in Figure 5. All couplings are in gauss; the calculations are done using the AM1 geometry, the PWP86 functional, and IGLO-III basis set for H, DZP for C. Exp. ref: [154]; Theoretical ref: [149].

	2,2'	3,3'	4,4'	5,5'	6,6'	β,β	β',β'	γ,γ
Experimental	2.1	0.4	3.8	0.8	2.6	6.6	2.9	0.4
Calculated	-1.8	0.2	-3.6	0.6	-2.2	7.0	2.8	-0.2

To give a flavour of the sizes of the systems that can be investigated with the present scheme, we present in table 27 some data for one of the substituted stilbene anions recently studied [149]. It consists of the ordinary *cis*-stilbene framework (1,2-diphenylethene), where the remaining ethene protons have been substituted for a saturated C_3H_6 fragment. The final form of the molecule is thus 1,2-diphenyl-pentene. The carbon framework, and the labelling of the different positions are displayed in figure 5. In total, the present system contains no less than 119 electrons and 415 basis functions. The study was conducted such, that we first optimized the geometries using semiempirical AM1 theory, and then performed single point PWP86/IGLO-III calculations (DZP basis set on carbon) to get the hyperfine structures. As seen from the table, the agreement in proton hfcc is most satisfactory. The possibility to actually start investigating larger and more realistic molecules of *e.g.*, biological significance now seems to be within reach.

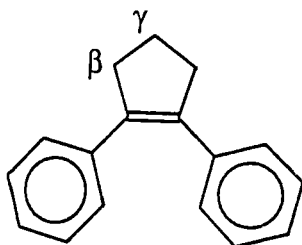


Figure 5. Schematic drawing of the 1,2-diphenyl-cyclopentene radical anion investigated in ref [149]. See table 27 for PWP86/IGLO-III computed proton hfcc's.

Other systems we have investigated in detail are the series of alkane and alkene radical cations [117, 121], fluoroethyl radicals [122](c), the NX_2 and PX_2 series ($\text{X}=\text{H}, \text{F}, \text{Cl}$) [116], and various small charged and neutral radicals [114, 122](a,b). Barone and coworkers have, *e.g.*, investigated the hfcc for vinyl and fluorovinyl radicals and various β -ketoenolyl radicals [118, 139, 7, 140]. Throughout, the conclusions have been the same, *i.e.* that the local spin density level is sufficiently accurate for proton couplings, whereas for heteroatoms either the B3LYP or the PWP86 gradient corrections are required. The basis sets should at least be of 'TZP' quality.

3.4.2 Heteroatom hyperfine coupling constants

As seen in the previous sections, the inclusion of gradient corrections are essential to get accurate isotropic hfcc for heteroatoms at the DFT level. Earlier, the data for the two systems H_2O^+ and NH_2 were presented in tables 20 (H_2O^+) and 21 (NH_2), respectively. In table 26, we include the data for the heteroatoms of the CH_3 , NH_3^+ , CH_4^+ , $\text{HCCH}^{+/-}$ and $\text{CCH}_2^{+/-}$ radicals. For most of these, however, only proton hfcc are available from previous theoretical or experimental studies. For those systems where experimental heteroatom hfcc are available, the results are generally rather satisfactory. In cases such as F_2^- (table 28), where the DFT approaches are unable to generate accurate geometries – DFT continuously predicts a too long bond length – the use of an appropriate geometry, in this case obtained at the MRCISD level, leads to hyperfine structures of MRCISD quality. It hence seems as if the determination of the magnetic properties are still most accurate, although the geometry determination especially for very weakly bonded systems can be a crucial factor.

One case where the DFT-ESR approach has been shown not to work very well, is the NO radical. This has a very large multireference character, as shown in the extensive ROHF-MRCISD work by Feller et al [156]. It was there concluded that it is necessary to go to the full CI limit in order to get accurate spin properties on the nitrogen atom ($A_{\text{iso}}(^{14}\text{N})=22.5$ G [157]). At the CISD level of theory, or using a MRCISD expansion with more than 400 reference configurations, values of 10-15 G were computed for $A_{\text{iso}}(^{14}\text{N})$, to be compared with our PWP86/IGLO-III value of 10 G. A similar analogy applies to the NH_2 radical, where we have found [158] that it is necessary to perform a MRCISD calculation with at least 80 reference configurations in order to accurately predict the hfs of the entire molecule. Using a smaller MRCI expansion, values close to those obtained at the PWP86/IGLO-III level (cf. table 21) were instead obtained.

Table 28: Variation of hfcc in $^{19}\text{F}_2^-$, calculated using the PWP86/IGLO-III method at varying F-F distances. The optimized distance is at this level 2.056 Å.

Method	R_{FF} (Å)	A_{iso}	A_{dip}	Ref
PWP86/IGLO-III	1.70	450	304	[6]
	1.80	350	306	
	1.90	270	304	
	2.00	220	302	
	2.10	180	301	
	2.20	150	300	
MRCISD/(9s,5p,3d)	1.896	260.3	308.3	[154]
EXP.		268-280	315-321	[155]

Recently, work has been initiated to calculate the hfs of metal containing systems, and to also incorporate the surrounding matrix in the treatment. Two examples of this are the interaction between an alkali metal atom (Li, Na, K) and acetylene/vinylidene [132]; and the hfs of Mg^+ or Mg_2^+ embedded in up to 10 neon or argon atoms [133]. The results obtained were throughout of very high accuracy. In table 29 we show some data for these systems. We note that we are in excellent agreement with the ESR data for both types of systems, and that we are in particular able to predict the shifts in metal hfcc when changing from HCCH to CCH_2 or when changing the surrounding matrix, to within one or two gauss. Since the DFT-ESR approach scales much more favourably than do conventional correlated HF approaches, the DFT-ESR method can be a very valuable method in order to obtain accurate data for systems of at least one order of magnitude larger size than the CI or CC based approaches, with comparable accuracy. In comparison with the stilbene example above, the present complexes have all been fully optimized at the PWP86 levels. The largest system ($\text{Mg}_2^+-\text{Ar}_{10}$) contains 203 electrons and 258 basis functions. We might hence very soon be able to predict, e.g., spin distributions in biological system, or to accurately predict interactions with surrounding materia.

Table 29: DFT-ESR calculations of metal containing systems. For the alkali metal - HCCH systems the data are presented for the two *cis*- M^+HCCH^- / $M^+C^+CH_2^-$ charge transfer complexes, respectively.

System	Method	Atom	A_{iso}	T_{xx}	T_{zz}
$Li^+C_2H_2^-$	PWP86/IGLO-III ^a	Li	-9.7 / -8.1	-2.5 / -1.5	2.2 / 1.2
		C'	74.4 / 16.6	-9.0 / -24.9	17.9 / 45.3
		C	74.4 / -16.3	-9.0 / -4.4	17.9 / 3.4
		H (2)	61.2 / 54.1	-4.1 / -1.6	5.1 / 2.6
	MRCISD/ 6-311++G(d,p) ^b	Li	-4.4 / -4.7		
		C'	69.7 / -4.1		
		C	69.7 / -16.9		
		H (2)	54.6 / 43.6		
	EXP ^c	Li	-7.0 / -5.7	-2.0 / -0.8	1.5 / 0.7
		C'	74 / -		
		C	74 / -		
		H (2)	66.5 / 57.0	-4.5 / -2.0	4.5 / 2.0
$Na^+C_2H_2^-$	PWP86/IGLO-III ^a	Na	-21.4 / -16.7	-3.6 / -1.8	6.4 / 2.3
		C'	91.1 / -20.5	-9.7 / -25.7	19.3 / 46.6
		C	91.1 / -15.9	-9.7 / -4.5	19.2 / 3.8
		H (2)	66.6 / 55.5	-4.2 / -1.6	5.4 / 2.8
	MRCISD/ 6-311++G(d,p) ^b	Na	-7.4 / -7.3		
		C'	86.3 / -3.3		
		C	86.3 / -16.1		
		H (2)	60.4 / 59.8		
	EXP ^c	Na	- / -12.7	- / -0.3	- / 0.2
		C'	- / 24.3	- / -20.8	- / 41.7
		C	- / 14	- / -	- / -
		H (2)	- / 59.8	- / -1.3	- / 2.2
$K^+C_2H_2^-$	PWP86/IGLO-III ^a	K	-3.4 / -3.2	-0.9 / -0.5	1.5 / 0.7
		C'	93.5 / 18.2	-9.4 / -25.8	18.8 / 46.3
		C	93.5 / -14.9	-9.4 / -4.4	18.8 / 3.9
		H (2)	67.0 / 55.2	-4.2 / -1.5	5.4 / 2.7
	EXP ^c	K	-3.3 / -2.7		
		H (2)	73.0 / 58.5		
$Mg^+ - Ne_6 / Ar_6$	PWP86/IGLO-III ^d	Mg	-211.7 / -201.6		
$Mg^+ - Ne_8 / Ar_8$	PWP86/IGLO-III ^d	Mg	-214.2 / -204.6		
$Mg^+ - Ne / Ar$	EXP ^e	Mg	-222.5 / -211.6		
$Mg_2^+ - Ne_{10} / Ar_{10}$	PWP86/IGLO-III ^d	Mg	-101.4 / -101.9		
$Mg_2^+ - Ne / Ar$	EXP ^e	Mg	-105.4 / -104.3		

^aRef [132]; ^bRef [159]; ^cRef [148]; ^dRef [133]; ^eRef [134].

Table 30: Isotropic and dipolar hfcc (MHz) of the B and Al atoms in the diatomic isovalent systems BO, BS, AlO and AlS, calculated at the PWP86/IGLO-III level (this work).

System	Method	Bond Length (Å)	Atom	A_{iso}	A_{dip}	Ref
BO	PWP86/IGLO-III	1.205	^{11}B	996.5	28.5	
	CISD/DZP	1.205		968	26	[3, 160]
	EXP			1025	27	[160, 161]
BS	PWP86/IGLO-III	1.619	^{11}B	759.7	32.2	
	EXP			795.6	28.9	[162]
AlO	PWP86/IGLO-III	1.636	^{27}Al	696.6	52.0	
	CISD/DZP	1.618		776	42	[3, 160]
	EXP			767	53.0	[163]
AlS	PWP86/IGLO-III	2.070	^{27}Al	780.39	49.60	

The anisotropic hfcc are generally very well described at all levels of theory, as was shown in a number of the previous tables. Also simple UHF theory seems to do well for anisotropic couplings. One interesting example is given by the BO molecule, where early neon matrix ESR experiments from codeposition of B and O vapor yielded a value for A_{dip} ($=1/2 T_z$) of 6.3 MHz for ^{11}B [160]. This strongly contradicts our calculated value of 28.5 MHz (PWP/IGLO-III), as well as that reported by Feller and Davidson, 26 MHz, at the CISD/DZP level [3]. This was somewhat surprising, given that anisotropic hfcc's generally are very accurately determined, and that the isotropic hfcc of boron was in very good agreement with experiment (cf. table 30). In a later microwave experiment, however, the dipolar coupling of 27.1 MHz was reported, in excellent agreement with the calculated data [161]. This and some related systems (BS, AlO, AlS) are listed in table 30. As seen, the calculations do rather well for both the B and Al nuclei, although the agreement is less satisfactory for the isotropic couplings than for the anisotropic part. This is hence in agreement with the findings on the smaller systems described above. It also shows that there are essentially no limits as to what types of systems that can be investigated with the DFT-ESR approach. As a rule of thumb, it seems that we get roughly 90-95% of the isotropic couplings, and a few percent better for the anisotropic data.

Table 31: Optimized geometries and hfcc of the $X^2\Sigma^+$ TiN and $X^3\Delta$ TiO systems. All calculations are done using the PWP86 functionals and uses the IGLO-III basis set on X (X=N,O).

System	Basis	R (Å)	$\langle S^2 \rangle$	$A_{iso}(Ti)$	$A_{dip}(Ti)$	$A_{iso}(X)$	$A_{dip}(X)$
TiN	DZP ^a	1.591	0.753	-580.3	-3.0	20.3	1.5
	DZPP ^a	1.598	0.753	-576.0	-4.9	19.8	1.3
	EXP ^b		0.750	-558.8 (-570 ^c)	-5	18.5	0.2
TiO	DZP ^a	1.645	2.011	-269.4	5.5	-6.0	-2.7
	DZPP ^a	1.650	2.010	-269.6	4.4	-5.9	-2.6
	EXP ^b		2.000	-240.4 ^d			

^aThis work; ^bRef [164]; ^cRef [165]; ^dDerived using the calculated value for A_{dip} .

As a final example, we present in table 31 the data for the hfcc of the TiO and TiN radicals. These are interesting from two aspects; it is one of the very first applications of the gradient corrected DFT method to transition metal systems, and the TiO radical has a triplet ground state. As seen from the table, the DFT method predicts both isotropic and anisotropic couplings very accurately, on both the titanium and the ligand atoms. Using a basis set of IGLO quality rather than the present DZP and DZPP ones (table 31) will most likely refine these numbers further. In this example we have also listed the spin contamination. As has been found in numerous examples earlier, the value of $S(S+1)$ is usually within 0.01 of the ideal value for the particular radical in question, indicating that we have a very good description of the singly occupied orbital.

4 Concluding Remarks

We have in the present paper investigated two fundamentally different, yet complementary, routes to computational studies of radical hyperfine structures. On the one hand, we have the highly accurate MRCI – based approaches, which are able to predict hyperfine structures of small systems to very high accuracy. The role and importance of higher than double excitations in the configuration expansions has been elucidated by means of detailed case studies on a number of first row atoms, as well some selected molecular systems. We have also demonstrated how a newly developed method, the MRD–CI/B_K method, by means of a perturbative method is able to incorporate the effects

of these higher excitations into the MRD-CI calculations, thus producing hfs results of high quality.

In the second part of the paper, we have explored an alternative route to the calculation of radical hfs, namely the DFT-based approaches. In this case, we trade in the extremely high accuracy of the MRCI approaches for applicability to systems up to a few hundred atoms in size. As shown in the above examples, the accuracy of the DFT based approaches is still well beyond conventional single determinant CIS or CISD data, provided an appropriate functional is used.

Future applications of the DFT based hfcc calculations will involve extending the sets of systems into areas such as surface chemistry, biophysics, and large transition metal complexes, where MRCI approaches again will serve as an extremely important tool for calibrating the calculations of the larger systems, to reveal possible pitfalls and explain deviations when these occur.

5 Acknowledgements

This work was supported by the Swedish Natural Science Research Council (NFR), the Swedish Institute (SI), the Natural Sciences and Engineering Council of Canada (NSERC), the Deutsche Forschungsgemeinschaft (DFG) and the Deutscher Akademischer Austauschdienst (DAAD). We would like to thank all our colleagues who took part in the work presented in this review, especially Professors S. D. Peyerimhoff, M. Perić, F. Grein, E. R. Davidson, R. J. Boyd, D. R. Salahub, and A. Lund with research groups. Special thanks go to Hans Ulrich Suter, Ming-Bao Huang and Vladimir and Olga Malkin for fruitful collaboration.

References

- [1] L.B. Knight, Jr., *Acc. Chem. Res.* **19** (1986) 313.
- [2] A. Lund, M. Lindgren, S. Lunell and J. Maruani, in *Molecules in Physics, Chemistry and Biology, Vol. III*, J. Maruani, Ed., Kluwer, Dordrecht, 1989, pp. 259 – 300.
- [3] D. Feller and E.R. Davidson, in *Theoretical Models of Chemical Bonding*, (Ed.: Z.B. Maksic), Springer, Berlin (1991).
- [4] A. Lund and M. Shiotani, Eds., *Radical Ionic Systems. Properties in Condensed Phases*, Kluwer, Dordrecht, 1991.
- [5] D. M. Chipman, *Magnetic Hyperfine Coupling Constants in Free Radicals*. In *Quantum Mechanical Electronic Structure Calculations with Chemical Accuracy* (Ed.: S.R. Langhoff), 1995, Kluwer Academic Publishers, Dordrecht, (The Netherlands), 1995.
- [6] V.G. Malkin, O.L. Malkina, L.A. Eriksson and D.R. Salahub, in *Theoretical and Computational Chemistry, Vol. 2; Modern Density Functional Theory: A Tool for Chemistry*, P. Politzer and J.M. Seminario, Eds, Elsevier, 1995.
- [7] V. Barone, in *Recent Advances in Density Functional Methods, Part 1*, D.P. Chong, Ed, World Scientific, Singapore, 1996.
- [8] C.W. Bauschlicher Jr., S.R. Langhoff, H. Partridge, D.P. Chong, *J. Chem. Phys.* **89** (1988) 2985; C.W. Bauschlicher Jr., *J. Chem. Phys.*, **92** (1990) 518.
- [9] K. Funken, B. Engels, S.D. Peyerimhoff, F. Grein, *Chem. Phys. Lett.*, **172** (1990) 180.
- [10] D.M. Chipman, I. Carmichael, D. Feller, *J. Phys. Chem.*, **95** (1991) 4702.
- [11] I. Carmichael, *J. Chem. Phys.* **91** (1989) 1072.
- [12] D.M. Chipman, *Theor. Chim. Acta* **82** 93 1992, and references cited therein.
- [13] B. Engels, *J. Chem. Phys.*, **100** (1994) 1380.
- [14] B. Engels, *Theor. Chim. Acta*, **86** (1993) 429.

- [15] D. Feller, E.R. Davidson, J. Chem. Phys. **88** (1988) 7580.
- [16] D. Feller, E.R. Davidson, Theor. Chim. Acta **68** 57 1985.
- [17] F.B. van Duijneveldt, Tech. Rep. RJ945, IBM Research Lab. San Jose, CA, 1971.
- [18] T.H. Dunning, J. Chem. Phys. **90** 1007 1989.
- [19] B. Engels, S.D. Peyerimhoff, E.R. Davidson, Mol. Phys. **62** 109 1987.
- [20] B. Engels, Chem. Phys. Lett., **179** 398 1991.
- [21] I. Carmichael, J. Phys. Chem., **93** 190 1989.
- [22] Z. Gershgorin, I. Shavitt, Intern. J. Quantum Chem. **2** 751 1968.
- [23] P.O. Löwdin, J.Chem.Phys, **19** 1396 (1951).
- [24] P.O. Löwdin, in *Perturbation Theory and its Applications in quantum mechanics*, ed. C.H. Wilcox, Wiley, New York (1966).
- [25] L.E. Nitzsche, E.R. Davidson, J. Chem. Phys. **68** 3103 (1977).
- [26] E.R. Davidson, L.E. McMurchie, S.I. Day, J. Chem. Phys. **74** 5491 (1981).
- [27] D.C. Rawlings, E.R. Davidson, Chem. Phys. Lett. **98** 424 (1983).
- [28] G.A. Segal and K. Wolf, Chem. Phys, **56** 321 (1981).
- [29] T.C. Steimle, D.R. Woodward, J.M. Brown, J.Chem.Phys **85** 1276 (1986).
- [30] C.R. Brazier, J.M. Brown, Can. J. Phys. **62** 1563 (1984).
- [31] MELDF-X was originally written by L. McMurchie, S. Elbert, S. Langhoff and E.R. Davidson. It has been substantially modified by D. Feller, R. Cave, D. Rawlings, R. Frey, R. Daasch, L. Nitzche, P. Phillips, K. Iberle, C. Jackels and E.R. Davidson.
- [32] B. Engels, S.D. Peyerimhoff, Mol. Phys. **67** 583 (1989).
- [33] R.J. Buenker, S.D. Peyerimhoff, Theor. Chim. Acta **35** 33 (1974); *ibid.* **39** 33 (1975); R.J. Buenker, S.D. Peyerimhoff, W. Butscher, Mol. Phys. **35** 771 (1978).

- [34] L.B. Knight, Jr., K.D. Johannessen, D.C. Cobbranchi, E.A. Earl, D. Feller, E.R. Davidson, *J. Chem. Phys.* **87** 885 (1987).
- [35] M.J. Frisch, M. Head-Gordon, H.B. Schlegel, K. Raghavachari, J.S. Binkley, C. Gonzalez, D.J. Defrees, D.J. Fox, R.A. Whiteside, R. Seeger, C.F. Melius, J. Baker, R.L. Martin, L.R. Kahn, J.J.P. Stewart, E.M. Fluder, S. Topiol, J.A. Pople, GAUSSIAN, INC., Pittsburgh PA.
- [36] J.A. Pople, M. Head-Gordon, K. Raghavachari, *J. Chem. Phys.*, **87** 5968 (1987).
- [37] D.M. Chipman, *Theor. Chim. Acta* **76**, 73 (1989).
- [38] D.M. Chipman, *J. Chem. Phys.* **91**, 5455 (1989).
- [39] C.F. Bender, E.R. Davidson, *Phys. Rev.* **183** 23 (1969).
- [40] P. Kristiansen, L. Veseth, *J. Chem. Phys.* **84**, 6336 (1986).
- [41] I. Carmichael, *J. Chem. Phys.* **94** 5734 (1990).
- [42] P. Bündgen, F. Grein, B. Engels, submitted for publication.
- [43] M.-B. Huang, H.U. Suter, B. Engels, *Chem. Phys.* **183** 27 (1994).
- [44] H.U. Suter, B. Engels, *J. Chem. Phys.*, **100**, 2936 (1994).
- [45] G. Marston and L.J. Stief, *Res. Chem. Intermediates* **12**, 161 (1989).
- [46] E.L. Cochran, F.J. Adrian and V.A. Bowers, *J. Chem. Phys.* **36**, 1938 (1962).
- [47] D. Banks and W. Gordy, *Mol. Phys.* **26**, 1555 (1973).
- [48] S. Yamamoto and S. Saito, *J. Chem. Phys.* **96**, 4157 (1992).
- [49] L.B. Knight and J. Steadman, *J. Chem. Phys.* **80**, 1018 (1984).
- [50] M.C.R. Symons, *Tetrahedron* **39**, 615 (1973); S.P. Mishra and M.C.R. Symons, *J. Chem. Soc. Chem. Comm.*, 909 (1975).
- [51] D. Feller and E.R. Davidson, *J. Chem. Phys.* **80**, 1006 (1984).
- [52] J.A. Pople, M. Head-Gordon and K. Raghvachari, *J. Chem. Phys.* **87**, 5968 (1987).
- [53] I. Carmichael, *J. Chem. Phys.* **93**, 863 (1990).

- [54] I. Carmichael, J. Phys. Chem. **95**, 108 (1991).
- [55] R.J. Cave, S.S. Xantheas and D. Feller, Theor. Chim. Acta **83**, 31 (1992).
- [56] R.J. Cave and E.R. Davidson, J. Chem. Phys. **89**, 6798 (1988).
- [57] H.J. McManus, R.W. Fessenden and D.M. Chipman, J. Phys. Chem. **92**, 3781 (1988).
- [58] P. Botschwina, M. Horn, S. Seeger and J. Flügge, Mol. Phys. **78**, 191 (1993).
- [59] S.R. Langhoff and E.R. Davidson, Int. J. Quantum Chem. **8**, 61 (1974); I. Shavitt, F.B. Brown and P.G. Burton, Int. J. Quantum Chem. **31**, 507 (1987).
- [60] T. Momose, H. Nakatsuji and T. Shida, J. Chem. Phys. **89**, 4185 (1988).
- [61] H. Nakatsuji and M. Izawa, J. Chem. Phys. **91**, 6205 (1989).
- [62] H. Sekino and R.J. Bartlett, J. Chem. Phys. **82**, 4225 (1985).
- [63] S. Huzinaga, *Approximate Atomic Functions 1* (University of Alberta, Edmonton, Canada, 1971); S. Huzinaga, J. Chem. Phys. **42**, 1293 (1965); S. Huzinaga and Y. Sakai, J. Chem. Phys. **50** (1969) 1371.
- [64] H.U. Suter, M.-B. Huang, B. Engels, J. Chem. Phys. **101** 7686 (1994).
- [65] D.E. Milligan and M.E. Jacox, J. Chem. Phys. **44**, 2850 (1966).
- [66] D.E. Milligan, M.E. Jacox and A.M. Bass, J. Chem. Phys. **43**, 3149 (1965).
- [67] D.E. Milligan, M.E. Jacox, J.J. Comefor and D.E. Mann, J. Chem. Phys. **43**, 756 (1965).
- [68] M.E. Jacox, D.E. Milligan, N.G. Moll and W.E. Thompson, J. Am. Chem. Soc. **43**, 3734 (1965).
- [69] B.E. Wurfel, A. Thoma, R. Schlacta and V.E. Bondybey, Chem. Phys. Lett. **190**, 119 (1992).
- [70] C. Devilles and D.A. Ramsay, Can. J. Phys. **49**, 2839 (1971).
- [71] A.J. Merer and D.N. Travis, Can. J. Phys. **43**, 1795 (1965); A.J. Merer and D.N. Travis, Can. J. Phys. **44**, 353 (1966).

- [72] K.R. Jennings and J.R. Linett, *Trans. Faraday Soc.* **46**, 1737 (1960).
- [73] G. Herzberg and D.N. Travis, *Can. J. Phys.* **42**, 1658 (1964); G. Herzberg, *Electronic Spectra of Polyatomic Molecules* (Van Nostrand, Reinhold, New York, 1966).
- [74] E. Wassermann, L. Barash and W.A. Yager, *J. Am. Chem. Soc.* **87**, 2075 (1965).
- [75] G.R. Smith and W. Weltner, *J. Chem. Phys.* **62**, 4592 (1975).
- [76] R.L. DeKock, R.S. Grev and H.F. Schaefer III, *J. Chem. Phys.* **89**, 3016 (1988).
- [77] J.F. Olsen and L. Burnelle, *Tetrahedron* **25**, 5451 (1969).
- [78] C. Thomson, *J. Chem. Phys.* **58**, 841 (1972); C. Thomson and B.J. Wishart, *Theor. Chim. Acta* **31**, 347 (1973).
- [79] Z.-L. Cai, G.-H. Sha, C.-H. Zhang and M.-B. Huang, *J. Mol. Struct. (THEOCHEM)* **253**, 303 (1992).
- [80] S.P. Walch, *J. Chem. Phys.* **72**, 5679 (1980).
- [81] C.F. Chabalowski, R.J. Buenker and S.D. Peyerimhoff, *J. Chem. Phys.* **84**, 268 (1986).
- [82] D.A. Dixon and R.L. DeKock, *J. Chem. Phys.* **97**, 1157 (1992).
- [83] C.W. Murray, G.J. Laming, N.C. Handy and R.D. Amos, *J. Phys. Chem.* **97**, 1868 (1993).
- [84] M. Perić, B. Engels, S. D. Peyerimhoff, *Theoretical Spectroscopy on Small Molecules: Ab Initio Investigations of Vibronic Structure, Spin-Orbit Splittings and Magnetic Hyperfine Effects in the Electronic Spectra of Triatomic Molecules*. In *Quantum Mechanical Electronic Structure Calculations with Chemical Accuracy*, (Ed.: S.R. Langhoff), 1995, Kluwer Academic Publishers, Dordrecht, (The Netherlands), 1995.
- [85] T. Koga and A.J. Thakkar, *Theor. Chim. Acta* **85**, 391 (1993).
- [86] C.E. Dykstra, S.-Y. Liu, D.J. Malik, *Adv. Chem. Phys.* **75**, 37, (1989).
- [87] S. Lunell and M.-B. Huang, *Chem. Phys. Letters* **168**, 63 (1990).

- [88] M.-B. Huang and S. Lunell, *Chem. Phys.* **147**, 85 (1990)
- [89] S. Lunell, D. Feller and E.R. Davidson, *Theor. Chim. Acta* **77**, 111 (1990)
- [90] A recent example is given by M.-B. Huang, H. U. Suter, B. Engels, S. D. Peyerimhoff and S. Lunell, *J. Phys. Chem.* **99**, 9724, (1995).
- [91] P. Hohenberg and W. Kohn, *Phys. Rev. B* **136** (1964) 864.
- [92] W. Kohn and L.J. Sham, *Phys. Rev. A* **140** (1965) 1133.
- [93] *Density Functional Methods in Chemistry*, J. Labanowski and J. Andzelm, Eds, Springer-Verlag, Berlin, 1993.
- [94] R.G. Parr and W. Yang, *Density Functional Theory of Atoms and Molecules*, Oxford, New York, 1989.
- [95] *Theoretical and Computational Chemistry, Vol. 2; Modern Density Functional Theory: A Tool for Chemistry*, P. Politzer and J.M. Seminario, Eds, Elsevier, 1995.
- [96] *Recent Advances in Density Functional Theory*, D.P. Chong, Ed, World Scientific, Singapore, 1995.
- [97] *Density Functional Methods in Chemistry and Materials Science*, M. Springborg, Ed, Wiley, New York, 1996.
- [98] J.C. Slater, *Quantum Theory of Molecules and Solids, Vol. 4: The Self-Consistent Field for Molecules and Solids*, McGraw-Hill, New York, 1974.
- [99] S.H. Vosko, L. Wilk and M. Nusair, *Can. J. Phys.* **58** (1980) 1200.
- [100] J.P. Perdew, *Phys. Rev. B* **33** (1986) 8822; idem *ibid* **34** (1986) 7406.
- [101] C. Lee, W. Yang and R.G. Parr, *Phys. Rev. B* **37** (1988) 785.
- [102] J.P. Perdew and Y. Wang, *Phys. Rev. B* **45** (1992) 13244; J.P. Perdew, in *Electronic Structures of Solids*, P. Ziesche and H. Eischrig, Eds, Akademie Verlag, Berlin, 1991; J.P. Perdew, J.A. Chevary, S.H. Vosko, K.A. Jackson, M.R. Pederson, D.J. Singh and C. Fiolhais, *Phys. Rev. B* **46** (1992) 6671.
- [103] D.C. Langreth and M.J. Mehl, *Phys. Rev. B* **28** (1983) 1809.
- [104] R. Colle and D. Salvetti, *Theor. Chim. Acta* **37** (1975) 329; idem, *J. Chem. Phys.* **79** (1983) 1404.

- [105] J.P. Perdew and Y. Wang, Phys. Rev. B **33** (1986), 8800.
- [106] A.D. Becke, Phys. Rev. A **38** (1988) 3098.
- [107] A.D. Becke, J. Chem. Phys. **98** (1993) 5648.
- [108] J.A. Pople, M. Head-Gordon, D.J. Fox, K. Raghavachari and L.A. Curtiss, J. Chem. Phys. **90** (1989) 5622; L.A. Curtiss, C. Jones, G.W. Trucks, K. Raghavachari and J.A. Pople, J. Chem. Phys. **93** (1990) 2537.
- [109] A.D. Becke, J. Chem. Phys. **98** (1993) 1372.
- [110] J. Andzelm and E. Wimmer, J. Chem. Phys. **96** (1992) 1280.
- [111] B.G. Johnson, P.M.W. Gill and J.A. Pople, J. Chem. Phys. **98** (1993) 5612.
- [112] J.P. Perdew and K. Burke, Int. J. Quantum Chem., in press.
- [113] V. Barone, J. Chem. Phys. **101** (1994) 6834.
- [114] L.A. Eriksson, O.L. Malkina, V.G. Malkin and D.R. Salahub, J. Chem. Phys. **100** (1994) 5066.
- [115] V. Tschinke and T. Ziegler, Can. J. Chem. **67** (1988) 460; L. Fan and T. Ziegler, J. Chem. Phys. **94** (1991) 6057.
- [116] M.A. Austen, L.A. Eriksson and R.J. Boyd, Can. J. Chem. **72** (1994) 695.
- [117] a) L.A. Eriksson, J. Wang and R.J. Boyd, Chem. Phys. Letters **211** (1993) 88; b) L.A. Eriksson, V.G. Malkin, O.L. Malkina and D.R. Salahub, J. Chem. Phys. **99** (1993) 9756.
- [118] V. Barone, C. Adamo and N. Russo, Chem. Phys. Letters **212** (1993) 5.
- [119] N. Ishii and T. Shimizu, Phys. Rev. A **48** (1993) 1691.
- [120] a) A. St-Amant and D.R. Salahub, Chem. Phys. Letters **169** (1990) 387; b) A. St-Amant, Ph.D. Thesis, Université de Montréal, 1991; c) D.R. Salahub, R. Fournier, P. Mlynarski, I. Papai, A. St-Amant and J. Ushio, in *Density Functional Methods in Chemistry*, J. Labanowski and J. Andzelm, Eds, Springer-Verlag, New York, 1991; d) C. Daul, A. Goursoot and D.R. Salahub, in *Grid Methods in Atomic and Molecular Quantum Calculations*, C. Cerjan, Ed, Nato ASI C142 (1993).

- [121] L.A. Eriksson, V.G. Malkin, O.L. Malkina and D.R. Salahub, *Int. J. Quantum Chem.* **52** (1994) 879.
- [122] a) J. Kong, L.A. Eriksson and R.J. Boyd, *Chem. Phys. Letters*, **217** (1993) 24; b) L.A. Eriksson, J. Wang, R.J. Boyd and S. Lunell, *J. Phys. Chem.* **98** (1994) 792; c) J.M. Martell, L.A. Eriksson and R.J. Boyd, *J. Phys. Chem.* **99** (1995) 623.
- [123] W. Kutzelnigg, U. Fleischer and M. Schindler, in *NMR - Basic Principles and Progress*, Vol. 23, Springer-Verlag, Heidelberg, 1990, p 165.
- [124] S.A. Perera, J.D. Watts and R.J. Bartlett, *J. Chem. Phys.* **100** (1994) 1425.
- [125] Gaussian 92/DFT, Revision F.2; M.J. Frisch, G.W. Trucks, H.B. Schlegel, P.M.W. Gill, B.G. Johnson, M.W. Wong, J.B. Foresman, M.A. Robb, M. Head-Gordon, E.S. Replogle, R. Gomperts, J.L. Andres, K. Raghavachari, J.S. Binkley, C. Gonzalez, R.L. Martin, D.J. Fox, D.J. De-frees, J. Baker, J.J.P. Stewart and J.A. Pople, Gaussian Inc., Pittsburgh PA, 1993.
- [126] W.R.M. Graham and W. Weltner, Jr, *J. Chem. Phys.* **65** (1976) 1516.
- [127] J.S.M. Harvey, L. Evans and H. Lew, *Can. J. Phys.* **50** (1972) 1719.
- [128] W.W. Holloway, Jr., E. Lüscher and R. Novick, *Phys. Rev.* **162** (1962) 2109.
- [129] S.M. Harvey, *Proc. R. Soc. London, Ser. A* **285** (1965) 581.
- [130] K.R. Leopold, K.M. Evenson, E.R. Comben and M.J. Brown, *J. Mol. Spectrosc.* **122** (1987) 440; J.A. Coxon, K.V.L.N. Sastry, J.A. Austin and D.H. Levy, *Can. J. Phys.* **57** (1979) 619.
- [131] L.B. Knight, Jr. and J. Steadman, *J. Chem. Phys.* **78** (1983) 5940.
- [132] L.A. Eriksson, J. Wang and R.J. Boyd, *Chem. Phys. Letters* **235** (1995) 422.
- [133] L.A. Eriksson, *J. Chem. Phys.* **103** (1995) 1050.
- [134] L.B. Knight, Jr., C.B. Cleveland, R.F. Frey and E.R. Davidson, *J. Chem. Phys.* **100** (1994) 7867.
- [135] J.P. Wittke and R.H. Dicke, *Phys. Rev.* **103** (1956) 620.

- [136] H.U. Suter, V. Pleß, M. Ernzerhof and B. Engels, *Chem. Phys. Letters* **230** (1994), 398.
- [137] G.W. Hills, *J. Mol. Spectry* **94** (1982) 385.
- [138] F. Sim, D.R. Salahub, S. Chin and M. Dupuis, *J. Chem. Phys.* **95** (1991) 4317; N. Godbout, D.R. Salahub, J. Andzelm and E. Wimmer, *Can. J. Chem.* **70** (1992) 560.
- [139] C. Adamo, V. Barone and A. Fortunelli, *J. Phys. Chem.* **98** (1994) 8648; V. Barone, N. Russo and C. Adamo, *Int. J. Quantum Chem.* **52** (1994) 963.
- [140] V. Barone, R. Fournier, F. Mele, N. Russo and C. Adamo, *Chem. Phys. Letters* **237** (1995) 189.
- [141] N. Ishii and T. Shimizu, *Chem. Phys. Letters* **225** (1994) 462.
- [142] N. Ishii and T. Shimizu, *Chem. Phys. Letters* **235** (1995) 614.
- [143] D.M. Chipman, *J. Chem. Phys.* **78** (1983) 3112.
- [144] W.J. Bouma, D. Poppinger and L. Radom, *Isr. J. Chem.* **23** (1983) 21; M.N. Paddon-Row, D.J. Fox, J.A. Pople, K.N. Houk and D.W. Pratt, *J. Am. Chem. Soc.* **107** (1985) 7696.
- [145] L.B. Knight, Jr., J. Steadman, D. Feller and E.R. Davidson, *J. Am. Chem. Soc.* **106** (1984) 3700.
- [146] K. Matsuura and H. Muto, *J. Phys. Chem.* **97** (1993) 8842.
- [147] E.A. Piosos, D.W. Werst, A.D. Trifunac and L.A. Eriksson, *J. Phys. Chem.*, in press (1996).
- [148] P. Kasai, *J. Am. Chem. Soc.* **114** (1992) 3299, and references therein.
- [149] J.E. Gano, E.J. Jacob, G. Subramaniam, D. Leoir, L.A. Eriksson and F. Gerson, *J. Org. Chem*, submitted for publication.
- [150] R.W. Fessenden, *J. Phys. Chem.* **71** (1967) 74.
- [151] R. Bonazzola, N. Leray, J. Roncin and Y. Ellinger, *J. Phys. Chem.* **90** (1986) 5573.
- [152] A.J. McKinley and J. Michl, *J. Phys. Chem.* **95** (1991) 2674.

- [153] F. Gerson, H. Ohya-Nishiguchi, M. Szwarc and G. Levin, *Chem. Phys. Letters* **52** (1977) 587.
- [154] S.P. Karna, F. Grein, B. Engels and S.D. Peyerimhoff, *Int. J. Quantum Chem.* **36** (1989) 255; D. Feller, *J. Chem. Phys.* **93** (1990) 579.
- [155] L.B. Knight Jr, E. Earl, A.R. Login and D.P. Cobranchi, *J. Chem. Phys.* **85** (1986) 1228, and references therein.
- [156] D. Feller, E.D. Glendening, E.A. McCullough Jr and R.J. Miller, *J. Chem. Phys.* **99** (1993) 2829.
- [157] P. Kristiansen, *J. Mol. Spectr.* **66** (1977) 177.
- [158] J. Kong, R.J. Boyd and L.A. Eriksson, *J. Chem. Phys.* **102** (1995) 3674.
- [159] M.T. Nguyen, T.-K. Ha and M. Yoshimine, *Mol. Phys.* **77** (1992) 921.
- [160] L.B. Knight, M.B. Wise, E.R. Davidson and L.E. McMurchie, *J. Chem. Phys.* **76** (1982) 126.
- [161] W. Weltner, Jr., *Magnetic Atoms and Molecules*, Van Nostrand-Reinhold, New York, 1983.
- [162] J.M. Brom and W. Weltner, Jr., *J. Chem. Phys.* **57** (1972) 3379.
- [163] L.B. Knight and W. Weltner, Jr., *J. Chem. Phys.* **55** (1971) 5066.
- [164] D.A. Fletcher, C.T. Scurlock, K.Y. Jung and T.C. Steimle, *J. Chem. Phys.* **99** (1993) 4288.
- [165] B. Simard, H. Niki and P.A. Hackett, *J. Chem. Phys.* **92** (1990) 7012.
- [166] G. Gazzoli, C.D. Espositi, P.G. Favero, G. Severi, *Nuovo Cimento B* **61** (1981) 243.
- [167] J.P. Perdew, *Int. J. Quant. Chem.: Quant. Chem. Symp.*, **27** (1993) 93.

This Page Intentionally Left Blank

Some Properties of Linear Functionals and Adjoint Operators.

By Per-Olov Löwdin*

Uppsala Quantum Chemistry Group, Box 518, S-75120, Uppsala, Sweden.
Quantum Theory Project, 362 Williamson Hall
University of Florida, Gainesville, FL 32611-8435

List of Contents:

Introduction.

1. Some Properties of Linear Functionals.

Matrix representation of operators.

Ket-bra operators.

The bi-orthogonality theorem connected with the eigenvalue problems for a pair of operators T and T^d .

Linear transformations of the basis X .

2. Mappings of the dual space A^d on the original space A .

Mapping through the vector representation.

Binary products in the space $A = \{x\}$ with two linear positions.

Case of a symmetric binary product.

Binary products with one linear and one anti-linear position.

Case of a binary product with hermitean symmetry.

3. Mapping of the dual space A^d on another linear space .

4. Mapping of a space $A = \{x\}$ on another space $B = \{y\}$.

Abstract: By using the dual space $A^d = \{l\}$ formed by all the functionals $l = l(x)$, defined on a given linear space $A = \{x\}$, it is shown that every linear operator T defined on A corresponds to a mapping T^d defined on A^d . If the dual space A^d in some way is mapped back onto the original space A , the dual operator T^d is mapped on another linear operator T^a defined on A called the *adjoint operator* to T , i.e. if $x \rightarrow l \rightarrow x$, then $Tx \rightarrow T^d l \rightarrow T^a x$. Since there are many ways to carry out the mapping $l \rightarrow x$, e.g. by various types of binary products, there is a multitude of adjoint operators T^a , which usually have the property $(T^a)^a \neq T^a$. Some of the main types, which are based on binary products linear in both positions or linear in one and anti-linear in the other, are discussed in somewhat greater detail. If the binary product in the latter case has hermitean symmetry, there exists an hermitean adjoint T^\dagger having the property $(T^\dagger)^\dagger = T^\dagger$. The features of these adjoint operators under linear transformations of the reference basis in the original space $A = \{x\}$ are also discussed. Some of the results are further applied to the mappings of the dual space on another linear space $B = \{y\}$, and to the mappings of the original space $A = \{x\}$ on this other linear space $B = \{y\}$.

*Professor Emeritus at Uppsala University, Uppsala, Sweden.
Graduate Research Professor Emeritus at the University of Florida.

Introduction. - Linear functionals and adjoint operators of different types are used as tools in many parts of modern physics [1]. They are given a strict and deep going treatment in a rich literature in mathematics [2], which unfortunately is usually not accessible to the physicists, and in addition the methods and terminology are unfamiliar to the latter. The purpose of this paper is to give a brief survey of this field which is intended for theoretical physicists and quantum chemists. The tools for the treatment of the linear algebra involved are based on the bold-face symbol technique, which turns out to be particularly simple and elegant for this purpose. The results are valid for finite linear spaces, but the convergence proofs needed for the extension to infinite spaces are usually fairly easily proven. but are outside the scope of the present paper.

1. Some Properties of Linear Functionals.

Let us consider a linear space $A = \{x\}$ of elements, e.g. a finite space or a Banach space with a basis. Any mapping $x \rightarrow l$ of the objects x on the field of complex numbers is referred to as a *functional*, and such a mapping $l(x)$ is called a *linear functional* if it satisfies the relation

$$l(x_1 \cdot \alpha_1 + x_2 \cdot \alpha_2) = l(x_1) \cdot \alpha_1 + l(x_2) \cdot \alpha_2, \quad (1.1)$$

where the coefficients α_1 and α_2 in general are complex numbers. Let us next consider two linear functionals l_1 and l_2 . It is evident that the combination $l(x) = l_1(x)\beta_1 + l_2(x)\beta_2$ or $l = l_1 \cdot \beta_1 + l_2 \cdot \beta_2$ is again a linear functional. The set $A^d = \{l\}$ of all linear functionals is again a linear space, which is called the *dual space* to $A^d = \{x\}$. Every linear functional $l(x)$ is represented by an element l in A^d , i.e. by a "point" in the space A^d

At this point it is convenient to introduce a new notation. If $l(x)$ is the value of the linear functional in the point x , then $l(x) = [l | x]$ may be considered as the *dual product* of the elements l and x , and one has immediately the two theorems:

$$[l | x_1 \cdot \alpha_1 + x_2 \cdot \alpha_2] = [l | x_1] \cdot \alpha_1 + [l | x_2] \cdot \alpha_2, \quad (1.2)$$

$$[l_1 \cdot \beta_1 + l_2 \cdot \beta_2 | x] = [l_1 | x] \cdot \beta_1 + [l_2 | x] \cdot \beta_2, \quad (1.3)$$

i.e. the dual product is linear in both the first and second position. An element l of A^d is further said to be *bi-orthogonal* (in the sense of the dual product) to an element x of A , if $[l | x] = 0$. A set l_1, l_2, l_3, \dots out of A^d

is said to be *bi-orthonormal* to a set of elements x_1, x_2, x_3, \dots out of A , if one has $[l_i | x_j] = \delta_{ij}$.

If T is a linear operator defined on the space $A = \{x\}$, so that $T(x_1 \cdot \alpha_1 + x_2 \cdot \alpha_2) = T(x_1) \cdot \alpha_1 + T(x_2) \cdot \alpha_2$, then $l_1 = [l | Tx]$ is another linear functional, and one says that the mapping $l \rightarrow l_1$ is performed by the *dual operator* T^d defined on the dual space A^d , so that $l_1 = T^d l$, and

$$[l | Tx] = [l_1 | x] = [T^d l | x], \quad (1.4)$$

It is evident that also T^d is a linear operator, and that one further has the relations

$$(T_1 + T_2)^d = T_1^d + T_2^d, \quad (T_1 \cdot \alpha)^d = T_1^d \cdot \alpha, \quad (T_1 T_2)^d = T_2^d T_1^d. \quad (1.5)$$

In the following we will study these concepts in greater detail.

Vector representations. - Let us now assume that the original space $A = \{x\}$ has a basis $\mathbf{X} = \{X_1, X_2, X_3, \dots\}$, so that one has an expansion theorem of the form

$$x = \sum_k X_k a_k = \mathbf{X} \mathbf{a}, \quad (1.6)$$

where $\mathbf{a} = \{a_k\}$ is a column vector with the elements a_k . Here and in the following we will use bold-face symbols to denote rectangular or quadratic matrices as well as row and column vectors with the understanding that the product $\mathbf{C} = \mathbf{A}\mathbf{B}$ has the matrix elements

$$C_{kl} = \sum_{\alpha} A_{k\alpha} B_{\alpha l}, \quad (1.7)$$

i.e. one multiplies the columns of the first factor \mathbf{A} with the rows of the second factor \mathbf{B} . We note that the expansion theorem (11.6) establishes a one-to-one mapping $x \leftrightarrow \mathbf{a}$ between the space $A = \{x\}$ and the vector space $\{\mathbf{a}\}$. For the linear functional l , one obtains directly

$$l(x) = l(\sum_k X_k a_k) = \sum_k l(X_k) a_k = \sum_k l_k a_k = \mathbf{l} \cdot \mathbf{a}, \quad (1.8)$$

where $l_k = l(X_k)$ and $\mathbf{l} = \{l_k\}$ is the row vector formed by the elements l_k . Through this relation, one establishes a one-to-one correspondence $l \leftrightarrow \mathbf{l}$ between the linear functional space $\{l\}$ and the vector space $\{\mathbf{l}\}$. One says that \mathbf{a} and \mathbf{l} are vector representations of x and l , respectively. For the column vector \mathbf{a} , one has now the decomposition

$$\mathbf{a} = \begin{pmatrix} a_1 \\ a_2 \\ a_3 \\ \vdots \end{pmatrix} = \begin{pmatrix} 1 \\ 0 \\ 0 \\ \vdots \end{pmatrix} a_1 + \begin{pmatrix} 0 \\ 1 \\ 0 \\ \vdots \end{pmatrix} a_2 + \begin{pmatrix} 0 \\ 0 \\ 1 \\ \vdots \end{pmatrix} a_3 + \dots = \sum_k \mathbf{e}_k a_k, \quad (1.9)$$

where the unit vectors \mathbf{e}_k form a basis for the vector space $\{\mathbf{a}\}$ with the one-to-one correspondence $X_k \leftrightarrow \mathbf{e}_k$. In the same way, one gets for the row vector \mathbf{l} :

$$\begin{aligned} \mathbf{l} &= (l_1, l_2, l_3, \dots) = \\ &= l_1(1, 0, 0, \dots) + l_2(0, 1, 0, \dots) + l_3(0, 0, 1, \dots) + \dots = \sum_k l_k \mathbf{f}_k, \end{aligned} \quad (1.10)$$

where the quantities \mathbf{f}_k are the unit vectors in the row vector space $\{\mathbf{l}\}$ and span this space. If F_k denotes the linear functional which corresponds to the vectors \mathbf{f}_k , one gets for an arbitrary linear functional that

$$\mathbf{l} = \sum_k l_k F_k = \mathbf{l} \cdot \mathbf{F}, \quad (1.11)$$

where $\mathbf{F} = \{F_k\}$ is the column vector formed by the elements F_k :

$$\mathbf{F} = \begin{pmatrix} F_1 \\ F_2 \\ F_3 \\ \vdots \end{pmatrix}. \quad (1.12)$$

It is evident that the elements F_k span the dual space $A^d = \{\mathbf{l}\}$. From the relation $\mathbf{l}(\mathbf{x}) = \mathbf{l} \cdot \mathbf{a}$, one gets now immediately

$$[F_k | X_j] = F_k(X_j) = \mathbf{f}_k \cdot \mathbf{e}_j = \delta_{kj}, \quad (1.13)$$

which implies that the two bases \mathbf{F} and \mathbf{X} are *bi-orthonormal* with respect to each other. In condensed form, one has

$$[\mathbf{F} | \mathbf{X}] = \mathbf{1}, \quad (1.14)$$

where $\mathbf{1}$ is the unit matrix. Starting from $\mathbf{x} = \mathbf{X} \cdot \mathbf{a}$, one gets further that $[\mathbf{F} | \mathbf{x}] = [\mathbf{F} | \mathbf{X} \cdot \mathbf{a}] = [\mathbf{F} | \mathbf{X}] \cdot \mathbf{a} = \mathbf{1} \cdot \mathbf{a}$. This gives the explicit formula for the expansion coefficients

$$\mathbf{a} = [\mathbf{F} | \mathbf{x}], \quad (1.15)$$

as the dual product between \mathbf{F} and the element \mathbf{x} under consideration. One has further for any linear functional $l = \mathbf{l} \cdot \mathbf{F}$, which gives $[l | \mathbf{X}] = [\mathbf{l} \cdot \mathbf{F} | \mathbf{X}] = \mathbf{l} \cdot [\mathbf{F} | \mathbf{X}] = \mathbf{l} \cdot \mathbf{1} = \mathbf{l}$, i.e. $l = [l | \mathbf{X}]$ or $l_k = [l | X_k]$ in accordance with the previous definition.

Matrix representation of operators. - If an operator T is defined on the space $A = \{\mathbf{x}\}$, then the quantity $T\mathbf{x}_l$ is also an element of this space and may be expanded in the form

$$T\mathbf{x}_l = \sum_k X_k T_{kl}, \quad (1.16)$$

where the expansion coefficients form a matrix $\mathbf{T} = \{T_{kl}\}$ which is said to be the matrix representation of the operator T in terms of the basis \mathbf{X} . In bold-face symbols, one may write this relation in the more condensed form

$$T \mathbf{X} = \mathbf{X} \cdot \mathbf{T}. \quad (1.17)$$

Multiplying to the left by $[\mathbf{F} |$, one gets $[\mathbf{F} | T \mathbf{X}] = [\mathbf{F} | \mathbf{X} \cdot \mathbf{T}] = [\mathbf{F} | \mathbf{X}] \cdot \mathbf{T} = \mathbf{1} \cdot \mathbf{T} = \mathbf{T}$, i.e.

$$\mathbf{T} = [\mathbf{F} | T \mathbf{X}] = [\mathbf{F} | T | \mathbf{X}], \quad (1.18)$$

where we have introduced a second "dummy" bar, which is often used by the physicists. By means of the definition (1.4), it is now possible to find the matrix representation $\tilde{\mathbf{R}}$ of the dual operator T^d , which is defined by the relation $T^d \mathbf{F}_l = \sum_k F_k R_{kl} = \sum_k \tilde{R}_{lk} F_k$, where $\tilde{\mathbf{R}}$ is the transposed of the matrix \mathbf{R} with the rows and columns interchanged. Observing that \mathbf{F} is a column vector, one may write this definition in the condensed form

$$T^d \mathbf{F} = \mathbf{F} \mathbf{R} = \tilde{\mathbf{R}} \mathbf{F}, \quad (1.19)$$

Multiplying this relation to the right by $|\mathbf{X}]$, one obtains

$$[T^d \mathbf{F} | \mathbf{X}] = [\tilde{\mathbf{R}} \mathbf{F} | \mathbf{X}] = \tilde{\mathbf{R}} [\mathbf{F} | \mathbf{X}] = \tilde{\mathbf{R}} \cdot \mathbf{1} = \tilde{\mathbf{R}}, \quad (1.20)$$

and further

$$\tilde{\mathbf{R}} = [T^d \mathbf{F} | \mathbf{X}] = [\mathbf{F} | T\mathbf{X}] = [\mathbf{F} | \mathbf{X} \mathbf{T}] = [\mathbf{F} | \mathbf{X}] \mathbf{T} = \mathbf{T}, \quad (1.21)$$

which means that \mathbf{R} is the transposed of the matrix \mathbf{T} . One may also write relation (1.19) in the form

$$T^d \mathbf{F} = \mathbf{T} \cdot \mathbf{F} , \quad (1.22)$$

which is a very simple result due to the fact that we are considering two bi-orthonormal bases.

Ket-bra operators. - The dual product $[\mathbf{l} | \mathbf{x}]$ is essentially different from the binary product $\langle \mathbf{x} | \mathbf{y} \rangle$, which is customarily used in quantum theory, but one can still pick up certain ideas from this field. Following Dirac, one can consider even the bracket $[\mathbf{l} | \mathbf{x}]$ as the "product" of a bra-vector $[\mathbf{l} |$ and a ket-vector $|\mathbf{x}\rangle$, which means that one can also introduce a *ket-bra operator* $G = |\mathbf{x}_1\rangle[\mathbf{l}_1|$ defined in the original space $A = \{\mathbf{x}\}$ through the relation

$$G = |\mathbf{x}_1\rangle[\mathbf{l}_1| , \quad G\mathbf{x} = \mathbf{x}_1[\mathbf{l}_1 | \mathbf{x}]. \quad (1.23)$$

Since one has $G\mathbf{x}_1 = \mathbf{x}_1[\mathbf{l}_1 | \mathbf{x}_1]$, it is clear that \mathbf{x}_1 is an eigenelement to the operator G associated with the eigenvalue $\lambda = [\mathbf{l}_1 | \mathbf{x}_1]$. It is also evident that, if $\lambda \neq 0$, this eigenvalue is non-degenerate: if \mathbf{z}_1 is another eigenelement associated with the same eigenvalue, one has $G\mathbf{z}_1 = \lambda\mathbf{z}_1 = \mathbf{x}_1[\mathbf{l}_1 | \mathbf{z}_1]$, i.e. $\mathbf{z}_1 \sim \mathbf{x}_1$, which proves the statement. For an arbitrary element \mathbf{x} , one has also $G^2\mathbf{x} = G\mathbf{x}_1[\mathbf{l}_1 | \mathbf{x}] = \mathbf{x}_1[\mathbf{l}_1 | \mathbf{x}_1][\mathbf{l}_1 | \mathbf{x}] = [\mathbf{l}_1 | \mathbf{x}_1] \mathbf{x}_1[\mathbf{l}_1 | \mathbf{x}] = [\mathbf{l}_1 | \mathbf{x}_1] G\mathbf{x}$, which means that the operator G satisfies the reduced Cayley-Hamilton equation

$$G(G - [\mathbf{l}_1 | \mathbf{x}_1]) = 0, \quad (1.24)$$

and that it has the eigenvalues $\lambda = 0$ and $\lambda = [\mathbf{l}_1 | \mathbf{x}_1]$. For the diagonal sum of the eigenvalues, one hence obtains

$$\text{Tr } G = \text{Tr } |\mathbf{x}_1\rangle[\mathbf{l}_1| = [\mathbf{l}_1 | \mathbf{x}_1]. \quad (1.25)$$

The ket-bra operators are useful in many connections. Using (1.15), the expansion theorem (1.6) may now be written in the form

$$\mathbf{x} = \sum_k X_k a_k = \mathbf{X} \mathbf{a} = \mathbf{X} [\mathbf{F} | \mathbf{x}] = |\mathbf{X}\rangle [\mathbf{F} | \mathbf{x}], \quad (1.26)$$

for all elements \mathbf{x} , and this means that one has the following resolution of the identity operator in the original space $A = \{\mathbf{x}\}$:

$$I = |\mathbf{X}\rangle[\mathbf{F}| = \sum_k |\mathbf{X}_k\rangle[\mathbf{F}_k|. \quad (1.27)$$

For an arbitrary operator T , one gets immediately

$$\begin{aligned}
 T &= T.I = T |X\rangle[F] = T X [F] = X T [F] = |X\rangle T [F] = \\
 &= \sum_{kl} |X_k\rangle T_{kl} [F_l] = \sum_{kl} T_{kl} |X_k\rangle [F_l] = \sum_{kl} T_{kl} P_{lk}, \quad (1.28)
 \end{aligned}$$

where the operators $P_{lk} = |X_k\rangle[F_l]$ apparently span the operator space $\{T\}$. It is interesting to observe that, once the carrier space $A = \{x\}$ has a basis, even the operator space $\{T\}$ has a basis. The operators P_{lk} are often referred to as the fundamental units in $\{T\}$, and - by using (1.13) - it is easily shown that they satisfy the algebraic relations

$$P_{kl}P_{mn} = \delta_{kn}P_{ml}, \quad I = \sum_k P_{kk}, \quad (1.29)$$

with the special cases $P_{kk}^2 = P_{kk}$, $\text{Tr } P_{kk} = 1$, and $P_{kl}^2 = 0$, for $k \neq l$. Our study shows that the linear functionals, the dual products and their ket-bra operators are valuable tools in treating both the original space $A=\{x\}$ and its operator space $\{T\}$.

The bi-orthogonality theorem connected with the eigenvalue problems for a pair of operators T and T^d .- For the sake of simplicity, we will consider a linear space $A = \{x\}$ of order n , and a linear operator T having only distinct eigenvalues $\lambda_1, \lambda_2, \lambda_3, \dots, \lambda_n$, and the eigenelements $C_1, C_2, C_3, \dots, C_n$, which form a basis in the space $A = \{x\}$, so that

$$T C_k = \lambda_k C_k, \quad x = \sum_k C_k a_k. \quad (1.30)$$

In such a case, the dual space $A^d=\{l\}$ of all the linear functionals is also of order n . Let us denote the eigenvalues and eigenelements of the adjoint operator T^d by D_l and μ_l , respectively, so that

$$T^d D_l = \mu_l D_l. \quad (1.31)$$

Using the definition (1.4), one gets directly

$$\mu_l [D_l | C_k] = [T^d D_l | C_k] = [D_l | T C_k] = \lambda_k [D_l | C_k], \quad (1.32)$$

i.e.

$$(\mu_l - \lambda_k) [D_l | C_k] = 0, \quad (1.33)$$

or

$$[D_l | C_k] = 0, \quad \text{whenever } \mu_l \neq \lambda_k. \quad (1.34)$$

This is the general *bi-orthogonality theorem* valid for a pair of adjoint operators. From the expansion theorem $x = \sum_k C_k a_k$, one gets further $[D_l | x] = \sum_k [D_l | C_k] a_k = [D_l | C_l] a_l$. Since the product $[D_l | x]$ cannot be

vanishing for all \mathbf{x} , one has necessarily $[D_1 | C_1] \neq 0$, and - according to (1.31) -, this implies $\mu_1 = \lambda_1$, i.e.

$$[D_1 | C_1] \neq 0, \quad \mu_1 = \lambda_1, \quad (1.35)$$

Putting $D_1' = [D_1 | C_1]^{-1} D_1$, one gets particularly $[D_1' | C_1] = 1$. It is evident that, in the distinct case, the operators T and T^d have the same eigenvalues and that one has the bi-orthonormalization relation:

$$[D | C] = 1. \quad (1.36)$$

It is illustrative to study these properties also by using the matrix representations, in which case one can also generalize the results to degenerate eigenvalues. Starting from (1.17), one knows that the matrix T may be brought to *classical canonical form* λ by a similarity transformation γ , so that

$$T X = X T, \quad \gamma^{-1} T \gamma = \lambda. \quad (1.37)$$

Putting $C = X \gamma$ and $X = C \gamma^{-1}$, one gets directly $T C = T X \gamma = X T \gamma = C \gamma^{-1} T \gamma = C \lambda$, i.e.

$$T C = C \lambda. \quad (1.38)$$

This is the *stability relation* which in the general case replaces the eigenvalue problem. From the relation (1.22), one gets further

$$T^d F = T F = \gamma \lambda \gamma^{-1} F, \quad (1.39)$$

and introducing a column vector D through the relation $D = \gamma^{-1} F$, one obtains after multiplying (1.39) to the left by γ^{-1} that

$$T^d D = \lambda D, \quad (1.40)$$

which relation indicates that the operator T^d has the same eigenvalue structure as the operator T . One has further

$$[D | C] = [\gamma^{-1} F | X \gamma] = \gamma^{-1} [F | X] \gamma = \gamma^{-1} 1 \gamma = 1, \quad (1.41)$$

which is the general bi-orthonormality relation.

Linear transformations of the basis X .- Let us now consider a linear transformation $X' = X \alpha$ of the basis for the space $A = \{\mathbf{x}\}$ with the inverse $X = X' \alpha^{-1}$. In the new basis the operator T has the matrix representation

\mathbf{T}' , defined by the relation $\mathbf{T} \mathbf{X}' = \mathbf{X}' \mathbf{T}'$, and one gets immediately $\mathbf{T} \mathbf{X}' = \mathbf{T} \mathbf{X} \alpha = \mathbf{X}' \mathbf{T} \alpha = \mathbf{X}' \alpha^{-1} \mathbf{T}' \alpha$ and the well-known similarity transformation

$$\mathbf{T}' = \alpha^{-1} \mathbf{T} \alpha, \quad (1.42)$$

Since the expansion theorem has the form $\mathbf{x} = \mathbf{X} \mathbf{a} = \mathbf{X}' \mathbf{a}' = \mathbf{X} \alpha \mathbf{a}'$, and for the vector transformations one gets the relations

$$\mathbf{a} = \alpha \mathbf{a}', \quad \mathbf{a}' = \alpha^{-1} \mathbf{a}. \quad (1.43)$$

For a linear functional, one gets according to (1.8) that $l(\mathbf{x}) = [l | \mathbf{x}] = \mathbf{l} \cdot \mathbf{a}$, where $\mathbf{l} = l(\mathbf{X})$. This gives directly $\mathbf{l}' = l(\mathbf{X}') = l(\mathbf{X} \cdot \alpha) = l(\mathbf{X}) \alpha = \mathbf{l} \cdot \alpha$, as well as $\mathbf{l}' \cdot \mathbf{a}' = \mathbf{l} \cdot \mathbf{a}$, which shows that the linear functional $l(\mathbf{x})$ is independent of the choice of basis in the space $A = \{\mathbf{x}\}$, and that the dual product $[l | \mathbf{x}]$ is a *scalar*. Since one has the transformation formula

$$\mathbf{l}' = \mathbf{l} \cdot \alpha, \quad \mathbf{l} = \mathbf{l}' \cdot \alpha^{-1}. \quad (1.44)$$

one says often that \mathbf{l} transforms as a *co-variant* vector, whereas \mathbf{a} transforms as a *contra-variant* vector. The two vector spaces $\{\mathbf{a}\}$ and $\{\mathbf{l}\}$ have hence essentially different transformation properties. According to (1.11) one has further $\mathbf{l} = \mathbf{l} \cdot \mathbf{F} = \mathbf{l}' \cdot \mathbf{F}' = \mathbf{l} \cdot \alpha \cdot \mathbf{F}'$, which implies that the basis in the dual space undergoes the transformation $\mathbf{F}' = \alpha \cdot \mathbf{F}$ with the inverse $\mathbf{F} = \alpha^{-1} \mathbf{F}'$, so that

$$\mathbf{F}' = \alpha \cdot \mathbf{F}, \quad \mathbf{F} = \alpha^{-1} \cdot \mathbf{F}'. \quad (1.45)$$

It is now easily checked that $[\mathbf{F}' | \mathbf{X}'] = [\alpha^{-1} \mathbf{F} | \mathbf{X} \alpha] = \alpha^{-1} [\mathbf{F} | \mathbf{X}] \alpha = \mathbf{1}$, and that further $[\mathbf{X}'] [\mathbf{F}'] = [\mathbf{X} \alpha] [\alpha^{-1} \mathbf{F}] = [\mathbf{X}] \alpha \alpha^{-1} [\mathbf{F}] = [\mathbf{X}] [\mathbf{F}] = \mathbf{I}$ is the identity operator. For the mapping of the adjoint operator \mathbf{T}^d in the dual space, one gets finally $\mathbf{T}^d \mathbf{l} = \mathbf{T}^d (\mathbf{l} \cdot \mathbf{F}) = \mathbf{l} \cdot \mathbf{T}^d \mathbf{F} = \mathbf{l} \cdot \mathbf{T} \cdot \mathbf{F}'$ as well as $(\mathbf{T}^d \mathbf{l})' = \mathbf{l}' \cdot \mathbf{T}' \cdot \mathbf{F}' = \mathbf{l} \cdot \alpha \cdot \alpha^{-1} \mathbf{T} \alpha \cdot \alpha^{-1} \mathbf{F} = \mathbf{l} \cdot \mathbf{T} \cdot \mathbf{F} = \mathbf{T}^d \mathbf{l}$; the result of the mapping is again an invariant.

2. Mappings of the dual space A^d on the original space A .

If one maps the dual space $A^d = \{\mathbf{l}\}$ back on the original space $A = \{\mathbf{x}\}$ through a mapping $\mathbf{l} \rightarrow \mathbf{y}$, one may transfer some of the concepts introduced above as to the dual space to the original space itself. For instance, one may say that two elements \mathbf{y} and \mathbf{x} are *bi-orthogonal*, if \mathbf{l} and \mathbf{x} are bi-orthogonal. To every linear operator \mathbf{T} on A , there exists further an *adjoint operator* \mathbf{T}^a on A , such that, if $\mathbf{l} \rightarrow \mathbf{y}$, then $\mathbf{T}^d \mathbf{l} \rightarrow \mathbf{T}^a \mathbf{y}$.

Unfortunately, there are many ways to construct the mapping $l \rightarrow y$, and this implies that there are many ways to carry out these extensions. We will here investigate only a few of the main types.

Mapping through the vector representation. The simplest mapping $l \rightarrow y$ possible is based on the fact that $l = \mathbf{l} \cdot \mathbf{F}$, where $\mathbf{l} = \mathbf{l} = (l_1, l_2, l_3, \dots)$ is a row vector, and one can then define the image element y through the relation

$$y = \sum_k X_k l_k = \mathbf{X} \tilde{\mathbf{l}}. \quad (2.1)$$

In such a case, one says that two elements y and x of the space $A = \{x\}$ are bi-orthogonal, if $[\mathbf{l} | x] = \tilde{\mathbf{l}} \mathbf{a} = 0$. For the dual operator T^d , one has further $T^d \mathbf{l} = T^d \mathbf{l} \cdot \mathbf{F} = \mathbf{l}$, $T^d \mathbf{F} = \mathbf{l} \cdot \mathbf{T} \cdot \mathbf{F} = (\mathbf{l} \cdot \mathbf{T}) \cdot \mathbf{F}$, and this gives

$$T^a y = \mathbf{X} \cdot (\mathbf{l} \cdot \mathbf{T})_{\text{trans}} = \mathbf{X} \cdot \tilde{\mathbf{T}} \cdot \tilde{\mathbf{l}}. \quad (2.2)$$

Since one has also $T^a y = T^a \mathbf{X} \tilde{\mathbf{l}}$, it follows that the adjoint operator is characterized by the relation

$$T^a \mathbf{X} = \mathbf{X} \cdot \tilde{\mathbf{T}}, \quad (2.3)$$

i.e. that T^a has the matrix representation $\tilde{\mathbf{T}}$, which seems to be a very natural result.

The disadvantage of this mapping $l \rightarrow y$ is that it is basis dependent. Considering an arbitrary non-singular transformation $\mathbf{X}' = \mathbf{X} \alpha$, one has $\mathbf{l}' = \mathbf{l} \alpha$, $\tilde{\mathbf{l}}' = \tilde{\alpha} \tilde{\mathbf{l}}$, and

$$y' = \mathbf{X}' \mathbf{l}' = \mathbf{X} (\alpha \tilde{\alpha}) \tilde{\mathbf{l}}, \quad (2.4)$$

which means that $y' = y$ only for transformations α having the special property

$$\alpha \tilde{\alpha} = \mathbf{1}, \quad \tilde{\alpha} = \alpha^{-1}. \quad (2.5)$$

For the matrix representation of the adjoint operator T^a in the basis $\mathbf{X}' = \mathbf{X} \alpha$, one should have the similarity transformation $\alpha^{-1} \tilde{\mathbf{T}} \alpha$, whereas the transposed matrix has the related special property $(\alpha^{-1} \cdot \mathbf{T} \alpha)_{\text{trans}} = \tilde{\alpha} \tilde{\mathbf{T}} (\tilde{\alpha})^{-1}$; these two expressions are identical, if and only if the relation (2.5) is satisfied.

Unless one restricts oneself to a very class of bases $\mathbf{X}' = \mathbf{X} \alpha$, connected by transformations α of the type (2.5), the mapping $l \rightarrow y$ discussed here leads hence to concepts which are basis dependent. We will now try to remove this restriction.

Binary products in the space $A = \{x\}$ with two linear positions.- As a tool, we will first use a binary product $(x_1 | x_2)$, which is a mapping of any ordered pair x_1, x_2 of elements of $A = \{x\}$ on the field of the complex numbers. It is assumed to be independent of any choice of basis, i.e. it is a *scalar*, and it is further assumed to be *linear* in both positions. For the moment, we don't need any symmetry property, i.e. there is no statement of the value of $(x_2 | x_1)$ in relation to $(x_1 | x_2)$. If $\mathbf{X} = \{X_1, X_2, X_3, \dots\}$ is an arbitrary basis for the space $A = \{x\}$, we will now consider the matrix

$$\Delta = (\tilde{\mathbf{X}} | \mathbf{X}), \quad (2.6)$$

having the elements $\Delta_{kl} = (X_k | X_l)$. According to the expansion theorem (1.6) one has $x = \mathbf{X}\mathbf{a}$, and this gives directly $(\tilde{\mathbf{X}} | x) = (\tilde{\mathbf{X}} | \mathbf{X}\mathbf{a}) = (\tilde{\mathbf{X}} | \mathbf{X}\mathbf{a}) = (\tilde{\mathbf{X}} | \mathbf{X})\mathbf{a} = \Delta\mathbf{a}$, or

$$\Delta\mathbf{a} = (\tilde{\mathbf{X}} | x), \quad (2.7)$$

which is an equation system for the column vector \mathbf{a} . Since this vector is unique, one must necessarily have $|\Delta| \neq 0$, and the matrix Δ has hence an inverse Δ^{-1} , and (2.7) has then the explicit solution

$$\mathbf{a} = \Delta^{-1}(\tilde{\mathbf{X}} | x), \quad (2.8)$$

For a pair of elements $x_1 = \mathbf{X}\mathbf{a}_1 = \tilde{\mathbf{a}}_1 \tilde{\mathbf{X}}$ and $x_2 = \mathbf{X}\mathbf{a}_2$, one gets further that

$$(x_1 | x_2) = (\tilde{\mathbf{a}}_1 \tilde{\mathbf{X}} | \mathbf{X}\mathbf{a}_2) = \tilde{\mathbf{a}}_1 (\tilde{\mathbf{X}} | \mathbf{X})\mathbf{a}_2 = \tilde{\mathbf{a}}_1 \Delta\mathbf{a}_2. \quad (2.9)$$

One may use such a binary product to define the length $||x||$ of an element x through the relation $||x|| = (x | x)^{1/2}$, which gives

$$||x||^2 = (x | x) = \tilde{\mathbf{a}} \Delta \mathbf{a} = \sum_{kl} a_k \Delta_{kl} a_l, \quad (2.10)$$

and for this reason the matrix Δ is often referred to as the *metric* matrix for the space $A = \{x\}$, in analogy with the "metric fundamental tensor" occurring in some other parts of physics.

In studying the mapping $l \rightarrow y = \mathbf{X} \mathbf{b}$, we observe by using (2.9) that $(y|x) = \tilde{\mathbf{b}} \Delta \mathbf{a}$ is equal to $l(x) = [l|x] = \mathbf{l} \mathbf{a}$, provided that $\tilde{\mathbf{b}} \Delta = \mathbf{l}$, i.e. that $\tilde{\mathbf{b}} = \mathbf{l} \Delta^{-1}$ or $\mathbf{b} = (\tilde{\Delta})^{-1} \tilde{\mathbf{l}}$, which gives

$$l(x) = [l|x] = (y|x), \quad (2.11)$$

which seems to be independent of any choice of the basis. The mapping $l \rightarrow y$ is now defined explicitly by the relation

$$y = \mathbf{X} \mathbf{b} = \mathbf{X} (\tilde{\Delta})^{-1} \tilde{\mathbf{l}}, \quad (2.12)$$

which differs from (2.1) by the extra factor $(\tilde{\Delta})^{-1}$. Let us now study how this mapping behaves under the basis transformation $\mathbf{X}' = \mathbf{X} \alpha$. Since $\Delta' = (\tilde{\mathbf{X}}' | \mathbf{X}') = (\tilde{\alpha} \tilde{\mathbf{X}} | \mathbf{X} \alpha) = \tilde{\alpha} (\tilde{\mathbf{X}} | \mathbf{X}) \alpha = \tilde{\alpha} \Delta \alpha$ and $\mathbf{l}' = \mathbf{l} \alpha$, one has

$$\begin{aligned} y' &= \mathbf{X}' \mathbf{b}' = \mathbf{X}' (\tilde{\Delta}')^{-1} \tilde{\mathbf{l}}' = \mathbf{X} \alpha (\tilde{\alpha} \tilde{\Delta} \alpha)^{-1} \tilde{\alpha} \tilde{\mathbf{l}} = \\ &= \mathbf{X} \alpha \alpha^{-1} (\tilde{\Delta})^{-1} (\tilde{\alpha})^{-1} \tilde{\alpha} \tilde{\mathbf{l}} = \mathbf{X} (\tilde{\Delta})^{-1} \tilde{\mathbf{l}} = y, \end{aligned} \quad (2.13)$$

Hence the mapping $l \rightarrow y$ defined by (2.12) is independent of the choice of basis.

According to the general definition, two elements are said to be bi-orthogonal if $[l|x] = (y|x) = 0$. Similarly a sequence y_1, y_2, y_3, \dots is said to be *bi-orthonormal* to a sequence x_1, x_2, x_3, \dots , if one has the relation

$$[l_i | x_j] = (y_i | x_j) = \delta_{ij}. \quad (2.14)$$

According to (1.14), one has the bi-orthonormality relation $[\mathbf{F} | \mathbf{X}] = \mathbf{1}$. By using (2.12), one can now carry out the mapping $\mathbf{F} \rightarrow \mathbf{Y}$ through the formula $\mathbf{Y} = \mathbf{X} (\tilde{\Delta})^{-1}$, which gives

$$\mathbf{Y} = \mathbf{X} (\tilde{\Delta})^{-1}, \quad [\mathbf{F} | \mathbf{X}] = (\tilde{\mathbf{Y}} | \mathbf{X}) = \mathbf{1}. \quad (2.15)$$

The basis $\mathbf{X}_r = \mathbf{Y}$ is often referred to as the *reciprocal basis* to the original basis \mathbf{X} , and it is a very important tool in many parts of modern physics. It is easily checked that it has the property $(\tilde{\mathbf{X}}_r | \mathbf{X}) = (\Delta^{-1} \tilde{\mathbf{X}} | \mathbf{X}) = \Delta^{-1}(\tilde{\mathbf{X}} | \mathbf{X}) = \Delta^{-1}\Delta = \mathbf{1}$. Hence one has

$$\mathbf{X}_r = \mathbf{X} (\tilde{\Delta})^{-1}, \quad (\tilde{\mathbf{X}}_r | \mathbf{X}) = \mathbf{1}, \quad (2.16)$$

whereas $(\tilde{\mathbf{X}} | \mathbf{X}_r) = (\tilde{\mathbf{X}} | \mathbf{X} (\tilde{\Delta})^{-1}) = (\tilde{\mathbf{X}} | \mathbf{X})(\tilde{\Delta})^{-1} = \Delta (\tilde{\Delta})^{-1}$, where - due to the lack of symmetry properties of the metric matrix Δ - no further simplification is possible.

From the relations $\mathbf{x} = \mathbf{X} \mathbf{a}$ and $\mathbf{T} \mathbf{X} = \mathbf{X} \mathbf{T}$, one gets - after multiplication to the left by $(\tilde{\mathbf{X}}_r |$ and using the fact that $(\tilde{\mathbf{X}}_r | \mathbf{X}) = \mathbf{1}$ - the explicit formulas

$$\mathbf{a} = (\tilde{\mathbf{X}}_r | \mathbf{x}), \quad \mathbf{T} = (\tilde{\mathbf{X}}_r | \mathbf{T} \mathbf{X}). \quad (2.17)$$

Let us now consider the operator mappings $\mathbf{T} \rightarrow \mathbf{T}^d \rightarrow \mathbf{T}^a$, which is defined through the relations

$$(\mathbf{y} | \mathbf{T} \mathbf{x}) = [\mathbf{l} | \mathbf{T} \mathbf{x}] = [\mathbf{T}^d \mathbf{l} | \mathbf{x}] = (\mathbf{T}^a \mathbf{y} | \mathbf{x}) \quad (2.18)$$

for all \mathbf{x} . This implies also that $[\mathbf{T}^d \mathbf{F} | \mathbf{X}] = (\mathbf{T}^a \tilde{\mathbf{F}} | \mathbf{X}) = (\mathbf{T}^a \tilde{\mathbf{X}}_r | \mathbf{X})$ and - putting $\mathbf{T}^a \mathbf{X}_r = \mathbf{X}_r \tilde{\mathbf{R}}$ - that $(\mathbf{T}^a \tilde{\mathbf{X}}_r | \mathbf{X}) = (\tilde{\mathbf{R}} \tilde{\mathbf{X}}_r | \mathbf{X}) = \tilde{\mathbf{R}} (\tilde{\mathbf{X}}_r | \mathbf{X}) = \tilde{\mathbf{R}}$. Using (1.22), one gets finally

$$\tilde{\mathbf{R}} = [\mathbf{T}^d \mathbf{F} | \mathbf{X}] = [\mathbf{T} \cdot \mathbf{F} | \mathbf{X}] = \mathbf{T} \cdot [\mathbf{F} | \mathbf{X}] = \mathbf{T}. \quad (2.19)$$

Hence one has the fundamental relations

$$\mathbf{T} \mathbf{X} = \mathbf{X} \mathbf{T}, \quad \mathbf{T}^d \mathbf{F} = \mathbf{T} \cdot \mathbf{F}, \quad \mathbf{T}^a \mathbf{X}_r = \mathbf{X}_r \tilde{\mathbf{T}}. \quad (2.20)$$

As a simple application, we will now consider the ket-bra operator $G = |x_1\rangle\langle l_1|$ defined by (1.23) so that $G \mathbf{x} = x_1 |l_1\rangle = x_1 (y_1 | \mathbf{x})$. The mapping $l_1 \rightarrow y_1$ gives hence

$$G = |x_1\rangle\langle l_1| = |x_1\rangle\langle y_1|, \quad (2.21)$$

and by using the relation $(G^a y | x) = (y | Gx) = (y | x_1(y_1 | x)) = (y | x_1)(y_1 | x) = ((y | x_1)y_1 | x)$ for all x , one finds for the adjoint operator that $G^a y = (y | x_1)y_1$. According to (1.27), one has a resolution of the identity $I = |X\rangle[F|$ which now takes the form

$$I = |X\rangle\langle X_r|, \quad (2.22)$$

and, for the operator T , one gets the expression

$$T = T |X\rangle\langle X_r| = |X\rangle T \langle X_r|, \quad (2.23)$$

which also gives the fundamental units in the operator space $\{T\}$. Let us now consider the adjoint operator T^a and the relation $T^a X_r = X_r \tilde{T}$, which implies that $T^a X (\tilde{\Delta})^{-1} = X (\tilde{\Delta})^{-1} \tilde{T}$ or

$$T^a X = X (\tilde{\Delta})^{-1} \tilde{T} (\tilde{\Delta})^{+1}, \quad (2.24)$$

which gives the matrix representation of the adjoint operator in the ordinary basis X . Using the resolution of the identity this gives finally

$$T^a = |X\rangle (\tilde{\Delta})^{-1} \tilde{T} (\tilde{\Delta})^{+1} \langle X_r|. \quad (2.25)$$

It is clear from the definition that the adjoint operator T^a is independent of the choice of basis, but is also illustrative to show that the expression (2.25) is invariant under the transformation $X' = X\alpha$. In order to understand the expression (2.25) somewhat better, one should observe that the reciprocal basis X_r has its own metric matrix:

$$\Delta_r = (\tilde{X}_r | X_r) = (\Delta^{-1} \tilde{X} | X) (\tilde{\Delta})^{-1} = \Delta^{-1} (\tilde{X} | X) (\tilde{\Delta})^{-1} = \Delta^{-1} \Delta (\tilde{\Delta})^{-1} = (\tilde{\Delta})^{-1} \quad (2.26)$$

which means that, for the reciprocal of the reciprocal basis, one gets

$$(X_r)_r = X_r (\tilde{\Delta}_p)^{-1} = X_r \Delta, \quad (2.27)$$

and (2.25) may then be written under the simple form

$$T^a = |X_r\rangle \tilde{T} \langle X_{rr}|. \quad (2.28)$$

Case of a symmetric binary product.- In many applications, it is convenient to have $X_{rr} = X$, and this is achieved if one assumes that the binary product $(x_1 | x_2)$ is *symmetric* in the two positions, so that

$$(\mathbf{x}_1 | \mathbf{x}_2) = (\mathbf{x}_2 | \mathbf{x}_1) . \quad (2.29)$$

In such a case, the metric matrix becomes symmetric so that $\tilde{\Delta} = \Delta$, which implies that $\mathbf{X}_{\text{rT}} = \mathbf{X}_{\text{r}} \Delta = \mathbf{X} (\tilde{\Delta})^{-1} \Delta = \mathbf{X}$. It is then also easily shown that $(T^a)^a = T$ and that, for $G = |\mathbf{x}_1\rangle\langle\mathbf{y}_1|$, one has $G^a = |\mathbf{y}_1\rangle\langle\mathbf{x}_1|$. One has e.g. $(\mathbf{y} | T\mathbf{x}) = (T^a\mathbf{y} | \mathbf{x}) = (\mathbf{x} | T^a\mathbf{y}) = (T^{aa}\mathbf{x} | \mathbf{y}) = (\mathbf{y} | T^{aa}\mathbf{x})$ and $G^a\mathbf{y} = (\mathbf{y} | \mathbf{x}_1)\mathbf{y}_1 = \mathbf{y}_1(\mathbf{x}_1 | \mathbf{y}) = |\mathbf{y}_1\rangle\langle\mathbf{x}_1| \mathbf{y}$, which proves the statement.

Binary products with one linear and one anti-linear position. - As another tool, which is perhaps more familiar to the physicists, we will now introduce a binary product $\langle \mathbf{y} | \mathbf{x} \rangle$ for two elements \mathbf{y} and \mathbf{x} out of the linear space $A = \{\mathbf{x}\}$, which is *anti-linear* in the first position and *linear* in the second, so that

$$\langle \beta_1 \mathbf{y}_1 + \beta_2 \mathbf{y}_2 | \mathbf{x} \rangle = \beta_1^* \langle \mathbf{y}_1 | \mathbf{x} \rangle + \beta_2^* \langle \mathbf{y}_2 | \mathbf{x} \rangle , \quad (2.30)$$

$$\langle \mathbf{y} | \alpha_1 \mathbf{x}_1 + \alpha_2 \mathbf{x}_2 \rangle = \langle \mathbf{y} | \mathbf{x}_1 \rangle \alpha_1 + \langle \mathbf{y} | \mathbf{x}_2 \rangle \alpha_2 , \quad (2.31)$$

but without any particular symmetry property. In (2.30) the star * indicates that one should take the complex conjugate. As before, the metric matrix has the form

$$\Delta = \langle \tilde{\mathbf{X}} | \mathbf{X} \rangle, \quad \Delta_{kl} = \langle \mathbf{X}_k | \mathbf{X}_l \rangle. \quad (2.32)$$

From the expansion theorem $\mathbf{x} = \mathbf{X} \mathbf{a}$, it follows that $\langle \tilde{\mathbf{X}} | \mathbf{x} \rangle = \Delta \cdot \mathbf{a}$, and - since the equation system $\Delta \cdot \mathbf{a} = \langle \tilde{\mathbf{X}} | \mathbf{x} \rangle$ - has a unique solution for the column vector \mathbf{a} - one has necessarily that $|\Delta| \neq 0$ and that

$$\mathbf{a} = \Delta^{-1} (\tilde{\mathbf{X}} | \mathbf{x}), \quad (2.33)$$

If $\mathbf{y} = \mathbf{X} \mathbf{b} = \tilde{\mathbf{b}} \tilde{\mathbf{X}}$, one has also

$$\langle \mathbf{y} | \mathbf{x} \rangle = \langle \tilde{\mathbf{b}} \tilde{\mathbf{X}} | \mathbf{X} \mathbf{a} \rangle = \tilde{\mathbf{b}}^* \langle \tilde{\mathbf{X}} | \mathbf{X} \rangle \mathbf{a} = \mathbf{b}^\dagger \Delta \mathbf{a} = \sum_{kl} b_k^* \Delta_{kl} a_l, \quad (2.34)$$

where $\mathbf{b}^\dagger = (\tilde{\mathbf{b}})^*$. In certain cases, it may be convenient to use this relation to *define* the binary product $\langle \mathbf{y} | \mathbf{x} \rangle$, e.g. by choosing real or complex values for the elements $\Delta_{kl} = \langle \mathbf{X}_k | \mathbf{X}_l \rangle$ in a specific representation \mathbf{X} , noting that, in the general case, one may have $\Delta_{lk} \neq$

Δ_{kl} . It should be observed that this binary product, in spite of this definition, is a true *scalar*, in the sense that it is invariant under linear transformations of the form $\mathbf{X}' = \mathbf{X} \alpha$. One has $\mathbf{a}' = \alpha^{-1} \mathbf{a}$ and $\mathbf{b}' = \alpha^{-1} \mathbf{b}$, as well as $\Delta' = \langle \tilde{\mathbf{X}}' | \mathbf{X}' \rangle = \langle \tilde{\alpha} \tilde{\mathbf{X}} | \mathbf{X} \alpha \rangle = \tilde{\alpha} \langle \tilde{\mathbf{X}} | \mathbf{X} \rangle \alpha = \alpha^\dagger \Delta \alpha$, where $\alpha^\dagger = (\tilde{\alpha})^*$ is the *hermitean adjoint* of the matrix α . This gives

$$\begin{aligned} \langle y | x \rangle' &= \langle y' | x' \rangle = (\mathbf{b}')^\dagger \Delta' \mathbf{a}' = \mathbf{b}^\dagger (\alpha^\dagger)^{-1} \alpha^\dagger \Delta \alpha \alpha^{-1} \mathbf{a} = \\ &= \mathbf{b}^\dagger \Delta \mathbf{a} = \langle y | x \rangle, \end{aligned} \quad (2.35)$$

which proves the statement.

Let us now consider a linear functional $l(x) = [l | x] = \mathbf{a}$. Putting $\mathbf{l} = \mathbf{b}^\dagger \Delta$, i.e. $\mathbf{b}^\dagger = \mathbf{l} \Delta^{-1}$ and $\mathbf{b} = (\Delta^{-1})^\dagger \mathbf{l}^\dagger = (\Delta^\dagger)^{-1} \mathbf{l}^\dagger$, one obtains directly

$$l(x) = [l | x] = \mathbf{b}^\dagger \Delta \mathbf{a} = \langle y | x \rangle, \quad (2.36)$$

and, to each linear functional l , there is uniquely associated an element y of the space $A = \{x\}$ through the binary product $\langle y | x \rangle$ and the relation

$$y = \mathbf{X} \mathbf{b} = \mathbf{X} (\Delta^\dagger)^{-1} \mathbf{l}^\dagger. \quad (2.37)$$

The mapping $l \rightarrow y$ is invariant under a linear transformation of the basis $\mathbf{X}' = \mathbf{X} \alpha$. One has $\mathbf{l}' = \mathbf{l} \alpha$ and $\mathbf{b}' = (\Delta'^\dagger)^{-1} (\mathbf{l}')^\dagger = (\alpha^\dagger \Delta^\dagger \alpha)^{-1} (\mathbf{l} \alpha)^\dagger = \alpha^{-1} (\Delta^\dagger)^{-1} (\alpha^\dagger)^{-1} \alpha^\dagger \mathbf{l} = \alpha^{-1} (\Delta^\dagger)^{-1} \mathbf{l} = \alpha^{-1} \mathbf{b}$, which means that $y' = \mathbf{X}' \mathbf{b}' = \mathbf{X} \alpha \alpha^{-1} \mathbf{b} = \mathbf{X} \mathbf{b} = y$, which proves the statement.

According to the general definition, two elements y and x are said to be bi-orthogonal if $[l | x] = \langle y | x \rangle = 0$. Similarly a sequence y_1, y_2, y_3, \dots is said to be *bi-orthonormal* to a sequence x_1, x_2, x_3, \dots , if one has the relation

$$[l_i | x_j] = \langle y_i | x_j \rangle = \delta_{ij}. \quad (2.38)$$

According to (1.14), one has the bi-orthonormality relation $[\mathbf{F} | \mathbf{X}] = \mathbf{1}$. By using (2.37), one can now carry out the mapping $\mathbf{F} \rightarrow \mathbf{Y}$ through the formula $\mathbf{Y} = \mathbf{X} (\Delta^\dagger)^{-1}$, which gives

$$\mathbf{Y} = \mathbf{X} (\Delta^\dagger)^{-1}, [\mathbf{F} | \mathbf{X}] = \langle \mathbf{Y}^\dagger | \mathbf{X} \rangle = \mathbf{1}. \quad (2.39)$$

The basis $\mathbf{X}_r = \mathbf{Y}$ is again referred to as the *reciprocal basis* to the original basis \mathbf{X} , and it is a very important tool in many parts of modern

physics. It is easily checked that it has the property $\langle \mathbf{X}_r^\dagger | \mathbf{X} \rangle = \langle \Delta^{-1} \mathbf{X}_r^\dagger | \mathbf{X} \rangle = \Delta^{-1} \langle \mathbf{X}_r^\dagger | \mathbf{X} \rangle = \Delta^{-1} \Delta = \mathbf{1}$. Hence one has

$$\mathbf{X}_r = \mathbf{X} (\Delta^\dagger)^{-1}, \quad \langle \mathbf{X}_r | \mathbf{X} \rangle = \mathbf{1}, \quad (2.40)$$

whereas $\langle \mathbf{X}^\dagger | \mathbf{X}_r \rangle = \langle \mathbf{X}^\dagger | \mathbf{X} (\Delta^\dagger)^{-1} \rangle = \langle \mathbf{X}^\dagger | \mathbf{X} \rangle (\Delta^\dagger)^{-1} = \Delta (\Delta^\dagger)^{-1}$, where - due to the lack of symmetry properties of the metric matrix Δ - no further simplification is possible.

Let us now consider the reciprocal to the reciprocal basis \mathbf{X}_r , which has the metric matrix $\Delta_r = \langle \mathbf{X}_r^\dagger | \mathbf{X}_r \rangle = \langle (\Delta)^{-1} \mathbf{X}^\dagger | \mathbf{X} (\Delta^\dagger)^{-1} \rangle = (\Delta)^{-1} \langle \mathbf{X}^\dagger | \mathbf{X} \rangle (\Delta^\dagger)^{-1} = (\Delta)^{-1} \Delta (\Delta^\dagger)^{-1} = (\Delta^\dagger)^{-1}$. For the reciprocal of \mathbf{X}_r , one hence obtains

$$(\mathbf{X}_r)_r = \mathbf{X}_r (\Delta_r^\dagger)^{-1} = \mathbf{X}_r \Delta = \mathbf{X} (\Delta^\dagger)^{-1} \Delta, \quad (2.41)$$

which means that, in the general case, $(\mathbf{X}_r)_r \neq \mathbf{X}$. From the relations $\mathbf{x} = \mathbf{X} \mathbf{a}$ and $\mathbf{T} \mathbf{X} = \mathbf{X} \mathbf{T}$, one gets immediately by using $\langle \mathbf{X}_r | \mathbf{X} \rangle = \mathbf{1}$ the explicit formulas

$$\mathbf{a} = \langle \mathbf{X}_r | \mathbf{x} \rangle \dots \mathbf{T} = \langle \mathbf{X}_r | \mathbf{T} \mathbf{X} \rangle = \langle \mathbf{X}_r | \mathbf{T} | \mathbf{X} \rangle, \quad (2.42)$$

Let us now consider the adjoint operator \mathbf{T}^d , which in the case of the binary product $\langle \mathbf{y} | \mathbf{x} \rangle$ will be given the special notation \mathbf{T}^\dagger . The operator mapping $\mathbf{T} \rightarrow \mathbf{T}^d \rightarrow \mathbf{T}^\dagger$, which is then defined through the relations

$$\langle \mathbf{y} | \mathbf{T} \mathbf{x} \rangle = [\mathbf{l} | \mathbf{T} \mathbf{x}] = [\mathbf{T}^d \mathbf{l} | \mathbf{x}] = \langle \mathbf{T}^\dagger \mathbf{y} | \mathbf{x} \rangle \quad (2.43)$$

for all \mathbf{x} . This implies also that $[\mathbf{T}^d \mathbf{F} | \mathbf{X}] = \langle \mathbf{T}^\dagger \mathbf{Y}^\dagger | \mathbf{X} \rangle = \langle \mathbf{T}^\dagger \mathbf{X}_r^\dagger | \mathbf{X} \rangle$ and - putting $\mathbf{T}^\dagger \mathbf{X}_r = \mathbf{X}_r \mathbf{R}$ or $\mathbf{T}^\dagger \mathbf{X}_r^\dagger = \mathbf{R}^\dagger \mathbf{X}_r^\dagger$ - that $\langle \mathbf{T}^\dagger \mathbf{X}_r^\dagger | \mathbf{X} \rangle = \langle \mathbf{R}^\dagger \mathbf{X}_r^\dagger | \mathbf{X} \rangle = \mathbf{R}^\dagger \langle \mathbf{X}_r^\dagger | \mathbf{X} \rangle = \mathbf{R}^\dagger$ and further that $\langle \mathbf{T}^\dagger \mathbf{X}_r^\dagger | \mathbf{X} \rangle = \langle \mathbf{X}_r^\dagger | \mathbf{T} \mathbf{X} \rangle = \langle \mathbf{X}_r^\dagger | \mathbf{X} \mathbf{T} \rangle = \langle \mathbf{X}_r^\dagger | \mathbf{X} \rangle \mathbf{T} = \mathbf{T}$, which gives $\mathbf{R}^\dagger = \mathbf{T}$ and $\mathbf{R} = \mathbf{T}^\dagger$. Hence one has the two relations

$$\mathbf{T} \mathbf{X} = \mathbf{X} \mathbf{T}, \quad \mathbf{T}^\dagger \mathbf{X}_r = \mathbf{X}_r \mathbf{T}^\dagger, \quad (2.44)$$

and from the latter one obtains $\mathbf{T}^\dagger \mathbf{X}_r = \mathbf{T}^\dagger \mathbf{X} (\Delta^\dagger)^{-1} = \mathbf{X} (\Delta^\dagger)^{-1} \mathbf{T}^\dagger$, i.e.

$$\mathbf{T}^\dagger \mathbf{X} = \mathbf{X} (\Delta^\dagger)^{-1} \mathbf{T}^\dagger (\Delta^\dagger)^{-1}, \quad (2.45)$$

which gives the matrix representation of the adjoint operator T^\dagger in terms of the original basis X . From the relation $\langle y | T^\dagger x \rangle = \langle T^\dagger y | x \rangle$, it is now possible to evaluate the operator $(T^\dagger)^\dagger = T^{\dagger\dagger}$, and - putting $T^{\dagger\dagger} X = X Q$ - one obtains $\langle T^\dagger y | x \rangle = \langle T^{\dagger\dagger} X b | x \rangle = \langle X Q b | x \rangle = \langle (Qb)^\dagger X^\dagger | X a \rangle = (Qb)^\dagger \langle X^\dagger | X a \rangle = b^\dagger Q^\dagger \Delta a = \langle y | T^\dagger x \rangle = \langle Xb | T^\dagger X a \rangle = b^\dagger X^\dagger | X (\Delta^\dagger)^{-1} T^\dagger (\Delta^\dagger)^{-1} a \rangle = b^\dagger \langle X^\dagger | X \rangle (\Delta^\dagger)^{-1} T^\dagger (\Delta^\dagger)^{-1} a = b^\dagger \Delta (\Delta^\dagger)^{-1} T^\dagger (\Delta^\dagger)^{-1} a$ for all a and b , which means that $Q^\dagger \Delta = \Delta (\Delta^\dagger)^{-1} T^\dagger (\Delta^\dagger)^{-1}$ or $Q^\dagger = \Delta (\Delta^\dagger)^{-1} T^\dagger (\Delta^\dagger)^{-1} \Delta^{-1}$ i.e.

$$Q = (\Delta^\dagger)^{-1} \Delta T (\Delta)^{-1} \Delta^\dagger, \quad (2.46)$$

It is evident that the matrix $(\Delta^\dagger)^{-1} \Delta$, which also occurred in (2.41), plays again a fundamental role. The main conclusion of this relation is that the operator $T^{\dagger\dagger}$ in the general case is different from T .

Even in this case, the ket-bra operator $G = |x_1\rangle\langle l_1|$ may be transformed to the space $A = \{x\}$, and one gets directly

$$G = |x_1\rangle\langle l_1| = |x_1\rangle\langle l_1|. \quad (2.47)$$

The resolution of the identity $I = |X\rangle\langle F|$ takes now the form

$$I = |X\rangle\langle X_r^{\dagger\dagger}|, \quad (2.48)$$

and, for the operator T , one gets now the resolution

$$T = T.I = T |X\rangle\langle X_r^{\dagger\dagger}| = |X\rangle T \langle X_r^{\dagger\dagger}|, \quad (2.49)$$

and this gives also a new set of fundamental units in the operator space $\{T\}$. By using (2.45) and (2.41), one gets similarly for the adjoint operator T^\dagger :

$$\begin{aligned} T^\dagger &= T^\dagger . I = T^\dagger |X\rangle\langle X_r^{\dagger\dagger}| = |X\rangle (\Delta^\dagger)^{-1} T^\dagger (\Delta^\dagger)^{-1} \langle X_r^{\dagger\dagger}| = \\ &= |X (\Delta^\dagger)^{-1} \rangle T^\dagger \langle \Delta^\dagger X_r^{\dagger\dagger}| = |X_r \rangle T^\dagger \langle X_{rr}^{\dagger\dagger}|, \end{aligned} \quad (2.50)$$

which is analogous to (2.49).

Case of a binary product with hermitean symmetry.- In many applications, it is convenient to have $X_{rr} = X$, and this is achieved if one assumes that the binary product $(x_1 | x_2)$ has a *hermitean symmetry* in the two positions, so that

$$\langle x_1 | x_2 \rangle = \langle x_2 | x_1 \rangle^*. \quad (2.51)$$

It implies that the length $||x||$ in square, $||x||^2 = \langle x|x \rangle$, is always a *real* quantity. which is of importance in many parts of physics. In such a case, the metric matrix shows an hermitean symmetry:

$$\Delta^\dagger = \Delta, \quad (2.52)$$

and one gets $(\Delta^\dagger)^{-1}\Delta = 1$, which implies that $\mathbf{X}_{rr} = \mathbf{X}$, and $T^{\dagger\dagger} = T$. In this particular case, one says that T^\dagger is the *hermitean adjoint* to the operator T . The relation $T^{\dagger\dagger} = T$ is easily proven directly, if one observes that $\langle T^{\dagger\dagger} y | x \rangle = \langle y | T^\dagger x \rangle = \langle T^\dagger x | y \rangle^* = \langle x | Ty \rangle^* = \langle Ty | x \rangle$ for all x and y .

For the hermitean adjoint of the ket-bra operator $G = |x_1\rangle\langle y_1|$, one gets immediately $G^\dagger = |y_1\rangle\langle x_1|$, since one has

$$\begin{aligned} \langle G^\dagger y | x \rangle &= \langle y | Gx \rangle = \langle y | x_1 \langle y_1 | x \rangle \rangle = \langle y | x_1 \rangle \langle y_1 | x \rangle = \\ &= \langle y | x_1 \rangle^* y_1 \langle x \rangle = \langle y_1 \langle x_1 | y \rangle | x \rangle = \langle (|y_1\rangle\langle x_1|) y | x \rangle, \end{aligned} \quad (2.53)$$

which proves the statement.

3. Mapping of the dual space A^d on another linear space .

Let us now introduce a second linear space $B = \{y\}$, which is of the same order as the original space $A = \{x\}$ but not necessarily identical with this space. The space $A = \{x\}$ is spanned by the basis $\mathbf{X} = \{X_1, X_2, X_3, \dots\}$, whereas the space B is assumed to be spanned by the basis $\mathbf{Y} = \{Y_1, Y_2, Y_3, \dots\}$. Let us further introduce a binary product $\langle y | x \rangle$, which is assumed to be anti-linear in the first position and linear in the second position. In this case, one cannot introduce any symmetry property whatsoever, but our reasonings above shows that such a property is by no means necessary to derive the fundamental concepts. Putting $y = \mathbf{Y} \mathbf{b} = \tilde{\mathbf{b}} \tilde{\mathbf{Y}}$ and $x = \mathbf{X} \mathbf{a}$, one obtains directly

$$\langle y | x \rangle = \langle \tilde{\mathbf{b}} \tilde{\mathbf{Y}} | \mathbf{X} \mathbf{a} \rangle = \mathbf{b}^\dagger \langle \tilde{\mathbf{Y}} | \mathbf{X} \rangle \mathbf{a} = \mathbf{b}^\dagger \Delta \mathbf{a}, \quad (3.1)$$

where $\Delta = \langle \tilde{\mathbf{Y}} | \mathbf{X} \rangle$ is the interrelation matrix between the two bases associated with different spaces.

In order to study the transformation properties, one has now to introduce two linear transformations

$$\mathbf{X}' = \mathbf{X} \alpha, \quad \mathbf{Y}' = \mathbf{Y} \beta, \quad (3.2)$$

which gives

$$\Delta' = \beta^\dagger \Delta \alpha. \quad (3.3)$$

It is interesting to observe that, since $\mathbf{x} = \mathbf{X} \mathbf{a}$, one has $\langle \tilde{\mathbf{Y}} | \mathbf{x} \rangle = \langle \tilde{\mathbf{Y}} | \mathbf{X} \mathbf{a} \rangle = \langle \tilde{\mathbf{Y}} | \mathbf{X} \rangle \mathbf{a} = \Delta \alpha$, which implies that $|\Delta| \neq 0$, that Δ^{-1} exists, and that

$$\mathbf{a} = \Delta^{-1} \langle \tilde{\mathbf{Y}} | \mathbf{x} \rangle. \quad (3.4)$$

Considering a linear functional $l(\mathbf{x}) = \langle \mathbf{l} | \mathbf{x} \rangle = \mathbf{l} \mathbf{a}$, one can now construct a mapping $\mathbf{l} \rightarrow \mathbf{y} = \mathbf{Y} \mathbf{b}$ by putting $\mathbf{l} = \mathbf{b}^\dagger \Delta$ in the relation $\langle \mathbf{l} | \mathbf{x} \rangle = \mathbf{l} \mathbf{a} = \mathbf{b}^\dagger \Delta \mathbf{a} = \langle \mathbf{y} | \mathbf{x} \rangle$. For the row vector \mathbf{b} , this gives $\mathbf{b}^\dagger = \Delta^{-1} \mathbf{l}$, $\mathbf{b} = (\Delta^{-1})^\dagger \mathbf{l}^\dagger$ and

$$\mathbf{y} = \mathbf{Y} \mathbf{b} = \mathbf{Y} (\Delta^{-1})^\dagger \mathbf{l}^\dagger. \quad (3.5)$$

The mapping $\mathbf{l} \rightarrow \mathbf{y}$ is invariant under the linear transformations (3.2), since one has $\Delta' = \beta^\dagger \Delta \alpha$ and $\mathbf{l}' = \mathbf{l} \alpha$, which gives

$$\begin{aligned} \mathbf{b}' &= (\Delta'^{-1})^\dagger (\mathbf{l}')^\dagger = (\alpha^\dagger \Delta^\dagger \beta)^{-1} (\mathbf{l} \alpha)^\dagger = \beta^{-1} (\Delta^\dagger)^{-1} (\alpha^\dagger)^{-1} \alpha^\dagger \mathbf{l}^\dagger = \\ &= \beta^{-1} (\Delta^\dagger)^{-1} \mathbf{l}^\dagger = \beta^{-1} \mathbf{b}, \end{aligned} \quad (3.6)$$

and

$$\mathbf{y}' = \mathbf{Y}' \mathbf{b}' = \mathbf{Y} \beta \cdot \beta^{-1} \mathbf{b} = \mathbf{Y} \mathbf{b} = \mathbf{y}. \quad (3.7)$$

The concept of bi-orthonormality $[\mathbf{F} | \mathbf{X}] = \mathbf{1}$, is now easily generalized to two different linear spaces $B = \{\mathbf{y}\}$ and $A = \{\mathbf{x}\}$. Starting from the mapping $\mathbf{F} \rightarrow \mathbf{Y}_r$ given by the formula (3.5) or

$$\mathbf{Y}_r = \mathbf{Y} (\Delta^\dagger)^{-1}, \quad (3.8)$$

one gets directly $\langle \tilde{\mathbf{Y}}_r | \mathbf{X} \rangle = \langle (\Delta^\dagger)^{-1} \tilde{\mathbf{Y}} | \mathbf{X} \rangle = (\Delta^{-1})^\dagger \langle \tilde{\mathbf{Y}} | \mathbf{X} \rangle = (\Delta^{-1})^\dagger \Delta = \mathbf{1}$. and \mathbf{Y}_r is said to be the basis in B which is *reciprocal* to the basis \mathbf{X} in A :

$$\langle \tilde{\mathbf{Y}}_r | \mathbf{X} \rangle = \mathbf{1}. \quad (3.9)$$

Using this relation, one gets immediately from the fundamental equations $\mathbf{x} = \mathbf{X} \mathbf{a}$ and $\mathbf{T} \mathbf{X} = \mathbf{X} \mathbf{T}$ that

$$a = \langle \tilde{\mathbf{Y}}_r | \mathbf{x} \rangle, \quad \mathbf{T} = \langle \tilde{\mathbf{Y}}_r | \mathbf{T} \mathbf{X} \rangle. \quad (3.10)$$

Let us now study also the adjoint operator \mathbf{T}^\dagger , which is defined through the mapping $\mathbf{T}\mathbf{x} \rightarrow \mathbf{T}^\dagger \mathbf{y}$. Observing that $[\mathbf{I} | \mathbf{T}\mathbf{x}] = \langle \mathbf{y} | \mathbf{T}\mathbf{x} \rangle$, one gets directly

$$\langle \mathbf{y} | \mathbf{T}\mathbf{x} \rangle = [\mathbf{I} | \mathbf{T}\mathbf{x}] = [\mathbf{T}^\dagger \mathbf{I} | \mathbf{x}] = \langle \mathbf{T}^\dagger \mathbf{y} | \mathbf{x} \rangle. \quad (3.11)$$

It is evident that \mathbf{T} is defined on the space $\mathbf{A} = \{\mathbf{x}\}$, whereas \mathbf{T}^\dagger is defined on the space $\mathbf{B} = \{\mathbf{y}\}$. For the matrix representation \mathbf{R} of the operator \mathbf{T}^\dagger with respect to the basis \mathbf{Y}_r , one has $\mathbf{T}^\dagger \mathbf{Y}_r = \mathbf{Y}_r \mathbf{R}$ or $\mathbf{T}^\dagger \tilde{\mathbf{Y}}_r = \tilde{\mathbf{R}} \tilde{\mathbf{Y}}_r$, and hence one has

$$\begin{aligned} \mathbf{R}^\dagger &= \mathbf{R}^\dagger \langle \tilde{\mathbf{Y}}_r | \mathbf{X} \rangle = \langle \tilde{\mathbf{R}} \tilde{\mathbf{Y}}_r | \mathbf{X} \rangle = \langle \mathbf{T}^\dagger \tilde{\mathbf{Y}}_r | \mathbf{X} \rangle = \langle \tilde{\mathbf{Y}}_r | \mathbf{T}\mathbf{X} \rangle = \\ &= \langle \tilde{\mathbf{Y}}_r | \mathbf{X}\mathbf{T} \rangle = \langle \tilde{\mathbf{Y}}_r | \mathbf{X} \rangle \mathbf{T} = \mathbf{T}, \end{aligned} \quad (3.12)$$

i.e. $\mathbf{R} = \mathbf{T}^\dagger$, and one gets the operator relations

$$\mathbf{T} \mathbf{X} = \mathbf{X} \mathbf{T}, \quad \mathbf{T}^\dagger \mathbf{Y}_r = \mathbf{Y}_r \mathbf{T}^\dagger. \quad (3.13)$$

From the last relation one gets further $\mathbf{T}^\dagger \mathbf{Y}_r = \mathbf{T}^\dagger \mathbf{Y} (\Delta^\dagger)^{-1} = \mathbf{Y} (\Delta^\dagger)^{-1} \mathbf{T}^\dagger$, i.e.

$$\mathbf{T}^\dagger \mathbf{Y} = \mathbf{Y} (\Delta^\dagger)^{-1} \mathbf{T}^\dagger \Delta^\dagger. \quad (3.14)$$

Even the ket-bra operator $\mathbf{G} = |\mathbf{x}_1\rangle[\mathbf{l}_1|$ may now be transferred to the space $\mathbf{A} = \{\mathbf{x}\}$, and one gets directly

$$\mathbf{G} = |\mathbf{x}_1\rangle[\mathbf{l}_1| = |\mathbf{x}_1\rangle\langle \mathbf{y}_1|. \quad (3.15)$$

The resolution of the identity $\mathbf{I} = |\mathbf{X}\rangle[\mathbf{F}|$ takes now the form

$$\mathbf{I} = |\mathbf{X}\rangle\langle \tilde{\mathbf{Y}}_r|, \quad (3.16)$$

and, for the operator \mathbf{T} , one gets the fundamental formula

$$\mathbf{T} = \mathbf{T} \mathbf{I} = \mathbf{T} |\mathbf{X}\rangle\langle \tilde{\mathbf{Y}}_r| = |\mathbf{X}\rangle \mathbf{T} \langle \tilde{\mathbf{Y}}_r|, \quad (3.17)$$

which also contains a new definition of the fundamental units in the operator space $\{T\}$. It is illustrative to check that this formula for the operator T is independent of the choice of bases for the two spaces involved. From the relations (3.2) and (3.3), it follows that $\tilde{Y}_r' = Y' (\Delta^\dagger) = Y \beta (\alpha^\dagger \Delta^\dagger \beta)^{-1} = Y \beta \cdot \beta^{-1} (\Delta^\dagger)^{-1} (\alpha^\dagger)^{-1} = Y_r (\alpha^\dagger)^{-1}$. This gives further

$$\begin{aligned} T' &= \langle \tilde{Y}_r' | T X' \rangle = \langle (\alpha^*)^{-1} \tilde{Y}_r | T X \alpha \rangle = \langle (\alpha^*)^{-1} \tilde{Y}_r | X T \alpha \rangle \\ &= \alpha^{-1} \langle \tilde{Y}_r | X \rangle T \alpha = \alpha^{-1} T \alpha, \end{aligned} \quad (3.18)$$

and

$$\begin{aligned} T' &= |X'\rangle T' \langle \tilde{Y}_r'| = |X \alpha\rangle (\alpha)^{-1} T \alpha \langle (\alpha^*)^{-1} \tilde{Y}_r| = \\ &= |X\rangle \alpha \alpha^{-1} T \alpha \alpha^{-1} \langle \tilde{Y}_r| = |X\rangle T \langle \tilde{Y}_r| = T, \end{aligned} \quad (3.19)$$

which proves the statement. We note that, in this approach, there is no resolution of the identity in the space $B = \{x\}$ and no resolution of the adjoint operator T^\dagger , but that it should be possible to obtain such expressions by starting from the space $B = \{y\}$ and its linear functionals. For this purpose, we need one more binary product $\{x|y\}$ in which the element x from A has the first position and the element y from B the second position. It will again be assumed that the first position is anti-linear and the second linear.

For the sake of simplicity, it may now be convenient to introduce the definition

$$\{x|y\} = \langle y|x \rangle^*, \quad (3.20)$$

which is by no means a symmetry relation. The fundamental interrelation matrix $(\tilde{X}|Y)$ has now the elements

$$\{X_k|Y_l\} = \langle Y_l|X_k \rangle^* = \Delta_{lk}^*, \quad (3.21)$$

i.e.

$$(\tilde{X}|Y) = \Delta^\dagger. \quad (3.22)$$

Using the results obtained above, one can now introduce a reciprocal basis $X_r = X \Delta^{-1}$, which has the property $(\tilde{X}_r|Y) = \{(\tilde{\Delta})^{-1} \tilde{X}_r|Y\} = (\Delta^\dagger)^{-1} \{\tilde{X}_r|Y\} = (\Delta^\dagger)^{-1} \Delta^\dagger = 1$. From $y = Y b$, one obtains $b = \{\tilde{X}_r|y\}$, and this gives $y = Y \{\tilde{X}_r|y\} = |Y\rangle \{\tilde{X}_r|y\}$ for all y , which means that one has the following resolution of the identity in the space $B = \{y\}$:

$$I = |\mathbf{Y}\rangle\langle\tilde{\mathbf{X}}_r|. \quad (3.23)$$

Using the relation (3.14), one gets further

$$\begin{aligned} T^\dagger = T^\dagger \cdot I = T^\dagger |\mathbf{Y}\rangle\langle\tilde{\mathbf{X}}_r| &= |\mathbf{Y}\rangle\langle\Delta^\dagger\rangle^{-1} T^\dagger \Delta^\dagger \langle\tilde{\mathbf{X}}_r| = \\ &= |\mathbf{Y}\langle\Delta^\dagger\rangle^{-1} T^\dagger \langle\tilde{\Delta} \tilde{\mathbf{X}}_r| = |\mathbf{Y}_r\rangle\langle\tilde{\mathbf{X}}|, \end{aligned} \quad (3.24)$$

which is the expression desired.

The operator $G = |x_1\rangle\langle y_1|$ is defined on the space $A = \{x\}$, and, by using (3.20), it is then easily shown that the adjoint operator has the form

$$G^\dagger = |y_1\rangle\langle x_1|. \quad (3.25)$$

It is evident that the formalism using bold-face symbol is a very simple and elegant tool in studying the properties of linear spaces and their functionals, particularly in showing the invariance features of certain quantities.

The main conclusion of Sections 2 and 3 is that, even if a linear space $A = \{x\}$ has a dual space $\{l\}$ defined by its linear functionals, and every linear operator T has a uniquely defined dual operator T^d , there is a *multitude* of adjoint operators T^a of which only a few of the main types have been discussed here.

4. Mapping of a space $A = \{x\}$ on another space $B = \{y\}$.

One can now utilize these results to study also mappings between two spaces $A = \{x\}$ and $B = \{y\}$ of the same order having the bases \mathbf{X} and \mathbf{Y} , respectively, defined by the relations

$$R x = y, \quad S y = x. \quad (4.1)$$

The operator SR maps A on A , whereas the operator RS maps B on B . The "mirror theorem" says that the two operators SR and RS have the same non-vanishing eigenvalues and the same type of classical canonical structure. The matrix representations are defined by the relations

$$R \mathbf{X} = \mathbf{Y} R, \quad S \mathbf{Y} = \mathbf{X} S. \quad (4.2)$$

As in the previous section, we will use two binary products $\langle y | x \rangle$ and $\langle x | y \rangle$ in which the elements are not interchangeable and without any connections. In this case, there are two interrelation matrices

$$\Delta = \langle \tilde{\mathbf{Y}} | \mathbf{X} \rangle, \quad \mathbf{D} = \langle \tilde{\mathbf{X}} | \mathbf{Y} \rangle. \quad (4.3)$$

Introducing the special basis sets

$$\mathbf{Y}_r = \mathbf{Y} (\Delta^\dagger)^{-1}, \quad \mathbf{X}_r = \mathbf{X} (\mathbf{D}^\dagger)^{-1}, \quad (4.4)$$

one gets immediately the two relations $\langle \tilde{\mathbf{Y}}_r | \mathbf{X} \rangle = \langle (\Delta^*)^{-1} \tilde{\mathbf{Y}} | \mathbf{X} \rangle = \Delta^{-1} \langle \tilde{\mathbf{Y}} | \mathbf{X} \rangle = \Delta^{-1} \Delta = \mathbf{1}$, and similarly $\langle \tilde{\mathbf{X}}_r | \mathbf{Y} \rangle = \mathbf{1}$, i.e.

$$\langle \tilde{\mathbf{Y}}_r | \mathbf{X} \rangle = \mathbf{1}, \quad \langle \tilde{\mathbf{X}}_r | \mathbf{Y} \rangle = \mathbf{1}, \quad (4.5)$$

and we will say that the basis \mathbf{Y}_r in the space B is *bi-reciprocal* to the basis \mathbf{X} in the space A, and that the basis \mathbf{X}_r is bi-reciprocal to the basis \mathbf{Y} . For the matrices R and S in (4.2), one gets immediately the explicit expressions

$$\mathbf{R} = \langle \tilde{\mathbf{X}}_r | \mathbf{R} \mathbf{X} \rangle, \quad \mathbf{S} = \langle \tilde{\mathbf{Y}}_r | \mathbf{S} \mathbf{Y} \rangle. \quad (4.6)$$

From the relations $\mathbf{x} = \mathbf{X} \mathbf{a}$ and $\langle \tilde{\mathbf{Y}}_r | \mathbf{X} \rangle = \mathbf{1}$, it follows further that $\mathbf{a} = \langle \tilde{\mathbf{Y}}_r | \mathbf{x} \rangle$, $\mathbf{x} = \mathbf{X} \langle \tilde{\mathbf{Y}}_r | \mathbf{x} \rangle = |\mathbf{X}\rangle \langle \tilde{\mathbf{Y}}_r | \mathbf{x}$, which gives the following resolution of the identity operator in the A-space: $I_A = |\mathbf{X}\rangle \langle \tilde{\mathbf{Y}}_r |$. From the relations $\mathbf{y} = \mathbf{Y} \mathbf{b}$ and $\langle \tilde{\mathbf{X}}_r | \mathbf{Y} \rangle = \mathbf{1}$, one gets similarly $\mathbf{b} = \langle \tilde{\mathbf{X}}_r | \mathbf{y} \rangle$, $\mathbf{y} = \mathbf{Y} \langle \tilde{\mathbf{X}}_r | \mathbf{y} \rangle = |\mathbf{Y}\rangle \langle \tilde{\mathbf{X}}_r |$ and $I_B = |\mathbf{Y}\rangle \langle \tilde{\mathbf{X}}_r |$, which is the resolution of the identity operator I_B in the B-space. Hence one has

$$I_A = |\mathbf{X}\rangle \langle \tilde{\mathbf{Y}}_r |, \quad I_B = |\mathbf{Y}\rangle \langle \tilde{\mathbf{X}}_r |. \quad (4.7)$$

For the resolutions of the operators R and S, one gets directly the expressions

$$\mathbf{R} = \mathbf{R} I_A = \mathbf{R} |\mathbf{X}\rangle \langle \tilde{\mathbf{Y}}_r | = |\mathbf{Y}\rangle \mathbf{R} \langle \tilde{\mathbf{Y}}_r |, \quad (4.8)$$

$$\mathbf{S} = \mathbf{S} I_B = \mathbf{S} |\mathbf{Y}\rangle \langle \tilde{\mathbf{X}}_r | = |\mathbf{X}\rangle \mathbf{S} \langle \tilde{\mathbf{X}}_r |, \quad (4.9)$$

Even in this case, it is possible to introduce "adjoint operators" through the special definitions

$$\{x_1 | Rx_2\} = \langle R^\dagger x_1 | x_2 \rangle^*, \quad \langle y_1 | Sy_2 \rangle = \{S^\dagger y_1 | y_2\}^*, \quad (4.10)$$

which are generalizations of those introduced in the previous section. These relations imply that the operator R^\dagger maps A on B and S^\dagger maps B on A , as the original operators R and S .

Let us first evaluate the matrix representation of the operator R^\dagger , which in analogy with (3.13) may be defined by the relation $R^\dagger \mathbf{X}_r = \mathbf{Y}_r \mathbf{Q}_1$, which also gives $R^\dagger \tilde{\mathbf{X}}_r = \tilde{\mathbf{Q}}_1 \tilde{\mathbf{Y}}_r$. One gets directly $\langle R^\dagger \tilde{\mathbf{X}}_r | \mathbf{X} \rangle = \langle \tilde{\mathbf{Q}}_1 \tilde{\mathbf{Y}}_r | \mathbf{X} \rangle = \mathbf{Q}_1^\dagger \langle \tilde{\mathbf{Y}}_r | \mathbf{X} \rangle = \mathbf{Q}_1^\dagger$, and further

$$\mathbf{Q}_1^\dagger = \langle R^\dagger \tilde{\mathbf{X}}_r | \mathbf{X} \rangle = \langle \tilde{\mathbf{X}}_r | R \mathbf{X} \rangle = \langle \tilde{\mathbf{X}}_r | \mathbf{Y} R \rangle = \langle \tilde{\mathbf{X}}_r | \mathbf{Y} \rangle R = R, \quad (4.11)$$

and

$$\mathbf{Q}_1 = R^\dagger, \quad R^\dagger \mathbf{X}_r = \mathbf{Y}_r R^\dagger. \quad (4.12)$$

Putting $S^\dagger \mathbf{Y}_r = \mathbf{X}_r \mathbf{Q}_2$, one gets similarly $\{S^\dagger \tilde{\mathbf{Y}}_r | \mathbf{Y}\} = \mathbf{Q}_2^\dagger \{ \tilde{\mathbf{X}}_r | \mathbf{Y} \} = \mathbf{Q}_2^\dagger$, and $\mathbf{Q}_2^\dagger = \{S^\dagger \tilde{\mathbf{Y}}_r | \mathbf{Y}\} = \langle \tilde{\mathbf{Y}}_r | S \mathbf{Y} \rangle = \langle \tilde{\mathbf{Y}}_r | \mathbf{X} S \rangle = S$, i.e.

$$\mathbf{Q}_2 = S^\dagger, \quad S^\dagger \mathbf{Y}_r = \mathbf{X}_r S^\dagger. \quad (4.13)$$

Since $\mathbf{X}_r = \mathbf{X} (\mathbf{D}^\dagger)^{-1}$ and $\mathbf{X} = \mathbf{X}_r \mathbf{D}^\dagger$, one gets also $R^\dagger \mathbf{X} = R^\dagger \mathbf{X}_r \mathbf{D}^\dagger = \mathbf{Y}_r \mathbf{R}^\dagger \mathbf{D}^\dagger = \mathbf{Y} \Delta^{-1} \mathbf{R}^\dagger \mathbf{D}^\dagger$ and similarly $S^\dagger \mathbf{Y} = S^\dagger \mathbf{Y}_r \Delta^\dagger = \mathbf{X}_r \mathbf{S}^\dagger \Delta^\dagger = \mathbf{X} (\mathbf{D}^\dagger)^{-1} \mathbf{S}^\dagger \Delta^\dagger$. For the adjoint operators R^\dagger and S^\dagger , one gets hence the following resolutions:

$$R^\dagger = R^\dagger I_A = R^\dagger | \mathbf{X} \rangle \langle \tilde{\mathbf{Y}}_r | = | \mathbf{Y}_r \rangle R^\dagger \mathbf{D}^\dagger \langle \tilde{\mathbf{Y}}_r |, \quad (4.14)$$

$$S^\dagger = S^\dagger I_B = S^\dagger | \mathbf{Y} \rangle \langle \tilde{\mathbf{X}}_r | = | \mathbf{X}_r \rangle S^\dagger \Delta^\dagger \langle \tilde{\mathbf{X}}_r |. \quad (4.15)$$

The operator SR maps A on A , and its adjoint operator has been defined in the previous section. At the same time, one has $\langle y | SR x \rangle = \{S^\dagger y | Rx\} = \langle R^\dagger S^\dagger y | x \rangle$, i.e.

$$(SR)^\dagger = R^\dagger S^\dagger, \quad (4.16)$$

which relation connects the two concepts of adjointness discussed here. Similarly, one gets $(RS)^\dagger = S^\dagger R^\dagger$. It is illustrative to check these formulas by using the resolutions of the various operators.

We have so far worked with two independent binary products $\{x|y\}$ and $\langle y|x \rangle$, and it is evident that one obtains a certain simplification if one introduces the interconnecting relation

$$\{x|y\} = \langle y|x \rangle^*. \quad (4.17)$$

which means that one can now work with a single binary product, say $\langle y|x \rangle$. In such a case, one has in particular for the matrix $\mathbf{D} = \{\tilde{\mathbf{X}}|\mathbf{Y}\}$, that $D_{lk} = \{X_l|Y_k\} = \langle Y_k|X_l \rangle^*$, $(\mathbf{D}^\dagger)_{kl} = D_{lk}^* = \langle Y_k|X_l \rangle$, which gives $\mathbf{D}^\dagger = \langle \tilde{\mathbf{Y}}|\mathbf{X} \rangle = \Delta$ and $\mathbf{D} = \Delta^\dagger$. The relation (4.14) will now take the form $\mathbf{R}^\dagger = |\mathbf{Y}_r\rangle \mathbf{R}^\dagger \mathbf{D}^\dagger \langle \tilde{\mathbf{Y}}_r| = |\mathbf{Y}_r\rangle \mathbf{R}^\dagger \mathbf{D}^\dagger \langle (\Delta^*)^{-1} \tilde{\mathbf{Y}}| = |\mathbf{Y}_r\rangle \mathbf{R}^\dagger \Delta \Delta^{-1} \langle \tilde{\mathbf{Y}}| = |\mathbf{Y}_r\rangle \mathbf{R}^\dagger \langle \tilde{\mathbf{Y}}|$. Instead of (4.14) and (4.15), one will now get the simpler relations

$$\mathbf{R}^\dagger = |\mathbf{Y}_r\rangle \mathbf{R}^\dagger \langle \tilde{\mathbf{Y}}|, \quad \mathbf{S}^\dagger = |\mathbf{X}_r\rangle \mathbf{S}^\dagger \Delta^\dagger \langle \tilde{\mathbf{X}}|. \quad (4.18)$$

All these definitions will reduce to the standard definitions in the case when A and B are subspaces of a bigger linear space C having a binary product with hermitean symmetry, so that $\{x|y\} = \{y|x\}^* = \langle y|x \rangle^* = \langle x|y \rangle$. In this case, the two binary products are identical, and some further simplifications are possible.

In some previous papers [3], the author has investigated the properties of pairs of adjoint operators T and T^\dagger in general, and the present paper may be considered as an extension of these studies. In the Uppsala group, there has also been a considerable interest in the properties of non-self-adjoint operators in connection with the method of complex scaling [4] with results which may be considered as illustrations of the more general theorems treated here.

Acknowledgment. - The author is indebted to Dr. Piotr Froelich and Dr. Erkki Brändas in the Uppsala group for some valuable discussions about linear functionals and the meaning of adjoint operators.

References:

1. See e.g. T. Kato, *Perturbation of Linear Operators*, (Springer Verlag, Berlin 1966); M. Read and B. Simon, *Methods of Modern Mathematical Physics*, (Academic Press, New York 1972).
2. See e.g. F. Riesz and B. Sz-Nagy, *Functional Analysis* (F. Ungar Publ.Co. New York, 1955); N.I. Akhiezer and I.M. Glazman, *Theory of Linear Operators in Hilbert Space*, vols. I and II (F. Ungar, New York 1961); M.A. Naimark, *Linear Differential Operators*, vols. I and II, (F. Ungar, London, 1967 and 1968); W. Rudin, *Real and Complex Analysis*, (McGraw Hill, New York 1987); N. Young, *An Introduction to Hilbert Space*, (Cambridge Univ. Press 1988).
3. P.-O.Löwdin, *Set Theory and Linear Algebra - Some Mathematical Tools to be Used in Quantum Theory*, Part I (Florida TN 490).; *Binary Product Spaces, and Their Operators*, Part II (Florida TN 491). *J. Math. Phys.* **24**, 70 (1983).
4. E. Brändas and P. Froelich, *Phys. Rev. A* **16**, 2207 (1977); P. Froelich, *J. Math. Phys.* **24**, 2762 (1983); P. Proelich and E. Brändas, *Int. J. Quantum Chem. S* **17**, 113 (1983); P.O. Löwdin, *Adv. in Quantum Chem.* **19**, 87 (Academic Press, New York 1987); P.Froelich, M. Mishra, and P.-O.Löwdin, *Int. J. Quantum Chem.* **36**, 93 (1989) ; *Adv. Quantum Chem.* **20**, 185 (Academic Press, San Diego 1989).

This Page Intentionally Left Blank

Index

A

- ABC theorem, description of complex scaling of Hamiltonian, 228–229
- Ab initio* calculations
 - in electron density fragmentation studies, 194–195
 - H₂CN and H₂CO⁺, 320
- Absorption bands, low-lying, ozone, triplet state role, 103–104
- Acetylene radical cation, proton hyperfine coupling constant, 350, 352
- Allyl radical
 - freeon Heisenberg superexchange Hamiltonian, 20
 - interpolated spectrum, 18
 - negative spin density, 22–23
 - spin-arrow diagram, 20
 - spin polarization, 21–22
 - spin superexchange Hamiltonian, 21
 - three-electron spaces, 18
 - valence bond structure, 19–20
- Ammonia radical cation, proton hyperfine coupling constant, 349, 351
- Aromatic compounds, phosphorescence, 129–130
- Atomic structure
 - application of freeon theory, 54–60
 - isomorphism with nuclear structure, 60–61
- Auger resonance
 - analysis with dilated electron propagator technique, 265
 - Be⁺ (1s⁻¹) ²S, energy and width, 260–263
 - equations, 225, 260
 - role of consistent decouplings, 263–266

- Auger satellites, numerical considerations, 266
- Azabenzenes, phosphorescence, 143–146
- Azanaphthalenes, phosphorescence, 146–148

B

- Baryons, quark structure, 65
- Basis sets
 - for DFT–ESR calculations
 - auxiliary set, 344
 - IGLO family, 340–344
 - Slater-type orbitals, 344
 - TZP set, 342
 - van Duijneveldt series, 342–343
- X**, linear transformations, in linear functionals, 378–379
- Benzene
 - phosphorescence
 - associated problem, 130–134
 - comparison with naphthalene and polyenes, 141–142
 - vibronic structure in response formalism, 134–140
 - role in development of freeon dynamics, 23–25
- Beryllium
 - e-Be ²P shape resonance, 244–246
 - shape resonance, analysis, 268–271
- Biorthogonality theorem, in linear functionals, 377–378
- Bipolarons
 - chemical structure, 46–48
 - wavefunction, amplitude effect on vibronic interaction, 52–53

- Boron, A_{iso} , effect of excitation classes, 301–308
- Butadiene, singlet–triplet transitions, 125–128

C

- Calcium
 - e-Ca ^2P shape resonance, 249–251
 - shape resonance, analysis, 274–276
- Cameron band system, CO singlet–triplet transitions, 116–122
- Carbon, A_{iso} , effect of excitation classes, 301–308
- Carbon monoxide
 - Cameron band system, 116–122
 - CO^{2+} , application of MCS equations, 96–98
 - e-CO, resonant Feynman–Dyson amplitude, 282–283
 - $^2\Pi$ e-CO, shape resonances, e-molecule scattering, 256–258
- Chemical bonds, as density domain relation
 - global density range, 184–185
 - localized density range, 184
 - properties, 181–183
- Condensation, 2D representation, in Ising small-bipolaron model, 43–44
- Conductivity, perfect
 - observations, 35–36
 - theory, 36–37
- Configuration interaction methods, in calculation of A_{iso}
 - effect of excitation classes, 301–308
- MRD-CI/ B_K method
 - isoelectronic molecules, 329–332
 - methine, 310–319
 - predictive abilities, 321–329
 - steps in calculation, 318–319
 - theory, 308–310
 - treatment, 300–301
- Conformation, approximate optimization from fragment models, 215–216
- Correlation, role in atomic shape resonances, 251–252
- Crystal field states, Gel'fand state correlation, 55–57
- Crystal structure, cuprate superconductors, 39–41
- Cuprate superconductors
 - bipolaron–lattice–parameter model, 50
 - crystal structure, 39–41
 - doping, 48–49

- freeon Gel'fand states, 47–48
- Ising small-bipolaron theory, 39
- phase diagram, 41
- site orbital space, 46–47
- two-electron space, 47

D

- Decouplings
 - consistent, role in Auger resonances, 263–266
 - dilated electron propagator, resonance orbital pictures, 266–267
- Density domain
 - chemical bond as
 - global density range, 184–185
 - localized density range, 184
 - properties, 181–183
 - in definition of functional groups, 178–180, 186–188
 - in local molecular property analysis, 178–180
 - MEDLA fragment selection based on, 195
- Density functional theory–electron spin resonance calculations
 - basis sets
 - atomic hyperfine coupling constants, 340–342
 - auxiliary set, 344
 - common approximation, 339–340
 - IGLO family, 340–344
 - Slater-type orbitals, 344
 - TZP set, 342
 - van Duijneveldt series, 342–343
 - heteroatom hyperfine coupling constants, 354–358
 - proton hyperfine coupling constants
 - acetylene radical anion, 350, 352
 - ammonia radical cation, 349, 351
 - 1,2-diphenylcyclopentene radical anion, 353–354
 - methane radical cation, 349, 351
 - methyl radical, 349, 351
 - vinylidene radical anion, 350, 352
 - radical hyperfine structure
 - H_2CN and H_2CO^+ , 344–348
 - theory, 333
 - role of gradient corrections, 333–339
- DFT–ESR, *see* Density functional theory–electron spin resonance calculations
- Dimension expansion–reduction method, for fuzzy electron density fragments, 199–201

1,2-Diphenylcyclopentene radical anion, proton
hyperfine coupling constant, 353–354

Doping

cuprate superconductors, 48–49
dependence of J_{BH} and T_C , 51

Dual space

A^d , mapping on linear space, 389–393
 A^d , mapping on original space A
binary product
with hermitean symmetry, 388–389
with linear and antilinear position,
385–388
in space $A = \{x\}$ with linear positions,
381–384
mapping concepts, 379–380
symmetric binary product, 384–385
via vector representation, 380–381

E

e-Atom scattering, shape resonances

e-Be 2P , 244–246

e-Ca 2P , 249–251

e-Mg 2P , 247–249

theory, 243–244

Eigenvalues

linear response, in response function theory,
80–84

for operators in linear functionals, 377–378

Electron affinity, calculation, 225–226

Electron density

fragmentation studies with *ab initio* calculations, 194–195

functional groups, direct computation with
MEDLA method, 192–195

fuzzy fragments

additivity, 175–178

in construction of molecular electron densities, 192

linear homotopies, 196–199

nonlinear transformations

by dimension expansion–reduction
method, 199–201

by weighted affine transformation
method, 201–206

molecular

construction with additive fuzzy electron
density fragmentation, 192

functional groups as fuzzy subsets,
188–191

fuzzy set formalism, 169–171

pseudo-density complement scheme, 174

pseudo-density scheme, 173–174

threshold value, late–early rule, 185–186

Electronic structure, polyenes, 10

Electron propagator

for analysis of resonances in electron scattering,
286–288

dilated

in analysis of Auger resonance, 265

based on real SCF, 238–239

biorthogonal, equations, 235–238

decouplings, resonance orbital pictures,
266–267

equations, 231–235

molecular resonances, 242–243

pole structure, 240–242

with Siegert boundary condition, 239

one-electron, ionization energy and electron
affinity from, 225–226

Electrons

in freeon dynamics, 4–5

two, irreducible representation spaces for, 11

Electron scattering, resonances, analysis,

286–288; *see also* e-Atom scattering;

e-Molecule scattering

Electron spectroscopy, spin-orbital coupling-

based interpretations, 74–76

e-Molecule scattering, shape resonances

$^2B_{2g}$ e-C₂H₄, 258–259

calculation, 252

$^2\Pi$ e-CO, 256–258

$^2\Pi_g$ e-N₂, 253–255

theory, 243–244

Energy

Be⁺ (1s⁻¹) 2S Auger resonance, 260–263

fragment interaction, theory, 214–215

ionization, calculation, 225–226

total, contribution of second order spin-orbit
coupling, 91–92

Ethylene

$^2B_{2g}$ e-C₂H₄, shape resonance, e-molecule
scattering, 258–259

e-C₂H₂, resonant Feynman–Dyson amplitude,
284–285

interpolated spectrum, 12–14

π theory, 11–17

singlet–triplet transitions, 124–125

spin-arrow diagrams, 16

valence bond structure, 14–15

Excitation class, effect on A_{iso} , 301–308

Excited states, perturbation theory formulation,
76–77

F

- Ferromagnetism, freeon theory
 - critique, 53–54
 - uniform interaction model, 32–34
- Feynman–Dyson amplitudes
 - in analysis of shape resonances
 - e-Be, 268–271
 - e-Ca, 274–276
 - e-C₂H₂, 284–285
 - e-CO, 282–283
 - e-Mg, 272–274
 - e-N₂, 278–282
 - as correlated orbital, 267–268
- Formaldehyde, ³A' → ¹A' emission, 106–107
- Formaldehyde radical cation, isotropic hyperfine coupling constant
 - configuration interaction method, 319–329
 - DFT–ESR calculation, 344–348
- Fragmentation
 - electron density, *ab initio* calculations, 194–195
 - fuzzy electron density
 - additivity, 175–178
 - in construction of molecular electron densities, 192
- Freeon dynamics
 - development, role of benzene, 23–25
 - Hückel–Hubbard Hamiltonian, 11
 - nuclear freeon dynamics, 67
 - polyenes, 10
 - properties, 4–5
 - unitary group formulation, 7–8
- Freeon theory
 - application to atomic structure, 54–60
 - ferromagnetism
 - critique, 53–54
 - uniform interaction model, 32–34
- Freeon waves
 - spectral theory, 29–30
 - spin paradigm, 30
- Functional groups
 - density domain definition, 178–180, 186–188
 - electron densities, direct computation with MEDLA method, 192–195
 - energy relations and interactions, 214–216
 - as fuzzy subsets of molecular electron density, 188–191
 - interacting, local shapes, 208–210
 - local shape complementarity measures for, 212–214
 - as MEDLA superfragments, 196

- noninteracting, local shapes, 207–208
- quantum chemical description, 165–167
- semiclassical model, 167–168
- shape similarity measures based on local shapes, 210–211

G

- Gel'fand states
 - (1s)^A isofreeon states, 61–62
 - correlation, crystal field states, 55–57
- ethylene
 - freeon atomic-orbital states, 12
 - freeon molecular-orbital freeon states, 12
- flavor, construction, 65–66
- freeon, cuprate superconductors, 47–48
- isospin paradigm, 62–63
- polyenes, 10
- Gradient corrections, role in DFT–ESR calculations
 - gradient expansion approximation, 334–335
 - for isotropic hyperfine coupling constants, 337–339
 - local density approximation, 333–339
 - random phase approximation, 334
- Gradient expansion approximation, for gradient corrections, 334–335
- Group theory
 - in d^N spectral analysis, 60
 - history of universe based on, 67–69
 - in p^N spectral analysis, 58–59

H

- Hamiltonian
 - complex-scaled, description by ABC theorem, 228–229
 - dilated atomic, bivariational SCF equations for, 229–231
 - group-theoretical, for atomic spectra, 57–58
- Heisenberg exchange
 - freeon antiferromagnetic, from Hückel–Hubbard Hamiltonian, 15–16
 - second-order perturbation theory, 27–28
 - theory, 25–27
- Heisenberg freeon
 - conversion to spin Heisenberg Hamiltonian, 28–29
 - derivation, 28
- Heisenberg superexchange, freeon, for allyl radical, 20

Hückel–Hubbard
 in calculation of ethylene spectrum, 12–14
 to freeon antiferromagnetic Heisenberg exchange Hamiltonian, 15–16
 freeon dynamics, 11
 negative-Hubbard Hückel–Hubbard, spectrum, 42–43
 spin exchange, from freeon antiferromagnetic Heisenberg Hamiltonian, 17
 spin Heisenberg, from freeon Heisenberg Hamiltonian, 28–29
 spin superexchange, allyl radical, 21
 Heavy atom, external, effect on singlet–triplet transitions, 148–152
 Heitler–London rule, in relation to spin paradigm, 17
 Hermitean symmetry, binary product with, 388–389
 Heteroatoms, hyperfine coupling constants, DFT–ESR calculations, 354–358
 Heterocycles, nitrogen-substituted, phosphorescence, 142–143
 Hexatriene, singlet–triplet transitions, 128
 Holes
 chemical structure, 46–48
 wavefunction, amplitude effect on vibronic interaction, 52–53
 Homotopy, linear, fuzzy electron density fragments, 196–199
 Hund's rule, in relation to spin paradigm, 17
 Hydrocarbons, conjugated, singlet–triplet transitions, 124
 Hyperfine coupling constants
 atomic, calculation with DFT–ESR/IGLO method, 340–342
 DFT–ESR calculations
 heteroatoms, 355–358
 NO radical, 354
 isotropic, *see* Isotropic hyperfine coupling constants
 proton, *see* Proton hyperfine coupling constants
 Hyperfine structure
 isoelectronic molecules, 329–332
 radical
 density functional calculations, 333
 theory, 298–299

I

Irreducible representation space, for two electrons, 11

Ising small-bipolaron theory, cuprate superconductors, 39
 Isodensity contours
 fragment, functional groups and molecular fragments, 168
 molecular, bodies, 167–168
 Isospin paradigm, Gel'fand states, 62–63
 Isotropic hyperfine coupling constants
 calculation with configuration interactions
 approaches, 300–301
 effect of excitation classes, 301–308
 equation, 298–299
 H_2CN and H_2CO^+ , 319–329
 methine, 310–319
 oxygen, 318–319
 DFT–ESR calculations, H_2CN and H_2CO^+ , 344–348
 gradient correction, 337–339

J

Jablonski diagram, singlet–triplet transitions, 104–106

L

Late–early rule, in electron density threshold value, 185–186
 Linear functionals
 biorthogonality theorem associations, 377–378
 ket-bra operator, 376–377
 linear transformations of basis \mathbf{X} , 378–379
 matrix representation of operators, 375–376
 properties, 372–373
 vector representations, 373–375
 Local density approximation, for DFT–ESR gradient corrections, 333–339
 Local shape
 changes, induction by molecular environment, 206
 complementarity measures for functional groups, 212–214
 interacting functional groups, 208–210
 noninteracting functional groups, 207–208
 in shape similarity measures of functional groups, 210–211
 Lowest unoccupied molecular orbital, as resonant orbital, 277–278
 LUMO, *see* Lowest unoccupied molecular orbital

M

Magnesium

- e-Mg ^2P shape resonance, 247–249
- shape resonance, analysis, 272–274

Mapping

- dual space A^d on linear space, 389–393
- dual space A^d on original space A
 - binary product
 - with hermitean symmetry, 388–389
 - with linear and antilinear position, 385–388
 - in space $A = \{x\}$ with linear positions, 381–384
 - mapping concepts, 379–380
 - symmetric binary product, 384–385
 - via vector representation, 380–381
- space $A = \{x\}$ on space $B = \{y\}$, 393–396

Matrices

- fragment density, 175–178
- pseudo-density, for analysis of electron density, 173–174
- representation of operators, in linear functionals, 375–376

MCS equations, *see* Multichannel Schrödinger equation

Mean-field theory

- description of superconductivity, 35
- Ising small-bipolaron model
 - ISB derivation, 44–46
 - 2D representation of condensation, 43–44
- second-order phase change, 30–31

MEDLA, *see* Molecular electron density lego assembler method

Meissner effect, in superconductivity, 37–39

Methane radical cation, proton hyperfine coupling constant, 349, 351

Methine, isotropic hyperfine coupling constant, 310–319

Methylene imino radical, isotropic hyperfine coupling constant

- configuration interaction calculation, 319–329

DFT–ESR calculation, 344–348

Methyl radical, proton hyperfine coupling constant, 349, 351

Models

- bipolaron–lattice–parameter, cuprate superconductors, 50
- fragment, approximate conformation optimization from, 215–216
- fuzzy set
 - for local molecular properties, 191

- for molecular electronic density, 169–171
- Ising small-bipolaron, mean-field theory derivation, 44–46
 - 2D representation of condensation, 43–44
- uniform interaction, for ferromagnetism, 32–34

Molecular body

- local properties, density domain analysis, 178–180
- quantum chemical representation, 171–173
- semiclassical model, 167–168
- subdivision with fragmentation schemes, 171–173

Molecular electron density lego assembler method

- for computation of electron densities of functional groups, 192–195
- database, linear homotopies of fuzzy electron density fragments, 196–199
- fragment selection, based on density domains, 195
- superfragments, functional groups as, 196
- and weighted affine transformations, 205–206

Molecules

- diatomic, singlet–triplet transitions, 107–110, 122–123
 - electronic density, fuzzy set formalism, 169–171
 - environment, induction of local shape changes, 206
 - free, optical and ultraviolet spectra, 101–104
 - global environment, local molecular fragments in, 206
 - isoelectronic, hyperfine structure, 329–332
 - local fragments, in global molecular environment, 206
 - properties
 - calculation, 80–84
 - local, fuzzy set model, 191
 - resonances
 - for dilated electron propagator, 242–243
 - LUMO as resonant orbital for, 277–278
 - spin-orbit coupling, response theory and calculations, 71
- Multichannel Schrödinger equation, application to CO^{2+} , 96–98

N

Naphthalene, phosphorescence, 140–142

Nitric oxide radical, hyperfine coupling constant, 354

Nitrogen

- A_{iso} , effect of excitation classes, 301–308
- $B^3\Sigma_u^- \leftarrow X^1\Sigma_g^+$ Ogawa–Tanaka–Wilkinson system, 114
- $C^3\Pi_u \leftarrow X^1\Sigma_g^+$ Tanaka system, 114–116
- e- N_2 , Feynman–Dyson amplitude, 278–282
- $^2\Pi_g$ e- N_2 , shape resonance, e-molecule scattering, 253–255
- Vegard–Kaplan system, 110–113
- $W^3\Delta_u \leftarrow X^1\Sigma_g^+$ Saum–Benesch system, 113–114
- Nuclear structure, isomorphism with atomic structure, 60–61
- Nuclei, light
 - $j = 3/2$ configurations, 64
 - (j)^A configurations, 63–64

O

- Ogawa–Tanaka–Wilkinson system,
 - $B^3\Sigma_u^- \leftarrow X^1\Sigma_g^+$, N_2 , 114
- Operators, in linear functionals
 - ket-bra operator, 376–377
 - matrix representation operator, 375–376
 - T and T^d operator, eigenvalue problems, 377–378
- Orbitals, correlated, Feynman–Dyson amplitude, 267–268
- Original space A, dual space A^d mapping on binary product
 - with hermitean symmetry, 388–389
 - with linear and antilinear position, 385–388
 - in space A = {x} with linear positions, 381–384
 - mapping concepts, 379–380
 - symmetric binary product, 384–385
 - via vector representation, 380–381
- Outer valence Green's function, for electron propagator calculations, 237
- Oxirane, application of spin-orbit response method, 99–101
- Oxygen, hyperfine coupling constant, 318–319
- Ozone, low-lying absorption bands, triplet state role, 103–104

P

- Periodic table, atomic theoretical explanation, 54–55
- Perturbation theory
 - in calculation of physical and chemical prop-

- erties
 - response functions, 77
 - summation over excited states, 76–77
- second-order, in Heisenberg exchange Hamiltonian, 27–28
- Phase change, second-order, mean-field theory, 30–31
- Phase diagram, cuprate superconductors, 41
- Phosphorescence
 - aromatic compounds, 129–130
 - azabenzenes, 143–146
 - azanaphthalenes, 146–148
 - benzene
 - associated problem, 130–134
 - vibronic structure in response formalism, 134–140
 - naphthalene, 140–142
 - nitrogen-substituted heterocycles, 142–143
- Pi theory, ethylene, 11–17
- Polyenes
 - electronic structure and spectra, 10
 - and naphthalene and benzene, phosphorescence, comparison, 141–142
 - singlet–triplet transition intensities, 28–129
- Proton hyperfine coupling constants, DFT–ESR calculations
 - acetylene radical anion, 350, 352
 - ammonia radical cation, 349, 351
 - 1,2-diphenylcyclopentene radical anion, 353–354
 - methane radical cation, 349, 351
 - methyl radical, 349, 351
 - vinylidene radical anion, 350, 352
- Pseudo-density complement, for analysis of electron density, 174

Q

- Quarks, structure of baryons, 65

R

- Radicals, *see also specific radicals*
 - experimental techniques for analysis, 298–299
 - reactions, intersystem crossings, 98–101
- Random phase approximation, for gradient corrections, 334
- Relaxation, role in atomic shape resonances, 251–252

Resonance exchange integral, dependence on doping parameter, 51

Resonances

in electron scattering, analysis, 286–288
molecular, LUMO as resonant orbital for, 277–278

Resonant pole, trajectory method for search, 240–242

Response functions

calculation of molecular properties, 80–84
multiconfiguration formalism, 78–80
perturbation theory formulation, 77–78
spin-orbit
 computation, 86–87
 computational features, 87–89
 in intersystem crossings of radical reactions, 98–101
vibronic structure of benzene phosphorescence, 134–140

Response theory

extended system applications, 154–155
spin catalysis applications, 153–154
spin-orbital coupling calculation, test, 89–91
spin orbitals, 84–86
for spin-orbit interaction in molecules, 71, 74–76

S

Saum–Benesch system, $W^3\Delta_u \leftarrow X^1\Sigma_g^+$, nitrogen, 113–114

SCF, *see* Self-consistent field

Schrödinger equation, theory, 227–228

Self-consistent field

bivariational approximation
 for biorthogonal dilated electron propagator, 235
 equations, for dilated Hamiltonians, 229–231
real SCF, 238–239

Shape, *see* Local shape

Shape resonances

analysis with Feynman–Dyson amplitudes, 267–268
 e-Be, 268–271
 e-Ca, 274–276
 e-Mg, 272–274
atomic, role of correlation and relaxation, 251–252
in e-atom scattering, 243–244
 e-Be 2P , 244–246

 e-Ca 2P , 249–251

 e-Mg 2P , 247–249

in e-molecule scattering, 243–244, 252

$^2B_{2g}$ e-C₂H₄, 258–259

$^2\Pi$ e-CO, 256–258

$^2\Pi_g$ e-N₂, 253–255

orbital picture, 266–267

Siegert boundary condition, electron propagator with, 239

Singlet–triplet transitions

butadiene, 125–128
CO Cameron band system, 116–122
conjugated hydrocarbons, 124
diatomic molecules, 107–110, 122–123
ethylene, 124–125
external heavy atom effect on, 148–152
formaldehyde, 106–107
hexatriene, 128
Jablonski diagram, 104–106
nitrogen

$B'^3\Sigma_u^- \leftarrow X^1\Sigma_g^+$ Ogawa–Tanaka–Wilkinson system, 114

$C^3\Pi_u \leftarrow X^1\Sigma_g^+$ Tanaka system, 114–116

Vegard–Kaplan system, 110–113

$W^3\Delta_u \leftarrow X^1\Sigma_g^+$ Saum–Benesch system, 113–114

polyenes, intensities, 128–129

Space

$A = \{x\}$, mapping on space $B = \{y\}$, 393–396

$B = \{y\}$, space $A = \{x\}$ mapping on, 393–396

dual, *see* Dual space

linear, dual space A^d mapping on, 389–393

original, *see* Original space A

site orbital, cuprate superconductors, 46–47

three-electron, allyl radical, 18

two-electron, cuprate superconductors, 47

Spectra

atomic, group-theoretical Hamiltonian for, 57–58

Auger, intensity rearrangement derivations, 92–94

d^N , group theoretical analysis, 60

electronic, intensity, modulation due to spin-orbit coupling, 92–94

freeon-wave, theory, 29–30

interpolated, ethylene, 12–14

negative-Hubbard Hückel–Hubbard Hamiltonian, 42–43

optical, free molecules, 101–104

p^N , group theoretical analysis, 58–59

polyenes, 10

ultraviolet, free molecules, 101–104

Spin-arrow diagrams
 allyl radical, 20
 ethylene, 16

Spin catalysis, application of response theory, 153–154

Spin configurations, light nuclei
 $j = 3/2$ configurations, 64
 $(j)^A$ configurations, 63–64

Spin density, negative, for allyl radical, 22–23

Spin-orbital coupling
 induced dynamic properties, 94–98
 intensity modulation of electronic spectra, 92–94
 response theory calculation
 in molecules, 71, 74–76
 test, 89–91
 role in experimental interpretation, 74–76
 second order, contribution to total energy, 91–92

Spin orbitals
 in freeon dynamics, 4–5
 response properties, 84–86

Spin paradigm
 features, 9
 from freeon Heisenberg Hamiltonian, 28–29
 freeon waves, 30
 in relation to Hund's rule and Heitler–London rule, 17

Spin polarization, allyl radical, 21–22

Superconductivity
 description by mean-field theory, 35
 Meissner effect, 37–39
 perfect conductivity
 observations, 35–36
 theory, 36–37

Superconductors, *see* Cuprate superconductors

Symmetry–quantization, for group-theoretical Hamiltonian, 57–58

T

Tanaka system, $C^3\Pi_u \leftarrow X^1\Sigma_g^+$, nitrogen, 114–116

Transformations
 linear, basis \mathbf{X} , in linear functionals, 378–379
 nonlinear, fuzzy electron density fragments
 by dimension expansion–reduction method, 199–201
 by weighted affine transformation method, 201–206

Triplet states
 electronic, isoelectronic molecules, 329–332
 ozone, role in low-lying absorption band analysis, 103–104

U

Unitary group, in freeon dynamic formulation, 7–8

Universe, group theoretical history, 67–69

V

Valence bond structure
 allyl radical, 19–20
 ethylene, 14–15

Vector representation
 linear functionals, 373–375
 in mapping dual space A^d on original space A , 380–381

Vegard–Kaplan system, nitrogen, 110–113

Vibronic interaction, effect of wavefunction amplitude, 52–53

Vibronic structure, benzene phosphorescence in response formalism, 134–140

Vinylidene radical anion, proton hyperfine coupling constant, 350, 352

W

Wavefunctions, bipolaron and hole, effect on vibronic interaction, 52–53

Weighted affine transformation method, for fuzzy electron density fragments, 201–206

This Page Intentionally Left Blank